Understanding Complex Systems

Springer : COMPLEXITY

Ekhard K.H. Salje
Avadh Saxena
Antoni Planes *Editors*

Avalanches in Functional Materials and Geophysics

Springer

Springer Complexity

Springer Complexity is an interdisciplinary program publishing the best research and academic-level teaching on both fundamental and applied aspects of complex systems—cutting across all traditional disciplines of the natural and life sciences, engineering, economics, medicine, neuroscience, social and computer science.

Complex Systems are systems that comprise many interacting parts with the ability to generate a new quality of macroscopic collective behavior the manifestations of which are the spontaneous formation of distinctive temporal, spatial or functional structures. Models of such systems can be successfully mapped onto quite diverse "real-life" situations like the climate, the coherent emission of light from lasers, chemical reaction-diffusion systems, biological cellular networks, the dynamics of stock markets and of the internet, earthquake statistics and prediction, freeway traffic, the human brain, or the formation of opinions in social systems, to name just some of the popular applications.

Although their scope and methodologies overlap somewhat, one can distinguish the following main concepts and tools: self-organization, nonlinear dynamics, synergetics, turbulence, dynamical systems, catastrophes, instabilities, stochastic processes, chaos, graphs and networks, cellular automata, adaptive systems, genetic algorithms and computational intelligence.

The three major book publication platforms of the Springer Complexity program are the monograph series "Understanding Complex Systems" focusing on the various applications of complexity, the "Springer Series in Synergetics", which is devoted to the quantitative theoretical and methodological foundations, and the "Springer Briefs in Complexity" which are concise and topical working reports, case studies, surveys, essays and lecture notes of relevance to the field. In addition to the books in these two core series, the program also incorporates individual titles ranging from textbooks to major reference works.

Understanding Complex Systems

Founding Editor: S. Kelso

Future scientific and technological developments in many fields will necessarily depend upon coming to grips with complex systems. Such systems are complex in both their composition – typically many different kinds of components interacting simultaneously and nonlinearly with each other and their environments on multiple levels – and in the rich diversity of behavior of which they are capable.

The Springer Series in Understanding Complex Systems series (UCS) promotes new strategies and paradigms for understanding and realizing applications of complex systems research in a wide variety of fields and endeavors. UCS is explicitly transdisciplinary. It has three main goals: First, to elaborate the concepts, methods and tools of complex systems at all levels of description and in all scientific fields, especially newly emerging areas within the life, social, behavioral, economic, neuro- and cognitive sciences (and derivatives thereof); second, to encourage novel applications of these ideas in various fields of engineering and computation such as robotics, nano-technology, and informatics; third, to provide a single forum within which commonalities and differences in the workings of complex systems may be discerned, hence leading to deeper insight and understanding.

UCS will publish monographs, lecture notes, and selected edited contributions aimed at communicating new findings to a large multidisciplinary audience.

More information about this series at http://www.springer.com/series/5394

Ekhard K.H. Salje · Avadh Saxena
Antoni Planes
Editors

Avalanches in Functional Materials and Geophysics

Springer

Editors
Ekhard K.H. Salje
Department of Earth Sciences
University of Cambridge
Cambridge
UK

Avadh Saxena
Theoretical Division
Los Alamos National Laboratory
Los Alamos
USA

Antoni Planes
Departament de Física de la Matèria Condensada
Universitat de Barcelona
Barcelona, Catalonia
Spain

ISSN 1860-0832 ISSN 1860-0840 (electronic)
Understanding Complex Systems
ISBN 978-3-319-45610-2 ISBN 978-3-319-45612-6 (eBook)
DOI 10.1007/978-3-319-45612-6

Library of Congress Control Number: 2016950384

Printed on acid-free paper

This Springer imprint is published by Springer Nature
The registered company is Springer International Publishing AG
The registered company address is: Gewerbestrasse 11, 6330 Cham, Switzerland

Preface

The topic Avalanches in Functional Materials and Geophysics is a highly researched area of science with significant cross-fertilization between approaches in the two fields. Avalanches occur in many physical systems spanning microscopic to macroscopic length scales. Beyond the usual snow avalanches and seismic activity, acoustic emission measurements identify avalanches during phase transitions, the collapse of porous materials under pressure and many other materials related processes. One of the major objectives of the book is to identify common experimental characterization, theoretical and simulation techniques as well as statistical data analysis, and similar predictive modelling and phenomenology in materials science and geophysics. The book is likely to be broadly accessible and caters to beginning researchers, graduate students as well as experts.

The book contains a dozen chapters, which represent partly a review with a wide perspective and original research aimed at identifying open issues. The first two chapters invoke the statistical mechanics approach to earthquakes and an associated mean-field theory to study avalanches. A series of simple models of earthquake faults is investigated. The role of fault geometry, friction and noise in determining the statistics of earthquakes is explored. The statistics and the dynamics of slip avalanches in slowly deformed solids are reviewed. These results have implications for materials testing, failure prediction, and hazard prevention. The next three chapters address how to mimic earthquakes in a laboratory setting ("labquakes") in porous materials as well as geological aspects such as the role of various rock types in earthquakes. A review of recent acoustic emission experiments during the compression of synthetic porous materials under controlled force rates is presented. The statistical analysis of the recorded signals of laboratory experiments allows a comparison with the statistics of earthquakes from available seismic data. Different methods to characterize individual acoustic emission avalanches and their time correlations are discussed. The results indicate that the failure dynamics of materials can be studied by measuring strain drops under slow compression, opening the possibility to study earthquake dynamics in the laboratory at non-ambient conditions.

Similarly, in rock physics sudden changes in internal stress associated with microscopically brittle rupture events lead to acoustic emissions that can be recorded on the sample boundary, and used to infer the state of internal damage. Crackling noise is inherently stochastic, but the population of events often exhibits remarkably robust scaling properties, in terms of the source area, duration, energy, and in the waiting time between events. Despite the stationary strain rate and the lack of any time-dependent weakening processes, the results are all characterized by emergent power law distributions over a broad range of scales, in agreement with experimental observation. As deformation evolves, the scaling exponents change systematically in a way that is similar to the evolution of damage in experiments on real sedimentary rocks. The potential for real-time forecasting of catastrophic failure obeying such scaling rules is then examined by using synthetic and real data tests, e.g. prior to volcanic eruptions.

Chapters 6–9 deal with avalanches in structural phase transitions, particularly in martensites, and more generally both the experimental and the simulation studies of pinning and avalanches in ferroelastics—materials in which strain serves as the order parameter for phase transitions. Solids subject to continuous changes of temperature or mechanical load often exhibit discontinuous avalanche-like responses, e.g. avalanche dynamics have been observed during plastic deformation, fracture, domain switching in ferroic materials or martensitic transformations. The statistical analysis of avalanches reveals a very complex scenario with a distinctive lack of characteristic scales. Efforts to understand the characteristics of avalanches in martensites through mathematical modelling are reviewed. Analogously, nano-scale multiferroics often display sudden, jerky domain movements under weak external fields. These domain movements include retracting twin domains, kinks in domain walls, jamming between walls and changes in complex tweed patterns. It is shown that the probability density function of the jerk distribution follows power law statistics at sufficiently low temperatures and thermally activated jumps at high temperatures, which explains the mixing of thermal and athermal events during acoustic emission.

Time-lapse optical microscopy of certain ferroelastic single crystals allows the propagation and retraction of individual needle domains to be observed under conditions of slowly varying shear stress. Optical observation and thermodynamic analysis show that the continuous behaviour is thermally activated. The avalanches follow power law behaviour in agreement with self-similar avalanches close to the depinning threshold. Singularities of the characteristic (Larkin) length occur when the front line breaks. Three physical systems are discussed in which the distributions of certain variables are centred around a most probable value. Each microstructural-related event proceeds through a multitude of smaller mesoscopic events that span several orders of magnitude. Statistical analyses of other variables, associated with the mesoscopic events, follow a scale-invariant power law distribution. The origins for the co-existence of events at different scales and their different statistical distributions are discussed for the physical characteristics of the explored systems.

Chapter 10 studies avalanches in metallic glasses whereas Chap. 11 deals with yield and irreversibility in amorphous solids. The atomistic mechanism of deformation in metallic liquids and glasses is discussed in view of the local topology of atomic connectivity. In crystals the topology of atomic connectivity network is fixed, and deviation from it defines lattice defects. In liquids and glasses, however, the topology is open and flexible, and fluctuates in time and space. Collective phenomena, including shear-transformation-zones and their avalanche, govern the macroscopic deformation in supercooled liquids and glasses. The description of the structure and dynamics of liquids and glasses through local topology is likely to advance the field. Similarly, a fundamental problem in the physics of amorphous materials is understanding the transition from reversible to irreversible plastic behaviour and its connection to the concept of yield. Under periodic shear, amorphous solids undergo a transition from deterministic, periodic behaviour to chaotic, diffusive behaviour as a function of strain. It has been related to a depinning-like transition in which cooperative avalanche events span the system. An overview of recent work focused on the nature of yield in amorphous systems from a cooperative and dynamical point of view is presented.

Finally, Chap. 12 describes avalanches in the context of fluid imbibition. In particular, the invasion of an open fracture by a viscous wetting fluid is reviewed in the context of research on the spatiotemporal dynamics of fronts in disordered media. Competition of forces at different length scales leads to an initially flat front undergoing a kinetic roughening process, leading to a statistically stationary state characterized by critical interfacial fluctuations and a collective avalanche dynamics. A scale-dependent statistical analysis of the temporal behaviour of the spatially averaged velocity of the front reveals the presence of non-Gaussian fluctuations, strongly intermittent dynamics and global avalanches.

These 12 chapters discuss a multitude of open questions and set the stage for future research in this highly multidisciplinary field. They also provide a much needed integration between two broad subject areas, materials and geophysics, which is expected to usher into further insights and a better understanding of avalanches. However, much remains to be improved such as the detailed analysis of avalanche processes. Besides seasoned researchers the book will also serve as a valuable resource for graduate students in materials science and engineering, condensed matter physics, geophysics and other related disciplines.

Cambridge, UK — Ekhard K.H. Salje
Los Alamos, USA — Avadh Saxena
Catalonia, Spain — Antoni Planes

Contents

Contributors

Jordi Baró Departament de Física de la Matèria Condensada, Universitat de Barcelona, Barcelona, Spain; University of Calgary, Calgary, AB, Canada

Andrew F. Bell School of Geoscience, Grant Institute, University of Edinburgh, Edinburgh, UK

Karin A. Dahmen Department of Physics, University of Illinois at Urbana-Champaign, Urbana, IL, USA

Xiandong Ding State Key Laboratory for Mechanical Behavior of Materials, Xi'an Jiaotong University, Xi'an, People's Republic of China

T. Egami Joint Institute for Neutron Sciences and Department of Materials Science and Engineering, University of Tennessee, Knoxville, TN, USA; Department of Physics and Astronomy, University of Tennessee, Knoxville, TN, USA; Oak Ridge National Laboratory, Oak Ridge, TN, USA

Y. Fan Oak Ridge National Laboratory, Oak Ridge, TN, USA

Eilon Faran Faculty of Mechanical Engineering, Technion, Haifa, Israel

Harvey Gould Department of Physics, Boston University, Massachusetts, USA; Department of Physics, Clark University, Massachusetts, USA

Tyler Gu Department of Physics, Boston University, Massachusetts, USA

R.J. Harrison Department of Earth Sciences, University of Cambridge, Cambridge, UK

T. Iwashita Joint Institute for Neutron Sciences and Department of Materials Science and Engineering, University of Tennessee, Knoxville, TN, USA

Javad Kazemian Western University, London, ON, Canada; University of Tehran, Tehran, Iran

W. Klein Department of Physics, Boston University, Massachusetts, USA

Ferenc Kun Department of Theoretical Physics, University of Debrecen, Debrecen, Hungary

Turab Lookman Center for Nonlinear Studies and Theoretical Division, Los Alamos National Laboratory, Los Alamos, NM, USA

Ian G. Main School of Geoscience, Grant Institute, University of Edinburgh, Edinburgh, UK

Jordi Ortín Dept. de Física de la Matèria Condensada, and University of Barcelona Institute of Complex Systems (UBICS), Facultat de Física, Universitat de Barcelona, Barcelona, Catalonia, Spain

Francisco J. Perez-Reche Institute for Complex Systems and Mathematical Biology, SUPA, University of Aberdeen, Aberdeen, UK

Antoni Planes Departament de Física de la Matèria Condensada, Universitat de Barcelona, Barcelona, Catalonia, Spain

Sabine Puchberger Faculty of Physics, University of Vienna, Wien, Austria

Ido Regev Jacob Blaustein Institutes for Desert Research, Ben-Gurion University of the Negev, Beersheba, Israel

J.B. Rundle Department of Physics, University of California Davis, Davis, CA, USA

Ekhard K.H. Salje Department of Earth Sciences, University of Cambridge, Cambridge, UK

Stéphane Santucci Laboratoire de Physique, CNRS UMR 5672, École Normale Supérieure de Lyon, Lyon Cedex 07, France

Wilfried Schranz Faculty of Physics, University of Vienna, Wien, Austria

C. Serino Department of Physics, Boston University, Massachusetts, USA; MIT Lincoln Laboratory, Massachusetts, USA

Doron Shilo Faculty of Mechanical Engineering, Technion, Haifa, Israel

James B. Silva Department of Physics, Boston University, Massachusetts, USA

Viktor Soprunyuk Faculty of Physics, University of Vienna, Wien, Austria

K.F. Tiampo CIRES ESOC and Department of Geological Sciences, University of Colorado at Boulder, Colorado, USA

Andreas Tröster Institute of Material Chemistry, Vienna University of Technology, Wien, Austria

Eduard Vives Facultat de Física, Departament d'Estructura i Constituents de la Matéria, Universitat de Barcelona, Barcelona, Catalonia, Spain

Chapter 1
Statistical Mechanics Perspective on Earthquakes

W. Klein, Harvey Gould, K.F. Tiampo, James B. Silva, Tyler Gu, Javad Kazemian, C. Serino and J.B. Rundle

Abstract We report on theoretical and numerical investigations of a series of simple models of earthquake faults. We find that the range of stress transfer, the nature of the friction force, the magnitude of the noise, and the "fault" geometry all play an important role in determining the statistics of earthquakes. In addition to providing some understanding of the nature of faults and fault systems, these studies raise interesting questions about the nature of equilibrium.

1.1 Introduction

Earthquakes are similar to avalanches in that there is a build up of a "force" which is relieved by a breakdown, or event that can vary in size. In the case of earthquakes the force is the stress, usually caused by tectonic plate motion, and the event or

W. Klein (✉) · H. Gould · J.B. Silva · T. Gu · C. Serino
Department of Physics, Boston University, Boston, Massachusetts 02215, USA
e-mail: klein@bu.edu

H. Gould
Department of Physics, Clark University, Worcester, Massachusetts 01610, USA

K.F. Tiampo
CIRES ESOC and Department of Geological Sciences, University of Colorado at Boulder, Boulder, Colorado 80309, USA

J. Kazemian
Western University, London N6A 3K7, ON, Canada

J. Kazemian
University of Tehran, Amir Abad, Tehran, Iran

C. Serino
MIT Lincoln Laboratory, Boston, Massachusetts 02420, USA

J.B. Rundle
Department of Physics, University of California Davis, Davis 95616, CA, USA

E.K.H. Salje et al. (eds.), *Avalanches in Functional Materials and Geophysics*,
Understanding Complex Systems, DOI 10.1007/978-3-319-45612-6_1

avalanche is an earthquake. One reason that these systems are of considerable interest is that there are aspects of earthquake phenomenology that are suggestive of phase transitions. One such aspect is Gutenberg–Richter scaling in which the number of events with seismic moment magnitude m, n_m, scales as a power law:

$$n_m \sim m^{-b} \tag{1.1}$$

Similar to "avalanches" in other systems the statistical distribution of earthquakes depends not only on an underlying self-organization or "phase transition," but there is also a strong influence of factors such as the roughness of the faults, the noise, the nature of the friction force, and the range of the stress transfer.

Unlike many other systems, the study of earthquakes is hampered by the lack of ability to perform controlled experiments, and the difficulty of observation because what we need to know, such as the structure of the fault, is hidden from view. For these reasons it is useful to study simple models of earthquake faults to understand the relation between the underlying self-organization and other factors, such as those mentioned, associated with structure.

Our approach was motivated by a block and spring model introduced by Burridge and Knopoff (BK) [1]. We will describe this fully dynamic model in detail in Sect. 1.2, as well as the details of the other models we study. Here we simply note that the BK model is computationally intensive and for that reason Rundle and collaborators [2, 3] formulated a cellular automaton (CA) version of the BK model. The Rundle, Jackson, Brown (RJB) model [2, 3] is also a block and spring model. Several years later Olami, Feder, and Christensen (OFC) introduced a lattice CA model [4], which, as we will show, is essentially equivalent to the RJB model, but is easier to simulate and modify to include structure. Although the OFC model is the simplest to simulate, the RJB model is easier to understand theoretically. The BK model can be used to probe the effect of the inertia and friction, which are both absent in the CA models.

In addition to the relation between structural factors and the underlying self-organization, the study of these models has raised important questions about the nature of driven dissipative systems and the nature of equilibrium.

The structure of the remainder of this paper is as follows: In Sect. 1.2 we introduce the BK, RJB and OFC models. In Sect. 1.3 we discuss the relation between the OFC and RJB models and present the results of both simulation and theory for these models where the "fault" is taken to be homogeneous. In Sect. 1.4 we present the results of simulations of the BK model and compare the results to those of the homogeneous RJB and OFC models. In Sect. 1.5 we introduce various forms of structure in the OFC model and discuss the results of simulations and compare them with those obtained from the homogeneous models. In Sect. 1.6 we discuss our results and possible areas of further research.

1.2 Models

1.2.1 Burridge-Knopoff Model

The BK model [1] consists of blocks with mass m connected by Hooke's law springs with spring constant K_C resting on a surface with a velocity dependent friction force. The blocks are also connected to a loader plate, which moves with a constant speed V, via Hooke's law springs with spring constant K_L (see Fig. 1.1). Due to the computational difficulty of this model, it has been simulated in one dimension [1, 5, 6] and two dimensions [7] for only a limited range of parameters. It was found that the nature of the statistical distribution of earthquakes depends on the nature of the friction force [6]. However, the system size was small and the time over which the system was simulated was short. These limitations contributed to the formulation of the RJB CA version of the BK model.

1.2.2 RJB Model

Rundle and collaborators use the same blocks and springs but instead of a friction force the blocks are assigned a failure threshold σ_F and a residual stress σ_R. The blocks are assigned initial positions and the stress (the sum of the forces due to the inter-block springs with spring constant K_C and the loader plate springs with a spring constant K_L) is calculated. If the stress on the ith block has a stress $\sigma_i < \sigma_F$, the block does not move. If the ith block has $\sigma_i \geq \sigma_F$, the block is moved a distance

$$\Delta x = \frac{\sigma_i - \sigma_R}{K_L + qK_C}, \tag{1.2}$$

where z is the number of neighbors of a block. In $d = 1$, $z = 2$. In this way the stress on the ith block is reduced from σ_i to σ_R. In many applications of the model noise is added, so that Δx is given instead by

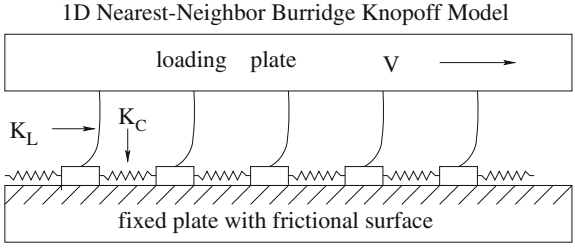

Fig. 1.1 Schematic of the one-dimensional Burridge-Knopoff model

$$\Delta x = \frac{\sigma_i - \sigma_R + \eta}{K_L + qK_C}, \tag{1.3}$$

where η is usually chosen from a flat random distribution. This procedure is followed until there is no block that has $\sigma_i \geq \sigma_F$. The loader plate is then moved until the block with the largest value of the stress is brought to failure. This procedure is referred to as the zero velocity update.

The number of blocks that failed before the loader plate is moved is the size of the "earthquake." The process is then repeated and the number of events that have s failed blocks is counted.

This model has also been studied in dimension $d = 1$, but because it is so much simpler to simulate, a more realistic two-dimensional model can also be studied. In the two-dimensional model the stress on the blocks is always parallel or anti-parallel to the direction that the loader plate moves, so that the springs that are perpendicular to the direction of the loader plate motion are leaf springs (see Fig. 1.2). The original model used only nearest neighbor springs. In real earthquake faults the stress transfer is due to an elastic force which is long range. For this reason we have also simulated the model with long-range springs between blocks. As we will see, the addition of long-range springs changes the model in significant ways. We can also calculate the energy for the system by simply summing up the energy stored in the springs. Obviously for this CA model there is no kinetic energy as there is in the BK model.

Why do the earthquakes stop in this model? To ask this question in another way, what dissipates the stress that is put into the system when the loader plate is moved? To answer this question we first note that if there were no loader plate springs, then a movement of a block would conserve the stress in the system because the springs are linear. Consequently, the stress dissipation comes only from the loader plate spring and the change Δx in the position of the block. Therefore, when a block is moved a distance Δx, the amount of stress dissipated $\Delta\sigma_{\text{diss}} = K_L \Delta x$. Using (1.3) we have that the amount of stress dissipated when a block is moved is given by

$$\Delta\sigma_{\text{diss, RJB}} = K_L \left[\frac{\sigma_i - \sigma_R + \eta}{K_L + qK_C} \right]. \tag{1.4}$$

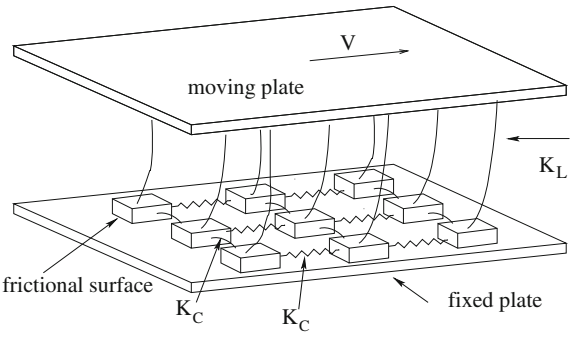

Fig. 1.2 Schematic of the two-dimensional Burridge-Knopoff and Rundle Jackson Brown model model

1.2.3 OFC Model

The OFC model is also a CA model and is, as we will see, almost identical to the RJB model. The OFC model is a lattice model, and we consider only a square lattice. In a way similar to the RJB model we assign a failure threshold σ_F and a residual stress σ_R to each site. Stress is initially distributed at random to each site. The stress on the ith site is checked to see if it is greater than σ_F. If $\sigma_i \geq \sigma_F$, we reduce the stress on the site to σ_R. We then take a fraction α of $\sigma_i - \sigma_R$ and throw it away and transfer $(1 - \alpha)(\sigma_i - \sigma_R)$ to the neighbors. We can transfer the stress to only the four nearest neighbors, or we could use a longer range stress transfer. We normally use a square neighborhood as shown in Fig. 1.3.

As with the RJB model we can add a noise so that the amount of stress dissipated is

$$\Delta\sigma_{\text{diss, OFC}} = \alpha(\sigma_i - \sigma_R + \eta). \tag{1.5}$$

As for the RJB model this process is continued until there are no sites with $\sigma_i \geq \sigma_F$. The site with the largest stress is then located and the amount of stress that brings the stress on that site to σ_F is added to all of sites in the system. This reloading process is also referred to as the zero velocity update. The process described above is then repeated. Similar to the RJB model, the size of the earthquake is the number of sites that failed before the system is reloaded.

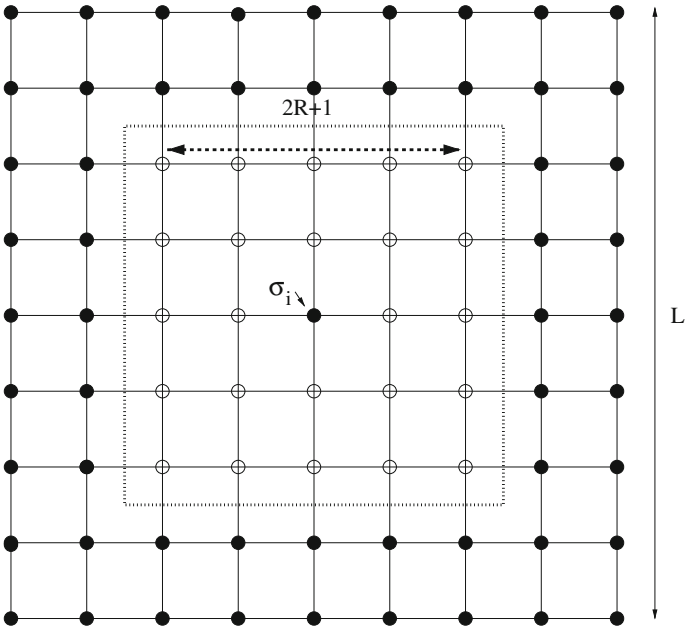

Fig. 1.3 Stress transfer region in the OFC model

1.3 Results for Homogeneous CA Models

In this section we discuss the similarity between the RJB and OFC models and present some results for the models with uniform failure thresholds and residual stress.

1.3.1 Equivalence of RJB and OFC Models

Assume that the initial conditions for the OFC and RJB models are identical and we are using the same random number generator and the same seed for both. In addition, we take both σ_F and σ_R to have the same values in the OFC model as they do in the RJB model. Note that this assumption requires that we have identified each block in the RJB model with a site in the OFC model. Consider first what happens to the stress on a block in the RJB model and a site in the OFC model that are both above the failure threshold. Because their initial stress is the same and the random number generated for the noise is the same, the stress on the two sites after the failure (that is, $\sigma_R + \eta$) will be identical. In the OFC model we now dissipate, or throw away, an amount of stress equal to

$$\alpha(\sigma_i - \sigma_R + \eta). \tag{1.6}$$

In the RJB model the amount of stress dissipated is given by (1.4), which we repeat here for convenience.

$$\Delta\sigma_{\text{diss, RJB}} = K_L\left[\frac{\sigma_i - \sigma_R + \eta}{K_L + q\,K_C}\right].$$

If we set

$$\alpha = \frac{K_L}{K_L + zK_C}, \tag{1.7}$$

then the amount of stress remaining to be transferred to the neighbors is the same for both models. Because we have identified each block in the RJB model with a site in the OFC model, the number of neighbors of each site z is the same for both models so that after the stress is transferred each block and its corresponding site has the same stress. These considerations imply that the stress on each site is identical to that on the corresponding block throughout the failure process. When no site has a stress greater than the failure threshold, the plate in the RJB model is moved so that the site with the largest stress is brought to the failure threshold. The amount of stress added to each site, given by $K_L\Delta x = \sigma_F - \sigma_{\max,i}$, is the same as the stress added in the OFC model. These considerations show that the stress on each block in the RJB model and the stress on the corresponding site in the OFC model are identical throughout out the simulation of the models. Hence, as far as the stress is concerned the models are the same, independent of dimension and stress transfer range.

1.3.2 RJB Model

Because the RJB and OFC models give identical results for the stress, we have performed most of our simulations using the OFC model because it is easier to simulate. However, one difference is that the RJB model has a natural definition of energy, namely, the energy stored in the springs, while there is no natural definition of the energy in the OFC model. The importance of a lack of a definition of energy in the latter is that it has been shown that the driven dissipated RJB model, which is in a steady state after it has been run long enough to eliminate transients, is in thermodynamic equilibrium in the limit that the stress transfer range goes to infinity [8]. To show that the RJB model is in thermodynamic equilibrium and not simply in a steady state, we can plot the ratio of the fraction of systems with energy E for two values of the noise. If the system is in equilibrium, then the probability that the system will have an energy E is proportional to a density of states, which is independent of the temperature, or noise, multiplied by $e^{-\beta E}$. Because the density of states is independent of the noise, a log-linear plot of the ratio of the probabilities versus E should be a straight line, consistent with the Boltzmann distribution. As the figure in [9] shows, this ratio is indeed a straight line.

We have also derived a Langevin equation that describes the evolution of the RJB model in the limit that the stress transfer range goes to infinity. The driving force in the Langevin equation is the functional derivative of an action [10, 11]. As shown in [12], the existence of a driving force guarantees that the system approaches equilibrium in the limit of infinite time.

1.3.3 OFC Model

Because we are interested in what we can learn about earthquake faults from these simple models, we will concentrate on the OFC model with long-range stress transfer. We will present our results for the OFC model with the understanding that all of these results are valid for the RJB model as well.

Although we have no definition of energy for the OFC model. there is a test that we can employ to check for ergodicity, a necessary condition for equilibrium. We will use a metric first proposed by Thirumalai and Mountain [13]. To construct the metric we take the time average of the stress on the ith site

$$\overline{\sigma}_i(t) = \int_0^t dt' \sigma_i(t'), \tag{1.8}$$

and the spatial average of the time average

$$<\overline{\sigma}(t)> = \frac{1}{N} \sum_{i=1}^{N} \overline{\sigma}_i(t), \tag{1.9}$$

where N is the number of sites in the system. The metric is defined as

$$\Omega(t) = \frac{1}{N}\sum_{i=1}^{N}\left[\overline{\sigma}(t) - <\overline{\sigma}(t)>\right]^2. \tag{1.10}$$

Thirumalai and Mountain [13] showed that for the system to be ergodic, a necessary, but not sufficient condition is that the metric $\Omega(t)$ approach zero as $1/t$ [13]. In Fig. 1.4 we plot the inverse of the metric normalized by $\Omega(t=0)$ for $R = 20$. The stress transfer is done within a square block $2R$ on a side so that the number of sites within the stress transfer range is $(2R+1)^2 - 1$. As can be seen the inverse metric is a straight line, which is consistent with the Boltzmann distribution found for the RJB model.

In Fig. 1.5 we plot the number of events (earthquakes) with s failed sites, n_s [14]. If a site fails more than once, we count it only once. However as the range of stress transfer R increases, the number of sites that fail more than once goes to zero as $R \to \infty$. For $R = 20$ the number of sites that fail more than once is exceedingly rare [15]. (Reference [15] considered the RJB model, but the isomorphism guarantees that the same conclusion holds for the OFC model [16]).

The derivation of a Langevin equation description of the RJB model [10, 11] indicates that the scaling of the events is associated with a spinodal. This association leads to an explicit prediction for the scaling exponent in Fig. 1.5. The histogram in Fig. 1.5 can be fit by the function

$$n_s = A\frac{\exp\left[-\Delta h s^{\sigma}\right]}{s^{\tau}}. \tag{1.11}$$

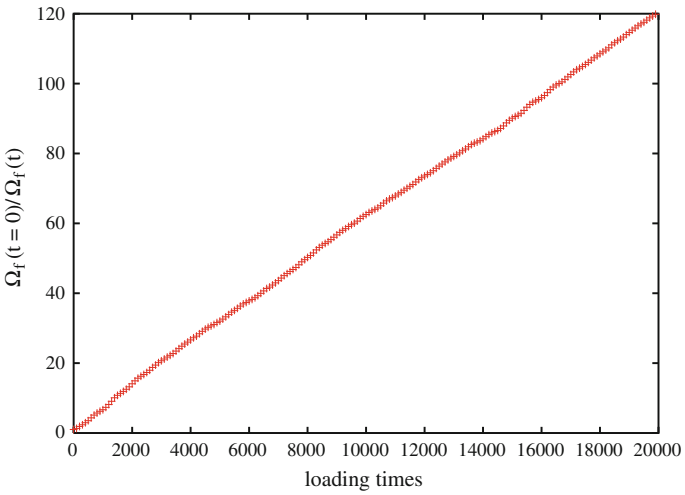

Fig. 1.4 The time-dependence of the inverse metric for the OFC model with $R = 20$

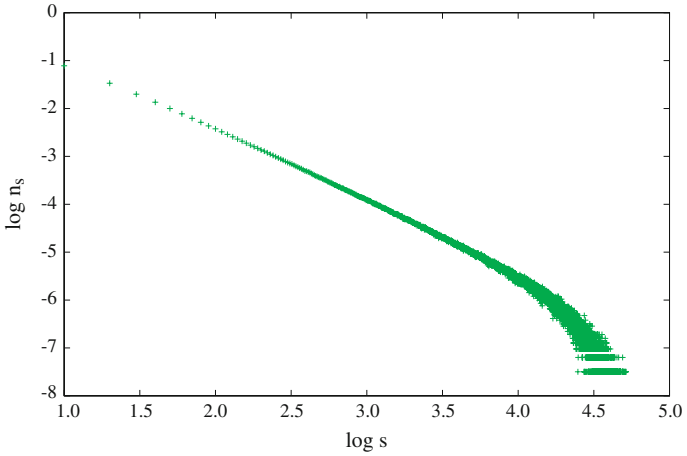

Fig. 1.5 Log-log plot of n_s for $\approx 5 \times 10^7$ events for $R = 30$. The slope is consistent with $\tau = 1.5$

Here A is a constant and Δh is the distance from the spinodal. If there is indeed a spinodal, we must have

$$\int_0^\infty ds\, s^2 n_s = \Delta h^{-\gamma} \tag{1.12}$$

$$\int_0^\infty ds\, s n_s = \Delta h^{\beta}, \tag{1.13}$$

where γ and β are the exponents associated with the susceptibility and the vanishing of the order parameter as the spinodal is approached. Hence, given the mean-field values of γ and β we have

$$\frac{3-\tau}{\sigma} = \frac{1}{2} \text{ and } \frac{\tau - 2}{\sigma} = \frac{1}{2}, \tag{1.14}$$

or $\tau = 5/2$ and $\sigma = 1$. These relations are similar to the mapping of the spinodal onto a percolation problem [17]. Here the clusters are grown from a seed so that the effective τ that we measure is equal to $\tau - 1 = 3/2$ [18] in agreement with simulations of the model.

1.4 Burridge-Knopoff Model

Before we consider the effect of structure, it is important to ask what is the effect of friction and inertia on the CA results we have obtained for systems with long-range stress transfer in the OFC model and long-range springs in the RJB model. To this end

we have simulated the BK model with long-range springs [6]. Our results indicate that the situation is somewhat complicated. We employed a velocity weakened friction force and found that the relation between the CA results and the BK results depend on how fast the friction force decreases with velocity. The decrease was parameterized by the parameter α (not to be confused with the dissipation parameter in the OFC model.) The larger the value of α, the faster the friction force decreases with velocity. For large stress transfer range (range of the springs) and $\alpha \geq 1$, the BK model appears to have the same scaling behavior as the RJB and OFC models. However, for smaller α the relation is more complicated. There is a lack of scaling, and quasi-periodic behavior and mode switching between scaling and periodic behavior appears. It is clear that more work needs to be done in order to understand the relation between the BK and the CA models.

1.5 CA Models with Structure

1.5.1 Role of Dissipation via Microcracks

We investigated the behavior of the CA models vary when we include structure. The first of the two variations that we have studied is the inclusion of different levels of fracture or microcracks in the fault. To mimic the effect of this structure we removed a fraction q of the sites from the OFC model. When stress is transferred to an empty site, it is simply dissipated as it would be with microcracks. If we were to run the model with every site in the stress transfer range of every other site, that is, a fully connected model, this removal would simply be equivalent to increasing the dissipation parameter α [14]. For a finite but long-range system it is somewhat more complicated. However, we find that the larger the value of q, the further the system is from the spinodal critical point mentioned above (see Fig. 1.6).

We can fit these curves by

$$n_s = \frac{1}{1-q}\frac{\exp[-q^2 s]}{s^{3/2}}. \tag{1.15}$$

What is more interesting about this approach is that it allows us to understand how it is possible to have fault systems that satisfy Guttenberg–Richter scaling, even though most of their individual faults exhibit very poor Gutenberg–Richter scaling, and how fault systems in different parts of the world can have Gutenberg–Richter scaling with different exponents (b values). From Fig. 1.6, we see that the smaller the value of q, the better the fit to Gutenberg–Richter scaling and a critical point picture. However, in a fault system there will be faults with different values of q. To obtain a Gutenberg–Richter distribution we need to integrate over different values of q. That is, for a fault system we have

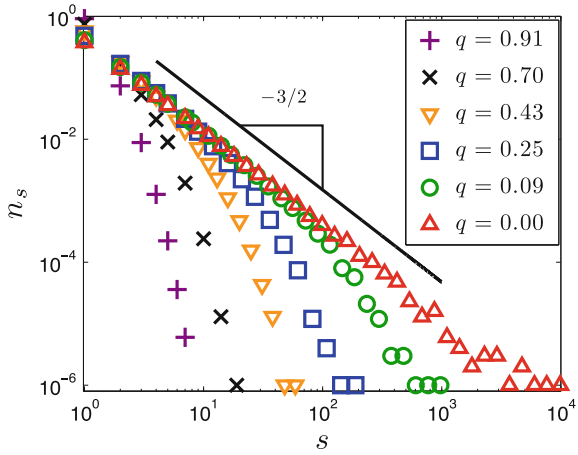

Fig. 1.6 The number of events of size s for different values of q

$$\tilde{n}_s = \int dq\, n_s \sim \int_0^1 dq\, \frac{D_q}{1-q}\, \frac{\exp[-q^2 s]}{s^{3/2}}, \tag{1.16}$$

where the weighting factor D_q is the fraction of faults with damage q between q and $q + dq$. If we associate the damage with microcracks, which are known to have a fractal distribution [19], then it is reasonable to assume a scale free or power law distribution $D_q \sim q^{-x}$, where the exponent x varies depending on the fault system. If we are interested in scaling, we can do an asymptotic expansion [14] for large s so that we can approximate (1.16) by

$$\tilde{n}_s \sim \frac{1}{s^{2-x/2}}. \tag{1.17}$$

Hence different fault systems, with different values of x, can have different b values. In addition, as can be seen in Fig. 1.7, which shows n_s versus s for different values of x, the range over which Gutenberg–Richter scaling fits the data is considerable larger than what is seen for most models with a fixed value of q.

If the mechanism we are proposing, that is, a critical-like point such as a spinodal, is responsible for the frequency-magnitude scaling of *single faults*, we expect the data obtained from real faults to vary from fault to fault. This variation is captured by a single parameter in an otherwise universal distributions in (1.11). By using scaling arguments, we can rewrite (1.11) as

$$n_A \propto \frac{\exp\left[-\Delta h A^{2/3}\right]}{A}, \tag{1.18}$$

where A is the slip area. In Fig. 1.8 we show the number of events with area A from the Advanced National Seismic System Catalog [20]. The fits (solid lines) are to (1.18) and the straight line has unit slope. This data appears to support the idea that at least

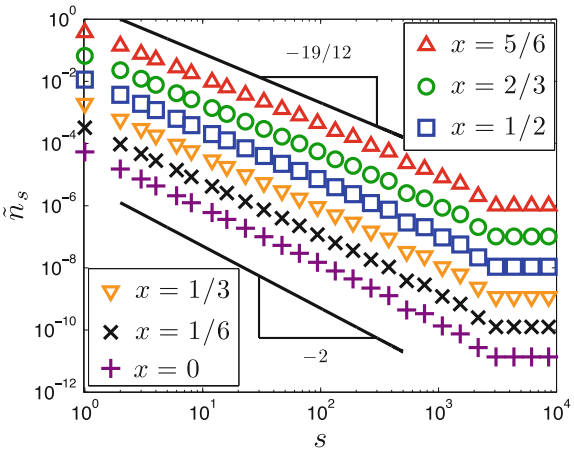

Fig. 1.7 The number of events of size s for different values of the parameter x, where the distribution of the number of microcracks is given by $D_q \sim q^{-x}$

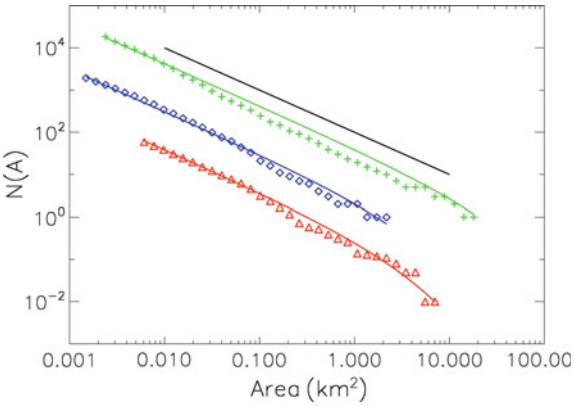

Fig. 1.8 The number of events with area A from the Advanced National Seismic System Catalog [20]. The plots are of the number of events with magnitude greater than or equal to the minimum magnitude of completeness [21] versus the area of each event occurring between 1980–2008 within a 20 km swatch on either side of the San Jacinto (*crosses*), Fort Tejon segment of the San Andreas fault (*diamonds*), and the creeping section of the San Andreas fault (*triangles*). To see the data clearly, the various faults have been offset by factors of ten

some faults have Gutenberg–Richter scaling that can be explained by an underlying critical point. However, there are faults, such as the Parkfield fault, that do not fit this pattern. This fault does not appear to have a range of Gutenberg–Richter scaling that can be fit by (1.18), and there is an event of magnitude approximately six every (roughly) twenty-two years.

1.5.2 Role of Structure

Large events on the Gutenberg–Richter scaling curve in the OFC model do not seem to have either foreshocks or aftershocks. To model these phenomena we introduce structure into the model.

One obvious deficiency of the CA models we have discussed so far is the fact that the failure thresholds are all the same. Because the failure thresholds are supposed to represent the breaking strength of the rock at that point in the fault, it is unrealistic to assume that they are all identical. The simplest way to account for their differences is to have a spatially varying failure threshold in the OFC model. In this paper we will only consider the effect of a large (compared to the other sites) failure threshold on a single site chosen at random. The inclusion of only one asperity is unrealistic, but it is important to understand the effect of one asperity before several asperities are included so that we can better separate the effect of a higher failure threshold from the interaction of the asperities with each other.

The single asperity acts as a sink for stress, that is, as an effectively larger dissipation coefficient α. The difference between the asperity and a larger dissipation coefficient is that when the single asperity fails, a large amount of stress is released into the system. One question is then does the single large asperity impose a periodicity on the event sequence which is associated with the failure of the asperity site? If the system has noise, we would not expect that the system would be exactly periodic, so we first look at the system with zero noise.

As can be seen in Fig. 1.9 the addition of a single asperity appears to enhance the GR scaling. The slope appears to be approximately the same, but the range of the scaling has increased due to the presence of larger events apparently caused by the release of a large amount of stress due to by the failure of the asperity.

In Fig. 1.10 we plot the stress in the system as a function of time for the system with and without the asperity. The stress with zero noise is almost periodic but the presence of the asperity makes the system somewhat less periodic. To understand this behavior we perform a spectrographic analysis of the system stress. In Fig. 1.12 we see that there is a clear band at 10 Hz with a sampling rate of 8000 indicating a

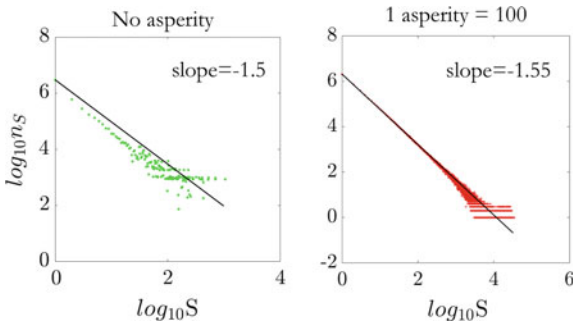

Fig. 1.9 The OFC model with zero noise with one asperity with $\sigma_F = 100$. The other sites have $\sigma_F = 2$. Note that the scaling is very good with a slope of ≈ -1.55. The maximum event size increases from 1000 to 15000. The simulations were with $R = 10$, linear dimension $L = 200$, and $\alpha = 0.025$

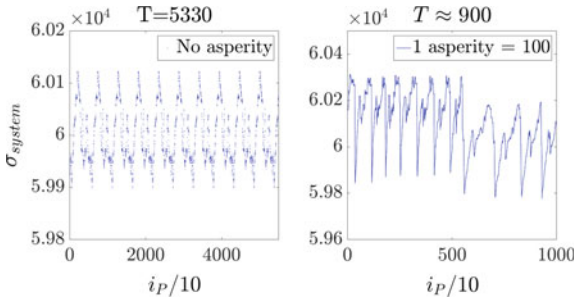

Fig. 1.10 Time series of the total stress for a system without asperities and a system with one asperity. The period with one asperity is around 900, which is much smaller than the period of 5330 for the system without an asperity. Also the periodic behavior of the system with one asperity is not as regular

periodicity of 800. In Fig. 1.12 we see that the period of the asperity is about 70,000 plate updates.

As can be seen in Fig. 1.9 the addition of a single asperity appears to enhance the Gutenberg–Richter scaling. The slope appears to be unchanged, but the range of the scaling has increased due to the presence of larger events apparently caused by the release of a large amount of stress due to the failure of the asperity.

In Fig. 1.10 we plot the stress in the system as a function of time (plate updates) for a system with and without the asperity. The stress with zero noise is almost periodic, but the presence of the asperity makes the system less periodic. To understand this behavior, we perform a spectrographic analysis of the system stress. In Fig. 1.11 we see that there is a clear band at 10 Hz with a sampling rate of 8000 indicating a periodicity of 800 updates. In Fig. 1.12 we see that the period of the asperity is about 70,000 plate updates. This behavior implies that the observed periodicity in the system with the single asperity in Fig. 1.9 is due to an interaction between the periodic behavior of the stress with zero noise and no asperity and the period associated with the failure of the asperity. This behavior suggests that the periodic behavior associated with single faults such as Parkfield is not a simple matter of an

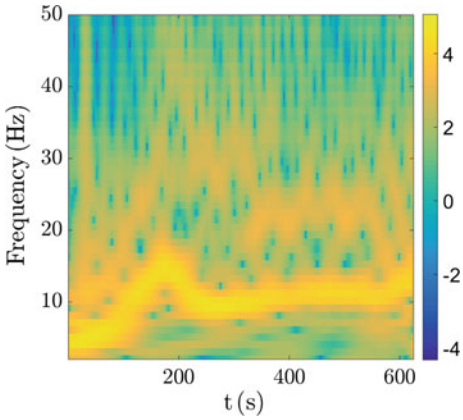

Fig. 1.11 Spectrogram of the total stress for the zero-noise OFC model with one asperity. A sampling rate of 8000 is used for the analysis and 5×10^6 plates updates were analyzed. The strong band around 10 Hz means the period is about 800. There is a transient of about 1.6×10^6 updates after which the periodic behavior becomes more regular

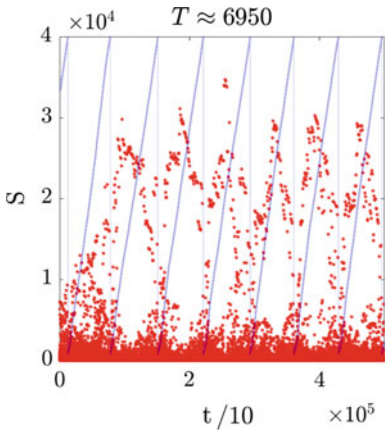

Fig. 1.12 Time series of event sizes (*red*) and stress on an asperity site (*blue*). The period of the stress on the asperity site is about 69500. The peak of the time series of the events may have the same period, but the periodic behavior is less regular. The failure of the asperity does not result in the largest event in the time series

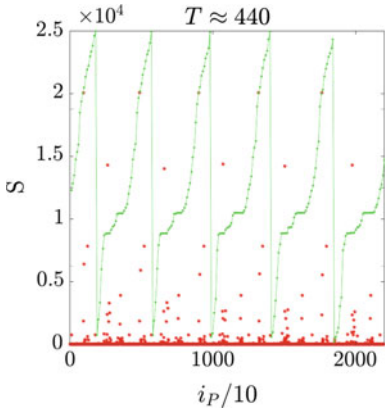

Fig. 1.13 Time series of the stress on the asperity site (*green curve*) and the corresponding time series of the event size (*red curve*). The asperity site failed 12 times in 5000 plate updates. The failure of the asperity site does not directly result in large events

asperity failing over and over with a set period, but is a more complicated interaction of the fault structure with the underlying dynamics.

To support this point of view, we plot in Fig. 1.12 the stress on the single asperity and the event size versus time. We see that, as mentioned, the period of the failure of the asperity is not the same as the period of the largest event in the system. Figure 1.12 shows the surprising result that the largest event does not occur when the asperity fails, but it lags the asperity failure by approximately 2–3 $\times 10^5$ plate updates. Why this lag occurs is not understood and further simulations are being done to test several hypotheses. We also investigated the effect of the strength of the asperity (all other parameters are the same as for the asperity strength of 100). The period associated with the failure of the asperity appears to depend linearly on the strength of the asperity [22]. As can be seen in Fig. 1.13 the fact that the failure of the asperity does not coincide with the largest events does not seem to depend on the size of the failure threshold of the asperity.

Finally we look at the effect of asperities for non-zero noise. If the noise is small, which is what we would expect in real earthquake faults, we would not expect much of a change from the zero noise case. However, as we can see in Fig. 1.14, there is a significant difference in the scaling with and without the asperity (with failure threshold of 100) for small noise [22]. As the noise increases, the two cases, asperity and no asperity, have less of a difference. In addition, the periodicity of the system is much less pronounced as seen in Fig. 1.15.

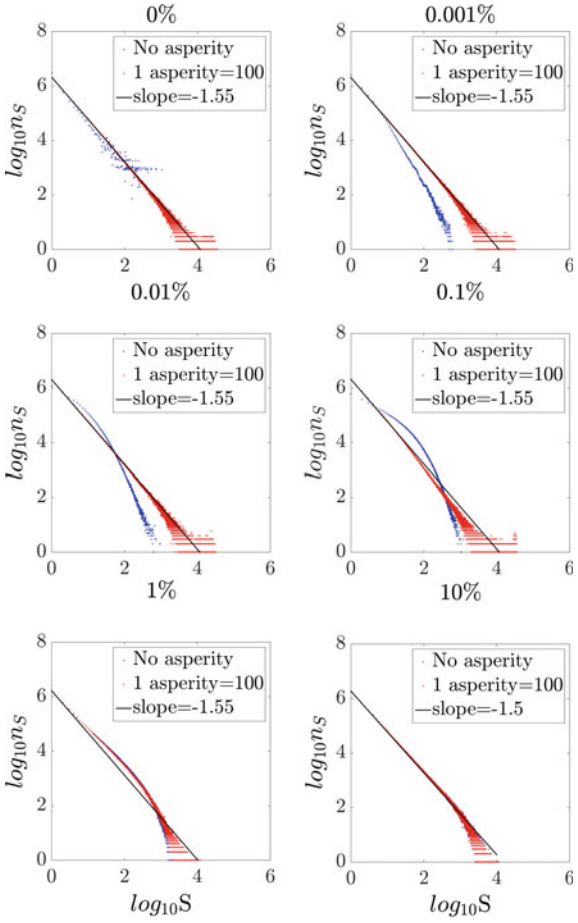

Fig. 1.14 Scaling for without asperities and one with $\sigma_F = 100$ for different values of the noise η. If $\eta < 0.1\%$, the asperity has a significant impact on the scaling; the scaling fits a power law better with the asperity than without. If $\eta > 1\%$, the asperity has little impact on the scaling

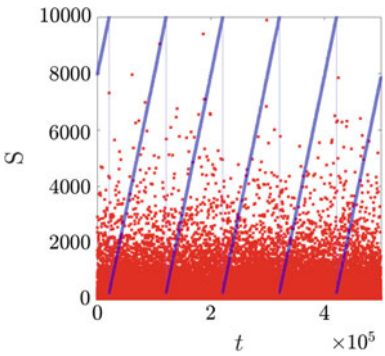

Fig. 1.15 Stress on the asperity (*blue line*) and size of the event (*red dots*) as a function of time for a system with a single asperity and a 10% noise. Compared to a system with 0% noise the evolution is less periodic

1.6 Conclusions

The study of CA models allows us to understand several aspects of the phenomenology of earthquake faults and fault systems. For example, we were able to construct a paradigm that can explain how we can have faults at different distances from an apparent critical point, but a fault system made up of those faults that exhibit a very good fit to Gutenberg–Richter scaling, with a larger range of the power law behavior than any one of the individual faults and a different exponent than the one that characterizes the scaling on the individual faults. This behavior indicates how the fault structure interacts with an underlying critical point. In addition, we begun the study of the interaction between asperities and the underlying critical phenomena.

Future studies will include the addition of several asperities with various distributions of strengths (failure thresholds) as well as their spatial distributions. We will also address the fact that when neighboring sections of the faults fail they do not always lead to a loading of adjacent sections but will sometimes result in a reduction of stress on the neighboring fault sections(sites), i.e. stress is a tensor in real faults. More studies are needed on how the behavior of the CA models is affected by the inclusion of friction and inertia to see if the results we obtained from the CA models are changed by their inclusion as we would have in the BK model.

Acknowledgments This work was funded by the DOE through grant DE-FG02-95ER14498.

References

1. R. Burridge, L. Knopoff, Bull. Seismo. Soc. Am. **57**, 341 (1967)
2. J.B. Rundle, D.D. Jackson, Bull. Seismo. Soc. Am. **67**, 1363 (1977)
3. J.B. Rundle, S.R. Brown, J. Stat. Phys. **65**, 403 (1991)
4. Z. Olami et al., Phys. Rev. Lett. **68**, 1244 (1992)
5. J.M. Carlson, J.S. Langer, Phys. Rev. A **40**, 884 (1991)
6. J. Xia et al., Phys. Rev. E **77**, 031132 (2008)
7. T. Mori, H. Kawamura, Phys. Rev. E **77**, 051123 (2008)

8. J.B. Rundle et al., Phys. Rev. E **56**, 293 (1997)
9. J.B. Rundle et al., Phys. Rev. Lett. **78**, 3798 (1997)
10. W. Klein et al., Phys. Rev. Lett. **78**, 3793 (1997)
11. W. Klein et al., in *GeoComplexity and the Physics of Earthquakes*, J. B. Rundle, D. L. Turcotte and W. Klein, eds. (Am. Geophys. Union, 2000)
12. R. Zwanzig, *Non-equilibrium Statistical Mechanics* (Oxford University Press, Oxford, 2001)
13. D. Thirumalai, R.D. Mountain, Phys. Rev. A **42**, 4574 (1990)
14. C.A. Serino et al., Phys. Rev. Lett. **106**, 108501 (2011)
15. C.D. Ferguson, Numerical Investigations of an Earthquake Fault Based on a Cellular Automaton, Slider Block Model, Ph.D. thesis, Boston University (1997)
16. C. A. Serino, Statistical Properties of Systems with Damage and Defects, Ph.D. thesis, Boston University (2012)
17. W. Klein et al., Phys. Rev. E **75**, 031114 (2007)
18. D. Stauffer, *Introduction to Percolation Theory* (Taylor and Francis, Abingdon, 1994)
19. M. Sahimi et al., Phys. A **191A**, 57 (1992)
20. The Advanced National Seismic System Catalog hosted by the Northern California Earthquake Data Center and the Northern California Seismic Network, U. S. Geological Survey, Menlo Park; Berkeley Seismological Laboratory, University of California, Berkeley, www.needc.org/anss
21. S. Wiemer, M. Wyss, Bull. Seismol. Soc. Am. **90**, 859 (2000)
22. X. Gu, Modified Earthquake Olami-Feder-Christensen Model with Low Noise and Asperities, Ph.D. thesis, Boston University (2016)

Chapter 2
Mean Field Theory of Slip Statistics

Karin A. Dahmen

Abstract A simple mean field model for the statistics and the dynamics of slip avalanches in slowly deformed solids is reviewed. Its universal scaling predictions are compared to experiments on slowly compressed single nanocrystals, microcrystals, bulk metallic glasses, and rocks, as well as to slowly sheared jammed granular materials, and to earthquakes. The remarkable agreement between model and experiments spanning 12 decades in length and a wide range of material structures implies that results on the slip statistics can be transferred from one solid material to another and from one scale to another. Potential applications of the results include materials testing, failure prediction, and hazard prevention.

2.1 Introduction

Slowly sheared crystals, bulk metallic glasses, composite materials, ferroelastic materials, densely packed granular materials, rocks, and the earth's crust all deform in a jerky way via (slip-) avalanches, such as earthquakes. These slip avalanches have a broad distribution $D(S)$ of sizes S, following simple functions that are independent of the microscopic details of the material. Recent experiments, analytic models, and simulations show that the avalanche size distribution typically follows a power law over a broad range of sizes, similar to the Gutenberg Richter law of earthquakes. The power law region is cut off at a size $S = S_{max}$ that may depend on the applied stress, strainrate, temperature, or sample size [1–5].

A simple mean field model [5] has proven useful not only for gaining an intuition for these slip avalanches (also called "serrations" of the stress strain curves), but also for organizing the experimental data. The model also predicts the observed statistics of the avalanches, the avalanche dynamics, the time series properties

K.A. Dahmen (✉)
Department of Physics, University of Illinois at Urbana-Champaign,
Urbana, IL 61801, USA
e-mail: dahmen@illinois.edu

E.K.H. Salje et al. (eds.), *Avalanches in Functional Materials and Geophysics*,
Understanding Complex Systems, DOI 10.1007/978-3-319-45612-6_2

of the avalanches, and their dependence on the experimental tuning parameters [1–4, 6, 11]. In the following we briefly review the model, its predictions, and its comparison to first experiments.

2.2 The Model

The model assumes that a solid material has weak spots [5]. As the material is slowly sheared the local shear stress increases everywhere. Each weak spot is stuck until the local shear stress exceeds its random failure threshold. When that happens it slips by a random amount, and the released stress is redistributed to the other weak spots. This may trigger some of the other weak spots to slip also, leading to a failure cascade, or slip avalanche. The avalanche stops when everywhere in the material the local stress is below its respective local failure threshold.

After an avalanche is completed, the applied stress is slowly increased further until the next weak spot slips, thereby triggering the next slip avalanche. The model can be written [5] either in a continuum description or a discrete description. Both are reviewed below.

2.2.1 Continuum Version of the Model

One can write the following equation of motion for the model [5, 8]:

$$\eta \quad \partial u(\mathbf{r},t)/\partial t = F + \sigma_{int}(\mathbf{r}, t) - f_R[u, \mathbf{r}, \{(u(\mathbf{r}, t' < t)\}] \tag{2.1}$$

where η is a damping constant, F is the applied shear stress in the x direction (using scalar elasticity). $u(\boldsymbol{r}, t)$, is the accumulated slip in the x direction at point $\boldsymbol{r}$ and at time t (e.g. the displacement discontinuity across the slip plane or shear band, or earthquake fault), and

$$\sigma_{int}(\mathbf{r}, t) = \int_{-\infty}^{t} dt' \int d^2r' \quad J(\mathbf{r} - \mathbf{r}', t - t') \times [u(\mathbf{r}', t') - u(\mathbf{r}, t)] \tag{2.2}$$

is the shear stress accumulated at point $\boldsymbol{r}$, at time t, resulting from elastic stress transfer from all previous slips in the solid since time $t = 0$ when the system started in a relaxed state. f_R represents the quenched random "pinning" stress, that prevents slips until the local stress exceeds the local failure threshold, as discussed above. This failure threshold may be history dependent (see also the discussion of the discrete version of the model below). A renormalization group analysis of the model for positive couplings shows that the coupling between slips of weak spots is sufficiently long range (for example, $J(\mathbf{r}) \equiv \int dt\, J(\mathbf{r}, t) \sim r^{-2}$ for parallel straight edge

dislocations) that mean field theory (MFT) gives the correct scaling behavior in all dimensions [5, 8]. For small patches slipping along a fault-like plane surrounded by elastic material $J(\mathbf{r}) \equiv \int dt\, J(\mathbf{r}, t) \sim r^{-3}$ and mean field theory is expected to apply for 2 and higher dimensional slip planes [5, 8]. In most solids the slips or slip avalanches organize predominantly along shear bands or glide planes, and the positivity of the coupling applies during avalanches [8–10]. In fact the predictions of MFT agree with the scaling behavior of the avalanche statistics seen in experiments on crystals, bulk metallic glasses, high entropy alloys, rocks, granular materials, and earthquakes [1–3, 6, 11].

2.2.2 Discrete Version of the Model

A simple discrete version of the model can be easily solved in mean field theory.

For a block of material two different loading conditions may be applied:

(I) a slowly increasing shear stress F applied to the boundaries
(II) a small strain rate imposed at the boundaries.

The model predicts that the scaling behavior for both boundary conditions is the same, as was recently also confirmed by experiments [32].

In the discrete version the material is modeled by N lattice points marked by $l=1,\ldots,N$. Each lattice point (or weak spot) has its own random *local* failure shear stress $\tau_{s,l}$. We assume it deforms elastically until the local shear stress exceeds this local threshold. When that happens, the weak spot slips until the local shear stress is reduced to a lower arrest stress $\tau_{a,l}$("sticking stress"). $\tau_{s,l}$ and $\tau_{a,l}$ vary randomly in space, to model the disorder in the material. After re-sticking the weak spot locally acts again elastically until the local stress again exceeds the failure stress.

Brittle materials: To model brittle (or hardening) materials, the failure stress is assumed to weaken (or strengthen, respectively) after the initial slip in an avalanche. For brittle materials, after a point l slips for the first time during an avalanche, the local failure threshold is weakened from the static value $\tau_{s,l}$ to a diminished value $\tau_{d,l}$ with $\tau_{a,l} < \tau_{d,l} < \tau_{s,l}$. The failure stress remains at $\tau_{d,l}$ until the avalanche has been completed. The amount of weakening is given by the weakening parameter $\varepsilon = (\tau_{s,l} - \tau_{d,l})/\tau_{s,l}$ [5, 8]. After the completion of an avalanche all weakened failure stresses are reset to their initial static values $\tau_{s,l}$.

Hardening Materials: In contrast, for hardening materials upon slipping the failure thresholds are strengthened by an amount proportional to $\varepsilon < 0$, to model the local energy absorption due to dislocation pair creation and entanglement etc. [4, 5].

Avalanches: The stress that is released during a slip is redistributed to all other cells in MFT. In MFT the coupling is replaced by a function that is constant in space: $J(\mathbf{r}) \equiv J/N$. The coupling causes slip avalanches. The local stress τ_l at a lattice point l is given by $\tau_l = J/N \Sigma_m (u_m - u_l) + F$ [5], where F is the applied stress and u_l is the local displacement discontinuity. As described above, each point fails when

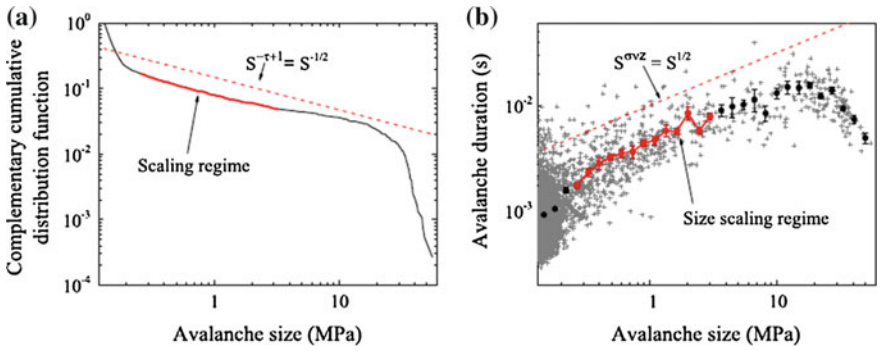

Fig. 2.1 Figures reprinted from [6]. Avalanche statistics for quasistatic uniaxial compression of two specimens of $Zr_{45}Hf_{12}Nb_5Cu_{15.4}Ni_{12.6}Al_{10}$. The predictions of the mean field model are shown by the *dashed red lines*. The data in the scaling regime are also highlighted in *red*. **a** The distribution of stress drop sizes for the 3744 avalanches; the data in the scaling regime have the expected mean field exponent of –1/2. **b** The avalanche duration as a function of avalanche size. The data in the scaling regime have the expected mean field exponent of 1/2

the local stress is bigger than the local failure threshold (slip stress) $\tau_{f,l} \equiv \tau_{s,l}$ (or $\tau_{d,l}$). When site l fails, it slips by an amount Δu_l resulting in a stress reduction $\tau_{f,l} - \tau_{a,l} \sim 2G\Delta u_l$ where $G \sim J$ is the elastic shear modulus. After a slip the site resticks and the released stress is redistributed to the other sites in the system. A local slip can then trigger other sites to slip in a slip-avalanche. The avalanche ends when at all sites the local stresses are below their local failure stresses $\tau_l < \tau_{f,l}$. In the adiabatic (slow driving) limit, the applied stress F is increased only after a slip avalanche has been completed, until the next site fails. For small applied strain rate Ω the stress F in the dynamical equation is replaced by $K_L(\Omega t - u_i)$ where K_L is an effective loading spring constant [5, 8], which is proportional to $G/N^{(1/2)}$.

This model can be solved analytically [5, 8]. It predicts the observed scaling behavior of the slip statistics without the need for any fitting parameters or any assumptions about length scales or material structures. As a result, it predicts the same slip statistics for a wide range of scales and materials (Fig. 2.1) [1, 5]. The key model parameters are: the weakening ε, the boundary conditions, $\tau_{s,r}, \tau_{a,r}$ and their distributions, the values of η and the elastic constants, and the form of $J(\boldsymbol{r}, t) > 0$. Among these, only ε, and the range of $J(\boldsymbol{r}, t)$ affect the universal (i.e. detail independent) aspects of the behavior on long length scales.

2.2.2.1 Model Predictions for Avalanche Statistics and Comparison to Experiments

For zero weakening (ε=0) the model predicts the scaling behavior of the slip statistics on long length scales for a wide range of materials, irrespective of the microscopic details. In particular it predicts the probability distributions of $D(S)$ of finding

avalanches of size S at applied shear stress F [5, 8]:

$$D(S, F) \sim 1/S^{\kappa} G_S(S(F - F_c)^{1/\sigma}) \quad \text{where in MFT } \kappa = 1.5 \text{ and } 1/\sigma = 2$$
$$\text{and } G_S(x) \sim A' exp(-B'x),$$

with A' and B' non-universal constants. F_c is the flow stress or critical stress. The avalanche size S could be the total slip for experiments with slowly increasing applied shear stress, or total stress drop for experiments at imposed slow strain rate. Similarly it predicts the probability of finding avalanches of energy E at stress $F$to scale as [12].

$D(E, F)$. $\sim 1/E^{-\eta} G_E(E(F_c - F)^{(2-\sigma \upsilon z)/\sigma})$ with η=*4/3* and $(2-\sigma \upsilon z)/\sigma = 3$, $\sigma \upsilon z = 0.5, \sigma = 0.5$ and $G_E(x)$ is another universal scaling function [3, 13]. Here the energy E scales as $E \sim \int v^2(t)\, dt$, and $v(t)$ is proportional to the instantaneous growth rate of the avalanche (either the slip rate for slowly increasing stress or the stress drop rate for slow strain rate boundary conditions). In some experiments histograms of avalanche energies or sizes are collected over the entire stress range, in that case $D(S, F)$ and $D(E, F)$are integrated over the applied stress F, from 0 to F_c, which yields the power law stress-integrated histograms $D_{int}(S) \sim S^{-(\kappa+\sigma)}\ G_{int,S}\,(S/S_{max})$. Here $S_{max}$is a measure for the largest observed avalanche size, which is usually a function of the tuning parameters in the system, such as temperature, sample size, etc. $G_{int,S}(x)$ is another scaling function. In some acoustic emission experiments the energy may be defined as $E_m \sim (v(t))^2_{max}$ i.e. as proportional to the highest slip-velocity squared during an avalanche [1]. In MFT histograms of this quantity scale as $D(E_m, F) \sim (E_m)^{-(\mu+1)/2}\ G_{Em}(E_m/E_{m,max})with E_{m,max} \sim (F_c - F)^{-2\rho}$ where $(\mu + 1)/2 = 1.5$ and $2\rho = 2$ in MFT and $G_{Em}(x)$ is yet another scaling function. Correspondingly the stress integrated distribution scales as $D_{int}(E_m) \sim (E_m)^{-[(\mu+1)/2+1/(2\rho)]}$ $G_{int,Em}(E_m/E_{m,max})) \sim (E_m)^{-2}\ G_{int,Em}(E_m/Em_{,max})$ [14, 15]. Table 2.1 summarizes some of the results from MFT. All symbols with a subscript "max" (or "min") denote maximum (or minimum) values of the scaling variable, that typically depend on experimental tuning parameters, such as temperature, sample size, and others. The results shown in Table 2.1 are compiled from references [1, 5, 12, 14, 15]. Table 2.1a, b show some of the scaling relations predicted by mean field theory, while Table 2.1c shows the comparison to a wide range of recent experiments. A comparison of some of these predictions to experiments on the slow shear of nanocrystals, amorphous materials, rocks, granular materials, and the earth's crust is shown in [1].

The most extensive comparison to experiments has probably been done for bulk metallic glasses (BMGs), which shows agreement with the model predictions for more than 12 different statistical quantities [6]. For BMGs that are compressed at slow strainrate, Fig. 2.1 shows the complementary cumulative stress drop size distribution $C(S) = \int_S^{\infty} D\left(S'\right) dS'$ which gives the probability to observe avalanches larger than size S. For deformation in the steady state, the mean field model

Table 2.1 Results form MFT

Statistical Distributions	**Scaling forms predicted by the model** *[5-7]*
D(S,F), of avalanche size, *S* (slip size or stress drop at stress *F*)	$D(S) \sim S^{-\kappa}\, G_S(S/S_{max})$
$D_{int}(S)$ of avalanche size S integrated over stress *F*	$D_{int}(S) \sim S^{-(\kappa+\sigma)}\, G_{int,S}(S/S_{max})$
D(v,F), of stress-drop rate, *v*	$D(v) \sim v^{-\psi}\, G_V(v/v_{max})$
D(T,F), of avalanche durations, *T*	$D(T) \sim T^{-\alpha} G_T(T/T_{max})$
$D_{int}(T)$ of avalanche durations integrated over stress F	$D_{int}(T) \sim T^{(\alpha+1/(\nu z))}\, G_{int,T}(T/T_{max})$
Power spectrum of the stress drop rate versus time, *P(ω,F),* at frequency, *ω*	$P(\omega) \sim \omega^{-(1/\sigma\nu z)} D_\omega(\omega/\omega_{min})$
D(E,F), of energy $E \sim \int v^2 dt$ released in a slip close to failure	$D(E,F) \sim E^{-\eta}\, G_E(E/E_{max})$
$D_{int}(E)$ of energy $E \sim \int v^2 dt$ integrated over stress *F*	$D_{int}(E) \sim E^{-(\eta+\sigma/(2-\sigma\nu z))}\, G_{int,E}(E/E_{max})$
$D(E_m, F)$ of peak velocity squared $E_m \sim v^2_{max}$	$D(E_m,F) \sim (E_m)^{-(\mu+1)/2} G_{Em}(E_m/E_{m,max})$
$D_{int}(E_m)$ of peak velocity squared $E_m \sim v^2_{max}$ integrated over stress *F*	$D_{int}(E_m) \sim (E_m)^{-[(\mu+1)/2+1/(2\rho)]} G_{int,Em}(E_m/E_{m,max})$
$D(v_m,F)$ of maximum velocities v_m during avalanche	$D(v_m,F) \sim (v_m)^{-\mu} G_{vm}(v_m/v_{m,max})$
$D_{int}(v_m)$ of max. velocities v_m integrated over stress *F*	$D_{int}(v_m) \sim (v_m)^{-(\mu+1/\rho)}\, G_{int,vm}(v_m/v_{m,max})$

(a)

Scaling relations	**Exponent values in Mean Field Theory (MFT)**	**Exponent relations**
$\langle E \mid S \rangle \sim S^2/\langle T \mid S \rangle \sim S^{2-\sigma\nu z}$	$2-\sigma\nu z=3/2$	$(\kappa-1)=(\eta-1)(2-\sigma\nu z)$, $\eta=4/3$ in MFT
$\langle S \mid T \rangle \sim T^{(1/\sigma\nu z)}$	$1/(\sigma\nu z)=2$	$\kappa_{int} \equiv \kappa+\sigma=2$ (in MFT for the stress integrated exponent of $D_{int}(S)$)
$\langle T \mid S \rangle \sim S^{\sigma\nu z}$	$\sigma\nu z=1/2$	$\eta_{int} \equiv \eta + \sigma/(2-\sigma\nu z)=5/3$ (in MFT for stress integrated exponent of $D_{int}(E)$)
$\langle v_m \mid S \rangle \sim S^{\sigma\rho}$	$\rho\sigma=1/2$	$(\kappa_{int}-1) = (\eta_{int}-1)(2-\sigma\nu z)$
$\langle v_m \mid T \rangle \sim T^{(\rho/(\nu z))}$	$\rho/(\nu z)=1$	
$\langle E \mid S \rangle \sim S^{2-\sigma\nu z}$	$2-\sigma\nu z=3/2$	
$\langle E_m \mid S \rangle \sim S^{2\sigma\rho}$	$2\sigma\rho=1$	
$\langle E \mid T \rangle \sim T^{(2-\sigma\nu z)/(\sigma\nu z)}$	$(2-\sigma\nu z)/(\sigma\nu z)=3$	$(\kappa-1)=(\alpha-1)\sigma\nu z$
$\langle E_m \mid T \rangle \sim T^{2\rho/(\nu z)}$	$2\rho/(\nu z)=2$	
Strain-rate $\langle v \mid F \rangle \sim (F-F_c)^{\beta}$ for $F > F_c$ (depinned)	$\beta=1$	

Fixed-stress loading conditions: slowly increasing stress, *F*, up to the failure stress, F_c	**Fixed-strain-rate loading conditions: moving the boundary at a slow strain rate, *Ω***
$S_{max} \sim (F_c-F)^{-1/\sigma}$	$S_{max} \sim \Omega^{-\lambda/(\sigma z\nu)}$
$v_{max} \sim (F_c-F)^{-1}$	$v_{max} \sim \Omega^{-1}$
$T_{max} \sim (F_c-F)^{-\nu z}$	$T_{max} \sim \Omega^{-\lambda}$
$\omega_{min} \sim (F_c-F)^{\nu z}$	$\omega_{min} \sim \Omega^{\lambda}$
$E_{max} \sim (F_c-F)^{-(2-\sigma\nu z)/\sigma}$	$E_{max} \sim \Omega^{-(2-\sigma\nu z)\lambda/(\sigma\nu z)}$
$E_{m,max} \sim (F_c-F)^{-2\rho}$	$E_{m,max} \sim \Omega^{-2\rho\lambda/(\nu z)}$
$v_{m,max} \sim (F_c-F)^{-\rho}$	$v_{m,max} \sim \Omega^{-\rho\lambda/(\nu z)}$

(b)

(continued)

Table 2.1 (continued)

Exponents	Sample Size	κ	$\kappa_{int}=\kappa+\sigma$	σ	$1/\sigma\nu z$	α	ψ	$\lambda\equiv\nu z/\beta$	η	μ	ρ	β
Model Predictions												
Mean Field Theory (MFT) [5,14,15]		**1.5**	2	0.5	2	2	1	1	4/3	2	1	1
Experimental Verifications*												
Nanocrystals (Molybdenum (Mo), Compression, see [3,16]	10^{-8} m	**1.5**	2	0.5	2							
Microcrystals (Nickel (Ni), Compression [4,17])	10^{-6} m	**1.5**			2							
Bulk Metallic Glass (BMG) ($Cu_{47}Zr_{47.5}Al_5$ [18], $Zr_{45}Hf_{12}Nb_5Cu_{15.4}Ni_{12.6}Al_{10}$ [6], and $Zr_{64.13}Cu_{15.75}Ni_{10.12}Al_{10}$ [2], atomic percent) Compression.	10^{-3} m	**1.5**	2	0.5	2	2						
Lab-scale rocks (Sidobre granite, Compression [19,20,21])	10^{-2} m	**~1.5**	1.66-2.2									
Lab-scale rocks (Westerly granite, Frictional sliding [22])	10^{-2} m	**~1.5**										
Jammed granular materials (Photo-elastic disks in Couette cells and other geometries also in 3 dimensions [23,24])	1 m	**~1.5**			1.8-2.5	~2						
Earthquakes [25,26,27]	10^{5} m	**~1.5**			2							

(c)

(continued)

Table 2.1 (continued)

Lab-scale rocks (Sidobre granite, Compression [19,20,21])	10^{-2} m	**~1.5**	1.66-2.2									
Lab-scale rocks (Westerly granite, Frictional sliding [22])	10^{-2} m	**~1.5**										
Jammed granular materials (Photo-elastic disks in Couette cells and other geometries [23])	1 m	**~1.5**			1.8-2.5	~2						
Earthquakes [25,26,27]	10^{5} m	**~1.5**			2							

(c)

**Exponents from experiments and observations quoted here have a 10% error range due to statistical fluctuations* [1]. *Exponents from previous rock experiments were obtained from* [19, 20] *at the largest stresses, using that the Gutenberg Richter exponent, b, in* [19] *is related to our exponents via b = 3(κ-1)/2 (see* [8, 21]*). For the relationship between the slip-size and the acoustic-emission signal see* [21]*, the Supplementary Information of* [3, 15]*, and references therein*

predicts $C(S) \sim S^{-(\kappa-1)}$ for a certain scaling regime range of (small) avalanche sizes $S_{min} < S < S_{max}$, with $\kappa = 1.5$. Power laws fitted to experimental data on crystals and bulk metallic glasses are consistent with mean field theory $\kappa - 1 = 0.51 \pm 0.03$ [3, 5, 6, 19]. For models of brittle materials, such as BMGs, the weakening parameter $\varepsilon > 0$ and the model predicts additional large (i.e. system spanning) avalanches that recur almost periodically, with the power law distributed smaller avalanches observed in between the occurrence of the large avalanches [5, 6, 23]. Both small and large avalanches have recently been observed in experiments on BMGs [6, 7].

2.3 Model Predictions for Avalanche Dynamics and Comparison to Experiments

The MFT model also predicts average temporal profiles of the avalanches, The time profile for the average stress drop rate $< -d\sigma/dt(t)|T >$, which is obtained by averaging the stress drop rate $-d\sigma/dt(t) > 0$ over all avalanches of the same duration T, is predicted by mean field theory to follow a parabola. (An avalanche starts when $-d\sigma/dt(t)$ first becomes positive and it stops when it becomes negative again.). The predictions for the scaling behavior of these profiles have recently been tested for

bulk metallic glasses for the first time [6]. Machine stiffness effects can flatten out the shape [6]. An asymmetric profile, i.e. one that is tilted to the right or to the left, can be an indication that either inertia or delay effects play an important role in the slip dynamics [5, 23, 28–31].

Also, the time profile for the average stress drop rate $< -d\sigma/dt(t)|S >$, which is obtained by averaging $-d\sigma/dt(t)$ over all avalanches of the same total stress drop size S, is predicted by MFT to follow a function of the form $< -d\sigma/dt(t)|S > \sim S^{1-\sigma\upsilon z} G'(t/S^{\sigma\upsilon z})$ with $\sigma\upsilon z = 0.5$ in MFT, and $G'(x) = A'x\exp(-B'x^2)$ where A' and B' are experiment-specific constants [1, 5, 6].

Examples of these shapes are shown in Fig. 2.2. References [2, 6] contain the comparison of many more statistical properties with the model predictions.

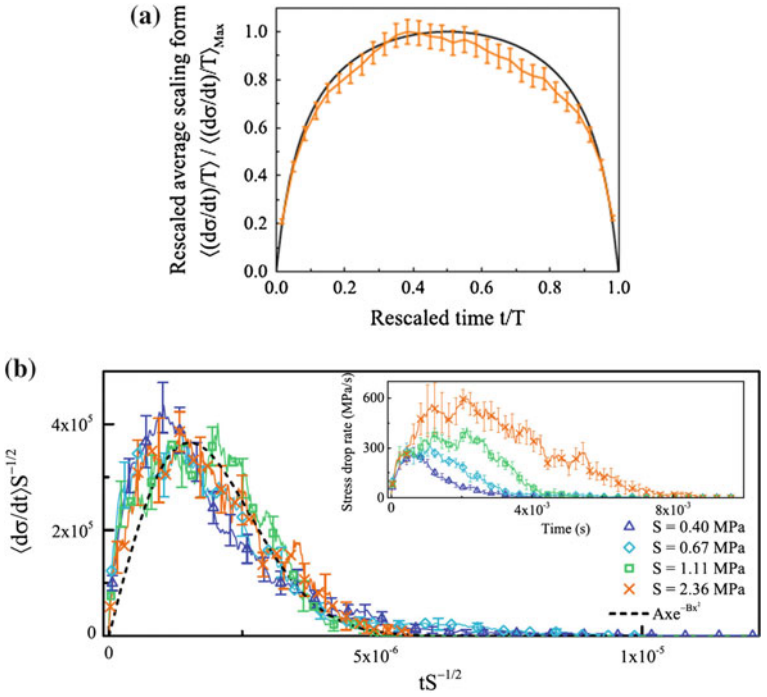

Fig. 2.2 Figures reprinted from [6]. **a** The average avalanche shape constructed from all avalanches in the scaling regime. The stress drop rate is scaled by the maximum stress drop rate for each avalanche on the vertical axis and by the avalanche duration on the horizontal time axis. The mean field prediction is also shown. **b** The unscaled shapes for several small avalanches of various sizes are shown in the *inset*. When both axes are scaled by $S^{-1/2}$, the shapes collapse to the form predicted by the mean field model (*black dashed line*). (From [6])

2.4 Conclusion

Initial measurements indicate that mean field theory makes many predictions for experiments, some of which have been tested for a range of materials. Initial comparisons of theory with experiments suggest that the universality class of the simple mean field model may be surprisingly large [1]. Table 2.1 shows that so far only a subset of the model predictions have been tested in experiments. More experimental tests, especially tests at high time resolution on a wide range of materials are needed to fully test all predictions of the model and to establish the size of the underlying universality class. Regardless of whether or not a material's slip statistics agree precisely with the predictions of the simple model for the scaling exponents and scaling functions, the model provides valuable intuition and guidance for organizing the data of experiments and simulations. As recent experiments show [1, 6], the model predictions agree with experiments on a surprisingly wide range of materials, including crystals, BMGs, rocks, granular materials, and earthquakes [1].The reason for this agreement of the simple mean field model with so many experiments likely lies in the fact that most experiments show some kind of slip localization so that the avalanches typically propagate in gilde planes, shear bands, or earthquake faults. For this kind of slip localization one can use tools from the theory of phase transitions, like the renormalization group, to show that the elastic interactions are positive along such shear bands and that the discussed mean field theory is expected to fully describe the scaling behavior on long length scales, in 3 dimensions (up to negligible logarithmic corrections) [8]. Experiments and simulations of other systems, such as ferroelastics also give related results [12, 33]. Potential applications of the model include materials testing, failure prediction and hazard prevention [34].

Acknowledgments We thank Michael LeBlanc, Ekhard Salje, Jonathan Uhl, and Wendelin Wright for key contributions to this short review article. This work was supported by the National Science Foundation under Grants CBET–1336634, and DOE DE-FE-0011194 (KAD). We especially thank the Kavli Institute for Theoretical Physics for hosting the author for a workshop during which parts of this paper were written and for support through grant NSF PHY11–25915.

References

1. J.T. Uhl, S. Pathak, D. Schorlemmer, X. Liu, R. Swindeman, B.A.W. Brinkman, M. LeBlanc, G. Tsekenis, N. Friedman, R. Behringer, D. Denisov, P. Schall, X. Gu, W.J. Wright, T. Hufnagel, A. Jennings, J.R. Greer, P.K. Liaw, T. Becker, G. Dresen, K.A. Dahmen, Universal quake statistics: from compressed nanocrystals to earthquakes. Sci. Reports **5**, 16493 (2015)
2. J. Antonaglia, X. Xie, M. Wraith, J. Qiao, Y. Zhang, P.K. Liaw, J.T. Uhl, K.A. Dahmen, Tuned critical avalanche scaling in bulk metallic glasses. Nature Sci. Reports **4**, 4382 (2014)
3. N. Friedman, A.T. Jennings, G. Tsekenis, J.-Y. Kim, J.T. Uhl, J.R. Greer, K.A. Dahmen, Statistics of dislocation slip-avalanches in nano-sized single crystals show tuned critical behavior predicted by a simple mean field model. Phys. Rev. Lett. **109**, 095507 (2012)
4. M. Zaiser, Scale invariance in plastic flow of crystalline solids. Adv. Phys. **55**, 185–245 (2006). (and references therein)

5. K.A. Dahmen, Y. Ben-Zion, J.T. Uhl, Micromechanical model for deformation in solids with universal predictions for stress strain curves and slip avalances. Phys. Rev. Lett. **102**, 175501 (2009)
6. J. Antonaglia , W.J. Wright, X.J. Gu, R.R. Byer, T.C. Hufnagel, M. LeBlanc M, J.T. Uhl, and K.A. Dahmen, Bulk Metallic Glasses Deform via Slip-avalanches. Phys. Rev. Lett. **112**, 155501/1–4 (2014)
7. W.J. Wright, Y. Liu, X. Gu, K.D. Van Ness, S.L. Robare, X. Liu, J. Antonaglia, M. LeBlanc, J.T. Uhl, T.C. Hufnagel, K.A. Dahmen, Experimental evidence for both progressive and simultaneous shear during quasistatic compression of a bulk metallic glass. J. Appl. Phys. **119**, 084908 (2016). doi:10.1063/1.4942004
8. D.S. Fisher, K.A. Dahmen, S. Ramanathan, Y. Ben-Zion, Statistics of earthquakes in simple models of heterogeneous faults. Phys. Rev. Lett. **78**, 4885–4888 (1997)
9. J.P. Sethna, Private communication
10. J.T. Uhl, Private communication
11. R. Carroll, C. Lee, C.-W. Tsai, J.-W. Yeh, J. Antonaglia, B. Brinkman, M. LeBlanc, X. Xie, S. Chen, P.K. Liaw, K.A. Dahmen, Experiments and model for serration statistics in low-entropy, medium-entropy, and high-entropy alloys. Sci. Reports **5**, 16997 (2015). doi:10.1038/srep16997
12. E.K.H. Salje, K.A. Dahmen, Crackling noise in disordered materials. Annu. Rev. Condens. Matter Phys. **5**, 233–254 (2014)
13. K. A. Dahmen, *Hysteresis, avalanches, and disorder-induced critical behavior: a renormalization group approach*. Ph.D. thesis, Cornell Univ., Ithaca, NY (1995) 233 pp
14. M. LeBlanc, L. Angheluta, K.A. Dahmen, N. Goldenfeld, Universal fluctuations and extreme statistics of avalanches near the depinning transition. Phys. Rev. E **87**, 022126 (2013)
15. M. LeBlanc, L. Angheluta, K. Dahmen, N. Goldenfeld, Distribution of maximum velocities in avalanches near the depinning transition. Phys. Rev. Lett. **109**, 105702 (2012)
16. S. Brinckmann, J.-Y. Kim, J.R. Greer, Fundamental differences in mechanical behavior between two types of crystals at nano-scale. Phys. Rev. Lett. **100**, 155502/1–4 (2008)
17. D. Dimiduk, C. Woodward, R. LeSar, M. Uchic, Scale-free intermittent flow in crystal plasticity. Science **312**, 1188–1190 (2006)
18. B.A. Sun et al., Plasticity of ductile metallic glasses: A self-organized critical state. Phys. Rev. Lett. **105**, 035501/1–4 (2010)
19. D. Amitrano, Brittle-ductile transition and associated seismicity: experimental and numerical studies and relationship with the *b*-value. Geophys. Res. **108**B1, 2044/1–15 (2003). doi:10.1029/2001JB000680
20. C.H. Scholz, The Frequency-magnitude relation of microfracturing in rock and its relation to earthquakes. Bull. Seismol. Soc. Am. **58**, 399–415 (1968)
21. D. Amitrano, Variability in the power-law distributions of rupture events. Eur. Phys. J. **205**, 199–215 (2012)
22. T.H.W. Goebel et al., Identifying fault heterogeneity through mapping spatial anomalies in acoustic emission statistics. J. Geophys. Res. **117**, B03310/1–18 (2012). doi:10.1029/2011JB008763
23. K.A. Dahmen, Y. Ben-Zion, J.T. Uhl, A simple analytic theory for the statistics of avalanches in sheared granular materials. Nat. Phys. **7**, 554–557 (2011)
24. D.V. Denisov, K.A. Lorincz, J.T. Uhl, K.A. Dahmen, P. Schall, Universality of slip avalanches in flowing granular matter. Nat. Commun. **7**, 10641 (2016). doi:10.1038/ncomms10641
25. Y. Ben-Zion, J.R. Rice, Slip patterns and earthquake populations along different classes of faults in elastic solids. J. Geophys. Res. **98**, 14109–14131 (1993)
26. Y. Ben-Zion, Collective behavior of earthquakes and faults: continuum-discrete transitions, progressive evolutionary changes and different dynamic regimes. Rev. Geophys. **46**, RG4006/1–70 (2008)
27. Y.Y. Kagan, Earthquake size distribution: power-law with exponent β=1/2? Tectonophysics **490**, 103–114 (2010)

28. S. Papanikolaou, F. Bohn, R.L. Sommer, G. Durin, S. Zapperi, J.P. Sethna, Universality beyond power laws and the average avalanche shape. Nat. Phys. **7**, 316 (2011)
29. S. Zapperi, C. Castellano, F. Colaiori, G. Durin, Signature of effective mass in crackling-noise asymmetry. Nat. Phys. **1**, 46 (2005)
30. A. Baldassarri, F. Colaiori, C. Castellano, Average shape of a fluctuation: universality in excursions of stochastic processes. Phys. Rev. Lett. **90**, 060601 (2003)
31. K.A. Dahmen, Nonlinear dynamics: universal clues in noisy skews. Nat. Phys. **1**, 13 (2005)
32. R. Maass, M. Wraith, J.T. Uhl, J.R. Greer, K.A. Dahmen, Slip statistics of dislocation avalanches under different loading modes. Phys. Rev. E **91**, 042403 (2015)
33. X. He, X. Ding, J. Sun, E.K.H. Salje, Parabolic temporal profiles of non-spanning avalanches and their importance for ferroic switching. Appl. Phys. Lett. **108**, 072904 (2016). doi:10.1063/1.4942387
34. B. Brinkman, M. LeBlanc, Y. Ben-Zion, J.T. Uhl, Karin A. Dahmen, Probing failure susceptibilities of earthquake faults using small-quake tidal correlations. Nature Commun. **6**, 6157 (2015). doi:10.1038/ncomms7157

Chapter 3
From Labquakes in Porous Materials to Earthquakes

Eduard Vives, Jordi Baró and Antoni Planes

Abstract A review of recent Acoustic Emission experiments during the compression of synthetic porous SiO_2 (Vycor© and Gelsil) under controlled force rates is presented. The statistical analysis of the recorded signals allows comparison with the statistics of earthquakes from available public seismological catalogues. We discuss different methods to characterize the properties of the individual acoustic emission avalanches and the time correlations between them.

3.1 Introduction

For quite a long time there has been a lot of interest in designing laboratory experiments that can be used as low-scale models for earthquakes with the final aim of predicting earthquake occurrence. To this end, the focus has been on brittle fracture experiments in heterogeneous materials [1–5] since both phenomena display crackling noise response under slow external stimulation. Actually, all these systems belong to a class that show scale invariant intermittent dynamics when externally driven. These processes occur as sequences of well-separated events, usually called avalanches, which occur in the absence of characteristic time and size scales. This intermittent collective dynamics has been reported in magnetization processes (Barkhausen noise), plasticity and martensitic transitions, among others. The existence of scale invariance associated with avalanches suggests that in spite of the disparity of scales expected in earthquakes and laboratory-scale experiments, the most fundamental laws that govern the statistical behavior of earthquakes may also

E. Vives (✉) · J. Baró · A. Planes
Departament de Física de la Matèria Condensada, Universitat de Barcelona,
Martí i Franquès 1, 08028 Barcelona, Catalonia, Spain
e-mail: eduard@ecm.ub.edu

E. Vives
Universitat de Barcelona Institute of Complex Systems (UBICS), Barcelona, Spain

J. Baró
University of Calgary, 2500 University Dr. NW Calgary, Calgary, AB T2N 1N4, Canada
e-mail: jordi.barourbea@ucalgary.ca

E.K.H. Salje et al. (eds.), *Avalanches in Functional Materials and Geophysics*,
Understanding Complex Systems, DOI 10.1007/978-3-319-45612-6_3

emerge in brittle fracture experiments. These empirical laws establish that a number of earthquake features are power-law distributed, which is the fingerprint of scale invariance. The Gutenberg–Richter, Omori, Productivity and Universal Scaling laws summarize this striking behavior.

The Gutenberg–Richter law describes the relation between magnitude and frequency of occurrence of earthquakes and can be expressed in the sense that earthquake energies are power-law distributed. Omori's law is concerned with the existence of aftershocks following a large event. It expresses how the rate of aftershocks decays with time and reveals the existence of correlations in the occurrence of earthquakes. The productivity law is connected with Omori's law and assumes that the rate of decay of aftershocks depends on the magnitude of the main event. However, these last two laws have raised some controversy since they depend on how the main event and the subsequent aftershocks are defined. When the study of correlations was acknowledged as providing a suitable method to forecast catastrophic events, numerical tools aimed at detecting earthquake correlations, which are independent of the definition of main event and aftershocks, were proposed. Along these lines, a new idea of universality has been suggested, which starts from analysis of the distribution of waiting or silent times between consecutive events. It has been noticed that while this distribution exhibits strong dependence on the studied catalogue (defined by the seismic process corresponding to a given region), distributions corresponding to different catalogues can be scaled into a universal function, which defines the Universal Scaling law.

The failure of porous materials subjected to compressional forces has recently received much attention not only in connection with earthquakes, but also due to its relevance in the collapse forecast of both natural and artificial structures such as mines, buildings, or bones. It has been shown that when mining materials are subjected to a compressive stress, failure can be heralded by significant precursor activity. In this precursor regime, the response of the system to the applied compressive stress has been shown to be not smooth and continuous as classically expected for elastoplastic materials, but, instead, occurs as a sequence of avalanches. Experimentally, it has been shown that avalanches stem from sudden changes of the internal strain field (displacement discontinuities), which usually lead to shrinking of the sample and can be detected by measuring the acoustic emission (AE) originating from contraction. AE avalanche behavior has been reported in a number of synthetic and natural (mineral) porous materials. The case of the porous glasses Vycor and Gelsil is especially appealing since the statistical characteristics of the AE events, or labquakes, has been shown to share strong similarities with seismicity arising from failure of the Earth's crust due to stresses induced from plate tectonics. In the present chapter we study the statistical features of energies, aftershocks and waiting times of labquakes detected from AE experiments in Vycor and Gelsil and compare the obtained behavior with those of earthquakes. The chapter is organized as follows:

In the two following subsections we present firstly a summary of the statistical laws that describe seismic activity in Sect. 3.1.1 and secondly the Epidemic Type Aftershock-Sequence (ETAS) model in Sect. 3.1.2 which is a phenomenological model that reproduces most of these laws. In Sect. 3.2 we present the experimental data. This includes details of the compression setup in Sect. 3.2.1, details of the

samples in Sect. 3.2.2, analysis of the shapes of individual signals in Sect. 3.2.3, correlations between different signal properties in Sect. 3.2.4, the statistical distribution of energies, amplitudes and durations of individual signals in Sect. 3.2.5, Omori's correlations in Sect. 3.2.6, distribution of waiting times in Sect. 3.2.7 and study of the local Poisson character of the signals in Sect. 3.2.8. Finally, in Sect. 3.3 we both summarize and draw conclusions.

3.1.1 Revisiting the Statistical Laws for Earthquakes

Earthquakes are complex phenomena that have been the focus of scientific studies in the last several hundred years. In this section we are mainly interested in reviewing the very general statistical and collective properties of earthquakes with the aim of comparing them with the acoustic emission that occurs during compression of materials in laboratory experiments. Thus, we will adopt a very simple, holistic description of earthquakes, reducing them to a sequence of events $k = 1, \ldots, N$ that occur at times t_k and at positions r_k, which can be characterized by a magnitude M_k. This is the standard information that can be found in the accessible public catalogues. Earthquake magnitudes are logarithmic estimations of the energy of an earthquake. Historically, the measurements were obtained from analysis of the consequences of the earthquake. Different quantitative methods have been proposed to measure magnitudes. Modern catalogues use the "moment magnitude" (M_w) which is obtained from the so-called seismic moment, which is an estimation of the energy released at the source of the event (fault area $\times$ mean displacement $\times$ shear rigidity). Despite the fact that such a measurement is not always accessible, we will systematically translate earthquake magnitudes to the so-called "minimum strain energy drop" using the commonly accepted relation:

$$\log_{10} E = (3/2)M_w + 4.8, \tag{3.1}$$

where the energy E is given in Joules. Typical recorded magnitudes are in the range 0–9, thus corresponding to a range of $\sim$14 orders of magnitude, from 10^4–10^{18} J. From now on, we will use the generic symbol M to denote the magnitude of earthquakes reported in catalogues, irrespectively of the exact details of its measurement.

To date, our laboratory experiments with porous materials (as will be reviewed in the next section) have been performed in small samples with typical sizes of several mm. Spatial location techniques are still not good enough to find the position of the source of the AE events at this resolution. Therefore, comparison with real earthquakes will be performed by neglecting the information related to their spatial correlations. In what follows, we will consider that an earthquake catalogue corresponds to the information $\{(t_k, E_k)\ k = 1, \ldots N\}$. Within mathematical language this is referred to as a marked stochastic point process [6].

Figure 3.1 shows examples of earthquake catalogues, which will be used to illustrate the examples in this section. Plots represent the cumulative number of events as a function of time and circle sizes indicate the energy of each event.

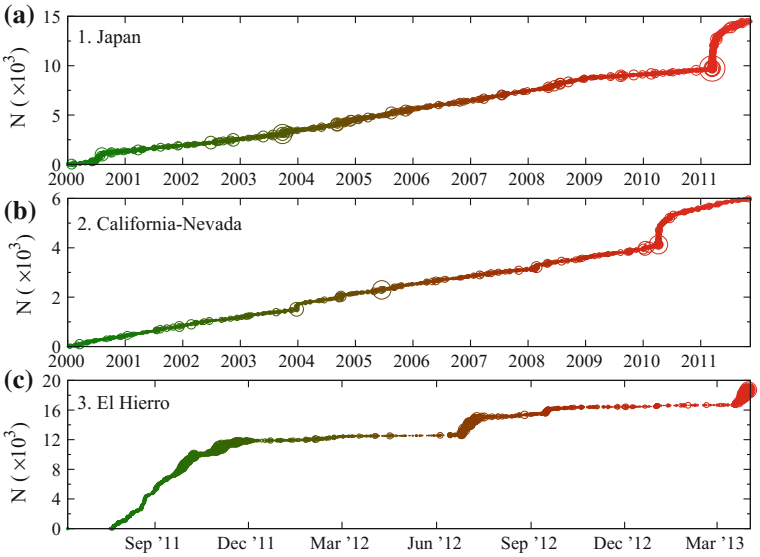

Fig. 3.1 Cumulative number of registered events as a function of time for three different catalogues defined in the text. The *circles* are proportional to the logarithm of the energy of each event. **a** Corresponds to Japan, **b** to California–Nevada and **c** to El Hierro

The first catalogue corresponds to the area of Japan and includes all the seismic events in the ANSS [7] catalogue from 2000/01/01,00:00:00 to 2011/11/09,17:32:36 within the region enclosed between latitudes 28 and 48°N and longitudes 128 and 148°E. The registered data correspond to the $N = 14509$ events above $M = 2.7$, where the Tōhoku earthquake of 2011/03/11 was the most serious event with an estimated magnitude of $M = 9.0$.

The second catalogue corresponds to the San Andreas Fault system beneath the region occupied by the states of California and Nevada. The data analyzed here corresponds to the seismic signals registered as earthquakes in the ANSS [7] catalogue with its epicenter located within the area of latitudes between 30 and 42°N and longitudes between 114 and 126°W during the period between 2000/01/01,00:00:00 and 2011/11/09,17:43:00. In order to avoid the presence of possible background noise, we selected only those earthquakes with a magnitude greater than $M = 0.4$. The largest earthquake, corresponding to Gorda plate, was recorded on 2005/06/15 off the Coast of Northern California with a magnitude of $M = 7.2$. The full data set has $N = 453372$ events.

As a third example we consider a completely different seismological phenomenon (very localized both in space and time): the recent submarine volcanic eruption of La Restinga off the island of El Hierro (Canary Islands), which started in the summer of 2011. The volcanic activity triggered an earthquake swarm [8] which was expected to have quite different behavior from typical tectonic processes. We considered the data obtained from the IGN [9] catalogue from 2011/06/08, 00:00:00 until 2013/02/04,

9:15:00 in the region limited by latitudes from 27.5 to 28.0°N and longitudes from 17.50 to 18.50°W. The data set has $N = 18877$ events.

There are four main empirical laws that describe the statistical properties of such stochastic processes:

1. **Gutenberg–Richter law** Given a sufficiently large catalogue, their energy distributions is such that the logarithm of the number of earthquakes with a magnitude larger than a certain value M, decreases linearly with M: $\log_{10} N_> \propto -bM$, with the slope b exhibiting values close to 1. Using the above-mentioned relation of the magnitude with the energy (3.1), the Gutenberg–Richter law [10] translates into a power-law distribution for energies:

$$p(E)dE \propto E^{-\varepsilon} dE, \tag{3.2}$$

with $\varepsilon = (2/3)b + 1$, that will typically take values close to $5/3 \simeq 1.67$. Nevertheless, it has also been suggested that ε could be closer to 1.33 (which corresponds to $b = 0.5$) [11]. Figure 3.2a shows examples of histograms corresponding to energy distributions of earthquakes in the three above-mentioned catalogues. As can be clearly seen the three catalogues render a power-law distribution of energies with almost the same slope when represented on log-log scales. The precise value of the exponent can be quantitatively fitted with the Maximum Likelihood (ML) method. A standard method to perform the fit consists of estimating ε while constraining the data to energies above a varying threshold E_{low}. The existence of a plateau extending for various decades in the plot of the fitted exponent versus E_{low} (as shown in Fig. 3.2b) indicates that data are well described by a power-law

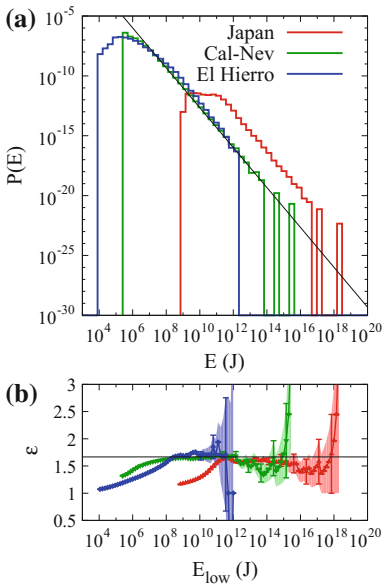

Fig. 3.2 **a** Energy distribution of earthquakes from three different catalogues as indicated by the legend. Note that bins are logarithmic. **b** Maximum likelihood fitted exponent as a function of the lower energy threshold E_{low}. The plateaus of the *three curves* reveal the value of a common critical exponent $\varepsilon \simeq 5/3$

distribution. In this case, the value $\varepsilon = 1.66$ is compatible with the three catalogues for a large number of decades. It should be mentioned that the ML method also renders an estimation of the error bars (also shown in Fig. 3.2b). However, these error bars do not take into account systematic sources of uncertainties and, therefore the true error bars should be enlarged significantly by comparing fits in different energy ranges, different catalogues, etc. More sophisticated methods have been described in [12–15].

2. **Omori's law** This is the first evidence of the non-Poisson character associated with instants of occurrence of earthquakes t_k. When a large earthquake (main shock, MS) has occurred in a certain region, there is a sudden increase in the rate of earthquake activity in the neighboring region [16, 17]. The subsequent extra events are called aftershocks. The rate of aftershocks r_{AS} (number of AS per unit time) after a time Δt from the mainshock decreases as:

$$r_{AS} = \frac{k}{(c + \Delta t)^p}, \tag{3.3}$$

where c is a constant that prevents the rate from diverging exactly after the mainshock, with values that range from 0.01 days to 1 day, k is a proportionality constant, and p is the Omori exponent that takes values in the range 1–1.6 [18, 19]. Note that the total number of AS after a certain MS will behave as

$$N_{AS} = \int_0^\infty r_{as} d\Delta t = k \frac{p-1}{c^{p-1}}. \tag{3.4}$$

If we want this number to be positive and finite, p should be larger than 1.
Two examples of Omori behavior can be seen in Fig. 3.3. They correspond to the aftershock sequences after the largest earthquakes in the Japan and California catalogues.

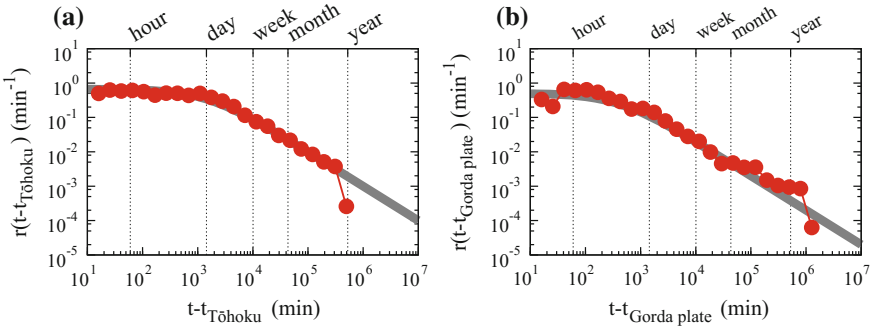

Fig. 3.3 Activity rate (number of aftershocks per minute) after two large earthquakes (Tohoku plate earthquake in Japan and Gorda plate earthquake in California–Nevada) as a function of the time to the mainshock, Note that time bins are logarithmic. The *thick gray lines* indicate the behavior of the theoretical Omori law with $p = 1$ and the constants $k = 1000$, $c = 1500$ min for Tohoku and $k = 200$, $c = 400$ min for Gorda-plate

Omori plots can be obtained not only for the largest earthquakes in a catalogue, but also for smaller ones. In fact, one might well consider as MS all the events in a certain energy range defined by two thresholds and then obtain the averaged Omori plots that reveal a similar trend to those corresponding to individual very large events.

3. **Productivity law** The productivity law [18] reveals the existence of correlations between the energies of the events and the aftershocks. It establishes a relation between the magnitude of the main shock M_{MS} and the total number of aftershocks induced by the MS. It can be expressed as:

$$\log_{10} N_{AS} = \alpha M_{MS} + \beta, \tag{3.5}$$

where β is a constant and α is an exponent that characterizes the power-law increase of the number of AS with the energy of the MS. The value of α has been found to be close to 0.8. When this law is expressed in terms of the main-shock energy E_{MS} and it is combined with the Omori law, the rate of aftershocks becomes

$$r_{AS} = k' \frac{E_{MS}^{\frac{2}{3}\alpha}}{(c + \Delta t)^p}, \tag{3.6}$$

where k' is a constant that depends on the energy threshold for the detection of events, and the time units selected for the definition of the rate. A consequence of this empirical formula is the so-called Båth's law that states that the strongest aftershock has typically a magnitude that equals $M_{MS} - 1.2$, as was shown by A. Helmstetter [18].

4. **Unified Scaling Law** This law has been discovered more recently [20]. It does not hold the same consensus as the previously mentioned laws within the seismology community. The Unified Scaling Law reveals the critical character of the earthquake random process. It refers to the statistical distribution of waiting times (or silent times) that we will denote as δ. These values can be recorded in a certain geographical region R, during a certain period T, after fixing a threshold E_0 for event detection. In general, the probability density for the waiting times $p(\delta)d\delta$ will depend on R, T and E_0, but it can be shown that all the spatial, temporal and energy dependences can be summarized within a unique function $\Delta(R, T, E_0)$, so that:

$$p_{R,T,E_0}(\delta)d\delta = \Phi\left(\delta/\Delta_{R,T,E_0}\right) \frac{d\delta}{\Delta_{R,T,E_0}}, \tag{3.7}$$

where Φ is a universal function expressing the Unified Scaling Law (USL). By integration, it is easy to check that the function Δ_{R,T,E_0} is proportional to the average waiting time $\langle\delta\rangle$ or equivalently, inversely proportional to the average rate $\langle r\rangle$. These quantities can be estimated from the total number of signals of the catalogue and the total duration of the catalogue T

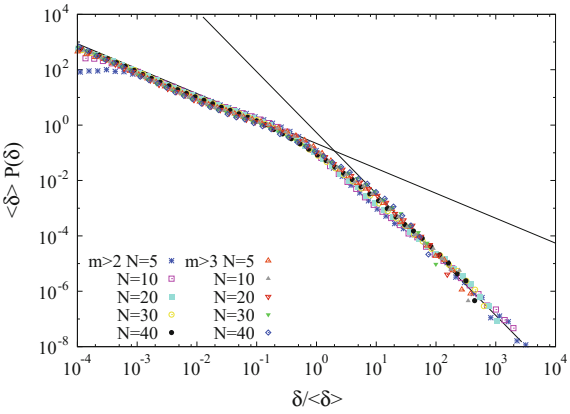

Fig. 3.4 Distribution of waiting times $p(\delta)$ corresponding to a small region with a width of 5° in latitude and longitude (31–36N, 120–115 W) for different magnitude (energy) thresholds. The *lines* show the double power-law behaviors, with exponents $-(1-\nu) = -0.75$ and $-(2+\xi) = -2.2$ as explained in the text

$$\langle \delta \rangle \simeq \frac{T}{N} \simeq \langle r \rangle^{-1}. \tag{3.8}$$

Consequently, the waiting time distributions from different regions, different time periods and corresponding to different energy thresholds should overlap when represented as $\langle \delta \rangle p(\delta)$ versus $\delta/\langle \delta \rangle$, or as $p(\delta)/\langle r \rangle$ versus $\delta \langle r \rangle$. There has been some discussion about the shape of the universal function Φ [21]. If the analyzed set of δ values correspond to mixtures of regions and include data from areas with clearly different activity rates, or if the durations of the studied catalogues are large enough so that there have been strong fluctuations in basal earthquake activity, the function Φ should show a double power law shape

$$\Phi(x) \propto \begin{cases} x^{-(1-\nu)} & \text{if } x \ll 1 \\ x^{-(2+\xi)} & \text{if } x \gg 1, \end{cases} \tag{3.9}$$

where the exponents are $\nu \sim 0$ and $\xi \sim 1$. Examples of these universal scaling laws can be obtained, for example, by restricting the data to sub-catalogues of small enough regions that have undergone repeated changes of activity rate within many orders of magnitudes. Figure 3.4 shows some of these examples corresponding to subregions of the California–Nevada catalogue. If the catalogues correspond to regions and time windows in which the basal activity rate is constant for the whole duration of the catalogue (as usually occurs when catalogues extend to vast regions), then Φ shows exponentially damped power-law behavior:

$$\Phi(x) \propto x^{-(1-\nu)} \exp -x/\theta, \tag{3.10}$$

where θ is a characteristic scale.

An example of this scaling can be seen in Fig. 3.5 which shows the behavior of $p(\delta)$ for the full catalogues corresponding to Japan and California–Nevada. For these large

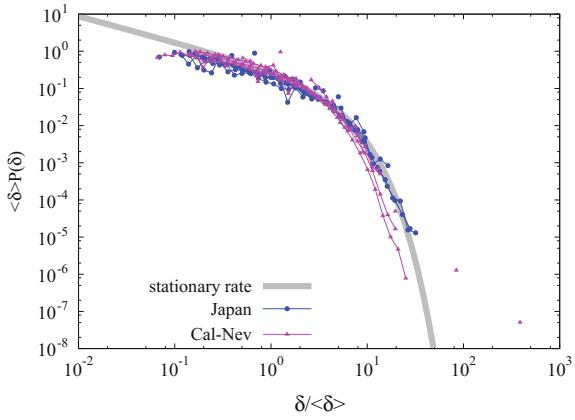

Fig. 3.5 Distribution of waiting times corresponding to the full catalogues of Japan and California–Nevada, as indicated by the colors. The *different lines* correspond to different energy thresholds. The *gray line* shows an exponentially damped power law with $-(1-\nu) = -1.45$

areas, activity rates are relatively constant, and thus one obtains the exponentially damped behavior for the Universal Scaling Law $\Phi(x)$.

Omori's law, the Productivity Law and the USL reveal the existence of correlations, but their behavior can be affected also by the non-homogeneous character of the activity rate.

Bi et al. [22] proposed an statistical test some years ago that reveals whether or not a process is locally compatible with a Poisson process (uncorrelated), independently of the fact that the activity rate may vary in time. The test considers all the events above a certain threshold occurring at times t_k with $k = 1, \ldots, n$. For each event we define a variable H_k as follows:

$$H_k = \frac{\delta t_k}{\delta t_k + \frac{1}{2}\delta\tau_k}, \tag{3.11}$$

where δt_k is the minimum of the temporal distances $t_{k+1} - t_k$, and $t_k - t_{k-1}$, and $\delta\tau_k$ is measured as

$$\delta\tau_k = \begin{cases} t_{k+2} - t_{k+1} & \text{if } t_{k+1} - t_k < t_k - t_{k-1} \\ t_{k-1} - t_{k-2} & \text{if } t_k - t_{k-1} < t_{k+1} - t_k. \end{cases} \tag{3.12}$$

A rather simple analysis shows that if the process is locally Poisson, the values H_k should be uniformly distributed between 0 and 1. Thus, one can apply a Kolmogorov–Smirnov test to check whether the values H_k are compatible with a uniform distribution. This is done by comparing the experimental cumulative distribution function $F_n(H)$ with the theoretical cumulative distribution function of a uniform random variable $F(H) = H$, both functions defined in the interval (0, 1). Bi test plots usually show the difference $\Delta f(H) = \sqrt{n}\,(F_n(H) - H))$. By fixing a confidence level it is possible to obtain the thresholds indicating the limits of acceptance of $\Delta f(H)$. The plots typically correspond to one of the three situations illustrated in Fig. 3.6.

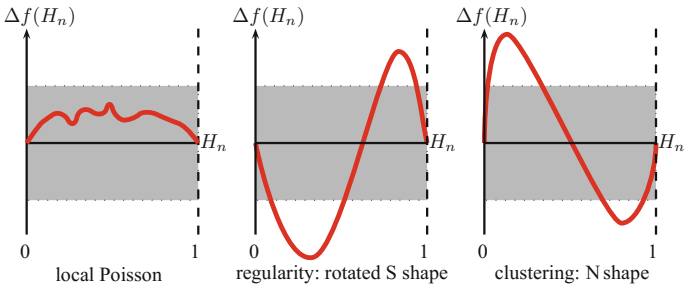

Fig. 3.6 The three kinds of outcomes expected from a Bi test for the local Poisson hypothesis. *Gray shadows* indicate the limits for acceptance of the hypothesis at a certain confidence level

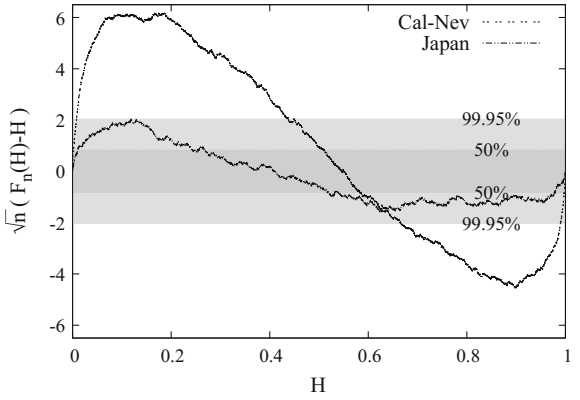

Fig. 3.7 Kolmogorov–Smirnov test revealing that data from the California–Nevada and Japan catalogues is not compatible with a Poisson hypothesis when one considers a 99.5% confidence level

If $\Delta f(H)$ never exceeds the thresholds (see left-hand panel in Fig. 3.6), the local Poisson hypothesis is accepted. If the curve exceeds the threshold levels, the local Poisson hypothesis cannot be accepted. The rotated "S" shape in the central panel of Fig. 3.6 reveals an excess of H_k values concentrating at $H = 2/3$. This is indicative of a process which is more regular than expected for a Poisson hypothesis. On the other hand, the "N" shape of the right-hand panel, evidences an excess of small H values, indicating the existence of data clustering. This N shape is what is expected when Omori's aftershocks occur. Figure 3.7 shows that the California–Nevada and Japan catalogues exhibit correlations, in particular clustering of data due to the aftershocks.

3.1.2 ETAS Model

The Epidemic Type Aftershock Sequence (ETAS) model was introduced by Ogata in 1988 [23]. Despite the fact that the model does not contain many physical ingredients, it provides understanding of the difference between events caused by endogenous effects (essentially aftershocks) and those caused by exogenous effects such as, for

instance, an increase of the driving rate. The model incorporates the Guttenberg–Richter law, Omori's law and the productivity law. As already mentioned, here we discuss a simple version of the model for which the location of the events is not taken into account.

The random occurrence of an event during an interval $(t, t + dt)$ is determined by an intensity function $\mu(t)$ that accounts for the rate of events at time t. In the trivial case, the intensity is constant $\mu(t) = \lambda$, and the model renders a pure Poisson process with independent occurrence of events. In a certain time interval Δt, the average number of events is $\langle N \rangle = \lambda \Delta t$ and the waiting times between events are exponentially distributed according to

$$p(\delta)d\delta = \lambda e^{-\lambda\delta} d\delta. \tag{3.13}$$

Instead, in the ETAS model, a key point is assumed that the intensity $\mu(t)$ increases additively each time t_k that an event occurs with energy E_k by a term $\phi_k(t)$ given by

$$\phi_k(t) = K \frac{(E_k/E_0)^{2\alpha/3}}{(c + t - t_k)^{1+\theta}} \quad \text{when } t > t_k. \tag{3.14}$$

The values of E_k are drawn randomly and independently according to a (Gutenberg–Richter) power-law normalized between E_0 and ∞, given by

$$p(E)dE = (\varepsilon - 1)\frac{E_0^{\varepsilon-1}}{E^{\varepsilon}} dE. \tag{3.15}$$

The dependence of ϕ_k on $E_k^{2\alpha/3}$ in (3.14) allows the productivity law to be reproduced. The denominator with an exponent θ is introduced in order to get Omori-like behavior. At a given time t the intensity $\mu(t)$ depends, therefore, on all the previous events as:

$$\mu(t) = \mu_0(t) + \sum_{k;t_k<t} \phi_k(t) = \mu_0(t) + \sum_{k;t_k<t} K \frac{(E_k/E_0)^{2\alpha/3}}{(c + t - t_k)^{1+\theta}}, \tag{3.16}$$

where $\mu_0(t)$ accounts for the external changes of the basal rate and the sum for all the cumulated endogenous effects.

Figure 3.8 shows an example of a numerical simulation giving a sequence of events generated by the ETAS model. It is interesting to compare qualitatively some of the features with Fig. 3.1. In particular, the existence of rounded steps in the cumulative number of events after large events. The lower panel shows the corresponding evolution of $\mu(t)$ with time.

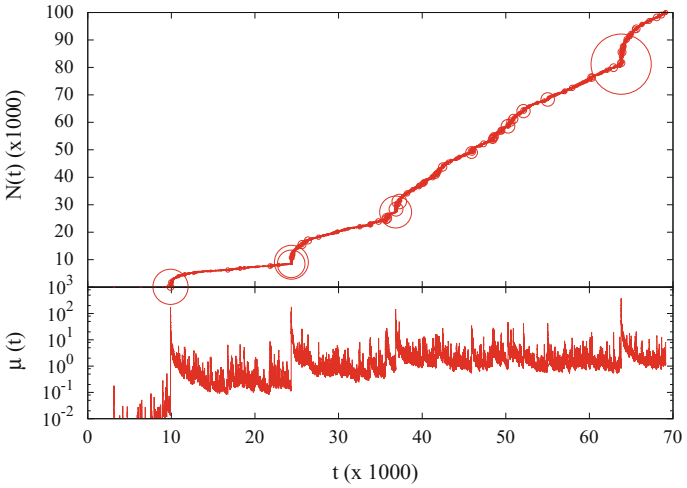

Fig. 3.8 Cumulative number of events as a function of time generated by an ETAS model with parameters $\theta = 0.3$, $c = 2$, $k = 0.1$, $\alpha = 0.5$, $\varepsilon = 1.67$ and a basal rate evolving in time according to $0.1(1 + cos(\pi t/100000))$

The average number of events that can be considered as directly generated by an individual main-shock at t_k with energy E_k can be estimated from (3.14) as [24]:

$$n = \int_{t_k}^{\infty} dt \int_{E_0}^{\infty} dE_k \phi_k(t) p(E_k) = K \frac{\varepsilon - 1}{c^{\theta}(\varepsilon - 1 - 2\alpha/3)} \int_0^{\infty} \frac{dz}{(1+z)^{\theta+1}} = \\ = K \frac{\varepsilon - 1}{\theta c^{\theta}(\varepsilon - 1 - 2\alpha/3)}. \tag{3.17}$$

The latter equality only holds if $\theta > 0$.

The relation between the exponent θ of the ETAS model and the exponent p of the observed Omori behavior is not fully evident. Essentially, when one considers the decrease of the rate after a large event in the ETAS model, one observes not only the direct events produced by the MS (first generation of AS), but also a second generation of AS, a third generation of AS, etc. Thus, the exponent θ does not correspond to the Omori exponent p.

It is interesting to note that analysis of the waiting times in simulations of the ETAS model do also reveal the existence of a Unified Scaling Law. When the basal rate term $\mu_0(t)$ is constant, one obtains the USL defined in (3.10). However, if one considers a basal activity rate that changes in time by many orders of magnitude, one gets the double power-law USL given in (3.9). For example, in Fig. 3.9 we show the distribution of waiting times obtained with an ETAS model for which the basal activity rate changes in time according to a sinusoidal function.

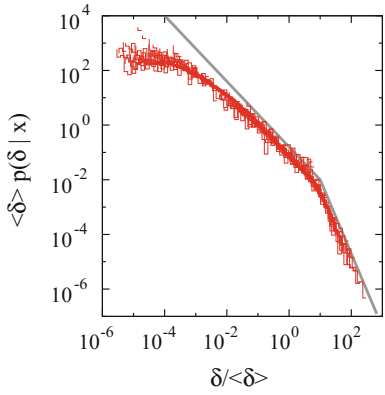

Fig. 3.9 Distribution of waiting times corresponding to different energy thresholds and scaled with the mean waiting time. Parameters for the simulation are the same as in the previous figure. *Lines* indicate the double power-law behavior

3.2 Experimental

3.2.1 Compression and Acoustic Emission Setup

The uniaxial compression setup consists of two parallel aluminum plates. The lower plate hangs from the load cell at the top of the arrangement and is static. The upper plate is pulled downwards at constant force rate dF/dt by guiding rods which slide along three Teflon-covered holes in the bottom plate. The contact zone of the upper and lower plates with the compressed sample is reinforced by embedded stainless steel disks in order to minimize noise due to indentation.

A mechanism allows a constant stress rate to be applied. It consists of a large container (up to 100 l) hanging from the guiding rods. The mechanical setup includes ball and socket joints that ensure a good alignment of the setup and the sample. A controlled water flow increases the weight of the container by means of a small pump that allows flows as small as 0.001 l/s.

A laser extensometer (*Fiedler Optoelektronik*) measures the vertical separation between the plates, h, with a nominal resolution of 50 nm. Unavoidable mechanical and electrical noise, nevertheless, increase the absolute uncertainty in h up to 200 nm. The load cell (1 kN range) signal is measured with a lock-in amplifier and has been calibrated with standard weights. The resolution is about 1 N. During compressive stress, the release of localized strain energy in the sample through acoustic emission (AE) is measured. The AE signal is detected by piezoelectrics transducers embedded in the compression plates and mechanically coupled by a thin layer of vaseline to the stainless steel disks. The transducers are centered at a distance of 2 mm from the sample surface. The sensors are encapsulated in stainless steel to reduce electrical noise. The electric signals from the transducers are pre-amplified (60 dB), band filtered (between 100 kHz and 2 MHz) and transferred to a PCI-2 acquisition system from Europhysical Acoustics (*Mistras group*) working at a nominal time resolution of 40 MHz. The registered signal is a voltage $U(t)$. For identification of individual

AE events (also called hits), a threshold U_{th} above the instrumental noise is set. In most of our experiments it is fixed at a value between 23 dB (=0.0141 V)–27 dB (=0.0224 V). A hit is defined to start with the first crossing of the threshold. The end time of a hit is the time at which the signal voltage falls below the threshold and remains below it for more than a preset hit detection time (HDT = 100 μs). After the hit has finished, the system re-arms again in a short time called the Hit Lockout Time, fixed at HLT= $2\mu s$, and is ready for the detection of new signals. Changes of these parameters do not affect the analysis presented below very much. Recently a detailed analysis of the influence of the threshold, HLT and HDT parameters on the critical exponents has been presented for the case of AE associated with dislocation movement [29].

Once individual signals are identified, several characteristic properties can be measured. Here we concentrate on hit energies E, amplitudes A and durations D. The system allows the energies of the hits to be determined by fast numerical integration of the square voltage $U(t)^2$, as

$$E = 1/R \int_{t_i}^{t_f} U^2(t)\, \mathrm{d}t, \tag{3.18}$$

where t_i and t_f are the starting and ending times of the signal and $R = 10k\Omega$ is a reference resistance. The duration of the events is given by $D = t_f - t_i$, and the amplitude A is a logarithmic measurement (given in dB) of the maximum voltage of the hit, U_{max} given by

$$A = 20 \log_{10} \left(\frac{U_{max}}{1V} \right) + 60. \tag{3.19}$$

Waiting times between signals correspond to the elapsed time between starting times of consecutive signals. The AE activity is defined as the number of hits registered per unit time (measured over large intervals, typically above 1 s).

3.2.2 Vycor and Gelsil Samples

In this chapter we will summarize the uniaxial compression experiments performed with different mesoporous synthetic silica (SiO_2) glasses [3, 26, 27]. Experiments on other synthetic compounds [25] and natural minerals [26, 28] have also been carried out. As a general trend, experiments performed with natural minerals or with synthetic porous materials but not based on SiO_2 render much fewer AE signals (above the threshold) during the compression experiments. This implies that statistical error bars associated with any measured property (exponents, averages, etc.) are much larger. Other observed deviations for natural minerals will be discussed in Sect. 3.3.

We have studied three types of synthetic SiO_2 materials: Vycor, Gelsil 2.6 and Gelsil 5. Porous Vycor 7930 is synthesized (Corning Inc. NY) via phase separation of a $Na_2OB_2O_3$-SiO_2 melt, followed by leaching, which leaves a 98% pure SiO_2

Table 3.1 Pore characteristics of the studied materials and Vycor. Data for Gel2.6, Gel5 and Vyc are from [30]. The density of quartz is 2.648 g/cm^3

	Gel2.6	Gel5	Vyc
Average pore diameter (nm)	2.6	5.0	7.5
Density (g/cm^3)	∼1.6	∼1.2	∼1.5
Porosity ϕ	0.36	0.54	0.40

skeleton containing interconnected pores of random length, direction and density. Pores in our samples show a mean diameter of 7.5 nm and a rather narrow pore-size distribution (as obtained from N_2-adsorption experiments and BET/BJH analysis). Nevertheless, it should be clarified that analysis of samples purchased in different years shows a certain variability of this mean diameter between 6 and 10 nm. After cutting and sanding, cleaning of these samples is carried out using a 30% solution of H_2O_2 for 24 h. Drying is done under vacuum at 400 K for another 24 h.

Gelsil monoliths are produced (4F International Co., Gensville, FL) in a sol-gel process by hydrolization of silica containing precursor liquids, followed by condensation and heat treatment. Silica molecules condense to spheres on stochastic sites within the hydrolized silica precursor. Subsequent gelation, drying and consolidation leads to a network-like arrangement of pure silica spheres or grains. The voids between these spheres constitute a random network of interconnected corridors and pockets and show a large pore size distribution. Mean void diameters of 2.6 and 5.0 nm are found in our Gelsil 2.6 and Gelsil 5 samples, respectively, from N_2-adsorption experiments and BET/BJH analysis [30]. Cylinder shaped samples were cut from the initial Gelsil samples. Before the compression experiments, Gelsil samples were cleaned with a 30% solution of H_2O_2, for 24 h and dried at 130 °C. The main characteristics of the three kinds of studied samples are summarized in Table 3.1.

Typical compressed specimens are prismatic, with initial heights of $5 \sim 6$ mm and transversal sections in the range $12 \sim 45$ mm^2. The exact values of the transversal sections are chosen in order to be able to fully break the sample with less than 1000 N (this is a limitation of our experimental setup). Different transversal shapes were studied: circular, semicircular, squared, and irregular. The results that we will discuss do not seem to depend on this shape. Note that the initial transversal section may well change after the first small avalanche events. Typical compression rates range between 0.2 to 7 kPa/s. For the case of Vycor a fast experiment was performed at 12.2 kPa/s.

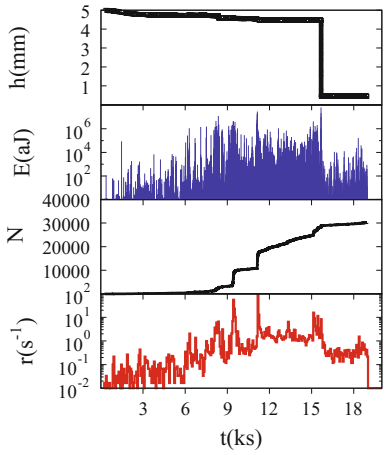

Fig. 3.10 Summary of a typical compression experiment of a Vycor sample. The *upper panel* shows the sample height as a function of time. The *second panel* indicates the energies of the individual AE signals recorded during the experiment. The *third panel* shows the cumulated number of signals and the *lower panel* shows an estimation of the rate evaluated in time intervals of 100 s

3.2.3 Avalanches During the Compression Process

Figure 3.10 shows a typical example of a compression experiment of a Vycor sample. The sample transversal section was 16.99 mm^2, and the compression rate 1.6 kPa/s. The top panel shows the evolution of the height of the sample as a function of time, as registered by the laser extensometer. One can clearly distinguish the existence of steps. The largest one corresponds to the collapse of almost the whole sample. The height decreases by a 80% of the initial sample height. The second panel corresponds to the energies of the individual AE signals recorded by the transducers in the compression plates. It is clear that AE events already start from the beginning of the experiment. For the first initial 4000 s it seems that the energy of the signals is not as large as for the remaining events. Note the vertical logarithmic scale. This could be due to the fact that the sample surface is in a process of adapting to the compression plate during the early stages. The most energetic events occur at times that correspond to the steps in the sample height, but not only at these times. Some large events are not clearly correlated with changes in sample height. It is also interesting to note that after the large collapse occurring at ∼15500 s, there are still many AE signals recorded, some of which have still quite large energies. This activity corresponds to the compression of the debris between the plates. As will be seen, from a statistical point of view, its behavior is pretty similar to the behavior of the initial sample.

The third panel shows the cumulated number of recorded signals, which reaches a number above 3×10^4 signals at the end of the experiment. The interest of this plot is that it reveals that there are steps corresponding to a clear increase of activity and that these steps occur abruptly but end smoothly, displaying a rounding behavior. This is an indication of the existence of aftershocks. It is interesting to compare this panel with the Figs. 3.1 and 3.8 corresponding to real earthquake catalogues and to ETAS model simulations, which shows similar trends. The lower panel in Fig. 3.10 shows the activity rate, calculated over time windows of 100 s. As can be seen, the

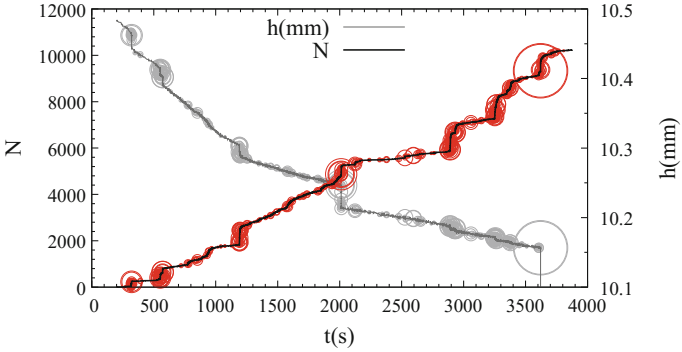

Fig. 3.11 Detail of the initial part of a typical compression experiment of a Vycor sample. The *decreasing curve* shows the evolution of the sample length in time, while the *increasing curve* shows the cumulated number of AE signals. *Circles* indicate the energy of the largest individual signals. The *smallest circles* correspond to signals with 10^2 aJ while the largest one represents a signal with more than 10^8 aJ. The value of h on the right-hand scale corresponds to the distance between marks on the compression plates. The real sample height was 9.80 mm

rate exhibits variations that expand several orders of magnitudes during the whole experiment, from 10^{-2} events per second to 10^2 events per second.

Interestingly many of the observed features remain unaltered when the plots are magnified $\times 10$ or $\times 100$. Figure 3.11 shows a magnification of the initial part of a compression experiment of another Vycor sample. In this case the sample is prismatic, with a transversal surface of 28.13 mm^2 and the compression rate was 7.0 kPa/s. Only the initial decrease corresponding to the first compression of 0.4 mm before the big collapse is shown. This plot allows us to see in detail the correlation between the most energetic events and the increase of activity in detail, in a very similar way to that described by the function μ of the ETAS model.

It is also interesting to study the response of the system under repeated cycling. Figure 3.12 corresponds to a sequence of compression-decompression loops, which reach, during each loop, higher and higher loads approaching the failure strength. In all cases the load after each loop is decreased back until 80 N. The left-hand panel shows height versus load trajectories and the right panel shows the height versus time, with circles indicating where large AE signals have been detected. Three interesting results should be pointed out: (a) Firstly, a large fraction of the strain is recoverable when the load is decreased. Part of the deformation is thus elastic. (b) Secondly, the decreasing-load branches show a certain degree of hysteresis and almost no AE. (c) As regards the loading branches, AE mostly occurs when the load exceeds the maximum load reached in the previous cycle. Associated with the existence of this AE at the end of a load branch, when the load is reversed, a certain amount of unrecoverable deformation occurs. Look at, for example, the third loop which exhibits a great deal of AE and, correspondingly, final strain after releasing the load increased by more than 0.05 mm.

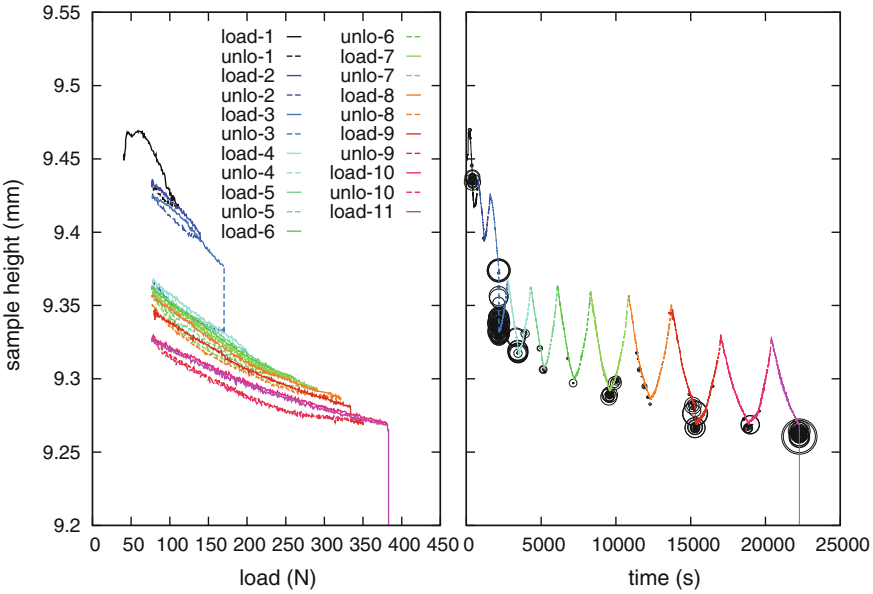

Fig. 3.12 Sequence of repeated compression experiments up to greater and greater loads. *Left-hand panel* shows the sample height against the applied load. *Right-hand panel* shows sample height against time. *Black circles* indicate the energies of the detected AE signals

This result shows that AE is essentially associated with fracture events. The deformation process, elastic or not, does not produce AE.

As in Vycor, uniaxial compression in Gelsil occurs very similarly, by jumps in strain release until the major collapse at the failure point [26]. The failure strength is, however, much higher in Vycor (∼30 MPa) than in Gelsil (∼1 MPa for Gel2.6 and ∼8 MPa for Gel5). This led us to perform experiments using much smaller transversal sections. The larger strength of Vycor has been suggested to be a consequence of its non-granular nature.

3.2.4 Correlations Between Properties of Individual Signals

An interesting preliminary analysis of the properties of the individual hits is to determine whether or not, the energy E, the duration D and the amplitude A are independent variables that carry information about different physical properties of the physics of the source events that generate the AE avalanches. This can be easily studied by plotting bivariate frequency maps of the signals recorded during the whole compression experiments [31]. Figures 3.13, 3.14 and 3.15 show the A versus D, the E versus A and the E versus D maps corresponding to three experiments done on Vycor at different compression rates: 0.2, 1.6 and 12.3 kPa/s. Color scale indicates the density of recorded signals.

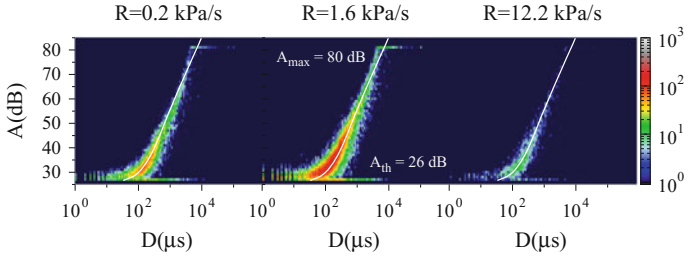

Fig. 3.13 Bivariate maps of Amplitudes versus Durations of recorded AE signals during the compression of Vycor samples for three different compression rates. The *white line* corresponds to the numerical solution of the model described in the text

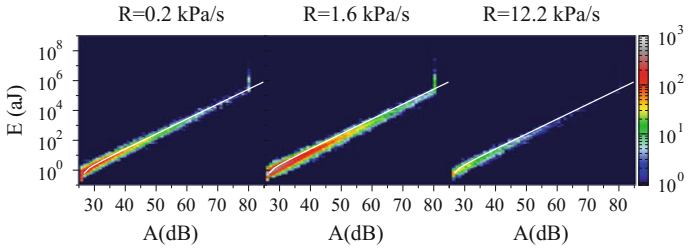

Fig. 3.14 Bivariate maps of Energies versus Amplitudes of recorded AE signals during the compression of Vycor samples for three different compression rates. The *white line* corresponds to the numerical solution of the model described in the text

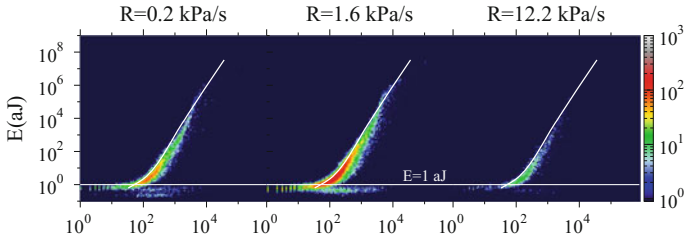

Fig. 3.15 Bivariate maps of Energies versus Durations of recorded AE signals during the compression of Vycor samples for three different compression rates. The *white line* corresponds to the numerical solution of the model described in the text

The first surprising result is that the bivariate distributions exhibit sharp crests along well defined lines, thus indicating strong statistical correlations between these three variables. This is a first indication that avalanches have an intrinsic shape $\phi(t)$ characterized by very few degrees of freedom. In fact, within the context of critical systems, it has been proposed [32] that avalanche profiles should follow a model that predicts a universal "shape" function Ξ according to:

$$\phi(t) = \begin{cases} 0 & \text{if } t < T \\ T^{\gamma}\,\Xi(t/T) & \text{if } 0 < t < T \\ 0 & \text{if } t > T, \end{cases} \tag{3.20}$$

where Ξ is typically chosen as a simple function exhibiting a peak, like a parabola. In the simplest case, even a rectangular shape with constant Ξ can be considered.

Therefore, avalanche signals are expected to be characterized by only two parameters: T which will be called true duration and the exponent γ. Note that γ relates the maximum value of $\phi(t)$ with T according to $\phi_{max} \propto T^{\gamma}$. Note that we have defined a true duration T differently from the measured duration D. One should take into account the fact that in the AE measurements the physical avalanche signal at the source $\phi(t)$ (which might correspond, for instance, to the speed of the advancing fractures) is distorted due to transmission through the sample, contact with the transducer, and due to the transducer and preamplifier responses. A very simple hypothesis is that the measured voltage signal (recorded by the experimental setup) is given by the following convolution:

$$U(t) = Ge^{i\omega_0 t} \int_{-\infty}^{t} dt' T^{\gamma}\,\Xi(t'/T) e^{-\frac{t-t'}{\tau}}\,, \tag{3.21}$$

where ω_0 is the characteristic frequency of the transducer and G and τ are the gain and the time constant of the acquisition system. Assuming that $\Xi(z)$ is a rectangular shape (with $\Xi = 1$ for $0 < z < 1$ and $\Xi = 0$, otherwise) it is possible to calculate the relation between the measured maximum voltage U_{max} and the measured duration D with the parameter T and the exponent γ [31]:

$$U_{max}(T) = \tau G T^{\gamma}\left(1 - e^{-T/\tau}\right) \simeq \begin{cases} G T^{\gamma+1} & \text{for } T \ll \tau \\ \tau G T^{\gamma} & \text{for } T \gg \tau \end{cases} \tag{3.22}$$

$$D(T) = \tau \ln\left(\frac{\tau G T^{\gamma}}{U_{th}}\left[e^{T/\tau} - 1\right]\right) \simeq \begin{cases} \tau \ln\left(\frac{G T^{\gamma+1}}{U_{th}}\right) & \text{for } T \ll \tau \\ T + \tau \ln\left(\frac{\tau G T^{\gamma}}{U_{th}}\right) & \text{for } T \gg \tau \end{cases} \tag{3.23}$$

Note that within this model we will get essentially $D \simeq T$ for signals with a true duration larger than the system characteristic response ($T \gg \tau$). From (3.22) one can then deduce that $U_{max} \propto D^{\gamma}$ and consequently $A = 20 \log_{10} U_{max} + 60 \propto 20\gamma \log_{10} D$. This justifies the linear behavior observed in the panels of Fig. 3.13. A straight line fit to the linear part of the crest renders $\gamma = 1.4$. The curvature observed for small values D is also justified by numerically fitting the model given by (3.22) and (3.23), as shown by the white line. From the fits, one can confirm the same value of γ, and also get $\tau = 75\mu$s and $\log_{10} G = 13.9$ V.

Deviations from the proposed model can be easily interpreted as arising from saturation of the amplifier for $A = 80$ dB, and the presence of background noise below $A = 26$ dB or $E = 1$ aJ which corresponds to the threshold in this case.

Using the preceding assumptions, one can compute the integral of the square detected signals $U(t)^2$ and obtain [31] the following expression for the energy of the individual hits:

$$E(T, U_{max}) = \frac{\tau}{2R}\left(\frac{\frac{T}{\tau} - 1 + e^{T/\tau}}{\left(1 - e^{-T/\tau}\right)^2} U_{max}^2 - \frac{1}{2}U_{th}^2\right). \tag{3.24}$$

This expression justifies the behavior $log_{10}E = 0.1A$ (equivalent to $E \propto U_{max}^2$) that can be observed in the panels of Fig. 3.14 for moderate and large amplitudes A. Similarly, the model does also explain the E versus D dependence in Fig. 3.15 as shown by plotting the numerical solution of the model (white line) over the experimental bivariate histogram map.

3.2.5 *Statistical Distributions of Energies, Amplitudes and Durations*

Figures 3.16, 3.17 and 3.18 show histograms corresponding to the marginal distributions of energies, amplitudes and durations for Vycor [3, 27] and the two Gelsil specimens [26]. Data correspond to the set of AE hits recorded from full compression experiments. The panels below show the ML analysis revealing that the right-hand tails of the three histograms can be well described by power-law distributions. As can be observed the distribution of energies $p(E)$ decays as $E^{-\varepsilon}$ with $\varepsilon = 1.40 \pm 0.05$

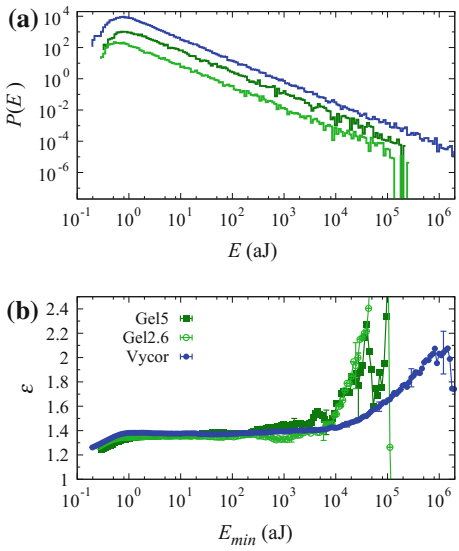

Fig. 3.16 **a** Distribution of energies corresponding to Vycor and Gelsil compression experiments. **b** Power-law exponents fitted with the ML method as a function of the lower energy cutoff

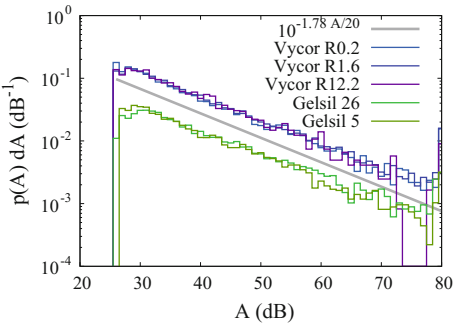

Fig. 3.17 Distribution of amplitudes corresponding to Vycor and Gelsil compression experiments. The line shown corresponds to the exponent $a = 1.78$

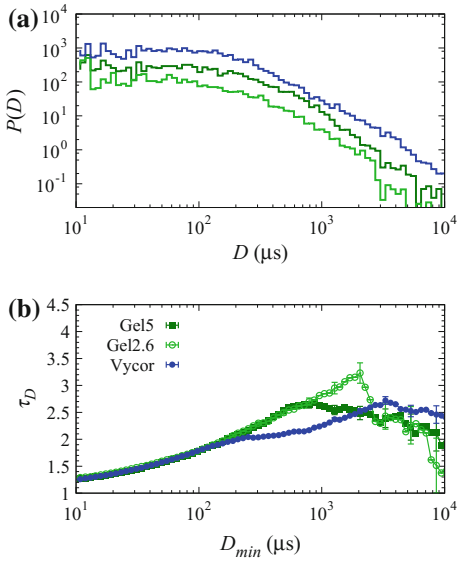

Fig. 3.18 **a** Distribution of durations corresponding to Vycor and Gelsil compression experiments. **b** Power-law exponents fitted with the ML method as a function of the lower energy cut-off

for at least 5 decades for the case of Vycor. Detailed fits also give $\varepsilon = 1.37 \pm 0.03$ and $\varepsilon = 1.36 \pm 0.03$ for Gelsil 2.6 and Gelsil 5, respectively, for at least 3 decades. This is good evidence of a lack of a characteristic scale of the AE events, in a way that is very similar to the Gutenberg–Richter Distribution for earthquakes. The three histograms could well be described by a common exponent. The distributions of amplitudes in Fig. 3.17 also shows very good linear behavior in this semilog plot. This means a dependence $p(A) \simeq 10^{-aA/20}$ with $a \simeq 1.78$. Note that, given that A is a logarithmic measure of U_{max} (see 3.19) this is equivalent to power-law behaviour for $p(U_{max}) \sim U_{max}^{-(a+1)}$.

The distribution $p(D)$ also shows a power-law tail but, apparently, with an anomalous plateau for low values of D. This is not surprising and can be easily understood from the bivariate maps in Figs. 3.13 and 3.15. The experimental lower cut-off in amplitudes at 26 dB (or energies at 1aJ) does not allow all the signals that with

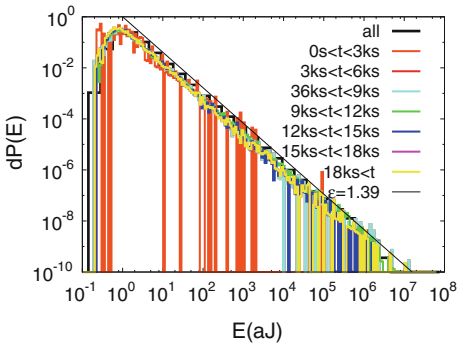

Fig. 3.19 Distribution of energies corresponding to a Vycor compression experiments. The different histograms correspond to different time windows throughout the full experiment, as indicated in the legend

exhibit small durations to be recorded, except for the fraction that turns out to have large enough amplitudes. Thus, the correct physical behavior describing our experimental data, which is not affected by the limitations of our set-up, corresponds to the right-hand tail of $p(D)$, which is also a power-law.

It is also very interesting to note that such distributions of energies, amplitudes and durations are quite stable throughout the duration of the experiment [3]. To illustrate this fact, we show the distributions of energies corresponding to the compression experiment of Vycor at a rate of 1.6 kPa/s in Fig. 3.19. The different histograms correspond to data recorded during time windows of 3000 s, as indicated by the legend. The AE activity of this experiment has been shown in Fig. 3.10. Note that the histogram of energies for the initial 3000 s corresponds to data recorded quite away from the large collapse of the sample. Despite this fact, the distribution of energies is very similar to the one corresponding to the central parts of the experiment. Something similar can be said about the final 3000 s of data, which correspond to signals recorded after the large collapse, when essentially only small pieces of debris are being compressed.

Finally, it should also be noticed that the distributions of energies are also quite stable when the compression rate is changed within reasonable values (0.2–12.2 kPa/s) [3, 27]. See Fig. 3.20 for an illustrative example. Fitting the exponents with the ML method does not see significant differences between the three studied rates, which fall in the range $\varepsilon = 1.40 \pm 0.05$.

Very recently we have repeated the measurements on more than 30 samples of Vycor with different shapes, aspect ratios, and corresponding to different synthesis processes with slightly different porosities. We have obtained a more conservative estimation of $\varepsilon = 1.37 \pm 0.06$, which is more similar to the values found for Gelsil.

3.2.6 Omori Correlations

The lack of characteristic scales in energies, durations and amplitudes suggests a strong similarity of the AE during the compression of porous materials and real

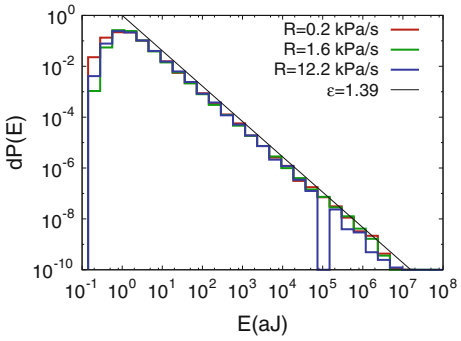

Fig. 3.20 Distribution of energies corresponding to Vycor compression experiments at three different compression rates. The *line* indicates the slope corresponding to the exponent $\varepsilon = 1.39$

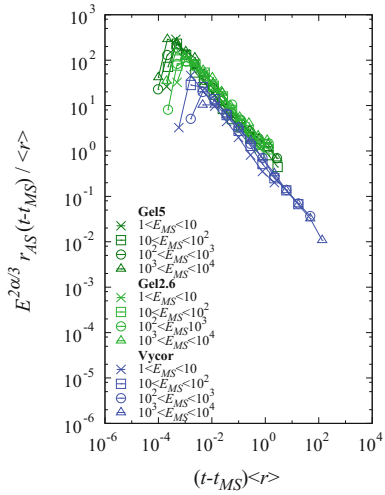

Fig. 3.21 Rate of aftershocks after MS above a certain threshold (as indicated by the symbols in the legend) as a function of the time distance from the mainshock. The vertical scale has been scaled by dividing by the mean activity rate $\langle r \rangle$ and the factor $E_{MS}^{2\alpha/3}$. The horizontal axis has been scaled by multiplying by $\langle r \rangle$

earthquakes. In the remaining subsections, we will see that these similarities also extend to the existence of time correlations in the sequence of recorded AE events.

The first possible analysis is to study the behavior of the activity rate after big events. One selects an arbirtrary threshold in energy E_{MS} and one denotes mainshocks (MS) as those events exceeding this threshold. After every MS we study the number of recorded events in logarithmic time windows, until a new MS is found. The obtained histograms are averaged over all events that have been classified as MS in the experiment. The results obtained for a Vycor sample [3] and two Gelsil samples [26] are presented in Fig. 3.21. In order to compare the different sets of data (corresponding to different samples and to different E_{MS} thresholds) on the same plot, we have normalized the horizontal (vertical) axis by multiplying (dividing) by the mean activity rate $\langle r \rangle$. In addition, in order to also test the existence of the productivity law, the vertical axis has been multiplied by $E^{2\alpha/3}$. The values of α used for each sample are detailed in Table 3.2. The collapse of the data is quite good and indicates a linear decay on a log-log scale. This is a clear demonstration that the occurrence

Table 3.2 Critical exponents reported for Gel2.6, Gel5 and Vycor. We also include the range of values found for the equivalent exponents in real earthquakes

	ε	p	α	$1-\nu$	$2+\xi$
Gel2.6	1.37 ± 0.03	0.71 ± 0.04	0.50 ± 0.10	1.02 ± 0.05	2.8 ± 0.3
Gel5	1.36 ± 0.03	0.73 ± 0.03	0.55 ± 0.05	1.05 ± 0.05	3.1 ± 0.3
Vycor	1.40 ± 0.05	0.75 ± 0.10	0.50 ± 0.10	0.93 ± 0.05	2.45 ± 0.1
Earthquakes	1.3–1.67	1–1.6	0.8	0.75–1.0	2.3–2.5

of AE events is not Poisson distributed, but instead are compatible with Omori-like behavior with exponent $p \simeq 0.75$. The particular fits for each sample are reported in Table 3.2. Note that a good collapse also suggests the existence of a productivity law, i.e. larger mainshocks induce more aftershocks than smaller mainshocks, as occurs with real earthquakes.

3.2.7 Waiting Times Distribution

A second interesting analysis is to test the Universal Scaling Law for the distribution of waiting times. Following a protocol similar to that in the preceding analysis, we define a threshold E_{min} and study the waiting times between signals above the threshold. We then study the distribution of the waiting times by performing histograms with logarithmic bins. The histograms obtained for Vycor [3] and Gelsil [26] samples are presented in Fig. 3.22. Data have been plotted in the scaling form proposed in (3.7).

The collapse is compatible with the double power law universal scaling law proposed in (3.9) with exponents $1-\nu \simeq 1$ and $2+\xi \simeq 2.5$ [3, 26]. Detailed fits for each sample are reported in Table 3.2. The fact that we obtain double power-law behavior for the Universal Scaling Law is not surprising since in our experiments the activity rate exhibits many increasing and decreasing ramps extending several orders of magnitude. This is similar to what happens in a long lasting catalogue of earthquakes corresponding to a small area of the Earth's crust. In similar experiments in porous rocks for which only time windows with constant activity rate were considered, a damped power law USL was obtained [1].

3.2.8 Bi Test

Finally, in order to check that the observed time correlations are not a consequence of the variation of the activity rate during the experiments we can perform a Bi test in order to check whether the events are locally Poisson or not. Figure 3.23 shows three

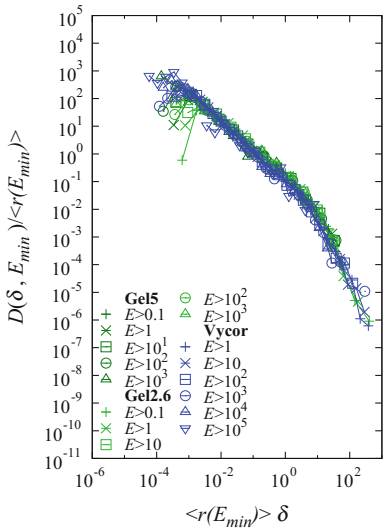

Fig. 3.22 Universal Scaling Law for the distribution of waiting times for Vycor and Gelsil experiments. Data have been analyzed by considering different thresholds E_{min}. The vertical scale has been scaled by dividing by the mean activity rate $\langle r \rangle$. The horizontal axis has been scaled by multiplying by $\langle r \rangle$

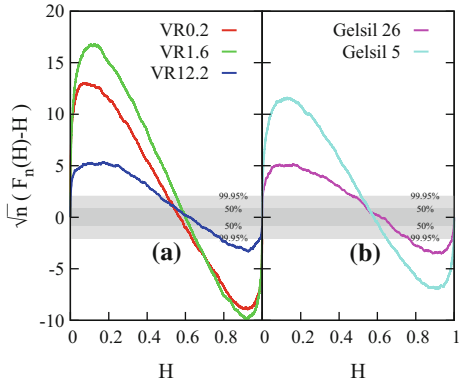

Fig. 3.23 Bi test for Vycor compression experiments at three compression rates and for two Gelsil samples. The "N" shape reveals clustering correlations between the AE events

examples of typical Bi test for Vycor (compressed at three different rates) and the two Gelsil samples [31]. As can be seen, the difference $\Delta f(H) = \sqrt{(n)}\,(F_n(H) - H))$ clearly exceeds any reasonable threshold of the Kolmogorov–Smirnov test. This occurs for most of the analysis performed. The only exception corresponds to the cases for which a very high energy threshold is used, and the number of signals above threshold is not large enough to rule out local Poisson behavior. The general trend is always an "N" shape, indicating a clustering of the events, as expected from Omori-like aftershocks.

3.3 Summary and Conclusions

We have presented results corresponding to the statistical analysis of AE avalanches detected during the compression of different synthetic porous materials based on SiO_2. The distribution of energies and the correlations between the signals can be described by statistical laws that show a lack of characteristic scales, and therefore reduce to simple or double power-law behavior.

From the evidence presented above two interesting conclusions can be drawn. First of all, the results establish clear common behavior in Vycor and Gelsil samples. In spite of having a distinct structural constitution giving rise to different macroscopic mechanical behavior, the statistical properties of AE avalanches are very similar in all the studied SiO_2 synthetic porous materials. Critical exponents that characterize energy distribution, aftershock time correlations, and waiting time distributions, summarized in Table 3.2, are equal to within error bars. Nevertheless, these exponents are different from those reported for other granular porous materials. This discrepancy could be explained as follows. For granular materials failure under uniaxial compression is known to occur by means of a double mechanism: breaking of bonds and relative grain displacements, which involve friction. However, only bond breaking is expected to occur in Vycor. It has been proposed that when only bond breaking occurs the system displays criticality; that is, in this case the failure process occurs with the absence of characteristic scales (length, time energy). The relative importance of the two mechanisms in granular materials determines the deviations from criticality. In Gelsil, the friction mechanism is less important than in other porous granular materials due to a strong adherence between SiO_2 grains. As a consequence, this material displays critical behavior to a very good approximation, within the same universality class of Vycor. In agreement with this scenario, it is worth noting that strong deviations from criticality have been found in some sandstones subjected to uniaxial compression and other porous minerals such as goethite. Sandstones are sedimentary rocks constituted of grains composed mainly of quartz (SiO_2). However, in contrast to synthetic Gelsil, in these materials the grains are cemented together by other minerals. In this case, the adherence of the grains is much less stronger than in Gelsil and friction occurs during the failure process which results in deviations from criticality.

The second important conclusion is the existence of a clear similarity between the statistics of AE events recorded during the compression of synthetic porous SiO_2-based materials and real earthquakes in the Earth's crust. In this case, the sets of exponents are not totally equivalent, but it should be remarked that the variability of the exponents characterizing real earthquakes is very large. This can be due to the fact that detection of earthquakes and measurements of their magnitudes are performed with different instruments over many years. Systematic recording of data with consistent instruments has been done only in recent years and only represents a very short period of time compared with the geological time needed to record the evolution of a fault.

The compression of SiO_2-based porous materials in the laboratory, with well-controlled parameters and systematically using the same wave detectors, amplifiers and recording instruments, gives excellent synthetic catalogues (labquakes) that can be very useful in the future, for testing algorithms with predictive power.

Acknowledgments We acknowledge Ministerio de Economia y Competitividad (Spain) for financial support (grants numbers MAT2013-40590-P and MAT2015-69777-REDT).

References

1. J. Davidsen, S. Stanchits, G. Dresen, Phys. Rev. Lett. **98**, 125502 (2007)
2. D. Bonamy, J. Phys. D Appl. Phys. **42**, 214014 (2009)
3. J. Baró, A. Corral, X. Illa, A. Planes, E.K.H. Salje, W. Schranz, D.E. Soto-Parra, E. Vives, Phys. Rev. Lett. **110**, 088702 (2013)
4. T. Makinen, A. Miksic, M. Ovaska, M. Alava, Phys. Rev. Lett. **115**, 055501 (2015)
5. H.V. Ribeiro et al., Phys. Rev. Lett. **115**, 025503 (2015)
6. D.J. Daley, D. Vere-Jones, *An Introduction to the Theory of Point Processes*, vol. II (Springer Science and Bussines Media, New York, 2008)
7. ANSS composite catalogue, http://www.ncedc.org.anss/catalog-search.html
8. S. Hainzl, J. Geodyn. **35**, 157 (2003)
9. Catálogo del Instituto Nacional de Geografia, http://www.ign.es/ign/layoutin/volcaformulariocatalogo.do
10. B. Gutenberg, C.F. Richter, Bull. Seismol. Soc. Am. **34**, 185–188 (1944)
11. Y.Y. Kagan, Tectonophysics **490**, 103–114 (2010)
12. E.P. White, B.J. Enquist, J.L. Green, Ecology **89**, 905–912 (2008)
13. A. Clauset, C.R. Shalizi, M.E.J. Newman, SIAM Rev. **51**, 661–703 (2009)
14. J. Baró, E. Vives, Phys. Rev. E **85**, 066121 (2012)
15. A. Deluca, A. Corral, Acta Geophys. **61**, 1351–1394 (2013)
16. F. Omori, J. Coll. Sci. Imp. Univ. Tokyo **7**, 111–200 (1894)
17. T. Utsu, Y. Ogata, R.S. Matsu'ura, J. Phys. Earth **43**, 1–33 (1995)
18. A. Helmstetter, Phys. Rev. Lett. **91**, 058501 (2003)
19. Y.Y. Kagan, D.D. Jackson, R.J. Geller, Seismol. Res. Lett. **83**, 951–953 (2012)
20. P. Bak, K. Christensen, L. Danon, T. Scanlon Phys. Rev. Lett **88**, 178501 (2002)
21. A. Corral, Phys. Rev. Lett. **95**, 028501 (2005)
22. H. Bi, G. Börner, Y. Chu, Astron. Astrophys. **218**, 19–23 (1989)
23. Y. Ogata, J. Am. Stat. Assoc. **83**, 9 (1988)
24. A. Helmstetter, D.Sornette, J. Geophys. Res. Solid Earth **107**, ESE 10–1 (2002)
25. P.O. Castillo-Villa, J. Baró, A. Planes, E.K.H. Salje, P. Sellappan, W.M. Kriven, E. Vives, J. Phys. Condens. Matter **25**, 292202 (2013)
26. G.F. Nataf, P.O. Castillo-Villa, J. Baró, X. Illa, E. Vives, A. Planes, E.K.H. Salje, Phys. Rev. E **90**, 022405 (2014)
27. E.K. Salje, D.E. Soto-Parra, A. Planes, E. Vives, M. Reinecker, W. Schranz, Phil. Mag. Lett. **91**, 554 (2011)
28. K.K.H. Salje, G.I. Lampronti, D.E. Soto-Parra, J. Baró, A. Planes, E. Vives, Am. Miner. **98**, 609 (2013)
29. M.A. Lebyodkin, I.V. Shashkov, T.A. Lebedkina, K. Mathis, P. Dobron, F. Chmelik, Phys. Rev. E **88**, 042402 (2013)
30. J. Koppensteiner, W. Schranz, M. Puica, Phys. Rev. B **78**, 054203 (2008)
31. J. Baró, Ph.D. Dissertation, University of Barcelona (2015)
32. J.P. Sethna, K.A. Dahmen, C.R. Myers, Nature **410**, 242 (2001)

Chapter 4
Towards a Quantitative Analysis of Crackling Noise by Strain Drop Measurements

Viktor Soprunyuk, Sabine Puchberger, Wilfried Schranz, Andreas Tröster, Eduard Vives and Ekhard K.H. Salje

Abstract The method of measuring strain drops with a Dynamic Mechanical Analyzer (DMA) at slowly varying stress has a considerable potential to become an interesting complementary tool for the study of mechanical failure and earthquake dynamics in micron-sized materials. Evidence for this claim is provided by measurements of the SiO_2-based porous materials Vycor and Gelsil under slow uniaxial compression at constant force rates of $10^{-4}-10^{-3}\,\mathrm{Ns}^{-1}$ using a Diamond DMA (Dynamical Mechanical Analyzer, Perkin Elmer). The jerky evolution of the sample's height with time is analyzed in order to determine the corresponding power-law exponents for the maximum velocity distribution, the squared maximum velocity distribution as well as the aftershock activity in the region before macroscopic failure. A comparison with recent results from acoustic emission (AE) data on the same materials (J. Baró, Á. Corral, X. Illa, A. Planes, E. K. H. Salje, W. Schranz, D. E. Soto-Parra, and E. Vives, Phys. Rev. Lett. **110**, 088702 (2013)) shows similitude in the statistics, although the two methods operate on different spatial and temporal scales. Moreover, the obtained power-law exponents are in reasonable agreement with theoretical mean-field values (M. LeBlanc, L. Angheluta, K. Dahmen, N. Goldenfeld, Phys. Rev. B **87**, 022126 (2013)). The results indicate that the failure dynamics of materials can be well studied by measuring strain drops under slow compression, which opens the possibility to study earthquake dynamics in the laboratory also at non-ambient conditions, i.e. at high temperatures or under confining liquid pore pressure.

V. Soprunyuk · S. Puchberger · W. Schranz (✉)
Faculty of Physics, University of Vienna, Boltzmanngasse 5, 1090 Wien, Austria
e-mail: wilfried.schranz@univie.ac.at

A. Tröster
Institute of Material Chemistry, Vienna University of Technology,
Getreidemarkt 9, 1090 Wien, Austria

E. Vives
Facultat de Física, Departament d'Estructura i Constituents de la Matéria,
Universitat de Barcelona, Martí i Franqués 1, E-08028 Barcelona, Catalonia, Spain

E.K.H. Salje
Department of Earth Sciences, University of Cambridge, Downing Street,
Cambridge CB2 3EQ, UK

E.K.H. Salje et al. (eds.), *Avalanches in Functional Materials and Geophysics*,
Understanding Complex Systems, DOI 10.1007/978-3-319-45612-6_4

PACS numbers 62.20.mm · 89.75.Da · 91.30.Dk

4.1 Introduction

The failure of porous materials [1–3] subjected to compressional forces is an example of a phenomenon that produces crackling noise [4, 5]. Other examples are the "Barkhausen effect" in magnetic materials [6, 7], plastic deformation in metals [8–11], martensitic transitions [12–14] or paper fracture [15–17]. All these systems have in common that upon variation of an external field (magnetic, mechanical stress, etc.) avalanches of the conjugated variable (magnetization, strain, etc.) appear due to inhomogeneities or disorder in the sample. Understanding the complex spatio-temporal behavior of the microstructure evolution that produces crackling noise is an important problem in Earth science and engineering [2, 18].

Measuring avalanche statistics is very difficult because large data sets with a high dynamical range of the signals are needed for any reliable statistical analysis. Signals are often short time singularities (referred to as 'jerks'). A reasonable avalanche analysis requires the observation of several 1000 such jerks. This is clearly a tall task for the experimentalist. Only very few experimental methods are available, with probably acoustic emission (AE) on large samples as the outstanding champion. Acoustic emission (AE) technique is a highly sensitive tool for extracting real-time information regarding a broad variety of microstructure evolution that produces crackling noise. In a series of compression experiments we have measured the AE during the stress induced collapse of porous materials including Vycor [2], Gelsil [19], berlinite [20] and alumina [21]. Their statistical characteristics concerning the energy of AE events, their duration as well as those of waiting times between events share striking similarities with the corresponding figures obtained in analyzing natural earthquake statistics. Nevertheless, even in case of AE only porous collapse and some martensite transformations can be measured with sufficient resolution. Furthermore, AE fails for micron-scale samples which are increasingly important for nano-technology applications. Ferroic transformations [22] and ferroelastic twinning are even harder to quantify and only few tens or hundreds of signals are usually available [23]. Alternatively, nano-indenters were used with some success [8] although their statistical relevance is at the very limit to show the anticipated power law behavior of the avalanche dynamics. Finally, heat flux measurements have been successful in martensitic transitions [12] but AE techniques were needed to extend the measurement range to equally analyze the waiting time distributions. Summarizing the situation, it is fair to say that no ideal method exists up to date. There is an urgent need to develop alternative methods which combine the advantages of these techniques, namely small sizes for nano-indentation and high dynamical range of AE.

In the present paper we investigate the potential of an approach based on measuring the strain-collapse as sample shortening under weak external stress with a Dynamic Mechanical Analyzer (DMA), possibly enhanced by a further instrument

development. To see how the numerical results obtained from such DMA data compare with those based on AE, we analyze the statistical characteristics of strain drop data $\Delta h(t)$ for porous silicates Vycor and Gelsil with different pore sizes measured by a Diamond DMA by Perkin Elmer. It turns out that the power-law exponents obtained from strain drop data of Vycor and Gelsil are in quite good agreement with the corresponding power-law exponents from AE. Admittedly, the limited time resolution ($\approx$1 s) of the present DMA apparatus, which is much lower in comparison to AE, produces a more restricted data set. Nevertheless, we find sufficient evidence to believe that this method will open the way to overcome one of the main obstacles of AE in Earth Science applications, namely its limited sensitivity under extreme conditions.

The paper is organized as follows. In Sect. 4.2 we provide basic sample information and describe the experimental arrangement. Experimental results for Vycor 7.5 nm, Gelsil 5 nm and Gelsil 2.6 nm are presented in Sect. 4.3 and the distribution functions are analyzed to determine corresponding power-law exponents. In the last section we discuss assets and drawbacks of the proposed method and summarize the main conclusions of the work.

4.2 Experimental

4.2.1 Sample Properties

We performed slow uniaxial compression experiments on mesoporous silica Vycor and Gelsil with different pore sizes. Vycor originates from spinodal decomposition, resulting in a skeleton of nearly pure SiO_2 containing a network of interconnected nm-sized pores of narrow pore size distribution, random in length and direction [25]. The mean ratio of pore length l over pore diameter d was found to be $l/d \approx 4$. Gelsil monoliths are produced in a sol-gel process by hydrolization of silica containing precursors liquids, followed by condensation and heat treatment. Silica molecules condensate to spheres on stochastic sites within the hydrolized silica precursor. Subsequent gelation leads to a network-like arrangement of spheres. Via heat treatment the gel turns either into a bulk-like powder or monoliths. Thus, the dried and consolidated end product can be approximated as an assembly of stochastically arranged and monodisperse pure silica spheres [26]. Spheres are touching and also penetrating each other. The voids between these spheres constitute a random network of interconnected corridors and pockets and show a larger pore size distribution compared to Vycor. Table 4.1 summarizes the main characteristics of the samples.

To produce samples for dynamic mechanical analysis measurements we cut the as-produced rods with a diamond wire saw into bars. Parallel faces and rectangular corners were gained using a steel u-formed tool on which samples are mechanically clamped and sanded with finely grained sandpaper. Gluing samples on surfaces as used for polishing crystals is not recommended, since the glue may permeate the

Table 4.1 Characteristics of the studied samples. From [27, 28]

Sample	Vycor 7.5	Gelsil 5	Gelsil 2.6
Average pore diameter (nm)	7.5	5	2.6
Porosity Φ (%)	40	54	36
Density (g/cm^3)	1.9	1.2	1.2
Surface area (m^2/g)	70	510	590
Surface fractal dimension D_s	2.3	2.24	–
Mass fractal dimension D_m	2.31	2.87	–
Approximate failure stress σ_f (MPa)	30	10	0.5

sample's pores. By mounting the sample, sanding, checking angles and shape with an optical microscope, rotating and mounting the sample again repeatedly, rectangular bars with a typical size of $0.5 \times 0.5 \times 1.0\,\text{mm}^3$ were produced. The geometrical accuracy of this method, measured by height variations along as-prepared sample faces, was better than 10 μm. Cleaning of all samples has been done in a 30 % solution of H_2O_2 for 24 h. Afterwards samples were dried in a high vacuum chamber at 10^{-6} mbar and 120 °C for another 24 h.

4.2.2 Dynamic Mechanical Analysis

The measurements were performed with a Diamond DMA (Perkin Elmer) at room temperature. Small parallelepipeds were mounted between steel rods with parallel faces and slowly compressed at constant force rates of $10^{-4}-10^{-3}$ N/s (Fig. 4.1). We performed various kinds of stress ramps, i.e. stress cycling until macroscopic failure occurs as well as slow stress increase up to a maximum stress. Corresponding results are shown below.

The maximum force that can be applied within the Diamond DMA setup is $F_{max} = 10\,\text{N}$, with a resolution of 0.002 N. To increase the maximum force we used for some experiments a home-made holder, which can add an extra constant load of few Newtons. Nevertheless, the small value of the maximum force required us to select small sections for samples in order to reach macroscopic collapse. Typical dimensions of the samples were $0.5 \times 0.5 \times 1.0$ mm^3 for Vycor and $1.0 \times 1.0 \times 1.7$ mm^3 for Gelsil, i.e. one order of magnitude smaller as compared to the ones used for AE measurements in [19]. When the sample did not collapse until the maximum force was reached, we sometimes repeated the compression ramp until failure. In some cases this required up to 9 cycles (Fig. 4.2), i.e. 15 h. The spatial resolution of the DMA apparatus of about 3 nm is well adapted to the heterogeneity of the mesoporous silica (pore sizes between 2.6 and 7.5 nm) samples. The temporal resolution is the weak point of this method. In acoustic emission experiments the temporal resolution is a few orders of magnitude better as compared with Dynamic Mechanical Analysis

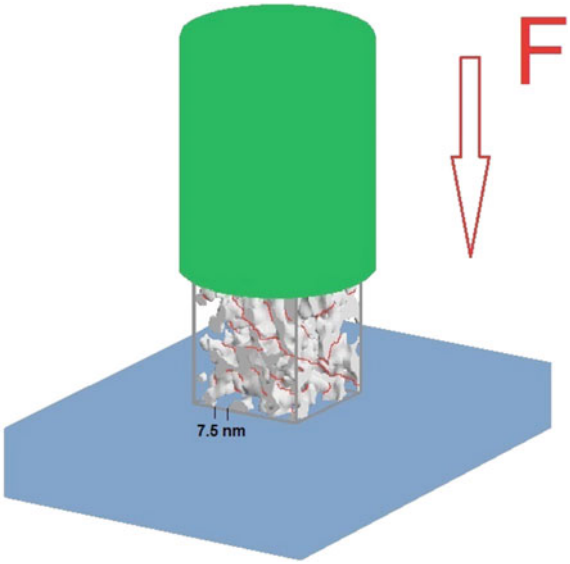

Fig. 4.1 Geometry of a typical compression experiment of Vycor or Gelsil using a Diamond DMA (Perkin Elmer)

while the possibility to put samples under extreme conditions is more restricted. Nevertheless, as we demonstrate in the present paper, the resolution of DMA is sufficient to collect a reasonable data set for calculating power law exponents that compare well with those obtained from AE and are presently not too far from those predicted by theory.

Altogether about 40 long time compression experiments with slowly increasing force on Vycor 7.5, Gelsil 5 and Gelsil 2.6 have been performed and analyzed to test reproducibility of the results and to compare with recent results from acoustic emission [1, 2, 19]. For more details about the DMA method see e.g. [24, 29].

4.3 Results

Figure 4.2 shows the time evolution of the sample height $h(t)$ (top graph) and its temporal derivative $v(t) = (dh/dt)$ (bottom graph) for the 11 cycle experiment of Vycor 7.5. From the shapes of $v(t)$ corresponding maxima $v_m = (dh/dt)_{max}$ can be identified, by finding local maxima including 2 neighboring points. To get a rough idea about the energies involved in the strain bursts we estimate $E_m = M v_m^2/2$, where the mass M that is moved is assumed to be of the order of the sample mass, i.e. $M \approx 3 \times 10^{-7}$ kg. With v_m varying between 1 and 1000 nm/s the burst energies vary between 10^{-5}–10^{1} aJ (Fig. 4.2). On the other hand, the elastic energy change E_{el} associated with a crack of size a is [30] $E_{el} \propto \sigma^2 a^3/E$, where σ is the applied stress, E the Young's modulus and a the typical crack size. An estimate of E_{el} using $\sigma \approx 1$ MPa, $E \approx 100$ GPa yields a release of elastic energy during the collapse of

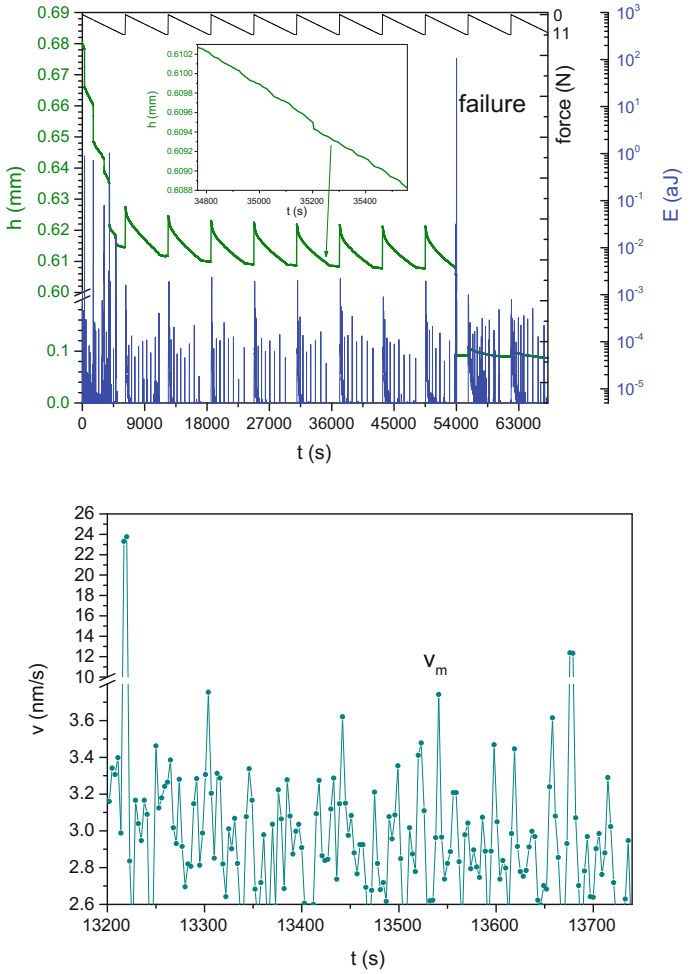

Fig. 4.2 *Top graph* Long time compression experiment of Vycor 7.5 showing 11 stress cycles (black line). The *green line* displays the measured sample height h with an initial height of h(t = 0) = 0.68 mm, sample area $A = 0.3\,\text{mm}^2$. The sample fails after 9 cycles at the force $F_f = 8.5\,\text{N}$, corresponding to a failure stress $\sigma_f = 94\,\text{MPa}$. h(t > t_f) ≈ 0.1 mm. *Blue lines* show the square of drop velocity maxima $v_m^2 = (dh/dt)^2_{max}$. The *inset* shows the jerky behavior of the sample height. *Bottom graph* Drop velocity peaks $v(t)$ on a magnified scale. v_m denotes peak maxima

one pore (plane of pores) of size $a \approx 10\,nm$ of $E_{el} \approx 10^{-5}$ aJ. The good agreement between these two estimates suggests that the elastic energy released by the collapse of the pores can be well determined by measuring the squared drop velocities, the smallest energies corresponding to the collapse of a single plane of pores of size a (approx. 10 nm for Vycor and 3–5 nm for Gelsils).

Peak heights in energy are observed to vary over more than 5 decades during the experiment (Fig. 4.2). More than 400 peaks corresponding to discontinuous strain drops where found for each cycle spanning about 6000 s. About 200 of these peaks with corresponding height jumps smaller than ca. 5 nm where identified as noise, but more than 200 peaks remained usable for the calculation of exponents within each cycle, implying a sample of about 2000 peaks for the 11 cycle experiment on Vycor (Fig. 4.2).

Figure 4.3 shows the distribution of the maxima of drop velocities $N(v_m)$ for Vycor in the region before failure. The histogram displays the accumulation of signals (peak maxima) over eight cycles [31], corresponding to about 1600 events (peaks). At small values of peak velocities the distribution has a maximum, whereas at large values of v_m it clearly follows a power-law, i.e. $N(v_m) \sim v_m^{-\mu}$. We may associate the two regions with two different physical processes. The peaks on the low-velocity side are most probably due to irregular oscillations of the DMA-machine producing a large number of small bursts and the large bursts produced by the intermittent cracking of the sample which display a power-law behavior.

Before analyzing the data in detail we always removed the large peak occurring at the end of each stress cycle (Fig. 4.2) as well as all other positive peaks (about 10–30 peaks for each stress cycle with positive drop velocity), since these correspond to

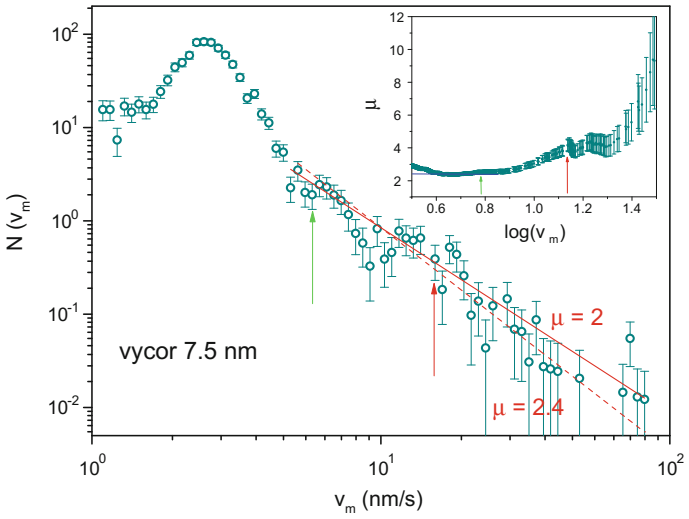

Fig. 4.3 Log–log plot of the distribution $N(v_m)$ of maximum drop velocities of Vycor 7.5 calculated from the height drop data of Fig. 4.2. The *solid red line* corresponds to $N(v_m) \propto v_m^{-\mu}$ with $\mu = 2$, implying good agreement with the corresponding mean-field value for constant stress [35]. The *inset* shows the ML-fitted exponent μ as a function of a lower threshold $v_{m,min}$. *Green* and *red arrows* mark the threshold values beyond which less than 200 and 50 data points contribute to the ML estimate (4.1), respectively. These threshold values are also marked by corresponding arrows in the main plot. The slopes corresponding to the mean-field value $\mu = 2$ and the ML estimate $\mu = 2.4$ are indicated by the *solid* and *broken red lines*, respectively

elastic recovery rather than to strain burst events. To assess the power-law exponents we employ the following method:

- In a first step, the data (e.g. v_m) are logarithmically binned (using the logarithm based on 10 for convenience), resulting in a histogram $\tilde{N}(\log_{10} x)$ which for power-law distributions has the advantage of reducing the number of zero and low count bins at larger values of e.g. v_m. To compensate for the effect of logarithmic binning in the accompanying probability measure, we then define corrected histogram bin entries $N(x) \equiv \tilde{N}(\log_{10} x)/x$. Assuming the non-Gaussian large-x "tail" of this histogram to follow a power law with exponent μ, a corresponding log–log plot of $\log N(x)$ against $\log_{10}(x)$ should exhibit a linear slope in the asymptotic range $x \to \infty$ with a slope equal to $-\mu$. Admittedly, choosing the fitting range (i.e. the smallest x-value from where one would expect the assumed power law to hold asymptotically) is to some extent a matter of taste. Moreover, simply applying a weighted linear regression to the logarithm of histogram entries is problematical, mainly because it is not clear how to deal with empty bin entries in this approach. In a log–log plot such bins must obviously be ignored, despite the fact that they also encode information about the underlying probability distribution, so ignoring them may introduce a bias to the resulting fit. On could try to avoid this problem by resorting to a log-linear fit instead. However, assuming Poissonian statistics for the bin entries of the original histogram $\tilde{N}(x)$, it is still unclear how to assign meaningful weights to the empty bins. Increasing the bin size may eventually eliminate the occurrence of empty bins, but at the expense of destroying an unacceptable amount of valuable statistical information. Apart from these statistical imponderables, a possible dependence of the obtained numerical results on the chosen bin size is expected to creep into such calculations anyhow, but for the examples we have studied so far, the resulting exponents turn out to be not very sensitive against binning with various meaningful intervals and well reproducible for all different experiments, provided the specimens are well prepared and close to macroscopic failure with failure stresses of $\sigma_f \approx 30$ MPa for Vycor, 10 MPa for Gelsil 5 and 0.5 MPa for Gelsil 2.6, respectively.
  Nevertheless, in view of all these difficulties log–log plots of logarithmically binned histograms must be taken with a pinch of salt. Therefore we complement this kind of evaluation by using the Maximum Likelihood (ML) approach.
- In theory, a Maximum Likelihood (ML) estimation of the power law exponent should be superior to the above heuristics [32, 33], the main reason being that there is no need to bin the data. Thus, in a ML analysis we neither have to juggle with empty bins, nor do we have to worry about error bar assignment to individual bins or how to deal with any spurious dependence of the obtained results on the chosen binning width. Furthermore, assuming that the power law holds for all observed values x_i, $i = 1, \ldots, n$ of x for which $x \geq x_{min}$, the analytical formula

$$\hat{\mu}(x_{min}) = 1 + n \left[\sum_{i=1}^{n} \ln \frac{x_i}{x_{min}} \right]^{-1} \tag{4.1}$$

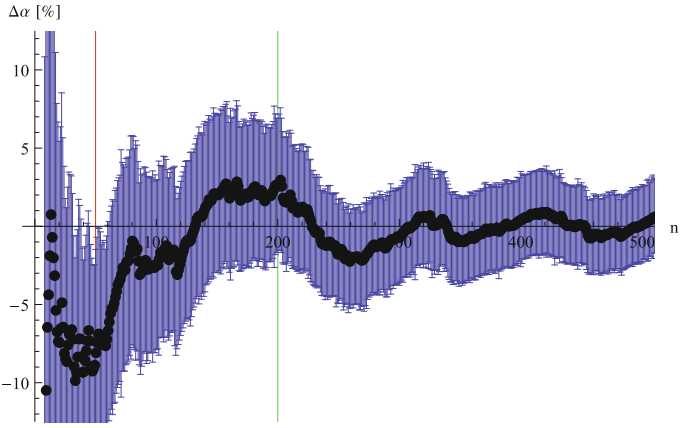

Fig. 4.4 Deviation (in percent) of the ML estimate (4.1) $\hat{\mu}(n) \equiv \hat{\mu}(x_{min}(n))$ from the exact value $\mu = 2.0$ as a function of the number n defined by $n \equiv |\{x_i > x_{min}\}|$ for an artificial dataset of 30,000 values generated from an ideal power law with exponent $\mu = 2.0$

which gives the ML estimate $\hat{\mu}$ for the exponent μ with a standard error of [32]

$$\sigma = \frac{\hat{\mu}(x_{min}) - 1}{\sqrt{n}} \tag{4.2}$$

represents the optimal guess based on the given data, with no need to perform any kind of fitting procedure. To study the dependence on the lower threshold x_{min}, we would expect that in a plot of $\hat{\mu}(x_{min})$ as a function of x_{min} the data range in which the power law distribution actually holds should be detectable by a corresponding plateau of $\hat{\mu}(x_{min})$ at the "true" value of the exponent μ. The caveat is, however, that the estimate (4.1) turns out to be biased unless n is large enough. In fact, in [32] on may find the recommendation that (4.1) and (4.2) should only be trusted for roughly $n \gg 50$. For (4.2) this is not a major issue, since the statistical error can always be alternatively assessed by standard methods of statistics like the jackknife or bootstrap estimates [34]. To illustrate the effect of n on the precision that can be expected from the estimate (4.1) in practice, we applied (4.1) to an artificial dataset of some 30,000 datepoints generated from a pure power law distribution with an exponent of, say, $\mu = 2$. As Fig. 4.4 reveals, even for this ideal case the ML estimate not only exhibits a very irregular behavior for less than 50 data points, but even for $n \approx 200$ systematic wavy oscillations of an amplitude of some 5 % around the true value $\mu = 2.0$ are still observed. Unfortunately, for experimental datasets in which only a relatively small number of the biggest values can be expected to contribute to the power-law tail of the distribution, these oscillations may therefore mask the flat plateau naively expected in a plot of the ML estimate for μ, thus hampering the detection of the power law region and thus a reliable numerical determination of the underlying exponent.

An attempt to determine the power-law exponent of $N(v_m) \propto v_m^{-\mu}$ for the case of Vycor 7.5 may serve to illustrate the resulting numerical ambiguities. From the inset of Fig. 4.3, which exhibits a plateau in the ML estimate of μ around a threshold value $v_{m,min}$ for which the condition $n > 200$ is already met, one would conclude that $\mu \approx 2.4$ would be a reasonable guess. Interestingly, this value of $v_{m,min}$ is also found to roughly coincide with the onset of the power law range visible in the main plot of Fig. 4.3. Indeed, a tentative linear regression of the corresponding log–log plot in this range then results in $\mu \approx 2.0$, in excellent agreement with recent mean-field calculations ($\mu = 2$) of maximum velocity distributions [35].

This trend persists for the distribution of the squared drop velocity maxima, which are fitted as $N(v_m^2) \sim (v_m^2)^{-\varepsilon'}$ with $\varepsilon' = 1.4 \pm 0.1$, which agrees equally well with the theoretical mean-field value $\varepsilon' = 1.5$ reported in [35], while the ML method would suggest a slightly higher value of $\varepsilon' \approx 1.7$. (Fig. 4.4). There is of course some redundancy when showing the distributions $N(v_m)$ and $N(v_m^2)$, since the corresponding exponents are related as $\varepsilon' = (\mu + 1)/2$. In terms of probability densities, this simple scaling relation may be understood by taking into account the Jacobian of the corresponding density measure. Alternatively, it can be directly derived from the ML exponent estimator (4.1). However, the behavior of other estimators (least squares, etc.) might be slightly altered e.g. in the crossover region from non-universal to power law behavior (compare Figs. 4.3 and 4.5). Thus, we decided to always present both distributions.

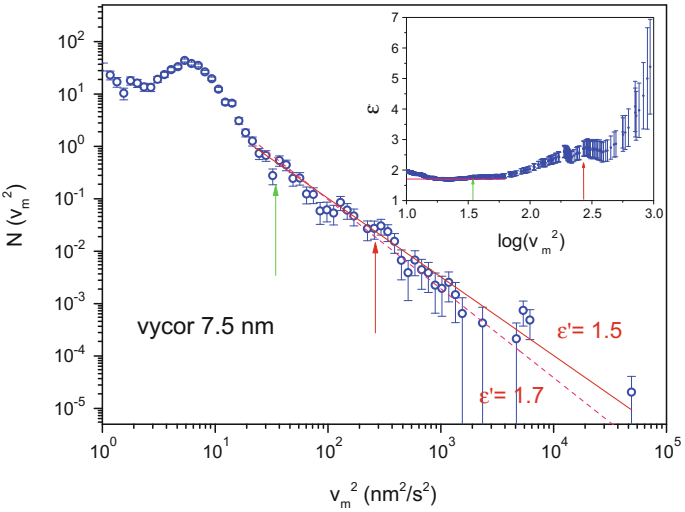

Fig. 4.5 Distribution of maximum drop velocities squared v_m^2 of Vycor 7.5. Logarithmic binning with increment of 0.05 was used. The *solid red line* corresponds to a power-law exponent $\varepsilon' = 1.5$. The *broken red line* shows the resulting slope for an exponent $\varepsilon' \approx 1.7$ as obtained from the ML method (*inset*)

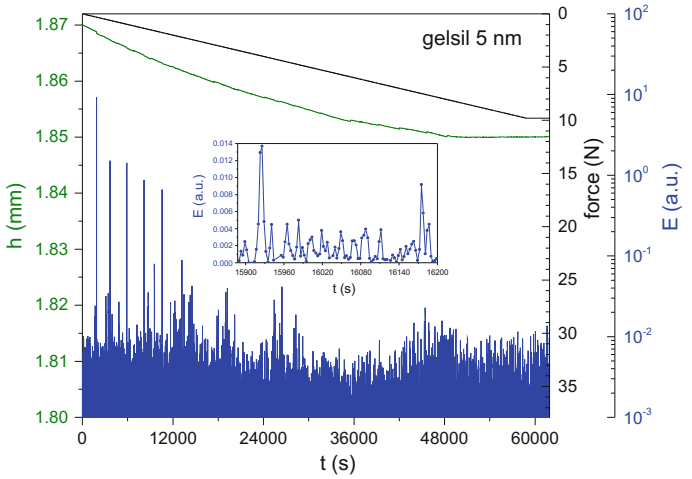

Fig. 4.6 Compression experiment of Gelsil 5 with force rate $\approx 10^{-4} Ns^{-1}$. The green line displays the measured sample height h(t), with h(t = 0) = 1.87 mm. *Blue lines* show the maxima of squared drop velocities $v_m^2 = (dh/dt)_m^2$ which are assumed to be proportional to the released Energy E of corresponding avalanches

An extremely small force rate of $\approx 10^{-4}$ Ns^{-1} was used to produce the strain drop data for Gelsil 5 (Fig. 4.6). Figures 4.7 and 4.8 show the resulting maximum velocity and squared maximum velocity distributions. Although the power-law character of the distributions - detectable as the onset of a linear slope in the corresponding log–log plots - is not masked by the noise produced by the DMA, one may conclude that in this case the quality of the dataset is insufficient for a reliable determination of the corresponding power-law exponents. Fortunately, we have observed that in most cases we could increase the quality of the observed data set significantly by performing experiments with many stress cycles. Based in the strain drop data of Figs. 4.9, 4.10 and 4.11 show the maximum velocity and squared maximum velocity distributions for Gelsil 2.6 obtained from such experiments. Here the power-law character of the distributions is clearly observed, allowing now for a good determination of the corresponding power-law exponents.

Summarizing the discussion so far, our strain drop data yield power-law exponents for the distributions of the maximum velocities as well as the squared maximum velocities of Vycor and Gelsils that are in good agreement with corresponding theoretical mean-field values [35] $\mu = 2$ and $\varepsilon' = 1.5$. Unfortunately, a direct comparison of results for the energy exponent of Vycor and Gelsil obtained from our approach with recent AE ones [1, 2, 19] is delicate: In AE the energy distribution is usually calculated from the squared voltage signal $U(t)$ measured in a detector by integration over the time period T of an event (avalanche) divided by a reference resistance R, i.e. $E_{AE} = 1/R \int_T U(t)^2 dt$. To compare the corresponding exponent with the one of our present DMA experiment, we would have to calculate the energy

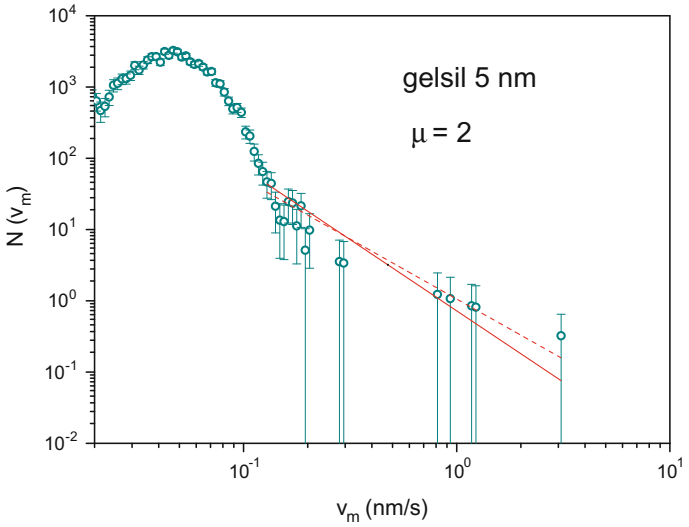

Fig. 4.7 Distribution of maximum drop velocities v_m of Gelsil 5. Logarithmic binning with increment of 0.05 was used. The *dashed red line* shows a fit using the relation $N(v_m) \propto v_m^{-\mu}$ with $\mu = 1.7 \pm 0.1$. The *red line* displays the theoretical power-law exponent $\mu = 2$ which would be expected from theory [35]

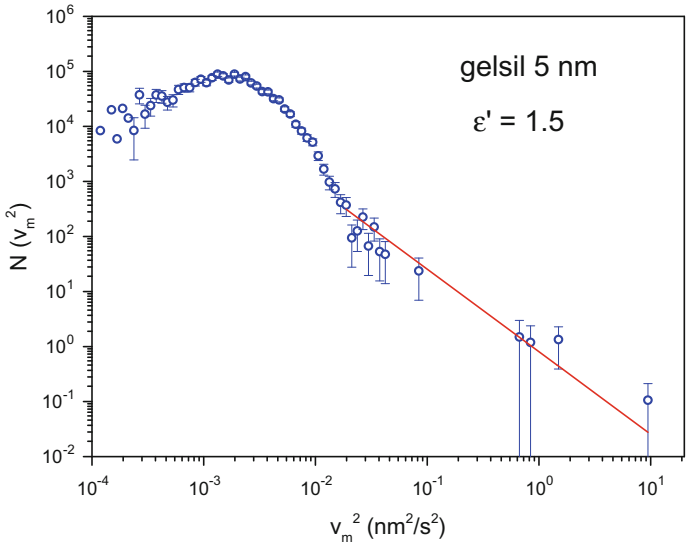

Fig. 4.8 Distribution of maximum drop velocities squared v_m^2 of Gelsil 5. Logarithmic binning with increment of 0.05 was used. The *solid line* corresponds to the theoretical value of $\varepsilon' = 2$

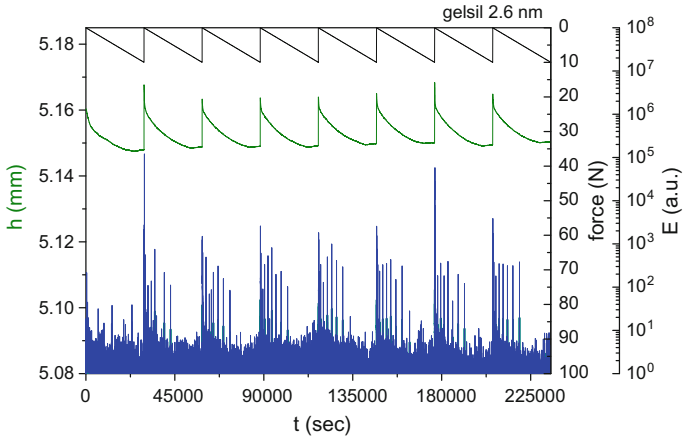

Fig. 4.9 Compression experiment of Gelsil 2.6 with compression rate of $3 \cdot 10^{-4}\,\mathrm{Ns}^{-1}$ with 8 stress cycles. The green line displays the measured sample height h(t). *Blue lines* show the square of drop velocity peaks $v_m^2 = (dh/dt)_m^2$ which appear due to the jerky behavior of h(t)

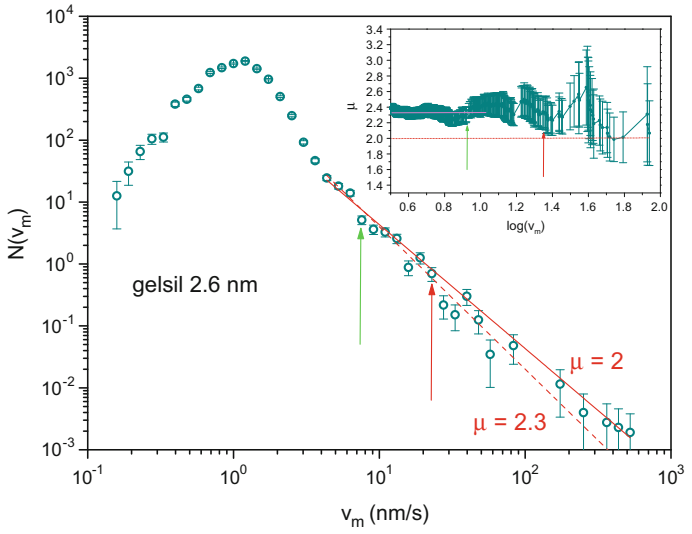

Fig. 4.10 Distribution of the drop velocity peaks of Gelsil 2.6 calculated from the data of Fig. 4.9. The *red line* corresponds to the exponent $\mu = 2$. The ML exponent (see *inset*) indicates also here a slightly higher value (*broken red line* in log–log plot) of $\mu \approx 2.3$

distribution from integration of squared drop velocities $v(t)$ over corresponding peaks, i.e. $E \propto 1/T \int_T v(t)^2 dt$. However, at present, our estimates of power-law exponents obtained from time integrated histograms are probably contaminated by relatively large systematic errors that creep in due to our rather coarse time resolution and so we are forced to postpone this kind of comparison to future experiments with

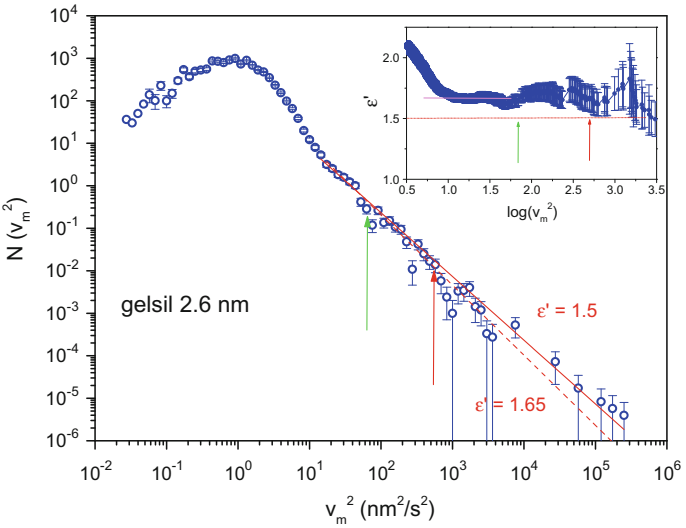

Fig. 4.11 Distribution of the squared drop velocity peaks of Gelsil 2.6 calculated from the data of Fig. 4.9. The red line corresponds to the exponent $\varepsilon' = 1.5$. ML treatment (*inset*) of the data yields $\varepsilon' = 1.65$, shown here as *broken red line* in the main plot

improved time resolution of DMA-techniques. Nevertheless, we can check consistency with AE data of Vycor and Gelsil by comparing the time dependence of the velocity *peaks* measured by DMA with the time dependence of energy *peaks* measured by AE. In doing so, it turned out that all events with peak velocities *below* the region where power-law holds for the distributions of $N(v_m)$ (Figs. 4.3, 4.7, 4.10) or $N(v_m^2)$ (Figs. 4.5, 4.8, 4.11) yield a Gaussian distribution of events in time (inset of Fig. 4.12). This is quite in agreement with the assumption that the "humps" in the distributions are due to irregular oscillations of the DMA-machine.

In contrast, events with peak velocities *above* the maximum value of the distributions show quite different time dependencies. A clear decay of the activity rate is observed (Fig. 4.12) for these jerks in agreement with Omori's law, which states that immediately following a main earthquake there is a sequence of aftershocks whose frequency decays with time [36]. For further analysis of these peaks we considered as mainshocks (MS) the largest events (largest $v_m's$) corresponding to strain *drops* and counted the number $r_{AS}(t) = dn/dt$ of events within time intervals $\Delta t = 300\,\mathrm{s}$ until an event with an energy of the same order than the energy of the MS was found. Based on the data treatment discussed mentioned, we report that the corresponding aftershock activities were indeed found to follow Omori's modified law (4.3)

$$r_{AS}(t) = \frac{k}{(t+c)^p} \tag{4.3}$$

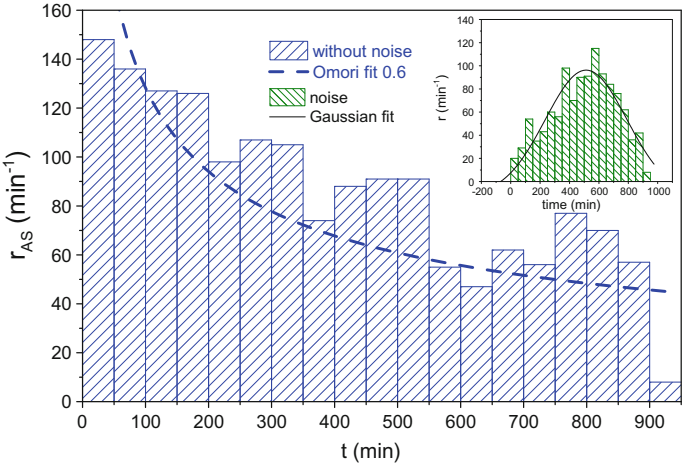

Fig. 4.12 *Blue* histogram displays the number of aftershocks per unit time r_{AS} as a function of time distance t to a main shock. The time dependence is calculated from the data of Fig. 4.6 of Gelsil 5 keeping only the events to the right of the peak maximum of the corresponding velocity distribution. The *blue broken line* displays Omori's law (4.3). The *inset* shows the corresponding histogram of the noise contribution to the data set built from velocities smaller than the location of the maximum of the maximum velocity distribution. It is well fitted by a Gaussian distribution function

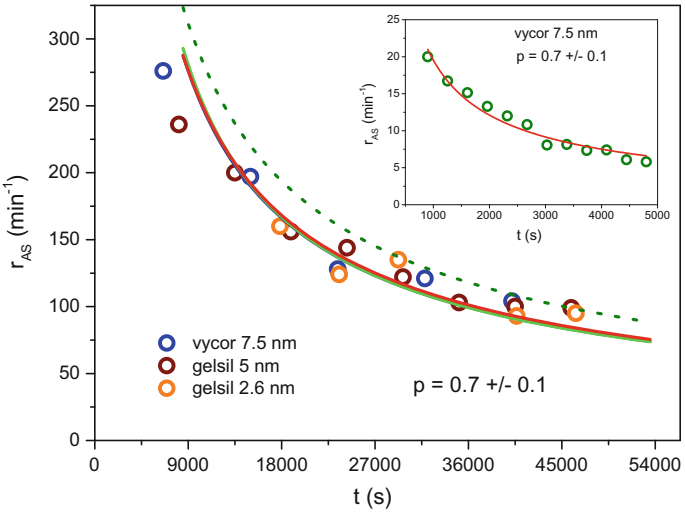

Fig. 4.13 Number of aftershocks per unit time r_{AS} as a function of time distance t to the main shock calculated from different long time experiments of Vycor and Gelsils. The *three coloured lines* shows fits with Omori's law with $c = 0\,\mathrm{s}$ (*cyan*; yielding $p = 0.6 \pm 0.08$), $c = 5\,\mathrm{s}$ (*green*; yielding $p = 0.7 \pm 0.09$) and $c = 10\,\mathrm{s}$ (*red*; yielding $p = 0.75 \pm 0.1$), all in good agreement with the value $p = 0.75 \pm 0.1$ of [2]. The *green dotted line* shows that for $c = 20\ s$ the fits deviate already significantly from the data. The *inset* shows data of the stress cycle experiment of Vycor (Fig. 4.2)

for earthquakes remarkably well (Fig. 4.13) for Vycor as well as Gelsil 5 and Gelsil 2.6. As shown in Fig. 4.13 we obtain fits of similar good quality for c-values varying between $c = 0\,\mathrm{s}$ and $c = 10\,\mathrm{s}$, yielding a power law exponent $p = 0.7 \pm 0.1$ which is quite compatible with the value found in [2] ($p = 0.75 \pm 0.1$). The fact that we cannot narrow down these limits in c-values results from our present coarse time scale.

From the present analysis it should be evident that from drop velocity measurements one can extract similar information on earthquake dynamics as from AE, albeit with somewhat reduced accuracy resulting from our sparser data set.

4.4 Discussion and Conclusions

We have presented a careful investigation of the fracture of porous SiO_2-based materials, i.e. Vycor and Gelsil by measuring and analyzing the statistics of corresponding strain drops under slow uniaxial compression (10^{-4}–$10^{-3}\,\mathrm{Ns}^{-1}$). The main motivation of this work was to propose a new experimental tool (Dynamic Mechanical Analyzer) for the study of failure dynamics of small size nanoporous materials. In addition we wanted to test a correspondence of Acoustic emission activity [2, 19] with strain bursts clarifying to which extent the AE signal is proportional to the dissipated energy during the failure process. A Dynamic Mechanical Analyzer (Diamond DMA, Perkin Elmer) turned out to be one of the rare devices that is capable of delivering an adequate resolution in the applied force (2 mN) as well as a sufficiently precise length detection (10 nm). Altogether we performed about 40 experiments on Vycor (7.5 nm pore size) and Gelsils (5 and 2.6 nm pore sizes). From the resulting strain drop data $h(t)$ we calculated the power-law exponents for the maximum velocity distribution $N(v_m)$ in avalanches and also the squared values $N(v_m^2)$ and carried out a comparison to Omori's law of aftershock activity rates.

It turns out that the peak-velocity distributions as well as the squared peak-velocity distributions follow power-laws $N(v_m) \sim v_m^{-\mu}$ and $N(v_m^2) \sim (v_m^2)^{-\varepsilon'}$ in regions spanning 2–4 orders of magnitude, respectively. Analyzing the data using the maximum likelihood method yields exponents for Vycor and Gelsils $\mu = 2.4$, (2.3) and $\varepsilon' = 1.7$, (1.6) that are slightly above the corresponding mean-field values [35, 37], whereas a simple log–log treatment of the data with logarithmically binned histograms yields exponents that are quite consistent with $\mu = 2$ and $\varepsilon' = 1.5$. Within the present resolution of the apparatus we are unable to draw a definite conclusion of the exponents, i.e. we can determine them only with an estimated accuracy of about 20 %. In addition to the velocity and the energy-distributions we also studied the dynamic behavior of the jerks. We found that the aftershock activity rates follow Omoris law for Vycor and Gelsils with an exponent $p \approx 0.7$ that is very similar to those found in AE [2] ($p = 0.75 \pm 0.1$), albeit on a much coarser time scale in the present case.

Of course, despite this nice agreement of our novel attempts with theoretical predictions and with recent AE data one may nevertheless question its absolute

significance due to the inherent limitations of our presently available data-set. Should such a DMA-technique can become an adequate tool for a precise study of avalanche statistics [38], these teething troubles, which at present are mainly due to a limited time resolution ($\approx$1 s) as well as due to the noise produced by the DMA-machine, should definitely be overcome. In future we should be able to increase the sampling rate by a factor of 100 by using another DMA system, which should then allow a more reliable comparison of advanced and more mature techniques like AE.

Summarizing, the present results demonstrate that - provided one can overcome the present limitations in the sampling rates - the proposed method of measuring strain drops with DMA at slowly varying stress could become a complementary tool for the study of mechanical failure and earthquake dynamics in micron-sized materials with the added benefit to be extendible also to non-ambient conditions, like high or low temperature or at pore filling with various liquids.

Acknowledgments We acknowledge financial support from the Austrian Science Fund (FWF) projects P28672-N36 and P27738-N28.

References

1. E.K.H. Salje, D.E. Soto-Parra, A. Planes, E. Vives, M. Reinecker, W. Schranz, Philos. Mag. Lett. **91**, 554 (2011)
2. J. Baró, Á. Corral, X. Illa, A. Planes, E.K.H. Salje, W. Schranz, D.E. Soto-Parra, E. Vives, Phys. Rev. Lett. **110**, 088702 (2013)
3. F. Kun, I. Varga, S. Lennartz-Sassinek, I.G. Main, Phys. Rev. Lett. **112**, 065501 (2014)
4. J.P. Sethna, K.A. Dahmen, C.R. Myers, Nature **410**, 242 (2001)
5. E.K.H. Salje, K.A. Dahmen, Crackling noise in disordered materials, ed. J.S. Langer. Annu. Rev. Condens. Matter Phys. **5**, 233–254 (2014)
6. G. Durin, S. Zapperi, in *The Science of Hysteresis*, vol. II, ed. by G. Bertotti, I. Mayergoyz (Elsevier, Amsterdam, 2006), pp. 181–267
7. F. Colaiori, Adv. Phys. **57**, 287 (2008)
8. D.M. Dimiduk, C. Woodward, R. LeSar, M.D. Uchic, Science **26**, 1188 (2006)
9. M.-C. Miguel, A. Vespignani, S. Zapperi, J. Weiss, J.-R. Grasso, Nature **410**, 667 (2001)
10. A. Vinogradov, I.S. Yasnikov, Acta Materialia **70**, 8 (2014)
11. M. Zaiser, J. Schwerdtfeger, A.S. Schneider, C.P. Frick, B.G. Clark, P.A. Gruber, E. Arzt, Philos. Mag. **88**, 30–32, 3861 (2008)
12. M.C. Gallardo, J. Manchado, F.J. Romero, J. del Cerro, E.K.H. Salje, A. Planes, E. Vives, R. Romero, M. Stipcich, Phys. Rev. B **81**, 174102 (2010)
13. J. Baró, J.-M. Martin-Olalla, F.J. Romero, M.C. Gallardo, E.K.H. Salje, E. Vives, A. Planes, J. Phys.-Condens. Matter **26**, 125401 (2014)
14. E.K.H. Salje, J. Koppensteiner, M. Reinecker, W. Schranz, A. Planes, Appl. Phys. Lett. **95**, 231908 (2009)
15. L.I. Salminen, A.I. Tolvanen, M.J. Alava, Phys. Rev. Lett. **89**, 185503 (2002)
16. S. Santucci, P.P. Cortet, S. Deschanel, L. Vanel, S. Ciliberto, Europhys. Lett. **74**(4), 595 (2006)
17. M. Stojanova, S. Santucci, L. Vanel, O. Ramos, Phys. Rev. Lett. **112**, 115502 (2014)
18. E.K.H. Salje, G.I. Lampronti, D.E. Soto-Parra, J. Bar, A. Planes, E. Vives, Am. Mineral. **98**, 609 (2013)
19. G.F. Nataf, P.O. Castillo-Villa, J. Baró, X. Illa, E. Vives, A. Planes, Phys. Rev. E **90**, 022405 (2014)

20. G. Nataf, P.O. Castillo-Villa, P. Sellappan, W.M. Kriven, E. Vives, A. Planes, E.K.H. Salje, J. Phys. Condens. Matter **26**, 275401 (2014)
21. P.O. Castillo-Villa, J. Baró, A. Planes, E.K.H. Salje, P. Sellappan, W.M. Kriven, E. Vives, J. Phys. Condens. Matter **25**, 292202 (2013)
22. E.K.H. Salje, X. Wang, X. Ding, J. Sun, Phys. Rev. B **90**, 064103 (2014)
23. E. Dul'kin, E.K.H. Salje, O. Aktas, R.W. Whatmore, M. Roth, Applied. Phys. Lett. **105**, 212901 (2014)
24. E.K.H. Salje, W. Schranz, Z. Kristallographie **226**, 1 (2011)
25. P. Levitz, G. Ehret, S.K. Sinha, J.M. Drake, J. Chem. Phys. **95**, 6151 (1991)
26. N. Eschricht, E. Hoinkis, F. Mdler, P. Schubert-Bischoff, Stud. Surf. Sci. Catal. **144**, 355 (2002)
27. J. Koppensteiner, W. Schranz, M.A. Carpenter, Phys. Rev. B **81**, 024202 (2010)
28. A. Ghaffar, *Confinement-Induced Structural Changes of Alkali Metals in Nanoporous Systems* (Universität Wien, Vienna, 2014)
29. W. Schranz, Phase Transit. **64**, 103 (1997)
30. Since we can measure length changes only when whole planes collapse, we have to multiply the typical crack length a by the number of broken bonds in one plane, but since the force that is acting on a bond is divided by the same number of broken bonds, the two terms cancel for the released elastic energy
31. We analyzed data only starting from the second cycle, since the first cycle seems to be contaminated by cracks due to tiny irregularities in the surface
32. A. Clauset, C.R. Shalizi, M.E.J. Newman, SIAM Rev. **51**, 661 (2009)
33. A. Deluca, A. Corral, Acta Geophys. **61**, 1351 (2013)
34. A.K. Hartmann, *Big Practical Guide to Computer Simulations*, 2nd edn. (World Scientific, Singapore, 2015)
35. M. LeBlanc, L. Angheluta, K. Dahmen, N. Goldenfeld, Phys. Rev. E **87**, 022126 (2013)
36. T. Utsu, Y. Ogata, R.S. Matsuura, J. Phys. Earth **43**, 1 (1995)
37. M. LeBlanc, L. Angheluta, K. Dahmen, N. Goldenfeld, Phys. Rev. Lett. **109**, 105702 (2012)
38. K. Dahmen, J.P. Sethna, Phys. Rev. B **53**, 14872 (1996)

Chapter 5
Crackling Noise in Digital and Real Rocks–Implications for Forecasting Catastrophic Failure in Porous Granular Media

Ian G. Main, Ferenc Kun and Andrew F. Bell

Abstract 'Crackling noise' occurs in a wide variety of systems that respond to steady-state external forcing in an intermittent way, leading to sudden bursts of energy release similar to those heard when crumpling a piece of paper or listening to a fire. In rock physics sudden changes in internal stress associated with microscopically-brittle rupture events lead to acoustic emissions that can be recorded on the sample boundary, and used to infer the state of internal damage. Crackling noise is inherently stochastic, but the population of events often exhibits remarkably robust scaling properties, in terms of the source area, duration, energy, and in the waiting time between events. Here we describe how these scaling properties emerge and evolve spontaneously in a fully-dynamic discrete element model of sedimentary rocks subject to uniaxial compression applied at a constant strain rate. The discrete elements have structural disorder similar to that of a real rock, and this is the only source of heterogeneity. Despite the stationary strain rate applied and the lack of any time-dependent weakening processes, the results are all characterized by emergent power law distributions over a broad range of scales, in agreement with experimental observation. As deformation evolves, the scaling exponents change systematically in a way that is similar to the evolution of damage in experiments on real sedimentary rocks. The potential for real-time forecasting of catastrophic failure obeying such scaling rules is then examined by using synthetic and real data from laboratory tests and prior to volcanic eruptions. The combination of non-linearity in the constitutive rules and an irreducible stochastic component governed by the material heterogeneity and finite sampling of AE data leads to significant variations in the precision and accuracy of

I.G. Main (✉) · A.F. Bell
School of Geoscience, Grant Institute, University of Edinburgh,
James Hutton Road, Edinburgh EH9 3FE, UK
e-mail: ian.main@ed.ac.uk

A.F. Bell
e-mail: a.bell@ed.ac.uk

F. Kun
Department of Theoretical Physics, University of Debrecen, P.O. Box 5,
Debrecen 4010, Hungary
e-mail: ferenc.kun@science.unideb.hu

E.K.H. Salje et al. (eds.), *Avalanches in Functional Materials and Geophysics*,
Understanding Complex Systems, DOI 10.1007/978-3-319-45612-6_5

the forecast failure time. This leads to significant proportion of 'false alarms' (forecast too early) and 'missed events' (forecast too late), as well as an over-optimistic assessments of forecasting power and quality when the failure time is known (the 'benefit of hindsight'). The evolution becomes progressively more complex, and the forecasting power diminishes, in going from ideal synthetics to controlled laboratory tests to open natural systems at larger scales in space and time.

5.1 Introduction

There is widespread interest in the prospect of forecasting system-sized catastrophic failure events in porous media and in the Earth, from the failure of stone-built bridges to landslides, rockfalls, volcanic eruptions and earthquakes, both natural and induced. Most methods for investigating this problem rely on the recording of elastic waves on the Earth's surface or the rock sample boundary, in turn caused by much smaller earthquakes or acoustic emissions that result from locally-brittle fracture and/or shear events. Such analysis is often combined with changes in bulk properties such as stress, strain, and elastic wave velocities where available. In the Earth it is not possible to measure the stress directly – a significant handicap compared to a controlled laboratory environment. Unfortunately, the search for reliable precursors to damaging earthquakes has not so far proven fruitful despite the large literature on candidate precursors [63]. The many claimed 'precursors' can largely be attributed to the unconscious biases that are associated with retrospective selection of data containing an irreducible stochastic component ([21], see also example in [35], their Fig. 5.5). This has in turn led to modern testing programmes that require forecasting of event probability to be made publically in real time as a 'blind test', and only then evaluated in retrospect by the community (e.g. http://www.cseptesting.org/).

Many current models for such forecasting are statistical, based on empirical scaling laws for seismicity that are also features of laboratory acoustic emissions on a smaller scale. In turn they are part of a much larger family of systems exhibiting 'crackling noise', where competition between local interactions and random fluctuations in disordered media results in broad-band power-law scaling and clustering in the resultant populations of discrete avalanches or 'bursts' of energy release [53, 57].

In this paper we first introduce some of the conceptual models that have been applied to populations of brittle rupture events in Earth materials on different scales in space and time. We then describe some of the phenomenology observed in the build-up to catastrophic failure in a controlled laboratory environment, and compare these to the results of some recent numerical simulations for the emergent scaling laws in space, time and event magnitude. Modern discrete element models are shown to reproduce much of the phenomenology of acoustic emissions in real rock samples, and highlight the fundamental role of structural disorder in controlling the emergent behaviour in the population dynamics, including the evolution from spatially-random

to localised brittle failure events. Finally we assess the implications of the emergent behaviour in forecasting system-sized brittle failure events on different scales in space, time and event magnitude.

5.2 Conceptual Models for the Population Dynamics of Brittle Rupture

The population dynamics of brittle failure events is often addressed using theories derived from the analysis of phase transitions in thermodynamics and statistical mechanics. This approach has a relatively long pedigree. Griffith's theory [15, 16] for crack nucleation closely parallels Gibbs' earlier theory [14] for the nucleation of raindrops, substituting intact or broken solid as phases rather than liquid or vapour, the specific surface energy for surface tension, the strain energy held in the bulk sample for the degree of super-saturation in the cloud, and critically the degree of permanent structural disorder (pre-existing micro-cracks or flaws) for fluctuations in temperature as a source of randomly-distributed potential nucleation sites. While raindrops eventually fall out of cloud under gravity at a critical size, the original Griffith nucleation theory allows arbitrarily large or system-sized avalanches to occur when the pre-existing stable crack exceeds a critical length associated with the maximum in free energy as a function of crack size. In practice a crack nucleating in a heterogeneous medium can also be stopped by random fluctuations in strength [51]. The growing crack can also be 'blunted' by a stress shadow caused by a cloud of damage or 'process zone' occurring ahead of the crack tip [4], also associated with random strength fluctuations [52].

In more recent times the notion of phase transitions has been extended to describe the population dynamics of far-from equilibrium systems, including earthquakes and acoustic emissions, notably the statistical physics of critical point or near-critical point systems. For example, in the laboratory the mean source crack length $y = < c >$ and the cumulative number of acoustic emissions $y = N$ inferred from acoustic emission data both increase according to an inverse power law under steady-state loading conditions of constant stress or constant applied strain rate

$$y = y_0 \left(1 - \frac{x}{x_c}\right)^{-\nu} \quad , \tag{5.1}$$

where x may be strain or time, which diverges at a critical value x_c, and the exponent $\nu > 0$ [28, 29]. At the same time the scaling in the frequency-size distribution of source energy (or seismic moment - the product of the shear modulus, the rupture area and the average source displacement) take the form of a power-law with an exponential cut-off

$$N = N_o \, (E/E_0)^{-B} \, \exp\left(-\frac{E}{E^*}\right) \quad , \tag{5.2}$$

where the exponent $B > 0$, subscripts zero denote characteristic values, and E^* is a characteristic energy related to the correlation length of the population of seismic sources (approximately the size of the largest cluster of broken elements). While a finite E^* is required to maintain a finite flux of strain energy [31], it can often be difficult to pin down in natural earthquake samples due to the small samples currently available in instrumental and historical data compared to the timescales of geological processes [7, 33]. Under these conditions the frequency-distribution can be approximated as a pure power law for seismic energy or moment, or an exponential one in magnitude m – a form known as the Gutenberg–Richter law, $\log(N) = a\text{-}bm$, where a is related to the total number of events and $b = 3B/2$ [31].

Equations (5.1) and (5.2) imply that the correlation length also diverges as in (5.1). This inverse power law acceleration of the correlation length and the power-law scaling of the size distribution are both characteristic of the approach to a critical point in a variety of physical systems [11]. The analogy is complete when we regard the stress drop (related to the difference in strain energy between intact and ruptured phases) as an appropriate 'order parameter' which diminishes to zero at the critical point [34].

The systems above require tuning of an external variable to bring the system to a critical state, represented by a system-sized rupture in our case. In the Earth (and many other systems driven slowly at a constant rate of external forcing, and which release energy intermittently in discrete dynamic events or avalanches) the system instead appears *spontaneously* to have arrived at a steady state of near-critical behaviour, where the system is perpetually in a state of near failure, including locations remote from plate boundaries [1]. This state is commonly referred to as 'self-organised criticality', a relatively loose term which includes near but not precisely critical behaviour [34]. It describes the long-term averages in the system, and explains much of the phenomenology of earthquakes and faulting in a single unified theory, including the observed power-law frequency-size distribution of events, the scale-invariant or self-affine nature of observed fault structures and the ease with which earthquakes can be triggered by relatively small natural or man-made stress perturbations in the subsurface [31]. It also provides a physical basis for the assumption of long-term stationarity in time-independent probabilistic seismic hazard estimation [30].

In a state of ideal strict self-organised criticality the timing of the next system-sized event would be random and unpredictable. Such temporally-random behaviour is also an explicit assumption in time-independent seismic hazard estimation. The size of an individual event, modelled as a cascade or avalanche of neighbouring failures, is an outcome of an inherently stochastic process in the absence of detailed direct knowledge of the state of stress at each microscopic location in the Earth. The question remains 'does an earthquake know how big it is going to be when it nucleates'? The answer is that it may to some extent, in that there is a weak correlation between the rate of seismic moment released in the first few seconds and the ultimate seismic moment of earthquakes, albeit with a large scatter [13]. The moment rate function is on average front-loaded, also consistent with the stacked data shown in Fig. 5.4 of [41] and laboratory experimental data [59]. These results are consistent

with each other despite the large differences in scale, but are inconsistent with the mean field model of ([57], see their Fig. 5.7).

The large scatter between the seismic moment release soon after earthquake or fracture nucleation and its eventual total originates from the large variability in the complexity of the moment rate function [24, 57], and places significant constraints on the precision with which one could estimate an ultimate earthquake size in time to provide early warning (Kanamori, 2008). This large scatter is also consistent with rupture propagation and arrest being controlled by details of the local strength and/or dynamics that would be inaccessible to direct observation before it has occurred. Together with the absence of systematic and reliable earthquake precursors [21], this has led to a reduction in confidence in the viability of reliable and accurate deterministic earthquake prediction as a realistic scientific goal (http://www.nature.com/nature/debates/earthquake/equake_frameset.html). Nevertheless, the small but finite stress drop in the Earth allows at least in principle a degree of 'intermittent criticality' [22, 34]. Unfortunately the search for the implied acceleration to failure of the form of (5.1) has so far not passed the rigorous statistical testing needed to establish this as a general phenomenon in natural earthquake populations [17].

On the other hand purely statistical models for the probability of earthquake triggering, including aftershocks, can lead to a significant probability gain in identifying periods of transiently-elevated hazard when compared with random process, even in real time [23]. Currently the best model for such 'operational earthquake forecasting' is based on an epidemic-type point process [49], itself a variant of a more general class of self-exciting processes [19]. This model combines a random background rate with a triggering probability for consequent events which satisfies a time-reversed form of (5.1) known as the Omori law. In cases of induced or volcanic seismicity, or during earthquake 'swarms' the background rate may be non-stationary. In the Epidemic-Type Aftershock Sequence model of [49] earthquake size is randomly sampled from the scaling relation (5.2) and the triggering rate depends on a 'productivity factor' related to the triggering event magnitude (a logarithmic measure of source energy or seismic moment). The magnitude difference can be negative in rare cases due to the random sampling, leading spontaneously to occasional triggering of larger events by a smaller one. The model can be expressed mathematically in the following form:

$$\lambda(t) = \mu + A\sum_{i,t_i<t} \exp[\alpha\,(m_i - m_C)]\left(1 + \frac{t - t_i}{c}\right)^{-p} \tag{5.3}$$

where $\lambda(t)$ is the event rate at time t, μ is the 'background' rate of independent events above a threshold magnitude m_C, c is a time constant ensuring finite event rate at $t = t_i$, p is the Omori–law exponent, α is the productivity factor for earthquake magnitude m_i, and A is an amplitude factor [49].

The model can be modified to include spatial clustering in the probability of triggering, either solely by distance or also by azimuth relative to the parent fault orientation, calculated by simulations of the immediate stress feedback and redistribution

after a large event (e.g. [40]). Longer-term 'stress renewal' models which incorporate ongoing loading and a stochastic element have also been used to estimate the effect of longer-term memory on the system, but their probability gains above a random process remain low [50].

5.3 Approach to Catastrophic Failure in a Laboratory Environment

In laboratory experiments on ceramic materials, glasses and rocks, catastrophic failure can occur below the critical stress for failure *in vacuo*, due to environmentally-assisted crack growth, even under static load. Sub-critical crack growth by thermally-activated chemical weakening processes under stress is also an intermittent, locally dynamic process that results in acoustic emissions – the macro-crack grows in jumps, and is associated with a cloud of damage associated with micro-cracks observed around the growing fracture, concentrated near the crack tip (e.g. [18]). The constitutive behaviour is often described empirically by a power law

$$V = \frac{dc}{dt} = V_0(K/K_0)^n \quad , \tag{5.4}$$

where V is velocity, K is stress intensity (a measure of stress concentration, proportional to the stress and the square root of nucleating crack length c), subscripts zero denote initial values and n is an exponent known as the 'stress corrosion index' [43]. Similar power-law behaviour can also be seen in the acoustic emission event rate dN/dt [42, 43]. This equation can be solved under conditions of constant stress to predict accelerating crack growth $c(t)$ or the total number of events $N(t)$ of the form of (5.1), with statistically-indistinguishable behaviour occurring under finite but slow stress loading conditions [32].

The intermittent and non-linear nature of quasi-static, sub-critical, crack growth is captured in the 'lattice-trapping' model, where the specific surface energy term in the Griffith nucleation theory is modulated by a sinusoid representing periodic strength variation in a crystal lattice, and the time-dependent intermittent crack growth rate is controlled by the height of the resulting local free energy barrier and hence the rate of the relevant chemical weakening reaction, modelled as a kinetic process ([27], Chap. 6). This results in a thermally-activated, intermittent crack growth even at constant stress, as well as other aspects of time-dependent behaviour such as static creep or fatigue. The theory predicts an approximately exponential dependence of V on K, but neglects the material disorder in the surrounding medium that is the origin of damage away from the crack tip, and also likely to be a fundamental control on the emergent power-law and the value of its exponent [28].

Time-dependent behaviour implies that the rate at which stress or strain is applied will affect the rheology. At high strain rates rocks produce much more brittle behaviour under compressive loading, but also more associated damage and associated

'crackling noise' in the surrounding medium that provide much more warning in the sub-critical stage. At lower strain rates (5.1) still holds, but the onset of detectable precursory acoustic emissions is delayed, the material becomes weaker (peak stress is reduced), the acceleration to failure curve becomes much sharper and the proportion of smaller events increases as the loading rate is reduced [48]. This strain-rate dependent behaviour has also been seen in other systems, including twinning avalanches occurring during high-speed impact events [53, 65].

In terms of spatial scale, the probability that one of the randomly-distributed Griffith flaws or stress concentrators being activated increases with the volume of the loaded specimen. Thus, catastrophic fracture initiates earlier for a large specimen and the macroscopically-deduced critical stress is smaller. In terms of observation and damage mechanics modelling, the material becomes both weaker and more brittle in this respect as it increases in size, behaving more like a continuum with a single flaw, as expected by the theory of Linear Elastic Fracture Mechanics [55]. Again in the limit of a very large system size, catastrophic failure would occur without warning in such a system.

On both counts we would expect predictability of individual system-sized events to degrade as the loading rate decreases and the system size increases. The logical deduction from such scaling effects is that prediction of individual earthquakes is intrinsically much harder than those of laboratory-scale fracture, and may not be possible in practical terms. This is consistent with our experience of the practical problem of deterministic earthquake prediction [23], including well-instrumented areas where a positive absence of precursors and sudden-onset rupture has been observed [2].

5.4 Squashing the Digital Rock

The above discussion has concentrated on empirical observation and models for fracture of disordered or damaged media based largely on mean-field approximations (damage mechanics), or simple cellular automaton models that capture the avalanche-like nature of the dynamics, at the expense of reducing the dimensionality of the problem to two, and the disorder to random processes acting on a geometrically-regular grid of elements (e.g. [1]). However, in critical phenomena the relevant critical exponents are known to depend to first order on the dimensionality of the model, and empirically the observed structural disorder of porous media is more amorphous than a grid. As a consequence it is necessary to tune the models to obtain the correct values of exponents such as B in (5.2), notably the dissipation factor on stress transfer after failure [34, 47].

Accordingly many researchers have turned to discrete element modelling of porous media. In the model of [25, 26]; see also [3] three-dimensional particles are represented by hard, unbreakable elastic spheres. Their diameter is selected randomly from a broad-band (log-normal) distribution, similar to that observed in a natural aquifer or hydrocarbon reservoir rock such as sandstone. The particles are

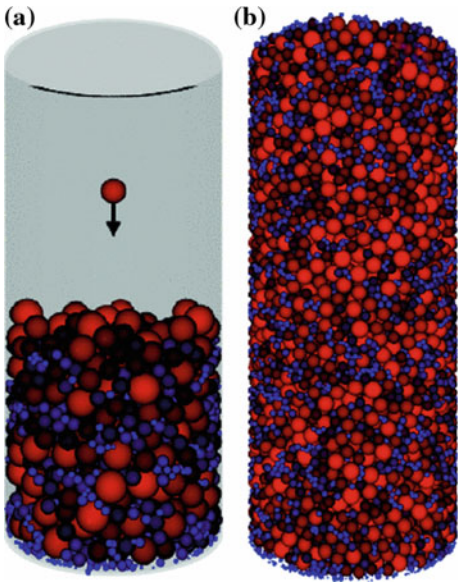

Fig. 5.1 The digital rock: **a** Illustration of its formation under sedimentation; **b** final configuration. Smaller particles are in *blue*, intermediate in *darker shades* of *red* and larger ones in *bright red* (from [25])

dropped into a cylinder under gravity, bounce around and settle in a sedimentation process that introduces a realistic structural disorder (Fig. 5.1). The particles are then cemented together by elastic bonds that can fail in either tension or torsion (shear), in both cases when the relevant stress exceeds a uniform local bond strength. The top few layers of particles are cemented by unbreakable bonds, effectively clamping the top and bottom of the sample to the boundaries where the load is applied. Some 20,000 particles were used in the above references. For a typical reservoir rock with a peak diameter at 200 microns, the equivalent bulk sample diameter is 6–7 mm. This is much smaller than the typical laboratory deformation testing range (2.5–10 cm diameter), but comparable to modern experiments aimed at elucidating the microscopic mechanisms of failure using high-resolution CT scanning using X rays [10] or neutron diffraction. At this stage of the modelling no layering or any other form of correlation above that produced by random sedimentation is introduced. This is not because we believe it to be unimportant. Instead it is because it is only with a controlled comparison with a randomly-uniform disordered medium that we could isolate the effect of such additional complexity at a later stage. The random uniform properties of the digital rock are shown in Fig. 5.2.

The digital rock is then squashed by applying a load at constant displacement rate to the upper surface of the cylinder, the lower one remaining fixed (see inset on Fig. 5.3). The combination of elastic interactions with initial structural disorder produces emergent stress heterogeneity, in the form of stress concentrations on 'force chains', and stress shadows in between. Once a bond is broken the particles are free to move dynamically and re-settle into a new configuration, arrested by the Hertzian forces acting between neighbouring spheres in contact. The Hertzian contact is the

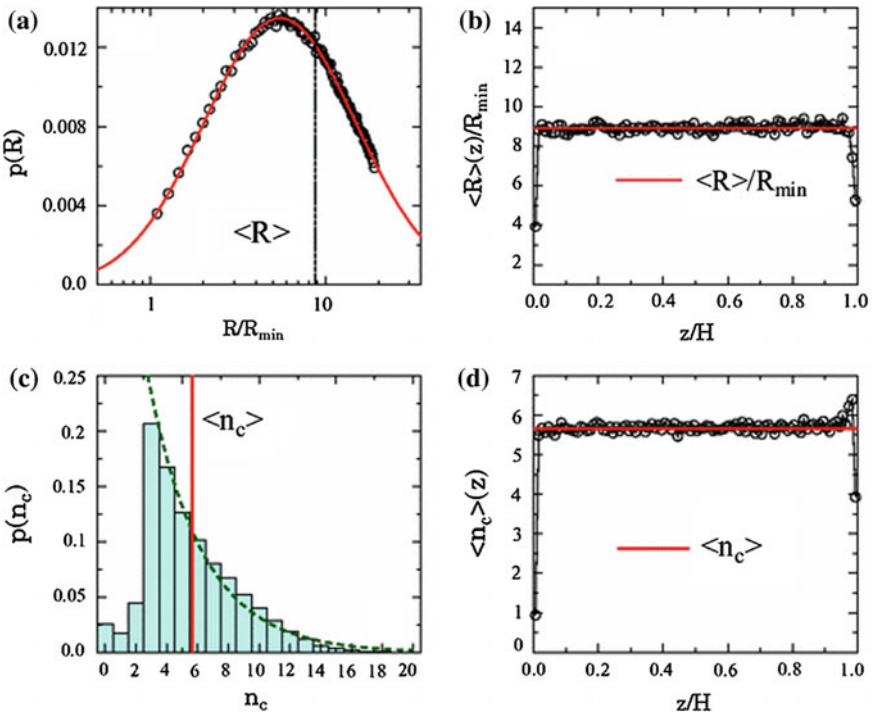

Fig. 5.2 Properties of the digital rock (from [25]). **a** Probability density function for particle radius R, normalised to its minimum value, based on sampling from a log-normal distribution. The *vertical line* indicates the average value <R>. **b** Variability of <R> as a function of vertical position z, normalized to the cylinder height H. **c** Probability density function for the number of contacts each particle has with its neighbours n_c. The *vertical red line* shows the average $< n_c >$ or 'co-ordination number'. **d** Co-ordination number as a function of z/H

basis for emergent frictional behaviour at the macroscopic level [56]. The broken bonds do not heal, and stress is redistributed dynamically to the neighbouring bonds, producing avalanches or cascades of bond ruptures representing correlated 'bursts' of energy release. While elastic radiation does take place, there is no need to put model transducers on the digital rock boundary and infer the source parameters. Instead parameters such as event time, hypocentre location, source energy, rupture area (or the number of broken bonds Δ as a proxy), average slip, the related seismic moment (product of shear modulus, rupture area and average slip), inter-event time can all be calculated directly from the model. The collective properties of this population are then a direct analogue for the source parameters of the 'crackling noise' observed in real rock samples during a laboratory test, with the advantage of having a complete sample of all local failure events.

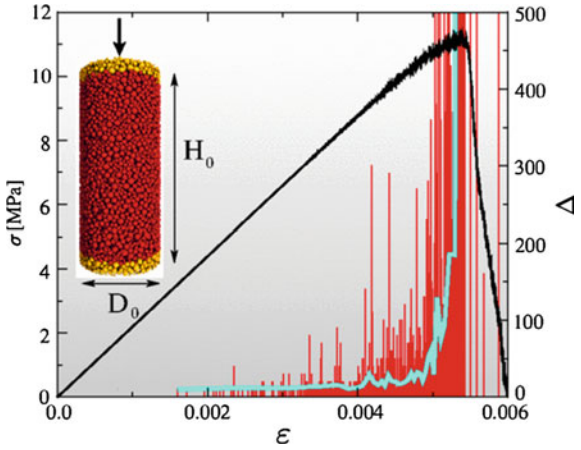

Fig. 5.3 Squashing the digital rock. The inset shows the digital rock, diameter D_0 and Height H_0, with the *top* few infinitely strong layers highlighted in *yellow*, and the direction of uniaxial force as an arrow. The *black curve* shows the stress σ as a function of strain ε, the *vertical red lines* represent the rupture area proxy Δ for each event, and the *blue line* the average $< \Delta >$ (from [26])

5.5 Properties of the Crackling Noise

The event sizes Δ are also shown in Fig. 5.3, both as a 'comb' plot of discrete individual events and as a running average. Crackling noise starts early – well before any sign of non-linearity in the stress-strain curve, and the mean event size accelerates rapidly after the yield point, in a manner similar to (5.1). The frequency-size distribution has the same form as (5.2) over a broad range of length scales in Fig. 5.4. As deformation progresses the best fit power-law exponent decreases (the slope becomes flatter) and the implied correlation length (related to the largest rupture size) increases. System-sized failure near the critical strain ε_c is marked by large apparent outlier events from the trend in (5.2) often termed 'dragon kings' [58] or, for natural seismicity, 'characteristic earthquakes'. Such a large gap between the largest and the next largest correlated cluster of broken bonds, allied with the large stress drop, is more reminiscent of a first order phase transition. However, establishing such 'dragon kings' are meaningful statistical outliers in natural data is often very difficult [45].

The event locations are dominated by the random disorder initially (see locations of nucleation points illustrated in Fig. 5.4), but increasingly localise on an incipient fault plane [25], just as occurs in experimental data on sandstone [28]. At the same time the correlation function of nucleation points spontaneously tends to a power law, with a power-law exponent (correlation dimension) decreasing to $D_2 = 2.25$ near the failure time [25]. This behaviour is in good quantitative agreement with the results of laboratory acoustic emission locations, where similar to the range observed in laboratory tests where D_2 starts off at around 2.75 when the deformation is more randomly distributed, and then decreases to around 2.25 near the failure time [20]. At the same time the incremental frequency-rupture area exponent (for the range of events shown) decreases from 1.1 to 0.4 (Fig. 5.4).

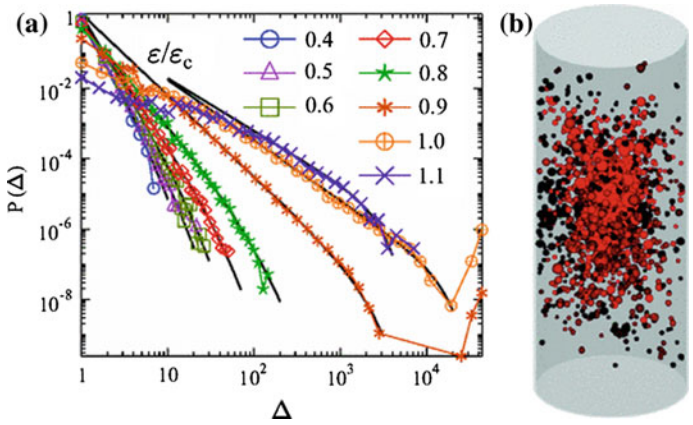

Fig. 5.4 The *left-hand* diagram shows the evolution of the probability density function for source size $p(\Delta)$, split up into consecutive increments of normalised strain indicated by the event numbers shown. The diagram on the *right plots* the location of the nucleation points for dynamic rupture cascades, an analogue for the location of acoustic emission sources

Figure 5.5 compares the results of the discrete element model with those of a laboratory test on natural sandstone. The mean event size for the digital rock increases in a similar way to that expected from combining (5.1) and (5.2), and the real data for event rate follow (5.1) directly, i.e. both are inverse power laws. The exponent ξ of the probability density function $p(\Delta)$ decreases monotonically in the model from around 4 to 1.5. The Gutenberg–Richter '*b*-value' shown for the real data is defined by the slope of the cumulative or incremental frequency curve for event magnitude, itself a logarithmic measure of energy. For a sensor acting as a velocity transducer and a constant stress drop model for acoustic emission sources, the *b*-value is related to B in (5.2) by $b = 3B/2$ with $E \sim \mathrm{A}^{1.5}$ and $p(A) \sim A^{-b-1}$ (e.g. [31]). Assuming rupture area scales linearly with the number of broken bonds, $A \sim \Delta$, the values of ξ imply a *b*-value decreasing from around 3 to 0.5 as failure approaches. This compares with the observation on Fig. 5.4 that $1.5 < b < 0.5$ in the laboratory tests. The absence of higher *b*-values early in the loading cycle in the laboratory tests could be due to a break down in the scale-independent stress drop model, or to data censoring of smaller events below ambient noise levels. Nevertheless, the inferred *b*-values for the later part of the real and laboratory tests are quantitatively similar, and exactly the same (around 0.5) immediately prior to catastrophic failure. A *b*-value prior to catastrophic failure of around half of the long-term average is also consistent with values reported for earthquake foreshocks, in cases where they are observed after the fact [44].

For the digital rock, the scaling may not be strictly self-similar. The energy of the bursts E scales with Δ as $E \sim \Delta^{1.15}$ [26]. This may be because the scaling of slip to rupture area is self-affine (power-law of slope less than 0.5) rather than self-similar, and/or because the parameter Δ (the number of broken bonds) does not scale

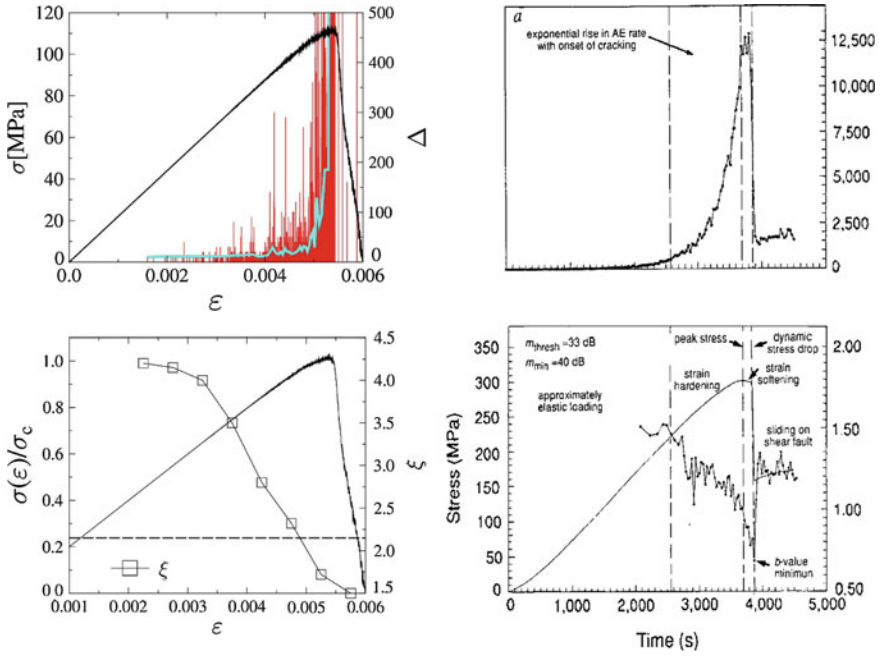

Fig. 5.5 Comparison of the model simulation results (*left hand* column, replotted after [25, 26]) with a real dry rock (*right-hand* column, from [54]). The *upper* diagrams show the acceleration of event size for the model (as in Fig. 5.3) compared to the event rate data (*top right* diagram). The *lower left* diagram show the power-law exponent of the probability density function for source size Δ (one curve for a constant strain window as in Fig. 5.4, and one for a constant number of events in each sub-sample) compared to the seismic *b*-value evolution in a laboratory test

linearly with rupture area A. If we assume instead that magnitude is a logarithmic function of energy, then the observed scaling range for ξ implies that the exponent B for the energy distribution ranges from 2.9 to 0.37 or so, or an implied b-value range for a scale-independent stress drop model of $4.3 < b < 0.55$, i.e. a slightly wider range for the early part of the loading cycle but a similar value immediately prior to system-sized failure.

After catastrophic failure the digital rock is broken in two main intact blocks, separated by a fault that takes the form of a deformation band of broken fragments - as observed in laboratory tests (Fig. 5.6). The deformation band contains a fault 'gouge' of fragments or isolated original particles with a broad bandwidth of sizes – with large fragments floating in a ground mass of smaller ones. There is significant damage (local micro-fractures) in the zone around the main fault, and a complex three-dimensional rugged geometry of the fault walls, with variable fault thickness along the fault trace. The probability density function for particle mass in the digital rock deformation band for particles containing at least two elements has the same form as (5.2) with a power law exponent $\tau = 2.1$ over two orders of magnitude [26],

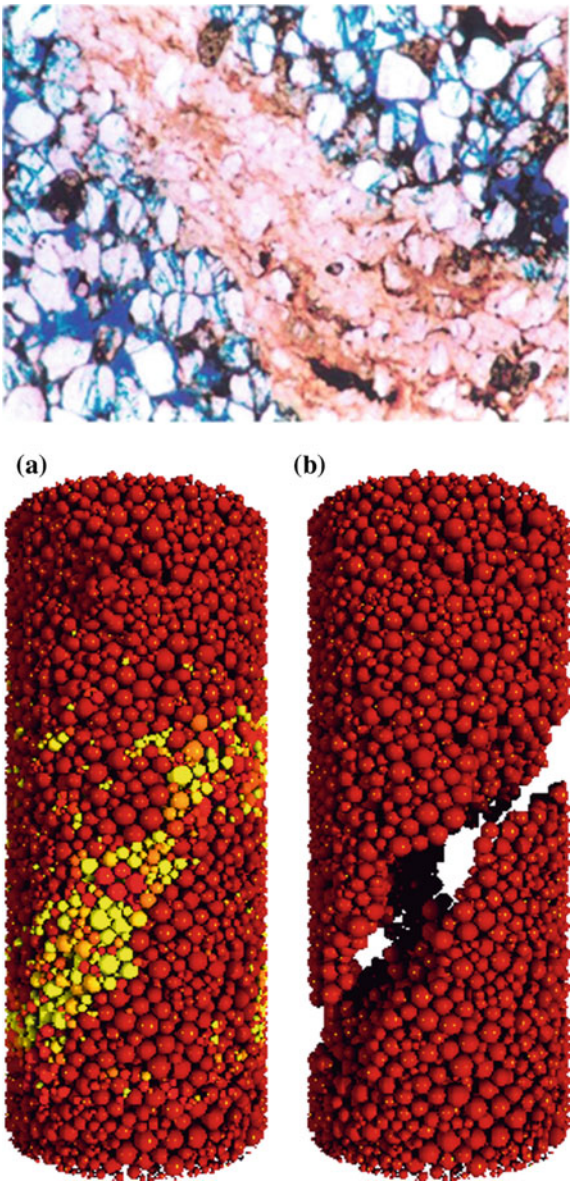

Fig. 5.6 Post-failure structure. The *upper* diagram shows a photo-micrograph of a thin section of a deformed laboratory sample of sandstone (colour version of the diagram shown in [37]). The rock has been injected with a fluorescent-dyed epoxy resin to preserve the structure and highlight locations of fracturing in *blue*. The lower diagram shows the digital rock after dynamic failure (from [25]): **a** The broken elements are shown in *yellow*, and the intact in *red*. **b** Image with broken elements removed

or (for the spherical particles of the discrete element model) an implied power-law exponent for the incremental frequency of particle diameter of $D = 3.3$. For real rocks the exponent of the frequency-particle length distribution for tests similar to those that produced the thin section in Fig. 5.6 (from [36], their Fig. 4.15), and those of real fault gouges (e.g. Table 3.1 of [61]) is $D \approx 2.6$. The main differences are likely

to be due to the angularity of the fragments in the real rock, the unbreakable nature of the discrete elements in the digital rock, and the lack of a confining pressure in the digital rock simulations. These remain a computational challenge that is currently being addressed in fully 3D simulations [38].

Emergent power laws of the form of (5.2) are also observed in the probability density functions for energy $p(E)$, duration $p(T)$, and waiting time between events $p(t_w)$ in the period before peak stress ([26], their Fig. 5.3). The distributions for energy and duration both show evidence of roll-offs in probability for smaller values associated with a lower cut-off to scale-invariant behaviour, whereas the source area proxy distribution $p(\Delta)$ does not. Best fits were obtained with the power-law exponents $\alpha = 2.02$, $\beta = 2.4$ and $z = 2.0$ for the probability density function of burst energy, duration and waiting time respectively, averaged over the period prior to the peak stress. This compares to an implied $\alpha = 1.67$ for an average $b = 1$ in the laboratory test of Fig. 5.5, and to $\alpha = 1.40 \pm 0.05$ for the uniaxial compression experiments of Vycor, a synthetic silica ceramic of ~40 % porosity [5].

The exponent for the waiting time distribution prior to peak stress in our numerical model $z = 2$ is significantly higher than that found by [5] with $z = 0.93 \pm 0.05$ for most of the time range of their laboratory tests. This discrepancy is most likely due to the absence of time-dependence in the properties of the digital rock at this stage of the modelling. References [5, 60] showed that a power-law inter-event time can be explained as an emergent property of the distribution of background and 'aftershock' events, based on the epidemic-type aftershock sequence (ETAS) model for earthquake populations. Even without aftershocks or more generally triggered events, a power law scaling in the inter-event time probability distribution can result from a non-stationary linear increase in the rate of independent events [64]. The lack of time dependence in our model means the properties of the digital rock do not depend on the loading rate, also in contrast to that seen in laboratory experiments [48], and would not result in long term creep and fatigue – another limitation compared to real rocks and other kinds of porous media. Despite these caveats, the similarity between the behaviour of the digital rock and laboratory samples, as well as the scaling to the properties of the Earth's crust are quite remarkable.

5.6 Implications for Forecasting

There are a number of clues to when catastrophic failure might occur, both in the models and in the observations collected in laboratory tests described above. These include event rate accelerating towards a singularity according to (5.1), reducing b-value, increased localisation of events in space along an incipient fault plane, and systematic changes to other exponents. In the laboratory or the digital rock a visual yield point is clear and the peak stress is a strong indicator of the onset of the final approach to failure. In the limit of an extremely brittle material catastrophic failure does occur at peak stress, but for many porous rocks system–sized failure occurs at a critical strain significantly beyond the peak stress, as captured in Fig. 5.5.

The most accurate failure forecasting model will then involve a combination of these metrics. This may be with a physical model (that also accounts for stochastic fluctuations), or a statistical approximation that may have more Information content (equally good fit with fewer free parameters). In practical scenarios there may be insufficient data for such a rigorous approach due to lack of data. For example practical volcano forecasting is often done using Bayesian 'event trees', where event rate and *b*-value changes can be included formally, along with other more subjective, 'expert' knowledge [39].

Let us now consider an ideal case, where the underlying AE rate accelerates to the critical point according to (1) plus or minus random fluctuations associated with material heterogeneity and/or finite sampling (counting errors). This defines the absolute limits of predictability of such an approach in an ideal case. By running several Monte-Carlo realisations [6, 8] mapped out the systematic and random errors involved in fitting (5.1) to infer the forecast failure time and its uncertainty for this case. To simulate a real-time or prospective forecast scenario they performed the inference at different times prior to the pre-determined failure time. First they showed that linearized versions of (5.1), often used for example in analysing seismicity associated with volcanic eruptions, introduce a systematic bias to the forecast failure time, even when data including the failure time are used. Instead a fully non-linear maximum likelihood fit to (1), assuming an underlying non-stationary Poisson process, produces a less biased fit. The random or statistical uncertainties are initially very large, and reduce significantly as more data are collected, and the most accurate forecast is after the system-sized event has occurred. This highlights the practical difficulties in evaluation of the significance of precursors retrospectively as descried by [21].

In evaluating such behaviour it is also critical to test competing hypotheses for the underlying behaviour of the time series. Accordingly [8] tested (i) stationary, (ii) exponential acceleration and (iii) (5.1) models concurrently, selecting the preferred model using a Bayesian Information Criterion, a modern form of Ockham's razor that accounts for the balance between the model residuals and the number of free parameters. A precursor is detected when the stationary model can be rejected, and a system-sized failure time cannot be defined unequivocally until (5.1) is the preferred model. The results showed that it is relatively easy to define a precursor, but an unequivocal failure time cannot be determined until relatively late in the cycle. Therefore it is possible to identify periods of enhanced probability of failure, but the precise failure time may not be known until very near or after the fact.

In real volcanic earthquake data the acceleration (determined after the fact) can be more complex that (5.1), leading to systematic errors in the best fit eruption time [7]. Such real data shows that accelerating sequences most often end in intrusions, where magma freezes in place underground rather than being extruded in eruptions [12]. Unfortunately the statistics of these two processes cannot currently be distinguished, so it is not possible to discriminate between them in real time unambiguously. This implies that local Civil Protection authorities would then have to live with many 'false alarms'. In real volcanic data (1) can be a good fit, but often the exponential model is preferred throughout or until just before the failure time. This limits the possibility of

a successful planned and orderly evacuation based on such a deterministic forecast. In this case there may be many 'misses' when the forecast time is after the eruption time, as well as 'hits' when the two are the same within the extrapolated uncertainty. Over time the ratio of 'hits', 'misses' and 'false alarms' will help quantify the hazard and risk probabilities, and also help educate the public on the practical limits of what science can do in forecasting such a complex, non-linear system [9]. Nevertheless, this probabilistic, risk-based approach has achieved some remarkable successes, leading to successful evacuations at the right time, for example at Mount St Helens, US, in 1980 and at Pinatubo, Philippines, in 1991.

5.7 Influence of Material Heterogeneity on Forecasting Power

The Griffith theory highlighted the important role of heterogeneity due to initial flaws (cracks and/or pores) in the fracture process of an otherwise intact material. Accordingly it would not be surprising if material heterogeneity would have a significant effect on the forecasting power. To test this notion Vasseur et al. [62] generate a suite of synthetic samples porous silicate liquids undergoing the glass transition with variable heterogeneity. A heterogeneity (disorder) parameter is defined by $H = \varphi - 0.5$, where φ is the porosity, such that $H = 0$ when φ=0 (perfect order) and $H = 1$ when φ=0.5 (perfect disorder). These synthetic porous media consisted of a range of samples of the same material, but with different porosity and microstructure (see their Fig. 5.1), in turn controlled by the gas volume fraction held in the cell during their synthesis. They then placed the synthetic rock under uniaxial compression, and recorded the AE generated in the approach to catastrophic failure.

In analysing the data (Fig. 5.7, from [62]) the exponential model is preferred when H is low, and the inverse power law when the degree of heterogeneity is high, as anticipated by the fibre bundle model of [46]. If a best-fit inverse power law is forced, then its prediction error (the normalised difference between the estimated failure time and the actual one) decreases significantly with the increasing material heterogeneity. In this sense catastrophic failure is easier to predict in heterogeneous materials. The material with high H has fewer events (Fig. 5.7a) most likely because of a greater proportion of 'silent' damage due to elastic pore closure as porosity increases. This variability in behaviour as a function of the degree of material heterogeneity may explain the large variability observed in real systems, and in time may improve the reliability and accuracy of operational forecasts, if it can be used to constrain the forecasting power in different settings.

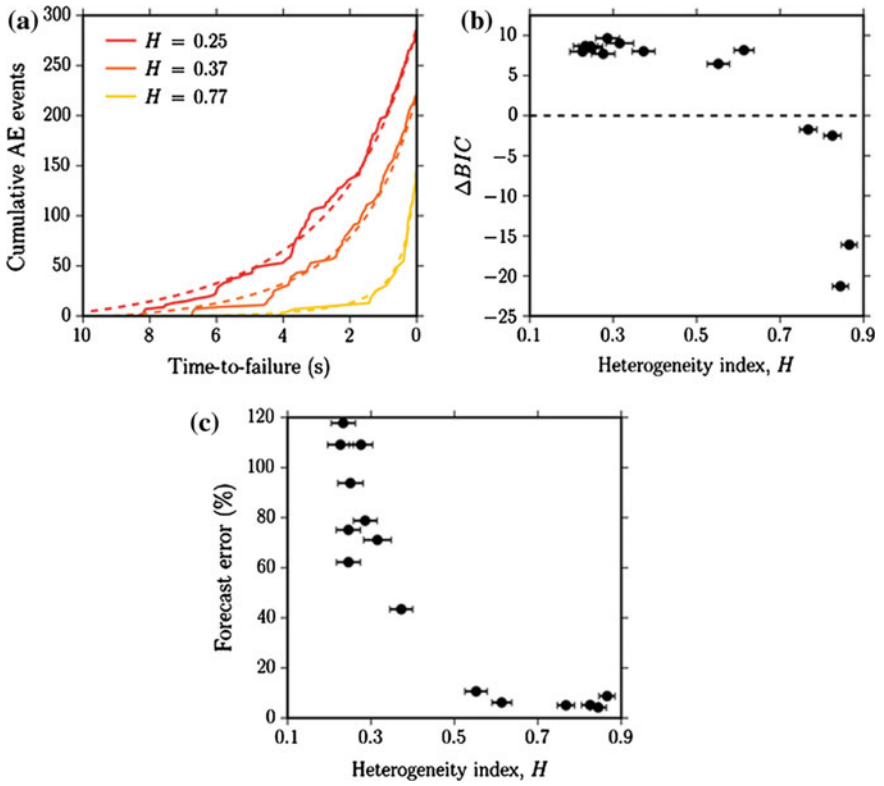

Fig. 5.7 Test of forecasting power as a function of the heterogeneity index $H = \phi - 0.5$, where ϕ is the porosity (from [62]). **a** Cumulative AE events (*solid lines*) and their maximum-likelihood best-fit curves (*dashed lines*). **b** Model selection using the difference in the Bayesian Information Criterion ΔBIC between exponential and inverse power-law acceleration in **(a)** The inverse power law is preferred when $\Delta\text{BIC} < 0$. **c** Heterogeneity-dependence of the forecast error, defined as the absolute difference between the predicted failure time and the experimental failure time, normalised by the deformation time, expressed as a percentage

5.8 Conclusion

A discrete element model with a particle size distribution similar to that of porous sandstone can now reproduce many of the scaling relationships observed in crackling noise in real rocks with similar properties. Despite the stationary loading rate and the lack of any time-dependent weakening processes, the results are all characterized by emergent power law distributions over a broad range of scales, in quantitative as well as qualitative agreement with experimental observation. As deformation evolves, the scaling exponents change systematically in a way that is similar to the evolution of damage in experiments on real sedimentary rocks. The combination of non-linearity in the constitutive rules and an irreducible stochastic component governed by the

material heterogeneity and finite sampling of AE data leads to significant variations in the precision and accuracy of the forecast failure time using constitutive rules derived from the model. The evolution of the crackling noise becomes progressively more complex, and the forecasting power diminishes, in going from the ideal behaviour revealed by the discrete element model to controlled laboratory tests to open natural systems at larger scales in space and time. Material heterogeneity plays a significant part in the emergent power-law scaling, and also affects the forecasting power. The results imply significant forecasting power above a random process that could be used in operational forecasting scenarios involving non-stationary seismicity, including seismicity induced by subsurface engineering projects and by magmatic processes leading up to volcanic eruptions.

Acknowledgments The bulk of this paper is based on the Néel lecture delivered by IGM at the 2014 European Union of Geosciences meeting in Vienna, and a shortened version delivered to the 'Avalanches in Functional Materials and Geophysics' meeting in Cambridge the same year. FK and AFB made significant material contributions to the presentations, and to the writing of this paper. IGM is grateful to Philip Meredith for many insights into rock physics that motivated the work described in the paper, as well as the many co-authors cited in the reference list, especially Jeremie Vasseur whose experimental results are reproduced in Fig. 5.7. Much of the work described in this paper was supported by the European Commission via the Complexity-NET pilot project 'LOCAT' and by the NERC project 'EFFORT', NE/H02297X/1.

References

1. P. Bak, C. Tang, Earthquakes as a self-organised critical phenomenon. J. Geophys. Res. **94**, 15635–15637 (1989)
2. W.H. Bakun et al., Implications for prediction and hazard assessment from the 2004 Parkfield earthquake. Nature **437**, 969–974 (2005). doi:10.1038/nature04067
3. P. Ball, How rocks break. Physics **7**, 16 (2014)
4. G.I. Barenblatt, The mathematical theory of equilibrium cracks in brittle fracture. Adv. Appl. Mech. **7**, 55 (1962)
5. J. Baró, Á. Corral, X. Illa, A. Planes, E.K.H. Salje, W. Schranz, D.E. Soto-Parra, E. Vives, Statistical similarity between the compression of a porous material and earthquakes. Phys. Rev. Lett. **110**, 088702 (2013)
6. A.F. Bell, M. Naylor, M.J. Heap, I.G. Main, Forecasting volcanic eruptions and other material failure phenomena: An evaluation of the failure forecast method. Geophys. Res. Lett. **38**, L15304 (2011). doi:10.1029/2011GL048155
7. A.F. Bell, M. Naylor, I.G. Main, Convergence of the frequency-size distribution of global earthquakes. Geophys. Res. Lett. **40**, 2585–2589 (2013a). doi:10.1002/grl.50416
8. A.F. Bell, M. Naylor, I.G. Main, The limits of predictability of volcanic eruptions from accelerating rates of earthquakes. Geophys. J. Int., (2013b), doi:10.1093/gji/ggt191
9. A.F. Bell, C.R.J. Kilburn, I.G. Main, Volcanic eruptions: real-time forecasting, in *Encyclopedia of Earthquake Engineering*, ed. by M. Beer, E. Patelli, I. Kougioumtzoglou, S.-K. Au (Springer, Berlin, 2015). doi:10.1007/978-3-642-36197-5_43-1
10. P. Bésuelle, G. Viggiani, N. Lenoir, J. Desrues, M. Bornert, X-ray micro CT for studying strain localization in clay rocks under triaxial compression. J. Strain Anal. Eng. Des. **40**(2), 185–197 (2006)
11. A., Bruce, D. Wallace, Critical point phenomena: universal physics at large lengthy scales, in Davies, P. (ed.) (The New Physics, Cambridge, 1989), p. 516

12. S.F.M. Chastin, I.G. Main, Statistical analysis of daily seismic event rate as a precursor to volcanic eruptions. Geophys. Res. Lett. **30**(13), 1671 (2003). doi:10.1029/2003GL016900
13. S. Colombelli, A. Zollo, G. Festa, M. Picozzi, Evidence for a difference in rupture initiation between small and large earthquakes. Nat. Commun. **5**, 3958 (2014). doi:10.1038/ncomms4958
14. J.W. Gibbs, *Elementare Grundlagen der Statistischen Mechanik* (Johann Ambrosius Barth, Leipzig, 1905)
15. A.A. Griffith, The phenomena of rupture and flow in solids. Phil. Trans. Roy. Soc. Lond. A **221**, 163 (1920)
16. A.A. Griffith, The theory of rupture,, ed. by C.B. Biezzo, J.M. Burgers, J. Waltman Jr., Proceedings of the First International Congress on Applied Mechanics, (Delft, 1924), p. 55
17. J.L. Hardebeck, K.R. Felzer, A.J. Michael, Improved tests reveal that the accelerating moment release hypothesis is statistically insignificant. J. Geophys. Res. **113**, B08310 (2008). doi:10.1029/2007JB005410
18. C.G. Hatton, I.G. Main, P.G. Meredith, A comparison of seismic and structural measurements of fractal dimension during tensile subcritical crack growth. J. Struct. Geol. **15**, 1485–1495 (1993)
19. A.G. Hawkes, Spectra of some self-exciting and mutually exciting point processes. Biometrika **58**(1), 83–90 (1971)
20. T. Hirata, T. Satoh, K. Ito, Fractal structure of spatial distribution of microfracturing in rock. Geophys. J. Roy. Astr. Soc. **90**, 369–37 (1987)
21. S. Hough, Predicting the Unpredictable: The Tumultuous Science of Earthquake Prediction (Princeton University Press, 2009) p. 272
22. S.C. Jaume, L.R. Sykes, Evolving towards a critical point: a review of accelerating seismic moment/energy release prior to large great earthquakes. Pure Appl. Geophys. **155**, 279–305 (1999)
23. T. Jordan, Y. Chen, P. Gasparini, R. Madariaga, I. Main, W. Marzocchi, G. Papadopoulos, G. Sobolev, K. Yamaoka, J. Zschau, Operational earthquake forecasting: state of knowledge and guidelines for utilization. Ann. Geophys. **54**(4), 361–391 (2011). doi:10.4401/ag-5350
24. H. Kanamori, Earthquake physics and real-time seismology. Nature **451**, 271–273 (2008). doi:10.1038/nature06585
25. F. Kun, I. Varga, S. Lennartz-Sassinek, I.G. Main, Approach to failure in porous granular materials under compression. Phys. Rev. E. **88**, 062207 (2013). doi:10.1103/PhysRevE.88.062207
26. F. Kun, I. Varga, S. Lennartz-Sassinek, I.G. Main, Rupture cascades in a discrete element model of a porous sedimentary rock. Phys. Rev. Lett. **112**, 065501 (2014). doi:10.1103/PhysRevLett.112.065501
27. B. Lawn, *Fracture of Brittle Solids*, 2nd edn. (Cambridge University Press, Cambridge, 1993). p. 371
28. S. Lennartz-Sassinek, I.G. Main, M. Zaiser, C. Graham, Acceleration and localization of subcritical crack growth in a natural composite material. Phys. Rev. E **90**, 052401 (2014). doi:10.1103/PhysRevE.90.052401
29. I.G. Main, A modified Griffith criterion for the evolution of damage with a fractal distribution of crack lengths: application to seismic event rates and b-values. Geophys. J. Int. **107**, 353–362 (1991)
30. I.G. Main, Earthquakes as critical phenomena: Implications for probabilistic seismic hazard analysis. Bull. Seismol. Soc. Am. **85**, 1299–1308 (1995)
31. I. Main, Statistical physics, seismogenesis, and seismic hazard. Rev. Geophys. **34**, 433–462 (1996)
32. I.G. Main, A damage mechanics model for power-law creep and earthquake aftershock and foreshock sequences. Geophys. J. Int. **142**, 151–161 (2000)
33. I.G. Main, L. Li, J. McCloskey, M. Naylor, Effect of the Sumatran mega-earthquake on the global magnitude cut-off and event rate. Nat. Geosci. **1**, p142 (2008)
34. I.G. Main, M. Naylor, Entropy production and self-organized (sub) criticality in earthquake dynamics. Phil. Trans. Roy. Soc. Lond. A **2010**(368), 131–144 (2010). doi:10.1098/rsta.2009.0206

35. I.G. Main, A.F. Bell, P.G. Meredith, S. Geiger, S. Touati, The dilatancy-diffusion hypothesis and earthquake predictability, in *Faulting, Fracturing and Igneous Intrusion in the Earth's Crust*, ed. by D. Healy, R.W.H. Butler, Z.K. Shipton, R.H. Sibson (Geological Society Special Publications, London, 2012), pp. 215–230. doi:10.1144/SP367.15
36. K. Mair, Experimental studies of fault zone development in a porous sandstone, Ph.D. thesis, University of Edinburgh (1997)
37. K. Mair, I.G. Main, S.C. Elphick, Sequential development of deformation bands in the laboratory. J. Struct. Geol. **22**, 25–42 (2000)
38. K. Mair, S. Abe, Breaking up: comminution mechanisms in sheared simulated fault gouge. Pure Appl. Geophys. **168**, 2277–2288 (2011). doi:10.1007/s00024-011-0266-6
39. W. Marzocchi, M. Bebbington, Probabilistic eruption forecasting at short and long time scales. Bull. Volcanol. **74**(8), 1777–1805 (2012)
40. J. McCloskey, S.S. Nalbant, S. Steacy, Indonesian earthquake: earthquake risk from co-seismic stress. Nature **434**, 291 (2005). doi:10.1038/434291a
41. A.P.K.A. Mehta, D.Y. Ben-Zion, Universal mean moment rate profiles of earthquake ruptures. Phys. Rev. E **73**, 056104 (2006)
42. P.G. Meredith, B.K. Atkinson, Stress corrosion and acoustic emission during tensile crack propagation in Whin Sill dolerite and other basic rocks. Geophys. J. Roy. Astron. Soc. **75**, 1–21 (1983). doi:10.1111/j.1365-246X.1983.tb01911.x
43. P.G. Meredith, B.K. Atkinson, Experimental fracture mechanics data for rocks and minerals, in *Fracture Mechanics of Rocks*, ed. by Atkinson B.K (Academic Press, London, 1987). chapter 11
44. G.M. Molchan, T.L. Kronrod, A.K. Nekrasova, Immediate foreshocks: time variation of the b-value. Phys. Earth Planet. Inter. **111**(3–4), 229–240 (1999). doi:10.1016/S0031-9201(98)00163-0
45. M. Naylor, J. Greenhough, J. McCloskey, A.F. Bell, I.G. Main, Statistical evaluation of characteristic earthquakes in the frequency-magnitude distributions of Sumatra and other subduction zone regions. Geophys. Res. Lett. **36**, L20303 (2009). doi:10.1029/2009GL040460
46. H. Nechad, A. Helmstetter, R. El Guerjouma, D. Sornette, Andrade and critical time-to-failure laws in fiber-matrix composites: experiments and model. J. Mech. Phys. Solids **53**(5), 1099–1127 (2005)
47. Z. Olami, H.J.S. Feder, K. Christensen, Self-organized criticality in a continuous, nonconservative cellular automaton modeling earthquakes. Phys. Rev. Lett. **68**, 1244 (1992)
48. I.O. Ojala, I.G. Main, B.T. Ngwenya, Strain rate and temperature dependence of Omori law scaling constants of AE data: implications for earthquake foreshock-aftershock sequences. Geophys. Res. Lett. **31**, L24617 (2004). doi:10.1029/2004GL020781
49. Y. Ogata, Statistical models for earthquake occurrences and residual analysis for point processes. J. Am. Stat. Assoc. **83**, 9–27 (1988)
50. M.D. Petersen, T. Cao, K.W. Campbell, A.D. Frankel, Time-independent and time-dependent seismic hazard assessment for the state of California: uniform California earthquake rupture forecast model 1.0. Seismol. Res. Lett. **78**, 99–109 (2007)
51. J. Rundle, E. Preston, S. McGinnis, W. Klein, Why earthquakes stop: growth and arrest in stochastic fields. Phys. Rev. Lett. **80**, 5698 (1998)
52. J.B. Rundle, W. Klein, Nonclassical nucleation and growth of cohesive tensile cracks. Phys. Rev. Lett. **63**, 171 (1989)
53. E.K.H. Salje, K.A. Dahmen, Crackling noise in disordered materials. Ann. Rev. Condens. Matter Phys. **5**, 233–254 (2014). doi:10.1146/annurev-conmatphys-031113-133838
54. P.R. Sammonds, P.G. Meredith, I.G. Main, Role of pore fluids in the generation of seismic precursors to shear fracture. Nature **359**, 228–230 (1992)
55. C. Saouridis, J. Mazars, Prediction of the failure and size effect in concrete via a bi-scale damage approach. Eng. Comput. **9**, 329–344 (1992)
56. D.R. Scott, Seismicity and stress rotation in a granular model of the brittle crust. Nature **381**, 592–595 (1996). doi:10.1038/381592a0

57. J.P. Sethna, K.A. Dahmen, C.R. Myers, Crackling noise. Nature **410**, 242–250 (2001). doi:10.1038/35065675
58. D. Sornette, G. Ouillon, Dragon-kings: mechanisms, statistical methods and empirical evidence. Eur. Phys. J. Spec. Top. **205**, 1–26 (2012)
59. D. Spasojevic, S. Bukvi, S. Miloevi, H.E. Stanley, Barkhausen noise: elementary signals, power laws, and scaling relations. Phys. Rev. E **54**, 2531–2546 (1996)
60. S. Touati, M. Naylor, I.G. Main, The origin and non-universality of the earthquake inter-event time distribution. Phys. Rev. Lett. **102**, 168501 (2009). doi:10.1103/PhysRevLett.102.168501
61. Turcotte, D.L., Fractals and chaos in geology and geophysics. (Cambridge, 1992), p. 221
62. J. Vasseur, F.B. Wadsworth, Y. Lavallée, A.F. Bell, I.G. Main, D.B. Dingwell, Heterogeneity: the key to failure forecasting. Sci. Rep. **5**, 13259 (2015). doi:10.1038/srep13259
63. M. Wyss (ed.), *Evaluation of Proposed Earthquake Precursors* (American Geophysical Union, Washington, DC, 1991). 94 pp
64. G. Yakovlev, J.B. Rundle, R. Shcherbakov, D.L. Turcotte, Inter-arrival time distribution for the non-homogeneous Poisson process. (Elsevier Science, 2005), http://arXiv.org/abs/cond-mat/0507657
65. L. Zhang, E.K.H. Salje, X. Ding, J. Sun, Strain-rate dependence of twinning avalanches at high speed impact. Appl. Phys. Lett. **104**, 162906 (2014)

Chapter 6
Modelling Avalanches in Martensites

Francisco J. Perez-Reche

Abstract Solids subject to continuous changes of temperature or mechanical load often exhibit discontinuous avalanche-like responses. For instance, avalanche dynamics have been observed during plastic deformation, fracture, domain switching in ferroic materials or martensitic transformations. The statistical analysis of avalanches reveals a very complex scenario with a distinctive lack of characteristic scales. Much effort has been devoted in the last decades to understand the origin and ubiquity of scale-free behaviour in solids and many other systems. This chapter reviews some efforts to understand the characteristics of avalanches in martensites through mathematical modelling.

6.1 Introduction

The physical properties of many materials follow a sequence of abrupt changes when the material is driven by smoothly varying the temperature or an external field. The abrupt changes are referred to as avalanches. Examples of processes exhibiting avalanche dynamics include plastic deformation [1, 2], fracture [3, 4], domain switching in ferroic materials [5, 6] or martensitic phase transitions [7–11]. In fact, avalanche dynamics are not exclusive to driven solids but have been reported for a wide variety of processes including earthquakes [12], stock market fluctuations [13], biological extinctions [14], epidemics [15], neural dynamics [16] or motion of animal herds [17].

A common feature to all these systems is that avalanches are typically characterised by a remarkable variability with magnitudes that extend over several decades. In most cases, the probability density function $\rho(x)$ for the magnitude x of avalanches is found to be long-tailed with a power-law decay, $\rho(x) \sim x^{-\alpha}$, in a wide interval of $x \in [x_{\min}, x_{\max}]$. A pure power-law distribution corresponds to the case $x_{\max} = \infty$ (i.e. a Pareto distribution) and implies a lack of characteristic scales [18]. In this

F.J. Perez-Reche (✉)
Institute for Complex Systems and Mathematical Biology, SUPA,
University of Aberdeen, Aberdeen, UK
e-mail: fperez-reche@abdn.ac.uk

E.K.H. Salje et al. (eds.), *Avalanches in Functional Materials and Geophysics*,
Understanding Complex Systems, DOI 10.1007/978-3-319-45612-6_6

case, the distribution of avalanche magnitudes is the same irrespective of the scale we look at it. Exact scale invariance is never detected in experiments due to several factors which may include limitations of the experimental devices, the finite size of systems or the very nature of the avalanche dynamics which may not be exactly scale-free (for instance, large characteristic events can coexist with power-law distribution [19, 20]). In spite of that, a power-law decay over a wide interval $[x_{\min}, x_{\max}]$ implies a large dispersion for x and defining a meaningful scale for the magnitudes of avalanches is essentially impossible (i.e. the statistics may be considered as scale-free in practice). For instance, the mean value $\mathrm{E}[x]$ is typically well defined for experimentally obtained distributions. However, taking $\mathrm{E}[x]$ as a characteristic scale for the magnitude of avalanches is typically meaningless since it is much smaller than the dispersion of the data and is not a representative quantity.

The large variability of magnitudes observed in non-equilibrium avalanche dynamics is reminiscent of the critical phenomena observed in equilibrium second-order phase transitions [21–23]. Following this similarity, the term criticality is broadly used to refer to scale-free avalanche dynamics [24, 25]. Avalanche criticality has indeed been associated with second-order phase transitions for a wide range of systems [5, 25, 26]. However, the mechanisms for robust scale-free avalanche behaviour are still a matter of debate for a number of systems, including martensites [9, 27, 28].

This chapter focuses on modelling of avalanche dynamics in martensitic transformations which are solid to solid first-order phase transitions responsible for unique phenomena such as shape memory and pseudoelasticity [29] or caloric effects [30]. In particular, we will mostly deal with avalanches in shape-memory alloys undergoing martensitic transitions from an open crystalline structure to a close-packed structure with lower symmetry [29, 31, 32]. The martensitic transformation can be induced by decreasing the temperature of the material or by applying a mechanical load. Avalanches in shape-memory alloys have been detected using a range of experimental techniques including acoustic emission [7, 8, 33, 34], calorimetry [10, 35], resistivity [9] or strain imaging [11]. Avalanches of similar origin have been also observed in ferroelastic materials with optical microscopy [36, 37] and are also predicted by molecular dynamics simulations [38, 39].

The specific details of phase transformations may depend on the material composition, the particular sample at hand, etc. However, avalanche statistics and other features are qualitatively similar for different materials. For instance, scale-free avalanches have been reported for many different phase transforming alloys and the value of the power-law exponent α only depends on generic features such as the crystal symmetry of the martensitic phase [33]. Following this observation, many theoretical studies have relied on toy models that aim for a basic understanding of key universal features exhibited by many systems. Within the context of martensites, it is common to use spin models with quenched randomness and metastable dynamics [40–45]. Most of these models can be viewed as extensions of prototype spin models such as the zero-temperature Random-Field Ising model (RFIM) which was originally proposed to study avalanches in fluid invasion [46] and magnetisation reversal [47]. In Sect. 6.2, we review these models which indeed capture important

features of martensites including their hysteresis and scale-free avalanches. In contrast, they are not suitable to study mechanically-induced transformations and, for instance, miss the fact that in most shape-memory alloys scale-free avalanches are only observed after a training process which consists in cycling several times through the phase transition [33, 48, 49]. During this process, shape-memory alloys develop dislocations [50–53] which are believed to play an important role in the scale-free character of avalanches in well-trained materials [27, 54]. In this respect, martensites are essentially different from many other apparently similar systems, say driven ferromagnets displaying Barkhausen noise, because in those systems training is not required to reach a scale-free behavior. Motivated by these facts, spin-like models were developed in [27, 28, 54, 55] which are applicable to both mechanically and thermally induced transformations. In addition, they are able to simultaneously handle the phase transition and dislocation activity. In order to unify these two processes, it is necessary to deal with the global symmetry group of crystals which includes large shearing and naturally account for the formation of dislocations [56–61]. These arguments are reviewed in Sect. 6.3 for homogeneous lattices and then extended in Sect. 6.4 to deal with heterogeneous deformations which are ubiquitous in martensites. After these general considerations, in Sect. 6.5 we formulate the Random Snap-Spring model (RSSM) which is a minimal framework to study avalanches in both thermally and mechanically driven transformations. Particular cases of the RSSM are studied in Sects. 6.6 and 6.7 for thermally-driven and mechanically-driven transformations, respectively.

6.2 Avalanches in Spin Models

The zero-temperature Random-Field Ising Model (RFIM) is a prototype model for avalanche dynamics that has been applied to study a wide range of phenomena including magnetisation reversal [47, 62], fluid invasion [46, 63], capillary condensation in porous media [64, 65] and even opinion shifts [66]. The RFIM is defined as a set of N spin variables $\{s_i = \pm 1;\ i = 1, 2, \ldots, N\}$ with Hamiltonian [62, 67]

$$\mathscr{H} = -\sum_{i,j}\left(J_{ij} - \frac{J_{\text{inf}}}{N}\right) s_i s_j - H\sum_i s_i - \sum_i h_i s_i. \tag{6.1}$$

Here $\mathbf{J} = \{J_{ij}\}$ is a matrix giving a positive interaction $J_{ij} = J > 0$ between nearest neighbours and zero otherwise. The term J_{inf}/N is an infinite-range interaction which, in the case of magnetic materials, is associated with demagnetising fields [67]; in martensites, it can be associated with the stiffness of mechanical loading devices (see Sect. 6.7). The spins are acted globally by an external homogeneous field, H, and locally by quenched random fields h_i which are often normally distributed with zero mean and standard deviation r. The parameter r gives an effective measure of the degree of disorder. The system is quasistatically driven by sweeping the field H

and thermal fluctuations are neglected. Two different spin flip dynamics have been considered in the past. *Nucleation* dynamics assume that any spin can flip provided this leads to a local decrease of the energy [47]. The other possibility corresponds to *front propagation* dynamics in which spins can only flip if this leads to a decrease of the energy *and* they are neighbouring a previously flipped spin [46, 63]. A necessary condition for a spin to flip in any of the two dynamics is that the flip induces a decrease of the energy. From (6.1), the energy change associated with the flip of a single spin s_i is $\Delta\mathscr{H}(s_i \to -s_i) = 2s_i\hat{f}_i$, where

$$\hat{f}_i = \sum_j \left(J_{ij} - \frac{J_{\text{inf}}}{N}\right) s_i + H + h_i, \tag{6.2}$$

is the local field acting on s_i. A stable configuration $\mathbf{s} = \{s_i\}$ is such that all those spins s_i that are allowed to flip must be aligned with their local field, i.e. $s_i\hat{f}_i > 0$. In this case, the energy cannot be decreased by flipping any single spin (the simultaneous flip of more than one spin might lead to a lower energy but this corresponds to other dynamics [68] that will not be considered here). Avalanches start when at least one spin becomes unstable under the driving. The unstable spin flips and may induce other spins to flip, thus generating an avalanche of spin flips which finishes when all the spins in the system are stable again. The number of spins flipped during the avalanche gives the avalanche size, S.

Many different numerical and analytical studies have been carried out to characterise the properties of magnetisation ($m = \sum_i s_i/N$) and avalanches in the zero-temperature RFIM. One of the most frequently analysed characteristic of avalanches is their size probability distribution which has been studied as a function of the applied field, $D(S, H)$, and also pooling avalanches observed at any field, $D_{\text{int}}(S) = \int_{-\infty}^{\infty} D(S, H)\mathrm{d}H$. The behaviour predicted by the model depends on the degree of disorder, the dynamics for spin flips and the presence ($J_{\text{inf}} > 0$) or absence ($J_{\text{inf}} = 0$) of infinite-range interactions. We now summarise the behaviour of the model for each dynamics assuming that H increases monotonically in the interval $[-\infty, \infty]$.

6.2.1 Propagation Dynamics

In order to study the propagation dynamics, the system is initially prepared with a finite domain of spins flipped up ($s = +1$) and the rest are down ($s = -1$). Upon increasing H, the domain of up spins grows and the transformation dynamics reduce to the propagation of the domain boundary in a disordered medium. Let us consider the case for $J_{\text{inf}} = 0$ first. The domain boundary remains pinned for small values of the applied field and depins at a critical field $H_p(r)$ which is a function of the degree of disorder, r. The morphology of the propagating front is self-affine for small disorder, $r < r_p$, and self-similar for $r > r_p$ [46, 63]. The avalanches at the pinning-depinning transition obey a power-law distribution, $D(S, H_p) \sim S^{-\tau_p}$, where the exponent τ_p depends on the morphology of the propagating front. For $r < r^p$, the

critical behaviour belongs to the quenched Edwards-Wilkinson (QEW) universality class of driven self-affine interfaces; the value of the exponent for a 3D system is $\tau_p \simeq 1.3$ [5, 46, 63]. In the high disorder regime, $r > r^p$, the avalanche size exponent takes the value $\tau_p \simeq 1.6$ which corresponds to the universality class of isotropic percolation [46, 63].

A positive value for infinite-range interaction J_{inf} brings a restoring force that keeps the domain boundary in the neighbourhood of the pinning-depinning transition generalisations of the Blume-Emery-Griffiths model with a three-stateion, thus providing a feedback mechanism which self-tunes the model to a critical state [67, 69, 70]. This phenomenology is interpreted as self-organized criticality. Within the framework of driven elastic interfaces, an analogous self-tuning to a pinning-depinning critical regime is obtained if the interface is driven through a weak spring which provides a feed-back mechanism [71, 72].

6.2.2 Nucleation Dynamics

Nucleation dynamics allow the flip of any spin that leads to the decrease of the energy. We assume an initial configuration with all the spins in the state $s = -1$ which is stable at the initial field $H = -\infty$. If $J_{\text{inf}} = 0$, one observes three different avalanche responses depending on the degree of disorder: pop, crackle and snap [25, 55]. Figure 6.1 shows examples of $D_{\text{int}}(S)$ for each regime. Pop behaviour is observed for large disorder when the transition proceeds through a

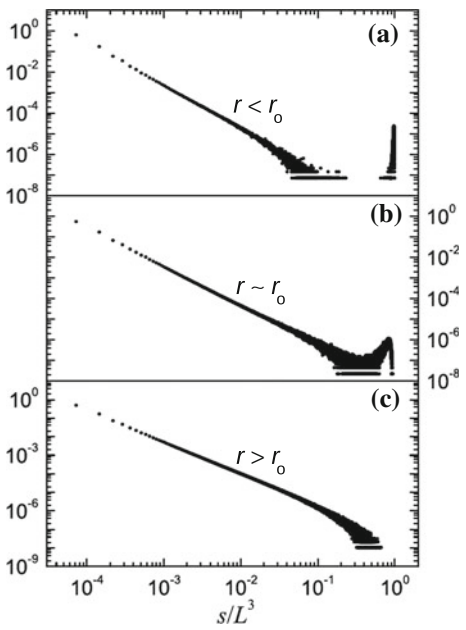

Fig. 6.1 Size probability distribution $D_{\text{int}}(S)$ for avalanches observed during the complete transformation in the RFIM with nucleation dynamics. Different panels correspond to different values of disorder: **a** $r = 1.7$, **b** $r = 2.21$ and **c** $r = 2.6$. The data correspond to a 3D system of linear size $L = 24$, i.e. with $N = L^3$ spins [From [80], Fig. 1, pp. 134421–4]

sequence of many avalanches of small size (see Fig. 6.1c). In this regime, the magnetisation exhibits a smooth hysteresis loop. Snap behaviour is observed in systems with disorder smaller than a critical value, r_o. In this regime, the magnetisation hysteresis loop exhibits a discontinuity associated with a macroscopically large avalanche that spans the system even in the thermodynamics limit. The peak at large avalanche sizes in Fig. 6.1a corresponds to the snap event. The pop and snap regimes are separated by a critical disorder (r_o) where avalanches have a broad range of sizes. This crackling regime corresponds to an order-disorder (OD) continuous phase transition associated with a $T = 0$ critical point (r_o, H_o) in the space spanned by the disorder and driving field [47, 68, 73–79]. The avalanche size distribution obeys a power law, $D(S, H_o) \sim S^{-\tau_o}$, at the critical point. The exponent τ_o depends on the dimensionality of the system and, for example, takes the value $\tau_o \simeq 1.6$ in 3D. At the critical disorder, the integrated avalanche size distribution also obeys a power-law decay, $D_{\text{int}}(S) \sim S^{-\tau_o'}$, with an exponent τ_o' that can be expressed as a function of τ_o and other exponents of the system. For a 3D system, $\tau_o' \simeq 2$ [80]. Such a decay is illustrated in Fig. 6.1b; the deviation from a pure power law at large avalanche sizes is a finite size effect which becomes negligible in large systems [80].

For $J_{\text{inf}} > 0$, the infinite-range interaction prevents avalanches from growing indefinitely. This implies that an infinite avalanche analogous to the one observed for $r < r_o$ in systems with $J_{\text{inf}} = 0$ cannot exist. In contrast, the system self-organises to display front-propagation critical behaviour [69, 70]. The size of avalanches follows a power-law distribution, $D(S) \sim S^{-\tau_p}$, where τ_p corresponds to the QEW universality class. In general, τ_p differs from its OD counterpart, τ_0, meaning that infinite-range interactions lead to a change of universality class. In Sect. 6.7 we will show that a change in universality class of this type can be induced for mechanically-induced martensitic transformations by varying the stiffness of the loading mechanical device [55].

6.2.3 *Spin Models for Martensites*

Several extensions of the zero-temperature RFIM with nucleation dynamics have been proposed to describe martensitic transformations (although avalanches have been only studied in few of them). A key feature of such extensions is the use of spin variables that take more than two values in order to capture the multiple variants of the martensitic phase. The simplest possibility in this direction corresponds to generalisations of the Blume-Emery-Griffiths model with a three-state spin variable, $s \in \{-1, 0, 1\}$, which allow the transition from austenite ($s = 0$) to two variants of martensite ($s = \pm 1$) to be described [40–44]. In particular, the avalanche size distribution in thermally-driven martensites was studied in [40] for a zero-temperature Random-Field Blume-Emery-Griffiths model (RFBEG) with Hamiltonian

$$\mathscr{H} = -\sum_{i,j} J_{ij} s_i s_j - \sum_i h_i s_i^2 - g(T) \sum_i s_i^2, \tag{6.3}$$

where $g(T)$ is a function of temperature that acts as a driving parameter. The fraction of martensite, $q = (1/N)\sum_i s_i^2$, is an increasing function of $g(T)$ so that the austenite and martensite phases are stable for sufficiently positive and negative values of $g(T)$, respectively. In common with the RFIM, the RFBEG predicts a critical regime with crackling noise associated with an OD critical manifold which separates snap and pop regimes at small and large disorder, respectively.

A Random-Field Potts model with vectorial three-state spins and more realistic dipolarlike interactions than previously considered for the RFBEG was proposed in [45]. The model predicts more realistic properties for microstructure and hysteresis than previously obtained with the RFIM or the RFBEG. Criticality is however associated with an OD transition analogous to those exhibited by simpler models.

Phenomenological extensions of the zero-temperature RFIM do not explicitly include elasticity. As a consequence, they are not suitable to describe the behaviour of mechanically-driven martensites. In contrast, mechanically-induced transformations were modelled using a different type of discrete systems consisting of interacting bi-stable elastic units which mechanically behave as *snap-springs*[1] [81–86]. Snap-spring models gave interesting insight on the stress–strain hysteresis of martensitic transformations. They were not designed however to capture the emergence of transformation-induced defects and the complexity of avalanches in martensites. Indeed, they traditionally aimed for analytical transparency by assuming simple topologies (e.g. 1D chains) and neglecting spatial heterogeneity.

6.3 Homogeneous Deformations of Bravais Lattices

The deformation of martensites is highly heterogeneous but, before dealing with such heterogeneities, it is instructive to study the subtleties of homogeneous deformations of crystalline solids [56–61]. Let us consider 2D crystals (nets) as a benchmark. Its structure is given by a simple Bravais lattice, defined mathematically as a discrete set of points in the Euclidean space,

$$\mathscr{L}(\mathbf{u}_a) = \{\mathbf{R} \in \mathbb{R}^2 : \mathbf{R} = n^a \mathbf{u}_a,\ n^a \in \mathbb{Z}\}. \tag{6.4}$$

Here, the Einstein's summation rule is used. $\mathbf{R}$ gives the position of atoms and $\{n^1, n^2\}$ are the components of $\mathbf{R}$ in the lattice basis defined by the independent pair of vectors $\{\mathbf{u}_1, \mathbf{u}_2\}$.

A homogeneous deformation transforms a lattice $\mathscr{L}(\mathbf{u}_a)$ into a new one, $\mathscr{L}(\mathbf{v}_a)$, spanned by basis vectors $\{\mathbf{v}_1, \mathbf{v}_2\}$ which are linearly related to the original lattice vectors, i.e. $\mathbf{v}_a = F_a^b \mathbf{u}_b$. Here, $\{F_a^b;\ a, b = 1, 2\}$ are real-valued elements of an invertible matrix $\mathbf{F}$. Figure 6.2 shows a homogeneous deformation of a square lattice by a direct shear of magnitude β given by the deformation matrix,

[1] A snap-spring in elastic materials can be viewed as the analogue of a spin in magnetic materials.

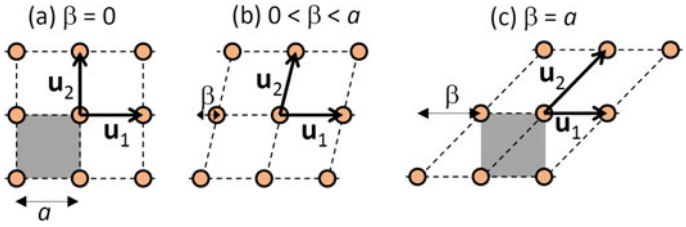

Fig. 6.2 Direct shear of a square lattice corresponding to the deformation matrix **F** given by (6.5). The lattice parameter is a. Different panels correspond to different values of the shear parameter β. The *shaded squares* in **a** and **c** show that the lattice is identical for $\beta = 0$ and $\beta = a$ (assuming that the lattices extend to infinity). In contrast, the lattice basis vectors, $\{\mathbf{u}_1, \mathbf{u}_2\}$, are not identical in **a** and **c**

$$\mathbf{F} = \begin{pmatrix} 1 & 0 \\ \beta/a & 1 \end{pmatrix}, \tag{6.5}$$

where a is the spacing of the square lattice.

Some deformations lead to new lattices that are identical to the original one, i.e. lattices are symmetric with respect to certain deformations. Such symmetries can be classified into two fundamental types. The first one is the symmetry under orthogonal transformations (i.e. rotations and reflections) and the second is linked to the fact that there are infinitely many different bases describing the same Bravais lattice. We discuss each symmetry type separately in Sects. 6.3.1 and 6.3.2. We then use the developed concepts to distinguish between weak and reconstructive transformations and describe the energy of a crystal under homogeneous deformations.

6.3.1 Orthogonal Transformations

The relative position of points in Bravais lattices remains unchanged for deformations induced by an orthogonal matrix, i.e. for $\mathbf{F} = \mathbf{Q} \in O(2)$. The physical properties of lattices must then be invariant under such transformations. This means that they must be functions of the lattice metric, **C**, which is a 2×2 Gram matrix with elements given by,

$$C_{ab} = \mathbf{u}_a^T \mathbf{u}_b. \tag{6.6}$$

Following this observation, a lattice $\mathscr{L}(\mathbf{u}_a)$ can be defined in terms of the corresponding metric and denoted as $\mathscr{L}(\mathbf{C})$. All nets can be represented by a point in the metric space $\mathscr{M}$ spanned by the elements of **C**. Due to the symmetry $C_{12} = C_{21}$, all 2D nets can in fact be described in terms of three independent matrix elements, $\{C_{11}, C_{12}, C_{22}\}$.

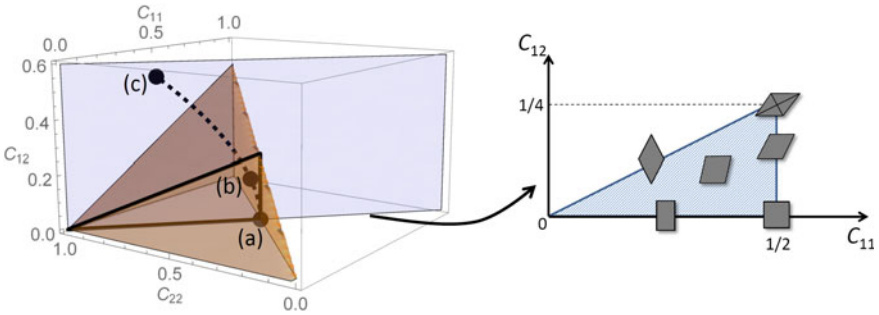

Fig. 6.3 Fundamental domain, *FD*, in the lattice metric space $\mathscr{M}$ spanned by the independent matrix elements, $\{C_{11}, C_{12}, C_{22}\}$. (*Left panel*) The *brown* (*dark gray*) wedge-shaped region shows the Lagrange *FD* (6.7). The *dashed line* indicates the path associated with the shear deformation given by the matrix in (6.5). The points **a**, **b** and **c** correspond to the lattices shown in Fig. 6.2. The *blue* (*light gray*) plane corresponds to the locus of points satisfying $C_{11} + C_{22} = 1$. The *thick black triangle* shows the boundaries of the region where *FD* intersects the plane $C_{11} + C_{22} = 1$. (*Right panel*) The *blue* (*light gray*) triangular domain shows the intersection of the *FD* with the plane $C_{11} + C_{22} = 1$ projected on the (C_{11}, C_{12}) plane. The *schematic shapes* indicate the different lattice groups: oblique (inside the *triangle*), *rectangular* (*horizontal line* with $C_{12} = 0$), fat rhombic (*vertical line* with $C_{11} = 1/2$), skinny rhombic (*diagonal line* with $C_{12} = \frac{1}{2}C_{11}$) and *hexagonal* ($C_{11} = 1/2$ and $C_{12} = 1/4$)

The six types of Bravais lattices in 2D can be represented in a subset of $\mathscr{M}$ referred to as a *fundamental domain* (*FD*). A possible choice for *FD* is the wedge-shaped domain shown in Fig. 6.3(left) which defines the Lagrange *FD* [59]:

$$FD = \left\{ \mathbf{C} \in \mathscr{M}, \quad 0 < C_{11} \leq C_{22}, \quad 0 \leq C_{12} \leq \frac{C_{11}}{2} \right\}. \tag{6.7}$$

As shown below, this is just one of the infinitely many possible choices for an *FD*. In Fig. 6.3(left), the points inside the domain (excluding the boundaries) correspond to oblique (O) lattices. Rectangular (R) lattices are located on the $C_{12} = 0$ plane; square (S) lattices correspond to the limiting case along the line $C_{11} = C_{22}$. Rhombic (R) lattices are located on the vertical plane along the line with $C_{11} = C_{22}$ and the inclined plane with $C_{11} = 2C_{12}$. Hexagonal (H) lattices are located at the intersection of the latter two planes. The location of different lattice types can be better visualised in the intersection of the *FD* with the plane $C_{11} + C_{22} = 1$ (Fig. 6.3(right)).

6.3.2 Equivalent Lattices

A lattice base defines a unique Bravais lattice but the contrary is not true. Indeed, there are infinitely many bases which generate the same lattice (Fig. 6.4 shows some examples). The necessary and sufficient condition for two bases, $\mathbf{u}_a$ and $\mathbf{v}_a$, to

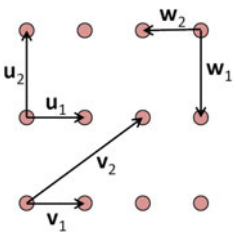

Fig. 6.4 Examples of different lattice bases generating a rectangular lattice

represent the same lattice is that $\mathbf{v}_a = m_a^b \mathbf{u}_b$. Here, m_a^b are integer entries of 2×2 matrices $\mathbf{m}$ with $\det \mathbf{m} = \pm 1$, i.e. matrices belonging to the general linear group $GL(2, \mathbb{Z})$. Figure 6.4 shows three different bases, $\mathbf{u}_a$, $\mathbf{v}_a$ and $\mathbf{w}_a$ spanning the same rectangular lattice. The bases $\mathbf{v}_a$ and $\mathbf{w}_a$ are related to $\mathbf{u}_a$ by the matrices

$$\mathbf{m}_v = \begin{pmatrix} 1 & 0 \\ 2 & 1 \end{pmatrix} \quad \text{and} \quad \mathbf{m}_w = \begin{pmatrix} -1 & 0 \\ 0 & -1 \end{pmatrix},$$

respectively. The metric $\mathbf{C}$ changes as $\mathbf{C}' = \mathbf{m}\mathbf{C}\mathbf{m}^T$ under the action of matrices $\mathbf{m} \in GL(2, \mathbb{Z})$.

The equivalence of lattices spanned by different basis vectors implies that there are infinitely many copies of each lattice type in $\mathscr{M}$. For instance, the three different lattice bases shown in Fig. 6.4 give three different copies $\mathbf{C}_u$, $\mathbf{C}_v$ and $\mathbf{C}_w$ in $\mathscr{M}$ of the same rectangular lattice.

The concept of fundamental domain introduced in Sect. 6.3.1 can be more rigorously defined as a subset of $\mathscr{M}$ containing *one and only one* copy of any given lattice under the action of $\mathbf{m} \in GL(2, \mathbb{Z})$. This means that a given point in a fundamental domain, *FD*, transforms to a different point in the metric space, $\mathbf{C}' = \mathbf{m}\mathbf{C}\mathbf{m}^T$, which is necessarily outside *FD* for any $\mathbf{m} \in GL(2, \mathbb{Z})$ different from the identity. In the example of Fig. 6.4, $\mathbf{C}_u$ belongs to the Lagrange *FD*; $\mathbf{C}_v$ and $\mathbf{C}_w$ are outside this domain. Lattice invariance under $\mathbf{m} \in GL(2, \mathbb{Z})$ also implies that there are infinitely many copies of a given fundamental domain in the metric space (see Fig. 6.5).

6.3.3 *Weak and Reconstructive Transformations*

Some matrices $\mathbf{m} \in GL(2, \mathbb{Z})$ correspond to orthogonal transformations, $\mathbf{Q} \in O(2)$, meaning that they induce a rotation or reflection which transforms the lattice back into itself, i.e. $\mathbf{C} = \mathbf{m}\mathbf{C}\mathbf{m}^T$. Such matrices provide a formal definition of the *lattice group* $\mathscr{G}(\mathbf{C})$ of any lattice $\mathscr{L}(\mathbf{C})$. As depicted in Fig. 6.3(right), there are six different lattice groups for nets [58, 59]: square (S), oblique (O), rectangular (R), fat rhombic (F-Rh), skinny rhombic (S-Rh) and hexagonal (H). Lattice groups are finite subgroups of the global symmetry group $GL(2, \mathbb{Z})$ and, as such, are not sufficient to capture all the symmetries of crystalline solids. In spite of that, a description in terms

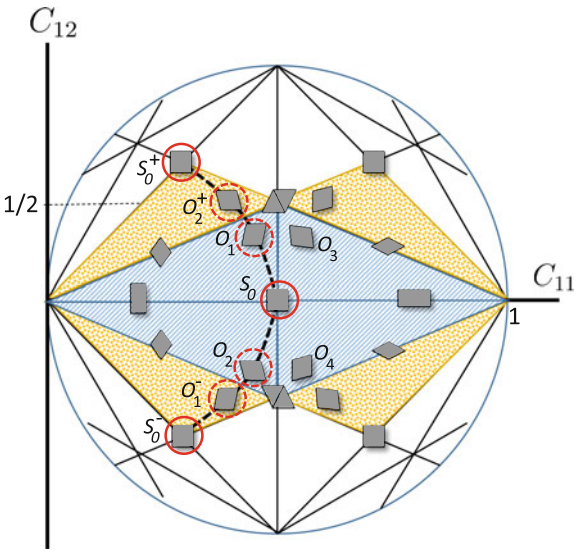

Fig. 6.5 Intersection of the metric space $\mathscr{M}$ with the plane $C_{11} + C_{22} = 1$ projected on the (C_{11}, C_{12}) plane. The *dashed domain* corresponds to the EPN of the square lattice at $(C_{11}, C_{12}) = (1/2, 0)$. The *dotted triangles* show copies of the fundamental domain outside the EPN of the square lattice. The *dashed thick line* shows the path of the lattice under a shear deformation. Energy wells for square austenite and oblique martensite are shown by *circles* with *solid* and *dashed lines*, respectively. The four variants of oblique martensite within the EPN of square S_0 are denoted as $O_1 - O_4$. O_1^-, O_2^+ and $S_0^\pm$ are copies of the lattices O_1, O_2 and S_0, respectively, which lay outside the S_0 EPN

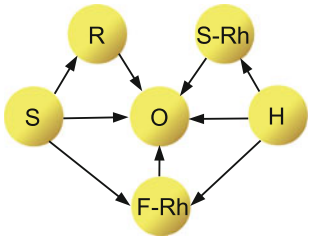

Fig. 6.6 Group-subgroup relationships between the six lattice groups of nets (*S*: square, *O*: oblique, *R*: rectangular, *F-Rh*: fat rhombic, *S-Rh*: skinny rhombic and *H*: hexagonal)

of only lattice groups can be suitable for *weak* structural phase changes between lattices $\mathscr{L}(\mathbf{C})$ and $\mathscr{L}(\mathbf{C}')$ that have a group-subgroup relationship, $\mathscr{G}(\mathbf{C}) \subseteq \mathscr{G}(\mathbf{C}')$. Figure 6.6 shows the possible structural changes in 2D with a lattice group-subgroup relationship. A number of Landau theories which only account for lattice group symmetries have been proposed to study structural phase transitions in ferroelastic materials and martensites [87–93]. Such theories can successfully describe phase transitions leading to small deformations which are typically the case in ferroelastics.

Indeed, a necessary condition for two lattices $\mathscr{L}(\mathbf{C})$ and $\mathscr{L}(\mathbf{C}')$ to have a group-subgroup relationship is that $\mathbf{C}'$ corresponds to a sufficiently small deformation of $\mathbf{C}$. More precisely, $\mathbf{C}'$ must be restricted to a sufficiently small open[2] neighbourhood of $\mathbf{C}$ in the space $\mathscr{M}$. This is the so-called Ericksen–Pitteri neighbourhood (EPN) of $\mathbf{C}$ which was formally introduced in [56, 94] (see also [58, 59, 61, 95]). For example, the dashed region in Fig. 6.5 is the EPN for the square lattice (the boundaries are excluded). To explore the concept, let us consider again the direct shear of magnitude β with deformation matrix given by (6.5); the deformed lattice describes the trajectory $\mathbf{C}'(\beta)$ in $\mathscr{M}$ indicated by the dashed line in Fig. 6.3(left). For values of $0 < \beta < a/2$, the deformed lattice is oblique (O_1) and it is a subgroup of the square lattice group (see Fig. 6.6). In contrast, for $\beta = a/2$, $\mathbf{C}'$ reaches the skinny rhombic lattice group which is not a subgroup of the square lattice. At this point, the system reaches the boundary of the EPN for the original square lattice, S_0. Note that the lattice group at the boundary does not have a group-subgroup relationship with the square lattice, thus illustrating the idea that the EPNs are open domains in $\mathscr{M}$.

Increasing β beyond the EPN of $\mathbf{C}$ leads to lattices that cannot be related to lattices in the EPN by elements of the lattice group $\mathscr{G}(\mathbf{C})$. Phase transitions inducing large deformations that go beyond the EPN of the parent lattice are *reconstructive* [96] and, strictly speaking, require dealing with the global symmetry group ($GL(2,\mathbb{Z})$ for nets). Nevertheless, dealing with the global symmetry group is challenging and the global periodicity of the lattice is often approximated using transcendental periodic order parameters [96–98].

6.3.4 The Energy of a Crystalline Solid

The energy of a lattice is a function of the relative position of atoms and the temperature, T. For homogeneous lattices, the relative position of atoms is fully determined by the lattice vectors and the energy must be invariant under the symmetry transformations described in Sects. 6.3.1 and 6.3.2. For a 2D Bravais lattice, these symmetries imply that the energy is a function $\tilde{\phi}(\mathbf{C};T)$ of the lattice metric $\mathbf{C}$ (cf. (6.6)) which must be invariant under the action of matrices $\mathbf{m} \in GL(2,\mathbb{Z})$, i.e.

$$\tilde{\phi}(\mathbf{C};T) = \tilde{\phi}(\mathbf{m}\mathbf{C}\mathbf{m}^T;T). \tag{6.8}$$

At a given temperature, stable lattices correspond to metrics $\mathbf{C}$ that minimise $\tilde{\phi}(\mathbf{C};T)$. Note that the global symmetry given by (6.8) implies that every stable lattice is represented by infinitely many energy wells in $\mathscr{M}$. Minimisers of $\tilde{\phi}(\mathbf{C};T)$ at high and low temperatures correspond to the structure in austenite and martensite, respectively. For instance, the EPN of the square lattice in a square to oblique

[2]Meaning that the boundaries of the neighbourhood do not belong to the neighbourhood itself.

transition contains the well for the square parent phase, S_0, and four wells of oblique ($O_1 - O_4$); these wells are infinitely replicated in $\mathscr{M}$ outside the S_0 EPN (see Fig. 6.5).

In the study of martensitic transformations, it is convenient to take the lattice in austenite as a reference and measure the change of energy associated with deformations from such structure. Let $\mathbf{u}_a$ and $\mathbf{v}_a = F_a^b \mathbf{u}_b$ be the lattice vectors of the austenite structure and a deformed lattice, respectively. The energy of the deformed lattice can be written as a function of the stretch tensor [58], $\mathbf{E} = (\mathbf{F}^T\mathbf{F} - \mathbf{I})/2$, as follows:

$$\phi(\mathbf{E}; T) = \tilde{\phi}(u_a^T(2\mathbf{E} + \mathbf{I})u_b; T) - \tilde{\phi}(u_a^T u_b; T), \tag{6.9}$$

where $\mathbf{I}$ is the identity matrix. The reference lattice corresponds to $\mathbf{F} = \mathbf{I}$ or, equivalently to $\mathbf{E} = \mathbf{0}$, and has energy $\phi(\mathbf{0}) = 0$.

For nets, $\mathbf{E}$ is a 2×2 symmetric matrix containing at most three independent elements. Any transformation path in $\mathscr{M}$ can therefore be parametrised by three scalar quantities e, e' and e''. Transitions between different energy wells in $\mathscr{M}$ are associated with non-convex dependence of the energy on one or more of these scalar parameters. Here we illustrate the effects of the energy periodicity following the assumption proposed in [27, 54] that $\phi(e, e', e'')$ is a non-convex function of one of the parameters, e, and it is convex with respect to e' and e''. More explicitly, we use the following expression for the energy:

$$\phi(e, e', e'') = f(e, h'; T) + \frac{C'}{2}(e')^2 + \frac{C''}{2}(e'')^2, \tag{6.10}$$

where C' and C'' are elastic constants and $f(e, h'; T)$ is a non-convex function of e; the variable h' is a stress coupled to e.

For a square-oblique transition as the one shown by the dashed line in Fig. 6.5, we approximate $f(e, h'; T)$ by a piece-wise parabolic function of the direct shear strain parameter, $e = \beta/a$ (cf. (6.5)):

$$f(e, h'; T) = \sum_{s=-1}^{1} \sum_{d \in \mathbb{Z}} \left[\frac{1}{2}(e - w(s, d))^2 + g(T)s^2 - h'e \right] \times \Theta(e - e^-(s, d))\Theta(e^+(s, d) - e). \tag{6.11}$$

Fig. 6.7 shows a plot of $f(e, h'; T)$ as a function of e at fixed temperature. In (6.11), $\Theta(x)$ is the Heaviside step function which is zero for $x < 0$ and one for $x \geq 0$. The domain of periodicity of the energy is given by the integer variable d which takes the value $d = 0$ for the EPN of S_0. For given d, the variable s may take the value 0 or ± 1 for austenite and the two variants of oblique martensite, respectively. The bottoms of the wells are located at $e = w(s, d) = d + \varepsilon s$, where ε is the transformation strain. Weak transformations correspond to values of $\varepsilon < 1/2$; reconstructive transformations correspond to the limiting value $\varepsilon = 1/2$. The energy difference between martensite and austenite wells is $g(T)$ which acts as a driving parameter for thermally driven phase transitions, analogous to the driving parameter in the RFBEG described

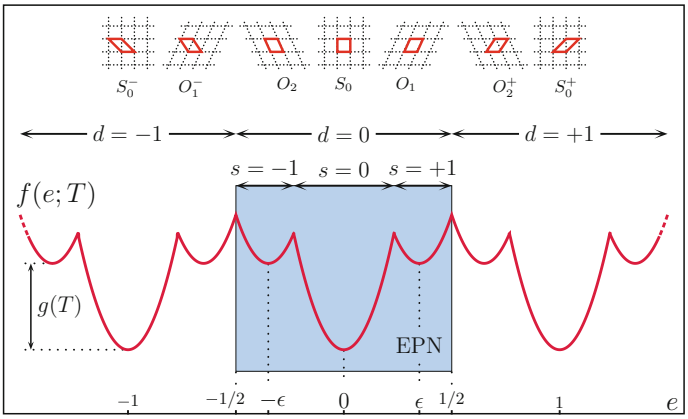

Fig. 6.7 Piece-wise parabolic approximation of the energy of a solid undergoing a square-oblique martensitic phase transition through a direct shear e (e.g. follows a path in $\mathscr{M}$ indicated by the *dashed line* in Fig. 6.5). The *shaded region* shows the EPN of the S_0 square net which is used as a reference frame. The insets on *top* show the shape of the element corresponding to the bottoms of the wells. The *dashed lines* indicate the lattice structure; the shapes of the mesoscopic elements are shown in *red*. The shapes in the domain with $d=0$ correspond to elements in *square* austenite, S_0, and two variants of martensite, O_1 and O_2. The rest of shapes are slipped lattices identical to those of the basic shapes (compare the *dashed lines*). [Adapted from [27], Fig. 1, pp. 075501–2]

in Sect. 6.2.3. The functions $e^{\pm}$ give the limits of stability of each well which depend on $g(T)$ and the well identity variables s and d as follows:

$$e^{\pm}(s,d)=\begin{cases}\varepsilon s+d\pm(\varepsilon/2+g/\varepsilon), & \text{AM phase change, } s=0\rightarrow s'=\pm 1,\\ \varepsilon s+d\pm(\varepsilon/2-g/\varepsilon), & \text{MA phase change, } s=\mp 1\rightarrow s'=0,\\ \varepsilon s+d\pm(1-2\varepsilon)/2, & \text{Slip, } (s,d)=(\pm 1,d)\rightarrow(s',d')=(\mp 1,d\pm 1).\end{cases} \tag{6.12}$$

Here, AM and MA refer to Austenite-Martensite and Martensite-Austenite phase changes, respectively.

6.4 Heterogeneous Deformations. Mesoscopic Description

In order to account for the complex microstructure of martensites, the theory described in Sect. 6.3 must be extended to incorporate heterogeneous deformations. Mesoscopic models [27, 54, 99] exploit the fact that the deformation in the martensitic phase is in fact homogeneous within domains of *linear dimensions* which range from several nanometres to millimetres. In 2D crystals, such domains represent homogeneous regions at mesoscopic scales between atomistic ($\sim$Å) and macroscopic ($\sim$cm) distances. Following this observation, mesoscopic models capture the heterogeneity of deformations by assuming a set of elastically compatible elements

which mechanically behave as multi-stable snap-springs [27, 54]. Each snap-spring represents a homogeneous deformation at mesoscopic scales but an ensemble of snap-springs can describe heterogeneous deformations at macroscopic scales. Similar approaches have been applied to study the plastic deformation of crystals [100, 101] and amorphous solids [102]. For crystals with typical lattice spacings around 5Å, the linear dimension of martensite domains corresponds to $10 - 10^6$ lattice units. Accordingly, a snap-spring can be well approximated by an infinite lattice in most cases so that its deformation obeys the rules given in Sect. 6.3. In the limit of very small snap-springs compared to the crystal, this assumption becomes equivalent to the Cauchy–Born rule used to derive continuum theories of lattices [58, 60]. In such theories, snap-springs become points $\mathbf{r}$ in the continuum space occupied by the solid. The Cauchy–Born rule assumes that, under a deformation field $\mathbf{F}(\mathbf{r})$, the lattice vectors at $\mathbf{r}$ transform as $\mathbf{v}_a(\mathbf{r}) = F_a^b(\mathbf{r})\mathbf{u}_b(\mathbf{r})$, i.e. transform as a homogeneous infinite lattice located at a point $\mathbf{r}$.

Elastic compatibility between adjacent snap-springs means that they must fit together perfectly. This imposes constraints on the discrete deformation field, $\mathbf{F}(\mathbf{r})$, defined by snap-springs [103]. Here, $\mathbf{r} = (i, j)$ is the coordinate of a snap-spring in the square grid of snap-springs, as indicated in Fig. 6.8. For relatively small deformations (linear elasticity), the constraints are given by the St. Venant compatibility [90, 91, 99],

$$\boldsymbol{\Delta} \times (\boldsymbol{\Delta} \times \mathbf{E}^l(\mathbf{r}))^T = \mathbf{0}, \tag{6.13}$$

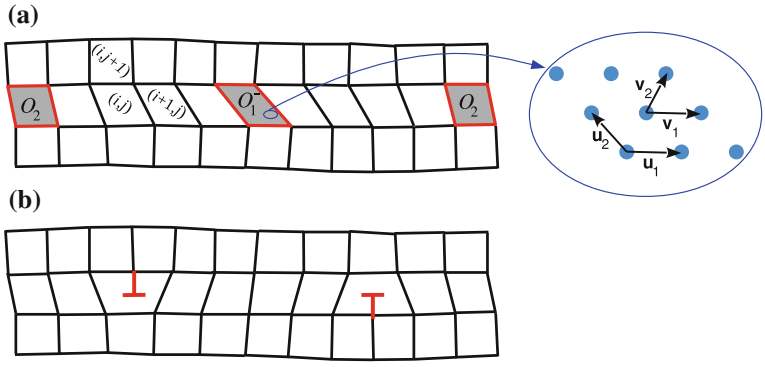

Fig. 6.8 **a** Description of the deformation of a 2D solid in terms of mesoscopic kinematically compatible elements (snap-springs) placed on a *square* grid. The lattice structure of the snap-springs marked by O_2 is oblique and belongs to the EPN of the square lattice S_0 (see Fig. 6.5). The snap-spring in the well O_1^- also corresponds to an oblique lattice but it is outside the EPN of S_0. Such lattice is shown in the inset where two possible bases are indicated. The base $\{\mathbf{v}_1, \mathbf{v}_2\}$ shows that the lattice is just a copy of the lattice O_1 outside the S_0 EPN. **b** Identical deformation field as in **a** showing that a mixture of snap-springs belonging to different EPNs (in this case O_2 and O_1^-) can be viewed as a solid with mesoscopic dislocations

where $\mathbf{E}^l(\mathbf{r})$ is the stress tensor which approximates the stretch tensor in linear elasticity. The symbol $\boldsymbol{\Delta}$ is a discrete difference operator analogous to the gradient vector in continuum systems. Given a field $A(\mathbf{r})$, it acts as $\boldsymbol{\Delta}A(\mathbf{r}) = (A(i+1,j) - A(i,j), A(i,j+1) - A(i,j))$.

The snap-spring model provides a unified description of phase transitions (between wells within an EPN) and slip (transitions between energy wells belonging to different EPNs). Note that a compatible deformation field $\mathbf{F}(\mathbf{r})$ can involve snap-springs that do not belong to the same EPN (cf. snap-springs in wells O_2 and O_1^- in Fig. 6.8). Therefore, slip does not necessarily lead to a violation of elastic compatibility between snap-springs.

An interesting consequence of elastic compatibility in heterogeneous deformation fields is that slip can occur locally [104] even when the phase transition of isolated snap-springs is weak (i.e. when martensite wells belong to the EPN of austenite). Recall that the theory described in Sect. 6.3.3 would only predict the occurrence of slip for reconstructive transitions. In contrast, local slip is indeed possible for heterogeneous *weak* deformations due to elastic compatibility which brings an interaction between snap-springs that may force some of them to explore regions of $\mathscr{M}$ outside the EPN of the parent phase. We then conclude that slip is much more frequent in heterogeneous deformations than it is for homogeneous crystals. In addition, the EPN concept is not enough to determine the conditions for slip in heterogeneous deformation fields.

Figure 6.9 shows a phase diagram presented in [54] that quantifies the possible slip within a snap-spring due to interaction with other snap-springs in the crystal. The stability boundaries for the martensite and the austenite phases can be derived

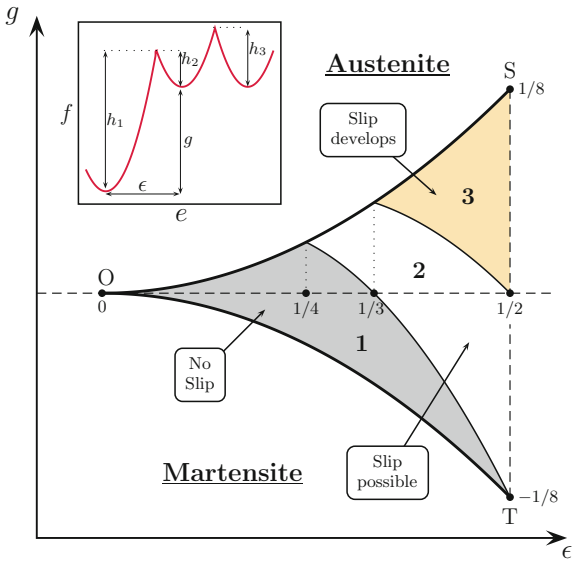

Fig. 6.9 Slip phase diagram for a snap-spring in the space $(\varepsilon, g(T))$. The *inset* indicates the energy barriers h_1, h_2 and h_3 used to define three characteristic zones in the domain of phase coexistence *SOT* [Adapted from [54], Fig. 5]

from the limits given by (6.12) and are indicated by the lines *OS* and *OT*, respectively. The possibility of slip in weak transformations can be heuristically analysed by comparing the energy barriers indicated in the inset of the figure for each transition type: austenite-martensite (h_1), martensite-austenite (h_2) and slip (h_3). One can distinguish three regions in the space $(\varepsilon, g(T))$. In region 1, $h_3 > h_1$ and slip can be typically neglected. In region 2, $h_2 < h_3 < h_1$ and slip is possible but not likely. Finally, in region 3 the barriers satisfy $h_3 < h_2 < h_1$ meaning that the barrier for slip is smaller than the rest and slip may easily develop. Note that region 3 is close to the limit $\varepsilon = 1/2$ for reconstructive transitions but plasticity can already develop for $\varepsilon < 1/2$.

Following the arguments presented in Sect. 6.3.4, the deformation of a snap-spring i can be given by three scalar parameters e_i, e_i' and e_i''. The energy of a solid consisting of N snap-springs can then be expressed as a sum over the energies of individual snap-springs as follows:

$$\Phi_{\text{solid}}(\mathbf{e}, \mathbf{e}', \mathbf{e}'') = \sum_{i=1}^{N} \phi(e_i, e_i', e_i''), \tag{6.14}$$

where $\mathbf{e} = \{e_i;\ i = 1, 2, \ldots, N\}$; the sets $\mathbf{e}'$ and $\mathbf{e}''$ are defined analogously. Here, one should also keep in mind that the parameters $\mathbf{e}$, $\mathbf{e}'$ and $\mathbf{e}''$ are not independent from each other due to elastic compatibility.

6.5 The Random Snap-Spring Model (RSSM)

Mesoscopic models of the type described in the previous section were proposed in [27, 28, 54] and [55] for thermally and mechanically driven materials, respectively. In this section, we present an extended formulation of these models to encompass the two types of driving.

The energy Φ of the system consists of two contributions, Φ_{solid} and Φ_{mech}, associated with the crystal (see (6.14)) and the mechanical load, respectively.

$$\Phi = \Phi_{\text{solid}} + \Phi_{\text{mech}}. \tag{6.15}$$

As shown in the scheme of Fig. 6.10, mechanical driving is applied through an elastic device attached to the system. The driving parameter is the global "elongation" of the system, e_G, which is assumed to be parallel to the order parameter e for simplicity. The energy associated with the loading device is

$$\Phi_{\text{mech}} = \frac{cN}{2}(e_G - \bar{e})^2, \tag{6.16}$$

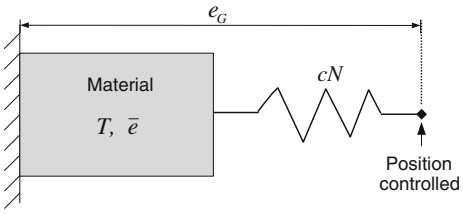

Fig. 6.10 Schematic representation of a solid attached to an elastic loading device with stiffness cN. Structural phase changes can be induced by sweeping the temperature, T, or the global strain of the system, e_G, by controlling the position of the loading device

where $\bar{e} = \frac{1}{N}\sum_{i=1}^{N} e_i$ is the average strain of the system of snap-springs. The stiffness of the loading device is $cN \geq 0$, where c is an specific stiffness which is assumed to be independent of the system size. The energy Φ_{solid} increases with the system size (i.e. it is extensive). By defining the stiffness cN as an extensive variable we make sure that the energy Φ_{mech} is also extensive and can represent a finite contribution to the total energy irrespective of the system size N. In addition, chosing an extensive stiffness ensures that finite elongations of the loading device, $e_G - \bar{e}$, can represent a non-zero driving force for the snap-spring system irrespective of N. The value of the specific stiffness, c, can vary between 0 and ∞. The limit as $c = \infty$ defines a hard device where the loading parameter must be $e_G = \bar{e}$ in order for Φ_{mech} and thus Φ to be finite. In this case, controlling e_G is equivalent to controlling the average strain of the system. In the opposite limit as $c \to 0$, the driving force vanishes unless $e \to \infty$ and the product ce_G remains finite. This is a situation in which the system is loaded by a very soft spring with large elongation and controlling e becomes equivalent to applying a stress $\sigma \equiv ce_G$.

The energy of the solid is assumed to be given by (6.14) with $\phi(e_i, e_i', e_i'')$ taking the form proposed in (6.10), i.e.

$$\Phi_{\text{solid}}(\mathbf{e}, \mathbf{e}', \mathbf{e}'') = \sum_{i=1}^{N} \left[f(e_i, h_i'; T) + \frac{C'}{2}(e_i')^2 + \frac{C''}{2}(e_i'')^2 \right], \tag{6.17}$$

where $f_i(e_i, h_i'; T)$ is given by (6.11). The local stress variables, $\{h_i'\}$, are defined as quenched random variables analogous to the random fields in random-field models (see Sect. 6.2). Within the context of the RSSM, random fields provide an effective description of the effects of, e.g. local impurities or dislocations at atomic scales (crystal dislocations). Point defects are responsible for interesting effects in martensites such as tweed precursors or strain-glass behaviour [105]. Such phenomena have been modelled for weak transformations using Landau theories [93, 106–108] and spin models [43, 109]. By including quenched random fields in the RSSM, we extend such theories to account for evolving disorder associated with transformation-induced slip and its interplay with quenched disorder (see Sect. 6.6). Crystal dislocations are also an important factor in martensites. Arbitrary distributions of crystal

dislocations within snap-springs may in general lead to a non-zero Burgers vector at mesoscopic scales and this translates into a lack of elastic compatibility between snap-springs. The non-compatibility effects were analysed in [110, 111] using Landau theories for weak phase transitions. In principle, such methods could be extended to be included in the model described here. We will however focus on systems with particular distributions of crystal dislocations giving a zero net Burgers vector within snap-springs so that snap-springs are elastically compatible.

The system is either thermally or mechanically driven through variation of the parameter $g(T)$ or the global elongation e_G, respectively. Under quasistatic driving and negligible thermal fluctuations [38, 112], the model exhibits avalanche dynamics which can be described in terms of automata [27, 54]. Avalanche dynamics are characterised by quiescent periods in which the system remains in a local energy minimum with fixed configuration fields $\mathbf{s} = \{s_{i,j}\}$ and $\mathbf{d} = \{d_{i,j}\}$ interrupted by avalanches leading to changes in $\mathbf{s}$ and/or $\mathbf{d}$. Avalanches start when the stability condition $e^- < e_i < e^+$ is violated by at least one snap-spring i and stop when the condition is again satisfied by all snap-springs. We now describe the steps followed to obtain an automaton representation of the model.

The relaxation of the harmonic variables $\mathbf{e}'$ and $\mathbf{e}''$ is assumed to be instantaneous with respect to the time scales of both driving and relaxation of the primary order parameter, $\mathbf{e}$. In this case, $\mathbf{e}'$ and $\mathbf{e}''$ can be adiabatically eliminated by setting $\partial \Phi / \partial e_i' = 0$ and $\partial \Phi / \partial e_i'' = 0$ subject to the elastic compatibility conditions [90, 91, 99]. This allows the energy of the system to be expressed in terms of the primary order parameter only [27, 28, 54]:

$$\tilde{\Phi}(\mathbf{e}) = \frac{1}{2} \sum_{i,j=1}^{N} K_{ij} e_i e_j + \sum_{i=1}^{N} f_i(e_i, h_i'; T) + \frac{cN}{2} (e_G - \bar{e})^2. \tag{6.18}$$

From this expression, the RSSM can be viewed as a set of snap-springs with energy $f_i(e_i, h_i'; T)$ which, due to elastic compatibility, interact with an interaction kernel $\mathbf{K} = \{K_{ij}\}$.

The variables $\mathbf{e}$ are assumed to obey overdamped dynamics given by the following set of equations:

$$\frac{1}{\gamma} \frac{\partial e_i}{\partial t} = -\frac{\partial \tilde{\Phi}}{\partial e_i}, \qquad i = 1, 2, \ldots, N, \tag{6.19}$$

where γ is the ratio between the rate of relaxation of the system to the local minimum of energy and the rate of driving. In the quasistatic limit, $\gamma \to \infty$, and the left hand side in (6.19) vanishes. As a result, the dynamics project onto the local minima of $\tilde{\Phi}$ which form a discrete set of branches with state variables $\mathbf{e}(e_G; \mathbf{s}, \mathbf{d})$. Each branch corresponds to a different configuration of $\mathbf{s}$ and $\mathbf{d}$. Minimization of $\tilde{\Phi}$ gives the following expression for the strain along equilibrium branches:

$$e_i = \frac{ck_i}{1+ck_\infty} e_G + \varepsilon \sum_{j=1}^{N} \left(J_{ij} - \frac{k_{ij}(c)}{N} \right) s_j + \sum_{j=1}^{N} \left(J_{ij} - \frac{k_{ij}(c)}{N} \right) d_j + h_i. \quad (6.20)$$

Here, $\{J_{ij}\}$ are the elements of a matrix $\mathbf{J} = (\mathbf{I} + \mathbf{K})^{-1}$, $h_i = \sum_j J_{ij} h'_j$ are renormalised disorder variables, $k_i = \sum_j J_{ij}$, $k_\infty = \frac{1}{N} \sum_i k_i$, and $\{k_{ij}(c)\}$ are the elements of an effective stiffness matrix defined as

$$k_{ij}(c) = \frac{ck_i k_j}{1+ck_\infty}. \quad (6.21)$$

The values taken by $k_{ij}(c)$ are limited to the interval $0 \leq k_{ij} < k_i k_j / k_\infty$ where the lower and upper bounds correspond to $c = 0$ and $c \to \infty$, respectively.

6.5.1 The RSSM as a Random-Field Model

Comparison of (6.20) with the local field for the RFIM (6.2) reveals that, along the equilibrium branches, the RSSM behaves as a random-field model with applied field proportional to e_G, and two types of random fields. The first type, h_i, represents generic heterogeneity while the second type,

$$h_i^{\mathrm{s}} = \sum_{j=1}^{N} \left(J_{ij} - \frac{k_{ij}(c)}{N} \right) d_j \quad (6.22)$$

is associated with slip. We will assume that random fields, h_i, are quenched and are given by a Gaussian distribution with zero mean and standard deviation r. In contrast, slip fields, h_i^{s} are not quenched in general since they are associated with the slip variables, $\mathbf{d}$, which evolve as the system is driven through the phase transition and slip is generated.

The behaviour of the RSSM along equilibrium branches reduces to that of a random-field model for the discrete variables s_i and d_i. The interaction between these variables consists of two contributions: the kernel $\mathbf{J} = \{J_{ij}\}$ originated by elastic compatibility and an infinite-range contribution $k_{ij}(c)/N$ associated with the stiffness of the mechanical constraint.

Substituting the strain given by (6.20) in (6.18) and using (6.11) with $w_i = \varepsilon s_i + d_i$ one gets the following energy for the RSSM along equilibrium branches:

$$\hat{\Phi} = \Phi_{\mathrm{ss}} + \Phi_{\mathrm{dd}} + \Phi_{\mathrm{sd}} + \Phi_{\mathrm{h}} + \Phi_{\mathrm{mech}}. \quad (6.23)$$

Here, we have neglected constant contributions and have defined

$$\hat{\Phi}_{\mathrm{ss}} = -\frac{\varepsilon^2}{2}\sum_{i,j}\left(J_{ij} - \frac{k_{ij}(c)}{N} - 2\frac{g(T)}{\varepsilon^2}\delta_{ij}\right)s_i s_j, \tag{6.24}$$

$$\hat{\Phi}_{\mathrm{dd}} = -\frac{1}{2}\sum_{i,j}\left(J_{ij} - \frac{k_{ij}(c)}{N}\right)d_i d_j, \tag{6.25}$$

$$\hat{\Phi}_{\mathrm{sd}} = -\varepsilon\sum_{i,j}\left(J_{ij} - \frac{k_{ij}(c)}{N}\right)s_i d_j, \tag{6.26}$$

$$\hat{\Phi}_{\mathrm{h}} = -\sum_{i} h_i(\varepsilon s_i + d_i), \tag{6.27}$$

$$\hat{\Phi}_{\mathrm{mech}} = \frac{cNe_G}{1+ck_\infty}\left(\frac{e_G}{2} - \frac{k_\infty}{N}\sum_i(\varepsilon s_i + d_i)\right). \tag{6.28}$$

The contribution $\hat{\Phi}_{\mathrm{ss}}$ gives the interaction between snap-springs associated with their phase state, $\mathbf{s}$. $\hat{\Phi}_{\mathrm{dd}}$ gives an analogous interaction for the slip state, $\mathbf{d}$. The energy $\hat{\Phi}_{\mathrm{sd}}$ gives the interaction between phase transition and slip. $\hat{\Phi}_{\mathrm{h}}$ accounts for the effects of snap-spring heterogeneity on the phase and slip states of snap-springs. Finally, $\hat{\Phi}_{\mathrm{mech}}$ is the energy associated with the mechanical loading.

6.6 Thermally-Driven Transformations

In order to illustrate the behaviour of thermally-driven structural transformations, we study the RSSM for mechanically unconstrained 2D solids by setting $c = 0$. The interaction kernel, $\mathbf{J}$, can in principle be explicitly calculated through minimisation of the energy of the system with respect to the strain fields $\mathbf{e}$, $\mathbf{e}'$, $\mathbf{e}''$, as described in Sect. 6.5. An explicit calculation of this type is presented in [28] for a highly anisotropic model which makes the calculation more tractable. A simpler alternative method consists in assuming periodic boundary conditions and then calculate the Fourier transform of the kernel $\mathbf{K}$ in (6.18) from which one can obtain $\mathbf{J} = (\mathbf{K} + \mathbf{I})^{-1}$ [90, 91, 100, 101, 107]. Irrespective of the method used to calculate the kernel $\mathbf{J}$, one always finds the following key features: anysotropy, sign indefiniteness and long-range decay. For illustration purposes, here we assume a short-range anisotropic and non-positive definite $\mathbf{J}$ as in [27, 54]; more realistic long-range interactions have been considered in [28] within a similar setting. We use the following kernel:

$$J_{ij} = \begin{cases} J_0, & i = j \\ J_1 > 0, & i \text{ n.n. } j \\ -J_2 < 0, & i \text{ n.n.n. } j \\ 0, & \text{otherwise,} \end{cases} \tag{6.29}$$

where 'n.n.' and 'n.n.n.' indicate nearest and next-to-nearest neighbors, respectively. We further assume that $\sum_{i,j} J_{ij} = 0$ which ensures that the inhomogeneity of the field $\mathbf{w} = \varepsilon\mathbf{s} + \mathbf{d}$ is penalised. For snap-springs on a square grid, this condition gives $J_0 = -4(J_1 - J_2)$.

In the following two subsections, we present results obtained through numerical simulation of a 501×501 ensemble of snap-springs placed on a square grid with open boundary conditions. The interaction terms are set to $J_1 = 0.062$ and $J_2 = 0.03$. The system is initially prepared in a homogeneous austenite phase with a minimal dislocation loop in the centre. Thermal loading is applied by cyclically sweeping $g(T)$ through the complete transformation.

6.6.1 *Evolution of Slip in Systems Without Quenched Disorder*

We now study the effect of transformation-induced defects in systems in which the only source of heterogeneity between snap-springs is associated with the slip field $\mathbf{d}$; Gaussian quenched disorder is set to $r = 0$.

Figure 6.11 shows the results for a system with $\varepsilon = 0.47$ inside region 3 in Fig. 6.9 where transformation-induced slip is expected. The upper panels in Fig. 6.11a show the spatial distribution of $\mathbf{s}$ in the martensitic phase after cycle 1 and after cycle 1000. The complexity of the phase microstructure clearly increases during the training period. In the lower panels one can see that the system develops some slip ($d \neq 0$) induced by the phase transition. The increase of slip with thermal cycling is clear in Fig. 6.11b which shows the density ρ of nearest neighbor snap-prings with differing values of d_i. As argued in Sect. 6.4 and illustrated in Fig. 6.8, neighbouring snap-springs with different values of d_i imply dislocations at a mesoscopic scale. Accordingly, the density ρ is a measure of the dislocation density at a mesoscale. The evolution of ρ is marked by a steep initial increase (training period) which after approximately 150 cycles leads to a steady regime (shakedown).

Figure 6.11c shows the distribution of avalanche sizes, $D_{\text{int}}(S)$, calculated by pooling avalanches observed during complete cooling runs. $D_{\text{int}}(S)$ evolves from a supercritical behaviour (peak at large values of S) during the first cycles towards a power law, $D_{\text{int}}(S) \sim S^{\tau'}$, in the steady state regime. A peak at large values of S indicates the occurrence of a snap event as in the low-disorder regime of random-field models presented in Sect. 6.2. The exponent of the power-law in the steady state regime takes a value $\tau' \simeq 1.2$ which is compatible with the exponent for a 2D RFBEG [40]. These results suggest that thermal cycling generates slip disorder that allows the system to cross a critical manifold associated with an OD transition of the type observed for random-field models with nucleation dynamics. In [28] we present a more detailed analysis of the origin of robust criticality in the RSSM and its link to OD critical transitions. We find a different value for the exponent $\tau'_{\text{LR}} \simeq 1.6$ when considering a more realistic long-range interaction kernel $\mathbf{J}$. Training effects predicted by

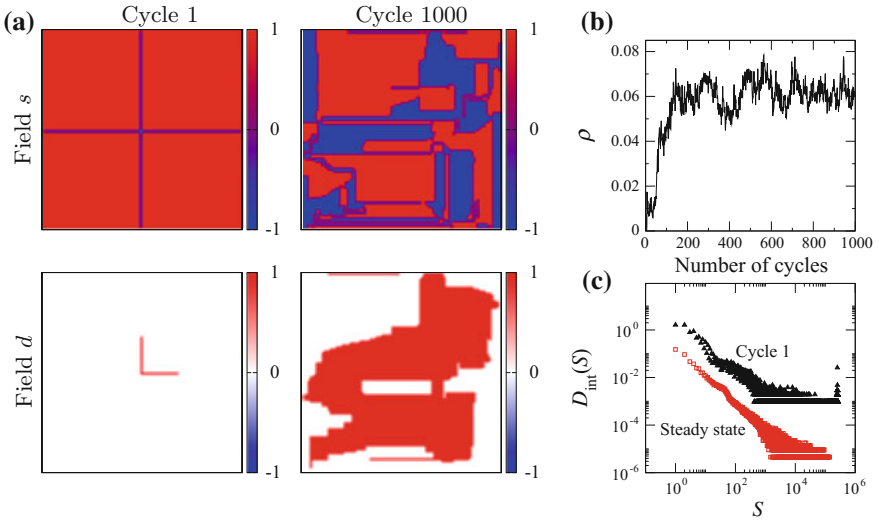

Fig. 6.11 Evolution under thermal cycling of a solid without quenched disorder undergoing a close to reconstructive transition with $\varepsilon = 0.47$. **a** The *upper* and *lower* panels show the phase (**s**) and slip (**d**) microstructures, respectively, after cycle 1 and cycle 1000. A dislocation loop was initially placed in the centre of the system. **b** Dislocation density ρ during the first 1000 cycles. **c** Distribution of the avalanche sizes, $D_{\text{int}}(S)$, after cycle 1 (*triangles*) and in the stationary state after 1000 cycles (*squares*)

models with short-range interactions are qualitatively similar to those observed for long-range interactions but the universality of critical avalanches is different.

6.6.2 *Interplay Between Quenched and Evolving Disorder*

We now explore the combined effect of Gaussian quenched disorder in intrinsically disordered solids and evolving slip disorder induced through thermal cycling. The predictions of this study are relevant to solids with impurities exhibiting, e.g., tweed precursors or strain-glass phases [105]. We consider a system with smaller transformation strain than in the previous section, $\varepsilon = 0.46$, such that slip generated in the absence of quenched disorder is negligible (see the panels for $r = 0$ in Fig. 6.12). In general, the amount of transformation-induced slip increases for increasing degree of quenched disorder (see panels for $r = 0.06$ and $r = 0.08$ in Fig. 6.12). In other words, the RSSM predicts that a large amount of quenched microscopic defects will typically induce larger amounts of transformation-induced slip. The density of dislocations in systems with quenched disorder, $r > 0$, takes larger values than for systems with $r = 0$ and also takes longer to reach a steady state (compare Fig. 6.13a

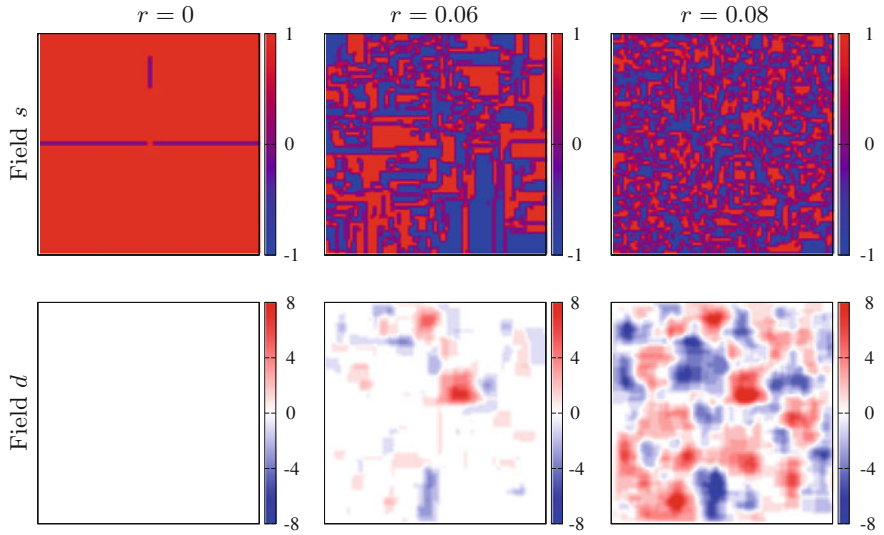

Fig. 6.12 Systems with quenched and evolving disorder after 1000 cycles. The transformation strain is $\varepsilon = 0.46$. The *upper* panels show the microstructure of phases, **s**, in the martensitic phase; the *lower* panels show the slip field **d**. Each column corresponds to a different degree of quenched disorder, $r = 0, 0.06, 0.08$

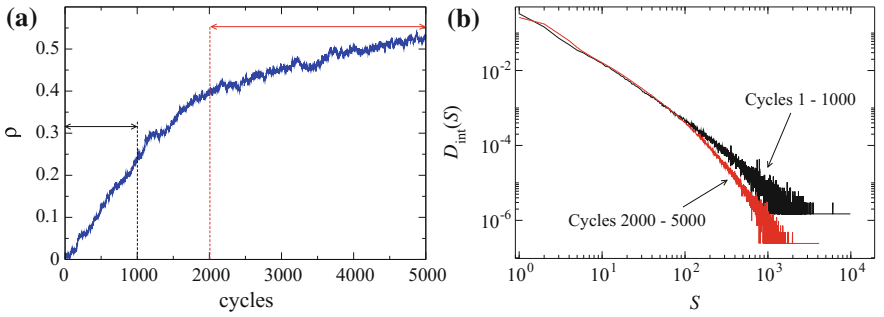

Fig. 6.13 **a** Dislocation density, ρ, during 5000 cycles in a system with quenched disorder $r = 0.06$ and transformation strain $\varepsilon = 0.46$. **b** Avalanche size distribution pooling avalanches registered during cycles $1 - 1000$ and $2000 - 5000$

and Fig. 6.11b). The avalanche size distribution, $D_{\text{int}}(S)$, is also affected by the degree of quenched disorder. Systems with large enough r develop high levels of slip under thermal cycling and obey a subcritical $D_{\text{int}}(S)$ (i.e. an exponential decay for large S), reminiscent of the response of random-field models in the pop regime. In addition, the cut-off of $D_{\text{int}}(S)$ at large avalanche sizes becomes increasingly pronounced as the levels of slip increase with cycling (see Fig. 6.13b).

6.7 Mechanically-Driven Transformations

This section presents some predictions of the RSSM for mechanically-driven systems [55]. We consider weak transformations with $\varepsilon \to 0$ so that slip can be neglected. In this regime, it is useful to set ε as the unit for strain in such a way that the bottom of the martensite wells are located at $e = \pm\varepsilon = \pm 1$. Let us also assume a particular case at low temperature, $g(T) < -\varepsilon^2/2$, so that all the snap-springs are in the martensitic phase. The resulting energy for a snap-spring, $f(e, h'; T)$ (cf. (6.11)), is illustrated in Fig. 6.14. These conditions correspond to the shape-memory regime in shape-memory alloys [31, 32]. In the following subsections, we present the stress–strain curves, transformation mechanisms and avalanche statistics predicted by the RSSM depending on the degree of quenched disorder, r, and stiffness of the loading device, c.

In the numerical simulations presented below, the system is initially prepared in a state with all snap-springs in the variant $s = -1$. The global elongation, e_G, is then quasistatically increased until all the snap-springs have transformed to the variant $s = +1$. We assume relatively simple settings for the snap-spring ensemble. The snap-springs are placed on the nodes of a simple cubic lattice of linear size $L = N^{1/3}$. This will allow us to compare with the well-studied zero-temperature RFIM in 3D. The interaction kernel $\mathbf{J}$ takes a short-range form with $J_{ii} = J_0 \geq 0$, $J_{ij} = J_1 > 0$ between nearest neighbors, and $J_{ij} = 0$ beyond nearest neighbors (in numerical simulations, we set $J_0 = J_1 = 1$). The non-negative character of the kernel ensures that the fraction $f_+ = (\sum_i s_i/N + 1)/2$ of snap-springs in the variant $s = +1$ increases monotonically with increasing e_G (i.e. no backward flips occur). We use periodic boundary conditions such that the quantity $k_i = \sum_j J_{ij}$ does not depend on i and takes the value $k_\infty = J_0 + 6J_1$ for snap-springs on a cubic lattice. The elements of the effective stiffness matrix k_{ij} defined in (6.21) are all equal to

$$k(c) = k_\infty \left[\frac{ck_\infty}{1 + ck_\infty} \right]. \tag{6.30}$$

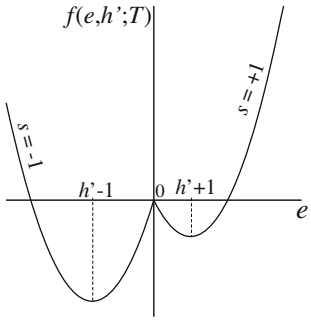

Fig. 6.14 Piece-wise parabolic energy for a snap-spring at low temperature in the limit of small transformation strain, ε, which is taken as the strain unit

Within this simplified setting, the behaviour of the RSSM along equilibrium branches can be mapped to the RFIM described in Sect. 6.2 with nearest-neighbour interaction, $\mathbf{J}$, and an infinite-range interaction, $J_{\text{inf}} = k(c)$.

6.7.1 Stress–Strain Curves

The stress is an intensive quantity defined as $\sigma = N^{-1} \frac{\partial \Phi}{\partial e_G}$ which, from (6.15), (6.16) and (6.17) reads as

$$\sigma = c(e_G - \bar{e}). \tag{6.31}$$

The average strain along the equilibrium branches can be obtained by introducing the equilibrium values e_i from (6.20) in the definition $\bar{e} = \frac{1}{N} \sum_i e_i$. One obtains,

$$\bar{e} = \frac{1}{1 + ck_\infty} \left(ck_\infty e_G + \frac{\sum_i k_i w_i}{N} \right). \tag{6.32}$$

The stress corresponding to the equilibrium branches can be obtained from (6.32) and (6.31) which give

$$\sigma = \frac{c}{1 + ck_\infty} \left[e_G - \frac{\sum_i k_i w_i}{N} \right]. \tag{6.33}$$

The soft-device limit corresponds to $c \to 0$ with finite ce_G which gives $k_i = 0$ and $\sigma = ce_G$, as argued in Sect. 6.5. The limit $c \to \infty$ corresponds to a hard device with stress

$$\sigma = \frac{1}{k_\infty} \left[e_G - \frac{\sum_i k_i w_i}{N} \right]. \tag{6.34}$$

The stress (6.32) can be alternatively expressed as a function of $\bar{e}$ as follows:

$$\sigma = \frac{1}{k_\infty} \left[\bar{e} - \frac{\sum_i k_i w_i}{N} \right]. \tag{6.35}$$

From this expression, it becomes clear that the stress consists of two contributions: a contribution proportional to the deformation of the sample (first term in the rhs of (6.35)) and a restoring component (second term in the rhs of (6.35)) associated with the configuration $\mathbf{w}$ of snap-springs. Note that (6.35) reduces to (6.34) in the hard-device limit when $\bar{e} = e_G$.

Figure 6.15 shows the stress–strain curves for two values of the disorder. For $k = 0$, a second-order phase transition occurs for a value of the disorder $r_o \simeq 2.2$. Such transition is associated with a critical point at $(r_o, \sigma_o) = (2.2, 0.34)$ which is equivalent to the OD critical point in the 3D-RFIM [62, 68, 80]. In the low disorder regime ($r < r_o$) the system exhibits snap behaviour marked by a macroscopic

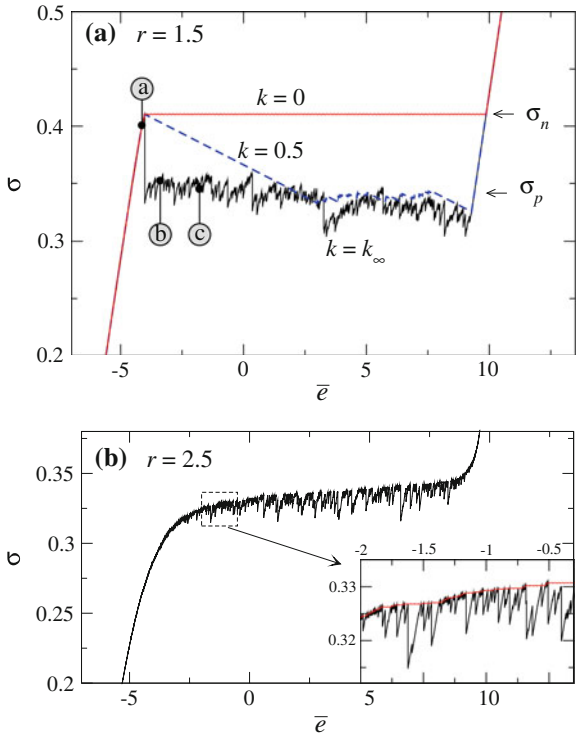

Fig. 6.15 Stress–strain curves obtained by increasing e_G in systems of size $L = 64$ with degree of disorder **a** $r = 1.5 < r_o$ and **b** $r = 2.5 > r_o$. The *three curves* plotted in a correspond to effective stiffness $k = 0$ (*dotted line*), $k = 0.5$ (*dashed line*), and $k = k_\infty$ (*continuous line*). The labels ⓐ, ⓑ, and ⓒ along the continuous line indicate the stress–strain values for the snapshots shown in Fig. 6.16a, b and c, respectively. The *curve* in b corresponds to a hard device loading with $k = k_\infty$. The *inset* in b shows the stress–strain curves for $k = k_\infty$ (*continuous line*) and $k = 0$ (*dotted line*) in the scale indicated by the *dashed square* in the main plot

discontinuity of the strain $\bar{e}$ associated with an infinite avalanche. Such avalanche occurs at a nucleation stress σ_n which is a decreasing function of r [55]. In the high disorder regime ($r > r_o$, Fig. 6.15b), the transition proceeds through a sequence of small avalanches characteristic of pop behaviour. A disorder-induced transition of this type can indeed be inferred from the results in [113] for impurity doped martensites. The martensite and strain-glass phases in doped martensites would correspond to the regimes with low and high disorder predicted by the RSSM.

The stiffness of the loading device does not play a significant role for systems in the pop regime (see the inset in Fig. 6.15b). In contrast, the snap behaviour in the low disorder regime is modified in a non-trivial manner for $k > 0$. As shown in Fig. 6.15a, the transformation starts at the stress σ_n as in the case with $k = 0$ but then decreases linearly with $\bar{e}$ (cf. (6.31)). More precisely, the behaviour of systems with k smaller than a certain value $k_\mathrm{p}(r)$, the behaviour is similar to that observed for $k = 0$ in the sense that the system is fully transformed in a single snap avalanche to the branch with $f_+ = 1$ (recall that f_+ is the fraction of snap-springs in the phase $s = +1$). In contrast, for $k > k_\mathrm{p}(r)$, the system reaches a stable branch with $0 < f_+ < 1$ and the transformation then proceeds along a saw-like path with lower values of the stress, σ_p, until the saturation branch with $f_+ = 1$ is reached. Section 6.7.2 shows that the

saw-like path corresponds to a propagation regime where the phase transformation is dominated by the growth of a single domain of the new phase.

The nucleation peak predicted by the RSSM at some stress σ_n is indeed observed experimentally in mechanically-driven shape-memory alloys [31, 114]. The existence of such peak suggests that the stability limit of equilibrium branches for the RSSM has a re-entrant behaviour in the space $(\bar{e}, \sigma)$. This behaviour is similar to that observed in the magnetisation-driven RFIM [115, 116] and is reminiscent of the re-entrant behaviour of the boundaries of the region of typical[3] states reported for the RFIM [117, 118].

Extending the conclusions of a recent study of the spinodal transition in the zero-temperature RFIM [119] to the RSSM studied here, one would expect the nucleation peak to be a finite-size effect disappearing in the thermodynamic limit ($L \to \infty$). The version of the RSSM studied in this section is however highly simplified and the size-dependence of the nucleation peak in more realistic settings with, e.g., a long-range and anisotropic $\mathbf{J}$, remains to be studied. In principle, an argument based on the RFIM or the simple version of the RSSM studied does not necessarily imply that the nucleation peak will disappear in the thermodynamic limit for martensites.

6.7.2 *Transformation Mechanisms: Nucleation and Propagation*

To illustrate the effect of the loading stiffness on the transformation mechanisms of the system, we consider the particular case with $k = k_\infty$. When increasing e_G as in Fig. 6.15a, the new phase nucleates in multiple isolated snap-springs for values of the stress smaller than σ_n (see the snapshot in Fig. 6.16a). At σ_n, one of the nuclei starts growing in a process reminiscent of the infinite avalanche occurring for $k = 0$. Such propagating domain is unique because the probability that two or more domains become unstable at the same stress, σ_n, is zero since σ_n is a real number.

During the growth of the propagating domain, the stress relaxes at constant driving, e_G, until a stable branch is reached. At this point, the new phase stops growing and e_G is increased again. The system evolves elastically (i.e. snap-springs do not change their energy well) along the reached equilibrium branch until the stability limit of such branch is reached. At this point, the transformation resumes. Figure 6.16a, b show that the transformation proceeds by the intermittent propagation of the boundary of the propagating domain. The domains of the new phase other than the propagating domain that nucleated before reaching σ_n were stable for $\sigma = \sigma_n$ and thus remain stable during the propagation regime which occurs at lower values of σ. Most of these domains are absorbed by the propagating domain.

The evolution of the system in the propagation regime consists of a sequence of pinning-depinning (PD) transitions of the boundary of the propagating domain

[3]Typical states have magnetisation m that can be represented by an exponentially large number of microscopic spin configurations, $\mathbf{s}$.

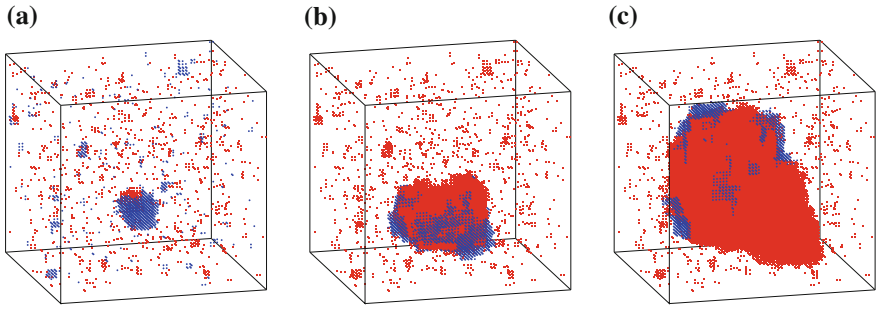

Fig. 6.16 Snapshots showing the transformed domains in the system following the stress–strain curve of Fig. 6.15a for $k = k_\infty$. The system size is $L = 64$ and disorder is $r = 1.5$. The *red regions* correspond to snap-springs that have already transformed to the phase $s = +1$ at **a** $f_+ = 0.005$ ($\bar{e} = -4.14$, ⓐ in Fig. 6.15a), **b** $f_+ = 0.04$ ($\bar{e} = -3.41$, ⓑ in Fig. 6.15a), and **c** $f_+ = 0.2$ ($\bar{e} = -1.79$, © in Fig. 6.15a). *Blue regions* show the transformed snap springs if the driving is slightly increased from the value corresponding to the configurations in red. Snapshot **a** illustrates the transformation mechanism in the nucleation regime before a propagating domain starts growing. Under a small increment of the driving, the transformation activity is spatially sparse. The propagation regime is illustrated by snapshots **b** and **c** where the snap-springs in *blue* show that *only* the propagating domain grows when increasing the driving

(henceforth referred to as the propagating front). The propagation stress σ_p corresponding to the upper limit of stability of each branch plays the role of a critical force for depinning of the propagating front.

Extrapolating the arguments of [119] to our model, one can argue that droplets of the new phase can in principle nucleate and start growing at the propagation stress, σ_p (i.e. can nucleate and grow before the driving reaches a larger nucleation stress, σ_n). The nucleation of such domains is however very unlikely and they are only expected to be frequent for very large systems where there are many possible nucleation events. If one of such nuclei leads to a rare droplet able to grow at the propagation stress, σ_p, the system will transform without a nucleation peak at $\sigma_n > \sigma_p$.

6.7.3 Universality Classes of Avalanches

The results of the previous section show that the transformation mechanisms strongly depend on the stiffness of the loading device, being nucleation-dominated for soft devices ($k < k_p(r)$) and propagation-dominated for harder devices ($k > k_p(r)$). The avalanche behaviour is different depending on the transformation dynamics. For $k < k_p(r)$, the model displays an OD transition between pop and snap regimes which belongs to the universality class of the zero-temperature RFIM with nucleation dynamics. For hard enough loading ($k > k_p(r)$), the system self-organizes to the QEW universality class for driven interfaces; in the RSSM, the interface corresponds to the phase boundary of a propagating domain. Interestingly, the driving-induced

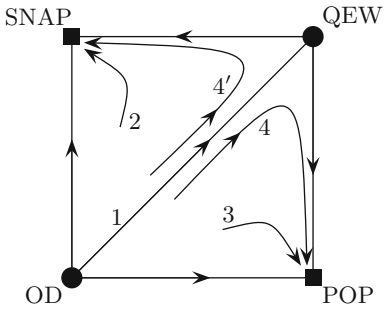

Fig. 6.17 Schematic RG flow for the RSSM model. Separatrix 1 is the QEW universality class manifold which indicates the RG flow from the neighborhood of the OD fixed point to the QEW fixed point. The RG-flow towards SNAP and POP regimes is indicated by *arrows* 2 and 3, respectively. *Lines* 4 and 4′ correspond to systems which display QEW critical exponents with supercritical or subcritical cut-offs for $k < k_{\mathrm{p}}(r)$ and $k > k_{\mathrm{p}}(r)$, respectively. [From [55], Fig. 4b, pp. 230601–4]

crossover between these two transformation mechanisms and critical behaviours was first proposed theoretically in [55] and then observed experimentally [120, 121].

The variety of nonequilibrium regimes observed in the mechanically-driven RSSM can be explained using Renormalization Group (RG) arguments [55]. The RG studies the way physical systems change under coarse-graining in order to understand the behaviour at large scales [22, 23, 25, 122]. Fixed points in the model parameter space remain invariant under the RG transformation and correspond to systems that remain invariant under coarse-graining. Under the RG transformation, systems flow towards a fixed point which dictates their behaviour at large scales. Four fixed points where assumed for the RSSM, see Fig. 6.17. Snap an pop behaviours are associated with trivial, fully attractive fixed points where the correlation length between snap-springs vanishes (these points are analogous to those of bulk phases in thermodynamics equilibrium [22]). In contrast, scale-free responses associated with OD and QEW universality classes are dictated by critical fixed points characterised by infinite correlation length between snap-springs.[4] The OD critical response is associated with a fully repulsive critical point which can be reached only by tuning all four parameters of the model: $\sigma = \sigma_o$, $r = r_o$, $k = 0$ and $L^{-1} = 0$. In contrast, QEW is a saddle point with a stable manifold which governs the large scale behaviour of the systems with $r < r_o$, $\sigma = \sigma_p(r)$, $k = 0$, and $L^{-1} = 0$; the corresponding systems lay on the critical manifold connecting the OD and QEW points [arrow 1 in Fig. 6.17]. Note that $k = 0$ is a necessary condition for pure critical behaviour of any type since $k > 0$ introduces a restoring force that prevents avalanches from growing indefinitely. This leads to a truncated power-law distribution for the avalanche sizes with a cut-off being increasingly pronounced for increasing k (see Fig. 6.18). This implies that finite systems which require $k \geq k_p(r) \geq 0$ to reach a propagation

[4] See [76] for an explicit calculation of the spin-spin correlation function near the OD transition.

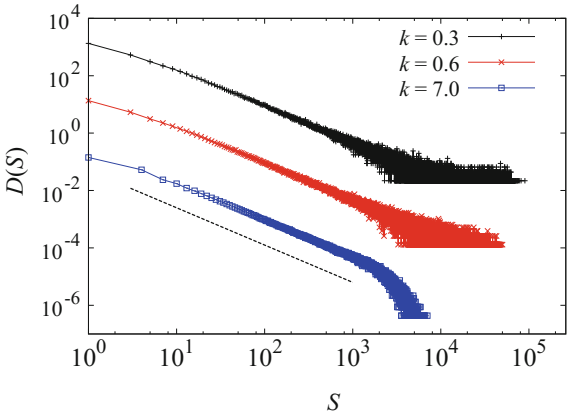

Fig. 6.18 Log-log plot of the distribution of sizes of avalanches exhibited by systems of size $L = 64$ and disorder $r = 1.5$ in the propagation regime. Different *symbols* correspond to different values of the stiffness k, as marked in the legend. The curves for $k = 0.6$ and $k = 7$ have been displaced vertically for clarity. The *dashed line* indicates a power-law $D(S) \sim S^{-\tau_p}$ with $\tau_p = 1.3$

regime are close to the critical QEW manifold [arrow 1 in Fig. 6.17] but eventually flow towards the POP fixed point under the RG transformation [arrow 4' in Fig. 6.17]. The situation in the thermodynamic limit can be different if rare droplets are able to grow by front propagation at σ_p [119]. In this case, there is no nucleation peak and the system can reach the propagation regime for arbitrarily small k so that the QEW criticality could be exactly reached.

6.8 Conclusions

In this chapter, it has been highlighted the idea that a complete description of the deformations occurring during martensitic transformations requires going beyond the usual assumption that the energy of solids is invariant under certain point group elements [56–61]. Indeed, crystallographic point groups are just finite subgroups of a global, infinite and discrete symmetry group which includes nonorthogonal and shearing deformations. Accounting for such deformations is crucial to model the emergence of defects such as dislocations induced by many martensitic phase changes. In essence, transformation-induced defects can be viewed as an inherent feature of many martensites which is built in their space of possible deformations. We have presented snap-spring (i.e. pseudo-spin) models which effectively account for such effects and provide an explanation for the emergence of scale-free avalanche behaviour after a training period. Such models account for both elastic and non-elastic properties of solids and this makes them ideal to study the interplay between

defects and the phase transition in both thermally and mechanically driven martensitic transformations.

Using a simple version of a random snap-spring model, it has been shown that criticality in mechanically-driven transformations depends on the stiffness of the loading device. The analysis presented here has only considered weak transformation and assumed short-range positive-definite interactions. Such simplification allowed us to compare with well-studied random-field models but a complete description of mechanically-induced transformations will require using long-range interactions and allowing for transformation-induced defects.

The role of transformation-induced defects was analysed for thermally-driven transformations. In this case, the evolution to criticality was initially interpreted in terms of the self-organized criticality (SOC) paradigm [27, 54]. This interpretation was however challenged by experiments on well-trained martensites which suggested that criticality requires tuning the driving parameter (temperature) to a critical value [9]. These results would support the existence of a critical point of the type displayed by random-field models rather than self-organized criticality. In a recent work [28] we extended the random-snap spring model reviewed here to propose an explanation that unifies the two seemingly conflicting interpretations proposed in [9, 27, 54, 92]. More explicitly, we identified a critical manifold in the temperature-disorder space of martensites where they are marginally stable [123]. The evolution of disorder during the phase transition allows the system to approach the critical manifold at a critical temperature without extrinsic tuning of disorder. This mechanism is reminiscent of the criticality paradigm proposed in [19] which postulated that a suitable coupling between driving and order parameters can lead to robust criticality. Our model predicts that a coupling of this type between the temperature and slip disorder explains the robustness of criticality in martensitic transformations.

Following the tradition of statistical mechanics, the models reviewed in this chapter are intended to capture generic properties of martensitic transformations. They are based on a number of simplifying hypotheses which include neglecting thermally activated effects or assuming infinitely slow driving fields. Thermal fluctuations are indeed a secondary factor for many shape-memory alloys [112]. The very fact that avalanches are observed as separated events in slowly driven systems indicates that thermally activated events are not frequent. In spite of that, some thermally activated events can occur [112] and spin models can be extended to study their effect on avalanches. This was done in [8] which focused on systems with weak thermal fluctuations and also investigated the effects of finite driving rates on avalanches. Both finite driving and thermal fluctuations promote the merging of avalanches that would be detected as separated events in athermal, quasistatically driven systems. As a consequence, the exponent for the distribution of avalanche sizes is smaller when thermal fluctuations are active and/or the driving is not quasistatic. In systems with stronger thermal fluctuations, individual avalanches are strictly speaking undetectable but bursts of transformation activity can still be distinguished. Molecular dynamics simulations show that the energy of such bursts deviates from the

power-law behaviour as thermally activated effects become stronger [38]. The mechanisms responsible for such deviations are still not fully understood.

Understanding the consequences of relatively strong thermal fluctuations within the framework of spin and/or snap-spring models is an interesting challenge for future studies. Another interesting task would consist in extending the proposed random-snap spring model to incorporate more realistic interactions and study generic phase transition paths in 2D and 3D systems. Such extensions will lead to a better understanding of the factors responsible for training effects and universality classes of avalanche dynamics in realistically complex materials. The random-snap spring model sets a good basis to achieve these goals.

Acknowledgments The author is grateful to Lev Truskinovsky and Giovanni Zanzotto for an enlightening collaboration on the topics covered in this chapter. The author is also grateful for insightful discussions and/or collaboration with a number of researchers including Eduard Vives, Antoni Planes, Lluís Mañosa, Jordi Ortín, Carles Triguero, Eckhard Salje, Sergei Taraskin, Stefano Zapperi, Turab Lookman and Avadh Saxena.

References

1. D.M. Dimiduk, C. Woodward, R. Lesar, M.D. Uchic, Scale-free intermittent flow in crystal plasticity. Science (New York) vol. 312, pp. 1188–1190. (2006). ISSN: 0036-8075
2. M.C. Miguel, A. Vespignani, S. Zapperi, J. Weiss, J.R. Grasso, Intermittent dislocation flow in viscoplastic deformation. Nature **410**, 667–671 (2001)
3. A. Petri, G. Paparo, A. Vespignani, A. Alippi, M. Costantini, Experimental evidence for critical dynamics in microfracturing processes. Phys. Rev. Lett. **73**, 3423–3426 (1994). ISSN: 0031-9007
4. J. Baró et al., Statistical similarity between the compression of a porous material and earthquakes. Phys. Rev. Lett. **110**(8), 088702 (2013). doi:10.1103/PhysRevLett.110.088702
5. G. Bertotti, I.D. Mayergoyz, G. Durin, S. Zapperi, *The Science of Hysteresis* (Elsevier, Amsterdam, 2006), pp. 181–267. doi:10.1016/B978-012480874-4/50014-2. http://www.sciencedirect.com/science/article/pii/B9780124808744500142
6. E.K. Salje, K.A. Dahmen, Crackling Noise in Disordered Materials. Annu. Rev. Condens. Matter Phys. **5**, 233–254 (2014). ISSN: 1947–5454
7. E. Vives et al., Distributions of avalanches in martensitic transformations. Phys. Rev. Lett. **72**, 1694–1697 (1994). ISSN: 0031-9007
8. F.-J. Pérez-Reche, B. Tadić, L. Mañosa, A. Planes, E. Vives, Driving rate effects in Avalanche-mediated first-order phase transitions. Phys. Rev. Lett. **93**, 195701 (2004). ISSN: 0031-9007
9. U. Chandni, A. Ghosh, H.S. Vijaya, S. Mohan, Criticality of Tuning in Athermal Phase Transitions. Phys. Rev. Lett. **102**, 25701 (2009)
10. M. Carmen Gallardo et al., Avalanche criticality in the martensitic transition of $Cu_{67.64}Zn_{16.71}Al_{15.65}$ shape-memory alloy: A calorimetric and acoustic emission study. Phys. Rev. B **81**, 174102 (2010). ISSN: 1098-0121
11. X. Balandraud, N. Barrera, P. Biscari, M. Grédiac, G. Zanzotto, Strain intermittency in shape-memory alloys. Phys. Rev. B **91**, 174111 (2015)
12. Y. Ben-Zion, Collective behavior of earthquakes and faults: Continuumdiscrete transitions, progressive evolutionary changes, and different dynamic regimes. Rev. Geophys. **46**, RG4006 (2008). ISSN: 8755-1209
13. D. Sornette, *Why Stock Markets Crash* (Princeton University Press, Princeton, 2003)

14. R.V. Solé, S.C. Manrubia, M. Benton, P. Bak, Self-similarity of extinction statistics in the fossil record. Nature **388**, 764–767 (1997). ISSN: 0028-0836
15. C.J. Rhodes, H.J. Jensen, R.M. Anderson, On the critical behaviour of simple epidemics. Proceedings. Biological sciences. R. Soc. **264**, 1639–1646 (1997). ISSN: 0962-8452
16. D. Plenz (ed.), *Criticality in Neural Systems* (Wiley, New York, 2014). doi:10.1002/9783527651009. http://onlinelibrary.wiley.com/book/10.1002/9783527651009. ISBN: 9783527651009
17. F. Ginelli et al., Intermittent collective dynamics emerge from conflicting imperatives in sheep herds, in *Proceedings of the National Academy of Sciences*, 12729–12734 (2015). ISSN: 0027-8424
18. M.E.J. Newman, Power laws, Pareto distributions and Zipf's law. Contemp. Phys. **46**, 323–351 (2004)
19. L. Gil, D. Sornette, Landau-Ginzburg theory of self-organized criticality. Phys. Rev. Lett. **76**, 3991–3994 (1996)
20. H.L.D. de S Cavalcante, M. Oriá, D. Sornette, E. Ott, D.J. Gauthier, Predictability and suppression of extreme events in a chaotic system. Phys. Rev. Lett. **111**, 198701 (2013)
21. H.E. Stanley, *Introduction to Phase Transitions and Critical Phenomena* (Oxford University Press, New York, 1983)
22. N. Goldenfeld, *Lectures on Phase Transitions and the Renormalization Group* (Addison-Wesley, Reading, MA, 1992)
23. J. Cardy, *Scaling and Renormalization in Statistical Physics* (Cambridge University Press, Cambridge, 1996)
24. P. Bak, *How Nature Works: the science of self-organized criticality* (Oxford University Press, Oxford, 1997)
25. J.P. Sethna, K.A. Dahmen, C.R. Myers, Crackling noise. Nature **410**, 242–250 (2001). ISSN: 0028-0836
26. D.S. Fisher, Collective transport in random media: from superconductors to earthquakes. Phys. Rep. **301**, 113–150 (1998). ISSN: 03701573
27. F.-J. Pérez-Reche, L. Truskinovsky, G. Zanzotto, Training-Induced Criticality in Martensites. Phys. Rev. Lett. **99**, 075501 (2007). ISSN: 0031-9007
28. F.J. Pérez-Reche, C. Triguero, L. Truskinovsky, G. Zanzotto, Origin of scale-free intermittency in structural first-order phase transitions. arXiv:1606.00607 (2016)
29. K. Otsuka, C.M. Wayman (eds.), *Shape Memory Materials* (Cambridge University Press, Cambridge, 1998)
30. L. Mañosa, A. Planes, M. Acet, Advanced materials for solid-state refrigeration. J. Mat. Chem. A **1**, 4925 (2013). ISSN: 2050-7488
31. J, Christian, The theory of transformations in metals and alloys, pp. 1102–1113 (Elsevier, Amsterdam, 2012). doi:10.1016/B978-008044019-4/50031-3. http://www.sciencedirect.com/science/article/pii/B9780080440194500313. ISBN: 9780080440194
32. G. Bertotti, I.D. Mayergoyz, J. Ortin, A. Planes, A, L. Delaey, The Science of Hysteresis, pp. 467–553 (Elsevier, Amsterdam, 2006). doi:10.1016/B978-012480874-4/50023-3. http://www.sciencedirect.com/science/article/pii/B9780124808744500233. ISBN: 9780124808744
33. L. Carrillo, L. Mañosa, J. Ortín, A. Planes, E. Vives, Experimental Evidence for Universality of Acoustic Emission Avalanche Distributions during Structural Transitions. Phys. Rev. Lett. **81**, 1889–1892 (1998)
34. J. Baró, E. Vives, Analysis of power-law exponents by maximum-likelihood maps. Phys. Rev. E **85**, 066121 (2012)
35. L. Carrillo, J. Ortín, Avalanches in the growth of stress-induced martensites. Phys. Rev. B **56**, 11508 (1997). ISSN: 0163–1829
36. R.J. Harrison, E.K.H. Salje, The noise of the needle: Avalanches of a single progressing needle domain in LaAlO[sub$_3$]. Appl. Phys. Lett. **97**, 021907 (2010). ISSN: 00036951
37. R. J. Harrison, E.K.H. Salje, Ferroic switching, avalanches, and the Larkin length: Needle domains in LaAlO3. Appl. Phys. Lett. **99**, 1077–3118 (2011). ISSN: 0003-6951

38. E.K.H. Salje, X. Ding, Z. Zhao, T. Lookman, A. Saxena, Thermally activated avalanches: Jamming and the progression of needle domains. Phys. Rev. B **83**, 104109 (2011)
39. X. Ding et al., Dynamically strained ferroelastics: Statistical behavior in elastic and plastic regimes. Phys. Rev. B **87**, 094109 (2013)
40. E. Vives, J. Goicoechea, J. Ortín, A. Planes, Universality in models for disorder-induced phase transitions. Phys. Rev. E **52**, R5–R8 (1995). ISSN: 1063-651X
41. J. Goicoechea, J.A. Ortín, Random field 3-State spin model to simulate hysteresis and avalanches in martensitic transformations. J. Phys. IV **5**, C2-71–C2-76 (1995)
42. S.R. Shenoy, T. Lookman, Strain pseudospins with power-law interactions: Glassy textures of a cooled coupled-map lattice. Phys. Rev. B **78**, 144103 (2008)
43. R. Vasseur, T. Lookman, Effects of disorder in ferroelastics: A spin model for strain glass. Phys. Rev. B **81**, 094107 (2010)
44. D. Sherrington, in *Disorder and Strain-Induced Complexity in Functional Materials*, ed. by T. Kakeshita, T. Fukuda, A. Saxena, A. Planes (Springer, Heidelberg, 2012), pp. 177–199. doi:10.1007/978-3-642-20943-7-10. ISBN: 978-3-642-20943-7
45. B. Cerruti, E. Vives, Random-field Potts model with dipolarlike interactions:hysteresis, avalanches, and microstructure. Phys. Rev. B **77**, 064114 (2008). ISSN: 1098-0121
46. H. Ji et al., M.O. Robbins, Percolative, self-affine, and faceted domain growth in random three-dimensional magnets. Phys. Rev. B **46**, 14519 (1992). ISSN: 0163-1829
47. J.P. Sethna et al., Hysteresis and hierarchies: dynamics of disorder-driven first-order phase transformations. Phys. Rev. Lett **70**, 12 (1993). ISSN: 0031-9007
48. F.J. Pérez-Reche et al., Kinetics of martensitic transitions in Cu-Al-Mn under thermal cycling: Analysis at multiple length scales. Phys. Rev. B **69**, 064101 (2004). ISSN: 1098-0121
49. F.J. Pérez-Reche, E. Vives, L. Mañosa, A. Planes, Acoustic emission studyof martensitic transition kinetics in Cu-based shape-memory alloys. J. Phys. IV **112**, 597–600 (2003)
50. G. Krauss, Fine structure of austenite produced by the reverse martensitic transformation. Acta Metall. **11**, 499–509 (1963). ISSN: 00016160
51. J. Pons, F. Lovey, E. Cesari, Electron microscopy study of dislocations associated with thermal cycling in a CuZnAl shape memory alloy. Acta Metallurgica et Materialia **38**, 2733–2740 (1990). ISSN: 09567151
52. T. Simon, A. Kröger, C. Somsen, A. Dlouhy, G. Eggeler, n the multiplication of dislocations during martensitic transformations in NiTi shape memory alloys. Acta Materialia **58**, 1850–1860 (2010). ISSN: 13596454
53. D.M. Norfleet et al., Transformation-induced plasticity during pseudoelastic deformation in Ni-Ti microcrystals. Acta Materialia **57**, 3549–3561 (2009). ISSN: 1359-6454
54. F.J. Pérez-Reche, L. Truskinovsky, G. Zanzotto, Martensitic transformations: from continuum mechanics to spin models and automata. Contin. Mech. Thermodyn. **21**, 17–26 (2009). ISSN: 0935-1175
55. F.J. Pérez-Reche, L. Truskinovsky, G. Zanzotto, Driving-induced crossover: From classical criticality to self-organized criticality. Phys. Rev. Lett. **101**, 230601 (2008). ISSN: 00319007
56. J.L. Ericksen, Some phase transitions in crystals. Arch. Ration. Mech. Anal. **73**, 99–124 (1980). ISSN: 0003-9527
57. I. Folkins, Functions of two-dimensional Bravais lattices. J. Math. Phys. **32**, 1965 (1991). ISSN: 00222488
58. M. Pitteri, G. Zanzotto, *Continuum Models for Phase Transitions and Twinning in Crystals* (Chapman & Hall/CRC, Boca Raton, 2003)
59. S. Conti, G. Zanzotto, A variational model for reconstructive phase transformations in crystals, and their relation to dislocations and plasticity. Arch. Ration. Mech. Anal. **173**, 69–88 (2004)
60. K. Bhattacharya, *Microestructure of Martensite: Why it Forms and How it Gives Rise to the Shape-Memory Effect* (Oxford University Press, Oxford, 2003)
61. K. Bhattacharya, S. Conti, G. Zanzotto, J. Zimmer, Crystal symmetry and the reversibility of martensitic transformations. Nature (London) **428**, 55–59 (2004)

62. G. Bertotti, I.D. Mayergoyz, J.P. Sethna, K.A. Dahmen, O. Perkovic, *The Science of Hysteresis* (Elsevier, Amsterdam, 2006), pp. 107–179. doi:10.1016/B978-012480874-4/50013-0. http://www.sciencedirect.com/science/article/pii/B9780124808744500130. ISBN: 9780124808744
63. B. Koiller, M.O. Robbins, Morphology transitions in three-dimensional domain growth with Gaussian random fields. Phys. Rev. B **62**, 5771–5778 (2000). ISSN: 0163-1829
64. E. Kierlik, P.A. Monson, M.L. Rosinberg, L. Sarkisov, G. Tarjus, Capillary vcondensation in disordered porous materials: hysteresis versus equilibrium behavior. Phys. Rev. Lett. **87**, 055701 (2001). ISSN: 0031-9007
65. T.P. Handford, F.J. Pérez-Reche, S.N. Taraskin, Capillary condensation in one-dimensional irregular confinement. Phys. Rev. E **88**, 012139 (2013)
66. Q. Michard, J.P. Bouchaud, Theory of collective opinion shifts: From smooth trends to abrupt swings. Europ. Phys. J. B **47**, 151–159 (2005). ISSN: 14346028
67. J.S. Urbach, R.C. Madison, J.T. Markert, Interface depinning, Self- organized criticality, and the Barkhausen effect. Phys. Rev. Lett. **75**, 276–279 (1995). ISSN: 0031-9007
68. F.J. Pérez-Reche, E. Vives, Spanning avalanches in the three-dimensional Gaussian random-field Ising model with metastable dynamics: Field dependence and geometrical properties. Phys. Rev. B **70**, 214422 (2004). ISSN: 1098-0121
69. M. C. Kuntz, J.P. Sethna, Noise in disordered systems: The power spectrum and dynamic exponents in avalanche models. Phys. Rev. B **62**, 11699–11708 (2000). ISSN: 01631829
70. J.H. Carpenter, K.A. Dahmen, A.C. Mills, M.B. Weissman, Historyinduced critical bahavior in disordered systems. Phys. Rev. B **72**, 052410 (2005)
71. R. Dickman, M.A. Muñoz, A. Vespignani, S. Zapperi, Paths to Self- Organized Criticality. Braz. J. Phys. **30**, 27 (2000)
72. M. Alava, Scaling in self-organized criticality from interface depinning. J. Phys.: Condens. Matter **14**, 2353–2360 (2002)
73. K. Dahmen, J.P. Sethna, Hysteresis, avalanches, and disorder-induced critical scaling: A renormalization-group approach. Phys. Rev. B **53**, 14872 (1996). ISSN: 0163-1829
74. O. Perković, K.A. Dahmen, J. P. Sethna, Disorder-induced critical phenomena in hysteresis: Numerical scaling in three and higher dimensions. Phys. Rev. B **59**, 6106–6119 (1999). ISSN: 0163-1829
75. S. Sabhapandit, P. Shukla, D. Dhar, Distribution of Avalanche sizes in the hysteretic response of random field ising model on a Bethe lattice at zero temperature. J. Stat. Phys. **98**, 103–129 (1999). ISSN: 00224715
76. T.P. Handford, F.-J. Perez-Reche, S.N. Taraskin, Exact spinspin correlation function for the zero-temperature random-field ising model. J. Stat. Mech.: Theor. Exp. **2012**, P01001 (2012)
77. T.P. Handford, F.J. Pérez-Reche, S.N. Taraskin, Mechanisms of evolution of avalanches in regular graphs. Phys. Rev. E **87**, 062122 (2013)
78. T.P. Handford, F.J. Pérez-Reche, S.N. Taraskin, Zero-temperature random-field Ising model on a bilayered Bethe lattice. Phys. Rev. E **88**, 022117 (2013)
79. I. Balog, M. Tissier, G. Tarjus, Same universality class for the critical behavior in and out of equilibrium in a quenched random field. Phys. Rev. B **89**, 104201 (2014). ISSN: 10980121
80. F.J. Pérez-Reche, E. Vives, Finite-size scaling analysis of the avalanches in the three-dimensional Gaussian random-field Ising model with metastable dynamics. Phys. Rev. B **67**, 134421 (2003)
81. I. Müller, P. Villaggio, A model for an elastic-plastic body. Arch. Rat. Mech. Anal. **65**, 25–46 (1977)
82. I, Müller, A model for a body with shape-memory. Arch. Ration. Mech. Anal. **70** (1979). doi:10.1007/BF00276382. http://link.springer.com/10.1007/BF00276382. ISSN: 0003-9527
83. B. Fedelich, G. Zanzotto, Hysteresis in discrete systems of possibly interacting elements with a double-well energy. J. Nonlinear Sci. **2**, 319–342 (1992)
84. G. Puglisi, L. Truskinovsky, Mechanics of a discrete chain with bi-stable elements. J. Mech. Phys. Solids **48**, 1–27 (2000)

85. L. Truskinovsky, A. Vainchtein, About the origin of the nucleation peak in transformational plasticity. J. Mech. Phys. Solids **52**, 1421–1446 (2004)
86. G.Puglisi, Hysteresis in multi-stable lattices with non-local interactions. J. Mech. Phys. Solids **54**, 2060–2088 (2006). ISSN: 00225096
87. E.K.H. Salje, *Phase transitions in ferroelastic and co-elastic crystals* (Cambridge University Press, Cambridge, 1993)
88. E.K.H. Salje, Ferroelastic Materials. Annu. Rev. Mater. Res. **42**, 265–283 (2012)
89. A.E. Jacobs, Solitons of the square-rectangular martensitic-transformation. Phys. Rev. B **31**, 5984–5989 (1985). ISSN: 1550-235X
90. S. Shenoy, T. Lookman, A. Saxena, A. Bishop, Martensitic textures: Multiscale consequences of elastic compatibility. Phys. Rev. B **60**, R12537–R12541 (1999). ISSN: 0163-1829
91. T. Lookman, S.R. Shenoy, K.O. Rasmussen, A.R. Saxena, A. Bishop, Ferroelastic dynamics and strain compatibility. Phys. Rev. B **67**, 024114 (2002). ISSN: 0163-1829
92. R. Ahluwalia, G. Ananthakrishna, Power-law statistics for Avalanches in a martensitic transformation. Phys. Rev. Lett. **86**, 4076–4079 (2001)
93. P. Lloveras, T. Castán, M. Porta, A. Planes, A. Saxena, Influence of elastic anisotropy on structural nanoscale textures. Phys. Rev. Lett. **100**, 165707 (2008)
94. M. Pitteri, Reconciliation of local and global symmetries of crystals. J. Elast. **14**, 175–190 (1984)
95. J.M. Ball, R.D. James, Proposed experimental tests of a theory of fine microstructure and the two-well problem. Philos. Trans. R. Soc. A: Math. Phys. Eng. Sci. **338**, 389–450 (1992). ISSN: 1364-503X
96. P. Tolédano, V. Dmitriev, *Reconstructive Phase Transitions* (World Scientific, Singapore, 1996)
97. D.M. Hatch, T. Lookman, A. Saxena, H.T. Stokes, Systematics of groupnonsubgroup transitions: Square to triangle transition. Phys. Rev. B **64**, 060104 (2001). ISSN: 0163-1829
98. V. Dmitriev, S. Rochal, Y. Gufan, P. Toledano, Definition of a transcendental order parameter for reconstructive phase transitions. Phys. Rev. Lett. **60**, 1958–1961 (1988). ISSN: 1079-7114
99. S. Shenoy, T. Lookman, A. Saxena, in *Magnetism and Structure in Functional Materials*, ed. by A. Planes, L. Mañosa, A. Saxena (Springer, Berlin, 2005). doi:10.1007/3-540-31631-2
100. O.U. Salman, L. Truskinovsky, Minimal Integer Automaton behind Crystal Plasticity. Phys. Rev. Lett. **106**, 175503 (2011)
101. O.U. Salman, L. Truskinovsky, On the critical nature of plastic flow: One and two dimensional models. Int. J. Eng. Sci. **59**, 219–254 (2012). ISSN: 00207225
102. D. Rodney, A. Tanguy, D. Vandembrouc, Modeling the mechanics of amorphous solids at different length scale and time scale. Modell. Simul. Mater. Sci. Eng. **19**, 083001 (2011). ISSN: 0965-0393
103. M. Braun, Compatibility conditions for discrete elastic structures. Rendiconti del Seminario Matematico 58, 37–48. ISSN: 0373-1243
104. X. Balandraud, G. Zanzotto, Stressed microstructures in thermally induced M9R-M18R martensites. J. Mech. Phys. Solids **55**, 194–224 (2007). ISSN: 00225096
105. T. Kakeshita, T. Fukuda, A. Saxena, A. Planes (eds.), *Disorder and Strain-Induced Complexity in Functional Materials* (Springer, Berlin, 2012). doi:10.1007/978-3-642-20943-7. ISBN: 978-3-642- 20943-7
106. S. Kartha, T. Castán, J. Krumhansl, J. Sethna, Spin-glass nature of tweed precursors in martensitic transformations. Phys. Rev. Lett. **67**, 3630–3633 (1991). ISSN: 1079-7114
107. S. Kartha, J.A. Krumhansl, J.P. Sethna, L.K. Wickham, Disorder-driven pretransitional tweed pattern in martensitic transformations. Phys. Rev. B **52**, 803–822 (1995)
108. D. Wang, Y. Wang, Z. Zhang, X. Ren, Modeling abnormal strain states in ferroelastic systems: the role of point defects. Phys. Rev. Lett. **105**, 205702 (2010). ISSN: 1079-7114
109. D. Sherrington, A simple spin glass perspective on martensitic shape-memory alloys. J. Phys. Condens. Matter **20**, 304213 (2008)
110. R. Gröger, T. Lookman, A. Saxena, Defect-induced incompatibility of elastic strains: dislocations within the Landau theory of martensitic phase transformations. Phys. Rev. B **78**, 184101 (2008)

111. R. Gröger, T. Lookman, A. Saxena, Incompatibility of strains and its application to mesoscopic studies of plasticity. Phys. Rev. B **82**, 144104 (2010). ISSN: 1098-0121
112. F.J. Pérez-Reche, E. Vives, L. Mañosa, A. Planes, Athermal character of structural phase transitions. Phys. Rev. Lett. **87**, 195701 (2001). ISSN: 0031- 9007
113. D. Wang et al., Superelasticity of slim hysteresis over a wide temperature range by nanodomains of martensite. Acta Materialia **66**, 349–359 (2014). ISSN: 13596454
114. E. Bonnot et al., Hysteresis in a system driven by either generalized force or displacement variables: Martensitic phase transition in single-crystalline Cu-Zn-Al. Phys. Rev. B **76**, 064105 (2007). ISSN: 10980121
115. X. Illa, M.-L. Rosinberg, E. Vives, Influence of the driving mechanism on the response of systems with athermal dynamics: The example of the random-field Ising model. Phys. Rev. B **74**, 224403 (2006). ISSN: 1098-0121
116. X. Illa, M.-L. Rosinberg, P. Shukla, E. Vives, Magnetization-driven random-field Ising model at T = 0. Phys. Rev. B **74**, 224404 (2006). ISSN: 1098-0121
117. F. J. Pérez-Reche, M.L. Rosinberg, G. Tarjus, Numerical approach to metastable states in the zero-temperature random-field Ising model. Phys. Rev. B **77**, 064422 (2008). ISSN: 10980121
118. M.L. Rosinberg, G. Tarjus, F.J. Pérez-Reche, The $T = 0$ random-field Ising model on a Bethe lattice with large coordination number: hysteresisand metastable states. J. Stat. Mech.: Theor. Exp. **2009**, P03003 (2009)
119. S. Nandi, G. Biroli, G.Tarjus, Spinodals with Disorder: from Avalanches in Random Magnets to Glassy Dynamics. Phys. Rev. Lett. **116**, 145701 (2016)
120. E. Vives, D. Soto-Parra, L. Mañosa, R. Romero, A. Planes, Drivinginduced crossover in the avalanche criticality of martensitic transitions. Phys. Rev. B **80**, 180101 (2009). ISSN: 1098-0121
121. E. Vives, D. Soto-Parra, L. Mañosa, R. Romero, A. Planes, Imaging the dynamics of martensitic transitions using acoustic emission. Phys. Rev. B **84**, 060101 (2011). ISSN: 1098-0121
122. K. G. Wilson, The renormalization group and critical phenomena. Rev. Mod. Phys. **55**, 583–600 (1983). ISSN: 00346861
123. M. Müller, M. Wyart, Marginal Stability in Structural, Spin, and Electron Glasses. Ann. Rev. Condens. Matter Phys. **6**, 177–200 (2015)

Chapter 7
Ferroelastic Domain Collapse and Acoustic Emission: Non-equilibrium Behaviour of Multiferroic Materials

Ekhard K.H. Salje and Xiandong Ding

Abstract Nano-scale multiferroics often display sudden, jerky domain movements under weak external fields. These domain movements include retracting twin domains, kinks in domain walls, jamming between walls and changes in complex tweed patterns. The time evolution of such patterns under weak forcing may also contain additional continuous movements such as the propagation of a twin wall under stress. Other movements remain jerky such as pinning-depinning events that may lead to acoustic emission. We show that the probability density function, PDF, of the jerk distribution follows power law statistics at sufficiently low temperatures and thermally activated jumps at high temperatures. The overall Vogel Fulcher distribution of the PDF is explained by the mixing of thermal and athermal events during AE.

7.1 Introduction

High memory capacities and electric wiring on a much finer scale than achievable with current technologies may be possible when the active elements in devices are not the bulk but where only domain boundary structures contain the desired functionalities [1–14]. The first step was to explore the possibility to generate highly conducting domain walls as a replacement of wires in device applications. Such domain boundaries were designed to carry high currents and it was indeed the discovery of superconducting twin boundaries that opened a wide field of applications in 'domain boundary engineering' where the domain boundary is the device and were the design of the device materials depends largely on tailoring the domain boundary structure [1, 4, 13, 15, 16].

E.K.H. Salje (✉)
Department of Earth Sciences, University of Cambridge, Cambridge CB2 3EQ, UK
e-mail: ekhard@esc.cam.ac.uk

X. Ding
State Key Laboratory for Mechanical Behavior of Materials, Xi'an Jiaotong University, 710049 Xi'an, People's Republic of China
e-mail: Dingxd@mail.xjtu.edu.cn

E.K.H. Salje et al. (eds.), *Avalanches in Functional Materials and Geophysics*, Understanding Complex Systems, DOI 10.1007/978-3-319-45612-6_7

The second step was to introduce polarity to the domain wall so that switchable ferroelectricity was confined to domain walls and would not interfere with depolarization fields and additional switching of domains in the bulk. The length scale of the active device was then restricted to the thickness of domain walls or even smaller structures such as Bloch walls inside domain walls [17–22]. Similar ideas were also explored in magnetic materials [23–30]. These approaches require – at least at the present sensitivity for the detection of ferroic functionalities – that many walls cooperate to induce a measurable macroscopic response to applied fields. If we use ferroelectricity as example, we would expect that a ferroelectric hysteresis requires at least 1% of all atoms to take part in a switching cycle in order to be observable on a macroscopic level. Domain wall ferroelectricity will have, in case of sparse domain walls, only ca. one in a million (1 ppm) particles switching, which will not be observable under currently available laboratory conditions. More sensitive means of detection may emerge in future, but the current analytical work is largely focused on materials were the domain boundary density is very high. Some materials such as cryogenic $SrTiO_3$ already contain very high domain boundary densities near the crystal surface [31, 32]. Computer simulations helped to identify alternative approaches to increase the domain wall densities, such as by external shearing of a sample (∼cold shearing) [33–36] instead of rapid temperature quenches.

The domain wall density seems to be limited when the intrinsic length scale of the wall, namely its intrinsic width w, competes with the wall-wall distances L. Empirical values for L for pattern with densely stacked walls under thermal quench are $L > 10w$. For higher wall concentrations (and $L < 10w$) a new type of global domain pattern was predicted: the domain glass with non-ergodic responses to external forcing. The concept of a domain glass was introduced only in 2014 [37] while 'domain' related glass states (such as encountered in polar nano-regions [38]) were long understood to exist in relaxor materials where non-ergodicity is one of the defining properties of the relaxor state [39–43]. Little it is known how the breaking of ergodicity occurs in the limiting case of weakly disordered systems, however. It is controversial whether highly structured ferroic materials can show glassy behaviour when the disorder is induced by nano-scale domain structures or whether they always follow the classic uniform transition pathway. One scenario is that decreasing the strength of defect related random fields in a ferroic phase transition will make the transition increasingly more ergodic and one may be tempted to assume that the fully ordered system undergoes a phase transition without any ergodicity breaking. This is not necessarily born out by experiments or by computer simulations. Lloveras et al. [44] have already shown that spatially heterogeneous states that occur in ferroelastic transitions depend crucially on the elastic anisotropy with tweed type microstructures for anisotropic interactions and mottled structures with almost spherical nano domains for isotropic interactions. Defect free systems (in computer simulations) or in materials that contain very small defect concentrations (experimentally) may show glassy behaviour - which has lead to claims that such materials are relaxors without the relaxor-type dispersion relations [45–53]. The glassiness in such systems is not related to some disorder in the structural matrix but stems entirely from ferroelastic, ferroelectric, or ferromagnetic microstructures, which perturbed the matrix only very slightly.

A key issue is how to monitor and ultimately control the formation of complex domain glasses with high domain boundary densities. Some classic spectroscopic techniques include hard mode Raman and Infrared spectroscopy [54–58]. Moreover, non-functional domain walls such as in $Pb_3(PO_4)2$, leucite and anti-ferroelectric materials such as titanite need to be identified and ultimately excluded from this research because the expectation of polarity based on group theory simply ignores some other fundamental restrictions on low-dimensional polar patterns [59–68]. This result shows that domain wall functionalities must be tested simultaneously with a careful assessment of how many walls are generated during the nucleation process. A significant breakthrough was achieved when resonant piezoelectric methods where applied to domain walls [69–80]. In Resonant Piezoelectric Spectroscopy, RPS, a weak electric field couples with local polarity to excite acoustic standing waves which can then be detected by mechanical transducers. This method can be combined with acoustic emission, AE, to detect the number density of domain walls. Neutron scattering, x-ray diffraction, and surface sensitive methods (AFM, PFM) were previously employed with much success [64, 81–89] in specific studies to explore the properties and thicknesses of domain walls. In addition, acoustic emission techniques are possibly the most promising avenue for future research in the dynamics of domain movements in ferroelastic materials [90] because they can be employed on a very small length scale during the production process of piezoelectric domain wall devices. This approach is new and depends on two key ingredients: firstly the AE equipment needs to be sensitive enough to detect nucleating and moving domain walls and, secondly, the ability to interpret the AE spectra with sufficient insight to correlate main wall-related events to specific AE signals or to specific statistical fingerprints such as avalanche activities and wall-wall correlation effects. None of this has been achieved yet but it is very likely that research in the next few years may lead to significant progress in this field. In this paper we summarize some of the relevant results known so far, hoping that they may constitute the starting point for much enhanced future research activities.

7.2 Acoustic Emission, AE

Domain patterning processes have been observed to be 'jerky' when measured with a very high time resolution. The reason is pattern formation, which involves nucleation, fast domain movements, jamming, and other heterogeneous processes [1, 2, 8, 14, 34–36, 91–95]. We call AE events and all other singularities dues to the pattern formation 'jerks' to indicate that they are observables with whatever statistical distribution. Jerks may not relate to avalanches but often they combine to produce 'crackling noise' [91–95] that may point towards the formation of avalanches where each nano-structural movement triggers others with bursts of activities and characteristic waiting times between such avalanches. The probability P(J) of a jerk J to occur is often power law distributed $P(J) \sim J^{-\varepsilon}$ F(J) where F(J) is some (exponential) cut-off function. Similar power law distributions exist for waiting times between

avalanches (for an extensive study we refer the reader to [93]). In most disordered materials such avalanches are described by a narrow range of dynamical exponents both for the energy distributions and the waiting times between avalanches [92–110].

Several experimental observations, theoretical models, and computer simulations of dynamical evolution of ferroic nano-structures [91–108] depict a fairly clear picture of transition dynamics involving domain pattern formation and reconstruction. Nevertheless, there is an obvious lack of experimental observations which prevents us from distinguishing between different local mechanisms. Experimental observations of 'jerks' over very short time scales are indeed difficult. We can compare the AE jerks with those of other experimental techniques. In case of ferroic transitions, we find suitable jerks in fast heat flux measurements (∼thermal jerks) [96], as acoustic emission (∼mechanical jerks) [93, 97] or spikes in the polarization (∼electric jerks) or magnetization (∼magnetic jerks or 'Barkhausen noise') [98, 99]. Acoustic emission, AE, plays a special role amongst these techniques because it appears to be more sensitive to small nano-structural changes than the other methods [100–102]. The key advantage is that AE carries the whole temporal and spatial information of the acoustic source mechanism with time series that enables us in the most successful measurements to determine the energy and duration of avalanches and waiting time between successive hits. Major advances were made when investigations focused on porous and martensitic materials where all quantities derived from AE display power law distributions corroborating the existence of avalanche criticality [103–107] (Fig. 7.1). In addition, space localization of the avalanches is also possible from AE measurements. Localization of the avalanches is important because it provides information regarding the spatial distribution of minima of the free energy landscape, which are the origin of criticality. This is only possible from surface observations in opaque martensites while most ferroic oxides are transparent which makes the localization of jerks rather easy [108]. The probably most advanced studies of martensitic transitions include [109, 110].

These examples show that great progress has been made for the AE for the detection of martensitic transitions and the investigations of the collapse of porous materials. Nevertheless, AE studies in ferroelectric and weakly ferroelastic materials are less advanced. The reason is that AE signals are usually very weak and often extremely sparse. In Ferroelectric materials only 90° boundaries carry sufficient strain to generate AE while the strain involved in 180° boundaries is much weaker [111–114]. Detailed computer simulations of AE in ferroelectrics have shown that most nano-structural changes in ferroic materials contain too little elastic energy to generate measurable AE signals [139]. This result also questions the way we analyze AE in ferroic materials: visible AE events are due to a complex combination of a multitude of various domain boundary movements over a very short time interval (large jerks) and it is virtually impossible to distinguish between individual events (the AE fine structure). Most importantly, the movement of jerks inside domain walls and the common movement of twin domain needles contain similar AE energies (and are hence indistinguishable from their energy spectrum). In virtually all cases investigated so far, one can only measure the energy of the total, complex pattern formation, such as the 'yield' in [34–36]. This generates a different perspective of AE

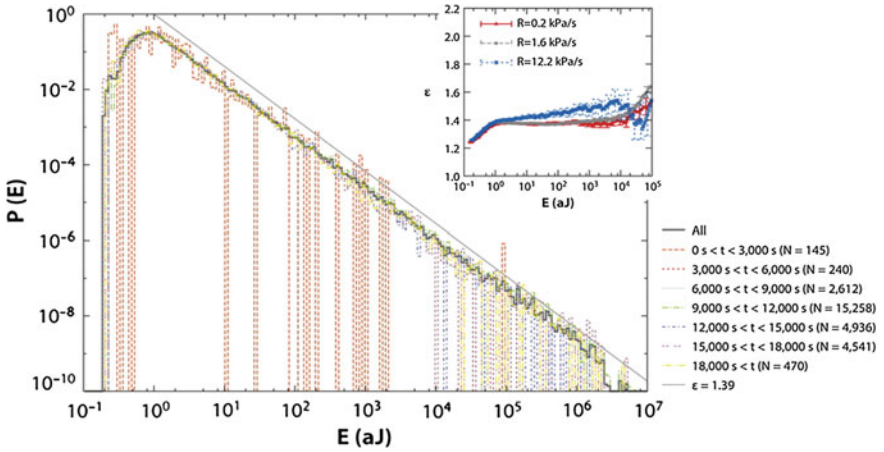

Fig. 7.1 Power law determined from AE determination of jerks emitted during the collapse of nano-scale, porous SiO_2

investigations in ferroic materials: the details of the structural changes may be hidden in the fine-structure of the AE spectrum while other parameters such as transition temperatures, the development of coherency in patterns at T*, the split of a transition point, etc. becomes prominent [115, 116].

Two serious limitations exist when the jerk-statistics is investigated by AE. Firstly, no continuous domain movements can be observed in the AE spectrum. Smooth domain movements are common in adaptive structures [8] and will simply be missed by AE. Secondly, jerks in ferroic materials can be observed when no avalanches occur. Examples are repeated pinning/depinning processes of a ferroelastic needle domain (serration), which generate several large jerks and cannot be distinguished from the more complex formation of avalanches where many depinning movements interact [117–119]. In these cases, the totality of all jerks may follow a power-law statistics but there is no fine-structures inside each jerks which is due to avalanche formation. AE can not distinguish between these two scenarios unless the time resolution is good enough to see the jerk fine-structure which has not been demonstrated so far.

A similar scenario was discussed for avalanches generated by dislocations [120]. These authors argued that two mechanisms coincide when, on one hand, correlations among individual dislocations are weak and fluctuations are roughly Gaussian, which makes the homogenized description adequate. On the other hand, a different point of view emerged from the analysis of high resolution acoustic emission (AE) data in plastically deforming crystals which showed that temporal fluctuations may be power-law distributed in size and energy [121] and may be clustered in both space [122] and time [123]. It has been long noticed that AE in plastically deformed crystals may include both continuous background and discrete bursts [124, 125]. While the continuous AE was thoroughly studied, the bursts were generally simply counted [126], or omitted as spurious even though sudden slips at irregular intervals could

be also observed directly [127–129]. The relative contribution of plastic avalanches responsible for bursts and simple Gaussian fluctuations were measured in [121] and showed that ice single and polycrystals generate nearly 100% of plastic movements were released through AE bursts. In contrast, for aluminum, the contribution due to avalanches is small, reaching under cyclic loading at most a few percent during the first cycles, when the dislocation substructure has not yet fully developed. Copper and CuAl alloys stay in between.

In other systems, jerks have been detected with a variety of other experimental techniques: induction by magnetic Barkhausen jumps [130, 131], magnetization measurements [132], calorimetry [96, 105], resistivity [133, 134] and capacitance measurements [135], and optical observations [14, 136]. In comparison with these techniques, AE appears to be the most popular method for the observation of intense jerks, with over 1500 publications per year in physics and material science journals. Despite this colossal effort, it often remains unclear which atomic processes are actually observed in AE experiments.

A very instructive comparison between the collapse of porous materials under stress and the effect of twinning of a martensite is discussed in [137]. Two sequences of AE signals were investigated in the same sample. The two processes occur simultaneously. De-twinning at the early stages of compression generated one AE sequence. Fracture dominated the later stages. Fracture also determines the catastrophic failure (big crash). For high-porosity samples, the AE energies of both sequences display power-law distributions with exponents $\varepsilon \simeq 2$ (twinning) and 1.7 (fracture). The two power laws confirm that twinning and fracture lead both to avalanche criticality during compression. This result shows that it is possible to observe highly resolved AE even when more than one process occurs at the same time in the same sample. The AE signal due to twinning is much weaker than the fracture signal.

7.3 Computer Simulation of AE During Nano-Patterning of a Ferroelastic Crystal

When twinning is identified as origin of AE, it remain unclear how the twinning actually occurs. A very detailed study [138] identified the AE signals of retracting needles, kinks, collapsing spanning domain walls and their combination in major yield events under shear strain based on the analysis of a very simple but generic model [34–36]. The model uses a generic two-body potential to represent the interactions of atoms in a 2D system. The potential energy U(r) contains three parts, the first- nearest atomic interactions of $20(\mathrm{r}-1)^2$, the second-nearest interactions $-10(\mathrm{r}-\sqrt{2})^2 + 2000(r-\sqrt{2})^4$, and the third- nearest interactions $-(\mathrm{r}-2)^4$, where r is the interatomic distance in units of the length of the crystallographic unit cell. This potential was developed based on Landau theory by choosing the shear angle as "order parameter". The details of properties obtained by this potential are described in [33–36]. Extensions of the model to three dimensions did not change the principal results of the simulations [139].

These simulations followed the tradition of large-scale simulations with open- (free-) boundary conditions and the equilibrated unit cell has the shape of the parallelogram with the shear angle of 4°. The equilibrium lattice constant is set to a = 0.1 nm and atomic mass to M = 100 amu.The initial configuration contains two horizontal twin boundaries (HTBs). The surface ratio of the intermediate layer to the whole sample is fixed to be 0.5. The size of the present simulations is based on a 400a × 402a box, except when a 200a × 202a box is used to capture the collapse of one single vertical needle domain under detwinning conditions. The calculated cell contains two buffer layers (each has three atomic layers) at the top and bottom of the 2D sheet. These buffer layers were sheared by the external boundary conditions (fixed external strain, hard boundary conditions). The system was first relaxed using a conjugate gradient refinement procedure to find the optimal position for each lattice point under the initial conditions of the sample shape. Molecular dynamics (MD) was then performed to anneal each configuration at a given temperature for 3×10^6 time steps. The only relaxations, which occurred during this procedure, were surface relaxations. After the relaxation and strain-free MD, external strain was applied via a global shear of the two buffer layers. We use a constant strain rate of 10^{-5}/ps and display our results as function of time to directly connect with the dynamics of AE. The temperature of the sample was held at T = 0.6 K by a Nose–Hoover thermostat (Fig. 7.2).

The time evolutions of the domain formation and the de-twinning sequence are shown on a long timescale in Fig. 7.3. The initial crystal (Fig. 7.4a) is heavily twinned during a yield event between time t_1, when the first twin nucleates, and time t_2, when the external strain is compensated by the shape change of the sample. The crystal decays into a multitude of twins (Fig. 7.4b). The twinned area then decreases under further shear (Fig. 7.4c–e), and a single crystal is recovered in Fig. 7.4f. The AE signal is largest during the yield event, where most experimental results were obtained. During the yield event, a complex mixture of domain movements will occur, with needle domains, kinks, and junctions all forming almost simultaneously. During de-twinning, the same movements occur, but they are spread out over a long time period. The AE of each event is much less than the total AE during yield,

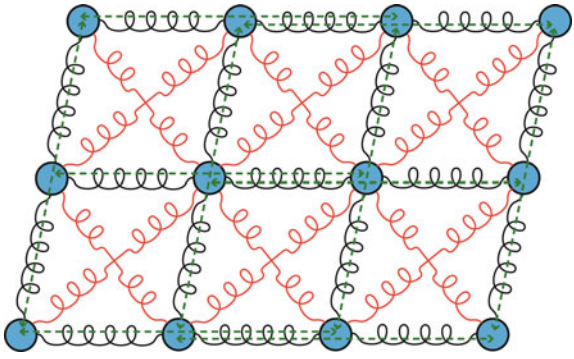

Fig. 7.2 The model with nearest-neighbor (*black* springs), next-nearest-neighbor (*red* springs), and third-nearest-neighbor (*green lines*) interactions

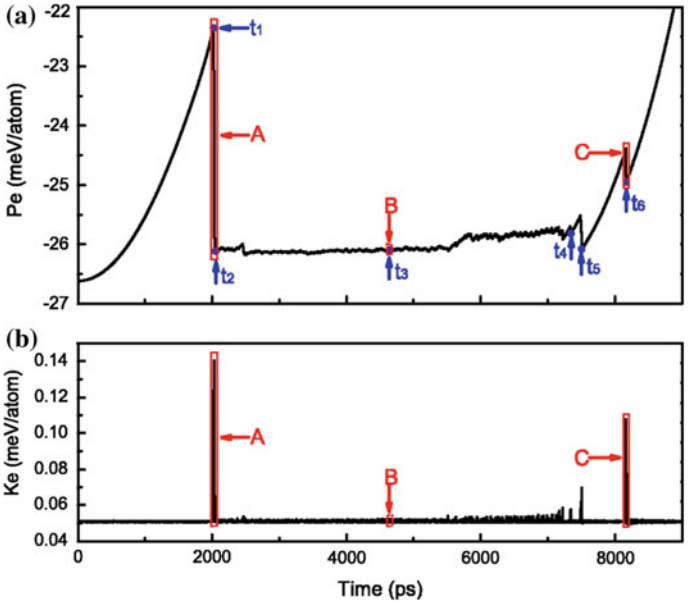

Fig. 7.3 Evolution of potential energy Pe (**a**) and kinetic energy Ke (**b**) during the shear deformation. The rectangles A, B, C correspond to the yield, kink, and horizontal needle regimes in Fig. 7.4

but, if the de-twinning AE could be accumulated in full, it would lead to the same energy change.

The main AE will usually happen when the strain passes the yield point. The yield point is characterized by the nucleation of a complex domain pattern, which consists of needle domains, spanning domain boundaries, and kinks inside domain boundaries. The yield event is sometimes visible in AE experiments and constitutes the "big bang" in ferroelastic and martensitic materials. The phonon energy in the twinning case decays very rapidly because the excess potential energy is transferred to the twin boundary energy, while no such twin boundaries exist in the de-twinning case, so that the kinetic energy leads to the ringing of the sample. AE under stress is composed of several events, which constitute the fine structure of the signal. They occur under strain increase (twinning) and strain release (de-twinning). The total avalanche energy is an extensive quantity for large samples. In the simulations shown in Figs. 7.3 and 7.4, a very small avalanche releases some 3.7 meV/atom, which is already a significant energy for AE. Most of this energy is consumed by lattice distortions and surface energies of the nucleating twin boundaries. Only a small part leads to increased vibrational amplitudes (ringing of the sample). Avalanches of this kind are the same as those generated during phase transformations and have been observed experimentally. Other events are part of such avalanches, both during twinning and de-twinning and constitute a fine structure of the AE signal which has so far eluded experimental observation.

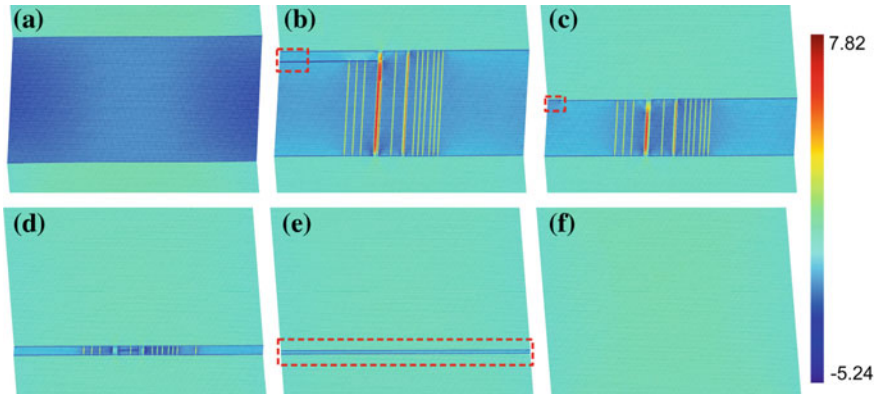

Fig. 7.4 Pattern evolution during shear deformation. Patterns shown in (**a**)–(**f**) correspond to the *blue dots* in Fig. 7.3 with the full time scale t_1–t_6, where t_1 is the time when the upper yield point is passed. The microstructure is shown before yield in (**a**) and after yield in (**b**). At time t_3, kinks move towards the surface (**c**). At times t_4–t_5, secondary patterns form (**d**), (**e**), while at t_6 (**f**), the single domain state is reestablished. The color scheme relates to the total shear angle between adjacent atoms. This angle is defined as $\theta = |\theta_{ver}| - 4 + \theta_{hor}$. θ_{ver} and θ_{hor} denote the local shear angle in the vertical direction and horizontal direction, respectively, and are calculated over three neighboring atoms

The energy release for kinks, vertical needles, and horizontal (spanning) domains is much smaller than the yield energy. This means that the energy of the pattern formation at the yield point corresponds to typically more than 10 elementary events such as needle formations or kink propagations. Only very high resolution spectra would allow the observation of time resolved sub-jerks. Ringing during de-twinning, when energy is transferred into vibrational energy, will be dampened in real systems by internal friction. We did not consider friction in our simulations because damping times are generally longer than our run times. We always find heat spikes near the collapse point. These heat spikes have similar energies as those in AE signals, which are determined by the longitudinal displacements of the surface atoms. These displacements are up to 1.8 Å for the major yield event, 0.7 Å for the collapse of the horizontal needle, 0.15 Å for the kink crashing into the surface, and 0.0014 A for the collapsing vertical needle. The equivalent energy releases are 3.7, 0.56, 0.017, and 0.017 meV/atom, respectively. We expect that AE can observe energies larger than 0.5 meV/atom so that the yield event and large needle domain nucleation and growth events can be observed while all other events may remain undetectable in AE.

7.4 Avalanche Exponents for Ferroelastics

The results of atomistic simulations show that the avalanches over the full strain regime at low temperatures follow power law statistics and become Vogel Fulcher

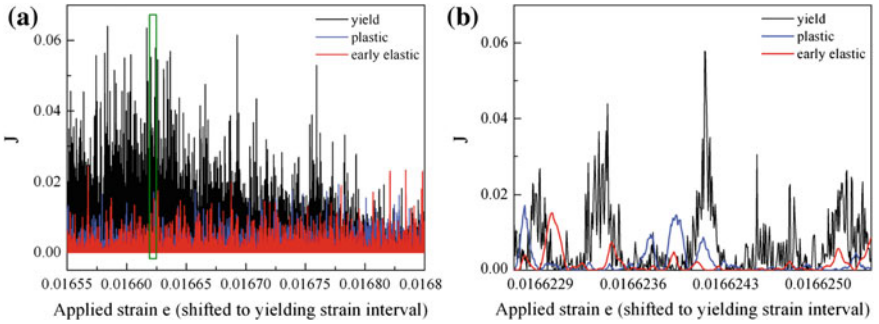

Fig. 7.5 The jerk spectra of three microstructural regimes at 10 K (**a**). **b** shows the expanded green rectangle region in (**a**), depicting the jerky energy signal profiles during yield events, while relatively smooth profiles occur in the early elastic and plastic regimes

distributed at higher temperatures [34–36]. Separating the Probability Distributions Functions, PDFs, of the strains in the yield regime and the plastic regime reveals a more complex pattern, however. The power law statistics of the yield regime is only weakly temperature dependent and shows energy exponents ε in the range between 1.3 and 2.3 for most ferroelastics and/or martensitic twinning. The value 1.3 coincides with the expected mean field value [92]. Avalanches in the plastic regime follow Vogel Fulcher statistics even for relatively low temperatures [139]. The overall behaviour is then determined by the mixture between the behaviours in the yield regime (large amplitudes at low temperatures) and the plastic regime (small amplitudes and low temperatures). In Fig. 7.5, we compare the jerks in the elastic, the yield, and the plastic regime. Figure 7.5a shows that the amplitudes of jerks are highest in the yield regime (black). Weak jerks are found in the elastic and plastic regime, where virtually all excitations are strongly temperature dependent. A surprising difference between the yield regime and the other regimes is that the individual jerks are smooth functions of the applied strain outside the yield regime. During yield, all the jerks are rugged with fine structures inside each event. This observation places emphasis on the scale invariance of jerks during yield: jerks represent avalanches, whereby each avalanche contains sub-avalanches that follow each other without the main avalanche coming to rest (Fig. 7.5b). This effect is even more obvious in the case of low-temperature avalanches in the yield regime. In Fig. 7.7, we show that the jerk distribution at low temperatures (0.5 and 1K) has a clear onset for small strains and remains active for very large strain intervals.

Collective jerks also occur in the elastic regime, which contains the low-temperature strain-tweed dynamics. The jerks become smooth and uncorrelated at higher temperatures, when the elastic regime is dominated by both tweed dynamics and some front propagation of the twin boundaries. Such individual, uncorrelated jerks dominate at high temperatures at all conditions outside the yield regime. The integrated distributions for the given regimes are summarized in Fig. 7.6. Jerks related to extended avalanches are approximately power-law distributed, with an

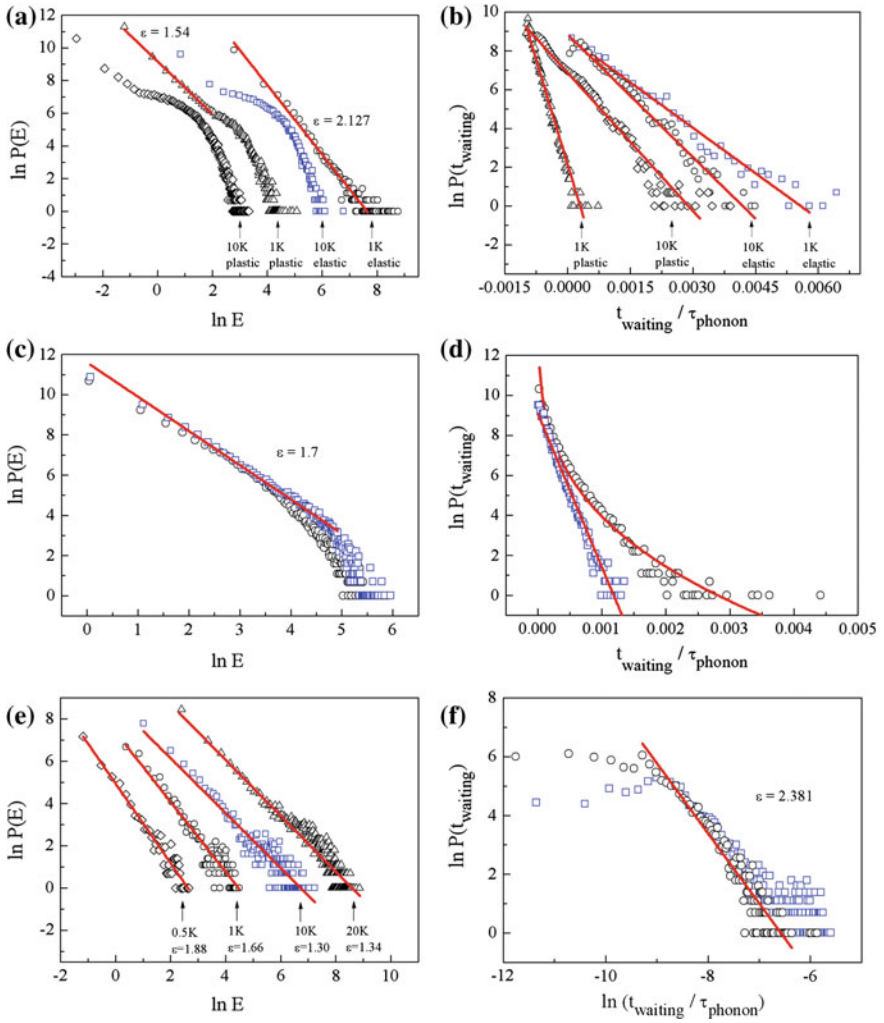

Fig. 7.6 The probability distribution of the jerk energy P(E) and waiting time $P(t_{waiting})$ in four regimes at 1 and 10 K. The black open circles and blue open squares represent 1 K and 10 K data, respectively. **a** Power-law–Vogel–Fulcher transitions of P(E) are shown in the elastic and plastic regimes. Their waiting times are exponentially distributed (**b**). **e** The P(E) in the yield regimes follows approximately a power-law distribution, and the data at 0.5 and 20 K show the variations in the power-law exponent. **f** The waiting times are also power-law distributed, with an exponent around 2.4. **c** The distributions of P(E) in the elastic regime just before the yield point are power law, while their waiting times show transitions from exponential to stretched exponential under cooling (**d**)

energy exponent $\varepsilon = 1.30$ at T = 10 K and $\varepsilon = 1.7$ at T = 1 K. The waiting time correlation follows a power law with an exponent of 2.0 at 1 K and a larger exponent at 10K. The yield behaviour is hence essentially athermal and scale-invariant,

but shows different inter-jerk correlations with power-law distributed waiting times between jerks [93]. Increasing the temperature from 1 to 10 K does not fundamentally change the avalanche mechanism (although the energy exponent changes slightly in the simulations). The main difference is that the large avalanche at 1 K is broken up at 10 K into smaller segments. The increase in the energy exponent at higher temperatures appears empirically to be related to this breakup. The waiting time distributions show strong correlations between the individual jerks, similar to the results for the collapse of porous materials and earthquakes [93]. The exponent of the waiting time power-law distribution is 2.4. The effect of temperature is much stronger outside the yield regime than in the yield regime. Thermal excitations, and hence the appearance of an energy scale, are very pronounced in the elastic and the plastic regimes, where we find that exponential distributions apply for jerks and for the waiting times between jerks. The only power-law distribution occurs just before the yield regime with a characteristically larger energy exponent and a strong exponential tail at high energies. At low temperatures, we find power-law distributions for jerks in all regimes besides the near-yield regime, where stretched exponentials characterize the crossover between the power law and the exponential regime.

Computer simulations hence confirm the earlier discovery of a temperature-generated crossover between thermal and athermal regimes [34, 95]. The origin of the crossover is related to the strain regimes outside the yield regime. These elastic and plastic regimes are thermally activated at high temperatures, while such activations are frozen out at sufficiently low temperatures. The spectra of the jerks show quasi-continuous profiles for each jerk, which relates to the continuous movement of kinks and needle domains under the applied strain field. These movements are thermally activated at sufficiently high temperatures. At low temperatures, we find that domain boundary freezing is in close agreement with the experimental observations [140, 141]. The Vogel Fulcher temperature is similar to that observed during a domain freezing process. Domain freezing is much less important during yield events with energies much larger than the thermal energy. Domain nucleation during yield is scale-invariant and not thermally activated.

Jerks during yield constitute geometrically one big avalanche at very low temperatures, while all the other events are jerks with very weak correlations. It is therefore crucial to distinguish between jerks related to avalanches during the yield events and other jerks, which can be thermally induced and do not lead to extended avalanches or power law PDFs. The jerk profiles can be used to identify the two types of jerks. Averaged jerk profiles were defined by summing over the interpolated profiles where the number of data points per jerk varies dramatically. The normalized profiles for the various regimes and temperatures are shown in Figs. 7.7 and 7.8. Subtle changes in the profiles show parabolic distributions in the yield regime (large-scale avalanches), while Gaussian distributions occur for cases where the excitation is mainly related to phonons in the plastic regime. In addition, AE signals in the yield regime show - at least in computer simulations – a fine structure of ‘jerks during jerks’ while the AE signals in the other regimes are much smoother.

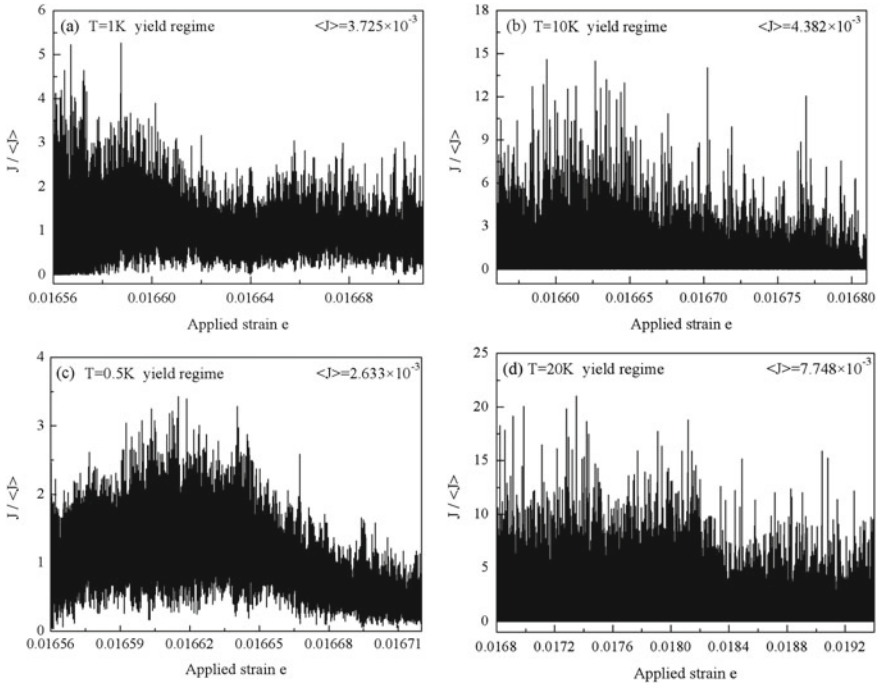

Fig. 7.7 Jerk distributions for yield regimes at four different temperatures. All the low-temperature distributions (**a**), **c** show the onset of avalanches and their continuation over an extended strain interval. These represent large-scale avalanches, while the thermal activations at 10 and 20 K (**b**), **d** show the collapse of jerks to zero energy between events. The 'avalanches' exist only over very small strain intervals and represent the advance of individual needle domains rather than collective avalanches, which are composed of large numbers of needle domains [135]

7.5 Conclusion

In the quest for domain boundary engineering, multiferroic domain patterns are designed to be the functional part of the material: the domain wall is the device. In this chapter we discussed how the characterization of domain patterns may be based on their dynamic behavior. Nucleation and growth of twin boundaries, as example, generate power law statistics at low temperatures. Glassy Vogel Fulcher statistics dominates at higher temperatures when thermal excitations become important. The emphasis was on the ferroelastic nature of the domain pattern.

The next step in research needs to incorporate effects like polarity and ferroelectricity into the patterns. A first attempt was made in [142] where nonconventional ferroelectric switching was shown to originate from a highly non-linear interaction between pattern-related dipoles and bulk dipoles. Typical antiferroelectric hysteresis loops were predicted despite the observation that neither the bulk not the walls were

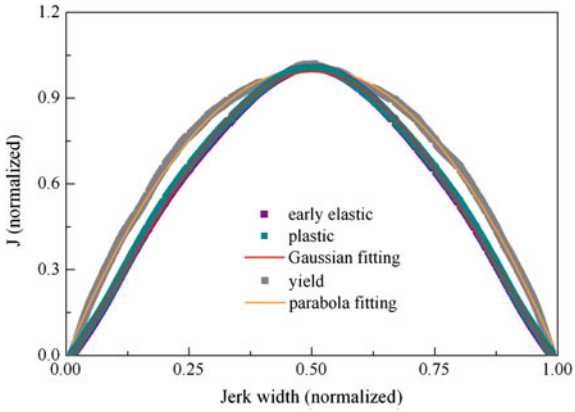

Fig. 7.8 The statistical jerk profiles in the early elastic, yield and plastic regimes. All the individual jerks are normalized in width, and the integration over all jerks results in the statistical jerk pro- files shown in this figure. The normalized statistical jerk profiles in the early elastic and plastic regimes show Gaussian distributions, while the jerk profiles in the yield regime are parabolic

antiferroelectric. Similar effects are expected in magnetic materials and, on an even smaller length scale, in ferroelectric Bloch wall states [22].

References

1. E.K.H. Salje, Multiferroic domain boundaries as active memory devices: trajectories towards domain boundary engineering. Chemphyschem **11**, 940–950 (2010)
2. E.K.H. Salje, H. Zhang, Domain boundary engineering. Ph. Transiti. **82**, 452–469 (2009)
3. J. Seidel, L.W. Martin, Q. He et al., Conduction at domain walls in oxide multiferr-oics. Nat. Mater. **8**, 229–234 (2009)
4. G. Catalan, J. Seidel, R. Ramesh et al., Domain wall nanoelectronics. Rev. Mod. Phys. **84**, 119–156 (2012)
5. A. Schilling, D. Byrne, G. Catalan et al., Domains in ferroelectric nanodots. Nano Lett. **9**, 3359–3364 (2009)
6. S. Farokhipoor, B. Noheda, Conduction through 71 degrees Domain Walls in$BiFeO_3$ Thin Films. Phys. Rev. Lett. **107**, 127601 (2011)
7. G. Catalan, A. Janssens, G. Rispens et al., Polar domains in lead titanate films under tensile strain. Phys. Rev. Lett. **96**, 127602 (2006)
8. D.D. Viehland, E.K.H. Salje, Domain boundary-dominated systems: adap-tive structures and functional twin boundaries. Adv. Phys. **63**, 267–326 (2014)
9. D.W. Wang, E.K.H. Salje, S.B. Mi et al., Multidomains made of different structural phases in multiferroic $BiFeO_3$: A first-principles-based study. Phys. Rev. B **8**, 134107 (2013)
10. J.F. Scott, E.K.H. Salje, M.A. Carpenter, Domain Wall damping and elastic softening in $SrTiO_3$: evidence for polar twin walls. Phys. Rev. Lett. **109**, 187601 (2012)
11. M.A. Carpenter, E.K.H. Salje, C.J. Howard, Magnetoelastic coupling and multiferroic fer-roelastic/magnetic phase transitions in the perovskite $KMnF_3$. Phys. Rev. B **85**, 224430 (2012)
12. E.K.H. Salje, D.J. Safarik, K.A. Modic et al., Tin telluride: a weakly co-elastic metal. Phys. Rev. B **82**, 184112 (2010)
13. J. Seidel, P. Maksymovych, Y. Batra et al., Domain wall conductivity in la-doped $BiFeO_3$. Phys. Rev. Lett. **105**, 197603 (2010)
14. R.J. Harrison, E.K.H. Salje, The noise of the needle: avalanches of a single progressing needle domain in $LaAlO_3$. Appl. Phys. Lett. **97**, 021907 (2010)

15. A. Aird, E.K.H. Salje, Sheet superconductivity in twin walls: experimental evidence of WO_{3-x}. J. Phys. Condens. Matter **10**, L377–L380 (1998)
16. A. Aird, E.K.H. Salje, Enhanced reactivity of domain walls in WO_3 with sodium. Eur. Phys. J. B **15**, 205–210 (2000)
17. S.V. Aert, S. Turner, R. Delville et al., Direct observation of ferrielectricity at ferroelastic domain boundaries in $CaTiO_3$ by electron micro-scopy. Adv. Mater. **24**, 523 (2012)
18. T. Zykova-Timan, E.K.H. Salje, Highly mobile vortex structures inside polar twin boundaries in $SrTiO_3$. Appl. Phys. Lett. **104**, 082907 (2014)
19. H. Yokota, H. Usami, R. Haumont et al., Direct evidence of polar nature of ferroelastic twin boundaries in $CaTiO_3$ obtained by second harmonic generationmicroscope. Phys. Rev. B **89**, 144109 (2014)
20. L. Goncalves-Ferreira, S.A.T. Redfern, E. Artacho et al., Ferrielectric twin walls in $CaTiO_3$. Phys. Rev. Lett. **101**, 097602 (2008)
21. E.K.H. Salje, O. Aktas, M.A. Carpenter et al., Domains within domains and walls within walls: evidence for polar domains in cryogenic $SrTiO_3$. Phys. Rev. Lett. **111**, 247603 (2013)
22. E.K.H. Salje, J.F. Scott, Ferroelectric Bloch-line switching: a paradigm for memory devices. Appl. Phys. Lett. **105**, 252904 (2014)
23. J.P. Ansermet, Perpendicular transport of spin-polarized electrons through magnetic nanostructures. J. Phys. Condens. Matter **10**, 6027–6050 (1998)
24. V.T. Zaspalis, V. Tsakaloudi, M. Kolenbrander, The effect of dopants on the incremental permeability of MnZn-ferrites. J. Mag. Mag. Mater. **313**, 29–36 (2007)
25. W. Koshibae, Y. Kaneko, J. Iwasaki et al., Memory functions of magnetic skyrmions. Jpn. J. Appl. Phys. **54**, 53001–53001 (2015)
26. I. Purnama, I.S. Kerk, G.J. Lim et al., Coupled Neel domain wall motion insandwiched perpendicular magnetic anisotropy nanowires. Sci. Rep. **5**, 8754 (2015)
27. J. Wang, L.S. Xie, C.S. Wang et al., Magnetic domain-wall motion twisted by nanoscale probe-induced spin transfer. Phys. Rev. B **90**, 224407 (2014)
28. W.L. Lim, R.H. Liu, T. Tyliszczak et al., Fast chirality reversal of the magnetic vortex by electric current. Appl. Phys. Lett. **105**, 222405 (2014)
29. M. Yamanouchi, D. Chiba, F. Matsukura et al., Current-induced domain-wall switching in a ferromagnetic semiconductor structure. Nature **428**, 539–542 (2004)
30. M.I. Mihai, T. Moore, H. Szambolics et al., Fast current-induced domain-wall motion controlled by the Rashba effect. Nat. Mater. **10**, 419–423 (2011)
31. J. Chrosch, E.K.H. Salje, Near-surface domain structures in uniaxially stressed $SrTiO_3$. J. Phys. Condens. Matter **10**, 2817–2827 (1998)
32. E.K.H. Salje, B. Wruck, Order parameter saturation at low temperatures- numerical results for displacive and O/D systems. Ferroelectrics **124**, 185–188 (1991)
33. S. Li, X. Ding, J. Ren et al., Strain-controlled thermal conductivity in ferroic twinned films. Sci. Rep. **4**, 6375 (2014)
34. E.K.H. Salje, X. Ding, Z. Zhao et al., Thermally activated avalanches: Jammingand the progression of needle domains. Phys. Rev. B **83**, 104109 (2011)
35. X. Ding, Z. Zhao, T. Lookman et al., High junction and twin boundary densities in driven dynamical systems. Adv. Mater. **24**, 5385–5389 (2012)
36. E.K.H. Salje, X. Ding, Z. Zhao et al., How to generate high twin densities in nano-ferroics: thermal quench and low temperature shear. Appl. Phys. Lett. **100**, 222905 (2012)
37. E.K.H. Salje, X. Ding, O. Aktas, Domain glass. Phys. Status Solidi B **251**, 2061 (2014)
38. E.K.H. Salje, M.A. Carpenter, Phys. Status Solidi in press, (2015)
39. L. Cross, Springer series in materials science. Piezoelectricity **114**, 131–155 (2008)
40. J. Hemberger, P. Lunkenheimer, R. Fichtl et al., Loidl, Relaxor ferroelectricity and colossal magnetocapacitive coupling in ferromagnetic $CdCr_2S_4$. Nature **434**, 364 (2005)
41. W. Kleemann, The relaxor enigma-charge disorder and random fields in ferroelectrics. J. Mater. Sci. **41**, 129–136 (2006)
42. E. Dul'kin, E.K.H. Salje, O. Aktas et al., Ferroelectric precursor behavior ofhighly cation-ordered $PbSc_{0.5}Ta_{0.5}O_3$ detected by acoustic emission: Tweed andpolar nanoregions. Appl. Phys. Lett **105**, 212901 (2014)

43. E.K.H. Salje, E. Dul'kin, M. Roth, Appl. Phys. Lett **106**, 152903 (2015)
44. P. Lloveras, T. Castán, A. Planes, A. Saxena, Disorder and strain-induced complexity in functional materials. Springer Ser. Mater. Sci. **148**, 227–247 (2012)
45. B. Dkhil, P. Gemeiner, A. Al-Barakaty, L. Bellaiche, E. Dul'kin, E. Mojaev, M. Roth, Intermediate temperature scale T* in lead-based relaxor systems. Phys. Rev. B **80**, 064103 (2009)
46. M. Pasciak, T.R. Welberry, J. Kulda, M. Kempa, J. Hlinka, Polar nanoregions and diffuse scattering in the relaxor ferroelectric $PbMg_{1/3}Nb_{2/3}O_3$. Phys. Rev. B **85**, 224109 (2012)
47. J. Hlinka, Do we need the ether of polar nanoregions. J. Adv. Dielectr. **02**, 1241006 (2012)
48. E.K.H. Salje, M.A. Carpenter, G.F. Nataf et al., Elastic excitations in $BaTiO_3$ single crystals and ceramics: mobile domain boundaries and polar nanoregions observed by resonant ultrasonic spectroscopy. Phys. Rev. B **87**, 014106 (2013)
49. B.P. Burton, E. Cockayne, U.V. Waghmare, Correlations between nanoscale chemical and polar order in relaxor ferroelectrics and the lengthscale for polar nanoregions. Phys. Rev. B **72**, 064113 (2005)
50. W.W. Schmahl, A. Putnis, E.K.H. Salje, P. Freeman, A. Graeme-Barber et al., Twin formation and structural modulations in orthorhombic and tetragonal $YBa_2(Cu_{1-x}Co_x)_3O_{7-\delta}$. Philos. Mag. Lett. **60**, 241 (1989)
51. K.Z. Baba-Kishi, M. Pasciak, An electron diffraction and Monte Carlo simulation study of an incommensurate antiferroelectric state in the relaxor ferroelectric Pb_2ScTaO_6. J. Appl. Crystallogr. **43**, 140–150 (2010)
52. A.M. Bratkovsky, S.C. Marais, V. Heine, E.K.H. Salje, The theory of fluctuations and texture embryos in structural phase transitions mediated by strain. J. Phys. Condens. Matter **6**, 3679 (1994)
53. K. Parlinski, V. Heine, E.K.H. Salje, Origin of tweed texture in the simulation of a cuprate superconductor. J. Phys. Condens. Matter **5**, 497 (1993)
54. E.K.H. Salje, Hard mode spectroscopy: experimental studies of structural phase transitions. Ph. Transit. **37**, 83–110 (1992)
55. E.K.H. Salje, U. Bismayer, Hard mode spectroscopy: the concept and applications. Ph. Transit. **63**, 1–75 (1997)
56. E.K.H. Salje, A. Ridgwell, B. Guttler et al., On the displacive character of the phase transition in quartz: a hard-mode spectroscopy study. J. Phys.: Condens. Matter **4**, 571–577 (1992)
57. Venkatraman Gopalan, V. Dierolf, D.A. Scrymgeour, Defect-domain wall interactions in trigonal ferroelectrics. Ann. Rev. Mater. Res. **37**, 449–489 (2007)
58. G. Blumberg, M.V. Klein, S.W. Cheong, Charge and spin dynamics of an ordered stripe phase in La12/3Sr1/3NiO4 investigated by Raman spectroscopy. Phys. Rev. Lett. **80**, 564–567 (1998)
59. M.T. Dove, T. Cool, D.C. Palmer, A. Putnis, On the role of AI-Si ordering in the cubic-tetragonal phase transition in leucite. Am. Miner. **78**, 486–492 (1993)
60. E.K.H. Salje, V. Devarajan, U. Bismayer, Phase transitions in $Pb_3(P_1\text{-}xAsxO_4)_2$: influence of the central peak and flip mode on the Raman scattering of hard modes. J. Phys. C: Solid State Phys. **6**, 5233–5243 (1983)
61. E.K.H. Salje, B. Wruck, Specific-heat measurements and critical exponents of the ferroelastic phase transition in $Pb_3(PO_4)_2$ and $Pb_3(P_{1-x}As_xO_4)_2$. Phys. Rev. B **28**, 6510–6518 (1983)
62. U. Bismayer, E.K.H. Salje, Ferroelastic phases in $Pb_3(PO_4)_2$-$Pb_3(AsO_4)_2$- X-ray and optical experiments. Acta Crystallogr. Sect. A **37**, 145–153 (1981)
63. E.K.H. Salje, A. Graeme-Barber, M.A. Carpenter et al., Lattice parameters, spontaneous strain and phase transitions in $Pb_3(PO_4)_2$. Acta Crystallogr. Sect. B: Struct. Sci. **49**, 387–392 (1993)
64. B. Wruck, E.K.H. Salje, M. Zhang et al., On the thickness of ferroelastic twin walls in lead phosphate $Pb_3(PO_4)_2$ an X-ray diffraction study. Ph. Transit. **48**, 135–148 (1994)
65. M. Zhang, E.K.H. Salje, U. Bismayer et al., Phase transition (s) in titanite $CaTiSiO_5$: an infrared spectroscopic, dielectric response and heat capacity study. Phys. Chem. Miner. **22**, 41–49 (1995)
66. E.K.H. Salje, C. Schmidt, U. Bismayer, Structural phase transition in titanite, CaTiSiO5: a ramanspectroscopic study. Phys. Chem. Miner. **19**, 502–506 (1993)

67. D.C. Palmer, E.K.H. Salje, W.W. Schmahl, Phase transitions in leucite: X-ray diffraction studies. Phys. Chem. Miner. **16**, 714–719 (1989)
68. E.K.H. Salje, R. Gehlig, K. Viswanathan, Structural phase transition in mixed crystals W_xMo_{1-x} O_3. J. Solid State Chem. **25**, 239–250 (1978)
69. O. Aktas, M.A. Carpenter, E.K.H. Salje, Polar precursor ordering in BaTiO3 detected by resonant piezoelectric spectroscopy. Appl. Phys. Lett. **103**, 142902 (2013)
70. O. Aktas, E.K.H. Salje, M.A. Carpenter, Resonant ultrasonic spectroscopy and resonant piezoelectric spectroscopy in ferroelastic lead phosphate, $Pb_3(PO_4)_2$. J. Phys. Condens. Matter **25**, 465401 (2013)
71. E.K.H. Salje, O. Aktas, M.A. Carpenter et al., Domains within domains and walls within walls: evidence for polar domains in cryogenic $SrTiO_3$. Phys. Rev. Lett. **111**, 247603 (2013)
72. O. Aktas, E.K.H. Salje, S. Crossley et al., Ferroelectric precursor behavior in $PbSc_{0.5}Ta_{0.5}O_3$ detected by field-induced resonant piezoelectric spectroscopy. Phys. Rev. B **88**, 174112 (2013)
73. N. Setter, D. Damjanovic, L. Eng et al., Ferroelectric thin films: review of materials, properties, and applications. J. Appl. Phys. **100**, 051606 (2006)
74. D. Damjanovic, Stress and frequency dependence of the direct piezoelectric effect in ferroelectric ceramics. J. Appl. Phys. **82**, 1788–1797 (1997)
75. D. Damjanovic, M. Demartin, Contribution of the irreversible displacement of domain walls to the piezoelectric effect in barium titanate and lead zirconate titanate ceramics. J. Phys. Condens. Matter **9**, 4943–4953 (1997)
76. T. Rojac, H. Ursic, A. Bencan et al., Mobile domain walls as a bridge between nanoscale conductivity and macroscopic electromechanical response. Adv. Funct. Mater. **25**, 2099–2108 (2015)
77. A. Biancoli, C.M. Fancher, J.L. Jones et al., Breaking of macroscopic centric symmetry in paraelectric phases of ferroelectric materials and implications for flexoelectricity. Nat. Mater. **14**, 224–229 (2015)
78. T. Rojac, A. Bencan, G. Drazic et al., Piezoelectric nonlinearity and frequency dispersion of the direct piezoelectric response of BiFeO3 ceramics. J. Appl. Phys. **112**, 064114 (2012)
79. R. Ahluwalia, A.K. Tagantsev, P. Yudin et al., Influence of flexoelectric coupling on domain patterns in ferroelectrics. Phys. Rev. B **89**, 174105 (2014)
80. T. Sluka, A.K. Tagantsev, D. Damjanovic, Enhanced electromechanical response of ferroelectrics due to charged domain walls. Nat. Commun. **3**, 748 (2012)
81. D. Navas, C. Redondo, G.A.B. Confalonieri et al., Domain-wall structure in thin films with perpendicular anisotropy: magnetic force microscopy and polarized neutron reflectometry study. Phys. Rev. B **90**, 054425 (2014)
82. J.S. Lee, A. Richardella, D.W. Rench et al., Ferromagnetism and spin-dependent transport in n-type Mn-doped bismuth telluride thin films. Phys. Rev. B **89**, 174425 (2014)
83. J. Seidel, R. Ramesh, Nanoscale Characterization of Multiferroic Materials. Mesoscopic Phenomena in Multifunctional Materials: Synthesis, Characterization, Modeling and Applications. Book Series: Springer Series in. Mater. Sci. **198**, 1–21 (2014)
84. M.T. Rekveldt, W.H. Kraan, Single domain wall chirality studies using polarised neutrons. J. Mag. Mag. Mater. **329**, 105–117 (2013)
85. P. Thibaudeau, F. Ott, A. Thiaville et al., Probing magnetic domain wall profiles by neutron spin precession. EPL **93**, 37003 (2011)
86. J.M. Tranquada, J.D. Axe, N. Ichikawa et al., Neutron-scattering study of stripe-phase order of holes and spins in $La_{1.48}Nd_{0.4}Sr_{0.12}CuO_4$. Phys. Rev. B **54**, 7489–7499 (1996)
87. J.F. Loffler, H.B. Braun, W. Wagner, Magnetic correlations in nanostructured ferromagnets. Phys. Rev. Lett. **85**, 1990–1993 (2000)
88. J. Chrosch, E.K.H. Salje, Temperature dependence of the domain wall width in $LaAlO_3$. J. Appl. Phys. **85**, 722–727 (1999)
89. S.R. Andrews, R.A. Cowley, X-ray scattering from critical fluctuations and domain walls in KDP and DKDP. J. Phys. C: Solid State Phys. **19**, 615–635 (1986)
90. E.K.H. Salje, Ferroelastic materials. Ann. Rev. Mater. Res. **42**, 65–283 (2012)
91. J.P. Sethna, K.A. Dahmen, C.R. Myers, Crackling noise. Nature **410**, 242 (2001)

92. E.K.H. Salje, K.A. Dahmen, Crackling noise in disordered materials. Ann. Rev. Condensed Matter Phys. **5**, 233 (2014)
93. J. Baro, A. Corral, X. Illa, A. Planes, E.K.H. Salje, W. Schranz, D.E. Soto-Parra, Statistical similarity between the compression of a porous material and earthquakes. Phys. Rev. Lett. **110**, 088702 (2013)
94. Z. Zhao, X. Ding, T. Lookman, J. Sun, E.K.H. Salje, Mechanical loss in multiferroic materials at high frequencies: friction and the evolution of ferroelastic microstructures. Adv. Mater. **25**, 3244 (2013)
95. X. Ding, T. Lookman, Z. Zhao, E.K.H. Salje, Dynamically strained ferroelastics: statistical behavior in elastic and plastic regimes. Phys. Rev. B **87**, 094109 (2013)
96. M.C. Gallardo, J. Manchado, J.J. Romero, J. del Cerro, E.K.H. Salje, A. Planes, E. Vives, M. Stipcich, Avalanche criticality in the martensitic transition of $Cu_{67.64}Zn_{16.71}Al_{15.65}$ shape-memory alloy: A calorimetric and acoustic emission study. Phys. Rev. B **81**, 174102 (2010)
97. Y. Zhang, T.T. Zuo, Z. Tang, M.C. Gao et al., K.A. Dahmen, P.K. Liaw, Microstructures and properties of high-entropy alloys. Prog. Math. Sci. **61**, 1 (2014)
98. K.S. Ryu, H. Akinaga, S.C. Shin, Tunable scaling behaviour observed in Barkhausen criticality of a ferromagnetic film. Nat. Phys. **3**, 547 (2007)
99. F. Colaiori, Exactly solvable model of avalanches dynamics for Barkhausen crackling noise. Adv. Phys. **57**, 287 (2008)
100. T. Castán, A. Saxena, A. Planes, in *Mesoscopic Phenomena in Multifunctional Materials*, ed. by A. Saxena, A. Planes (Springer, Berlin, 2014)
101. E. Vives, J. Ortín, L. Mañosa, I. Ràfols, R. Pérez-Magrane, A. Planes, Distributions of avalanches in martensitic transformations. Phys. Rev. Lett. **72**, 1694 (1994)
102. J. Baró, S. Dixon, R.S. Edwards, Y. Fan, D.S. Keeble, L. Mañosa, A. Planes, E. Vives, Simultaneous detection of acoustic emission and Barkhausen noise during the martensitic transition of a Ni-Mn-Ga magnetic shape-memory alloy. Phys. Rev. B **88**, 174108 (2013)
103. E.K.H. Salje, J. Koppensteiner, M. Reinecker, W. Schranz, A. Planes, Jerky elasticity: avalanches and the martensitic transition in $Cu_{74.08}A_{l23.13}Be_{2.79}$ shape-memory alloy. Appl. Phys. Lett. **95**, 231908 (2009)
104. Z. Balogh, L. Daroczi, L. Harasztosi, D.L. Beke, T.A. Lograsso, D.L. Schlagel, Magnetic emission during austenite-martensite transformation in Ni_2MnGa shape memory alloy. Mater. Trans. **47**, 631–634 (2006)
105. L. Carrillo, J. Ortín, Avalanches in the growth of stress-induced martensites. Phys. Rev. B **56**, 11508 (1997)
106. S. Sreekala, R. Ahluwalia, G. Ananthakrishna, Precursors and power-law statistics of acoustic emission and shape memory effect in martensites. Phys. Rev. B **70**, 224105 (2004)
107. E. Vives, D. Soto-Parra, L. Mañosa, R. Romero, A. Planes, Imaging the dynamics of martensitic transitions using acoustic emission. Phys. Rev. B **84**, 060101 (2011)
108. R. Harrison, E.K.H. Salje, The noise of the needle: avalanches of a single progressing needle domain in $LaAlO_3$. Appl. Phys. Lett. **97**, 021907 (2010)
109. R. Niemann, J. Kopeček, O. Heczko, J. Romberg, L. Schultz, S. Fähler, E. Vives, L. Mañosa, A. Planes, Localizing sources of acoustic emission during the martensitic transformation. Phys. Rev. B **89**, 214118 (2014)
110. J. Baro, J.M. Martin-Olalla, F. Javier Romero, M.C. Gallardo, E.K.H. Salje, E. Vives, A. Planes, Avalanche correlations in the martensitic transition of a Cu-Zn-Al shape memory alloy: analysis of acoustic emission and calorimetry. J. Phys. Condens. Matter **26**, 125401 (2014)
111. G.B. Stephenson, K.R. Elder, Ferromagneticlike closure domains in ferroelectric ultrathin films: first-principles simulations. Appl. Phys. Lett. **100**, 051601 (2006)
112. P.V. Yudin, A.K. Tagantsev, N. Setter, Bistability of ferroelectric domain walls: Morphotropic boundary and strain effects. Phys. Rev. B **88**, 024102 (2013)
113. Y. Ishibashi, E.K.H. Salje, A theory of ferroelectric 90 degree domain wall. J. Phys. Soc. Jpn. **11**, 2800–2803 (2002)

114. V. Gopalan, T.E. Mitchell, Large-angle electro-optic laser scanner on $LiTaO_3$ fabricated by in situ monitoring of ferroelectric-domain micropatterning. J. Appl. Phys. **83**, 941–954 (1994)
115. E.K.H. Salje, E. Dul'kin, M. Roth, Acoustic emission during the ferroelectric transition Pm(3)over-barm to P4mm in $BaTiO_3$ and the ferroelastic transition R(3)over-barm-C2/c in $Pb_3(PO_4)_2$. Appl. Phys. **106**, 152903 (2015)
116. E. Dul'kin, E.K.H. Salje, O. Aktas, Ferroelectric precursor behavior of highly cation-ordered $PbSc_{0.5}Ta_{0.5}O_3$ detected by acoustic emission: Tweed and polar nanoregions. Appl. Phys. Lett. **105**, 212901 (2014)
117. J. Antonaglia, X. Xie, G. Schwarz, Tuned critical avalanche scaling in bulk metallic glasses. Sci. Rep. **4**, 4382 (2014)
118. J. Antonaglia, X. Xie, Z. Tang, Temperature effects on deformation and serration behavior of high-entropy alloys (HEAs). JOM **66**, 2002–2008 (2014)
119. J. Antonaglia, W.J. Wendelin, X. Gu, R.R. Byer, Bulk metallic glasses deform via slip avalanches. Phys. Rev. Lett. **112**, 155501 (2014)
120. J. Weiss, W.B. Rhouma, T. Richeton, From mild to wild fluctuations in crystal plasticity. Phys. Rev. Lett. **114**, 105504 (2015)
121. M.C. Miguel, A. Vespignani, S. Zapperi, J. Weiss, Intermittent dislocation flow in viscoplastic deformation. Nature **410**, 667–671 (2001)
122. J. Weiss, D. Marsan, Three-dimensional mapping of dislocation avalanches: clustering and space/time coupling. Science **299**, 89–92 (2003)
123. J. Weiss, M.C. Miguel, Dislocation avalanche correlations. Mater. Sci. Eng. A. **387–389**, 292–296 (2004)
124. D. Rouby, P. Fleischman, C. Duvergier, Complexity in dislocation dynamics: experiments. Mag. B **47**, 671 (1983)
125. N. Kiesewetter, P. Schiller, The acoustic emission from moving dislocations in aluminium. Phys. Status Solidi (a) **38**, 569(1976)
126. D.R. James, S.H. Carpenter, Relationship between acoustic emission and dislocation kinetics in crystalline solids. J. Appl. Phys. **42**, 4685 (1971)
127. E.N.C. Andrade, On the viscous flow in metals, and allied phenomena. Proc. R. Soc. A **84**, 1 (1910)
128. R. Becker, E. Orowan, Advancing towards constitutive equations for the metal industry via the LEDS theory. Z. Phys. **79**, 566 (1932)
129. J. Weiss, T. Richeton, F. Louchet, F. Chmelik, P. Dobron, Evidence for universal intermittent crystal plasticity from acoustic emission and high-resolution extensometry experiments. Phys. Rev. B **76**, 224110 (2007)
130. G. Durin, S. Zapperi, Sci. Hysteresis: Phys. Model. Micromag. Magn. Dyn. **2**, 181 (2006)
131. H. Barkhausen, Zwei mit Hilfe der neuen Verstärker entdeckte Erscheinungen. Phys. Z. **20**, 401 (1919)
132. V. Hardy, S. Majumdar, S.J. Crowe, M.R. Lees, D.M.K. Paul, Field-induced magnetization steps in intermetallic compounds and manganese oxides: the martensitic scenario. Phys. Rev. B **69**, 020407(R) (2004)
133. W. Wu, P.W. Adams, Avalanches and slow relaxation: dynamics of ultrathin granular superconducting films in a parallel magnetic field. Phys. Rev. Lett. **74**, 610 (1995)
134. J.C. Lashley, K. Gofryk, B. Mihaila, J.L. Smith, E.K.H. Salje, Thermal avalanches near a Mott transition. J. Phys. Condens. Matter **26**, 035701 (2014)
135. M.P. Lilly, P.T. Finley, R.B. Hallock, Memory, congruence, and avalanche events in hysteretic capillary condensation. Phys. Rev. Lett. **71**, 4186 (1993)
136. D.H. Kim, S.B. Choe, S.C. Shin, Direct observation of Barkhausen avalanche in Co thin films. Phys. Rev. Lett. **90**, 087203 (2003)
137. D. Soto-Parra, X. Zhang, S. Cao, E. Vives, E.K.H. Salje, Avalanches in compressed Ti-Ni shape-memory porous alloys: an acoustic emission study PRE in press. Phys. Rev. E **91**, 060401(R) (2015)
138. E.K.H. Salje, X. Wang, X. Ding, Simulating acoustic emission: the noise of collapsing domains. Phys. Rev. B **90**, 064103 (2014)

139. Z. Zhao, X. Ding, J. Sun, Thermal and athermal crackling noise in ferroelastic nanostructures. J. Phys. Condens. Matter **26**, 142201 (2014)
140. A.V. Kityk, W. Schranz, P. Sondergeld, D. Havlik, Low-frequency superelasticity and nonlinear elastic behavior of SrTiO3 crystals. Phys. Rev. B **61**, 946–956 (1999)
141. R.J. Harrison, S.A.T. Redfern, E.K.H. Salje, Dynamical excitation and anelastic relaxation of ferroelastic domain walls in LaAlO3. Phys. Rev. B **69**, 144101 (2004)
142. E.K.H. Salje, S. Li, Z. Zhao, Polar twin boundaries and nonconventional ferroelectric switching. Appl. Phys. Lett. **106**, 12907 (2015)

Chapter 8
Avalanches and the Propagation and Retraction of Ferroelastic Needle Domains

R.J. Harrison and Ekhard K.H. Salje

Abstract Time-lapse optical microscopy of single crystal $LaAlO_3$ allows the propagation and retraction of individual needle domains to be observed under conditions of slowly varying shear stress. The propagation of a single ferroelastic needle domain consists of two parts: a continuous front propagation and jerky avalanches. Optical observation and themodynamic analysis show that the continuous behavior is thermally activated. The avalanches follow power law behavior with an energy exponent $\varepsilon = -1.8 \pm 0.2$ in agreement with self-similar avalanches close to the depinning threshold. Twin walls remain smooth during propagation, whereas the one-dimensional front line of the needle tip shows "wiggles" caused by interactions with defect fields. The front line becomes highly distorted during approach to, or retraction from, the sample surface. Singularities of the characteristic (∼Larkin) length occur when the front line breaks. Elastic forces produce planar twin walls with very large Larkin lengths, whereas the front line is not restrained by the compatibility energy and displays considerably shorter Larkin lengths.

8.1 Introduction

Avalanche statistics in granular and porous materials have been extensively investigated [1–3]. The collapse of porous media under uniaxial stress is a prime example for the self-similarity of avalanche dynamics, with six or more orders of magnitude of stresses yielding the same power law dependence of the acoustic emission during the collapse [4, 5]. The sizes of the collapsing cavities range from some nanometers to millimeters. While the acoustic emission, AE, of the collapse is easily measurable, it proved impossible to observe the actual geometrical collapse and other, related structural modifications using any of the currently available experimental methods. This limitation can be overcome when the movement of ferroelastic microstructures replaces the geometrical origin of the avalanche, namely the collapse of holes [6–10].

R.J. Harrison (✉) · E.K.H. Salje
Department of Earth Sciences, University of Cambridge, Downing Street, Cambridge CB2 3EQ, UK
e-mail: rjh40@esc.cam.ac.uk

E.K.H. Salje et al. (eds.), *Avalanches in Functional Materials and Geophysics*, Understanding Complex Systems, DOI 10.1007/978-3-319-45612-6_8

The advantage of this approach is that switching of ferroelastic microstructures is often limited to the movement of needle domains on a scale, that is easily observed optically [6]. Furthermore, the close connection of avalanche dynamics of ferroelastic movements under stress has been explored in much detail by computer simulation [11]. It has been shown that the prime candidate for emission of acoustic waves is the propagation and retraction of needle domains and that its dynamics is identical to that of hole collapses [12]. This means that we can investigate optically observable changes of ferroelastic microstructures under stress as a model case for a much wider class of crackling noises and self-similar avalanche dynamics by 'jerk' movements [6, 7].

8.2 Propogation of Ferroelastic Needle Twins

Careful investigations of the forced propagation of domain walls in ferroelastic materials have found that propagation happens by a superposition of ballistic movements and jerks [6, 8, 13–18]. These jerks are associated with pinning by extrinsic defects and can also be generated by mutual jamming of domain walls [19, 20]. Ferroelastic movements [21] play a special role amongst ferroic and multiferroic materials because most walls, such as ferroelectric 90° boundaries or magnetostrictive magnetic walls, have strong coupling to an elastic degree of freedom. Understanding the forced movement of ferroelastic walls, therefore, is essential for the analysis of a much wider class of walls [22, 23].

Microscopic observation shows that wall movement in the archetypal ferroelastic material $LaAlO_3$ occurs predominantly as propagation of needle domains. One single needle sufficed to produce noise signals $P(E) \sim E^{-\varepsilon}$ with characteristic energy exponents of $\varepsilon = 1.8$, as in the case of collective avalanches [1]. Such collective noise patterns could be rationalized if a multitude of defects pin a wall, leading to significant deformations of the wall profile on several length scales. This was not found, however. The twin walls at the shafts of the needles [24] remain smooth and no geometric indication of elastic interactions was observed (Fig. 8.1). The restoring forces, namely, the wall bending and compatibility energy, appear to exceed the pinning energies and ensure the shape invariance of the needle domain. It is sufficient, therefore, to analyse the behaviour of the front of the wedge-shaped domain. This front, FL, is a straight line under standard boundary conditions (cube shaped sample, no defects, weak shear forces); while under forcing in a sample with defects, this line meanders and moved locally with slightly different speeds (Fig. 8.1).

Harrison and Salje [7] observed the front line (FL) in an optical microscope under crossed polars. The sample is a 0.25 mm thick single crystal of $LaAlO_3$ cut parallel to the (001) faces of the pseudocubic unit cell. They observed a set of (101) needle twins, with walls oriented at 45° to the sample surface. Contrast is caused by the 90° rotation of the optical indicatrix inside the needle, which leads to a change in birefringence that is proportional to the projected thickness of the needle. The projected thickness becomes vanishingly small at the FL (Fig. 8.1) [25], resulting in a complete loss of

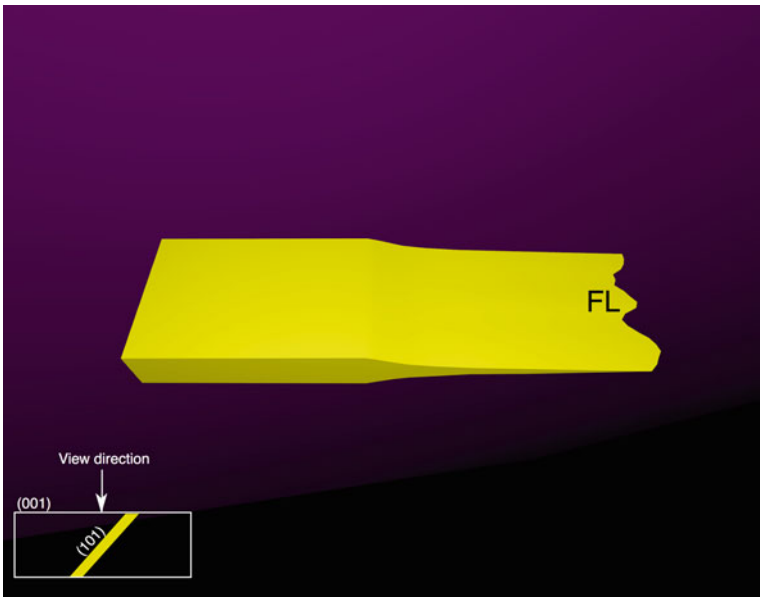

Fig. 8.1 The tip of a wedge-shaped needle domain, with the shaft at the left and the propagating front at the right. Note that the twin walls at the shaft and at the needle end are smooth, while only the FL "wiggles" as it adapts to the various defect fields. Inset shows view direction for the experimental setup

contrast ahead of the FL. The advancement and retraction of a single needle domain in the crystal are followed optically by time-lapse digital microscopy (interval of 60 s between each frame). The propagation of the FL in Fig. 8.2 shows characteristic behaviour in several frames: the initial sample (a) shows vertical twin walls along the elastically easy direction (see Fig. 8.2, enhanced online for time-lapse movie). An applied shear stress [6] leads to a retraction of the inner domain. The FL remains partly attached to the crystal surface (left hand side) and joins the main domain after some rough and wiggly stretch (b). A very small further movement of the domain leads to a thinning of the surface attached FL (c), and finally, the FL snaps and loosens from the surface (d). Without the surface attachment, the FL is short and appears to be relatively smooth. The following experiments were performed after the FL detached from the surface.

Under additional applied force, the FL first retracts to its equilibrium position, and then slowly creeps back towards the sample surface. The typical profiles in Fig. 8.3 show that the FL is first a collection of rather smooth segments (a), (b) which suddenly break at the left hand side when the FL is sufficiently stretched by the elastic driving force (c), (d) (see Fig. 8.3, enhanced online for time-lapse movie). The singularity appears as a break of the FL near the surface. The break indicates that we have now two wedge shaped domains with the same shaft but different FLs. This means that a kink must exist in the thinned end of the wedge, although this kink

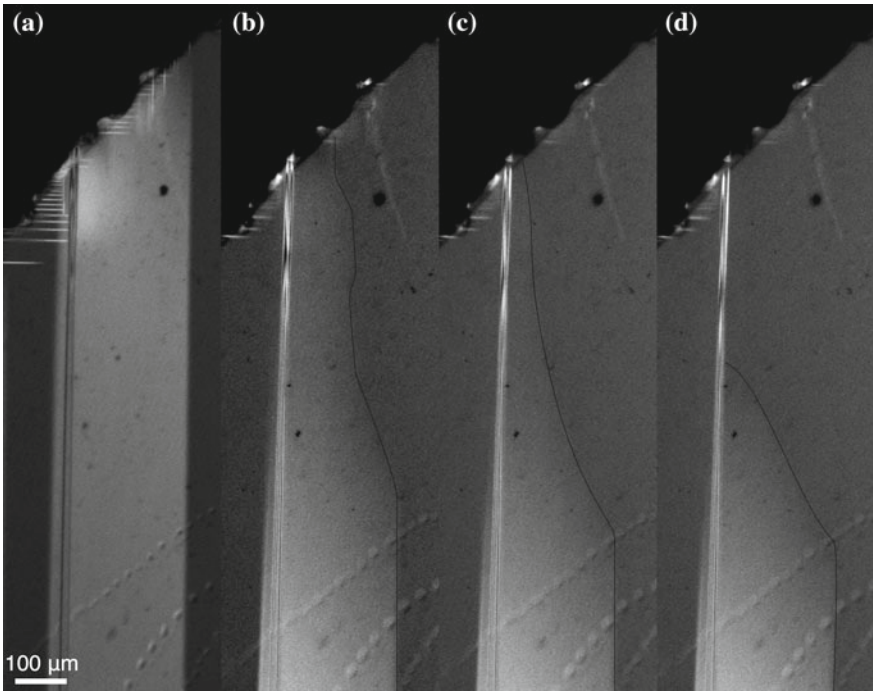

Fig. 8.2 Time evolution of a wedge shaped domain after attachment to the surface (**a**), partial attachment (**b**) and (**c**), and after the link snapped (**d**). *Black lines* (guides to the eye) show the position of the FL

is very short and exists only at the very thin end of the wedge. The FL is digitized from the intensity changes in the photographic image in the microscope (Fig. 8.3). Here, it becomes clear that any break of the FL is amended when the profile is taken further inside the domain. The second (red) profile in Fig. 8.3 is close to linearity and shows the equilibrium profile of the wedge away from the FL, while the FL itself remains rough and wiggly. We measure the degree of "wiggliness" by subtracting the observed profiles from the averaged linear profile (Fig. 8.4b) and then measure the autocorrelation of the profile $A(x) = \int \delta r(x)\delta r(x + \Delta)d\Delta$, where δr is the height of the wiggle of the FL at the position x of the linearized FL. Profiles $A(x)$ away from the FL are flat and show purely random autocorrelations. At the FL, the function $A(x)$ changes dramatically with strong positive correlations for small shifts x and a massive anti-correlation for larger distances. The length scale of the anticorrelation (90 µm in Fig. 8.3c) is a measure of a macroscopic Larkin length (L_c), which represents the length scale over which the elastic energy of the FL is balanced by the defect pinning potential. Comparing our results with simulations [26] shows that their main conclusion, namely, the breakup of the FL for sufficiently long sample length scales L ($L_c \ll L$), is indeed observed [27]. These simulations are based on an elastic string moving though a random potential. It is now tempting to identify such a string with

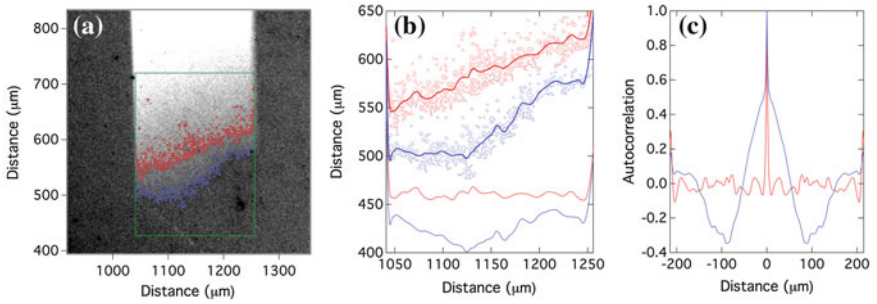

Fig. 8.3 Digitalization of the FL (*lower*) and a similar profile slightly inside the wedge domain (*upper*). Smoothed versions of the profiles are shown in **b**, both before and after sub- traction of the average slope of the upper profile (shifted vertically for clarity). The autocorrelation of the profile **c** shows random noise inside the domain but strong correlations and anti-correlations for the FL

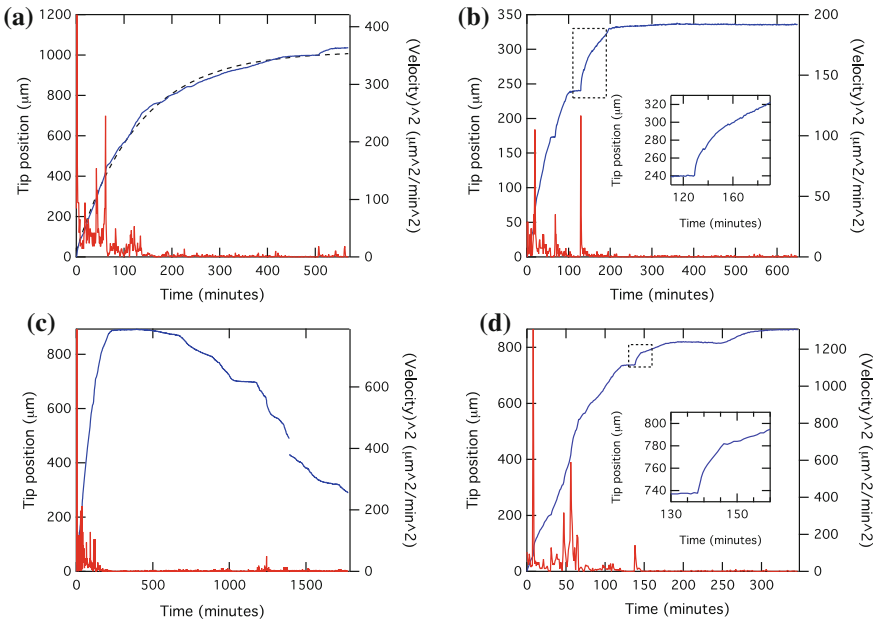

Fig. 8.4 Representative examples of the time evolution of the needle tip position (*black line*; *blue* in online version) and the differentiated curve (*grey line*; *red* in online version) where the height of each peak measures the energy of the jerk. The *insets* in **b** and **d** show the depinning transitions near a deep pinning center (expansions of the regions shown by *dashed rectangles*)

our FL. The condition for the breakup is that the dynamical roughness coefficient is positive, so that for long length there is an unlimited extension of the FL, leading inevitably to its break up. A direct determination of the roughness exponent is not possible for our wedge domains because the fluctuations are too course. However, we

have demonstrated successfully that (a) fluctuations and roughness during the jerky propagation of ferroelastic needles occurs at the FL, rather than in the ferroelastic twin walls themselves, (b) that these fluctuations are strongly influenced by surfaces and defects, and (c) that the fluctuations are large enough to warrant the frequent breakup of the FL, in agreement with the model in [27].

8.3 Noise Exponent for Needle Domain Propogation

The size/energy exponent of the jerky wall propagation was investigated in [6]. Defining the time dependence of the needle front requires a good knowledge of the needle shape and its invariance under the applied stress. Although the exact shape of a full needle domain and its wall profile next to the needle tip is very well understood, its dynamical behaviour is much less clear. Using DMA experiments [28, 29] it was found that the propagation and retraction of needles could be described by an extended Debye model. The dynamical response followed the momentum driven susceptibility of Cole-Cole semicircles. Similarly, Jacobs et al. [30] presumed for the dynamical behaviour of domain walls ballistic propagation where the dynamical force is balanced by the first time derivative of the loci of the needle tip $\mathrm{m}\mathrm{d}x/\mathrm{d}t \sim \mathrm{d}G/\mathrm{d}e \sim \sigma_{\mathrm{external}}$, where G is the Gibbs free energy of the system, e is the stress coordinate, and $\sigma_{\mathrm{external}}$ is the applied stress.

The advance of the jerky part of the front propagation follows power law dependence with an energy exponent of $\varepsilon = 1.8$ (Figs. 8.4, 8.5). The idea of avalanches as critical phenomena is generally related to a multitude of individual jerks which, statistically are described by power laws related to the probability to observe an

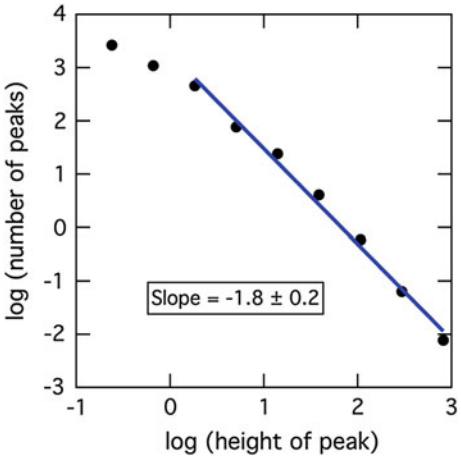

Fig. 8.5 Log–log plot of the jerks observed for one needle both propagating and retracting (combining data from 12 individual propagation/retraction cycles). Data were analyzed using logarithmic bins. The power law exponent is -1.8 ± 0.2, obtained after fitting to the range of data indicated by the fit line. The same exponent was obtained using linear binning (Color figure online)

avalanche with a certain energy or amplitude [1]. Alternatively, Natterman and collaborators have argued that interfaces themselves can show power law behaviour close to the depinning force [31].

8.4 Outlook

The simultaneous measurement of ferroelastic avalanche exponents and the direct optical observation of the underlying microstructural changes constitute a unique opportunity with no similar experimental observations reported previously. Nevertheless, future work may identify other ferroelastic systems where avalanche behaviour during the fluid dynamics part of the switching ferroelastic hysteresis will be measured [21]. Typical examples are the archetypal ferroelastic materials $Pb_3(PO_4)_2$ [32] and leucite [33], where ferroelastic switching was previous confirmed but where no correlations between the avalanche formation and the domain movement was reported. Other systems exist in the geological context [34] or in metal-insulator transitions [35]. Martensitic alloys show very similar switching properties, although the domain movements are not usually optically visible. In a recent study Soto-Para et al. [10] showed that even in porous, twinned materials, the stress collapse maintains two crucial ingredients, namely the power law for the de-twinning process and a second power law for the porous collapse. The two sequences of events have been found that have been identified as de-twinning and fracture, respectively. The energies of de-twinning signals display a power-law distribution with a characteristic exponent that is independent of porosity. For fracture signals, the energy distribution seems to approach the power-law behavior only for samples of high enough porosity. The corresponding exponent is in agreement with the exponent reported for other porous minerals under compression. Therefore, for high porosity the criticality associated with both twinning–de-twinning and fracture mechanisms occurs simultaneously during the compression process and is characterized by different critical exponents. Fitting procedures found $\varepsilon = 2.0 \pm 0.1$ for signals of the lower branches (twinning and detwinning), which can be assumed to be independent of porosity within the errors. Acoustic emission signals originating from de-twinning have the same values of the energy exponent expected for a martensitic transition taking place from cubic to monoclinic (as in the studied sample) [36, 37]. Interestingly, the exponent $\varepsilon \simeq 1.7$ estimated for signals originating from fracture is in good agreement with values obtained during failure under compression of porous minerals such as goethite [5] or different kinds of sandstone [38] but not in porous SiO_2 ceramics such as Vycor and Gelsil [39]. This result is of fundamental importance because it demonstrates that it becomes possible, under rather optimal circumstances, to investigate complex avalanches, which may originate from very distinct physical processes. It appears that ferroelastic switching corresponds in this case to energy exponents between 1.8 and 2. They are hence slightly greater than the predicted mean field exponents.

Computer simulations of the ferroelastic switching process demonstrate a limitation of the current approach: athermal switching was found only below a Vogel-

Fulcher temperature [14] while thermally activated movements become important at higher temperatures [40]. The Vogel Fulcher temperature is often near the upper stability temperature of the ferroelastic phase where atomic movements become thermally activated (such as Ti switching in $BaTiO_3$) and small needle domains and kinks can be driven in a temperature field. The details of the domain switching process (kinks and needle movements) were simulated in detail in [11].

Finally we comment on the highly disordered ferroelastic domain structures. It has been argued that so-called domain glasses can nucleate if the local domains interact, jam and form complex patterns such as structural tweed [41]. Domain glasses share the same characteristic temperatures as structural glasses (the glass temperature, the coherency temperature, the Vogel-Fulcher and the Kauzmann temperature) [41–43]. Domain glasses are hence expected to display thermally assisted avalanche dynamics between the Vogel-Fulcher temperature where full domain structures nucleate and the Kauzmann temperature below which domains freeze. No experimental observations are known to the authors, which could clarify the domain movements in this regime and characterize the avalanche exponent.

References

1. E.K.H. Salje, K.A. Dahmen, Annu. Rev. Condens. Matter Phys. **5**, 233 (2014)
2. K.A. Dahmen, Y. Ben-Zion, J.T. Uhl, Nat. Phys. **7**, 554 (2011)
3. Y. Ben-Zion, K.A. Dahmen, J.T. Uhl, Pure Appl. Geophys. **168**, 2221 (2011)
4. J. Baró, Á. Corral, X. Illa, A. Planes, E. Salje, W. Schranz, D. Soto-Parra, E. Vives, Phys. Rev. Lett. **110**, 088702 (2013)
5. E.K.H. Salje, G.I. Lampronti, D.E. Soto-Parra, J. Baró, A. Planes, E. Vives, Am. Mineral. **98**, 609 (2013)
6. R. Harrison, E. Salje, Appl. Phys. Lett. (2010)
7. R.J. Harrison, E.K.H. Salje, Appl. Phys. Lett. **99**, 151915 (2011)
8. M.C. Gallardo, J. Manchado, F.J. Romero, J. del Cerro, E.K.H. Salje, A. Planes, E. Vives, R. Romero, M. Stipcich, Phys. Rev. B **81**, 174102 (2010)
9. E. Faran, E. K. H. Salje, D. Shilo, Appl. Phys. Lett. **107** (2015)
10. D. Soto-Parra, X. Zhang, S. Cao, E. Vives, E.K.H. Salje, A. Planes, Phys. Rev. E **91**, 60401 (2015)
11. E.K.H. Salje, X. Wang, X. Ding, J. Sun, Phys. Rev. B **90**, 64103 (2014)
12. E.K.H. Salje, Y. Ishibashi, J. Phys. Condens. Matter **8**, 8477 (1996)
13. F.J. Romero, J. Manchado, J.M. Martín-Olalla, M.C. Gallardo, E.K.H. Salje, Appl. Phys. Lett. **99**, 011906 (2011)
14. E. Salje, X. Ding, Z. Zhao, T. Lookman, A. Saxena, Phys. Rev. B **83**, 104109 (2011)
15. P. Chauve, T. Giamarchi, P. Le Doussal, Phys. Rev. B **62**, 6241 (2000)
16. E. Bonnot, E. Vives, L. Mañosa, A. Planes, R. Romero, Phys. Rev. B **78**, 94104 (2008)
17. F.-J. Pérez-Reche, B. Tadić, L. Mañosa, A. Planes, E. Vives, Phys. Rev. Lett. **93**, 195701 (2004)
18. K.J. Måløy, S. Santucci, J. Schmittbuhl, R. Toussaint, Phys. Rev. Lett. **96**, 045501 (2006)
19. S. Papanikolaou, F. Bohn, R.L. Sommer, G. Durin, S. Zapperi, J.P. Sethna, Nat. Phys. **7**, 316 (2011)
20. S. Zapperi, P. Cizeau, G. Durin, H.E. Stanley, Phys. Rev. B **58**, 6353 (1998)
21. E.K.H. Salje, Annu. Rev. Mater. Res. **42**, 265 (2012)
22. E.K.H. Salje, ChemPhysChem **11**, 940 (2010)
23. S. Conti, S. Müller, A. Poliakovsky, E.K.H. Salje, J. Phys. Condens. Matter **23**, 142203 (2011)

24. E.K.H. Salje, A. Buckley, G. Van Tendeloo, Y. Ishibashi, G. Nord, Am. Mineral. **83**, 811 (1998)
25. J. Novak, U. Bismayer, E.K.H. Salje, J. Phys. Condens. Matter **14**, 657 (2002)
26. A.I. Larkin, Y.N. Ovchinnikov, J. Low Temp. Phys. **34**, 409 (1979)
27. H.J. Jensen, J. Phys. A. Math. Gen. **28**, 1861 (1995)
28. R. Harrison, S. Redfern, E. Salje, Phys. Rev. B **69**, 10 (2004)
29. R.J. Harrison, S.A.T. Redfern, A. Buckley, E.K.H. Salje, J. Appl. Phys. **95** (2004)
30. A.E. Jacobs, S.H. Curnoe, R.C. Desai, Phys. Rev. B **68**, 224104 (2003)
31. T. Nattermann, S. Stepanow, L.-H. Tang, H. Leschhorn, J. Phys. II **2**, 1483 (1992)
32. E. Salje, B. Wruck, Phys. Rev. B **28**, 6510 (1983)
33. D.C. Palmer, E.K.H. Salje, W.W. Schmahl, Phys. Chem. Miner. **16**, 714 (1989)
34. E. Salje, Phys. Chem. Miner. **14**, 181 (1987)
35. E. Salje, R. Gehlig, K. Viswanathan, J. Solid State Chem. **25**, 239 (1978)
36. A. Planes, L. Mañosa, E. Vives, J. Alloys Compd. **577**(Supplement 1), S699 (2013)
37. R. Niemann, J. Kopeček, O. Heczko, J. Romberg, L. Schultz, S. Fähler, E. Vives, L. Mañosa, A. Planes, Phys. Rev. B **89**, 214118 (2014)
38. G.F. Nataf, P.O. Castillo-Villa, J. Baró, X. Illa, E. Vives, A. Planes, E.K.H. Salje, Phys. Rev. E **90**, 22405 (2014)
39. J. Baró, Á. Corral, X. Illa, A. Planes, E.K.H. Salje, W. Schranz, D.E. Soto-Parra, E. Vives, Phys. Rev. Lett. **110**, 88702 (2013)
40. X. He, X. Ding, J. Sun, E.K.H. Salje, Appl. Phys. (2016 in press)
41. E.K.H. Salje, Am. Mineral. **100**, 343 (2015)
42. E.K.H. Salje, M.A. Carpenter, Phys. Status Solidi **252**, n/a (2015)
43. E.K.H. Salje, X. Ding, O. Aktas, Phys. Status Solidi **251**, 2061 (2014)

Chapter 9
Microstructural Effects During Crackling Noise Phenomena

Eilon Faran and Doron Shilo

Abstract Crackling noise phenomena typically exhibit scale-free statistical distributions (e.g., power law) of the measured variables. Such a universal behavior reveals little information regarding the physical mechanisms and microstructures that are either responsible and/or affect crackling behavior. Here, we address this issue and show three physical systems in which the distributions of certain variables are centered around a most probable value, which is related to a characteristic size of the internal microstructure. These variables represent microstructural-related events. At the same time, each microstructural-related event proceeds through a multitude of smaller mesoscopic events that span several orders of magnitude. Statistical analyses of other variables, which are associated with the mesoscopic events, follow a scale-invariant power law distribution. The origins for the co-existence of events at different scales and their different statistical distributions are discussed in light of the physical characteristics of the investigated systems.

9.1 Introduction to Crackling Noise and Open Questions

Numerous physical systems respond by discrete impulsive events when subjected to a slow and continuous change applied on their boundary conditions (e.g., an elongation/contraction of a material, a change in the temperature, or an application of external magnetic/electric field) [1, 2]. Individual events are termed 'jerks', which are formed during changes of temporal patterns and constitute 'crackling noise phenomena'. This term relates to the acoustically emitted noise that often appears as a result of the emitted energy during impulsive events (see, e.g., [3] and references therein). Crackling noise phenomena are commonly analyzed based on the statistical distribution of the magnitude ω of individual events. For infinite systems at criticality, the

E. Faran (✉) · D. Shilo
Faculty of Mechanical Engineering, Technion, 3200003 Haifa, Israel
e-mail: eilonfa@techunix.technion.ac.il

D. Shilo
e-mail: shilo@tx.technion.ac.il

E.K.H. Salje et al. (eds.), *Avalanches in Functional Materials and Geophysics*,
Understanding Complex Systems, DOI 10.1007/978-3-319-45612-6_9

probability density function (PDF) p of finding an event with a magnitude ω reveals a power law of the form [1–4]:

$$p(\omega) \propto \omega^{-\alpha} \tag{9.1}$$

with exponents α predicted for various universality classes and amplitude/energy distributions. Equation (9.1) exhibits the same behavior if plotted on different scales (ω can span many decades [5]), and is hence scale-invariant. The symbol ω in (9.1) may represent different measured variables that are used for quantifying the size of individual events. For example, ω can be related to emitted energy in acoustic emission (AE) tests [6–8], to heat flux in calorimetric measurements [9, 10], to changes of the magnetization during magnetic domain switching [2], or to magnitudes of stress drops in mechanical experiments [11]. Deviations from criticality (see e.g., [12, 13]), as well as measurement errors and limited time resolution, which are inherent to every experimental data, impose truncation of pure power law behavior. As a result, experimental data are sometimes analyzed using the following PDF [12–15]

$$p(\omega) \propto \omega^{-\alpha} exp(-\lambda\omega) \tag{9.2}$$

where the parameter λ measures the deviation from a power law distribution. In other cases, stretched exponential PDFs of the form [9, 11, 14, 16, 17]:

$$p(\omega) \propto \omega^{\beta-1} exp(-\lambda\omega^{\beta}) \tag{9.3}$$

with $\beta < 1$, have been used to account for finite size effects of otherwise power law distributed data [18].

The PDFs described in (9.1)–(9.3) are different, but they share several similarities. First, all are monotonously decreasing functions that have no peak related to a most probable value around which the PDF is distributed. Second, although (9.2) and (9.3) have a characteristic size, this size represents either a deviation from criticality [12, 13] or a detection limit of the experimental system [9, 11, 14, 17]. In both cases, it does not represent a most probable value around which the PDF is distributed.

Several types of models that explain and predict a power law distribution of avalanche events (9.1) in terms of classical criticality [2] or self-organized criticality [19] have been suggested. In general, power law behavior appears in dynamic systems that have numerous degrees of freedom and interactions between them that lead to numerous locally stable states [20, 21] or to an energy landscape that is characterized by numerous metastable states [22]. As a result, the system responds to a change of the boundary conditions through a sequence of transitions between different locally stable states. Each transition is characterized by a different energy barrier and forms an avalanche with a different magnitude. Different models provide different conditions, e.g., a specific relation between the amount of disorder and the strength of long range interactions, at which the collection of all avalanche magnitudes is distributed according to a power law. In all models, it is assumed that thermal

fluctuations are negligible compared with the energy barriers separating the locally stable states, such that the transitions between states occur in an athermal process. In cases where the latter condition is not met, avalanche PDFs follow an exponential law in accordance with the Vogel–Fulcher behavior [16, 23].

The above-described conditions can appear in many different dynamic systems and therefore the power-law distribution has been interpreted as a universal law, which is valid for many different physical processes regardless of the specific characteristics of each physical system [2, 4]. However, the universality comes at a price: the power law behavior does not provide information about the forms (spatial arrangement) of metastable states; the barriers and mechanisms of transitions between states; and material properties that govern all these aspects [1]. The latter information is often obtained by means of theoretical models and experimental methods different than those used for studying the crackling noise phenomenon. An example for such knowledge, related to one physical system, twin boundary motion in Ni-Mn-Ga, at which crackling noise phenomenon has been observed, is presented in Sect. 9.2. The relations between the type of barriers, the mechanisms of motion for overcoming them, and the resulted distributions of crackling noise, are still open issues.

A more critical unsolved problem is related to the scale-less nature of the power-law distribution, which implies that either the physical system has no characteristic length-scale or the length-scale has no effects on the crackling noise response. Common theoretical models that explain and predict the power-law behavior, such as the random field Ising models (e.g., [2, 24]) and mean field models (e.g., [17, 25, 26]), require some amount of disorder in the material/physical system. However, in these models the disorder is quantified only in terms of its strength, assuming that it has a uniform or arbitrary spatial distribution, without any characteristic length-scale. In practice, the disorder arises due to material defects, which usually have a characteristic length-scale (e.g., average distance between defects). Moreover, many of the physical systems at which scale invariant behavior have been reported have some characteristic length scale, which comes from the microstructure of the involved materials (e.g., grain, twin, or domain sizes). The microscopic mechanisms responsible for crackling noise are expected to be sensitive to the material microstructure or to the average distance between defects. Such sensitivity is expected to unfold through the PDF of ω, e.g., by being distributed around some characteristic value that is related to the characteristic length scale.

In this chapter, we investigate three very different physical systems that share one common feature: all systems have an intrinsic ‘microstructure’, with a characteristic length-scale that is expected to affect crackling noise response. In all systems we show that the internal ‘microstructure’ separates the material into volume elements that tend to respond separately, thus forming large-scale ‘macroscopic’ events, which are distributed in accordance with the characteristic length-scale of the microstructure. Yet, the dynamic response of each volume element is composed of numerous smaller ‘microscopic’ events, which are scale-free.

The latter distinction between ‘macroscopic’ and ‘microscopic’ events calls for a deeper understanding on different types of events. Since events occur due to barriers between locally stable states, we seek to obtain information not only on the intensities

(energy) of the barriers, but also on their sizes (length-scale) and spatial distribution. Therefore, in order to deeply understand the investigated physical problem, one has to consider not only the statistical data of the crackling noise, but also other experimental and theoretical information about the specific barriers and the processes for overcoming them.

In light of the above understanding, this chapter starts (Sect. 9.2) by focusing on one physical system, twin boundary motion in Ni-Mn-Ga. This section provides a comprehensive discussion about the barriers and mechanisms of motion relevant for this system. In Sect. 9.3, we use the knowledge presented in Sect. 9.2 to distinguish between three different types of events and evaluate the orders of magnitude of their volume, duration, and energy. In particular, we correlate the 'macroscopic' events to microstructural features (typically at the μm-scale) and refer to them as microstructural-related events. At the same time, the 'microscopic' events are correlated with lattice-scale (i.e., nm-scale) phenomena. While Sect. 9.3 is based on information obtained for twin boundary motion in Ni-Mn-Ga, it also presents several broad concepts related to types and length-scales of avalanche events and to detection capabilities of different experimental methods (including calorimetry and AE), which are relevant for a variety of physical systems. Sections 9.4–9.6 present experimental results and analysis of crackling noise during twin boundary motion in Ni-Mn-Ga, martensitic transformation in Cu-Al-Ni, and the collapse of a stack of corrugated fiberboards (see [27, 28]). All these studies are based on low-rate uniaxial compression tests. Finally, a brief summary is presented in Sect. 9.7.

9.2 Barriers and Mechanisms for Twin Boundary Motion in Ni-Mn-Ga

Ni-Mn-Ga exhibits both shape memory and ferromagnetic behaviors and is the most common ferromagnetic shape memory alloy (FSMA) [29, 30]. As common to shape memory alloys, Ni-Mn-Ga is characterized by a high symmetry (austenite) crystallographic phase and a low symmetry (martensite) crystallographic phase. The low symmetry phase is associated with a spontaneous strain and exhibits a twinned microstructure, in which the crystal is divided into different twin variants separated by twin boundaries [31, 32]. Each of these variants has a different orientation of the unit cell and in accordance different magnetic easy axis (an energetically favorable direction of the magnetization). When subjected to an external driving force (either mechanical or magnetic in the case of Ni-Mn-Ga), one twin variant may expand at the cost of the other through nucleation and propagation of twin boundaries, in a process collectively known as twinning or martensitic reorientation. The twinning transformation is associated with a significant strain change (i.e., beyond elasticity) and is therefore used in a variety of actuation applications [33–39].

A quantitative description of a twinning–based macroscopic response requires the knowledge of a kinetic relation. This fundamental material law describes the velocity of an individual twin boundary v_{TB} as a function of the external driving force g [40]. For example, following the common 'discrete twin boundary dynamics' modeling approach, which is similar to the discrete dislocation dynamics approach (see, e.g., [41]) but is more simple and straightforward, the macroscopic strain rate $\dot{\varepsilon}$ can be described by the relation:

$$\dot{\varepsilon} = 1/V_0 \sum_n A_{TB}^{(n)} N^{(n)}{}_{TB} \cdot \varepsilon_T^{(n)} v_{TB}^{(n)}(g) \tag{9.4}$$

The index (n) represents a twinning system, i.e., a transformation between two specific twin variants. V_0 is the crystal volume and A_{TB} is the area of a twin boundary. N_{TB} is the number of mobile twin boundaries, ε_T is the strain jump across the twin boundary (i.e., the twinning strain), and $v_{TB}(g)$ is the kinetic relation. In most of the cases, only one twinning system is activated and there is no interaction between twin boundaries beyond the nm-scale. In addition, N_{TB} is often constant and known for a given crystal (e.g., when active twin boundaries are stabilized [42]). The only unknown variable in (9.4) is $v_{TB}(g)$. Consequently, knowledge of $v_{TB}(g)$ is crucial for the simulation of twinning-based response. Generally, different types of kinetic relations arise for different ranges of the driving force and temperature, reflecting on the different mechanisms of motion that are active under different loading conditions [43–45].

While a kinetic relation bares fundamental importance in the quantitative description of twinning dynamics, the concept of such a relation assumes that the twin boundary velocity depends only on the driving force, thus ignoring local barriers and temporal processes by which the twin boundary overcomes these barriers. Consequently, a kinetic relation is meaningful for describing the average twin boundary velocity over length-scales much larger than those of relevant barriers for motion. This understanding emphasizes the need for the identification and characterization of the energy landscape under which a twin boundary propagates. This landscape may be generated by barriers of different intensities (amplitude) and widths (length scale), as well as different spatial distributions within a given crystal. Knowledge about the physical characteristics of the different barriers, as well as the mechanisms of motion is required both for modeling twinning transformation and for the development of new and improved materials.

The energy barriers for twin boundary motion can be classified according to their typical length scale. In particular, we distinguish between atomistic-scale lattice barriers to much longer range (typically μm scale) barriers. The former arises from resistance imposed by the lattice potential [46–48], while the latter is associated with larger scale interactions due to microstructural features and various crystal defects [49–52]. Twin boundaries can overcome the different energy barriers through different mechanisms of motion. Each of these mechanisms can be viewed as a collection of individual "events" with different length, energy and temporal scales, which can be estimated based on the physical characteristics of the different energy barriers.

The effects of the different barriers on the kinetics of individual twin boundaries in Ni-Mn-Ga were identified and analyzed through a combination of analytical and experimental investigations [27, 43–45, 53, 54]. It was shown that atomistic scale barriers result in different kinetic relations at different ranges of the driving force, while μm scale barriers are responsible primarily for the threshold driving force below which twin boundary motion does not take place. This important material property is commonly referred to as the twinning stress.

9.2.1 Twin Boundary Motion Under the Lattice Potential

At the atomistic scale, the periodicity of the crystal induces several energy barriers, which exist even in a crystal free of imperfections (see Fig. 9.1). First, we consider the lattice barrier that resists the uniform motion of a twin boundary as a flat plane. This 2D potential represents the change of the twin boundary energy (per unit area) as a function of its position (see, for example, [43, 44, 46, 48, 55–58]), and follows the periodicity of the lattice in the direction normal to the twin boundary. In a similar way, we can consider the 1D lattice potential for twinning dislocations, which are line defects that represent steps on an existing twin boundary and possess the characteristics of ordinary dislocations [59, 60]. The 1D lattice potential, also known as the Peierls potential [61], represents the periodic change of the twinning dislocation energy as a function of its position on the twinning plane. Depending on the driving force and rate limiting step, both the 1D and 2D lattice potentials can give rise to several possible mechanisms of motion, which result in different kinetic relations.

The effects of the lattice barrier on twin boundary motion in Ni-Mn-Ga single crystals have been studied by means of a pulsed magnetic field method. In this method, a pulse with a constant amplitude (driving force) and tunable duration in the range of $10 - 120\,\mu s$ is applied and the displacement of individual twin boundaries is measured by optical visualization before and after the pulse. The average velocity, v_{TB} of a twin boundary is calculated by dividing the measured distance traveled during a single pulse by the pulse duration. Figure 9.2 demonstrates an example for experimental results obtained using this method, showing average velocity measurements over a relatively large range of the driving force. All measurements shown in Fig. 9.2 were obtained from the same twin boundary. The scattering in the measured velocity values indicates the presence of interactions with crystal defects, which lead to the slowing down of the twin boundary motion. At the same time, for a large enough number of data points, there are instances in which the twin boundary does not meet a defect. In these cases, the average velocity is approximately equal to the instantaneous velocity under the driving force value of the pulse amplitude because the driving force is nearly constant throughout most of the pulse duration. Therefore, the maximum velocities under each value of the driving force represent the kinetic relations in a defect-free crystal, which are governed by the lattice barrier [7–9].

Studies using the above described method [43, 44] showed that above a certain transition driving force (denoted as g_{trans} in Fig. 9.2) the twin boundary overcomes

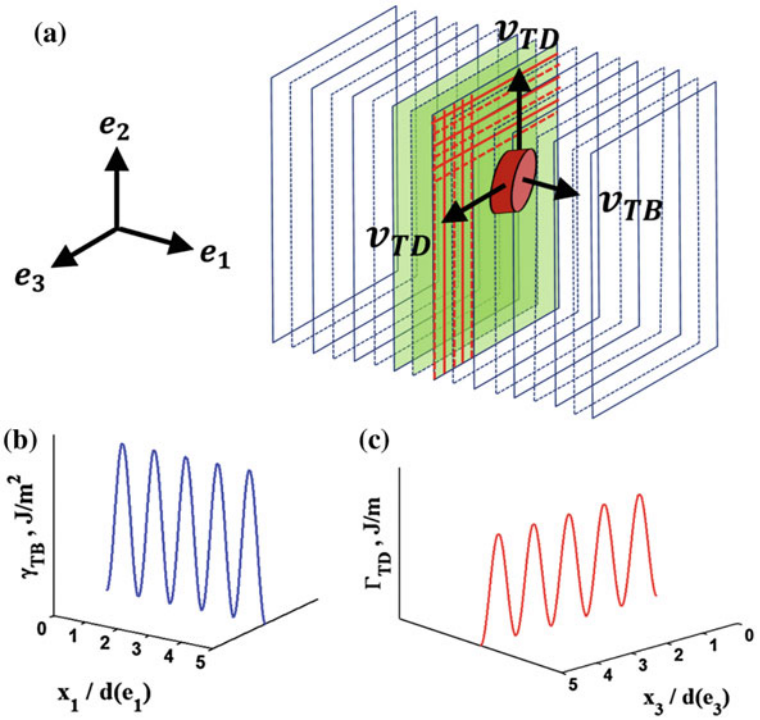

Fig. 9.1 **a** A schematic representation of the lattice potentials that form barriers for twin boundary motion. The boundary plane is marked in light *green*, and contains a step whose edges (marked in *red*) are twinning dislocations. *Black solid* and *dotted rectangles* represent "hills" and "valleys" (respectively) of the periodic 2D potential, which resists the motion of a twin boundary as a flat plane along the e_1 direction at velocity v_{TB}. *Red solid* and *dotted lines* represent "hills" and "valleys" (respectively) of the 1D potential, which resists the lateral propagation of twinning dislocations along the e_2 and e_3 directions at velocity v_{TD}. The periodic energy landscapes induced by the 2D and the 1D potentials are shown schematically in (**b**) and (**c**), respectively

the 2D lattice potential in an athermal manner and moves as a flat plane. This type of motion is described by a kinetic relation that follows a square root dependence on the driving force (see pink trend line in Fig. 9.2), and can lead to twin boundary velocities as high as several meters per second [33, 43, 44, 54]. Below the transition driving force, slower motion proceeds through nucleation and motion of twinning dislocations. This type of motion is described by an exponential type kinetic relation (see green trend line in Fig. 9.2), which reflects the thermally activated mechanisms that dictate the overall boundary motion [43, 44].

For the thermally activated type of motion, one can evaluate the physical characteristics of individual events that constitute the overall boundary propagation. For example, the transformed volume due to nucleation of a twinning dislocation, which can be described as a two dimensional circular step on the twin boundary plane, is given by:

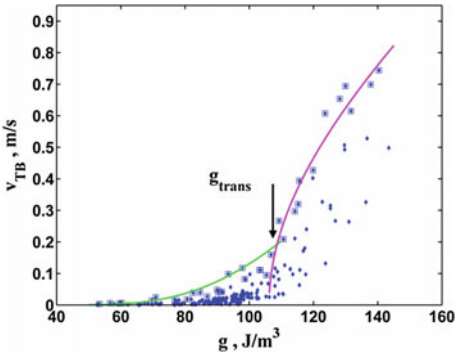

Fig. 9.2 Velocities of an individual twin boundary as a function of the driving force, obtained from high rate pulsed magnetic field measurements in Ni-Mn-Ga. The maximal velocity values are marked by *empty squares* and follow two trends that are fitted by two types of kinetic relations (see text for details). The transition value, at which slow thermally-activated motion switches to fast a-thermal motion is marked as g_{trans}

$$\Delta V = dr_c^2 \tag{9.5}$$

Here, $d \cong 4 \cdot 10^{-10}$ m, is the minimal thickness of the step (which is equivalent to the lattice spacing between adjacent twinning planes) and r_c is the critical radius of the step. The actual value of r_c in Ni-Mn-Ga can be extracted by fitting an analytical kinetic relation to experimental results, as was done in [44], resulting in $r_c \cong 20$ nm. Substituting these values in (9.5) results a value of $\Delta V \cong 5 \cdot 10^{-7}\,\mu\text{m}^3$. The energy associated with a nucleation of a twinning dislocation step is [44]:

$$\Delta E = gdr_c^2 \tag{9.6}$$

A substitution of a typical driving force value, e.g., $g = 100\,\text{kJ/m}^3$ (see Fig. 9.2) in (9.6) provides $\Delta E \cong 5 \cdot 10^{-20}$ J. The nucleation rate of such steps can be estimated based on standard nucleation theory:

$$\dot{N} = dc_0 f_0 exp\left(-\frac{Q}{kT}\right) \tag{9.7}$$

Here, c_0 is the atomic density, f_0 is the typical vibration frequency of atoms in the metal, Q is the activation energy for nucleation and kT is the thermal energy. The activation energy Q can be extracted based on an expression for the overall twin boundary velocity, which, for a process governed by nucleation of two dimensional steps, is given by [44]:

$$v_{TB} = v_0 exp\left(-\frac{Q}{3kT}\right) \tag{9.8}$$

Here, v_0 is the pre-exponential velocity term which can be obtained by fitting an expression for the kinetic relation to the measured data (see, e.g., [44]). Combining (9.7) and (9.8) results:

$$\dot{N} = dc_0 f_0 \left(\frac{v_{TB}}{v_0} \right)^3 \tag{9.9}$$

Equation (9.9) allows estimating the magnitude of $\dot{N}$ from the values of v_{TB} and v_0, which can be obtained from fitting an exponential type kinetic relation to the measured data [44, 45]. This procedure leads to nucleation rates on the order of $10^{21} - 10^{23}\,\mathrm{s}^{-1}$ (depending on the value of g). The duration of individual nucleation events is determined by f_0^{-1} and is at the pico-second scale.

9.2.2 *Long Range Energy Barriers: The Origin and Characteristics of the Twinning Stress*

Another experimental method for studying the dynamics of the twinning transformation is based on low-rate displacement-controlled uniaxial loading. In this method, the prescribed displacement rate dictates the average twin boundary velocity, and the driving force required for obtaining this velocity is measured. Traditionally, this method is used for measuring a fundamental property of SMA, which is termed the twinning stress. This value, which is taken as the average value of the stress plateau in the loading curve of the martensite phase, represents the threshold stress required to initiate twin boundary motion at low velocities. Figure 9.3a shows a typical uniaxial loading curve of a type I twin boundary in a NiMnGa single crystal, which was measured at a loading rate that corresponds to an average boundary velocity of $\bar{v}_{TB} = 2.8 \times 10^{-6}$ m/s (smaller by three orders of magnitude than the minimal velocity that can be detected by magnetic pulse tests described in Sect. 9.2.1). The load profile shows a typical plateau-type response, which, upon magnification reveals a saw tooth pattern (see Fig. 9.3b). The average value of the plateau stress (marked by the black line in Fig. 9.3a) represents the twinning stress σ_{ts}, which, for this boundary type equals about 0.85 MPa. This value corresponds to a driving force of $g_{ts} \approx 50\ \frac{\mathrm{kJ}}{\mathrm{m}^3}$ that is smaller than the transition driving force associated with the lattice potential ($g_{trans} \approx 110\ \frac{\mathrm{kJ}}{\mathrm{m}^3}$, see the pulsed field data in Fig. 9.2). Mechanical experiments conducted at different loading rates, which correspond to different average twin boundary velocities in the range of 10^{-7}–10^{-2} m/s (all slower than the typical values measured in the pulsed field method), reveal no significant change in the value of the twinning stress [54]. This result indicates that the twinning stress property represents a threshold driving force value below which twin boundaries are immobile. This observation implies that although $g_{trans} > g_{ts}$, the barrier associated with the lattice potential (related to g_{trans}) can be overcome by thermally activated processes while the twinning stress barrier (related to g_{ts}) cannot. Consequently, the length scale of the barrier responsible for the twinning stress is expected to be much larger than that

of the lattice potential, and as such may be responsible for the scattering observed in our pulsed magnetic field experimental data.

At length scales larger than the atomistic scale, possible barriers for twin boundary motion can arise from interactions with other crystal defects (e.g., dislocations [62], clusters of point defects and surface defects [63]) as well as barriers imposed by the complex internal twinning microstructure often found in various types of SMA and ferroelastic materials. The latter type is characteristic to Ni-Mn-Ga, in which the internal microstructure consists of a hierarchical laminated micro-twinning structure [52, 64–66], as well as a conjugate 180° magnetic domain pattern [67]. Recently, we have shown that the barriers for twin boundary motion at low velocities (i.e., barriers related to the twinning stress property) are determined primarily by the mechanical microstructure, and that the contribution of the 180° magnetic domains to the barrier is negligible [68].

The internal twinning microstructure in Ni-Mn-Ga originates from the small monoclinic distortions of the otherwise tetragonal 10M martensite phase [64]. This gives rise to additional twinning systems (shown as grey and white layers in Fig. 9.4) that exhibit much smaller strains compared to the strain jump across a macro-twin boundary. These finer twins are often referred to as $a-b$ laminates [64] and share a common c axis direction of the nearly tetragonal unit cell. The resulting microstructure on both sides of a macro twin boundary consists of alternating $a-b$ twinning laminates with a typical laminate width of few tens of microns [69]. Twinning laminates are oriented differently at different sides of the macro twin boundary [64] (see Fig. 9.4), but at the same time must satisfy strain compatibility across the macro twin boundary [52, 70]. Full compatibility (i.e., minimal strain energy) is achieved when laminates of the same kind meet across the entire twin boundary (see Fig. 9.4a, b).

The internal twinned volume on either sides of the macro twin boundary maintains its self-similar strain compatible structure each time the macro twin boundary advances by a distance Δx that is directly determined by the lamella thicknesses (Fig. 9.4b). We note that according to our optical observations during pulsed field tests in NiMnGa, the macro twin boundary remains relatively flat as it propagates, at least down to the sub-μm scale [43, 44]. Contrary, advancement by a distance smaller than Δx leads to a situation in which laminates of different kinds meet across parts of the macro twin boundary (as illustrated in Fig. 9.4c) and results in an excess energy due to strain incompatibility. In order to reduce this excess energy, needle twins may nucleate and grow inside the laminated structure, as illustrated in Fig. 9.4d. We note that while nucleation and growth of needle laminates dictate the overall motion of the macro twin boundary, it introduces a negligible amount of macroscopic strain change (due to the relatively small twinning strain associated with $a-b$ laminates). The macroscopic strain change is induced primarily by the motion of the macro-twin boundary.

The above discussion indicates that the motion of the macro twin boundary, which is commonly described by a single parameter (the twinning stress), is expected to follow a sequence of locally metastable states (e.g., Fig. 9.4a, b), which are dictated by the typical width of twinning lamellas. Between these metastable states, local events at much smaller scales are expected to take place (as in Fig. 9.4d).

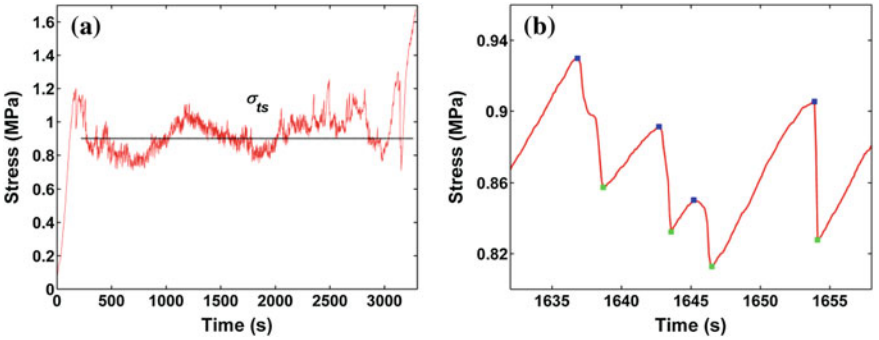

Fig. 9.3 **a** Low rate, displacement controlled uniaxial stress-strain curve showing a plateau type response at a nominal value of σ_{ts}. **b** A zoom in on the plateau region reveals a saw tooth pattern of the load profile. The *blue* and *green* markers represent local maxima and minima points, respectively, which define individual μm scale events (color figure online)

The "jerky" load profile shown in Fig. 9.3 implies that the twin boundary propagates from one local metastable state to the next through individual events. The orders of magnitude of some of the physical characteristics of these events can be evaluated from the experimental curve. For example, the energy change associated with a single event can be roughly evaluated based on the change in the total elastic energy due to a stress drop of magnitude $\Delta\sigma$:

$$\Delta E = V_0 \frac{\Delta\sigma \cdot \sigma}{Y} \tag{9.10}$$

Here, σ is the nominal stress value (i.e., the twinning stress), $Y \cong 5\,\text{GPa}$ is the elastic constant [71] and V_0 is the volume of the crystal, which is typically on the order of several mm^3. For stress drops $\Delta\sigma$ in the range of 0.001–0.1 MPa, we obtain $\Delta E \approx 10^{-6}$–$10^{-8}\,\text{J}$. Another way to roughly evaluate the energy of an individual event is through the product of the transformed volume ΔV and the mechanical work ($\sigma\varepsilon_T$) associated with twin boundary motion (note that in mechanical tests $g = \sigma\varepsilon_T$):

$$\Delta E = \Delta V \sigma \varepsilon_T \tag{9.11}$$

Here, $\varepsilon_T = 0.06$ is the twinning strain [72]. Combining (9.10) and (9.11) provides an evaluation for the transformed volume:

$$\Delta V = V_0 \frac{\Delta\sigma}{Y\varepsilon_T} \tag{9.12}$$

Inserting typical values in (9.12) results $\Delta V \approx 10^5$–$10^7\,\mu m^3$. The representative stress drops shown in Fig. 9.3b allow estimating the durations of individual events $\Delta t \approx 0.2$–$2\,s$, and the frequency at which they occur $f \approx 0.05$–$3\,s^{-1}$.

9.3 Different Types of Events and the Order of Magnitude of Their Volume, Energy, Duration and Rate

The analysis performed in the previous section for the Ni-Mn-Ga material system provides estimations of the orders of magnitude of several physical characteristics of individual events that constitute the overall motion of a twin boundary at different scales. These values are summarized in Table 9.1, and provide several important insights, which can be relevant for transformation phenomena in other material systems.

First, events associated with the lattice barrier are below the lateral, energetic and temporal resolutions of any experimental method that has been used for studying crackling noise. In addition, the high rate of the lattice-scale events indicates that at any moment there are numerous events that occur simultaneously. The small energy of these events, which is on the order of the thermal energy ($kT \approx 10^{-21}\,J$), allows their thermal activation and therefore their statistical distribution does not follow a power-law.

Second, the lattice-scale and microstructural-scale events are separated by a range of twelve orders of magnitude of volume, energy and duration. Within this vast range, there are probably other types of events, which we denote as mesoscopic-scale events. An example for such an event may be the formation of a needle twin (or needle domain) as illustrated in Fig. 9.4d and as observed in many ferroelastic materials [31, 73, 74]. It is possible, for example that a 'large' microstructural-scale event occurs through a formation of many needle twins and their subsequent motion. This means that any microstructural-scale event is composed of numerous mesoscopic-scale events (see the illustration of Fig. 9.4d). The mesoscopic-scale events are not sensitive to the microstructure and are therefore expected to exhibit a scale-free probability distribution.

Third, the relatively large size of microstructural-scale events is not unique to Ni-Mn-Ga. Many shape memory and ferroelastic single crystals, as well as polycrystals

Table 9.1 Different types of events during twin boundary motion in Ni-Mn-Ga and the orders of magnitude of their volume, energy, duration and rate

Barrier/scale	Volume (μm^3)	Energy (J)	Duration (s)	Rate (s^{-1})
Lattice barrier	10^{-7}–10^{-6}	10^{-20}–10^{-19}	10^{-12}–10^{-11}	10^{21}–10^{23}
Microstructural-related barrier	10^{6}–10^{8}	$5 \cdot 10^{-8}$–$5 \cdot 10^{-6}$	0.2–2	0.05–3

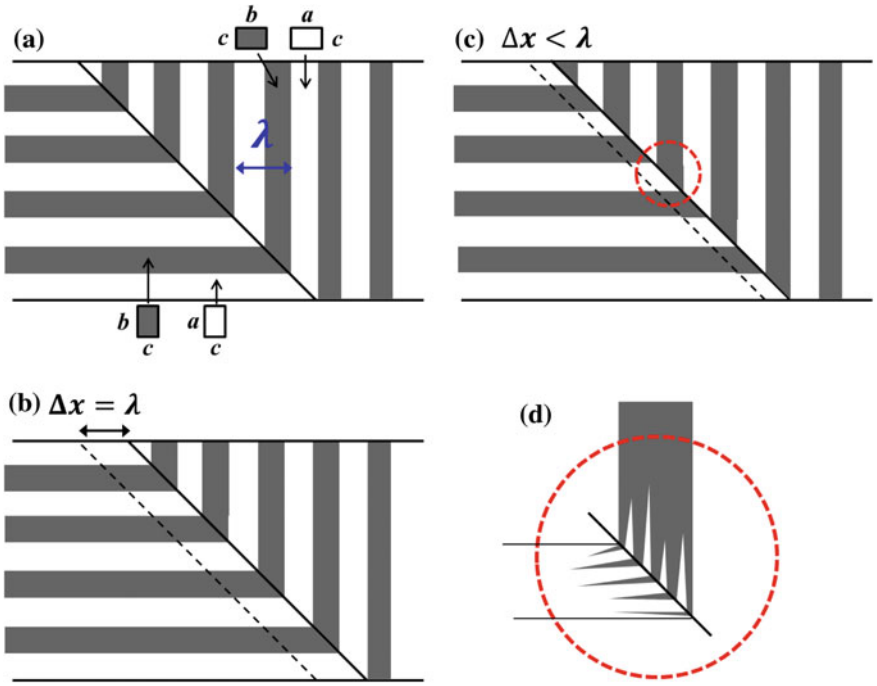

Fig. 9.4 **a** A schematic representation of the macro twin boundary (*solid black line*) in Ni-Mn-Ga. The single crystal is cut along {100} planes of the parent austenite phase, such that the macro twin boundary forms an inclination angle of 45° with regard to the crystal surface. A laminated twinning microstructure ("*grey*" and "*white*" stripes) is present on either side of the macro twin boundary with an equilibrium thickness of a pair lamella, λ. The lattice parameters of the nearly tetragonal unit cells represent the orientations of each laminate. **b** An advancement of the phase boundary by a distance $\Delta x = \lambda$ maintains the self-similar structure of the laminated volume. **c** An advancement of the twin boundary by a distance smaller than λ leads to excess strain energy due to incompatible laminated twins. **d** The excess energy associated with the incompatible structure shown in (**c**) can be reduced by formation of needle twins inside the laminated structure

with large grains exhibit an internal twin/domain microstructure at this length-scale [31, 75, 76]. One such example is given in Sect. 9.4, in which we present a study of crackling noise during a martensitic phase transformation in Cu-Al-Ni single crystal. On the other hand, there are materials with much finer microstructure, e.g., nano-grained materials, in which the microstructural-scale is smaller than the scale of mesoscopic events. In these cases, each mesoscopic-scale event spans over many grains and therefore it is not sensitive to the microstructure. An example for such situation is demonstrated in [77], in which all detected events span over many grains and exhibit a scale-free power-law distribution.

It is worthwhile to compare the orders of magnitude presented in Table 9.1 with the detection capabilities of common methods for measuring avalanche events. Calorimetric measurements with state of the art instruments, which are designed to obtain

the best resolution for small events, and under extremely slow rates (10^{-6}–10^{-5} K/h), are able to detect avalanche events with energy as small as 10^{-5} J (see [9]). This experimental setup has been applied for studying crackling noise during martensitic transformation in Cu-Zn-Al and demonstrated well-separated avalanche events distributed according to a power law within an energy range of 10^{-5}–10^{-2} J [9]. Taking into account the latent heat of Cu-Zn-Al (370 J/mole = 48.7 J/cm^3, [9]), the latter energy range is related to a range of transforming volume of $2 \cdot 10^5$–$2 \cdot 10^8 \mu m^3$. This volume range overlaps with the volume range related to the microstructural-scale events observed in Ni-Mn-Ga (see Table 9.1). Note that in the above mentioned calorimetric studies [9, 10] the martensitic transformation has been induced by a temperature change, which resulted in no preference for a specific martensitic variant. In Sect. 9.4 we present results for stress induced martensitic variant, in which the transformation to a single variant results in a well-ordered microstructure with a characteristic length scale.

Studies which combined calorimetry with AE [10, 78] showed that AE can detect a larger number of avalanche events (at least an order of magnitude). This indicates that AE is more sensitive to smaller events and can detect events typical to the mesoscopic scale in Table 9.1. Setups for AE filter the emitted waves usually in the range of kHz–MHz. As a result, event durations are usually limited to the range of 10^{-6}–10^{-3} s. Therefore, the duration of microstructural-scale events in Ni-Mn-Ga are too long to be detected by AE. It is likely that AE will detect such events as a collection of numerous smaller mesoscopic-scale events. While AE measurements can provide important information on mesoscopic-scale events, they may miss the fact that groups of such events constitute larger microstructural related events.

9.4 Crackling Noise During Twin Boundary Motion in Ni-Mn-Ga

The uniaxial loading curve presented in Fig. 9.3 provides the essential database for a statistical analysis of avalanche events [27]. The identification and evaluation of individual events is based on the following analytical analysis. Under constant displacement rate conditions that are applied by a much stiffer loading frame compared to the tested samples, the total strain ε, which is dictated by the constant displacement rate c, is expressed as the sum of two contributions:

$$\varepsilon = \frac{ct}{L_0} = \frac{\sigma}{Y} + \varepsilon_{trans} \tag{9.13}$$

Here, t represents the elapsed time, L_0 is the sample's initial length along the loading direction and Y is the elastic constant. The first term on the right hand side of (9.13) is the uniform elastic strain while ε_{trans} represents the strain due to the twinning transformation, which in our case occurs through the motion of a single macro twin boundary.

We note that the jerky load profile (a representative part of which is shown in Fig. 9.3b) is composed of alternating linear rising segments and rapid load drop segments. During the linear rising segments the sample responds as a linear elastic material (i.e., deforms uniformly) and ε_{trans} is constant, i.e., the boundary velocity is practically zero. Complementary, when the time derivative of the load is negative, i.e., during the load drop segments where $\dot{\sigma} < 0$, the transformation strain rate exceeds the average value imposed by the external displacement rate, c/L_0. In this case, avalanche events can be characterized by the displacement x_{TB} of the twin boundary, which induces a macroscopic strain change

$$\varepsilon_{trans} = (x_{TB}/L_0) \cdot \varepsilon_T \tag{9.14}$$

where ε_T is the strain associated with such motion (i.e., the twinning strain). Equations (9.13) and (9.14) lead to explicit relations for the boundary's displacement:

$$x_{TB} = \frac{ct}{\varepsilon_T} - \frac{L_0\sigma}{\varepsilon_T E} \tag{9.15}$$

The first step in analyzing the experimental loading curve (Fig. 9.4) is the identification of points along the loading curve, which are associated with the beginning and finish of twin boundary motion events. In the case of saw tooth pattern shown in Fig. 9.3, these points are the local maxima $x_{TB,max,i}$ and minima $x_{TB,min,i}$ points, at which stress is maximal or minimal (see markings in Fig. 9.3b). The difference $x_{TB,max,i} - x_{TB,min,i}$ between adjacent extrema points defines the irreversible twin boundary displacement $\Delta x_{TB,i}$. Next, the distributions of all values of Δx_{TB} are evaluated statistically. Interestingly, the distribution of Δx_{TB} (Fig. 9.5) reveals a clear peak, which represents the most probable value around which the PDF is distributed. The characteristic value of $\Delta x_{TB} \cong 15\,\mu m$ associated with the peak of the PDF, is in excellent agreement with the thickness λ of $a-b$ twinning laminates [52, 64, 69] (see Fig. 9.4). The exact shape of Δx_{TB} distribution is determined by the distribution of the length-scales of the internal microstructure in the Ni-Mn-Ga crystal. Curve fittings of log-normal PDF to the measured distribution exhibits reasonable agreements.

Recalling the values given in Table 9.1, we note that the transformed volume associated with twin boundary advancement by $\Delta x_{TB} \cong 15\,\mu m$ is about $5 \cdot 10^7\,\mu m^3$ (the twin boundary area is about $3\,mm^2$). Based on Table 9.1 and the related discussion, one can expect that a single microstructural-related event is composed of a multitude of much smaller mesoscopic events. Naturally, our experimental resolution does not allow capturing the mesoscopic events, but rather provide some average information over many of them. Yet, we wish to explore what type of information can be obtained on the mesoscopic events based on our experimental results.

To answer the above question we study another variable that characterizes the crackling noise events, i.e., the velocity of the process, v_{TB}. An analytical expression for the velocities of the twin boundary can be directly obtained by taking the time derivative of (9.15):

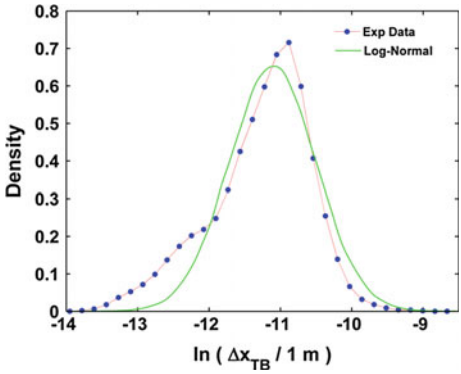

Fig. 9.5 Distribution of twin boundary displacement Δx_{TB} in NiMnGa. Individual values are calculated according to (9.15) and divided by 1 m to obtain unit-less variables. The peaks around which the PDF is distributed reveal a characteristic value that is associated with the internal microstructure. Fittings of the measured distributions to a log-normal function provide R^2 value 0.95

$$\dot{x}_{TB} = v_{TB} = \frac{c}{\varepsilon_T} - \frac{L_0 \dot{\sigma}}{\varepsilon_T Y} \tag{9.16}$$

Equation (9.16) indicates that the velocities of interest (i.e., positive velocity values) take place primarily during the load drop segments of the curves (in which $\dot{\sigma}$ is negative). In addition, we observe that different microstructural-related events of similar total displacement exhibit very different shapes of the displacement versus time curves. This is demonstrated in Fig. 9.6, which shows five representative curves of x_{TB} versus time (curves were calculated based on (9.15)). While all paths describe similar total displacements of 10–20 μm, each exhibits different local variations in the slope, i.e., in the temporal velocity. This observation indicates that the velocity of the twin boundary v_{TB} varies during an individual microstructural-related event, as well as between separate events. Thus, load drops are not accompanied by a single determined "path" in terms of v_{TB}, but rather exhibit noticeable variations, which can be attributed to the existence of many microscopic events. In addition, we notice that the global maximal measured value of v_{TB}, in all measured microstructural-related, is smaller by at least an order of magnitude than the velocity measured under the same driving force but higher loading rates [54]. This means that any temporal measured value of v_{TB} is a contribution of numerous mesoscopic events separated by waiting times which are much longer than the propagation times.

Such behavior motivates a statistical analysis of all temporal values of v_{TB}. Using (9.16), temporal velocities during all load drops along the curves in Fig. 9.3a are calculated and evaluated statistically. The distribution of twin boundary velocity is found to follow a scale invariant power law $p(v_{TB}) \propto {v_{TB}}^{-\alpha}$, with $\alpha = 2.02$, over the vast majority of the measured velocity range (see Fig. 9.7). The small deviation from power law at $v_{TB} > 10^{-4}$ m/s can be attributed to the finite temporal resolution, which may limit our detection capabilities at the higher velocities range or to a deviation

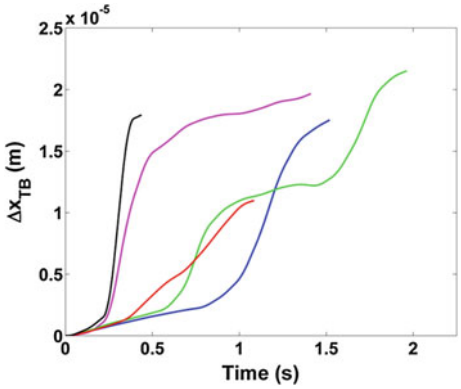

Fig. 9.6 Representative displacement-time paths of a twin boundary in NiMnGa during several microstructural-related events. The paths, marked by different color curves, are calculated using (9.15) for five representative load drops along the stress-time curve

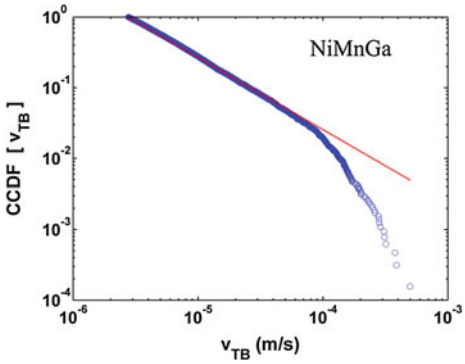

Fig. 9.7 Complementary cumulative distribution functions (CCDF) of temporary velocity values v_{TB}. The *red line* shows a power law statistical trend (color figure online)

from criticality. The distribution of v_{TB} implies that the mesoscopic events follow the monotonously decreasing statistical distributions according to (9.1). Yet, at the larger microstructural-related length scale, our analysis clearly shows that twin boundary motion is influenced by typical microstructural characteristics.

It is also worthwhile to discuss the distribution of the potential energy release rate $\dot{U}_p$, which is related to the magnitude of AE events. We note that the potential (elastic) energy is given by:

$$U_p = AL_0 \frac{\sigma^2}{2Y} \tag{9.17}$$

Taking the time derivatives of both sides in (9.17) results:

$$\dot{U}_p = \frac{AL_0}{Y} \sigma(\dot{\sigma}) \tag{9.18}$$

The nominal stress σ during the load-drop typically varies by less than 10%, while $(\dot{\sigma})$ varies by several orders of magnitude. Thus, to a good approximation, $\dot{U}_p$

is proportional to $(\dot{\sigma})$. Combining (9.16) and (9.18) we get that $\dot{U}_p$ is proportional to v_{TB}, and exhibits the same type of scale-free statistical distribution.

Previous experimental measurements of crackling noise during the phase transformation in NiMnGa exhibited a power law distribution with no signs for a characteristic length scale [79–82]. These observations can be explained taking into account that the austenitic parent phase had no internal twinned microstructure and that the phase transformation took place simultaneously in different places in the crystal.

9.5 Crackling Noise During Martensitic Transformation in Cu-Al-Ni

Materials undergoing stress-induced martensitic transformations are often characterized by a unique internal microstructure at the austenite martensite phase boundary (see, e.g., [66, 83–85]). The microstructure originates from the absence of a coherent interface between the austenite and any single martensite variant. As a result, a laminated structure of two twin-related variants of martensite (see Fig. 9.8) is formed near the phase boundary with the austenite. The lamella thickness ratio, i.e., the ratio between the thicknesses of the "black" and "white" twins in Fig. 9.8, is dictated by average strain compatibility requirements [86, 87]. In addition, the local mismatch strain between the austenite and each of the martensite twin variants results in a local strain energy field. This energy is smaller for a finer twinned structure. However, a finer structure increases the total area of twin boundaries and thus the amount of twin boundary energy. Consequently, there exists a characteristic size for the thickness of a lamella pair (marked as λ in Fig. 9.8a), which minimizes the total energy [86].

Cu-Al-Ni is a widely investigated shape memory material, which undergoes a martensitic transformation. In this alloy, several possible microstructures can form along the austenite-martensite phase boundary (see, e.g., [83, 84, 87–89]). Despite differences between the possible microstructures, all of them contain a laminated twinned structure (similar to that shown in Fig. 9.8a), with a typical lamella-pair thickness that is on the order of few tens of microns [84].

The twinned volume maintains its self-similar strain-compatible structure, as shown in Fig. 9.8b, each time the phase boundary advances by a distance Δx_{PB} that is directly determined by the twin lamella thicknesses. For example, for a lamella-pair thickness ratio of one, $\Delta x_{PB} = \lambda/2\sin\theta$. Contrary, advancement by a distance smaller than Δx_{PB} results in deviations from the equilibrium thickness ratio in the two lamella pairs located at the edges of the phase boundary (pairs 1 and 4 in Fig. 9.8c). This leads to local strain incompatibilities and to an increase in the total strain energy.

An advancement of the phase boundary by Δx_{PB} does not necessarily occur via a uniform propagation of the phase boundary as illustrated in Fig. 9.8b, c. It is more likely that this advancement proceeds through several sub-processes at much smaller scales (e.g., the mesoscopic scale events discussed in Sect. 9.3). These include the nucleation, motion and annihilation of twin boundaries, as well as the local nucleation

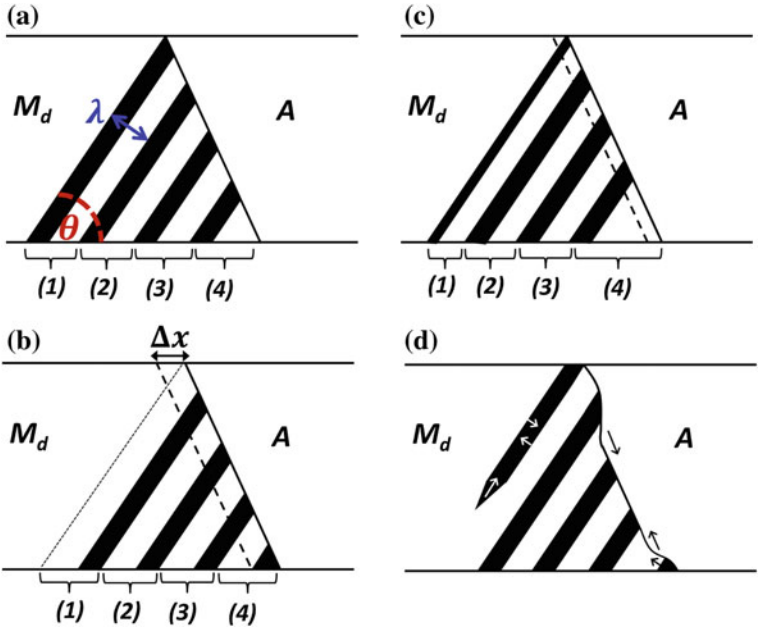

Fig. 9.8 **a** A schematic representation of the interface between a single martensite variant (M_d) and austenite (A) in Cu-Al-Ni single crystal. Near the phase boundary, the martensite forms a laminated twinning structure with a fixed ratio between the two twins ("black" and "white"). The thickness of a pair lamella, which are numbered 1 to 4, is λ. The inclination angle of the twins with regard to the crystal surface is θ. **b** An advancement of the phase boundary by a distance Δx_{PB} that maintains the self-similar structure of the laminated volume and the thickness ratio between the two twinning laminates. **c** An advancement of the phase boundary by a distance smaller than Δx_{PB} leads to strain incompatibilities due to deviations from the optimal thickness ratio in pairs 1 and 4. **d** Possible intermediate sub-processes that occur during the advancement of the phase boundary from state **a** to state **b**. The *small arrows* indicate the direction of motion of twin and phase boundaries

and motion of steps on the austenite-martensite phase boundary (see, for example, the sub-processes sketched in Fig. 9.8d). Yet, the microstructure sketched in Fig. 9.8d has a higher energy than the microstructures sketched in Fig. 9.8a, b. Each of these sub-processes, which can occur simultaneously at different locations along at the phase boundary, is accompanied by a different amount of local strain change, and can proceed at a different rate. In particular, we note that the nucleation and motion of twin boundaries induce significant local strains, due to the twining strain associated with the two types of twin variants. At the same time, an advancement of the phase boundary by Δx_{PB}, from the state illustrated in Fig. 9.8a to the state illustrated in Fig. 9.8b, induces a change in the macroscopic strain $\Delta\varepsilon_{trans}$:

$$\Delta\varepsilon_{trans} = (\Delta x_{PB}/L_0) \cdot \varepsilon_{PT} \tag{9.19}$$

Here, L_0 is the relevant sample's dimension and ε_{PT} is the strain associated with the phase transformation from austenite to a single martensite twin variant.

The above discussion indicates that the martensitic transformation is expected to follow a sequence of locally stable states (e.g., Fig. 9.8a, b), which are dictated by the microstructure of the twinned martensite. Switching between these states is expected to form relatively large jerky events. Yet, within each of these microstructural-related events, the martensitic phase transformation proceeds by a multitude of smaller mesoscopic events that can span over various length and temporal scales.

For the experimental part of the investigation, a prismatic shaped $2.65 \times 2.65 \times 11.5$ mm single crystal of Cu-14.3Al–4.2 Ni (wt. %) is tested (see also [84, 90]). The faces of the crystal are parallel to the {100} planes of the cubic austenite phase. In this crystal, the austenite phase is stable at room temperature ($M_s \approx 10\,^{\circ}\mathrm{C}$). Uniaxial compression along the long axis at room temperature results in a stress induced transformation to a single martensite twin variant, which is preferred by the external load [85]. Optically, it is observed that the stress induced transformation proceeds by the propagation of a single phase boundary along the main axis of the crystal. The resulting stress induced martensite is metastable at room temperature, due to the excess energy associated with the nucleation of the twinned volume at the interphase boundary [90]. Consequently, the reverse transformation to austenite requires heating the crystal to a temperature above 90°C. Several compression experiments are conducted at a constant strain rate of $1.5 \times 10^{-5}\,\mathrm{s}^{-1}$. The load is measured by a 250 kg full scale load cell, and the overall noise level of the measurement system is about ± 0.02 MPa (see inset in Fig. 9.9b).

A typical stress-time curve is shown in Fig. 9.9a, and is characterized by a nominal transformation stress on the order of 100 MPa. The overall strain associated with the transformation of the entire crystal is approximately 8%. Zooming in on the plateau region of the loading curve reveals the existence of fine features (Fig. 9.9b). The features are relatively "smooth" and do not display the distinct saw-tooth pattern as in the case of twin boundary motion in Ni-Mn-Ga. Therefore, our analytical analysis is slightly different and the identification of individual "events" is performed based on the strain rate profile.

Tests are performed under constant velocity of the cross-head bridge, c, that imposes a constant strain rate $\dot{\varepsilon} = c/L_0$. Similar to (9.13), the overall strain is written as:

$$\varepsilon = \frac{ct}{L_0} = \frac{\sigma}{Y} + \varepsilon_{trans} \tag{9.20}$$

where t is the elapsed time, L_0 is the sample's initial length, σ is the stress, Y is the elastic constant, and ε_{trans} represents the strain due to the phase transformation. Taking the time derivative results an expression for the transformation strain rate, $\dot{\varepsilon}_{trans}$:

$$\dot{\varepsilon}_{trans} = \frac{c}{L_0} - \frac{\dot{\sigma}}{Y} \tag{9.21}$$

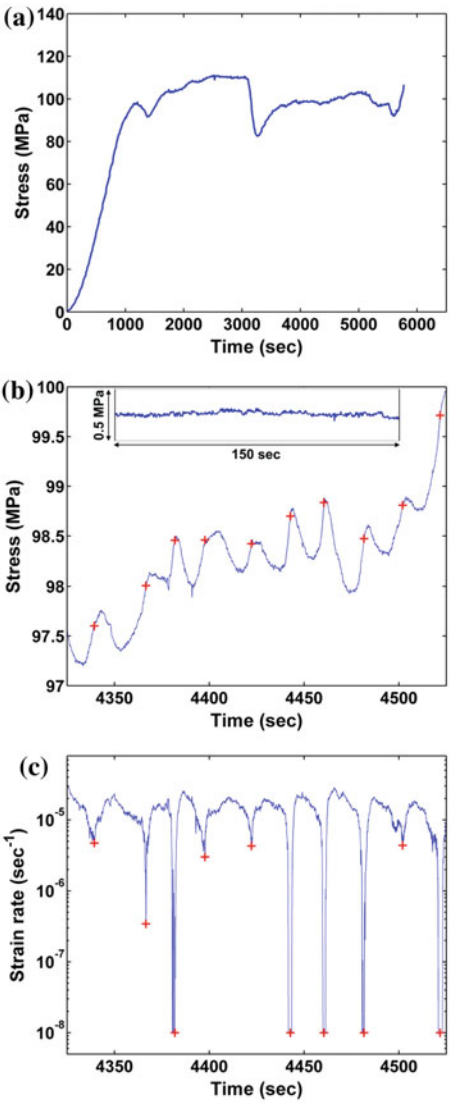

Fig. 9.9 **a** A typical loading curve of a Cu-Al-Ni single crystal. The plateau region corresponds to the stress induced martensite phase transformation. **b** Zoom in on the stress profile showing local variations in the stress along the plateau region. The *inset* at the top shows a typical noise profile of the measurement system, indicating that it is much smaller compared to the local stress variations. **c** Zoom in on the transformation strain rate profile, calculated according to (9.21), shown on a logarithmic scale. The local minima's correspond to instants at which the transformation temporarily halts. The same points are marked also in (**b**), where they correspond to the maximal positive derivative of the stress profile. The locations of these points in the stress profile are used to calculate propagation distances of the phase boundary according to (9.22)

Equation (9.21) allows us to calculate individual values of $\dot{\varepsilon}_{trans}$ over the entire loading profile. A representative portion of the calculated $\dot{\varepsilon}_{trans}$ profile is shown in Fig. 9.9c, revealing a pattern that consists of relatively short periods during which $\dot{\varepsilon}_{trans}$ drops (up to few orders of magnitude) below the average value of $c/L_0 = 1.5 \times 10^{-5}\,\mathrm{s}^{-1}$. These periods are separated by longer periods during which $\dot{\varepsilon}_{trans}$ is higher than c/L_0 and changes in a more moderate manner. The identified minima points in the strain rate profile (Fig. 9.9c) correspond to points in the stress profile where the local (positive) time derivative of the stress is maximal (see Fig. 9.9b).

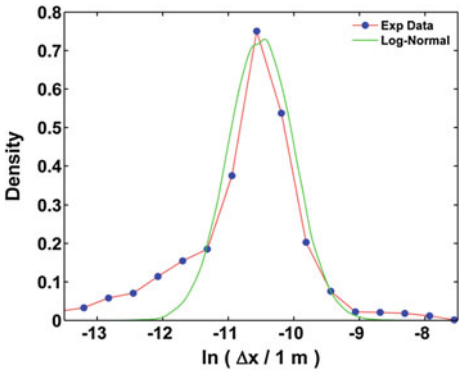

Fig. 9.10 The density function of phase boundary displacements Δx_{PB} during stress induced martensite transformation. The distribution exhibits a log-normal behavior that is centered around a value of about 30 μm

We can assume that the local minima points in the strain rate profile, at which the transformation practically halts, correspond to instances at which the phase boundary has reached a position of local equilibrium, as shown in Fig. 9.8a, b.

The above observation motivates us to calculate the intermediate displacements of the phase boundary Δx_{PB} that take place between sequential minima points in the $\dot{\varepsilon}_{trans}$ profile. The combination of (9.19) and (9.20), provides

$$\Delta x_{PB} = \frac{c}{\varepsilon_{PT}} \Delta t - \frac{L_0}{\varepsilon_{PT} Y} \Delta \sigma \tag{9.22}$$

where Δt and $\Delta \sigma$ are the time and stress differences between these points, respectively. Events with a stress drop larger than 0.06 MPa (i.e., three times the noise level) were taken into account. The PDF of the calculated Δx_{PB} values (see Fig. 9.10) follows a log normal distribution, which is centered around a most probable value of ∼30 μm. This value is in agreement with the typical thickness of the twinning lamellas near the phase boundary [83–85, 89], and indicates on a the direct relation between the microstructure and locally stable states during the phase transformation.

As evident from Fig. 9.9c, the temporal propagations of the phase boundary proceed at strain rates that span several orders of magnitude. Next, we evaluate the statistics of all temporal strain rate values $\dot{\varepsilon}_{trans}$ (calculated according to (9.21)). The resulting PDF of $\dot{\varepsilon}_{trans}$ (see Fig. 9.11) exhibits scale-free behavior and fits well to a power law of the form $(\dot{\varepsilon}_{trans}) \sim \dot{\varepsilon}_{trans}{}^{-\alpha}$, with $\alpha \cong 2.7$, over the majority of the data range. Similar values of α were reported in AE measurements that revealed the crackling noise response during martensitic phase transformation in Cu-Al-Ni alloys [78, 82, 91–93].

The scale-free distribution of $\dot{\varepsilon}_{trans}$ implies that the phase transformation proceeds through a multitude of mesoscopic events that takes place at various scales, smaller than the ∼30 μm value of Δx_{PB}, but larger than the atomistic-scale mechanisms, as discussed in Sect. 9.3. The broad range of strain rate values can be attributed to the various sub-processes, as sketched in Fig. 9.8(d).

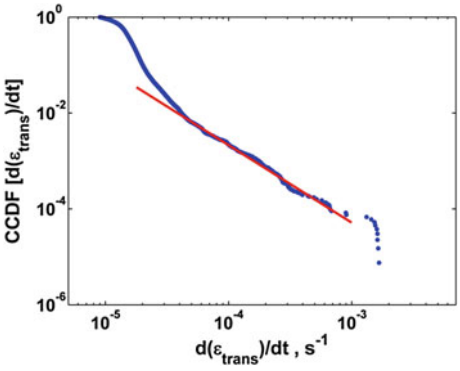

Fig. 9.11 Complementary cumulative density function (CCDF) of the temporary $\dot{\varepsilon}_{trans}$ values, showing scale-less behavior. The *red line* is the best fit of a power law of the form $p\,(\dot{\varepsilon}_{trans}) \sim \dot{\varepsilon}_{trans}{}^{-\alpha}$, with an exponent $\alpha = 2.7$

We note that previous investigations on the dynamics of martensitic phase transformation in Cu-based shape memory alloys using calorimetric and AE measurements (see, e.g., [8–10, 78, 93]), usually revealed power law distributions of the measured variables. The absence of microstructural effects in these works may be attributed to the fact that the martensitic transformation was thermally induced under no mechanical constraints. These loading conditions promote a twinned martensite structure, which evolves from the parent austenite phase through numerous nucleation events at different locations inside the tested volume. These nucleation events may not be affected by the internal microstructure. In our case, the stress induced transformation under uniaxial loading leads to an energy preference of a single twin variant. As a result, a twin laminated structure with a well-defined characteristic thickness is formed near the phase boundary with the austenite, as illustrated in Fig. 9.8. Moreover, stress-induced martensitic transformation at low rates often takes place through the propagation of one (or few) austenite-martensite interphases, as in our case (see, e.g., [94–96]).

In summary, analysis of temporary strain rate during stress induced martensitic transformation in Cu-Al-Ni reveals the influence of the internal microstructure on the crackling noise response. The characteristic size of the twinned microstructure dictates "discrete" μm-scale propagation events of the phase boundary. These microstructural-related events take place through numerous mesoscopic events that display no characteristic scale, and can be correlated to the various sub-processes by which internal interfaces (e.g., twin boundaries) propagate locally at the vicinity of the austenite-martensite phase boundary.

9.6 Crackling Noise During the Collapse of a Stack of Corrugated Fiberboards

Another example of a physical system, which exhibits direct effects of the internal microstructure on crackling noise behavior, is an engineered stack of corrugated fiberboards (for basic details on corrugated fiberboards see [97]). The corrugated

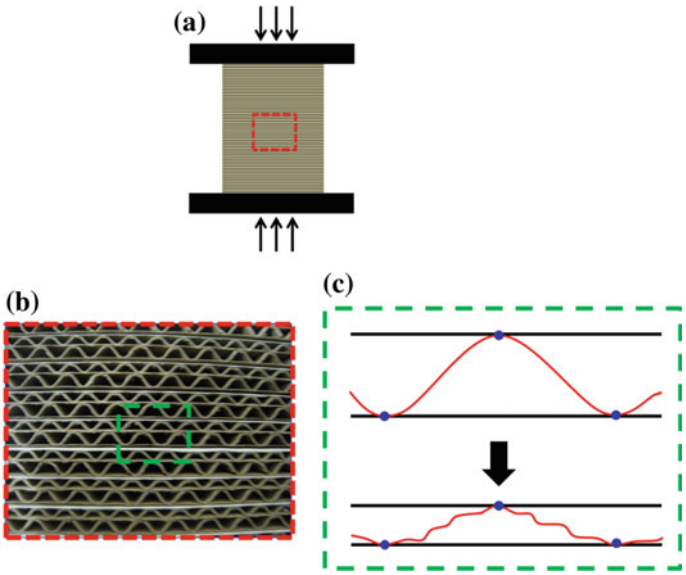

Fig. 9.12 **a** Schematic description of compression setup of an engineered corrugated fiber board structure. The structure consists of 15 identical fiber board sheets with a total initial height of about 100 mm. Each sheet is square shaped, B/C flute commercial type, cut to lateral dimensions of 94×94 mm^2 **b** An optical image of the cardboard structure showing individual sheets with a flute structure. **c** A schematic description of the collapse process of a single layer, which takes place through multiple local buckling events between adjacent anchoring points (marked as *blue circles*) (color figure online)

fiberboard structure (see Fig. 9.12) is characterized by a well-defined length-scale, i.e., the flute size or the thickness of individual layers within the boards. Under uniaxial compression, this structure also exhibits a jerky loading profile (Fig. 9.13a), which is related to local collapses of fluted sheets within the fiberboards.

Compression tests were performed at constant displacement rates of c=5 mm/min (corresponds to strain rate of $8.33 \times 10^{-4}\,\mathrm{s}^{-1}$). Under these conditions, the total displacement of the loaded sample u is given by

$$u = ct = \frac{F}{k} + u_p \tag{9.23}$$

where t represents the elapsed time. The first term on the right hand side of (9.23) is the uniform elastic deformation, where F and k are the instantaneous force and stiffness of the loaded sample, respectively. The term u_p represents the local "plastic" displacement, i.e., the displacement due to the collapse of individual fiberboards. Rearranging (9.23) results an expression for u_p:

$$u_p = ct - \frac{F}{k} \tag{9.24}$$

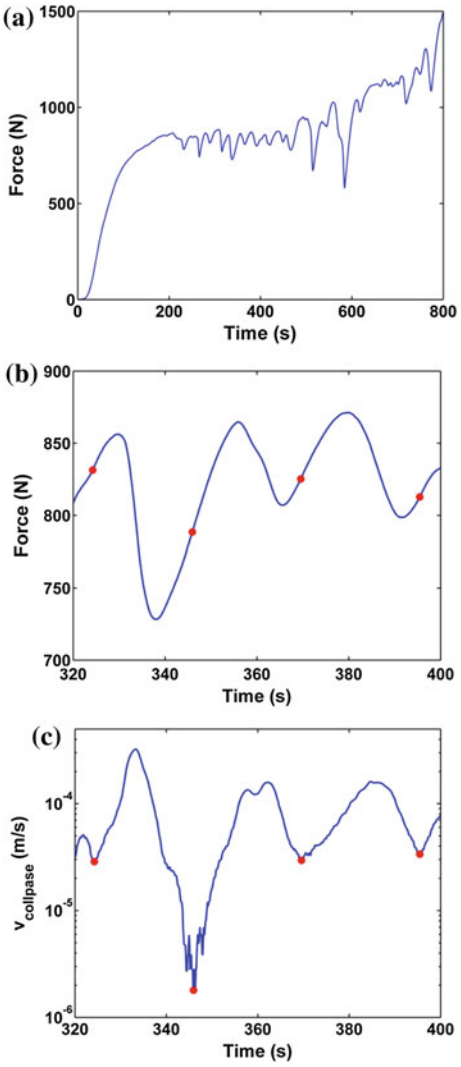

Fig. 9.13 **a** A typical compression loading curve of a stack of corrugated fiberboards. **b** Zooming in reveals local variations in the load profile. **c** The corresponding velocity profile of the collapse process ((9.25), shown on a logarithmic scale) is characterized by local minima that are used for the identification of individual events. The temporal locations of these minima points are marked by red points, and are shown also on the load profile in (**b**)

As in the case of the Cu-Al-Ni system, the jerky loading curve of the corrugated fiberboards does not exhibit sharp saw tooth pattern but rather smooth variations of the force (see Fig. 9.13). Consequently, individual collapse events are identified based on local minima of the plastic-displacement rate profile (see Fig. 9.13c), i.e., time periods at which the velocity of the collapse process is substantially lower compared to the majority of data points. The displacement rate profile is obtained by taking the time derivatives of (9.24):

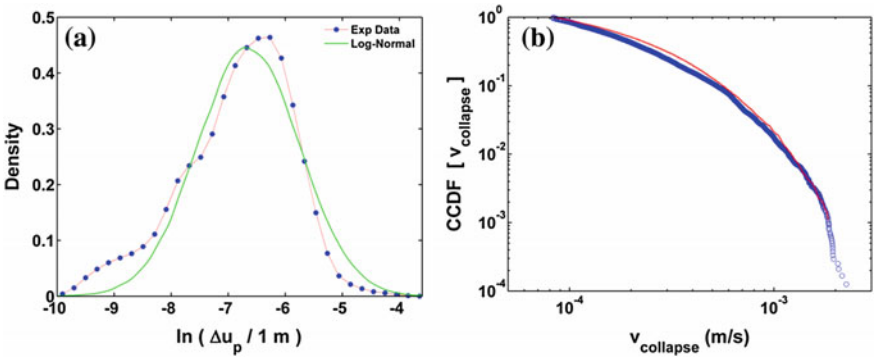

Fig. 9.14 **a** PDF of fiberboard displacements that take place during individual events marked in Fig. 9.13. The distribution is well fitted by a log normal function and is centered around a most probable value that is directly related to the internal structure of the fiberboard stack. **b** Complementary cumulative distribution function of the temporal velocities during the collapse process, showing a stretched exponential type distribution

$$\dot{u}_p = v_{collapse} = c - \frac{\dot{F}}{k} \tag{9.25}$$

We note that the local minima in the velocity profile are not as "sharp" as in the case of the Cu-Al-Ni (compare Figs. 9.9c and 9.13c). This indicates that the time periods during which the collapse velocity of the fiberboard stack is either slower or higher than the average value are comparable.

The distribution of irreversible displacements that take place within individual events (calculated using (9.24) for ten similar experiments) reveal a clear peak, which represents the most probable value around which the PDF is distributed. The characteristic values of $\Delta u_p = 1.5$–2.5 mm is excellent agreement with the thickness of an individual layer in the corrugated structure. Curve fitting of log-normal PDF to the measured distribution exhibit reasonable agreement.

Similar to the previous systems, we evaluate the temporary velocity values, i.e., all values obtained by (9.25) and shown graphically in Fig. 9.13c. Such an analysis results a distribution that follows a stretched exponential function (9.3), with $\beta = 0.74$. This implies that each microstructural related event, which is associated with a collapse of a complete fiberboard layer, is composed of a multitude of much smaller (mesoscopic) events (see, e.g., the schematic in Fig. 9.12c), that may span several orders of magnitude and follow a scale–less, monotonously decreasing, distribution function (Fig. 9.14).

9.7 Summary

This work unfolds the effects of an internal microstructure on the dynamics of systems undergoing crackling noise phenomena. We show experimental evidences for such effects in three different physical systems that are characterized by an internal microstructure. In all the investigated systems, the mechanical process proceeds through numerous events at different length, energy and time scales. These originate from the different energy barriers that separate metastable states and resist the overall process. In the cases of twin boundary motion in Ni-Mn-Ga and the stress induced martensitic phase transformation in Cu-Al-Ni, we identify atomistic and μm-scale events that originate from the lattice barrier and the fine twinned microstructure, respectively. While atomistic events (or rather mesoscopic events that contain a multitude of atomistic events) follow typical scale-less statistics over several orders of magnitude, the μm-scale events are dictated by a characteristic length scale that is directly related to the internal microstructure. A similar observation, only at larger length scales, is demonstrated for a stack of corrugated fiberboards undergoing mechanical collapse. In this system, the internal layered microstructure dictates mm-size events, which proceed through a multitude of smaller local collapse events.

This work demonstrates the ability to extract important physical insights from crackling noise experimental data through identification and quantitative analysis of different variables. This allows quantifying microstructural effects on crackling behavior, which contribute to a better understanding of the physical mechanisms that are responsible for this unique and important behavior in a variety of physical systems at various scales. We believe that this approach provides new perspectives on crackling noise phenomena and promotes further theoretical and experimental work on other physical systems.

Acknowledgments This research was supported by the Israel Science Foundation (grant No. 1268/14).

References

1. E.K.H. Salje, K.A. Dahmen, Crackling noise in disordered materials. Annu. rev. condens. matter phys. **5**(1), 233–254 (2014). doi:10.1146/annurev-conmatphys-031113-133838
2. J.P. Sethna, K.A. Dahmen, C.R. Myers, Crackling noise. Nature **410**(6825), 242–250 (2001)
3. P.A. Houle, J.P. Sethna, Acoustic emission from crumpling paper. Phys. Rev. E **54**(1), 278–283 (1996)
4. J.P. Sethna, Statistical mechanics: crackling crossover. Nat. Phys. **3**(8), 518–519 (2007)
5. J. Baró, Á. Corral, X. Illa, A. Planes, E.K.H. Salje, W. Schranz, D.E. Soto-Parra, E. Vives, Statistical similarity between the compression of a porous material and earthquakes. Phys. Rev. Lett. **110**(8), 088702 (2013)
6. E.K.H. Salje, D.E. Soto-Parra, A. Planes, E. Vives, M. Reinecker, W. Schranz, Failure mechanism in porous materials under compression: crackling noise in mesoporous SiO2. Philos. Mag. Lett. **91**(8), 554–560 (2011). doi:10.1080/09500839.2011.596491

7. P.O. Castillo-Villa, J. Baró, A. Planes, E.K.H. Salje, P. Sellappan, W.M. Kriven, Crackling noise during failure of alumina under compression: the effect of porosity. J. Phys. Condens. Matter **25**(29), 292202 (2013)
8. E. Vives, J. Ortín, L. Mañosa, I. Ràfols, R. Pérez-Magrané, A. Planes, Distributions of avalanches in martensitic transformations. Phys. Rev. Lett. **72**(11), 1694–1697 (1994)
9. F.J. Romero, J. Manchado, J.M. Martín-Olalla, M.C. Gallardo, E.K.H. Salje, Dynamic heat flux experiments in $Cu_{67.64}Zn_{16.71}Al_{15.65}$: separating the time scales of fast and ultra-slow kinetic processes in martensitic transformations. Appl. Phys. Lett. **99**(1), 011906 (2011). doi:10.1063/1.3609239
10. M.C. Gallardo, J. Manchado, F.J. Romero, J. del Cerro, E.K.H. Salje, A. Planes, E. Vives, R. Romero, M. Stipcich, Avalanche criticality in the martensitic transition of $Cu_{67.64}Zn_{16.71}Al_{15.65}$ shape-memory alloy: a calorimetric and acoustic emission study. Phys. Rev. B **81**(17), 174102 (2010)
11. J. Antonaglia, W.J. Wright, X. Gu, R.R. Byer, T.C. Hufnagel, M. LeBlanc, J.T. Uhl, K.A. Dahmen, Bulk metallic glasses deform via slip avalanches. Phys. Rev. Lett. **112**(15), 155501 (2014)
12. F.F. Csikor, C. Motz, D. Weygand, M. Zaiser, S. Zapperi, Dislocation avalanches, strain bursts, and the problem of plastic forming at the micrometer scale. Science **318**(5848), 251–254 (2007). doi:10.1126/science.1143719
13. R.M. Costello, K.L. Cruz, C. Egnatuk, D.T. Jacobs, M.C. Krivos, T.S. Louis, R.J. Urban, H. Wagner, Self-organized criticality in a bead pile. Phys. Rev. E **67**(4), 041304 (2003)
14. A. Clauset, C. Shalizi, M. Newman, Power-law distributions in empirical data. Siam rev. **51**(4), 661–703 (2009). doi:10.1137/070710111
15. Y. Virkar, A. Clauset, Power-law distributions in binned empirical data. Ann. Appl. Stat. **1**, 89–119 (2014). doi:10.1214/13-aoas710
16. X. Ding, T. Lookman, Z. Zhao, A. Saxena, J. Sun, E.K.H. Salje, Dynamically strained ferroelastics: statistical behavior in elastic and plastic regimes. Phys. Rev. B **87**(9), 094109 (2013)
17. N. Friedman, A.T. Jennings, G. Tsekenis, J.-Y. Kim, M. Tao, J.T. Uhl, J.R. Greer, K.A. Dahmen, Statistics of dislocation slip avalanches in nanosized single crystals show tuned critical behavior predicted by a simple mean field model. Phys. Rev. Lett. **109**(9), 095507 (2012)
18. J. Laherrere, D. Sornette, Stretched exponential distributions in nature and economy: "fat tails" with characteristic scales. Eur. Phys. J. B **2**(4), 525–539 (1998). doi:10.1007/s100510050276
19. M.J. Aschwanden, *Self-Organized Criticality Systems* (Open Academic Press, Berlin, 2013)
20. P. Bak, C. Tang, K. Wiesenfeld, Self-organized criticality: an explanation of the 1/*f* noise. Phys. Rev. Lett. **59**(4), 381–384 (1987)
21. P. Bak, C. Tang, K. Wiesenfeld, Self-organized criticality. Phys. Rev. A **38**(1), 364–374 (1988)
22. F.-J. Pérez-Reche, L. Truskinovsky, G. Zanzotto, Driving-induced crossover: from classical criticality to self-organized criticality. Phys. Rev. Lett. **101**(23), 230601 (2008)
23. Z. Zhao, X. Ding, J. Sun, E.K.H. Salje, Thermal and athermal crackling noise in ferroelastic nanostructures. J. Phys. Condens. Matter **26**(14), 142201 (2014)
24. A. Travesset, R.A. White, K.A. Dahmen, Crackling noise, power spectra, and disorder-induced critical scaling. Phys. Rev. B **66**(2), 024430 (2002)
25. K.A. Dahmen, Y. Ben-Zion, J.T. Uhl, Micromechanical model for deformation in solids with universal predictions for stress-strain curves and slip avalanches. Phys. Rev. Lett. **102**(17), 175501 (2009)
26. J. Antonaglia, X. Xie, G. Schwarz, M. Wraith, J. Qiao, Y. Zhang, P.K. Liaw, J.T. Uhl, K.A. Dahmen, Tuned critical avalanche scaling in bulk metallic glasses. Sci. Rep. **4**, 1 (2014). doi:10.1038/srep04382. http://www.nature.com/srep/2014/140317/srep04382/abs/srep04382.html#supplementary-information
27. E. Faran, E.K.H. Salje, D. Shilo, The exploration of the effect of microstructure on crackling noise systems. Appl. Phys. Lett. **107**(7), 071902 (2015). doi:10.1063/1.4928928
28. E. Faran, H. Seiner, M. Landa, D. Shilo, The effects of microstructure on crackling noise during martensitic transformation in Cu-Al-Ni. Appl. Phys. Lett. **107**(17), 171601 (2015). doi:10.1063/1.4934694

29. V.A. Chernenko, E. Cesari, V.V. Kokorin, I.N. Vitenko, The development of new ferromagnetic shape memory alloys in Ni-Mn-Ga system. Scripta Metallurgica et Materialia **33**(8), 1239–1244 (1995). doi:10.1016/0956-716X(95)00370-B
30. R.D. James, M. Wuttig, Magnetostriction of martensite. Philos. Mag. A **77**(5), 1273–1299 (1998). doi:10.1080/01418619808214252
31. E.K. Salje, *Phase Transitions in Ferroelastic and Co-elastic Crystals* (Cambridge University Press, Cambridge, 1993)
32. K. Bhattacharya, *Microstructure of Martensite* (Oxford University Press, Oxford, 2003)
33. O.Y. Kanner, D. Shilo, J. Sheng, R.D. James, Y. Ganor, Ferromagnetic shape memory flapper for remotely actuated propulsion systems. Smart Mater. Struct. **22**(8), 085030 (2013)
34. A. Nespoli, S. Besseghini, S. Pittaccio, E. Villa, S. Viscuso, The high potential of shape memory alloys in developing miniature mechanical devices: a review on shape memory alloy mini-actuators. Sens. Actuators A: Phys. **158**(1), 149–160 (2010). doi:10.1016/j.sna.2009.12.020
35. J. Mohd Jani, M. Leary, A. Subic, M.A. Gibson, A review of shape memory alloy research, applications and opportunities. Mater. Des. **56**, 1078–1113 (2014). doi:10.1016/j.matdes.2013.11.084
36. Y. Ganor, D. Shilo, N. Zarrouati, R.D. James, Ferromagnetic shape memory flapper. Sens. Actuators A: Phys. **150**(2), 277–279 (2009). doi:10.1016/j.sna.2009.01.001
37. E. Pagounis, A. Laptev, J. Jungwirth, M. Laufenberg, M. Fonin, Magnetomechanical properties of a high-temperature Ni-Mn-Ga magnetic shape memory actuator material. Scr. Mater. **88**, 17–20 (2014). doi:10.1016/j.scriptamat.2014.06.013
38. J.M. Stephan, E. Pagounis, M. Laufenberg, O. Paul, P. Ruther, A novel concept for strain sensing based on the ferromagnetic shape memory alloy NiMnGa. Sens. J. IEEE **11**(11), 2683–2689 (2011). doi:10.1109/JSEN.2011.2157489
39. E. Pagounis, R. Chulist, M.J. Szczerba, M. Laufenberg, High-temperature magnetic shape memory actuation in a Ni-Mn-Ga single crystal. Scr. Mater. **83**, 29–32 (2014). doi:10.1016/j.scriptamat.2014.04.001
40. R. Abeyaratne, J.K. Knowles, *Evolution of Phase Transitions: A Continuum Theory*, vol. v. 10 (Cambridge University Press, Cambridge, 2006)
41. D. Mordehai, E. Clouet, M. Fivel, M. Verdier, Introducing dislocation climb by bulk diffusion in discrete dislocation dynamics. Philos. Mag. **88**(6), 899–925 (2008). doi:10.1080/14786430801992850
42. Y. Ezer, O. Sozinov, L. Straka, A. Soroka, N. Lanska, Magnetic Shape Memory Alloys and Specimens Thereof. European Patent Number EP2710161: Filing Date: 21.05.2012, Publication Date: 2029.2011.2012 (2012)
43. E. Faran, D. Shilo, The kinetic relation for twin wall motion in NiMnGa. J. Mech. Phys. Solids **59**(5), 975–987 (2011). doi:10.1016/j.jmps.2011.02.009
44. E. Faran, D. Shilo, The kinetic relation for twin wall motion in NiMnGa–part 2. J. Mech. Phys. Solids **61**(3), 726–741 (2013). doi:10.1016/j.jmps.2012.11.004
45. E. Faran, D. Shilo, Dynamics of twin boundaries in ferromagnetic shape memory alloys. Mater. Sci. Technol. **30**(13a), 1545–1558 (2014). doi:10.1179/1743284714Y.0000000570
46. R. Abeyaratne, C. Chu, R.D. James, Kinetics of materials with wiggly energies: theory and application to the evolution of twinning microstructures in a Cu-Al-Ni shape memory alloy. Philos. Mag. A **73**(2), 457–497 (1996). doi:10.1080/01418619608244394
47. F. Hildebrand, R. Abeyaratne, An atomistic investigation of the kinetics of detwinning. J. Mech. Phys. Solids **56**(4), 1296–1319 (2008). doi:10.1016/j.jmps.2007.09.006
48. W.T. Lee, E.K.H. Salje, L. Goncalves-Ferreira, M. Daraktchiev, U. Bismayer, Intrinsic activation energy for twin-wall motion in the ferroelastic perovskite $CaTiO_3$. Phys. Rev. B **73**(21), 214110 (2006)
49. D.I. Paul, W. McGehee, R.C. O'Handley, M. Richard, Ferromagnetic shape memory alloys: a theoretical approach. J. Appl. Phys. **101**(12), 123917 (2007). doi:10.1063/1.2740328
50. D.I. Paul, R.C. O'Handley, B. Peterson, Ferromagnetic shape memory alloys: theory of interactions. J. Appl. Phys. **97**(10), 10M312 (2005). doi:10.1063/1.1854871

51. M. Chmielus, K. Rolfs, R. Wimpory, W. Reimers, P. Müllner, R. Schneider, Effects of surface roughness and training on the twinning stress of Ni-Mn-Ga single crystals. Acta Mater. **58**(11), 3952–3962 (2010). doi:10.1016/j.actamat.2010.03.031
52. O. Heczko, L. Straka, H. Seiner, Different microstructures of mobile twin boundaries in 10M modulated Ni-Mn-Ga martensite. Acta Mater. **61**(2), 622–631 (2013). doi:10.1016/j.actamat.2012.10.007
53. E. Faran, D. Shilo, Multi-scale dynamics of twinning in SMA. Shape Mem. Superelasticity **1**, 180–190 (2015). doi:10.1007/s40830-015-0012-5
54. E. Faran, D. Shilo, Implications of twinning kinetics on the frequency response in NiMnGa actuators. Appl. Phys. Lett. **100**(15), 151901–151904 (2012)
55. S.A. Kibey, L.L. Wang, J.B. Liu, H.T. Johnson, H. Sehitoglu, D.D. Johnson, Quantitative prediction of twinning stress in fcc alloys: application to Cu-Al. Phys. Rev. B **79**(21), 214202 (2009)
56. S. Kibey, H. Sehitoglu, D.D. Johnson, Energy landscape for martensitic phase transformation in shape memory NiTi. Acta Mater. **57**(5), 1624–1629 (2009). doi:10.1016/j.actamat.2008.12.008
57. F.E. Hildebrand, R. Abeyaratne, An atomistic investigation of the kinetics of detwinning. J. Mech. Phys. Solids **56**(4), 1296–1319 (2008). doi:10.1016/j.jmps.2007.09.006
58. L. Truskinovsky, A. Vainchtein, Peierls-Nabarro landscape for martensitic phase transitions. Phys. Rev. B **67**(17), 172103 (2003)
59. R.C. Pond, S. Celotto, Special interfaces: military transformations. Int. Mater. Rev. **48**(4), 225–245 (2003). doi:10.1179/095066003225010245
60. J.M. Howe, R.C. Pond, J.P. Hirth, The role of disconnections in phase transformations. Prog. Mater. Sci. **54**(6), 47–47 (2009). doi:10.1016/j.pmatsci.2009.04.001
61. R. Peierls, The size of a dislocation. Proc. Phys. Soc. **52**(1), 34 (1940)
62. D.I. Paul, W. McGehee, R.C. O'Handley, M. Richard, Ferromagnetic shape memory alloys: a theoretical approach. J. Appl. Phys. **101**(12) (2007). doi:10.1063/1.2740328
63. M. Chmielus, I. Glavatskyy, J.-U. Hoffmann, V.A. Chernenko, R. Schneider, P. Müllner, Influence of constraints and twinning stress on magnetic field-induced strain of magnetic shape-memory alloys. Scr. Mater. **64**(9), 888–891 (2011). doi:10.1016/j.scriptamat.2011.01.025
64. L. Straka, O. Heczko, H. Seiner, N. Lanska, J. Drahokoupil, A. Soroka, S. Fähler, H. Hänninen, A. Sozinov, Highly mobile twinned interface in 10M modulated Ni-Mn-Ga martensite: analysis beyond the tetragonal approximation of lattice. Acta Mater. **59**(20), 7450–7463 (2011). doi:10.1016/j.actamat.2011.09.020
65. O. Heczko, J. Kopeček, L. Straka, H. Seiner, Differently mobile twin boundaries and magnetic shape memory effect in 10M martensite of Ni-Mn-Ga. Mater. Res. Bull. (2013). doi:10.1016/j.materresbull.2013.04.034
66. H. Seiner, L. Straka, O. Heczko, A microstructural model of motion of macro-twin interfaces in Ni-Mn-Ga 10M martensite. J. Mech. Phys. Solids **64**, 198–211 (2014). doi:10.1016/j.jmps.2013.11.004
67. Y.W. Lai, N. Scheerbaum, D. Hinz, O. Gutfleisch, R. Schafer, L. Schultz, J. McCord, Absence of magnetic domain wall motion during magnetic field induced twin boundary motion in bulk magnetic shape memory alloys. Appl. Phys. Lett. **90**(19), 192503–192504 (2007)
68. E. Faran, I. Benichou, S. Givli, D. Shilo, The effects of internal microstructures on barriers for twinning reorientation in Ni-Mn-Ga. J. Appl. Phys. (submitted)
69. R. Chulist, L. Straka, N. Lanska, A. Soroka, A. Sozinov, W. Skrotzki, Characterization of mobile type I and type II twin boundaries in 10M modulated Ni-Mn-Ga martensite by electron backscatter diffraction. Acta Mater. **61**(6), 1913–1920 (2013). doi:10.1016/j.actamat.2012.12.012
70. H. Seiner, L. Straka, O. Heczko, A microstructural model of motion of macro-twin interfaces in Ni-Mn-Ga 10 M martensite. J. Mech. Phys. Solids **64**, 198–211 (2014). doi:10.1016/j.jmps.2013.11.004
71. L. Dai, Intermartensitic transformation in a NiMnGa alloy. J. Appl. Phys. **95**(11), 6957 (2004). doi:10.1063/1.1687203

72. N. Glavatska, G. Mogylny, I. Glavatskiy, V. Gavriljuk, Temperature stability of martensite and magnetic field induced strain in Ni-Mn-Ga. Scr. Mater. **46**(8), 605–610 (2002). doi:10.1016/S1359-6462(02)00019-2
73. E.K.H. Salje, X. Ding, Z. Zhao, T. Lookman, A. Saxena, Thermally activated avalanches: jamming and the progression of needle domains. Phys. Rev. B **83**(10), 104109 (2011)
74. R.J. Harrison, E.K.H. Salje, Ferroic switching, avalanches, and the Larkin length: needle domains in LaAlO3. Appl. Phys. Lett. **99**(15), 151915 (2011). doi:10.1063/1.3650475
75. K. Otsuka, X. Ren, Physical metallurgy of Ti-Ni-based shape memory alloys. Prog. Mater. Sci. **50**(5), 511–678 (2005). doi:10.1016/j.pmatsci.2004.10.001
76. K. Otsuka, C.M. Wayman, *Shape Memory Materials* (Cambridge University Press, Cambridge, 1999)
77. D.-H. Kim, S.-B. Choe, S.-C. Shin, Direct observation of barkhausen avalanche in Co thin films. Phys. Rev. Lett. **90**(8), (2003). doi:10.1103/PhysRevLett.90.087203
78. F.-J. Pérez-Reche, M. Stipcich, E. Vives, L. Mañosa, A. Planes, M. Morin, Kinetics of martensitic transitions in Cu-Al-Mn under thermal cycling: analysis at multiple length scales. Phys. Rev. B **69**(6), 064101 (2004)
79. R. Niemann, J. Baró, O. Heczko, L. Schultz, S. Fähler, E. Vives, L. Mañosa, A. Planes, Tuning avalanche criticality: acoustic emission during the martensitic transformation of a compressed Ni-Mn-Ga single crystal. Phys. Rev. B **86**(21), 214101 (2012)
80. Z. Balogh, L. Daróczi, L. Harasztosi, D. Beke, T.A. Lograsso, D.L. Schlagel, Magnetic emission during austenite-martensite transformation in Ni2MnGa shape memory alloy. Mater. Trans. **47**(3), 631–634 (2006). doi:10.2320/matertrans.47.631
81. J. Baró, S. Dixon, R.S. Edwards, Y. Fan, D.S. Keeble, L. Mañosa, A. Planes, E. Vives, Simultaneous detection of acoustic emission and Barkhausen noise during the martensitic transition of a Ni-Mn-Ga magnetic shape-memory alloy. Phys. Rev. B **88**(17), 174108 (2013)
82. R. Niemann, J. Kopecek, O. Heczko, J. Romberg, L. Schultz, S. Fähler, E. Vives, L. Mañosa, A. Planes, Localizing sources of acoustic emission during the martensitic transformation. Phys. Rev. B **89**(21), 214118 (2014)
83. H. Seiner, M. Landa, Non-classical austenite-martensite interfaces observed in single crystals of Cu-Al-Ni. Phase Transit. **82**(11), 793–807 (2009). doi:10.1080/01411590903366160
84. H. Seiner, P. Sedlák, M. Landa, Shape recovery mechanism observed in single crystals of Cu-Al-Ni shape memory alloy. Phase Transit. **81**(6), 537–551 (2008). doi:10.1080/01411590801891616
85. V. Novák, P. Šittner, S. Ignacová, T. Černoch, Transformation behavior of prism shaped shape memory alloy single crystals. Mater. Sci. Eng. A **438–440**, 755–762 (2006). doi:10.1016/j.msea.2006.02.192
86. K. Bhattacharya, Microstructure of Martensite: Why it Forms and how it Gives Rise to the Shape-memory Effect. OUP Oxford (2003)
87. T.W. Shield, Orientation dependence of the pseudoelastic behavior of single crystals of Cu-Al-Ni in tension. J. Mech. Phys. Solids **43**(6), 869–895 (1995). doi:10.1016/0022-5096(95)00011-7
88. C. Chu, R.D. James analysis of microstructures in Cu-14.0%Al-3.9%Ni by Energy Minimization. J Phys IV France **05**(C8), C8-143-C148-149 (1995)
89. H. Seiner, O. Glatz, M. Landa, Interfacial microstructures in martensitic transitions: from optical observations to mathematical modeling. Int. J. Multiscale Comput. Eng. **7**(5), 445–456 (2009). doi:10.1615/IntJMultCompEng.v7.i5.60
90. J.M. Ball, K. Koumatos, H. Seiner, Nucleation of austenite in mechanically stabilized martensite by localized heating. J. Alloys Compd. 577 Suppl. **1**, S37–S42 (2013). doi:10.1016/j.jallcom.2011.11.070
91. M. Landa, V. Novak, M. Blahacek, P. Sittner, Transformation processes in shape memory alloys based on monitoring acoustic emission activity. J. Acoust. Emiss. **20**, 163–171 (2002)
92. L. Carrillo, L. Mañosa, J. Ortín, A. Planes, E. Vives, Experimental evidence for universality of acoustic emission avalanche distributions during structural transitions. Phys. Rev. Lett. **81**(9), 1889–1892 (1998)

93. F.-J. Pérez-Reche, B. Tadić, L. Mañosa, A. Planes, E. Vives, Driving rate effects in avalanche-mediated first-order phase transitions. Phys. Rev. Lett. **93**(19), 195701 (2004)
94. J.A. Shaw, S. Kyriakides, Thermomechanical aspects of NiTi. J. Mech. Phys. Solids **43**(8), 1243–1281 (1995). doi:10.1016/0022-5096(95)00024-D
95. J.A. Shaw, S. Kyriakides, On the nucleation and propagation of phase transformation fronts in a NiTi alloy. Acta Mater. **45**(2), 683–700 (1997). doi:10.1016/S1359-6454(96)00189-9
96. K. Kim, S. Daly, Martensite strain memory in the shape memory alloy Nickel-Titanium under mechanical cycling. Exp. Mech. **51**(4), 641–652 (2011). doi:10.1007/s11340-010-9435-2
97. Wikipedia, Corrugated fiberboard. (2015). https://en.wikipedia.org/wiki/Corrugated_fiberboard

Chapter 10
Mechanical Deformation in Metallic Liquids and Glasses: From Atomic Bond-Breaking to Avalanches

T. Egami, Y. Fan and T. Iwashita

Abstract The atomistic mechanism of deformation in metallic liquids and glasses is discussed from the view point of local topology of atomic connectivity, based mainly on the results of computer simulation. In crystals the topology of atomic connectivity network is fixed, and deviation from it defines lattice defects. In liquids and glasses, however, the topology is open and flexible, and fluctuates in time and space. We focus on the action of atomic bond being cut or formed, which changes the local topology of atomic connectivity, and discuss how the bond cutting and forming determine viscosity of liquids. We then discuss how collectivity of such actions, including shear-transformation-zone (STZ) and their avalanche, governs the macroscopic deformation behavior in supercooled liquids and glasses. The collectivity of topological change is directly connected to the local potential energy landscape (PEL), particularly the density of the local minima in PEL. The density of PEL minima defines the effective temperature, and is influenced by processing conditions, such as cooling rate through the glass transition. The description of the structure and dynamics of liquids and glasses through local topology of atomic connectivity and the atomic-level stress could advance the field to the level the current mean-field approach would not be able to attain.

T. Egami (✉) · T. Iwashita
Joint Institute for Neutron Sciences and Department of Materials Science and Engineering, University of Tennessee, Knoxville, TN 37996, USA
e-mail: egami@utk.edu

T. Iwashita
e-mail: tiwashit@utk.edu

T. Egami
Department of Physics and Astronomy, University of Tennessee, Knoxville, TN 37996, USA

T. Egami · Y. Fan
Oak Ridge National Laboratory, Oak Ridge, TN 37831, USA
e-mail: fany@ornl.gov

E.K.H. Salje et al. (eds.), *Avalanches in Functional Materials and Geophysics*, Understanding Complex Systems, DOI 10.1007/978-3-319-45612-6_10

10.1 Introduction

In crystalline materials mechanical deformation occurs through motion of lattice defects, such as dislocations and vacancies. However, in glasses and liquids defects cannot be easily defined because of extensive structural disorder, and consequently it is more difficult to discuss how deformation takes place at the atomic level. At present the concept of shear-transformation-zone (STZ) is the most successful approach in explaining mechanical deformation in metallic glasses [1–3], but the microscopic details of STZ remain elusive.

The most persistent and dangerous obstacle in developing understanding of the glassy state could be our tendency to apply our approaches developed for crystalline materials directly to glasses, rather than developing a new description unique to liquids and glasses. The concept of defect is one of such examples. In crystalline materials defects can readily be identified as local deviations from the lattice periodicity. In liquids and glassy materials defects cannot be uniquely defined in the absence of the reference structure. Of course because of the structural heterogeneity the response to shear stress varies from place to place, and one can find correlations between local properties, such as local softness, and the start of plastic deformation [4–8]. However, such correlations are usually weak. Furthermore efforts to ascribe local weakness to particular structural features have been largely futile. Given a structural model it still is virtually impossible to predict where the next plastic deformation event will start. In other words, it is impossible to tell where the STZs are in a structural model. Then the logical conclusion is that STZ does not pre-exist; STZ is recognized *only after* deformation happens. Therefore STZ formation is an *emergent process*. This emergent nature of deformation and STZ was recognized by early leaders [1, 3, 9] and was suggested in a recent work [10], but it is often misunderstood or unrecognized in the community at large.

A major reason why deformation is an emergent process is the fact that the local atomic displacements involved in plastic deformation are relatively large in magnitude. For each local deformation event some atoms move as much as 1 Å or more [11, 12]. Such a distance is way out of the range of applicability of linear elasticity, whereas various concepts we use, such as strain or elastic modulus, are based upon linear expansion with infinitesimal strain increment. Furthermore a number of atoms are involved in the process, and the many-body nature of the process makes it virtually impossible to predict the course of event before it happens. The structure before deformation is quite different from the structure after. The process of local plastic deformation is much closer to a chaotic process than one would assume. This is very different from what happens in a crystalline material. One can easily recognize the motion of a dislocation in a crystal, because the local structure of a dislocation is the same before and after the motion because of lattice periodicity. In glasses, however, the structure is different from place to place, and every action of atomic rearrangement produces different outcome. Details of the process of deformation, therefore, are different each time.

In this article we discuss our recent progress on this subject based upon the concept of the dynamics of local topology of atomic connectivity, derived mainly from the results of computer simulation. The mechanism of deformation in glasses is a subject which has been discussed by many researchers. Also the concept of atomic connectivity is an old one, used mainly for oxides and other network glasses. However, focusing on its dynamics is relatively new, and brings new perspective and deeper understanding of old problems. Even though we primarily discuss metallic glasses [13] because they represent a simplest type of glasses having atoms as the structural unit, some of the discussions here could be applied to other groups of more complex glasses and liquids including polymers, polymer melts and colloids.

10.2 Topology of Atomic Connectivity and Local Topological Excitations

The structure of a crystal is well-defined by the lattice symmetry and the lattice constants. In comparison we lack effective metrics to specify the structure of liquids and glasses. It is usually described by the pair-density correlation function (PDF) which gives the distribution of interatomic distances [14, 15]. The PDF has a major advantage that it can be directly determined by scattering experiments [16, 17]. However, often two-body correlation alone is insufficient to elucidate properties of liquid or glass, and higher level many-body correlations have to be considered. To go beyond two-body correlation in describing the structure of a physical or computer model, Voronoi polyhedral analysis of the local atomic structure is frequently used [14, 15]. This analysis is certainly useful and conveys some three-dimensional information, but still the results do not directly allow qualitative elucidation of properties.

We prefer a related but slightly different approach, based upon atomic connectivity. In analyzing the structure of a simulated model we focus on the topology of atomic connectivity, rather than the actual position of each atom. This approach represents tremendous simplification of our view of the structure. Firstly this allows us to separate the vibrational and configurational degrees of freedom. The configurational degrees of freedom are important even below the glass transition as we discuss below, and become dominant in the liquid state. Secondly, this allows us to define the multiplicity of the state in liquids and glasses, and to construct new statistical mechanics of the liquid state. The analysis of atomic connectivity is augmented by the concept of the atomic-level stresses which facilitate linking local topology to physical properties [18].

In metals covalency of atomic bond usually is weak. Thus it might appear that defining atomic connectivity in metals is fraught with serious ambiguity. However, arguments below justify this approach. The PDF of a liquid or glass shows separation of the first and second peaks, as shown in Fig. 10.1 [19]. This implies there is a force to separate the nearest neighbors from the second neighbors. There are two principal components of this force.

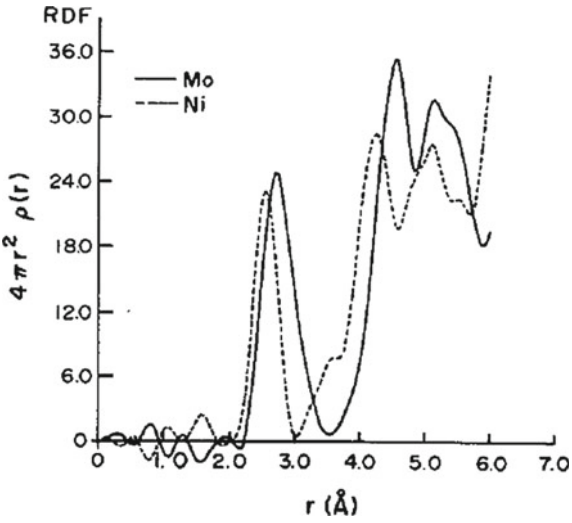

Fig. 10.1 Differential pair-distribution function (PDF with Ni or Mo at the center) of glassy $Ni_{50}Mo_{50}$ determined by resonant (anomalous) x-ray scattering [19]

(1) Steric effect: When an atom is already surrounded by large enough number of nearest neighbors, the second neighbor cannot go too close to the atom at the center.
(2) Potential effect: The interatomic potential tends to have a negative curvature over a range beyond the nearly harmonic part. In metallic materials often there is a maximum between the first and second neighbors because of the Friedel oscillation [20]. A pair of atoms at a distance in this range are unstable and tend to be either attracted or separated.

Because of these effects atoms are less stable at the minimum of the PDF between the first and the second peak. Therefore, we can use this distance as the cut-off, r_c, to define the nearest neighbors and thus define the network of atomic connectivity. Thus we are justified to define the atomic *bond* between the nearest neighbors.

Note that this definition of the cut-off distance is not related to the actual range of the interatomic potential. The long-range part of the potential may contribute to cohesion, but usually does not influence the structure very much. The structure of liquid and glass is dominantly determined by the steric effect due to the repulsive part of the potential and the short-range attraction. This explains why the all PDFs of liquid look alike, except for the size effect. The Voronoi polyhedral analysis is very similar to this approach of defining connectivity, but has a slight problem that all Voronoi faces are counted equally. Often a neighbor with a very small Voronoi face is counted as the nearest neighbor even though the actual interatomic distance is not short. Consequently the coordination number, the number of nearest neighbors, N_C, is overestimated. The value of N_C for the close-packed crystal structure (*f.c.c.* and *h.c.p.*) is 12, and our estimate of the ideal N_C in the glassy state is $4\,\pi = 12.56$ [21]. In comparison the value of N_C in the Voronoi analysis tends to be around 14 [14].

Once we define the "bond" between the adjacent atoms, we can define the action of *breaking* or *forming* bonds for two atoms crossing the cut-off distance [22]. Such a description is meaningful because r_c represents a distance at which a pair of atoms are unstable; they tend to decrease or increase the distance when the distance between them is close to r_c. The action of bond-breaking or bond-forming changes the local connectivity of atoms, therefore they are *local topological excitations*. We named these topological excitations *anankeons* [23], after Greek Goddess, Ananke, who represents force, constraint and destiny. From now on, we will discuss the atomic dynamics in liquids and glasses in terms of the anankeons. At high temperatures anankeons are independent of each other, but as temperature is lowered they interact and show collective dynamics. In supercooled liquid and in glass a small number of anankeons organize themselves into STZs and produce mechanical deformation.

As shown in Fig. 10.1 the PDF of a glass has a deep minimum between the first and the second peaks at r_c, but the value there is not zero. For atoms near the cut-off distance the separation of vibrational and configurational degrees of freedom (phonons and anankeons) is not straightforward, because regular vibration results in crossing the cut-off distance at each vibration, and appears to alter the configuration. The best way to separate these two is to quench the system at each time to the so-called inherent structure [24], the structure without kinetic energy, obtained by quenching the model to $T = 0\,\mathrm{K}$ and relaxing the model by the steepest descent method. Vibrational motion (phonon) is eliminated by going to the inherent structure, and only the configurational change (anankeon) survives. Alternatively we can time-average the structure over a time long enough to average out regular vibrations, e.g. ten times the inverse Debye frequency. Either way we can distinguish vibrational motion from configuration-altering motion even for atoms at a distance close to r_c.

10.3 Atomic-Level Stress

Topology has no lengthscale, and describes only the connectivity network. However, in reality the bond lengths have a relatively narrow distribution defined by the width of the first peak of the PDF, because atoms cannot be too close to each other due to strong repulsion and the cut-off at r_c which limits the upper end of the bond length. This constraint introduces interplay and correlation between topology and geometry. For instance the coordination number N_C is related to volume [25]. As shown in Fig. 10.2 [21] when an element A with the atomic size R_A is embedded in the glass of element B with the size R_B, the value of N_C depends on the size ratio $x = R_A/R_B$, and increases with the atomic size ratio; the larger is the atom at the center the larger is N_C. Also high-symmetry Voronoi polyhedra, such as icosahedra, are more stable [14]. Actually because an icosahedron has such a beautiful symmetry and as first pointed out by Frank [26] it is well-known as the example of local topology which resists crystallization, there have been a number of attempts to associate the liquid stability directly to formation of icosahedra [27–29], or related local topology [30]. However, in multi-component liquids icosahedra are not necessarily the most

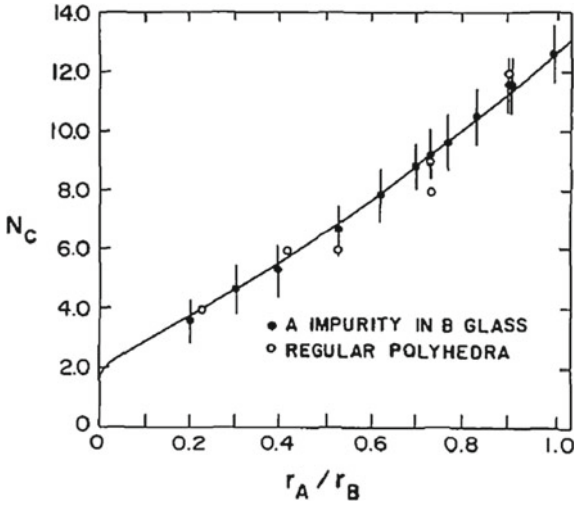

Fig. 10.2 Coordination number of element A with the atomic radius of r_A in glass of element B with the atomic radius of r_B [21]. The curve expresses 10.1

preferred local atomic arrangement. The preferred local atomic arrangement depends on atomic sizes and chemistry. Therefore it may be a misguided effort to focus on particular topology such as an icosahedron in discussing liquid stability. A more general approach is required to discuss the structure-property relationship in liquids and glasses.

The concept of the atomic-level stress was introduced for such a purpose. As shown in Fig. 10.2 N_C depends on the atomic size ratio, $x = r_B/r_A$. Our approximate expression is [21]

$$N_C(x) = 4\pi\left(1 - \frac{\sqrt{3}}{2}\right)(1+x)\left(1 + x + \sqrt{x(x+2)}\right). \tag{10.1}$$

This gives $N_C(1) = 4\,\pi$. A converse is that if one places an atom in a wrong environment it will be under pressure (negative or positive). Similarly if one places a spherical atom in non-spherical environment it will suffer a shear stress. This situation is analogous to the case of a continuum model of inclusion by Eshelby [31]. When one places an elastic object into a hole in a large elastic matrix as an inclusion, if the shapes of the inclusion and the hole in the matrix are not identical the inclusion will be under stress.

Stress is a concept usually defined for a continuum elastic body. However, the definition can be expanded to the network system as long as the two-body force can be defined. For an assembly of atoms the atomic-level stress tensor on the i-th atom, $\bar{\bar{\sigma}}_i$, can be given by [18],

$$\sigma_i^{\alpha\beta} = \frac{1}{\Omega_i}\sum_j f_{ij}^{\alpha} r_{ij}^{\beta}, \tag{10.2}$$

where α and β are Cartesian indices, Ω_i is the atomic volume of the atom i, $\boldsymbol{f}_{ij}$ is the two-body force and $\boldsymbol{r}_{ij}$ is the separation, between the atoms i and j. Hydrostatic pressure is given by its trace,

$$p_i = \frac{1}{3} Tr\left(\bar{\bar{\sigma}}_i\right) = \frac{1}{3}\left(\sigma_i^{xx} + \sigma_i^{yy} + \sigma_i^{zz}\right) , \tag{10.3}$$

and the volume strain and the local volume are given by

$$\varepsilon_i^v = \frac{p_i}{B_i}, \quad \Omega_i = \left(1 + \varepsilon_i^v\right) \langle \Omega \rangle , \tag{10.4}$$

where B_i is the atomic-level bulk modulus, and $< .... >$ represents volume average. It is convenient to use the spherical harmonics equivalents, for which the $\ell = 0$ term corresponds to pressure and the five $\ell = 2$ terms are the shear stresses [25]. The atomic-level stresses can readily be calculated for a model with a classical potential, and can also be evaluated with the ab-initio quantum-mechanical calculation, for instance using the density functional theory [32].

The atomic-level stress enables us to connect the topology of atomic connectivity network with physical properties as discussed in more detail in [33]. For instance (10.1) gives the size of an atom for which $p = 0$ given the value of N_C. Thus if the actual atom size is not equal to this value this atom will not fit the atomic cage of the nearest neighbors *a la* Eshelby, and will be under non-zero pressure. At high temperatures the equipartition theorem is valid, and

$$\frac{\langle \Omega \rangle \left\langle p^2 \right\rangle}{2 \langle B \rangle} = \frac{\langle \Omega \rangle \left\langle \sigma_s^2 \right\rangle}{2 \langle G \rangle} = \frac{kT}{4} . \tag{10.5}$$

where σ_s is any of the five shear stress components [34, 35]. This is because at high temperatures phonons are no longer elementary excitations of atomic vibration and are replaced by anankeons, as discussed below. Consequently the magnitudes of fluctuation in the atomic-level stresses, expressed by the second moments as in (10.5), are the order parameters [22, 23].

10.4 Atomic Dynamics in Liquids

10.4.1 Origin of Viscosity

Viscosity is one of the most fundamental properties of a liquid. Nevertheless the origin of viscosity at the atomic level has not been understood. This long-standing problem was solved by focusing on the atomic connectivity. Viscosity, η, defines the timescale for liquid dynamics, the Maxwell relaxation time,

$$\tau_M = \frac{\eta}{G_\infty}, \tag{10.6}$$

where G_∞ is the instantaneous shear modulus [36]. Through the molecular dynamics (MD) simulation of various metallic liquids at high temperatures it was found that at temperatures above the crossover temperature, T_A,

$$\tau_M = \tau_{LC}\,, \tag{10.7}$$

as shown in Fig. 10.3 [22]. Here τ_{LC} is the time for an atom to gain or lose one nearest neighbor by forming or breaking the atomic bond, i.e. by anankeons. Therefore, this equation means that the anankeon excitation determines the viscosity, providing the atomic-scale explanation of the origin of viscosity. T_A is the crossover temperature above which the Angell plot (a plot of $log\eta$ vs. T_g/T, where T_g is the glass transition temperature [37]) shows an Arrhenius behavior.

The reason why anankeon excitation determines viscosity is as follows. Through the Green–Kubo equation of fluctuation-dissipation theorem [36] viscosity and G_∞ are given in terms of the shear stress auto-correlation by,

$$\eta = \frac{V}{kT}\int \langle \sigma^{xy}(0)\,\sigma^{xy}(t)\rangle\, dt, \quad G_\infty = \frac{V}{kT}\left\langle (\sigma^{xy}(0))^2\right\rangle\,, \tag{10.8}$$

where V is the sample volume. We can express the shear stress in terms of the atomic-level shear stresses;

$$V\sigma^{xy}(t) = \sum_i \Omega_i \sigma_i^{xy}(t)\,. \tag{10.9}$$

Thus,

$$V^2\langle \sigma^{xy}(0)\,\sigma^{xy}(t)\rangle = \sum_{i,j}\Omega_i\Omega_j\left\langle \sigma_i^{xy}(0)\,\sigma_j^{xy}(t)\right\rangle. \tag{10.10}$$

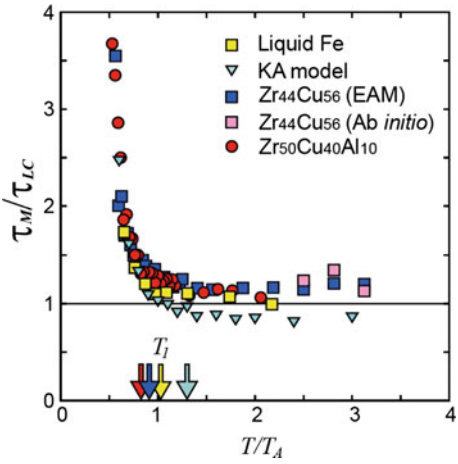

Fig. 10.3 The ratio τ_M/τ_{LC} (see text for definition) for various models as a function of T/T_A, where T_A is the crossover temperature [22]

Therefore the Maxwell relaxation time is equal to the correlation time of the atomic-level shear stress [38, 39]. Now the atomic-level stress depends on the local topology of the nearest neighbors. So excitation of an anankeon, the action of losing or gaining a neighbor which changes the local topology of atomic connectivity, changes the atomic-level stress enough to lose the stress correlation. This is why (10.7) is observed above T_A. This is a very significant result, because it directly connects a macroscopic property, η, to a microscopic quantity, τ_{LC}, the time-scale of anankeon, and explains the atomistic origin of viscosity.

Now above T_A, it was found that the phonon propagation length, $\xi = c_T \tau_M$, where c_T is the transverse phonon velocity, is shorter than the mean atomic distance, a, as shown in Fig. 10.4 [22]. In the Debye model, $\omega_D \sim c_T \pi / a$, so that $1/\nu_D \sim 2a/c_T$. In other words when the time-scale of phonon becomes equivalent to τ_M the structure changes so fast that it changes before the phonon travels between the nearest neighbor atoms. Thus anankeons cannot communicate with each other, and are independent. That is why a single anankeon excitation determines viscosity at $T > T_A$. Below T_A, however, anankeons communicate by exchanging phonons. Consequently they become more collective, and actions of local atomic rearrangements involve more than one anankeons. Thus the ratio, τ_M/τ_{LC}, is unity only above T_A, and below T_A it increases as temperature is decreased.

Equation (10.10) needs a bit more explanation. At high temperatures the self- and distinct stress correlations,

$$\Sigma_{self} = \sum_i \Omega_i \Omega_i \left\langle \sigma_i^{xy}(0)\, \sigma_i^{xy}(t) \right\rangle, \quad \Sigma_{dist} = \sum_{i \neq j} \Omega_i \Omega_j \left\langle \sigma_i^{xy}(0)\, \sigma_j^{xy}(t) \right\rangle, \tag{10.11}$$

have similar lifetimes, because anankeons are independent, and one anankeon excitation changes the stresses on one atom and one of its nearest neighbors. Thus the

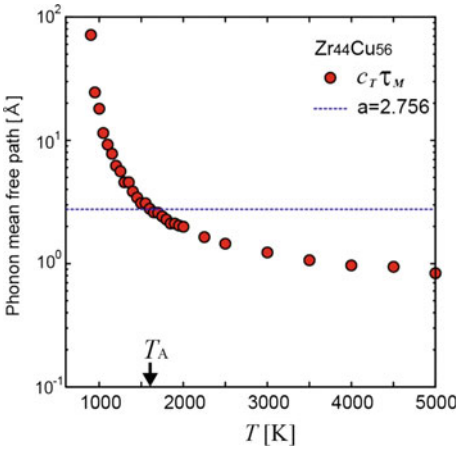

Fig. 10.4 Phonon mean free path as a function of temperature for liquid $Zr_{44}Cu_{56}$ [22]

self-correlation and the nearest neighbor correlation are affected at the same time, whereas long-range correlations are weak.

Above T_A, the dynamics of anankeons can be described by the local potential energy landscape (PEL) of one atom, as a function of its coordination number as shown in Fig. 10.5 [40]. In the conventional PEL picture the system is supposed to fly above the PEL at high temperatures, and start to feel the PEL only below T_A [41]. This picture is not correct, because viscosity shows thermally activated Arrhenius behavior above T_A [37]. The correct picture is that at high temperatures collectivity in dynamics is absent, therefore the local PEL of a single anankeon describes the behavior of the system.

A recent study of liquid viscosity in metallic liquids suggests remarkable universality in the temperature dependence of viscosity in many liquid alloys as shown in Fig. 10.6 [42]. Whereas the full implications of this result need further studies, it justifies a simple view of viscosity as thermally activated process with temperature dependent activation energy,

$$\eta\,(T) = \eta_\infty \exp\left(\frac{E_a\,(T)}{kT}\right), \tag{10.12}$$

where η_∞ is nearly independent of composition. Above T_A, E_a is independent of temperature [22, 41, 42], and is similar in magnitude with the atomic bond energy, justifying the picture that a single anankeon excitation controls liquid flow. By simulation the value of $\tau_\infty = \eta_\infty / G_\infty$ is of the order of 10^{-14} s (~300 meV), similar to the bond energy. However, the experimental value of τ_∞ is about 3×10^{-16} s [40], corresponding to $h/\tau_\infty = 12$ eV. Therefore, it is entirely possible that electronic excitations are determining these values. At high temperatures as the anankeon frequency increases the Born-Oppenheimer adiabatic approximation would fail, and the dynamics of bond cutting may be dictated by the electronic excitation between the

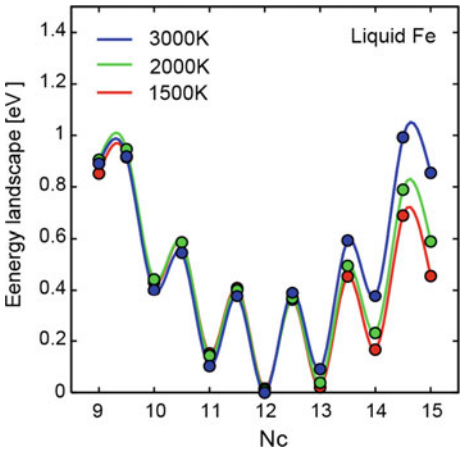

Fig. 10.5 Local potential energy landscape as a function of coordination number calculated for liquid Fe [40]

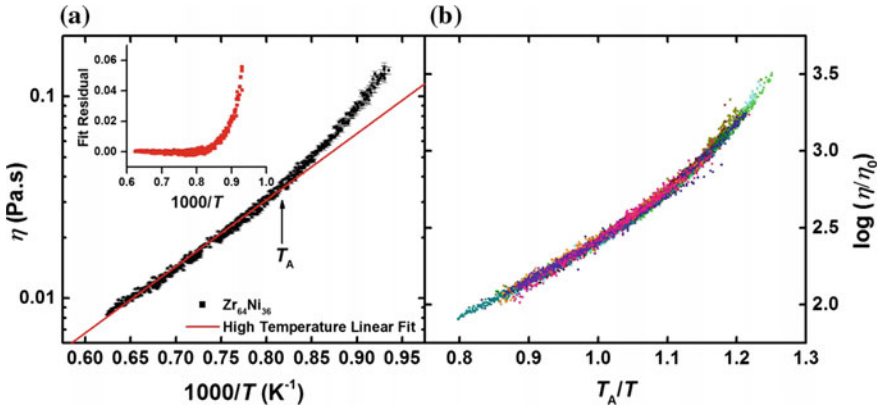

Fig. 10.6 **a** Viscosity of liquid $Zr_{64}Ni36$ plotted against $1000/T$. **b** Scaled viscosity, η/η_0, against T_A/T [42]

bonding and anti-bonding states. Most of liquid alloys studied are transition metal alloys, where bonding is primarily determined by d-electrons. Indeed the width of the d-band ($\sim$10 eV) is comparable to h/τ_∞.

Below T_A, anankeon dynamics slows down, and a single anankeon excitation would induce only locally confined atomic rearrangements without resulting in flow. Thus multiple anankeon excitations are necessary for shear flow, and the ratio, τ_M/τ_{LC}, increases from unity, as shown in Fig. 10.3. It is not difficult to image that this would increase E_a, resulting in a super-Arrhenius behavior in the Angell plot, culminating in the glass transition.

10.4.2 Second Crossover: Comparison to Relaxor Ferroelectrics

Before the glass transition is reached, however, another crossover phenomenon is observed, just in-between T_A and T_g. This is the point where high-temperature equipartition law, (10.5), starts to fail, and shear stresses start to become spatially correlated below T_s, as shown in Fig. 10.7 for supercooled liquid Fe. For this system $T_A = 2300\,\mathrm{K}$ [22], $T_s \sim 1500\,\mathrm{K}$ and $T_g = 900\,\mathrm{K}$ [34]. Also the statistics of local icosahedral cluster is changed around T_s [29]. Recently a pronounced change in behavior was observed by the MD simulation of $Cu_{44}Zr_{56}$ at a temperature, $T_c \sim 1.4T_g$ [43]. Furthermore a maximum in the second derivative of relaxation time with respect to temperature was observed at a temperature significantly above T_g in some, but not all, glass forming liquids [44]. Dynamic heterogeneity (DH) is also observed in a similar temperature range [4, 45–47]. These observations

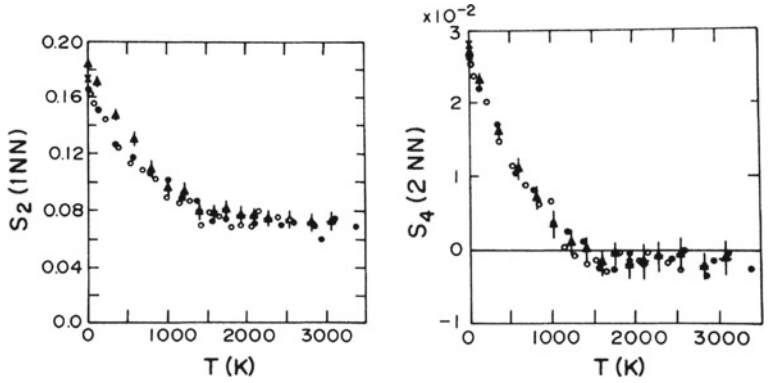

Fig. 10.7 Temperature dependence of the shear stress correlation for the nearest neighbor with $\ell = 2$ (*left*) and the second neighbor with $\ell = 4$ (*right*) [34]

suggest that the nature of a supercooled liquid changes in a subtle but important manner before it freezes into a glass. However, the nature and origin of this change is unclear.

It is instructive to make reference to relaxor ferroelectrics in which a very pronounced second crossover is observed. Relaxor ferroelectrics are strongly disordered ferroelectrics, such as $Pb(Mg_{1/3}Nb_{2/3})O_3$ (PMN) [48]. PMN maintains the simple perovskite structure at a macroscopic scale at all temperatures, with Pb occupying the A site. But the B site is occupied by both Mg^{2+} and Nb^{5+}, with only partial chemical order. Because of the strong chemical and electrostatic disorder in the B site ferroelectric order is heavily disturbed, and a glassy, strongly frequency dependent dielectric behavior is observed [49]. The ferroelectric transition is diffuse, and the ordering temperature (Curie temperature) is frequency dependent. For applications diffuse transition is advantageous, because a sharp transition results in strong temperature dependence of permittivity, which is problematic for application, whereas relaxor ferroelectrics show high permittivity over a wide temperature range.

The dielectric response of PMN becomes frozen, frequency independent, below $T_f = 217\,\mathrm{K}$ [49]. This clearly corresponds to the glass transition in regular glasses. Above T_f there are local dynamic polarizations [50], which disappear above the Burns temperature, $T_d \sim 600\,\mathrm{K}$ [51]. The Burns temperature is very similar to the crossover temperature, T_A, in liquids. Now diffuse ferroelectric transition occurs around $T_C \sim 300\,\mathrm{K}$, between T_g and T_d. Below T_C PMN forms dynamic nano-scale ferroelectric domains called polar nano-regions (PNR) [52]. At the same time because of piezoelectricity the lattice becomes locally and dynamically distorted, which can be observed by pulsed neutron pair-density function (PDF) analysis as shown in Fig. 10.8, in terms of distinct temperature variations of some of the PDF peaks [53].

In relaxor ferroelectrics, T_C is obviously the Curie temperature made diffuse because of structural disorder. Because of strong piezoelectricity the lattice becomes locally distorted below T_C, making PNR readily observable by the PDF method [53]. In supercooled liquid metals such obvious local distortions are not observed.

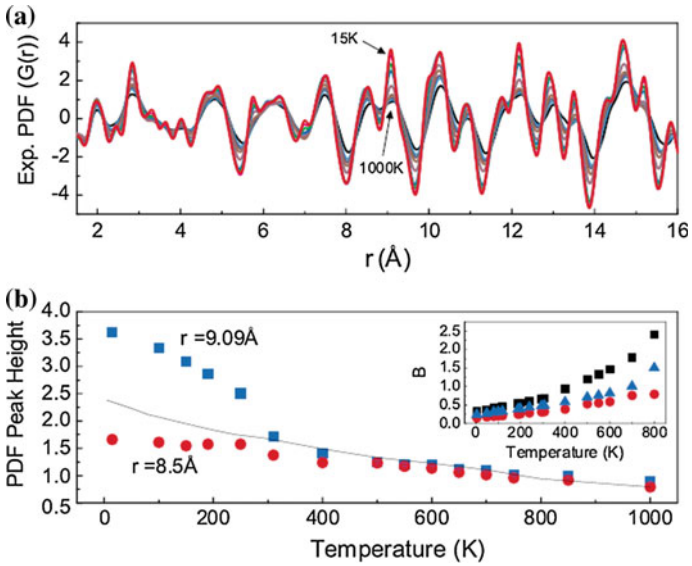

Fig. 10.8 The PDF of PMN at various temperatures (above) and temperature dependence of the PDF peak height at $r = 9.09$ and 8.5 Å [53]

Nevertheless, there could be a certain hidden phase transition well-defined in the mean-field approximation but made diffuse and frustrated by disorder. Such an idea has been discussed by many. Kivelson et al. [54, 55] used this as the central idea for glass transition.

A possible transition is the transition to the icosahedral state. A thirteen atom icosahedral cluster is locally more stable than the *f.c.c.* or *h.c.p.* clusters, and is often found in liquids, contributing to its stability and preventing crystallization, as pointed out by Frank [26]. As a liquid is cooled indeed the population of icosahedral clusters grows rapidly [27–30]. However, its five-fold symmetry prevents it from filling the space; the icosahedral order is frustrated in three-dimensional (Euclidian) space [56]. Consequently the growth is halted, resulting in a glass. But it may be wrong to associate the crossover with a particular geometry such as an icosahedron, because icosahedra are frequently found in monoatomic systems, but not in liquids with different compositions. The more fundamental principle is more efficient local packing of space [14, 15, 30, 57]. An icosahedron is just an example of efficient local packing.

Now the principle of local packing is appropriate for a hard-sphere systems, whereas metals are not hard-sphere systems [58, 59]. Therefore, it is possible that a different principle dictates the local ordering in metallic liquids. A strong candidate is the elastic stress field. Because atoms are deformable, they are under strong atomic-level stresses as discussed above. In the supercooled liquid below T_A the atomic-level stresses interact via the elastic Eshelby field [60]. Correlations are created to minimize the elastic field energy by locally rearranging atoms [61]. A possible correlation thus

produced is a bond-orientational correlation (BOC) with $\ell = 2$ *nematic* order [62]. This local order is very similar to the piezoelectric local distortion that forms PNR in relaxor ferroelectrics, making the comparison with the relaxor ferroelectrics very relevant.

The glass transition in the mode-coupling theory (MCT) is similar in character [63]. Because of the mean-field approximation invoked in the MCT, viscosity diverges at T_C^{MCT}, which is about 1.2 T_g, and the MCT fails to explain viscosity below this temperature [63, 64]. Various changes in the behavior is predicted to occur at T_C^{MCT}, such as the temperature dependence of viscosity changing from the Vogel–Fulcher type to power law [63]. However, the MCT is based solely on two-body density correlations, and will not be able to describe the BOC which is a four-body correlation. Even though the equation of motion in the MCT includes four-body density correlations, they are decoupled into the products of two-body correlation functions in the random-phase approximation. Our earlier simulation clearly shows the emergence of shear stress correlation below T_s (Fig. 10.8 [34]) which represents real four-body correlation, suggesting that the decoupling may not be justified. For this reason we raised caution against such decoupling in the MCT [34]. Thus, even though the MCT predicts viscosity divergence in the mean-field sense, the physics involved is different, and could not be related to the BOC based upon the spatial elastic interaction.

10.4.3 Equivalence of Stress and Temperature

Viscosity of a liquid depends on shear rate, and decreases as shear rate is increased. This phenomenon is called *shear thinning*, and is very widely observed for all liquids. Nevertheless, its origin has been controversial [65, 66]. One way to explain shear thinning is to invoke the concept of effective temperature. Because driving a liquid with shear exerts mechanical work on the liquid, it infuses kinetic energy. Consequently the structure becomes more disordered and viscosity goes down. This process can be described in terms of the increase in the effective temperature, T_{eff}, although its definition is slightly controversial [3, 13, 67, 68]. This approach is based upon the idea that applying shear stress to a liquid is similar to increasing temperature [69, 70]. The plot of equal viscosity lines as a function of temperature T and stress σ in Fig. 10.9 illustrates this equivalence. It was found that T and σ are scaled by [70]

$$\frac{T}{T_0(\eta)} + \left(\frac{\sigma}{\sigma_0(\eta)}\right)^2 = 1. \tag{10.13}$$

Note that reversing the sign of σ simply reverses the direction of shear and does not change physics. Thus only the terms with even power of σ should appear in the equation, and indeed only the σ^2 term is seen in (10.13). The glass transition temperature is defined by $T_g = T_0(\eta_g)$, where η_g is arbitrarily chosen (conventionally

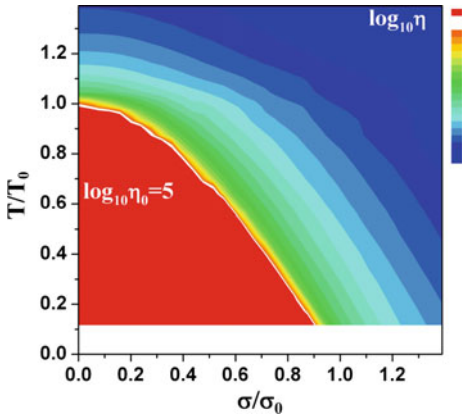

Fig. 10.9 The equal viscosity line in the normalized temperature-stress diagram obtained by the simulation of steady state flow for glassy $Zr_{50}Cu_{40}Al_{10}$ [70]

10^{13} poise $= 10^{12}$ Pa s for experiment, and a much lower value for simulation) to define glass transition. At $T = T_1 = T_0(\eta_1)$, for $\sigma \neq 0$,

$$T_0(\eta) = T_1 + \frac{\partial T_0}{\partial \eta}\Delta\eta = \frac{T_1}{1 - \left(\frac{\sigma}{\sigma_0(\eta)}\right)^2} = T_1\left[1 + \left(\frac{\sigma}{\sigma_0(\eta)}\right)^2 + \ldots.\right]. \quad (10.14)$$

Thus,

$$\Delta\eta = \frac{T_1}{\frac{\partial T_0}{\partial \eta}(\sigma_0(\eta_1))^2}\sigma^2. \quad (10.15)$$

Because $\partial T_0/\partial\eta < 0$, (10.15) naturally explains shear thinning.

Now it is instructive to examine (10.13) in the spirit of (10.12). Extending (10.12) to include the effect of stress we may write,

$$\eta(T, \sigma) = \eta_\infty \exp\left(\frac{E_a(T, \sigma)}{kT}\right), \quad (10.16)$$

Then,

$$\frac{E_a(T, 0)}{kT_0(\eta)} = \frac{E_a(T, 0)}{kT}\left(1 - \left(\frac{\sigma}{\sigma_0(\eta)}\right)^2\right) = \frac{E_a(T, \sigma)}{kT},$$
$$E_a(T, \sigma) = E_a(T, 0)\left(1 - \left(\frac{\sigma}{\sigma_0(\eta)}\right)^2\right). \quad (10.17)$$

Thus the applied stress reduces the activation energy, and results in shear thinning. We will return to this equation when we discuss the activation volume concept for glasses.

10.4.4 Atomistic Mechanism of Flow and Glass Transition in Correlated Liquids

As temperature is lowered below T_A anankeon excitations become more correlated in time and space. One anankeon excitation can induce another in the neighborhood, creating cascade action, or local avalanche. Consequently anankeon distribution in space will not be homogeneous, producing dynamic heterogeneity (DH). In a simple binary picture, DH leads to bifurcation of the liquid-like regions and solid-like regions. The distribution of the atomic-level pressure can be used in defining these two states [71], and the loss of percolation of the liquid-like states results in the glass transition [72, 73]. The glass transition temperature thus calculated agrees quite well for metallic glasses as shown in Fig. 10.10 [73].

When a liquid is subjected to external shear stress field the flow of atoms will not be homogeneous, reflecting DH. Simulation at temperatures below T_g indicates that locally elastic zones develop in liquid, as shown in Fig. 10.11 [40]. The size of the elastic zone, ξ, depends on shear rate, and decreases with increasing shear rate, $\dot{\gamma}$, as

$$\xi = \xi_T \left(\ln \frac{\dot{\gamma}_c}{\dot{\gamma}} \right)^{\frac{1}{2}}. \tag{10.18}$$

where $\dot{\gamma}_c$ is the critical shear rate above which no elastic zone is formed [40]. Also the shear stress, σ, is dependent on ξ by,

$$\sigma = \sigma_c \exp\left(-\frac{\xi}{\xi_\sigma} \right). \tag{10.19}$$

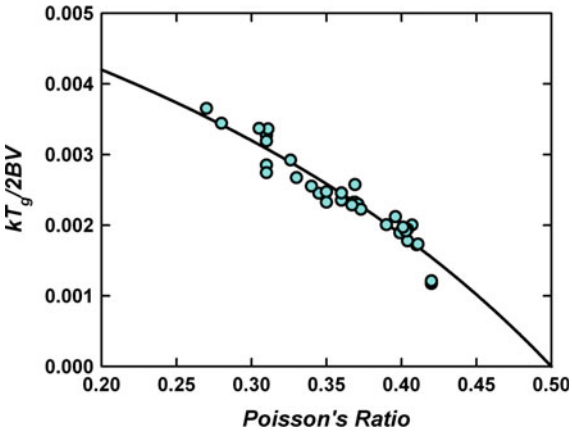

Fig. 10.10 Normalized glass transition temperature, $kT_g/2BV$, plotted against the Poisson's ratio. The *solid line* represents theory [73]

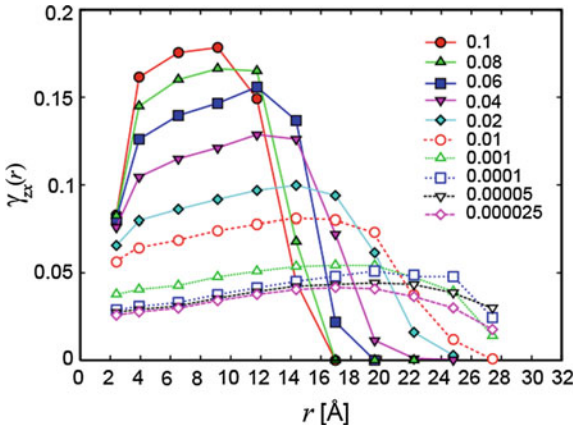

Fig. 10.11 Atomic-level shear strain between atoms apart by r during the steady state flow as a function of strain rate simulated for Fe at $T = 300$ K [40]

Simulation on supercooled liquid Fe indicates $\xi_T \sim \xi_\sigma \sim 4a$, where a is the average nearest neighbor distance [40]. Now viscosity is related to shear rate by $\eta = \sigma/\dot{\gamma}$, so from (10.18) and (10.19),

$$\eta = \frac{\sigma_c}{\dot{\gamma}_c} \exp\left(-\frac{\xi}{\xi_\sigma} + \left(\frac{\xi}{\xi_T}\right)^2\right). \tag{10.20}$$

Because $\xi > \xi_T \sim \xi_\sigma$ and ξ is reduced as shear rate is increased by (10.18), (10.20) indicates that viscosity is reduced as shear rate is increased. Thus (10.20) provides a microscopic elucidation of shear thinning.

10.5 Deformation of Metallic Glasses

10.5.1 Absence of Elasticity in Glass at Atomic Level

In the glassy state below T_g viscosity becomes so large that τ_M exceeds the experimental time-scale. When the applied stress is less than the yield stress, σ^Y, the strain response to the external stress is linear, so that the Hook's law, $\varepsilon = C\sigma$, where C is the elastic constant, appears to hold. However, at the atomistic scale that is not the case. The local strain tensor may be defined by

$$\boldsymbol{R}_i' = \left(1 + \bar{\bar{\varepsilon}}_i\right) \boldsymbol{R}_i \tag{10.21}$$

where $\boldsymbol{R}_i$ is the position of the i-th atom before deformation, $\boldsymbol{R}_i'$ is the position after deformation and $\bar{\bar{\varepsilon}}_i$ is the strain tensor. If deformation is *affine*, $\bar{\bar{\varepsilon}}_i$ is the same for all atoms. In a crystal deformation is affine for small strains because all atoms are in the

same environment. However, in glasses they are not, and $\bar{\bar{\varepsilon}}_i$ is different for each atom. Consequently atomic displacements are not collinear, resulting in reduction of the shear modulus [12, 74]. In addition, some atoms move so much even for small stress that some atomic bonds are cut or formed (anankeon excitation). In other words local topological changes are induced by stress [13, 75]. Because the number of bonds affected is linear with strain deformation appears to be elastic, but microscopically it is plastic. This effect is particularly pronounced for shear deformation. Strictly speaking, therefore, there is no elasticity in glasses [76].

For small strain these plastic events are localized and damages are contained. However, as strain is increased more of these events occur, and finally they percolate through the system to result in macroscopic yield. At temperatures close to T_g deformation is macroscopically uniform and shows a typical creep behavior [13, 77]. At lower temperatures deformation becomes localized as shear bands [9, 78]. In this article we will not discuss these mesoscopic behaviors, but will focus on the atomic-level phenomena.

10.5.2 Plastic Deformation as Stress-Induced Glass Transition

The plot in Fig. 10.3 shows that the glass transition is not a point in the diagram, but is represented by a line. Glass transition can be induced by stress, and this naturally explains the nature of mechanical failure as stress-induced glass transition. Earlier there have been experimental reports that the temperature within the shear band is significantly raised, suggesting that this local heating could explain shear band formation [79, 80]. However, it is more likely that heating is a consequence of flow in the shear band rather than the cause [80]. Spaepen [81] proposed increased volume, rather than temperature, is enough to initiate shear bands, based upon the free-volume theory [56]. But the free-volume theory is less successful for metals [56, 57], and indeed the pressure dependence of strength is quite small for metallic glasses [82]. On the other hand, simulation to produce Fig. 10.9 was done with constant volume and temperature. It shows shear stress alone, without the aid by volume or temperature, can induce glass transition and resultant mechanical failure.

Most theories of glass deformation [1–3, 77] assumes the double-well structure and the effect of stress is expressed by the activation volume, Ω, which changes the energy of the defect by,

$$E_D^{\pm}(\sigma) = E_D(0) \pm \frac{\Omega\sigma}{2}. \tag{10.21}$$

Thus the rate equation becomes,

$$\begin{aligned} \dot{\gamma} &= \gamma_0 \nu_\infty \left[e^{-(E_S - E_D^+)/kT} - e^{-(E_S - E_D^-)/kT} \right] \\ &= \gamma_0 \nu_\infty e^{-E_a/kT} \sinh\left(\frac{\Omega\sigma}{kT}\right) \approx \frac{\Omega}{kT} \gamma_0 \nu_\infty e^{-E_a/kT} \sigma \end{aligned}. \tag{10.22}$$

where γ_0 is the critical shear strain and ν_∞ is the attack frequency [77]. This picture presumes the presence of a defect with the volume Ω on which the applied stress exerts force. However, deformation in glass is an *emergent phenomenon* without pre-existing defects. In glasses once local deformation occurs, or the STZ is activated, the structure changes extensively, so that even when a reverse stress is applied the system almost never goes back to where it was. Therefore the concept of a double-well potential is very misleading. Indeed in the STZ theory the STZ disappears after it is activated [2, 3]. The concept of the activation volume requires careful scrutiny as we will discuss below.

It is interesting to note that in the liquid state the effect of stress on the activation energy is *quadratic* as in (10.17), rather than *linear* as in (10.21). This is most likely related to the issue of the back-stress in the glassy state which breaks the symmetry. In the liquid state anankeons are nearly independent, and the applied stress alters the local elastic energy through (10.17). In the glassy state each atom already has a static atomic-level stress. The applied stress merely adds to the existing stress, so the activation energy for the i-th atom is,

$$\begin{aligned} E_a^i\left(T,\sigma_a\right) &= E_a\left(T,0\right)\left(1-\left(\frac{\sigma_i+\sigma_a}{\sigma_0\left(\eta\right)}\right)^2\right) \\ &= E_a\left(T,0\right)\left(1-\left(\frac{\sigma_i}{\sigma_0\left(\eta\right)}\right)^2-\frac{2\sigma_i}{\left(\sigma_0\left(\eta\right)\right)^2}\sigma_a\right). \end{aligned} \tag{10.23}$$

where σ_a is the externally applied stress and only the linear term in σ_a was retained because σ_a is much smaller than the atomic-level stresses. Thus the atomic site with a large atomic-level stress with the same sign as the applied stress gets activated, because the existing atomic-level stress becomes added to the applied stress. Therefore we have the definition of an apparent activation volume,

$$\Omega_a^i\gamma_0 = \frac{2E_a\left(T,0\right)\sigma_i}{\left(\sigma_0\left(\eta\right)\right)^2}. \tag{10.24}$$

This implies that the stress sensitivity, the activation volume, varies greatly from atom to atom, and is proportional to the local atomic-level shear stress, σ_i. However, because atomic displacements involved in deformation are large, σ_i keeps changing as deformation proceeds. Therefore, the initial value of σ_i is not the most representative of the whole emergent process. Therefore, it may be more reasonable to assume,

$$\left\langle\Omega_a\right\rangle\gamma_0 = \frac{2E_a\left(T,0\right)}{\left(\sigma_0\left(\eta\right)\right)^2}\left\langle\left(\sigma^2\right)\right\rangle^{\frac{1}{2}}. \tag{10.25}$$

Equation (10.25) also suggests that the distribution of the activation energies should reflect the effective temperature. Indeed the internal friction measurement shows that is the case. The activation energy spectrum depends on the annealing temperature in the Arrhenius fashion [83]. Equation (10.25) represents a simplest picture in which

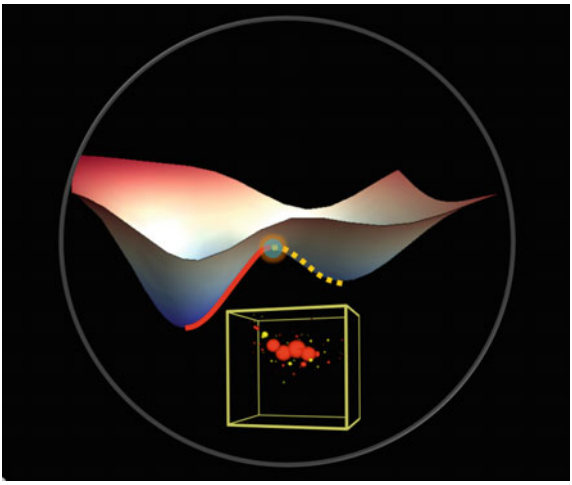

Fig. 10.12 Potential energy landscape with the saddle point (*middle*) and the final relaxed point [12]. The *inset* shows the atoms involved in rearrangement

the activation energy depends on one atom. This is not realistic, because the atomic motions are more collective as we discuss below. Nevertheless it conveys the idea of competition and cooperation between the existing atomic-level stress and the applied stress in determining the local dynamics of atoms under stress.

10.5.3 Atomistic Mechanism of Deformation

We now discuss the atomistic mechanism of mechanical deformation in metallic glasses using the language we introduced above. We focus on two steps in the PEL, the saddle point which represents the activation barrier, and the final point to which the system relaxes after going over the saddle point (Fig. 10.12) [12, 84]. To study this behavior we have to go beyond the MD simulation, because the longest time that MD can simulate is of the order of nanosec., which is too short for our purpose. If we use a conventional thermal activation model,

$$\tau = \tau_0 \exp\left(\frac{E_a}{kT}\right) \tag{10.26}$$

where τ_0 is the inverse of the attempt frequency, usually about 10^{-13} s corresponds to 9 kT, or 0.23 eV at room temperature. Processes with higher activation energies are not accessible by MD. For this reason we used the activation-relaxation-technique (ART) to simulate thermal activation. Using this method we simulated a large number of local deformation events ($>10^3$), and examined the atomic displacement for each event.

We prepared two models of $Cu_{56}Zr_{44}$ glassy alloy, one quenched from 2000 K (liquid state far above $T_g \sim 700$ K) and relaxed at 0 K, System I, and the other equilibrated at 1000 K and cooled slowly (10^{12} K/s) through T_g, System II [85]. System I is highly unstable and the spectrum of activation energies is approximately Gaussian around zero, as shown in Fig. 10.13. System II represents a stable glass, and the spectrum of activation energies shows a large pseudo-gap up to 1 eV within which activation is suppressed. If we plot the changes in the atomic-level shear stress due to deformation against the atomic displacement for each atom most atoms behave in an elastic manner (within the dashed lines), but some show non-elastic behavior, as shown in Fig. 10.14a. Atoms outside the elastic range are called "atoms involved in the plastic event". These atoms are clustered, and the spectrum of displacements shows deviation from the exponential distribution for elastic atoms [12].

Surprisingly the distribution of the number of atoms involved in the plastic event at the saddle point (Fig. 10.14b triangles) was found to be almost the same for Systems I and II, in spite of vast difference in stability [12]. The average is just about five, much smaller in number than discussed in experimental literature [86–89], but closer to those by simulation or theory. Now even though the distribution of the activation energies was similar for Systems I and II, the displacements involved, D_a, were not the same (Fig. 10.15). Larger displacements were involved in System II than for System I. Because the magnitude of displacement needed to overcome the activation barrier, d^{ave}, is related to the general distance between the PEL minima, L [90], it can be argued that in System I the PEL minima are more closely spaced than in System II as shown in Fig. 10.16. The density of the PEL minima, thus the STZ density, ρ_{STZ}, is related to L, and d^{ave}, and the effective temperature, T_{eff}, by

$$\rho_{STZ} = e^{-\chi} = \frac{1}{L^{3n}} \sim \frac{1}{(d^{ave})^{3n}}, \tag{10.27}$$

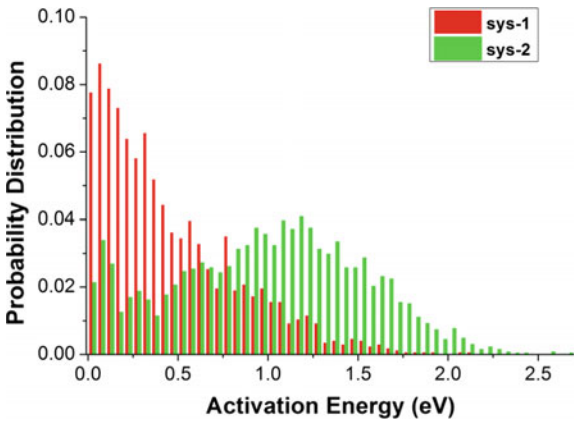

Fig. 10.13 Distribution of activation energies for unstable system (sys-1) and stable system (sys-2) [85]

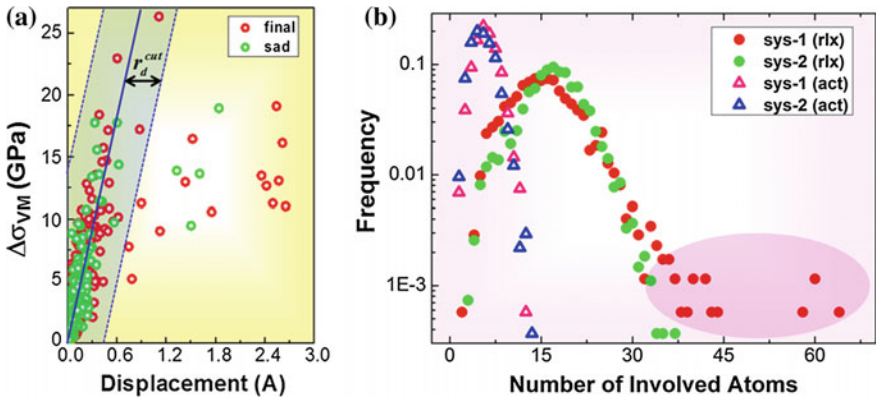

Fig. 10.14 **a** Change in the atomic-level shear stress against displacement indicating that most atoms behave elastically but some do not. **b** Distribution of number of atoms involved at the saddle point (*triangles*) and at the relaxed point (*circles*) [84]

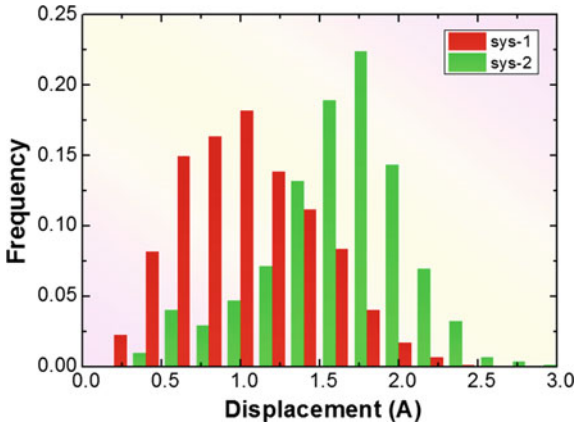

Fig. 10.15 Distribution of magnitudes of atomic displacement to reach the saddle point for two systems [12]

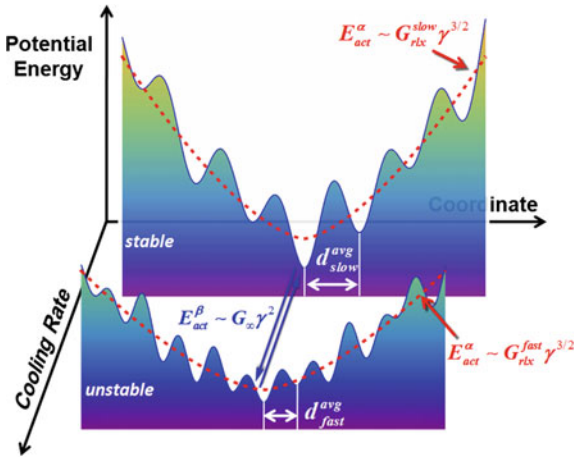

Fig. 10.16 Schematic PEL of stable and unstable systems. In a stable system local minima are less in density and far in-between [12]

where

$$\chi = \frac{E_{STZ}}{kT_{eff}}, \tag{10.28}$$

n is close to the number of atoms involved, and E_{STZ} is the STZ creation energy [2, 3].

In addition we note that the height of the activation barrier is determined at the saddle point, but the process goes on to relax the system down to the next minimum in PEL (Fig. 10.12). After relaxation more atoms are involved (Fig. 10.14b), with the average number of 15, which again is the same for Systems I and II [83]. The distribution of the number of atoms involved is nearly Gaussian, but distribution in System I was more spread beyond the Gaussian distribution, forming a tail at high end as shown in Fig. 10.14b. The distribution of the energy of relaxation, $E_{rlx} = E_{saddle} - E_{final}$, also has a long tail as shown in Fig. 10.17. The distribution at the high end approximately follows the power law, $P(E) \sim E_{rlx}^{-\tau}$ with $\tau = 1.6$, whereas the low energy portion follows the exponential law. Such a power law is commonly seen for the avalanche phenomena, with τ typically equal to 1.5 [91]. Thus the results show that in the unstable System I STZ can cause avalanche of other STZs.

It is most likely that the large values of activation volume observed by experiments are due to these avalanches. In other words deformation observed in most experiments is caused by a collection of STZs in avalanche, not due to a single isolated STZ. So-called dynamic heterogeneity (DH) observed in supercooled liquid also reflects multiple STZ chain reaction in avalanche, because the time-scale of DH represented by χ_4, the four-body correlation function, is of the order of 10 ps [44], much longer than the STZ time-scale of 1 ps or less.

Another reason of discrepancy between the magnitude of activation volume determined by experiment and simulation could be the definition of activation volume. Let

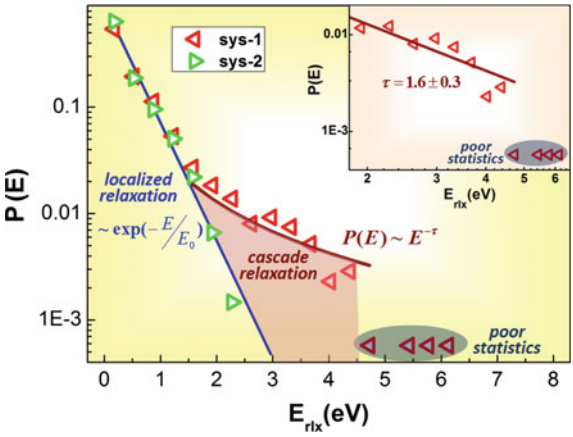

Fig. 10.17 Distribution of the relaxation energy ($E_{saddle} - E_{final}$). Localized events have an exponential distribution, whereas the avalanche events have a power law distribution [84]

us examine the number of atoms involved in light of the apparent activation volume given by (10.25). If we assume,

$$E_a(T,0) = N_a V_a \frac{(\sigma_c(\eta))^2}{2G}, \tag{10.29}$$

where N_a is the number of atoms involved, V_a is the atomic volume and $\sigma_c(\eta)$ is the stress on these atoms at the saddle point, then,

$$\Omega_a = N_a V_a \left(\frac{\sigma_c(\eta)}{\sigma_0(\eta)}\right)^2 \frac{\varepsilon_0}{\gamma_0}, \tag{10.30}$$

where $\varepsilon_0 =< \sigma^2 >^{1/2} / G$. If $\sigma_c(\eta) = \sigma_0(\eta)$, and $\varepsilon_0 = \gamma_0$, Ω_a is indeed the activation volume. However, if these equalities are not realized some multiplying factor would appear. It will be instructive to examine these quantities by simulation.

The STZ avalanche will have a profound effect on the mechanical properties. A single STZ activation is local and causes either anelastic effect or uniform flow (creep), but STZ avalanche will lead to percolation of STZ actions and local plastic flow. Therefore high propensity of STZ avalanche will result in ease of plastic deformation and ductility. Metallic glasses become brittle after annealing [13], most probably because the reduced STZ density due to annealing prevents STZ avalanche. Conversely if we find the way to keep the STZ high in spite of annealing we should able to develop ductile glass which does not lose ductility even after annealing. Understanding the mechanism of deformation could lead to such engineering possibilities.

10.6 Conclusion

Mechanical deformation of glass and liquid is a complex phenomenon and presents a major challenge to the effort toward its accurate microscopic description. However, through careful analysis of the simulation results and introduction of new concepts we should be able to make progress. The first step is to recognize that it is advantageous to describe an amorphous structure as a random network system of atoms and molecules, even when we deal with metallic glasses. Once we define the nearest neighbors and connectivity of atoms, we can define the structural state in terms of the topology of atomic connectivity or the bond network. An action to change it, local topological excitation, is breaking and forming of a bond. In high temperature liquid such excitations are directly linked to viscosity, and can be identified as a microscopic origin of viscosity. They replace phonons as elementary excitations, as phonons are overdamped and marginalized. We name them anankeons.

Anankeons are independent of each other in high temperature liquid above the crossover temperature, T_A, but below T_A they are coupled through elastic fields

(phonons), and in supercooled liquids they form a collective action unit called shear-transformation-zone (STZ). In the glassy state below T_g STZ is responsible for anelastic behavior. STZs, however, are not pre-existing defects such as lattice defects in crystals. They are emergent, and disappear after activation. The propensity of activation depends on the structure in a subtle way, defined in terms of the effective temperature. In a system with high effective temperature, an unstable system, STZ activation can cause avalanche of other STZs, resulting in plastic, ductile deformation. Thus through the hierarchy of dynamic topological changes, from anankeon, STZ, to STZ avalanche, we should be able to achieve microscopic elucidation of seemingly complex deformation phenomenon of glasses.

Acknowledgments The authors acknowledge stimulating and helpful discussions with J. S. Langer, K. F. Kelton, A. J. Liu, K. A. Dahmen, M. Atzmon, C. Maloney, I. Procaccia, A. Lemaître and J. R. Morris, and the support by U.S. Department of Energy, Office of Science, Basic Energy Sciences, Materials Science and Engineering Division.

References

1. A.S. Argon, Acta Met. **27**, 47 (1979)
2. M.L. Falk, J.S. Langer, Phys. Rev. E **57**, 7192 (1998)
3. J.S. Langer, Phys. Rev. E **70**, 041502 (2004)
4. A. Widmer-Cooper, P. Harrowell, Phys. Rev. Lett. **96**, 185701 (2006)
5. M. Tsamados, A. Tanguy, C. Goldenberg, J.-L. Barrat, Phys. Rev. E **80**, 026112 (2009)
6. M.L. Manning, A.J. Liu, Phys. Rev. Lett. **107**, 108302 (2011)
7. J. Ding, S. Patinet, M.L. Falk, Y. Cheng, E. Ma, PNAS **111**, 14052 (2014)
8. E.D. Cubuk, S.S. Schoenholz, J.M. Rieser, B.D. Malone, J. Rottler, D.J. Durian, E. Kaxiras, A.J. Liu, Phys. Rev. Lett. **114**, 108001 (2015)
9. C.A. Schuh, T.C. Hufnagel, U. Ramamurty, Acta Mater. **55**, 4067 (2007)
10. O. Gendelman, P.K. Jaiswal, I. Procaccia, B.S. Gupta, J. Zylberg, Euro. Phys. Lett. **109**, 16002 (2015)
11. C. Maloney, A. Lemaître, Phys. Rev. E **74**, 016118 (2006)
12. Y. Fan, T. Iwashita, T. Egami, Nature Commun. **5**, 5083 (2014)
13. T. Egami, T. Iwashita, W. Dmowski, Metals **3**, 77 (2013)
14. J.D. Bernal, Nature **183**, 141 (1959)
15. J.L. Finney, Proc. Roy. Soc. London A **319**, 479 (1970)
16. B.E. Warren, *X-ray Diffraction* (Dover, New York, 1969)
17. T. Egami, S.J.L. Billinge, *Underneath the Bragg Peaks: Structural Analysis of Complex Materials*, 2nd edn. (Pergamon Press, Elsevier Ltd., Oxford, 2003/2012)
18. T. Egami, K. Maeda, V. Vitek, Phil. Mag. A **41**, 883 (1980)
19. S. Aur, D. Kofalt, Y. Waseda, T. Egami, H.S. Chen, B.-K. Teo, R. Wang, J. Non-Cryst. Solids **61/62**, 331 (1984)
20. J. Hafner, *From Hamiltonian to Phase Diagrams* (Springer, Berlin, 1987)
21. T. Egami, S. Aur, J. Non-Cryst, Solids **89**, 60 (1987)
22. T. Iwashita, D.M. Nicholson, T. Egami, Phys. Rev. Lett. **110**, 205504 (2013)
23. T. Egami, Mod. Phys. Lett. B **28,** 1430006 (2014)
24. S. Sastry, P. Benedetti, F.H. Stillinger, Nature **393**, 554 (1998)
25. T. Egami, D. Srolovitz, J. Phys. F **12**, 2141 (1982)
26. F.C. Frank, Proc. Roy. Soc. London A **215**, 43 (1952)
27. P.J. Steinhardt, D.R. Nelson, M. Ronchetti, Phys. Rev. Lett. **47**, 1297 (1981)

28. S. Sachdev, D.R. Nelson, Phys. Rev. B **32**, 1480 (1985)
29. T. Tomida, T. Egami, Phys. Rev. B **52**, 3290 (1995)
30. Y.Q. Cheng, E. Ma, Progr. Mater. Sci. **56**, 379 (2011)
31. J.D. Eshelby, Proc. Roy. Soc. Lond. A **241**, 376 (1957)
32. D.M. Nicholson, M. Ojha, T. Egami, J. Phys. Condens. Matt. **25**, 435505 (2013)
33. T. Egami, Progr. Mater. Sci. **56**, 637 (2011)
34. S.P. Chen, T. Egami, V. Vitek, Phys. Rev. B **37**, 2440 (1988)
35. V.A. Levashov, R.S. Aga, J.R. Morris, T. Egami, Phys. Rev. B **78**, 064205 (2008)
36. J.-P. Hansen, I.R. McDonald, *Theory of Simple Liquids*, 3rd edn. (Academic Press, London, 2006)
37. C.A. Angell, Science **267**, 1924 (1995)
38. V.A. Levashov, J.R. Morris, T. Egami, Phys. Rev. Lett. **106**, 115703 (2011)
39. V.A. Levashov, J.R. Morris, T. Egami, J. Chem. Phys. **138**, 044507 (2013)
40. T. Iwashita, T. Egami, Phys. Rev. Lett. **108**, 196001 (2012)
41. P.G. Debenedetti, F.H. Stillinger, Nature **410**, 259 (2001)
42. M.E. Blodgett, T. Egami, Z. Nussinov, K.F. Kelton, Sci. Rep. **5**, 13837 (2015)
43. N.B. Weingartner, R. Soklaski, K.F. Kelton, Z. Nussinov, Phys. Rev. B. **93**, 214201 (2016)
44. V.N. Novikov, A.P. Sokolov, Phys. Rev. E. **92**, 062304 (2015)
45. S.C. Glotzer, V.N. Novikov, T.B. Schröder, J. Chem. Phys. **112**, 509 (2000)
46. A.S. Keys, L.O. Hedges, J.P. Garrahan, S.C. Glotzer, D. Chandler, Phys. Rev. X **1**, 021013 (2011)
47. L. Berthier, G. Biroli, Rev. Mod. Phys. **83**, 587 (2011)
48. G.A. Smolensky, *Ferroelectrics and Related Materials* (Gordon and Breach, New York, 1981)
49. D. Viehland, S.J. Jang, L.E. Cross, M. Wutting, Phys. Rev. B **46**, 8003 (1992)
50. W. Dmowski, S.B. Vakhrushev, I.-K. Jeong, M.P. Hehlen, F. Trouw, T. Egami, Phys. Rev. Lett. **100**, 137602 (2008)
51. G. Burns, F.H. Dacol, Solid State Commun. **48**, 853 (1983)
52. G. Xu, G. Shirane, J.R.D. Copley, P.M. Gehring, Phys. Rev. B **69**, 064112 (2004)
53. I.-K. Jeong, T.W. Darling, J.K. Lee, T. Proffen, R.H. Heffner, J.S. Park, K.S. Hong, W. Dmowski, T. Egami, Phys. Rev. Lett. **94**, 147602 (2005)
54. D. Kivelson, S.A. Kivelson, X. Zhao, Z. Nussinov, G. Tarjus, Physica A **219**, 27 (1995)
55. Z. Nussinov, J. Rudnick, S.A. Kivelson, L.N. Chayes, Phys. Rev. Lett. **83**, 472 (1999)
56. D.R. Nelson, Phys. Rev. B **28**, 5515 (1984)
57. D.B. Miracle, Nature Mater. **3**, 697 (2004)
58. M.H. Cohen, D. Turnbull, J. Chem. Phys. **31**, 1164 (1959)
59. T. Egami, J. Metals **62**(2), 70 (2010)
60. B. Wu, T. Iwashita, T. Egami, Phys. Rev. E **91**, 032301 (2015)
61. B. Wu, T. Iwashita, T. Egami, Phys. Rev. E **92**, 052303 (2015)
62. B. Wu, T. Iwashita, T. Egami (unpublished)
63. W. Götze, *Complex Dynamics of Glass-forming Liquids* (Oxford University Press, Oxford, 2009)
64. E. Leutheusser, Phys. Rev. A **29**, 2765 (1984)
65. B.J. Ackerson, J. van der Werff, C.G. de Kruif, Phys. Rev. A **37**, 4819 (1988)
66. X. Cheng, J.H. McCoy, J.N. Israelachvili, I. Cohen, Science **333**, 1276 (2011)
67. T.K. Haxton, A. Liu, Phys. Rev. Lett. **99**, 195701 (2007)
68. J.-L. Barrat, L. Berthier, Phys. Rev. E **63**, 012503 (2002)
69. L. Berthier, J.-L. Barrat, Phys. Rev. Lett. **89**, 095702 (2002)
70. P. Guan, M.-W. Chen, T. Egami, Phys. Rev. Lett. **104**, 205701 (2010)
71. T. Egami, Mater. Sci. Eng. A **226–228**, 261 (1997)
72. M.H. Cohen, G.S. Grest, Phys. Rev. B **20**, 1077 (1979)
73. T. Egami, S.J. Poon, Z. Zhang, V. Keppens, Phys. Rev. B **76**, 024203 (2007)
74. D. Weaire, M.F. Ashby, J. Logan, M.J. Weins, Acta Met. **19**, 779 (1971)
75. Y. Suzuki, T. Egami, J. NonCryst, Solids **75**, 361 (1985)

76. W. Dmowski, T. Iwashita, C.-P. Chuang, J. Almer, T. Egami, Phys. Rev. Lett. **105**, 205502 (2010)
77. F. Spaepen, Acta Metall. **25**, 407 (1977)
78. R. Dasgupta, O. Gendelman, P. Mishra, I. Procaccia, C.A.B.Z. Shor, Phys. Rev. E **88**, 032401 (2013)
79. B. Yang, C.T. Liu, T.G. Nieh, M.L. Morrison, P.K. Liaw, R.A. Buchanan, J. Mater. Res. **21**, 915 (2006)
80. J.J. Lewandowski, A.L. Greer, Nature Mater. **5**, 15 (2006)
81. F. Spaepen, Nature Mater. **5**, 7 (2006)
82. J. Caris, J.J. Lewandowski, Acta Mat. **58**, 1026 (2010)
83. N. Morito, T. Egami, Acta Metall. **32**, 603 (1984)
84. Y. Fan, T. Iwashita, T. Egami, Phys. Rev. Lett. **115**, 045501 (2015)
85. Y. Fan, T. Iwashita, T. Egami, Phys. Rev. E **89**, 062313 (2014)
86. J.D. Ju, D. Jang, A. Nwankpa, M. Atzmon, J. Appl. Phys. **109**, 053522 (2011)
87. I.-C. Choi, Y. Zhao, B.-G. Yoo, Y.-J. Kim, J.-Y. Suh, U. Ramamurty, J.-I. Jang, Scr. Mater. **66**, 923 (2012)
88. C.A. Schuh, A.C. Lund, T.G. Nieh, Acta Mater. **52**, 5879 (2004)
89. D. Pan, A. Inoue, T. Sakurai, M.W. Chen, Proc. Nat. Acad. Sci. **105**, 14769 (2008)
90. D.J. Wales, Science **293**, 2067 (2001)
91. J.P. Sethna, K.A. Dahmen, C.R. Myers, Nature (London) **410**, 242 (2001)

Chapter 11
The Irreversibility Transition in Amorphous Solids Under Periodic Shear

Ido Regev and Turab Lookman

Abstract A fundamental problem in the physics of amorphous materials is understanding the transition from reversible to irreversible plastic behavior and its connection to the concept of yield. Currently, continuum materials modeling relies on the use of phenomenological yield thresholds, however, in many cases the transition from elastic to plastic behavior is gradual, which makes it difficult to identify an exact yield criterion. Recent work has shown that under periodic shear, amorphous solids undergo a transition from deterministic, periodic behavior to chaotic, diffusive behavior as a function of the strain amplitude. Furthermore, this transition has been related to a depinning-like transition in which cooperative avalanche events become system-spanning at the same point. Here we provide an overview of recent work focused on an understanding of the nature of yield in amorphous systems from a cooperative and dynamical point of view.

11.1 Introduction

Amorphous solids such as plastics, window glass and amorphous metals are an important and ubiquitous form of matter. Industrial processing of such materials commonly involves plastic deformation. Although a microscopic mechanism of plastic deformation in these materials was identified [1–3], the collective behavior on the mesoscale is still being debated [4–7]. The main issues are the definition and nature of yield, how to describe the structural changes that occur during plastic deformation (this is related to the topics of ergodicity and entropy production which are some of the main issues in the general problem of the statistical mechanics description of glasses) and the role of long-range elastic interactions. As we will explain below, these issues

I. Regev
Jacob Blaustein Institutes for Desert Research, Ben-Gurion University of the Negev, Sede Boqer Campus, 84990 Beersheba, Israel

T. Lookman (✉)
Center for Nonlinear Studies and Theoretical Division, Los Alamos National Laboratory, Los Alamos, NM 87545, USA
e-mail: txl@lanl.gov

E.K.H. Salje et al. (eds.), *Avalanches in Functional Materials and Geophysics*, Understanding Complex Systems, DOI 10.1007/978-3-319-45612-6_11

play a role in the irreversibility transition discovered not long ago. Recent experiments and simulations on superconductor vortices, dilute colloidal dispersions and loosely packed granular materials show that these materials undergo a transition from reversible to irreversible diffusive behavior by varying the strength of an oscillatory external field [8–17]. These transitions have been ascribed to chaotic scattering [11] and/or to an absorbing phase transition [10].

11.2 Yield as an Irreversibility Transition

Recently, a similar transition was observed in amorphous solids under oscillatory shear, in simulations and experiments performed by several groups [8, 17–28]. These simulations and experiments studied highly condensed jammed materials (well above the jamming transition) under oscillatory shear and showed that for small strain amplitudes, after a transient, the system reaches a configuration which is completely reversible in the sense that particles return to the same position after one or more cycles (see Fig. 11.1). For large strain amplitudes, however, the particles are always diffusing (see Fig. 11.2). There have been several suggestions as to what causes this transition. One suggestion is that the transition from reversible to irreversible dynamics is an absorbing phase transition [24], which is a second order non-equilibrium phase transition, possibly of the directed percolation universality class [18]. The motivation behind this interpretation is that if one looks at the displacement of the particles from their positions before and after a cycle, at low strain amplitudes, one observes transient patches of moving particles which keep decreasing in size until one cannot observe any motion. This is very similar to the dynamics in directed percolation systems where below the percolation threshold there is random dynamics which stops after some time. The state where there is no dynamics is called the "absorbing phase" [29]. While this description is appealing, a closer look shows that there are states in which there is no overall diffusion but the particles do not return to their original positions after one cycle. However, after several cycles, the particles do return to their original positions and for that reason there is no overall diffusion. Furthermore, in all cases the dynamics during a cycle exhibits random particle rearrangements of considerable sizes [30, 31]. These rearrangements are dissipative and thus result in energy fluctuations, but they are completely repetitive (see Fig. 11.3). Therefore, the work being done on the material is transformed wholly into heat and structural rearrangements are reversible. Above a critical strain amplitude, the system does not settle into a limit cycle and the motion is chaotic with a positive maximal Lyapunov exponent. This allows us to define a yield point with a physical meaning. A yield point can be difficult to determine from a standard stress–strain curve since the behavior can be monotonic and there need not be a stress–peak as this depends on the way that the system is prepared. For example, the green curve in Fig. 11.6 was prepared by a fast quench compared to the blue curve in the inset which was prepared via a slow quench. Identifying and understanding the underlying dynamical behavior opens the

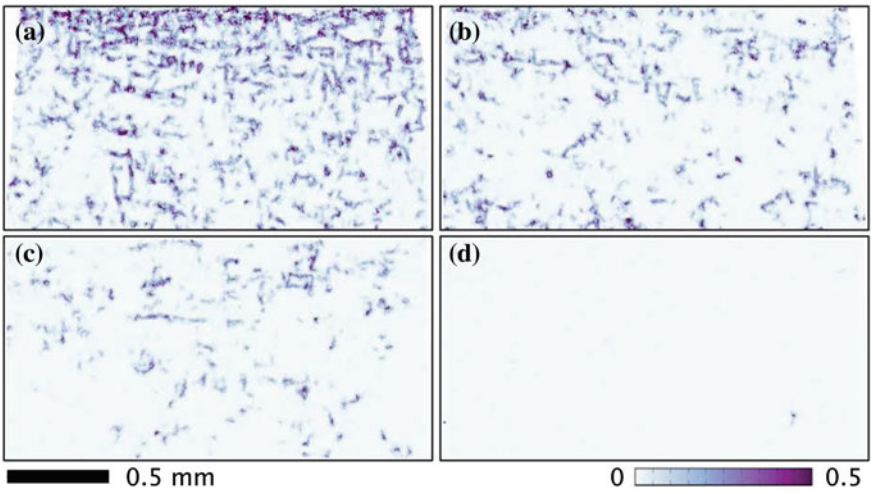

Fig. 11.1 (color online) Experimental evidence for the existence of irreversible states in a sheared colloidal suspension: *dark colors* represent areas that did not return to their original positions after a different number of cycles: **a** the first cycle of deformation with $\gamma_0 = 0.07$, **b** after 7 cycles, **c** cycles 1–3 and **d** cycles 10–12 (Taken from Keim et al. [17])

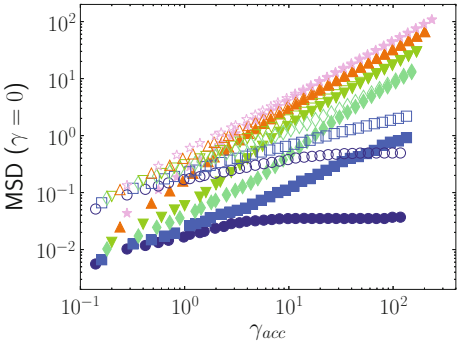

Fig. 11.2 Mean square displacement from simulations with different values of the maximal strain amplitude: $\gamma_{max} = 0.07$ (*dark blue circles*), 0.08 (*blue squares*), 0.09 (*greed diamonds*), 0.1 (*green down facing triangles*), 0.12 (*orange up facing triangles*), and 0.14 (*purple stars*). The simulations were averaged over different runs with samples of $N = 4000$ particles quenched from $T = 0.466$ (closed symbols) and $T = 1.0$ (open symbols). Note the transition between an arrested and diffusive regime as γ_{max} is increased (Taken from Fiocco et al. [18])

possibility for a quantitative description of the structural changes in these systems after yield and their relation to the dynamics.

In all of the experiments and simulations that are mentioned, the strain is applied in a periodic manner: either in a "sawtooth" fashion or as a sinusoidal function [17]. For the "sawtooth" strain profile, the strain is applied in the following manner: First, positive strain steps are applied. When a maximal pre-decided strain ϵ_{max} is reached,

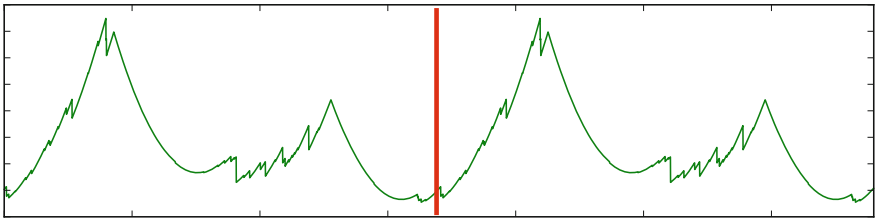

Fig. 11.3 (color online) The potential energy as a function of cumulative strain during two cycles (*red line* marks the end of the first cycle)

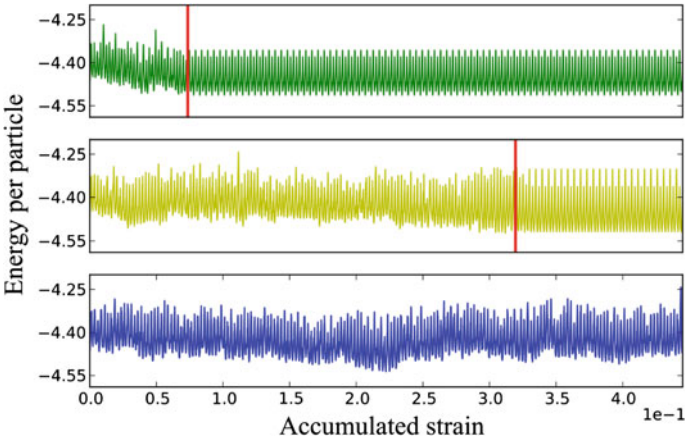

Fig. 11.4 (color online) Transient behavior of the potential energy before reaching a limit-cycle for three different strain-amplitudes (strain amplitude growing from *top* to *bottom*). *Red lines* are the point at which periodic behavior begins

the strain is reversed by applying strain steps in the opposite direction. This proceeds until the strain reaches the negative value of the maximal strain $-\epsilon_{max}$. At this point the strain steps are reversed until the system returns to zero strain, completing the elementary cycle of a specific maximal strain amplitude. The elementary cycle is then repeated and the response of the material per cycle is observed.

Different experiments and simulations [8, 17–24, 27, 28] have found that for small strain amplitudes these systems show random dynamics which gradually settles into a periodic limit-cycle (see Fig. 11.4). As the strain amplitude is increased, the transient times increase accordingly, until the transient time is so large that the system does not reach a limit cycle. Two main approaches have been suggested for describing the level of periodicity of the system. The first approach focuses on comparing the positions of particles before and after a limit-cycle. The long-time dynamics is than analysed by comparing how many particles changed their positions after a cycle [24], how much particles diffused and how the potential energy changed [18]. A limitation of this approach is that the dynamics inside the limit-cycle, which has interesting characteristics, as we will see below, is ignored. A different approach, is based on examining the dynamics inside the limit-cycle and comparing consecutive cycles in

order to understand what happens as the system approaches the critical point [19]. In order to measure the time it takes for the system to reach a periodic limit cycle, a cycle decorrelation function was defined using the total potential energy of the system $U(t)$:

$$R(n) = \int dt |U(t,n) - U(t,n-p)|. \tag{11.1}$$

When $p = 1$, this function compares the difference between potential energy fluctuations in two consecutive cycles (n is the number of cycles that the system underwent). For small strain amplitudes this function reaches a value close to zero after n cycles. However, in some cases the system reaches a limit cycle of periodicity p larger than one. Therefore, if periodic behavior is not observed p is increased by one and the function is recalculated. The process was repeated until a value of p for which the function reaches $R(n) = 0$ for some n was reached. If periodicity smaller than $p = 11$ was not observed p was set to its default value $p = 1$. In all cases periodicity larger than $p = 5$ was not observed. Figure 11.5 shows this function averaged over 30 different samples of size $N = 16{,}384$, each prepared from a different initial condition in the liquid state and than quenched using the same protocol that was used to create the green curve in Fig. 11.6. One can observe that for the strain amplitudes $\gamma = 0.06, 0.07, 0.75, 0.85, 0.88, 0.09, 0.093, 0.095$ the function relaxes, after a transient time, to zero, while for larger strain amplitudes ($\gamma = 0.12, 0.15$) the function $R(n)$ does not decay to zero but relaxes to some asymptotic finite value. In the inset to Fig. 11.7 we can see that the relaxation time, the time it takes the cycle-decorrelation function to go below 1% of its initial value, follows a power-law with a critical point at $\gamma_c = 0.11$. This critical strain amplitude is close to the yield strain as estimated from the blue linear stress–strain curve in the inset of Fig. 11.6, even though for the oscillatory shear that was used the faster quench protocol that corresponds to the green curve in Fig. 11.6. The transition from a repetitive to random behavior in a deterministic, dissipative system (no external noise is added) suggests that the transition might be a "transition to chaos" which is a well known phenomenon observed in various dynamical systems from the low-dimensional Lorenz system [32] to the high dimensional coupled chaotic maps [33] and involves a divergence (usually power-law) in the time it takes the system to reach periodic behavior as a parameter is varied. A transition to chaos might be associated with a phase transition as we will discuss below, though the connection between the two was not studied extensively, as much as we are aware. The main indication that a system exhibits chaotic behavior is sensitivity to initial conditions: trajectories starting from close-by initial conditions diverge exponentially [34, 35] (see Fig. 11.8). The sensitivity to initial conditions is estimated by measuring the maximal Lyapunov exponent λ which describes the rate of growth of the distance between two phase-space trajectories (solutions of the equations of motion with different initial conditions) $\mathbf{x}(t)$ and $\mathbf{x}_\epsilon(t)$ which are initially separated by a diminishing distance $|\mathbf{x}(0) - \mathbf{x}_\epsilon(0)| = \epsilon$:

$$\lambda_{max} = \lim_{t\to\infty} \lim_{\epsilon\to 0} \frac{1}{t} \ln \frac{|\mathbf{x}(t) - \mathbf{x}_\epsilon(t)|}{\epsilon}. \tag{11.2}$$

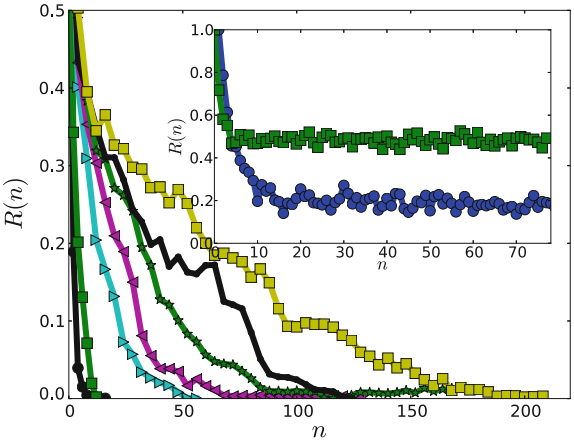

Fig. 11.5 Cycle decorrelation function as a function of the number of cycles, for system size $N = 16{,}384$ particles for strain amplitudes $\gamma = 0.06, 0.07, 0.75, 0.85, 0.88, 0.09, 0.093, 0.095$ (from left to right). (*inset*) The same function for strain amplitudes $\gamma = 0.12$ (*blue*), $\gamma = 0.15$ (*green*)

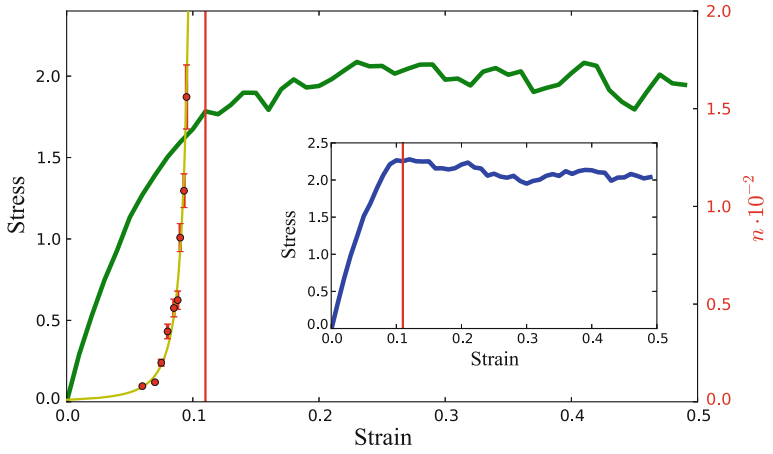

Fig. 11.6 (color online) Stress–strain curve from molecular dynamics simulations for 16,384 particles under quasi-static shear. *Red dots* represent the number of cycles, n, required to reach periodic behavior under oscillatory shear (scale is on the right side of the figure in *red*). The *red line* is the strain amplitude for which the time to reach reversible behavior diverges. *Inset* Stress–strain behavior for the same parameters as the *green curve* but with different initial particle configurations - the *red line* is the same as in the larger figure

For a periodic system $\lambda_{max} = 0$ whereas a chaotic system will have $\lambda_{max} > 0$ [34]. There are different methods for calculating the maximal Lyapunov exponent. In [19] the method suggested by Kantz [35, 36] which extracts the largest Lyapunov exponent from a time-series of one of the observables (in our case the potential energy: $u_i = \{u_0, u_1, u_2, \ldots\}$) was used. The advantages of this method is that it

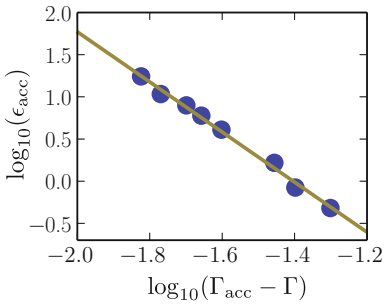

Fig. 11.7 (color online) Slowing down: Accumulated strain to reach a limit-cycle as a function of the maximal strain amplitude minus the critical strain amplitude $\Gamma_c = 0.11$

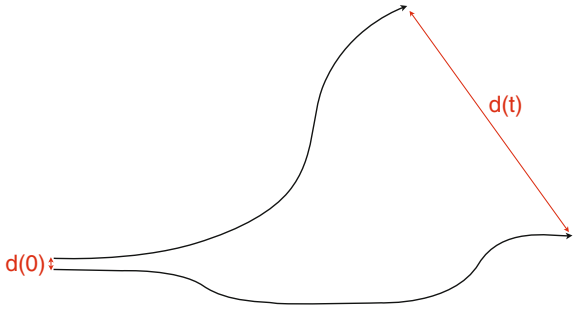

Fig. 11.8 (color online) In a chaotic system, the distance between phase-space trajectories diverges exponentially fast

has been widely tested, a highly tested code is available in the author's website and that the results give a relatively clear distinction between chaotic and non-chaotic time-series, as we shall see below. Since we are analyzing a time-series, instead of looking at the distance between two different solutions of the equations of motion, we look for points in the time-series which are at some-point close to each other, i.e. $|u_i - u_k| < \epsilon$ and check how the distance grows over time $d_\ell = |u_{i+\ell} - u_{k+\ell}|$. However, since u_i is a one dimensional function of the multi-dimensional phase-space, a simple measure of the distance between them does not reflect the actual distance of the phase-space coordinates that generated them. To overcome this we use Taken's delay embedding theorem [37] which asserts that for an embedding dimension $m > 2D_A$ where D_A is the dimension of the chaotic attractor (the part in phase-space at which the chaotic behavior occurs), a set of m variables generated by sampling the time-series at regular intervals τ m:

$$(u_{n-(m-1)\tau}, u_{n-(m-2)\tau}, \ldots, u_{n-\tau}, u_n), \tag{11.3}$$

will have an attractor with the same topological properties as the underlying attractor. As an example we show the reconstruction for the Lorenz system:

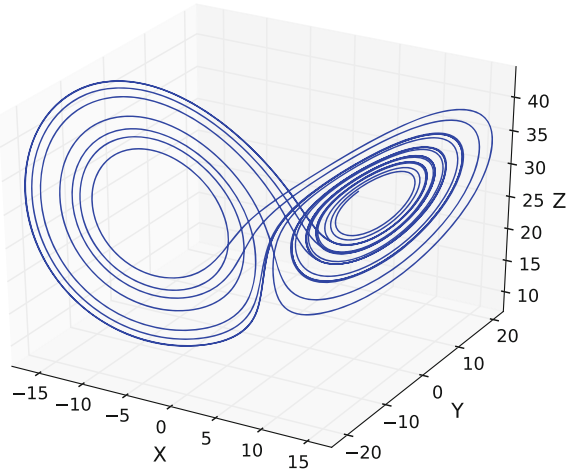

Fig. 11.9 Phase space trajectory which is part of the "strange" attractor of the Lorenz system

$$\begin{aligned}\frac{dx}{dt} &= \sigma(y-x)\,,\\ \frac{dy}{dt} &= x(\rho-z)-y\,,\\ \frac{dz}{dt} &= xy-\beta z.\end{aligned} \tag{11.4}$$

In Fig. 11.9 we show the dynamics as a function of all three coordinates which shows the famed Lorenz attractor which is chaotic for the parameters that we chose. To demonstrate reconstruction we take the time-series of one of the coordinates (Fig. 11.10) and construct three new coordinates using time-delay:

$$(x_{n-2\tau}, x_{n-\tau}, x_n), \tag{11.5}$$

where we chose $m = 3$ and an appropriate τ. We now plot the new coordinates in Fig. 11.11. One can see the resemblance in the structure of the reconstructed attractor and the original one (Fig. 11.9).

Typically, in a dissipative system, a chaotic attractor will have a smaller dimensionality than the phase space-dimension. Defining:

$$\mathbf{s}_n = (u_{n-(m-1)\tau}, u_{n-(m-2)\tau}, \ldots, u_{n-\tau}, u_n). \tag{11.6}$$

as the delay-coordinates vector, for large enough τ and m, the distance $d = |\mathbf{s}_i - \mathbf{s}_k|$ will represent the actual phase-space distance and if the underlying dynamics is chaotic, $d_\ell = |\mathbf{s}_{i+\ell} - \mathbf{s}_{k+\ell}|$ will grow exponentially fast. The value of τ is usually taken to be the de-correlation time of the time-series ($\tau \approx 600$ in this case) but m is unknown since we do not know a-priori the dimension of the attractor. In order to find a numerical estimate of the largest Lyapunov exponent the algorithm calculates

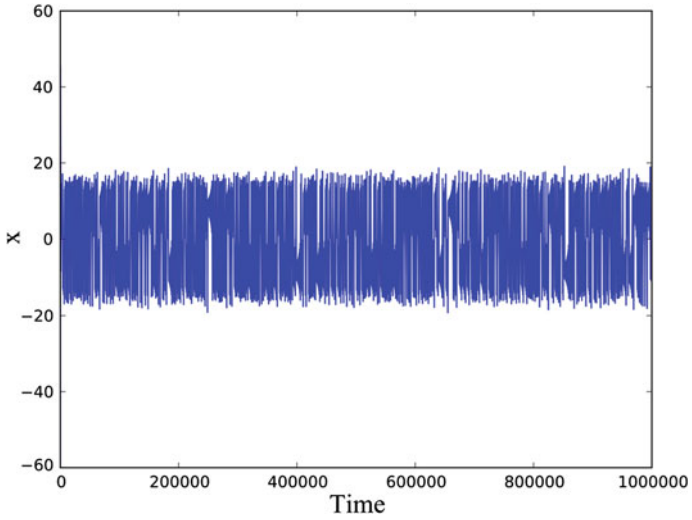

Fig. 11.10 A representative time-series of the x-coordinate of the Lorenz system in the chaotic regime

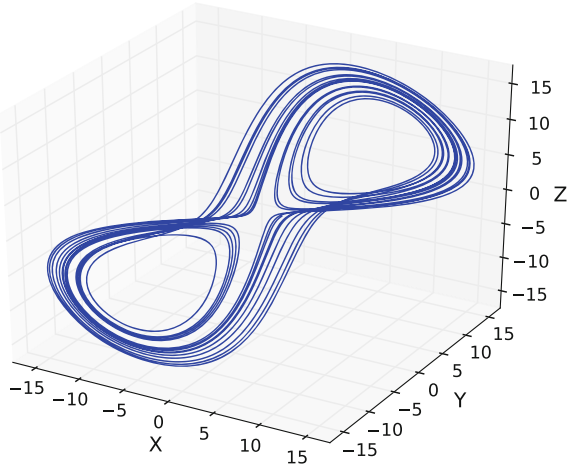

Fig. 11.11 Attractor reconstructed from the x coordinate which shares the same topological structure as the original attractor

the finite-time maximal Lyapunov exponent for a trajectory starting at a point i:

$$\lambda_\ell^i = \frac{1}{\ell} \ln \frac{||\mathbf{s}_{i+\ell} - \mathbf{s}_{k+\ell}||}{\epsilon}. \tag{11.7}$$

where $||\mathbf{s}_i - \mathbf{s}_k|| < \epsilon$ with respect to some norm $||..||$ (the actual norm used in the algorithm is $||\mathbf{s}_i - \mathbf{s}_k|| = |u_i - u_k|$ for reasons explained in [35]). For each point $\mathbf{s}_i$ and a small distance ϵ a set of points $\mathbf{s}_k$ such that $||\mathbf{s}_i - \mathbf{s}_k|| < \epsilon$ is gathered which allows to calculate the average distance from the point $\mathbf{s}_i$ as a function of ℓ:

$$\lambda_\ell^i = \frac{1}{\ell} \ln \frac{1}{\mathcal{U}_i} \sum_k \frac{||\mathbf{s}_{i+\ell} - \mathbf{s}_{k+\ell}||}{\epsilon}. \tag{11.8}$$

where $\mathcal{U}_i$ is the total number of points $\mathbf{s}_k$ that are ϵ close to $\mathbf{s}_i$. The process is repeated for different initial points $\mathbf{s}_i$ which leads to further averaging. The actual function that we calculate is:

$$S_\ell = \frac{1}{\mathcal{W}} \sum_i \ln \left(\frac{1}{\mathcal{U}_i} \sum_k \frac{||\mathbf{s}_{i+\ell} - \mathbf{s}_{k+\ell}||}{\epsilon} \right). \tag{11.9}$$

where $\mathcal{W}$ is the number of starting points i collected. Since this function describes the ln of the averaged growth of distances as a function of time, we expect that in a chaotic system ($\lambda_{max} > 0$) S_ℓ will show linear behavior with a positive slope for large enough ℓ. However, there are two caveats for this: the maximal Lyapunov exponent becomes dominant only after several time steps ℓ_0:

$$||\mathbf{s}_{i+\ell} - \mathbf{s}_{k+\ell}|| = \sum_i a_i e^{\lambda_i \ell} \approx_{\ell > \ell_0} a_{max} e^{\lambda_{max} \ell}. \tag{11.10}$$

The second caveat is that for large ℓ the distance $||\mathbf{s}_{i+\ell} - \mathbf{s}_{k+\ell}||$ can reach the size of the attractor and thus the trajectories start to fold back. When that happens S_ℓ saturates. In Fig. 11.12 one can see the function S_ℓ for a potential energy time-series of a system of size $N = 4096$ sheared at maximal strain amplitudes $\gamma = 0.12, 0.15, 0.2$ which are all above the critical amplitude [19]. Since the dimension of the attractor is not known a-priory all the values of m starting from $m = 1$ were checked until the shape of S_ℓ did not change under further increase (remember that according to Takens theorem the delay coordinates should give the right result for any $m > 2D_A$ where D_A is the dimension of the attractor). For m values 5, 6, 6 respectively, the function S_ℓ shows a linear regime with a positive slope which indicates a positive maximal Lyapunov exponent.

In Fig. 11.13 we can see the result of applying the algorithm for one of the periodic limit-cycles with different values of m. One can see that the behavior is significantly different from that observed for the chaotic time-series: there is no linear regime and the values of S_ℓ are negative for large enough values of m. This function shows a distinct behavior when calculated for chaotic time-series: for an intermediate range of ℓ it will have a linear, positive slope where the value of the slope is the value of the Lyapunov exponent. In Fig. 11.12 we can see the function S_ℓ for a time-series of potential energy values for a system of size $N = 4096$ sheared at maximal strain amplitudes $\gamma = 0.12, 0.15, 0.2$ all above the critical amplitude. In all three cases the function shows linear behavior for intermediate values of ℓ indicating a positive Lyapunov exponent and hence chaotic behavior. These results are consistent with previous results for the maximal Lyapunov exponent for amorphous solids under *linear* shearing obtained in experiments [38] and simulations [39]. These results suggest that amorphous solids undergo a transition to chaos at a strain amplitude

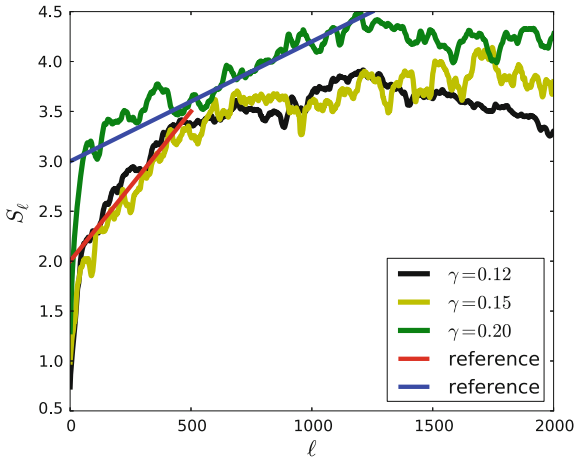

Fig. 11.12 Estimation of Lyapunov exponents: The function S_ℓ of the time delay ℓ for a system of size $N = 4096$ under oscillatory shear in different strain amplitudes larger than the critical amplitude. The *straight lines* are shown as a guide to the eye

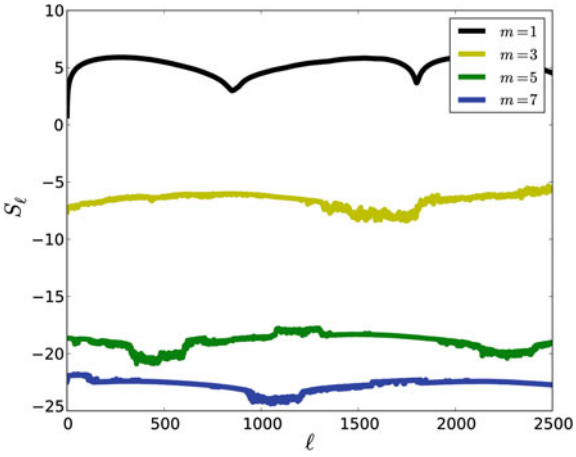

Fig. 11.13 The function S_ℓ applied for a periodic limit-cycle. The behavior is strikingly different than the one shown in Fig. 11.12 and includes negative values

coincident with yield at least under oscillatory shear. One should note that a transition to chaos is not necessarily accompanied by a nonequilibrium phase transition and although it shows behavior similar to critical slowing down, it is not necessarily accompanied by critical fluctuations and a growing correlation length, which are expected in a non equilibrium phase transition such as directed percolation. However, it has been suggested that in high dimensional systems, such as fluid turbulence and ecological systems, a transition to chaos (or turbulence) can be accompanied and even be a result of, a non equilibrium phase transition such as directed percolation [40, 41]. Below we discuss how the transition to chaos is related to a different non equilibrium phase transition.

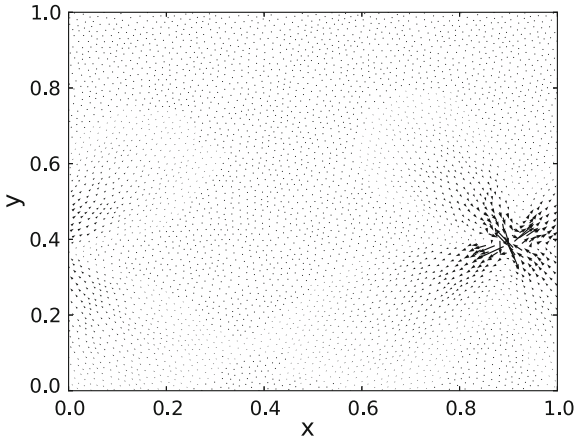

Fig. 11.14 Displacement field after a local particle rearrangement. *Arrows* indicate the direction and magnitude of displacement of each of the particles

11.2.1 Analysis of Periodic Behavior

As we explained above, for strain amplitudes smaller than the critical value, after a transient regime, the system shows fluctuating but periodic behavior. This resembles the reversible regime of dilute colloidal systems, of the types studied in [10, 11]. However, in these systems, the dynamics in a limit-cycle is quite trivial since the response becomes periodic only once the particles reach a configuration in which they do not touch each other during the cycle. On the contrary, in a highly condensed amorphous solid, particles change positions and rearrange in a non trivial manner, causing non affine deformation, even during a reversible limit cycle. Typically, this involves a large number of rearrangements of the T1 type (two next-nearest neighbours becoming nearest neighbors) which generate elastic-inclusion like displacement fields (see Fig. 11.14) and appear as energy drops in the potential energy time-series. The repetitive behavior can also be observed by following the trajectory of any single particle over consecutive cycles (blue and red lines in Fig. 11.15). The non-affine nature of the displacement of the particle is clearly seen in the figure. One should note that contrary to the usual notion the rearrangement events that are observed in the limit cycles are completely repetitive so that one can think of the dynamics inside a limit-cycle as a special form of non-linear elasticity rather than plasticity. It seems that the oscillatory loading reveals a distinction between plastic and nonlinear elastic rearrangements (for example, the phenomenon of super-elasticity in shape memory alloys [42–44]) which is somewhat subtle.

In Fig. 11.16 energy drops (rearrangement events) are identified and marked as black lines. The points in the limit cycle where these drops occur are marked as black dots in the columns of Fig. 11.17 where time advances from bottom to top. The x-axis in Fig. 11.17 is the strain amplitude. This is repeated for different strain amplitudes with the same initial conditions. It was found that for small strain amplitudes limit-cycles that start from the same initial conditions are similar to each other and an

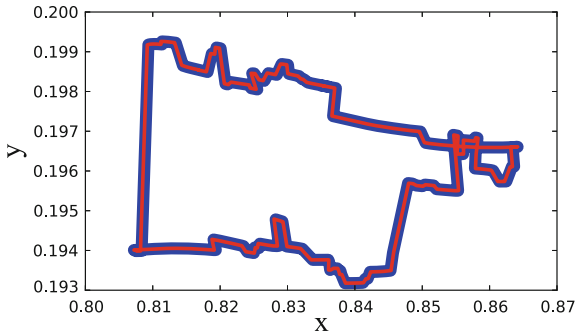

Fig. 11.15 Two consecutive trajectories of one particle taken when the system is in a limit-cycle: *blue* is the first cycle and *red* is the one just after it. The trajectories are very similar

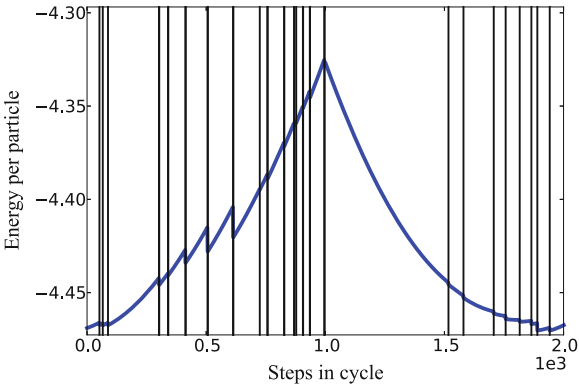

Fig. 11.16 (color online) Analysis of one limit cycle with a certain strain amplitude: Energy drops (rearrangement events) are identified and marked as *black lines* on this curve

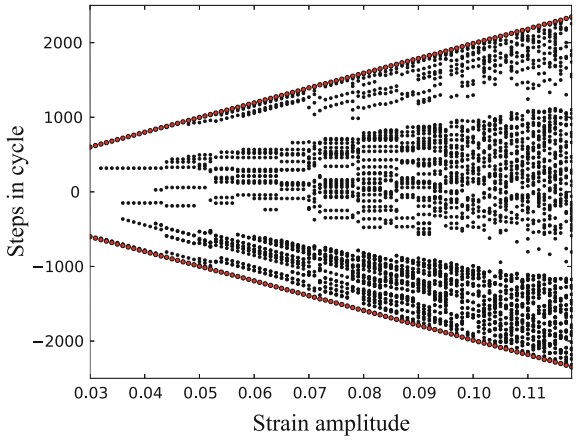

Fig. 11.17 (color online) A plot of the position of energy drops (marked as *black dots*) on the limit cycle as a function of the strain amplitude (x-axis) for one system of size $N = 1024$. The y-axis is the time inside a limit-cycle

increase of the strain amplitude changes the limit-cycle in a gradual manner. However, for large strain amplitudes small increments in the strain amplitude result in a completely different limit-cycle. This might be a manifestation of the coexistence of many different limit-cycles which occupy different parts of the state-space and of the

existence of "riddled basins of attraction" where infinitesimally close initial points in state-space lead to completely different attractors [34, 45]. In Fig. 11.18 we can see the effect of applying Langevin noise to a system that is already in a limit-cycle (these simulations were performed using overdamped dynamics). After a few cycles the system escapes from the initial limit-cycle and settles in a different limit-cycle. This is another indication that there are a large number of nearby limit-cycles and also shows that a limit-cycle can survive a small level of thermal noise. While the limit cycle that is shown in Fig. 11.15 repeat themselves after one cycle, for large strain amplitudes cycles that repeat themselves after 2, 3, 4 and 5 cycles were observed (see Figs. 11.19, 11.20) which is a phenomenon observed in many dynamical systems and in some cases can lead to a transition from periodic to chaotic behavior. This can happen in systems that show "frequency locking" or "period doubling bifurcations". In a system showing a transition to chaos due to period doubling, the period of the limit-cycle doubles for certain values of the control parameters. A succession of period doubling bifurcations (a period doubling cascade) leads to an infinite period and chaos. Below we will describe a possible explanation for the connection between the observed period doubling and the transition to chaos in amorphous solids.

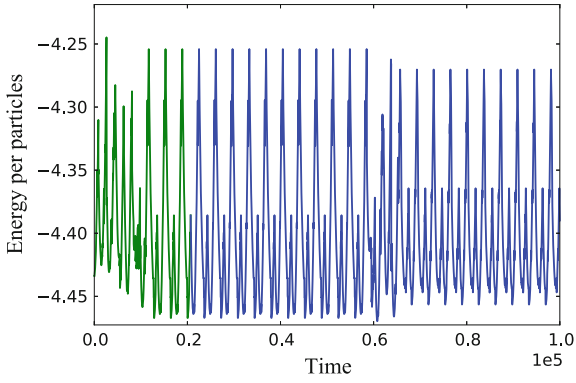

Fig. 11.18 Effect of thermal noise: System relaxes into a limit-cycle after initial overdamped dynamics (*green*). It is then subject to the same dynamics accompanied by a small Langevin noise. After some time it "hops" to another limit-cycle

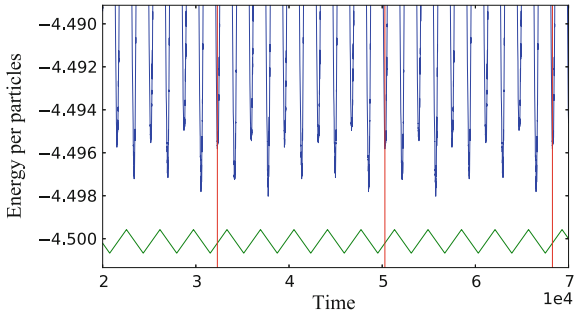

Fig. 11.19 (color online) Periodic limit cycles with period 5 at strain amplitude $\gamma = 0.09$. The *green curve* is the applied strain (not to scale). *Red lines* represent the start and the end of a cycle

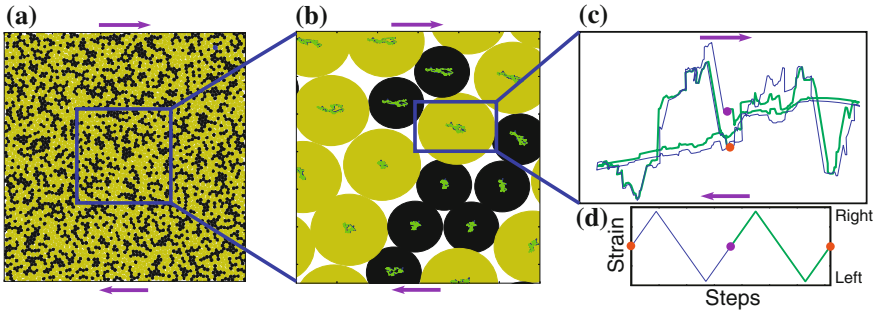

Fig. 11.20 Limit cycles: Repetitive particle trajectories in a period-two limit-cycle. **a** shows the entire system, **b** shows local environment and the trajectories that each particle is undergoing and **c** shows the trajectory of one particle. **d** shows the strain applied using the Lees Edwards boundary conditions (purple arrows show how the Lees-Edwards boundaries move with respect to the simulation square when the system is sheared in the positive direction). Since the limit cycle has period two the trajectories repeat themselves only after two shearing cycles (the *blue* and *green lines* in **d**). The particle starts from the orange initial point and moves to the right on the blue trajectory, due to the external strain that shears the material to the right, then moves back to the center and to the right, when the strain is changed accordingly (*blue curve* on **d**). When the strain is set back to zero, the particle reaches the purple point. Then, when the strain is applied again to the right, the particle moves accordingly, but this time on the green trajectory. The particle then moves to the center and to the left due to the applied strain (*green curve* in **d**). Eventually the particle comes back to the orange point, the initial condition. The next two cycles repeat the same two trajectories, and the same for the following cycles

11.3 Ergodicity

The emergence of chaotic behavior can explain an important aspect of the physics of amorphous solids. In previous studies [46–48] it was shown that the effective or "fictive" temperature that describes the structure of an amorphous solid depends on the initial quench of the system. However, when the material is deformed, the effective temperature of systems that were quenched using different cooling protocols converge to the same steady-state value which depends on the work performed on the system (and on the thermal bath temperature, when it is larger than zero). This has been described as overaging or rejuvenation of the amorphous solid [46], depending on whether the effective temperature increases or decreases. We can understand this behavior in terms of the onset of chaos. The existence of a positive maximal Lyapunov exponent is an indication that the system is not only chaotic, but that the dynamics is ergodic on a chaotic attractor which occupies part of the state-space (this is different than ergodicity in Hamiltonian systems in which the entire state-space for a given energy is explored). Since every initial condition ends up on the attractor, and the dynamics on the attractor is ergodic, averaged observables will eventually show the same values independent of the initial configuration. In Fig. 11.21 we see three different limit cycles all simulated with the same system size and sub-yield strain amplitude but with different initial conditions. We observe that whereas the

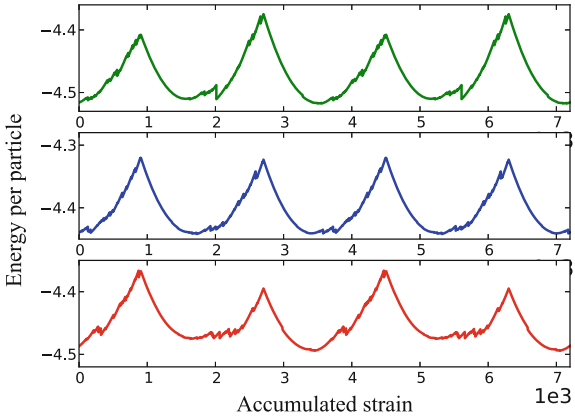

Fig. 11.21 (color online) Several different limit-cycles that were obtained using the same control parameters (number of particles, shearing steps, amplitude of shear) but different initial conditions

period is the same, the details of the cycles (energy fluctuations) depend on the initial configuration which indicates that the final state depends on the initial conditions, as we expect from a non-ergodic system. This dependence on initial conditions is clearly seen when one looks at the average potential energy as a function of the cumulative strain (Fig. 11.22 taken from Fiocco et al. [18]). One can observe that starting from two different initial quenches, with different potential energies, the final potential energy depends on the initial quench when the maximal strain amplitude is sub-yield and does not depend on the initial conditions when the maximal strain amplitude is above-yield which indicates that the system regains some kind of ergodicity above yield.

11.4 Interactions and a Non-equilibrium Phase Transition

It is well known that solids under plastic deformation exhibit power-law noise due to large correlated plastic events which resemble avalanches [31, 49] (see Fig. 11.23). A connection between the avalanche statistics and the irreversibility transition was explored by studying the avalanche statistics for different maximal strain amplitudes and system sizes [30]. Since the simulations were athermal, potential energy drops were identified with plastic rearrangement events. For each simulation, all of the energy drops in the last shear cycle (to avoid transient effects), were extracted and used to create a histogram of the energy drops which was used to calculate the average energy drop for each maximal strain amplitude [30]. We observe in Fig. 11.24 a cusp in the average potential energy at the point at which the irreversibility transition occurs, followed by saturation to a value which depends on the system size, at large strain amplitudes. The cusp suggests that the irreversibility transition is related to a change in the avalanche dynamics, and the system size dependence of the saturation

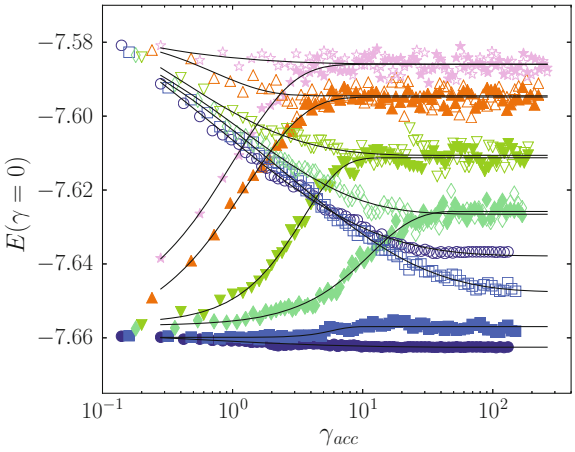

Fig. 11.22 Ergodicity breaking - Potential energy per particle E for zero-strain configurations, for different maximal strain amplitude γ_{max} [0.07 (*dark blue circles*), 0.08 (*blue squares*), 0.09 (*green diamonds*), 0.1 (*green down facing triangles*), 0.12 (*orange up facing triangles*), and 0.14 (*purple stars*)], averaged over different runs with samples of $N = 4000$ particles quenched from $T = 0.466$ (*closed symbols*) and $T = 1.0$ (*open symbols*). (Taken from Fiocco et al. [18])

suggests that there is a saturating correlation length both indicative of critical behavior [50, 51].

The avalanche statistics was interpreted using a simple model [52] that belongs to the same universality class as the theory of front depinning which was originally developed to explain the motion of an interface in a random media. This motion involves parts of an interface overcoming local energy barriers due to external forcing and neighbouring locations in the interface "pulling" the site back. The forward motion of the interface occurs in avalanches. In the case of long-range interactions, such as the ones that exist in elasto-plastic systems, the notion of a "front" becomes more abstract since sites that are far apart affect each other and the notion of locality becomes blurred (see Fig. 11.25 for illustration). This explains why the same equations can also describe avalanche behavior associated with the plasticity of amorphous solids in which the dynamics involves overcoming random energy barriers and long-range interactions, even if an actual front may not exist. The equations of motion describing the time evolution of the plastic displacement field $u(\mathbf{r}, \mathbf{t})$ controlled by overdamped dynamics are [52]:

$$\eta \frac{\partial u(\mathbf{r}, \mathbf{t})}{\partial t} = F + \int d^2 r' J(\mathbf{r} - \mathbf{r}') [\mathbf{u}(\mathbf{r}', \mathbf{t}) - \mathbf{u}(\mathbf{r}, \mathbf{t})] - \mathbf{f_R}(\mathbf{u}, \mathbf{r}), \tag{11.11}$$

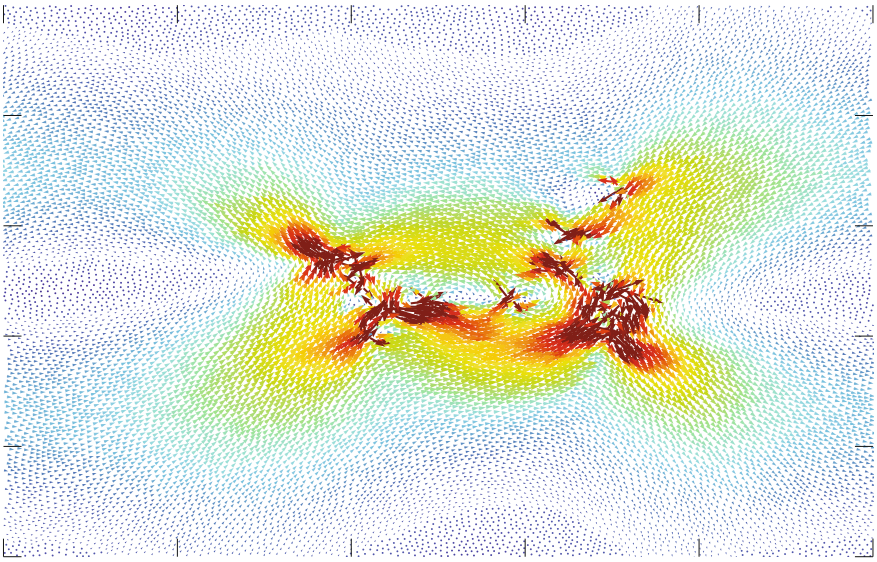

Fig. 11.23 Reversible (repetitive) Avalanches. An avalanche in a sub-critical limit-cycle for a system with $N = 16{,}384$ particles and maximal strain amplitude $\Gamma = 0.1$. Even though the avalanche spans a large part of the system, it is repeated under repeating strain cycles of identical strain amplitude. The *arrows* mark the displacement during the avalanche and the colors represent the magnitude of the displacement (warm - large displacement, cold - small displacement)

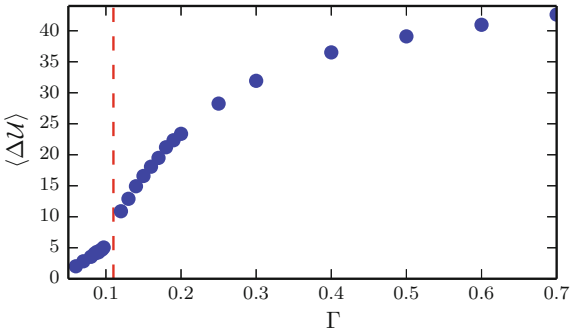

Fig. 11.24 Mean energy drops. The mean energy drop as a function of the maximal strain amplitude for the largest system size. Note the distinct cusp at the irreversibility point

where η is the viscosity, F is an externally applied force, $\mathbf{r}$ is a position of a deformable region (Shear transformation zone), $J(\mathbf{r} - \mathbf{r}')$ is the Green's function for the elastic interaction between different "soft" regions located at points $\mathbf{r}$ and $\mathbf{r}'$ and $f_R(u, \mathbf{r})$ is a random pinning potential representing the structural disorder inherent to such systems. This model assumes that the nature of the structure (the distribution of the random pinning forces $f_R(u, \mathbf{r})$) does not change as a function of time. In amorphous solids the randomness is self-generated and can (and typically does) change under plastic deformation. However, when the system is at a steady-state under linear or cyclic shearing, one can assume that the disorder is fixed. Also, the scaling behavior

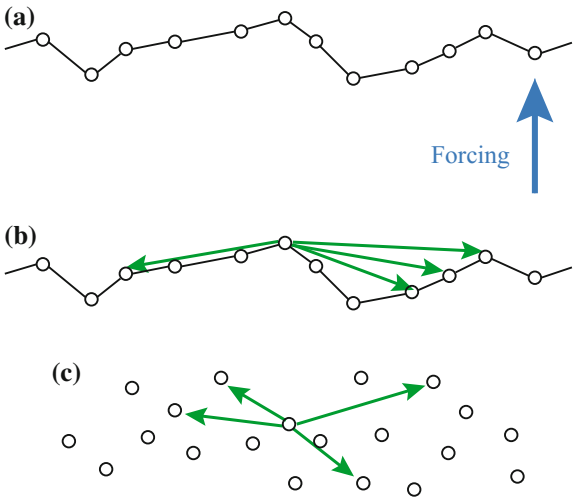

Fig. 11.25 Depinning theory in the amorphous plasticity context. **a** Depinning theory describes the motion of an elastic interface (here a one-dimensional front) in a random potential. The *circles* represent the (plastic) displacement of each point in the front. The front is subject to an applied force which causes it to move but elements of the front are pinned locally and need to overcome energy barriers. The different elements of the front are connected by springs so that if one pinned site overcomes the energy barrier it is pulling its nearest neighbors (and only them). **b** If the interactions are long range, different pinned elements of the front interact with distant elements and the actual structure of the front becomes immaterial. **c** In this case there is no real difference between the equations that describe a front and the equations that describe the interaction of some collection of pinning sites distributed in the material. A simple model of plasticity [52] that belongs to the depinning universality class, has been shown to describe the dynamics of an amorphous solid under shear where "shear transformation zones" or "weak spots" are dispersed in the material and affect each other with long-range elastic interactions

of the model predictions do not change if the pinning stresses randomly change in time. This model exhibits a non-equilibrium phase transition between a pinned, static state and a flowing state as the stress is slowly increased past a critical force F_c [52]. The transition is a critical point involving correlated displacement jumps. These correlations are described in terms of a scaling theory, which was derived from a mean-field (infinite interaction range) approximation and renormalization group theory [52, 53]. This theory was indeed shown to give a good description of the statistics of avalanches during plastic deformation in crystals [54–57] and is now also being applied to amorphous solids [58–60]. For an applied external force, at zero velocity (quasi-static limit) it was found that at a critical force F_c the avalanche size distribution scales as:

$$D(\mathcal{S}) \sim \mathcal{S}^{-\tau}, \tag{11.12}$$

where $\mathcal{S}$ is the avalanche size and τ is a universal critical exponent. Below F_c the distribution follows the same power law but with a maximal size (cutoff):

$$\mathcal{S}_{\max} \sim (F_c - F)^{-1/\sigma}, \tag{11.13}$$

where σ is the cutoff exponent. Then the distribution function takes the form:

$$D(\mathcal{S}, F) \sim \mathcal{S}^{-\tau}\mathcal{D}(\mathcal{S}/\mathcal{S}_{\max}) \sim \mathcal{S}^{-\tau}\mathcal{D}(\mathcal{S}(F_c - F)^{1/\sigma}), \tag{11.14}$$

where $\mathcal{D}(x) \sim A\, e^{-Bx}$ is a universal cutoff scaling function but the constants A and B are system specific [52, 53].

11.4.1 Statistics Under Oscillatory Shear

The application of depinning theory for amorphous solids under oscillatory shear involves modifying the theory to take into account different factors that were not included in the theory described above which assumes a steady force. One issue is that the disorder in amorphous solids is not quenched which can affect the statistics. For example, there could be weakening effects during an avalanche event, where the same site can be triggered more than once. This has been addressed by Dahmen et al. [52] and was shown to affect the stress–strain curve but not the scaling exponents [53]. The second effect of having dynamic disorder is that the distribution which describes the random variable $f_R(u, \mathbf{r})$ can change during a cycle. This issue was avoided by performing statistics only for avalanches in "steady-state" cycles, when the avalanche statistics is stable. It is known that the exact distribution of the disorder does not affect the avalanche statistics so even if the disorder is different in different cycles, that should not change the scaling functions. Another issue is that the forcing is a "sawtooth", periodic strain profile. In order to take that into account (11.14) was rewritten in terms of the strain and integrate over the different strain amplitudes. The relation between the stress and the strain shows hysteresis due to the nonlinear nature of plastic deformation. One immediate consequence of the existence of avalanches (and plastic events in general) is that the stress–strain curve becomes non-linear and exhibits hysteresis - the stress becomes a multivalued function of the strain (see Fig. 11.26). In principle, this nonlinearity can be deduced directly from the avalanche statistics. In the case of amorphous plasticity, however, in order to get an analytical solution certain approximation were needed as will be explained below. Since the forward and reverse straining branches of the hysteresis curve are statistically identical, we take into account only the forward direction. For the forward branch, we can model the relation between stress and strain using the scaling relation:

$$(\Sigma_c - \Sigma) \sim (\Gamma_c - \Gamma)^{\delta}. \tag{11.15}$$

where Γ_c is the critical strain and Σ_c is the critical stress which is related to the critical force F_c in a manner which will be explained below. The exponent δ was found to be $\delta = 1.25$ by fitting (see Fig. 11.27). The increment in plastic displacement u_p due to an infinitesimal change in the force is [52]:

$$du_{\mathrm{p}} \sim \langle \mathcal{S} \rangle_{\mathrm{F}} dF, \tag{11.16}$$

for a small force increment dF over the current force F (the avalanche size $\mathcal{S}$ is the amount of slip or displacement in an avalanche event and $\langle \mathcal{S} \rangle_F$ is the average avalanche size for a constant applied force F). This can be translated to an equation for the force-displacement behavior, using the theoretical scaling law for $\langle \mathcal{S} \rangle_F$:

$$\frac{du_{\mathrm{p}}}{dF} = \mathcal{C} \left(\frac{F_{\mathrm{c}}}{F_{\mathrm{c}} - F} \right)^{\alpha} = \mathcal{C} f^{-\alpha}, \tag{11.17}$$

where $\mathcal{C}$ is a constant with dimensions of length/force, $f = \frac{F_{\mathrm{c}} - F}{F_{\mathrm{c}}}$ and α is a critical exponent. When the avalanche size diverges, the behavior will be affected by finite size effects. If we assume that the irreversibility transition under oscillatory shear occurs at the same maximal strain amplitude as the non-equilibrium phase transition one can explain the finite-size dependence the results obtained by Fiocco et al. [18] which observed that the critical strain amplitude for the irreversibility transition decreases with system size: The maximal strain amplitude Γ is related to the maximal displacement by $\Gamma = u/L$. If we integrate (11.17) directly, we expect to get $u_{\mathrm{p}} \sim \ln L^{-1/\nu}$ when $F \to F_{\mathrm{c}}$, where ν is the critical exponent associated with the correlation length since the correlation length $\xi \propto f^{-\nu}$ must be smaller than the system size L. This gives a system size dependence of the plastic critical strain amplitude:

$$\Gamma_{\mathrm{p,c}} \sim \frac{\ln L}{L}. \tag{11.18}$$

However, the total yield strain is the sum of the elastic $\Gamma_{\mathrm{p,c}}$ and the plastic $\Gamma_{\mathrm{e,c}}$ yield strains:

$$\Gamma_{\mathrm{c}} = \Gamma_{\mathrm{p,c}} + \Gamma_{\mathrm{e,c}} \sim b \frac{\ln L}{L} + \Sigma_{\mathrm{c}}/\mu \tag{11.19}$$

such that for $L \to \infty$

$$\Gamma_{\mathrm{c}} \to \Sigma_{\mathrm{c}}/\mu, \tag{11.20}$$

where μ is the shear modulus, b is a constant and Σ_{c} is the critical stress for depinning. This prediction is compared in Fig. 11.28 to the transition to chaos points obtained from our simulations for three different system sizes. By fitting the critical strain was estimated to be $\Gamma_{\mathrm{c}} \approx 0.11$ for infinite systems. This should also be compared with other theoretical results that predict a yield strain due to the appearance of a system spanning plastic event [61]. We substitute (11.15) into (11.14) and obtain a scaling relation for the avalanche size distribution as a function of the strain amplitude:

$$D(\mathcal{S}, \Gamma) \sim \mathcal{S}^{-\tau} \mathcal{D}(\mathcal{S}(\Gamma_{\mathrm{c}} - \Gamma)^{\delta/\sigma}), \tag{11.21}$$

which would be expected to describe the avalanche statistics close to the critical strain amplitude. However, for oscillatory driving, the scaling function $D(\mathcal{S}, \Gamma)$

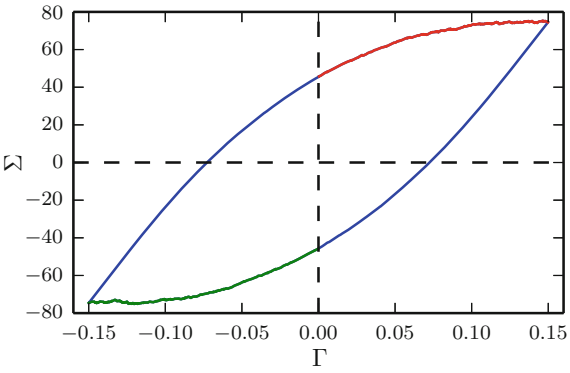

Fig. 11.26 Stress–strain curve exhibiting Hysteresis. *Red* and *green* branches are the relevant parts of the curve for the avalanche statistics. In the calculation we assume that they provide identical statistics

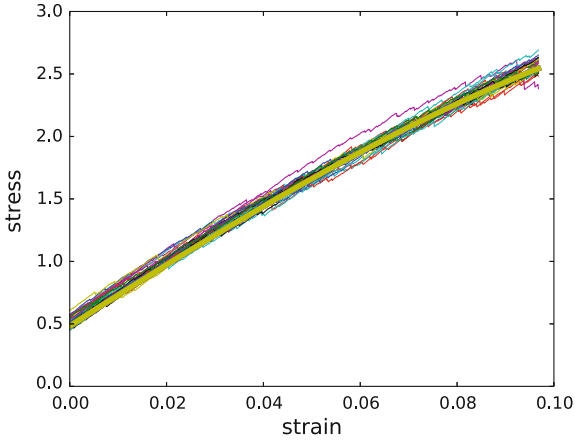

Fig. 11.27 Comparison of 30 stress–strain curves from simulations ($N = 16{,}384$, $\Gamma = 0.097$) with (11.5) in the main text, (*thick dark-yellow curve*) with a critical exponent $\delta = 1.25$

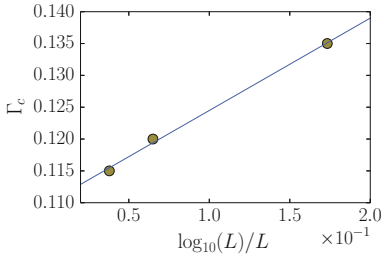

Fig. 11.28 Finite size effects in the critical strain amplitude

requires corrections since the avalanche size distribution measured is a result of integration over a varying amount of applied strain. Since the strain increases and decreases periodically, the system spends time both below and above the critical strain amplitude. Because we are averaging over cycles, we need to integrate over the different strain amplitudes.

Below the transition we get the equation:

$$P(\mathcal{S},\Gamma) \sim \int_{-\Gamma}^{\Gamma} d\varepsilon\, \mathcal{S}^{-\tau}\mathcal{D}(\mathcal{S}(\Gamma_c-\varepsilon)^{\delta/\sigma}), \tag{11.22}$$

where $P(\mathcal{S},\Gamma)$ is the distribution of avalanche sizes at maximal strain amplitude Γ, and ε is the instantaneous strain amplitude during a cycle $\varepsilon \in [-\Gamma,\Gamma]$.

By changing the variable of integration in (11.22), we get:

$$\begin{aligned} P(\mathcal{S},\Gamma) &\sim \int_{-\Gamma}^{\Gamma} d\varepsilon\, \mathcal{S}^{-\tau}\mathcal{D}(\mathcal{S}(\Gamma_c-\varepsilon)^{\delta/\sigma}) \\ &= \int_{0}^{\Gamma} d\varepsilon\, \mathcal{S}^{-\tau}\mathcal{D}(\mathcal{S}(\Gamma_c-\varepsilon)^{\delta/\sigma}) \\ &+ \int_{-\Gamma}^{0} d\varepsilon\, \mathcal{S}^{-\tau}\mathcal{D}(\mathcal{S}(\Gamma_c-\varepsilon)^{\delta/\sigma}). \end{aligned} \tag{11.23}$$

Next, we make two simplifications: first, we perform the integral only in the forward shearing direction (the red part of the curve in Fig. 11.26) since the statistics are symmetric to the shearing direction, second, we neglect the second integral because for strain amplitudes that are away from the critical point (the blue parts of the curve in Fig. 11.26) the fluctuations are very small (the distribution function is an exponential). Substituting for $\mathcal{D}(x)$, we get:

$$P(\mathcal{S},\Gamma) \sim \int_{0}^{\Gamma} d\varepsilon\, \mathcal{S}^{-\tau}\mathcal{D}(\mathcal{S}(\Gamma_c-\varepsilon)^{\delta/\sigma}) \tag{11.24}$$

$$= \int_{0}^{\Gamma} d\varepsilon\, \mathcal{S}^{-\tau} A e^{-B\mathcal{S}(\Gamma_c-\varepsilon)^{\delta/\sigma}} \tag{11.25}$$

substituting

$$x = B\mathcal{S}(\Gamma_c-\varepsilon)^{\delta/\sigma} \tag{11.26}$$

$$\varepsilon = \Gamma_c - \left(\frac{x}{B\mathcal{S}}\right)^{\sigma/\delta} \tag{11.27}$$

we get:

$$P(\mathcal{S},\Gamma) = -\mathcal{S}^{-\tau-\sigma/\delta}\frac{A\sigma/\delta}{B^{\sigma/\delta}} \int_{B\mathcal{S}(\Gamma_c)^{\delta/\sigma}}^{B\mathcal{S}(\Gamma_c-\Gamma)^{\delta/\sigma}} dx\, x^{\sigma/\delta-1}e^{-x} \tag{11.28}$$

close to the critical point $\Gamma \to \Gamma_c$ the typical avalanche size $\mathcal{S}$ is very large. Therefore, we assume that taking the lower limit to infinity will contribute a negligible change to the result:

$$\sim -\mathcal{S}^{-\tau-\sigma/\delta}\frac{A\sigma/\delta}{B^{\sigma/\delta}} \int_{\infty}^{B\mathcal{S}(\Gamma_c-\Gamma)^{\delta/\sigma}} dx\, x^{\sigma/\delta-1}e^{-x} \tag{11.29}$$

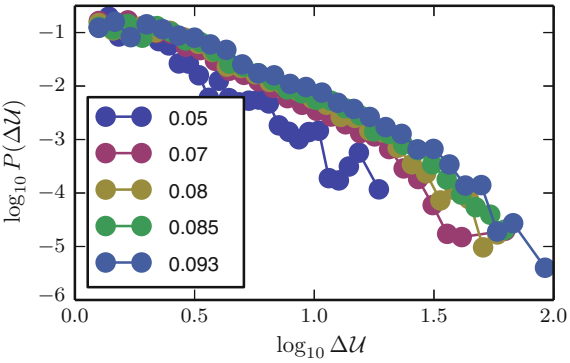

Fig. 11.29 Fluctuations: Energy drop distribution generated from log histograms for five different maximal strain amplitudes below the transition for strain amplitudes $\Gamma = 0.05, 0.07, 0.08, 0.085$ and 0.093

This gives the scaling function for the fluctuations below the critical point:

$$P(\mathcal{S}, \Gamma)\mathcal{S}^{\lambda} \sim \mathcal{F}(\mathcal{S}(\Gamma_c - \Gamma)^{\chi}), \tag{11.30}$$

where $\lambda = \tau + \sigma/\delta$ and $\chi = \delta/\sigma$. The scaling function is generally unknown. However, for mean-field depinning theory it was calculated to be $\mathcal{F}(x) = -\gamma(1/\chi, -x)$, where $\gamma(a, x)$ is the complementary gamma function and seems to agree with the data collapse (see Figs. 11.29, 11.30). Avalanche sizes in plasticity are usually associated with the amount of slip, which is proportional to the stress drop. However, as was shown in refs [49, 62], in the steady-state the fluctuations of stress and potential energy drops are proportional due to a sum rule. This was assumed to apply here as well. If the maximal strain amplitude Γ is larger than the critical value, we have to average over the statistics both below and above the critical strain amplitude. Due to the quasi-static forcing (zero strain-rate), for strains larger or equal to the critical strain amplitude, the system is expected to be exactly at criticality [63], and the avalanche statistics is expected to behave as a pure power-law:

$$D(\mathcal{S}, \varepsilon \geq \Gamma_c) \sim \mathcal{S}^{-\tau}. \tag{11.31}$$

Substituting, we obtain:

$$P(\mathcal{S}, \Gamma) \sim \int_0^{\Gamma_c} d\varepsilon\, \mathcal{S}^{-\tau} A e^{-B\mathcal{S}(\Gamma_c - \varepsilon)^{\delta/\sigma}} + (\Gamma - \Gamma_c)\, \mathcal{S}^{-\tau},$$

where we have performed the integral over the last term.

As demonstrated by Lerner et al. [62] and further developed by Salerno et al. [64] when the system is in a steady-state, there is a simple relation between an energy drop and the concurrent stress drop. The relation stems from the fact that at the steady-state, the work done on the system by the straining is balanced by the energy

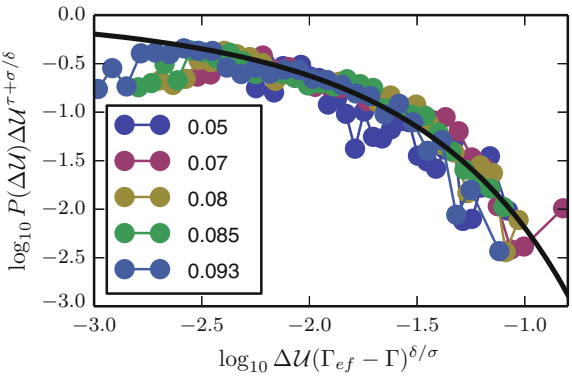

Fig. 11.30 Data collapse: Data collapse for five different maximal strain amplitudes below the transition compared to the mean-field scaling function $\mathcal{F}(x) = -\gamma(\sigma/\delta, -x)$, where $\gamma(a, x)$ is the complementary gamma function (marked by a *black line*)

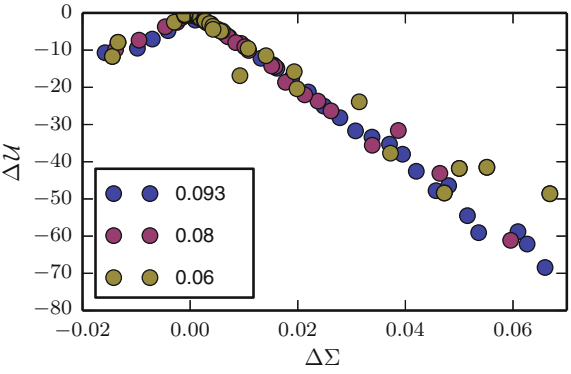

Fig. 11.31 Average energy drops versus stress drops for three different maximal strain amplitudes. The figure shows that the energy drops grow linearly with the stress drops

drops. Thus, they got the sum rule:

$$\frac{\langle \Sigma_s \rangle}{4\mu} \sum_i \Delta\Sigma_i = \sum_j \Delta\mathcal{U}_j \tag{11.32}$$

where μ is the shear modulus, $\Delta\Sigma_i$ is a stress drop, $\Delta\mathcal{U}_j$ is an energy drop and we have assumed that there is a well-defined average stress $\langle \Sigma_s \rangle$ at the steady-state. Under oscillatory shear conditions the steady-state stress depends on the strain amplitude, but for a small strain interval this relation should still hold. Therefore, at the steady-state the sum of the energy drops is proportional to the sum of the stress drops. For large avalanches, which are dominant in determining the power-laws, this suggests that individual stress and energy drops are also proportional. This was confirmed in the simulations by Salerno et al. [64]. Indeed, this behavior was also observed for oscillatory shear where the stress and energy drops were found to be proportional (see Fig. 11.31).

Using (11.30), data collapse was found for five maximal strain amplitudes $\Gamma = 0.05, 0.07, 0.08, 0.085$ and 0.093 at system size $N = 16{,}384$ (Figs. 11.29, 11.30) from which λ and χ were extracted.

We expect to have data collapse only for intermediate strain amplitudes - for strain amplitudes smaller than $\Gamma = 0.05$ the statistics are not good enough because there are not many energy drops (about 10 per cycle or less). Furthermore, far from the critical point the avalanche statistics is not expected to show the same behavior since the system is far from the singularity. For strain amplitudes that are too close to the critical point, finite size effects dominate. Close to the critical point we typically use the following expression:

$$g(f) = \xi^{\alpha/\nu} g_0(L/\xi) \tag{11.33}$$

where $\xi = f^{-\nu}$ is the correlation length, $f = \frac{F - F_c}{F_c}$ is the rescaled force, $g(x)$ is our scaling function, L is the system size, α and ν are the critical exponents (ν is the critical exponent of the correlation length) and $g_0(x)$ is the finite size scaling function who's properties are:

$$g_0(x) \to x^{\alpha/\nu},\ x \to \infty \tag{11.34}$$

and:

$$g_0(x) \to C,\ x \to 0 \tag{11.35}$$

where C is a constant. Therefore, close to the critical point we get:

$$g(f) \sim L^{\alpha/\nu} \tag{11.36}$$

which means that one cannot use the same function to describe the scaling behavior for maximal strain amplitudes in the intermediate range and close to the transition.

Using the estimate of δ, the critical exponents values $\tau = 1.04[0.26]$, $\sigma = 0.59[0.04]$ were found from the data collapse. The exponents deviate from the exponents found using mean-field depinning theory, which are $\tau = 1.5$ and $\sigma = 0.5$. There are several possible reasons for that. The first possibility is that inertia effects are changing the exponents as was suggested by Salerno et al. [49], for simulations under direct shear (not alternating). This might be an issue since in [19, 30] the FIRE (Fast Inertial Relaxation Engine) algorithm was used to minimise the potential energy. Another possibility is that since the elastic interactions can be both positive and negative, contrary to the only positive interactions exhibited by most depinning models, the mean field is in a "marginal state" [65] which dictates different scaling behavior. The main caveat to this approach, as we see it, is that the theoretical predictions that assume such behavior, based on scaling arguments [66, 67] and analytic calculations for hard spheres at infinite dimensionality [68] does not show the behavior that we are observing here. We believe that the discrepancy from both depinning theory and marginal stability might be a result of having anisotropic interactions which causes the formation of plastic events in specific directions [69], something that as much as we are aware, is not been taken explicitly into account in both theories. Another possibility is that the upper critical dimension is higher in amorphous solids than in

standard depinning and in that case one may have to take into account corrections to the critical exponents. We hope that further work will clarify these points.

11.4.2 Average Fluctuations

From the relevant critical exponents we can obtain the average energy fluctuations introduced in Fig. 11.24 using similar analysis as above. In order to calculate the average fluctuation size in a cycle we integrate over the same probability distributions but divide by the strain amplitude:

$$\langle \mathcal{S}^n \rangle_\Gamma \sim \int_0^{\mathcal{S}_{\rm co}} d\mathcal{S}\, \mathcal{S}^n \mathcal{S}^{-\tau} \frac{2}{\Gamma} \int_0^{\Gamma} d\varepsilon\, A e^{-B\mathcal{S}(\Gamma-\varepsilon)^{\delta/\sigma}} \tag{11.37}$$

for $\Gamma < \Gamma_{\rm c}$ and:

$$\langle \mathcal{S}^n \rangle_\Gamma \sim \int_0^{\mathcal{S}_{\rm co}} d\mathcal{S}\, \frac{2}{\Gamma} \int_0^{\Gamma_{\rm c}} d\varepsilon\, \mathcal{S}^n \mathcal{S}^{-\tau} A e^{-B\mathcal{S}(\Gamma_{\rm c}-\varepsilon)^{\delta/\sigma}} \tag{11.38}$$

$$+ \int_0^{\mathcal{S}_{\rm co}} d\mathcal{S} \frac{2}{\Gamma} \int_{\Gamma_{\rm c}}^{\Gamma} \mathcal{S}^n \mathcal{S}^{-\tau} \tag{11.39}$$

for $\Gamma > \Gamma_{\rm c}$. After integration:

$$\langle \mathcal{S}^n \rangle_\Gamma \sim \int_0^{\mathcal{S}_{\rm co}} d\mathcal{S}\, \frac{2}{\Gamma} \int_0^{\Gamma_{\rm c}} d\varepsilon\, \mathcal{S}^n \mathcal{S}^{-\tau} A e^{-B\mathcal{S}(\Gamma_{\rm c}-\varepsilon)^{\delta/\sigma}} \tag{11.40}$$

$$+ \int_0^{\mathcal{S}_{\rm co}} d\mathcal{S}\, \mathcal{S}^n \mathcal{S}^{-\tau} \frac{(\Gamma - \Gamma_{\rm c})}{\Gamma} \tag{11.41}$$

$$\langle \mathcal{S} \rangle \sim \int_0^{\mathcal{S}_{\rm co}} d\mathcal{S}\, \frac{2}{\Gamma} \int_0^{\Gamma_{\rm c}} d\varepsilon\, \mathcal{S}^{1-\tau} A e^{-B\mathcal{S}(\Gamma_{\rm c}-\varepsilon)^{\delta/\sigma}}$$
$$+ \frac{(\Gamma - \Gamma_{\rm c})}{\Gamma} \int_0^{\mathcal{S}_{\rm co}} d\mathcal{S}\, \mathcal{S}^{1-\tau}, \tag{11.42}$$

where $\mathcal{S}_{\rm co}$ is a cutoff avalanche size which depends on the system size in an unknown way, and the integral was divided by Γ in order to perform a cycle-average. The values of the critical exponents τ and σ that where used where $\tau = 1.04$ and $\sigma = 0.59$ which were obtained from the data collapse shown in Figs. 11.29 and 11.30. For the critical maximal strain amplitude the values $\Gamma_{\rm c} = 0.135$ for $N = 1024$, $\Gamma_{\rm c} = 0.12$ for $N = 4096$ and $\Gamma_{\rm c} = 0.115$ for $N = 16{,}384$ were chosen since they correspond to the values found for the transition to chaos. The maximal cluster size $\mathcal{S}_{\rm co}$ was

assumed to be proportional to a power-law of the system size since at the steady-state the correlations span the entire system ($\xi \sim L$):

$$\mathcal{S}_{\text{co}} = \mathcal{K} N^{\Delta}. \tag{11.43}$$

where $\mathcal{K}$ and Δ are constants. The parameter values $\mathcal{K} \sim 0.4$, $A \sim 4.547$, $B \sim 30.51$ and $\Delta \sim 0.482$ were found by minimising the normalised L_2 norm of (11.42) with respect to the data from simulations:

$$L_2 = \frac{1}{N}\sqrt{\sum_i (\langle \Delta \mathcal{U} \rangle_{\text{sim,i}} - \langle \mathcal{S} \rangle_{\text{theory,i}})^2} \tag{11.44}$$

the best fit resulted in $L_2 \sim 0.114$. Note that the value of $\Delta \sim 0.482$ is approximately consistent with avalanches concentrated along a shear-band and thus proportional to the linear system size $L \sim N^{1/2}$. Figure 11.32 shows the first moment of the potential energy fluctuations $\langle \Delta \mathcal{U} \rangle$ obtained from the simulations as a function of the maximal strain amplitude Γ, compared to (11.42) for three different system sizes. The most obvious features of $\langle \Delta \mathcal{U} \rangle$ as a function of the maximal strain amplitudes is the crossover (cusp) in behavior at the critical point (Figs. 11.32, 11.33), which was mentioned above, and the system size dependent saturation of $\langle \Delta \mathcal{U} \rangle$ for very large strain amplitudes. As one can see in the figures, both of these features are described by the theory. The saturation, and dependence on system size can be explained by noting that for very large maximal strain amplitudes $\Gamma \to \infty$, the normalized distribution function converges to the usual power-law statistics $P(\mathcal{S}) \sim \mathcal{S}^{-\tau}$ and respectively $\langle \Delta \mathcal{U} \rangle \sim \langle \Delta \mathcal{S} \rangle \to \mathcal{S}_{\text{co}}^{-\tau}$. One feature that was observed in the simulations that is not explained by the current theory is that Γ_{c} changes slightly with the strain amplitude due to structural rearrangements. In the theory (11.11), structural rearrangements will amount to a change in the properties of the distribution of the random pinning $f_R(u, t)$. However, this effect is small (changes in Γ_{c} are less than 5%) and was not taken into account when fitting the data to the theory. By analyzing the avalanche statistics using scaling forms predicted by depinning theory, it was shown that there is a critical point at a critical strain amplitude $\Gamma = \Gamma_{\text{c}}$ which is the same strain amplitude at which the system undergoes an irreversibility transition. However, this raises the question of why the two occur at the same point. An explanation for this intriguing concurrency will be provided below.

11.5 Connection Between Dynamics and Critical Behavior

The most interesting question that arises in view of the findings mentioned above is the connection between depinning and the observed dynamics in the reversible and irreversible regimes. The essence of this connection is that at depinning, the external force F suppresses all the energy barriers (see Fig. 11.34a, b) which changes the

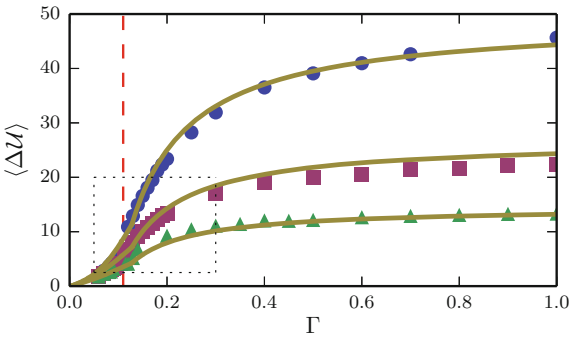

Fig. 11.32 First moment: Average potential energy drops versus maximal strain amplitude for different system sizes: N = 16,384(●), N = 4096(■), N = 1024(▲). The *yellow lines* are the theoretical results (11.42) where the integral was calculated numerically. The *red dashed line* marks the transition to chaos point for N = 16,384

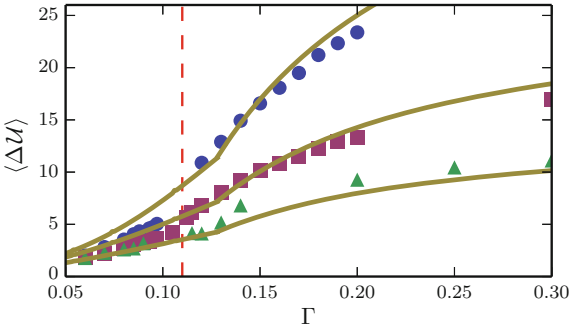

Fig. 11.33 Transition point: Scaled up version of Fig. 11.32. Note the change in curvature at the critical points $\Gamma_c = 0.115$, 0.12, 0.135 for N = 16,384(●), N = 4096(■), N = 1024(▲) respectively. *Yellow lines* are theoretical results

topology of the energy landscape - instead of a set of disconnected energy minima, we have a fully connected set of energy minima in terms of strain. This affects the dynamics and reversibility of the system (a related explanation was suggested for the dynamics of supercooled liquids, see [70]).

Limit cycles: Since the system is dissipative, it will always flow to an attractor occupying a limited part of phase-space (see Fig. 11.34c and [34]). This attractor will be composed of a finite or infinite set of configurations of the system connected to each other by elastic or plastic displacement (see Fig. 11.34d). For a system under linear shear, when the external forcing is below depinning, it is guaranteed that after some amount of strain the system will find a local minimum of the potential energy (will become pinned). For cyclic strain, if the maximal strain amplitude is below depinning, the system will find, after transient dynamics, a set of configurations all below the critical stress. Since the stress is lower than the critical depinning stress, this set of states is guaranteed to be linearly stable or nonlinearly stable. In the case that is nonlinearly stable, if the stress is increased, the system will overcome a close-by energy barrier but will "fall" into an adjunct energy barrier (see also Fig. 11.34a) which means that the next configuration in the attractor is separated by a finite energy barrier. Therefore, in this case, the attractor is not chaotic and it must be a limit-cycle (periodic). This situation is not so different to an absorbing phase transition, which was suggested as an explanation for similar phenomena [10, 24],

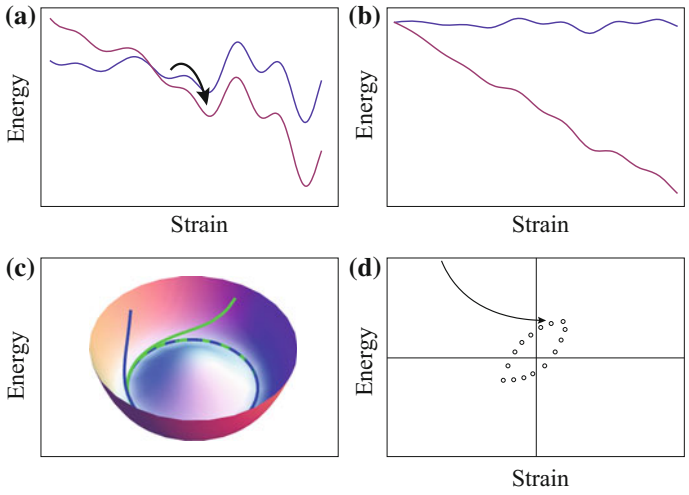

Fig. 11.34 Nonlinear stability: **a** Tilted energy landscape - nonlinearly stable. **b** Tilted energy landscape - completely unstable. Chaotic behavior is possible in this scenario. **c** A simple example of an attractor: for a dissipative system, different initial conditions which are in the same basin of attraction result in trajectories (*blue* and *green lines*) which end-up in the same limit-cycle. **d** Below the critical strain amplitude, for each strain amplitude, the system finds, after a transient (*arrow*), a stable configuration (*circles*)

although we suggest that depinning provides greater physical insight into the reason for the system to reach an absorbing state.

Chaotic attractor: When the stress is close to depinnig values, a small increase in stress, due to a strain step will supress all of the energy barriers (see Fig. 11.34b). In this case the system will be completely unstable, for a short time. In the quasi-static shearing scenario, the system will reach another minimum of the potential energy when the minimization algorithm or dissipation lowers the energy again but before that happens it will spend some time in boundless motion. Since there are effectively no energy barriers in this time, there are no retrieving forces and chaotic motion is possible (in some systems with *quenched* disorder and with a "no passing" property fulfilled [71], such as charge density waves and certain random magnets, chaotic motion is not possible and there always is a limit-cycle [72], but this is not the case in plasticity in amorphous solids in which disorder is not strictly quenched and for which the no passing rule is broken).

Period doubling: when the system is close but still not exactly at criticality, there are less and less stable "pinned" configurations. Therefore, the likelihood of the system being able to "construct" a limit-cycle that returns to the same point after one period is smaller and it may be required to have more than one cycle before the system can return to the initial configuration.

To summarize, if the strain amplitude is below depinning, the system can always self organize into cycles composed of states in which the stress fluctuations never

reach depinning values. In that case the dynamics will always be bounded, either linearly or nonlinearly (overcoming one energy barrier). If the strain amplitude is large enough, there are always states in which the stress is very close to depinning. In that case small increase in the stress, due to straining, will generate stresses that are larger than the depinning value, and thus will cause unbounded motion which can lead to sensitivity to initial conditions and chaos.

11.5.1 Relaxation Dynamics

Depinning mean-field theory predicts that close to a depinning transition, the system will "slide" for a long time before it becomes pinned due to critical slowing-down. Therefore, the accumulated strain to reach a steady-state (the number of cycles times 4Γ) is expected to diverge as function of the applied force:

$$\epsilon_{\text{acc}} \sim (F_{\text{c}} - F)^{-z\nu}, \tag{11.45}$$

with mean-field depinning theory, which was derived for linear shear, predicting a value of $z\nu = 1$ [52]. Since the steady-state is a limit-cycle composed of a set of pinned states, we expect that also under oscillatory shear, the accumulated strain to reach a steady-state will scale in the same way as the strain needed to pin one state. Since the control parameters was the maximal strain amplitude, we obtain on substituting:

$$\epsilon_{\text{acc}} \sim (\Gamma_{\text{c}} - \Gamma)^{-z\nu\delta}. \tag{11.46}$$

The simulations found [30] power-law scaling with $z\nu \sim 2.4$ for a choice $\Gamma_{\text{c}} = 0.11$ (Fig. 11.7), and $z\nu \sim 1.38$ for a slightly smaller $\Gamma_{\text{c}} = 0.1$ for the largest system that was ($N = 16{,}384$). The dynamical exponent $z\nu = 1$ predicted by mean-field theory is in rough agreement with the scaling of the time to reach steady-state measured in the experiments of Nagamanasa et al. [24] on colloidal glasses which gave $z\nu \sim 1.1/\delta \sim 0.88$.

11.6 Summary

The recent discovery of a reversibility transition connected to yield has raised the possibility that yield is a result of a transition from periodic to chaotic behavior. However, a number of questions arise regarding the nature of the transition and the implications to ergodicity and entropy production in these systems. The results described in this chapter suggest that the critical behavior might be caused by a transition to chaos [19], a phenomenon well studied in dynamical systems theory, which seems to be a result of a change in the topology of the energy landscape [30].

Furthermore, it is suggested that the change in energy landscape topology may be a result of a depinning-like dynamical non-equilibrium phase transition.

The existence of an irreversibility transition is supported by several experimental results based on the shearing of colloidal suspensions [17, 20, 24]. Similarly, experiments on granular piles have also shown that the onset of irreversible behavior is associated with the appearance of system spanning events [12], consistent with our findings. Therefore, it appears that the existence of an irreversibility transition/transition to chaos in colloidal systems is reasonably well substantiated. However, it is still not clear what happens in the thermodynamic limit and in molecular amorphous solids, such as bulk metallic glasses. Furthermore, the existence and nature of a non-equilibrium critical point at yield is still under debate. There are suggestions that the transition is actually first-order in nature rather than showing critical behavior [73, 74]. It will be interesting to see if one can explain the irreversibility transition based on a first-order non equilibrium phase transition.

References

1. A. Argon, Acta metallurgica **27**, 47 (1979)
2. C. Maloney, A. Lemaître, Phys. Rev. E **74**, 016118 (2006)
3. P. Schall, D.A. Weitz, F. Spaepen, Science **318**, 1895 (2007)
4. M. Falk, J. Langer, Phys. Rev. E **57**, 7192 (1998)
5. P. Sollich, Phys. Rev. E **58**, 738 (1998)
6. P. Sollich, F. Lequeux, P. Hébraud, M. Cates, Phys. Rev. Lett. **78**, 2020 (1997)
7. L. Bocquet, A. Colin, A. Ajdari, Phys. Rev. Lett. **103**, 36001 (2009)
8. N.V. Priezjev, Phys. Rev. E **87**, 052302 (2013)
9. N. Mangan, C. Reichhardt, C. Reichhardt, Phys. Rev. Lett. **100**, 187002 (2008)
10. L. Corté, P. Chaikin, J. Gollub, D. Pine, Nat. Phys. **4**, 420 (2008)
11. D. Pine, J. Gollub, J. Brady, A. Leshansky, Nature **438**, 997 (2005)
12. S. Slotterback, M. Mailman, K. Ronaszegi, M. van Hecke, M. Girvan, W. Losert, Phys. Rev. E **85**, 021309 (2012)
13. G. Petekidis, A. Moussaïd, P. Pusey, Phys. Rev. E **66**, 051402 (2002)
14. M. Lundberg, K. Krishan, N. Xu, C. O'Hern, M. Dennin, Phys. Rev. E **77**, 041505 (2008)
15. C.F. Schreck, R.S. Hoy, M.D. Shattuck, C.S. O'Hern (2013). arXiv preprint arXiv:1301.7492
16. N.C. Keim, S.R. Nagel, Phys. Rev. Lett. **107**, 10603 (2011)
17. N.C. Keim, P.E. Arratia, Soft Matter (2013)
18. D. Fiocco, G. Foffi, S. Sastry, Phys. Rev. E, **020301**(**R**) (2013)
19. I. Regev, T. Lookman, C. Reichhardt, Phys. Rev. E **88**, 062401 (2013)
20. N.C. Keim, P.E. Arratia, Phys. Rev. Lett. **112**, 028302 (2014)
21. N. Perchikov, E. Bouchbinder, Phys. Rev. E **89**, 062307 (2014)
22. N.V. Priezjev, Phys. Rev. E **89**, 012601 (2014)
23. R. Jeanneret, D. Bartolo, Nat. Commun. **5** (2014)
24. K.H. Nagamanasa, S. Gokhale, A. Sood, R. Ganapathy, Phys. Rev. E **89**, 062308 (2014)
25. M.C. Rogers, K. Chen, L. Andrzejewski, S. Narayanan, S. Ramakrishnan, R.L. Leheny, J.L. Harden, Phys. Rev. E **90**, 062310 (2014)
26. E. Tjhung, L. Berthier, Phys. Rev. Lett. **114**, 148301 (2015)
27. D. Fiocco, G. Foffi, S. Sastry, J. Phys.: Condens. Matter **27**, 194130 (2015)
28. M. Schulz, B.M. Schulz, S. Herminghaus, Phys. Rev. E **67**, 052301 (2003)
29. H. Hinrichsen, Adv. Phys. **49**, 815 (2000)

30. I. Regev, J. Weber, C. Reichhardt, K.A. Dahmen, T. Lookman, Nat. Commun. **6** (2015)
31. D. Fiocco, G. Foffi, S. Sastry, Phys. Rev. Lett. **112**, 025702 (2014)
32. J. Yorke, E. Yorke, J. Stat. Phys. **21**, 263 (1979)
33. T. Tél, Y. Lai, Phys. Rep. **460**, 245 (2008)
34. E. Ott, *Chaos in Dynamical Systems* (Cambridge University Press, Cambridge, 2002)
35. H. Kantz, Phys. Lett. A **185**, 77 (1994)
36. H. Kantz, T. Schreiber, R. Mackay, *Nonlinear Time Series Analysis*, vol. 2000 (Cambridge University Press, Cambridge, 1997)
37. F. Takens, in *Dynamical Systems and Turbulence, Warwick 1980* (Springer, Heidelberg, 1981), pp. 366–381
38. Z. Liu, G. Wang, K. Chan, J. Ren, Y. Huang, X. Bian, X. Xu, D. Zhang, Y. Gao, Q. Zhai, J. Appl. Phys. **114**, 033521 (2013)
39. E.J. Banigan, M.K. Illich, D.J. Stace-Naughton, D.A. Egolf, Nat. Phys. **9**, 288 (2013)
40. J. Knebel, M.F. Weber, E. Frey, Nat. Phys. **12**, 204 (2016)
41. H.-Y. Shih, T.-L. Hsieh, N. Goldenfeld, Nat. Phys. (2015)
42. S. Li, X. Ding, J. Deng, T. Lookman, J. Li, X. Ren, J. Sun, A. Saxena, Phys. Rev. B **82**, 205435 (2010)
43. T. Lookman, S. Shenoy, K. Rasmussen, A. Saxena, A. Bishop, Phys. Rev. B **67**, 024114 (2003)
44. A. Kityk, W. Schranz, P. Sondergeld, D. Havlik, E. Salje, J. Scott, Phys. Rev. B **61**, 946 (2000)
45. E. Ott, J. Sommerer, Phys. Lett. A **188**, 39 (1994)
46. D.J. Lacks, M.J. Osborne, Phys. Rev. Lett. **93**, 255501 (2004)
47. E. Bouchbinder, J. Langer, I. Procaccia, Phys. Rev. E **75**, 036108 (2007)
48. L. Boué, H. Hentschel, I. Procaccia, I. Regev, J. Zylberg, Phys. Rev. B **81**, 100201 (2010)
49. K.M. Salerno, C.E. Maloney, M.O. Robbins, Phys. Rev. Lett. **109**, 105703 (2012)
50. N. Goldenfeld, *Lectures on phase transitions and the renormalization group* (Addison-Wesley, Advanced Book Program, 1992)
51. M. Kardar, *Statistical Physics of Fields* (Cambridge University Press, Cambridge, 2007)
52. K.A. Dahmen, Y. Ben-Zion, J.T. Uhl, Phys. Rev. Lett. **102**, 175501 (2009)
53. D.S. Fisher, K. Dahmen, S. Ramanathan, Y. Ben-Zion, Phys. Rev. Lett. **78**, 4885 (1997)
54. P.Y. Chan, G. Tsekenis, J. Dantzig, K.A. Dahmen, N. Goldenfeld, Phys. Rev. Lett. **105**, 015502 (2010)
55. N. Friedman, A.T. Jennings, G. Tsekenis, J.-Y. Kim, M. Tao, J.T. Uhl, J.R. Greer, K.A. Dahmen, Phys. Rev. Lett. **109**, 095507 (2012)
56. D.M. Dimiduk, C. Woodward, R. LeSar, M.D. Uchic, Science **312**, 1188 (2006)
57. F.F. Csikor, C. Motz, D. Weygand, M. Zaiser, S. Zapperi, Science **318**, 251 (2007)
58. J. Antonaglia, X. Xie, G. Schwarz, M. Wraith, J. Qiao, Y. Zhang, P.K. Liaw, J.T. Uhl, K.A. Dahmen, Sci. Rep. **4** (2014)
59. J. Antonaglia, W.J. Wright, X. Gu, R.R. Byer, T.C. Hufnagel, M. LeBlanc, J.T. Uhl, K.A. Dahmen, Phys. Rev. Lett. **112**, 155501 (2014)
60. A.R. Jie Lin, E. Lerner, M. Wyart (2014). arXiv:1403.6735v2 [cond-mat.soft]
61. R. Dasgupta, H. Hentschel, I. Procaccia, Phys. Rev. Lett. **109**, 255502 (2012)
62. E. Lerner, I. Procaccia, Phys. Rev. E **79**, 066109 (2009)
63. J.P. Sethna, K.A. Dahmen, C.R. Myers, Nature **410**, 242 (2001)
64. K.M. Salerno, M.O. Robbins, Phys. Rev. E **88**, 062206 (2013)
65. J. Lin, A. Saade, E. Lerner, A. Rosso, M. Wyart, EPL (Europhys. Lett.) **105**, 26003 (2014)
66. J. Lin, T. Gueudré, A. Rosso, M. Wyart, Phys. Rev. Lett. **115**, 168001 (2015)
67. P.D. Ispánovity, L. Laurson, M. Zaiser, I. Groma, S. Zapperi, M.J. Alava, Phys. Rev. Lett. **112**, 235501 (2014)
68. C. Rainone, P. Urbani, H. Yoshino, F. Zamponi, Phys. Rev. Lett. **114**, 015701 (2015)
69. B. Tyukodi, S. Patinet, S. Roux, D. Vandembroucq (2015). arXiv preprint arXiv:1502.07694
70. A. Cavagna, Phys. Rep. **476**, 51 (2009)
71. J.P. Sethna, K. Dahmen, S. Kartha, J.A. Krumhansl, B.W. Roberts, J.D. Shore, Phys. Rev. Lett. **70**, 3347 (1993)
72. A.A. Middleton, D.S. Fisher, Phys. Rev. B **47**, 3530 (1993)
73. P. Jaiswal, I. Procaccia, C. Rainone, M. Singh (2016). arXiv preprint arXiv:1601.02196
74. T. Kawasaki, L. Berthier (2015). arXiv preprint arXiv:1507.04120

Chapter 12
Avalanches, Non-Gaussian Fluctuations and Intermittency in Fluid Imbibition

Jordi Ortín and Stéphane Santucci

Abstract We review our work on the invasion of a model open fracture by a viscous wetting fluid, in the context of research on the spatiotemporal dynamics of fronts in disordered media. The model consists on a Hele-Shaw cell with randomly-distributed dichotomic variations of gap thickness. Distortions of the advancing front produced by fluctuations in capillary pressure and permeability are damped by interfacial tension and fluid viscosity. Competition of forces at different length scales makes that an initially flat front undergoes a kinetic roughening process, leading to a statistically-stationary state characterized by critical interfacial fluctuations and a collective avalanche dynamics. Using fast and high-resolution imaging we are able to track the evolution of the advancing front in space and time with high accuracy. The motion of the front takes place by localized bursts whose lateral sizes, areas and durations are found to be power-law distributed–up to a cutoff scale which diverges as the capillary number of the displacement $\mathrm{Ca} \to 0$, a limit corresponding to a critical depinning transition. A scale-dependent statistical analysis of the temporal behavior of the spatially-averaged velocity of the front reveals the presence of non-Gaussian fluctuations, strongly intermittent dynamics and global avalanches.

12.1 Introduction

Many nonequilibrium systems with spatial degrees of freedom respond to a smooth and continuous external driving with jerky and discontinuous events of correlated activity. These fast, abrupt events, separated by intervals of slow or no activity, receive

J. Ortín (✉)
Dept. de Física de la Matèria Condensada, and University of Barcelona Institute of Complex Systems (UBICS), Facultat de Física, Universitat de Barcelona.,
C/ Martí i Franqués 1, 08028 Barcelona, Catalonia, Spain
e-mail: jordi.ortin@ub.edu

S. Santucci
Laboratoire de Physique, CNRS UMR 5672, École Normale Supérieure de Lyon,
46 Allée D'Italie, 69364 Lyon Cedex 07, France
e-mail: stephane.santucci@ens-lyon.fr

E.K.H. Salje et al. (eds.), *Avalanches in Functional Materials and Geophysics*,
Understanding Complex Systems, DOI 10.1007/978-3-319-45612-6_12

the generic name of *avalanches*. They have been observed in physical and geological settings with very different time and length scales, from motion of vortex flux lines in superconductors to slip motions of the Earth's crust (earthquakes) [6, 14, 29, 35, 48, 54, 60, 62, 68, 85, 95, 100]

Among model systems of slowly driven interfaces with complex interfacial dynamics, fluid fronts in disordered media have received substantial attention in recent years [1, 49]. Theoretical and experimental studies have addressed the motion of contact lines in the presence of wettability defects or obstacles [10, 19, 41, 50, 61, 79, 86], the collective motion of the interface formed by the different fluid menisci that invade the pores and throats of a porous medium during capillary rise [4, 20, 45], and the imbibition of a fluid by a Hele-Shaw cell with wettability defects [28, 65, 66], glass-beads [22, 87], or randomly-varying gap thickness [1, 3, 23, 56, 70, 75, 85].

In this paper we focus on stable imbibition displacements. A fluid that preferentially wets the walls of the disordered medium (e.g. oil) displaces a less wetting and less viscous fluid (e.g. air) originally residing in the medium. The advancement is highly intermittent. Local capillary bursts induce front distortions, which eventually trigger a cooperative motion of the invading front.

Advances in the understanding of the dynamics of imbibition displacements in disordered media in the 80 and 90s were reviewed in depth, from a statistical physics perspective, by Alava, Dubé and Rost in a celebrated review paper [1]. The emphasis at the moment was put on the kinetic roughening of the imbibition front. Comparatively, avalanches of imbibition fronts received then much less attention. In this chapter we deal with new studies of the dynamics of stable imbibition displacements that have been done since the publication of the review by Alava and coworkers in 2004. Specifically we focus on the burst-like dynamics of slowly-driven stable imbibition fronts. We review the insights gained from new experiments that have been carried out in our laboratory model in Barcelona through the last ten years. Advances in image acquisition have allowed us to record the front dynamics with unprecedented spatial and temporal resolution, which has made possible to investigate velocity correlations, velocity fluctuations, and front avalanches in great detail.

In order to make this chapter self-contained, we begin by introducing in Sect. 12.2 basic concepts of the dynamics of two-phase flows in disordered media which are relevant for our results. The experimental setup and the experimental methods that give access to local front velocities are described in Sect. 12.3. The setup consists on a horizontal Hele-Shaw cell with a two-valued gap thickness that fluctuates randomly in space, following a predefined pattern. The invading fluid moves in the free gap between the two parallel plates, but fluctuations in gap thickness give rise to localized and abrupt distortions of the advancing front. The dynamics of the invading front are studied in Sect. 12.4. We begin this section with a brief introduction of the linearized interfacial equation that describes stable imbibition displacements in this particular setup, following the work of Pauné and Casademunt [67]. The presence of disorder leads to a jerky, collective motion of the front. The front moves by *avalanches*, i.e. localized front displacements in which local front velocities are very high and spatially correlated. They are studied in Sect. 12.4.2. In very slow displace-

ments, where the flow is dominated by capillary forces, avalanches are expected to be scale-invariant in a wide range of sizes and durations. Local velocity bursts in stable imbibition displacements have been studied experimentally [17, 22, 72, 85], theoretically [24, 56, 75, 80] and numerically with phase-field simulations [56, 75, 80]. In Sect. 12.4.3 we study the front dynamics at increasing spatial scales. We focus on V_ℓ, the average velocity of the front in a window of lateral size ℓ–typically much smaller than the lateral width of the system L. We study different statistical properties of this *global*–on scale ℓ–temporal signal, which plays the role of a *crackling* noise in our system. First we show that its normalized values exhibit anomalous (non-Gaussian) fluctuations. The non-gaussianity is a consequence of the non applicability of the central limit theorem to correlated systems [7, 11, 12]. Non-Gaussian fluctuations of the global velocity in stable imbibition have been observed in phase-field numerical simulations [77, 80] and in experiments [18, 70, 77]. Next, we study the statistics of the temporal increments of $V_\ell(t)$. We show that this global velocity displays the characteristic features of an intermittent signal: periods of low velocities alternate with periods of very large velocity excursions. In the former, the acceleration is small and strongly correlated to the velocity, while in the latter the acceleration fluctuates strongly. This temporal intermittent behavior reflects spatial correlations along the front as well as strong temporal correlations in the direction of front advancement, related to the heterogeneities of the medium [16]. Finally, we study the statistics of avalanches of the *crackling* signal $V_\ell(t)$ [18, 70, 77, 80]. The chapter concludes in Sect. 12.5 with a recollection of the results presented and their interpretation. We discuss also new promising research directions, particularly the study of avalanche shapes.

12.2 Flows in Disordered Media: Basic Concepts

Flow in porous and fractured media occurs in geological, agricultural and industrial processes of capital importance, including secondary oil recovery and underground water flow. Fluid flow through disordered media is thus a central problem in the fields of petrology, hydrology, and chemical engineering [21, 27, 84]. The complexity of flows in disordered media arises from the heterogeneous structure of the media. Relevant features encompass a very wide range of spatial scales, from pore-size scales–1–50 nm–to field scales–which may extend over kilometers.

Darcy's Law

Flow at pore scales is described by the classical hydrodynamic equations of motion, supplemented with appropriate boundary conditions to take into account wetting effects and capillary forces that are essential at this scale of description. A continuum description on a coarse-grained (or Darcy) scale, above the scale of the disorder, is obtained by proper averaging over a *representative volume element* of the pore space–the minimal volume for which the properties of the porous medium and of the fluid flow within it remain statistically similar everywhere [84]. Single-phase fluid flow

at this scale is described by Darcy's law, a phenomenological relation which can be derived from Stokes equation by dimensional arguments and which plays a central role in the equations of continuum mechanics of porous media. Darcy's law states that in every point of the flow the fluid velocity is proportional to the pressure gradient, i.e. $\langle \boldsymbol{q} \rangle = -(\kappa/\mu)\,(\nabla p - \rho \boldsymbol{g})$, where $\langle \boldsymbol{q} \rangle$ is the average volume of fluid transported per unit time per unit cross-section of the porous medium, κ is the average hydraulic permeability (or simply the permeability) of the medium, μ is the dynamic viscosity of the fluid, ρ its density, and $\boldsymbol{g}$ is Earth's gravitational acceleration. In order to describe the flow at the field scale, finally, large-scale heterogeneities in the physical properties of the medium must be taken into account for a proper up-scaling.

Two-phase Flows

Many porous-media flows of interest involve the presence of an interface separating two different phases. Important examples include the displacement of oil with water in enhanced oil recovery, soil irrigation and ground-water contamination, printing and coating, and filtering of chemicals and contaminants. In two-phase flows a fluid originally residing in the disordered medium is displaced by a second, invading fluid. If the fluids are immiscible, and precursor films of the wetting phase can be ignored, there is a well defined (though eventually highly distorted) interface separating the two fluids.

The dynamics of the invasion process depends essentially on two conditions. The first one is the relative ability of the two fluids (displacing and displaced) to wet the walls of the disordered medium (Fig. 12.1, left panel). If the invading fluid wets preferentially the medium the displacement is favored by capillary forces, and is called *imbibition*. Conversely, when the preferentially wetting fluid is the displaced one capillary forces oppose the displacement of the menisci inside the pores. The corresponding process–which plays a central role in hydrology–is called *drainage*.

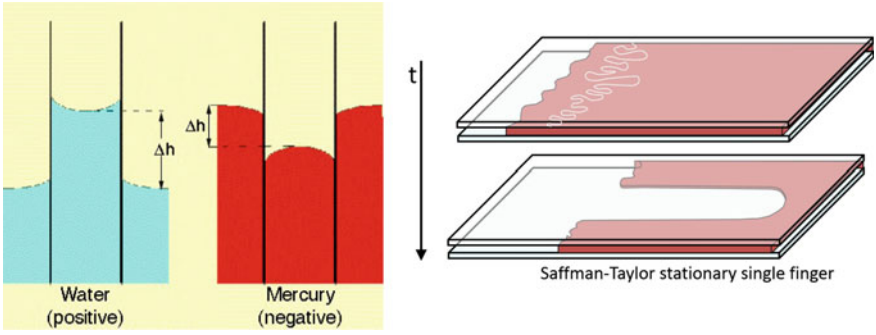

Fig. 12.1 The *left panel* shows how wetting properties influence liquid-air displacements in capillaries, by either favouring the invasion of the more wetting fluid (water), in *imbibition*, or hindering the invasion of the less wetting fluid (mercury), in *drainage*. The *right panel* shows the Saffman-Taylor instability that takes place when a less viscous fluid displaces a more viscous fluid in a Hele-Shaw cell. The initially flat interface develops viscous fingers. These fingers undergo a dynamic competition, leading finally to a wide, stationary single finger

Table 12.1 Classification of two-phase displacements resulting from the relative wetting properties and relative dynamic viscosities of the fluids involved

Invading fluid (μ) $\Rightarrow$ Defending fluid (μ_0)	$\mu < \mu_0$	$\mu > \mu_0$
Less wetting $\Rightarrow$ More wetting	Unstable drainage	Stable drainage
More wetting $\Rightarrow$ Less wetting	Unstable imbibition	Stable imbibition

The second important condition is the stability of the interface separating the two fluids. The displacement may be either stable or unstable, depending on the relative viscosities of the fluids involved. The displacement is stable when the invading fluid is more viscous than the defending fluid. Because of capillary pressure fluctuations at the pore scale, the front at large scales is slightly irregular, but front disturbances cannot grow because the viscous pressure gradient on the side of the invading fluid is larger than on the side of the defending fluid. When the invading fluid is less viscous than the defending fluid (e.g. when water displaces oil, as in Fig. 12.1, right panel) the situation is just the opposite. Front disturbances of small amplitude become amplified, and growing fingers of the invading fluid rapidly penetrate the defending fluid, limiting the effectiveness of the displacement process [38, 83]. Table 12.1 summarizes the four types of two-phase displacements that emerge from this picture.

In the absence of gravitational forces (e.g. for horizontal displacements) the stability of the interface is controlled by the viscosity ratio μ/μ_0 and by the capillary number Ca–given by $\mathrm{Ca} = \mu \mathrm{v}/\sigma$ when $\mu \gg \mu_0$. The capillary number is a dimensionless ratio of viscous to surface tension forces. Here μ is the dynamic viscosity of the invading fluid, v is the average velocity of the invading front, and σ is the interfacial tension between the two fluids.

Observations of two-phase fluid displacements in micromodels of porous media confirm that Ca and μ/μ_0 are the relevant controlling parameters [51, 52, 94]. In very slow drainage, either stable or unstable, the less wetting fluid invades the available channels in the sequential order dictated by the values of the capillary pressure jump across the meniscus in each channel. This sequential invasion is well described by the model of *Invasion Percolation*, and the resulting pattern is a self-similar fractal [97, 98]. Unstable drainage at larger Ca results in a highly ramified pattern of invaded pores, also a self-similar fractal but of smaller fractal dimension. Its morphology and growth dynamics correspond to a process of *Diffusion Limited Aggregation*, which describes the pattern formed by a growing unstable interface in an external field that obeys Laplace's equation [57, 64, 99]. Stable drainage displacements at larger Ca, in contrast, produces compact patterns. Concerning imbibition displacements, in which the invading fluid wets preferentially the medium, the invasion process is complicated by the presence of precursor wetting films of the invading fluid. Fast imbibition displacements lead to similar morphologies than fast drainage, because the dynamic contact angle increases with Ca and makes the injected fluid to invade the central part of the channels, as in drainage. But the outcome of slow imbibition displacements depends essentially on the pore-to-channel aspect ratio. In this case the presence of prewetting layers may render an interfacial description meaningless, since the essential dynamics are ruled by prewetting [1, 52].

Stable Imbibition Displacements

In this chapter we focus our attention on *stable imbibition* displacements in disordered media. Capillary-driven, spontaneous liquid invasion of a cookie dunked into a glass of milk or of a paper towel in contact with water, and the rise of sap in plants, belong to this type of two-phase fluid displacements. Imbibition has been less studied than drainage. Compared to its unstable counterpart, stable imbibition is a more simple process since viscous fingering is absent. Complications due to precursor wetting films can be avoided by considering displacements in fully prewetted media.

In a two-dimensional disordered medium, local capillary-pressure fluctuations and permeability variations (which play the role of quenched disorder) give rise to local fluctuations in the front height $h(x, t)$–the position of the interface between displacing and displaced fluids at lateral distance x and time t. In stable imbibition those fluctuations are damped not only by the surface tension of the interface, on short length scales, but also by the difference in fluid viscosity across the interface on larger length scales through the Saffman-Taylor mechanism. This situation presents many analogies with the generic problem of the motion of a slowly-driven elastic interface in a random potential [30, 49]. For this reason stable imbibition displacements have attracted a lot of interest also in nonequilibrium statistical physics. The question is whether the morphology and dynamics of stable imbibition fronts in disordered media can be described statistically in terms similar to other interfacial problems such as fire fronts or rupture lines. In those systems the competition between stabilizing and destabilizing (random) forces on different time and length scales leads to the unbounded growth of correlations and to the emergence of scale–invariant asymptotic properties [5, 30, 44]. The hope finally is that a universal description can be built in terms of a few basic features.

Kinetic Roughening

In the presence of competing interactions at different length scales, an initially smooth front undergoes a kinetic roughening process in which fluctuations grow in time due to the progressive correlation of adjacent points [5]. In the 90's, stable imbibition displacements attracted a great deal of attention as a model system of kinetic roughening. Results of experiments carried out in models of porous media consisting on glass-bead packings or in paper showed that flat fronts evolved indeed into morphologically rough, self-affine fractal objects [13, 36, 39, 40, 81]. The values of the scaling exponents, however, appeared to differ from one system to another, making difficult to classify stable imbibition displacements in porous media in a particular universality class of interfacial growth. It was soon recognized that the origin of this difficulty could be the essentially non-local character of the dynamics, which arises from mass continuity [24–26, 32, 33, 36, 37, 43, 67].

The properties of the disorder were found also to have a clear impact on the kinetic roughening of stable imbibition fronts. In glass-bead packings the transient regime preceding the statistically-stationary state of saturated roughness was generally too short to measure the exponent β that characterizes the temporal growth of interfacial fluctuations. In order to make this regime longer, and specially to have better control

of the disorder properties, we developed a new model of disordered medium that mimicked an open fracture [90]. Details of the model will be given in Sect. 12.3. Modifying the disorder properties of this model systematically in a controlled way (in particular its persistency in the direction of the displacement) we showed that the kinetic roughening of the front can exhibit 'anomalous' scaling, with local and global scales following a different dynamics [91, 92]. This kind of 'anomalous' scaling appears in interfacial problems in which the mean local slope of the front diverges in time, introducing a new correlation length in the growth direction [55, 78]. More recently it has been shown that in a nanoporous glass (Vycor), with highly elongated pores, the motions of different menisci in the imbibition front are uncorrelated. This leads to distinct scaling properties of the front roughness, because the stabilizing role of surface tension is absent in this type of displacements [34, 82].

We refer the reader to the extensive review by Alava, Dubé and Rost for further details on kinetic roughening in imbibition [1].

Driving Modes and Characteristic Length Scales

Stable imbibition displacements have been classified into *spontaneous* and *forced*. Spontaneous imbibition occurs under the sole influence of capillary forces. Forced imbibition, in contrast, involves capillary forces together with an externally imposed flow rate or pressure difference. However, it is more relevant for our purposes to classify stable imbibition displacements in terms of the mode used to drive the invading fluid into the medium–as defined by the boundary condition prescribed at the inlet. Indeed, different boundary conditions lead to different dynamics.

In the first mode of driving the displacement is driven by a *constant pressure difference* between inlet and outlet. This is usually implemented by applying a constant additional pressure at the inlet, e.g. by means of an auxiliary reservoir. Spontaneous imbibition is a particular case that corresponds to zero pressure difference. In the absence of gravity (for horizontal displacements) Darcy's law implies that the average position of the interface follows Washburn's law, $\langle h \rangle \sim \sqrt{t}$, so that $\mathrm{Ca} \sim 1/\sqrt{t}$ and the front slows down in time but never arrests (Fig. 12.2). This is only true however when the fluid displaced can easily leave the disordered medium. Similarly inertial effects, fluid evaporation, swelling of fibers in fibrous media, and several other complications, can make actual displacements depart from simple Washburn behaviour. A more complete discussion can be found in [1].

In the second driving mode the prescribed magnitude is the average velocity v of the fluid at the inlet, e.g. by means of an external pump. The usual prescription is a *constant flow rate*. The average position of the interface then is simply a (prescribed) linear function of time, $\langle h \rangle \sim t$, and Ca is well defined and does not depend on time. Experimental limitations associated with the smooth operation of fluid pumps prevent approaching the interesting limit $\mathrm{Ca} \to 0$. It is important to mention that this driving mode imposes a global constraint of mass conservation of the invading fluid per unit time. This constraint introduces large scale correlations between local velocities at distant points, which become increasingly important as the invading front is progressively more distant from the inlet [1].

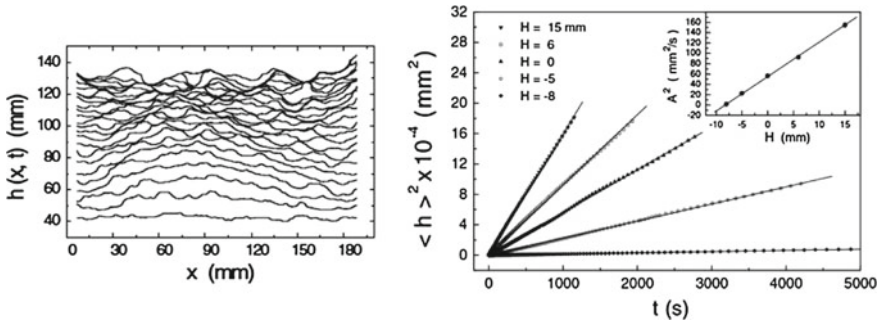

Fig. 12.2 Imbibition displacements driven by a constant pressure difference in a horizontal disordered Hele-Shaw cell. The *left panel* shows a series of fronts, $h(x,t)$, recorded at equal time intervals. The *right panel* shows the average front position, squared, versus time, for displacements corresponding to different applied pressures. The displacements follow Washburn's law, $\langle h \rangle = At^{1/2}$, quite accurately. The inset shows the dependence of Washburn's law prefactor A (squared) on applied pressure difference (in units of oil column height). Both panels are reproduced from [92]

In either mode of driving, local fluid conservation ($\nabla \cdot \boldsymbol{v} = 0$) and Darcy's law ($\boldsymbol{v} \sim \nabla p$) imply that the pressure field in the bulk of both the displacing and the displaced fluid obeys Laplace's equation, $\nabla^2 p = 0$. This is true for the undisturbed pressure field in a homogeneous medium and for the average pressure field in a disordered medium [67]. Motions of different parts of the imbibition front are thus coupled through the pressure field in the bulk of the fluids, and the interfacial dynamics is therefore intrinsically non-local–as mentioned earlier.

Indeed, several authors [1, 46, 67] have shown that fluid conservation introduces a characteristic length scale in the problem, $\ell_c \sim \mathrm{Ca}^{-1/2}$, which defines the maximum lateral extent of correlated interfacial fluctuations. To understand the physical origin of this length scale, consider the displacement of air by a viscous oil in a two-dimensional medium and suppose–as shown in Fig. 12.3–that a region of the front of lateral extent ℓ experiences a perturbation $\delta h(x) = A\cos(kx)$, where $k = 2\pi/\ell$. In a quasistatic approximation the concomitant pressure jump across the interface is linked to the local curvature through the Young–Laplace relation, $\Delta p \simeq \sigma(\partial^2 \delta h(x)/\partial x^2) \simeq \sigma A/\ell^2$, where σ is the oil–air surface tension. This pressure change makes that advanced segments of the front slow down. According to Darcy's law, on the other hand, the viscous pressure drop across the same distance in the flow direction is $\Delta p = (\mu/\kappa)\mathrm{v}A$, where μ is the dynamic viscosity of the oil and κ is the permeability of the medium. Comparing these two damping mechanisms yields a lateral length scale for interfacial fluctuations:

$$\ell_c = \sqrt{\frac{\kappa}{\mathrm{Ca}}}, \tag{12.1}$$

where $\mathrm{Ca} = \mu \mathrm{v}/\sigma$ is the capillary number.

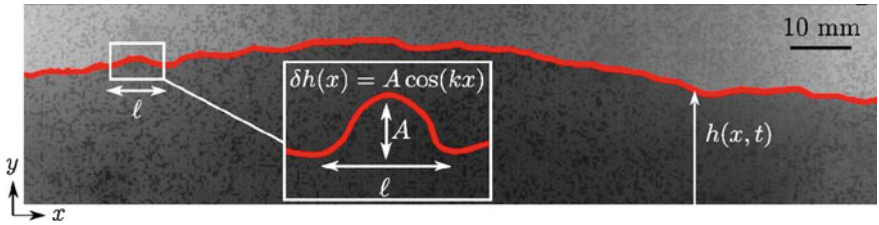

Fig. 12.3 Snapshot of a stable imbibition front (silicone oil displacing air) in a horizontal disordered Hele-Shaw cell. See the text for details. The figure is reproduced from [15]

Starting from an initially smooth interface, lateral correlations between front displacements grow in time up to the value ℓ_c; the interface reaches then a statistically-stationary state of saturated roughness [1, 24, 85]. Notice that in imbibition displacements driven at constant flow rate, ℓ_c can be tuned by changing either the imposed flow rate or the fluid properties (viscosity or surface tension). Notice also that ℓ_c diverges when $\mathrm{Ca} \to 0$, highlighting the importance of low capillary number experiments. The consequences on the scaling properties of front roughness have been extensively studied, both theoretically [1, 67] and experimentally [69, 90]. In this chapter we review the consequences on the spatiotemporal dynamics of the imbibition fronts [17, 85]. The prediction is that correlations extend over larger distances as $\mathrm{Ca} \to 0$, and diverge at $\mathrm{Ca} = 0$ where collective fluid motion is expected to occur in the form of critical avalanches spanning the whole system size. The precise condition $\mathrm{Ca} = 0$ defines thus a critical pinning-depinning transition, characterized by lateral correlations of infinite extent and an infinite susceptibility of the system to front distortions in the thermodynamic limit. Even though this condition cannot be reached experimentally, at least by simply tuning the injection rate to 0, we will show that the presence of the critical point is already noticeable on the wide probability distributions of avalanche lateral extents, sizes and durations, and on the strong divergence of their cutoffs as $\mathrm{Ca} \to 0$. The possibility of tuning the distance to criticality through the capillary number makes stable imbibition displacements particularly interesting in order to study complex spatiotemporal avalanche dynamics.

Front distortions are triggered by the heterogeneous, quenched structure of the disordered medium. At low capillary numbers the dominant role is played by the capillary pressure fluctuations across the interface. The interface moves slowly in average, with localized bursts of activity which are directly coupled to the quenched disorder. However, the fluid behind the interface feels also local fluctuations in the hydraulic permeability of the medium. Fluctuations in the permeability are translated into fluctuations of the advancing front by the pressure field in the fluid. We will show in Sect. 12.4.1 that a second crossover length scale, given now by $\ell_\times = \sqrt{\kappa}/\mathrm{Ca}$, separates front fluctuations induced by capillary disorder from those induced by permeability disorder. For slowly advancing fronts $\ell_\times \gg \ell_c$, so that capillarity-induced fluctuations prevail, and permeability noise and its possible correlations with capillary disorder can be ignored [67].

The effect of thermal fluctuations is considered negligible in front of the other forces involved–except maybe right at the critical pinning point $\mathrm{Ca} = 0$, a situation that remains largely unexplored.

Anomalous Dynamics of Capillary Rise in Porous Media

The simplest realization of spontaneous imbibition is the capillary invasion of a porous medium by a wetting fluid brought in contact with the medium outer surface. To focus on the basic physics of the invasion process we consider a simple model system where the displaced fluid has negligible viscosity (e.g. air) and the medium is essentially homogeneous beyond the Darcy scale.

As discussed earlier, in the absence of gravity (for horizontal displacements) the average position of the front as a function of time is well described by Washburn's law, $\langle h \rangle \sim \sqrt{t}$. When gravity opposes capillary invasion (for inclined or vertical displacements) a simple theory based also on Darcy's law predicts a crossover between Washburn behavior at early times and an exponential slowing down at late times that would finally take the front to rest–in infinite time. The average position reached asymptotically by the front is known as Jurin's height. It is given by $\Delta p_c/(\rho g \sin \psi)$, where Δp_c is the average capillary-pressure jump at the liquid-air interface, ρ is the liquid density and $g \sin \psi$ is the effective gravity. Traditionally this approach has been considered an appropriate description of capillary rise in disordered media, since it predicts the fast stages of invasion and the dramatic slowing down associated with approaching Jurin's height observed experimentally (see [53] for a recent overview).

Some years ago capillary rise in porous media was investigated for very long times in vertical cylindrical columns packed with glass spheres [20, 45]. Washburn behavior was indeed observed in the initial stages of invasion, followed by the predicted exponential slowing down for a few minutes. When the front had practically come to rest, however, the dynamics switched over unexpectedly into a motion in small-amplitude jumps on the pore scale that went on for hours. The average position followed a power law in time, rather than the predicted exponential dynamics, and was not found to approach an equilibrium height asymptotically. These unexpected observations did not find an explanation until Shikhmurzaev and Sprittles, in 2012, proposed a different approach to capillary rise in disordered media [89]. Their theory considers different modes of motion that menisci go through on the pore scale, in the framework of a hydrodynamic description at Darcy's scale. Three main modes are considered: a *wetting mode*, which describes the motion of the contact line on the pore scale driven by capillary forces, essentially in the Washburn regime, with a shape practically unchanged but with a velocity-dependent contact angle. A *threshold mode*, which describes the local pinning of the contact line upon reaching a pore, followed by the deformation of the meniscus until the contact angle reaches a critical value at which the contact line can resume its motion. The third mode, called *subcritical depinning*, introduces a new mechanism of motion. On the pore scale there are pressure fluctuations, due to the mutual influence of menisci that are in different modes of motion at one given moment. These fluctuations are unimportant when the local pressure is capable of pushing the meniscus through the threshold mode. But when this is not the case the front remains locally pinned, so that the effectiveness of

the fluctuations grows in time until, finally, the interface may depin subcritically due to random fluctuations. This mode of motion, responsible for the long-time behavior of capillary invasion, is associated with avalanches of the invading menisci that had been indeed observed experimentally in the long-time regime of capillary rise. The two first modes alone reproduce the essential features of the short-time dynamics. Jurin's height, however, is attained in finite time and depends only on the threshold value of the contact angle. Remarkably the third mode of motion is able to reproduce very accurately the power-law long-time dynamics, and also to capture the observed behavior for disordered media of different porosities. The theory predicts also that capillary rise eventually comes to a halt at very long times–but these fall beyond the range of available measurements.

12.3 Experimental Setting: A Model Open Fracture

Laboratory models designed to study imbibition displacements from a statistical physics perspective are idealizations of actual disordered (porous and fractured) media. They try to capture the relevant effects of the heterogeneous structure of the medium in some form of quenched disorder [3, 23]. Often they adopt a quasi-two-dimensional geometry in the form of Hele-Shaw cells, formed by two parallel glass plates with a very narrow gap in between. Hele-Shaw cells have the advantage of providing visual access to the local front dynamics while granting also–because of the small gap thickness–that fluid flow in the bulk is governed by Darcy's law. Experiments have addressed the imbibition of a fluid by a Hele-Shaw cell with wettability defects [28, 65, 66], random packings of glass-beads [22, 87], or randomly-varying gap thickness [70, 85].

The experiments that will be discussed in the remainder of this chapter belong to the last case. They emulate the stable invasion of an open fracture by a wetting, viscous fluid. The model open fracture is a horizontal Hele-Shaw (HS) cell with a two-valued gap thickness that fluctuates randomly in the plane of the cell. A sketch is shown in Fig. 12.4. The model consists of two parallel, large glass plates (190×500 mm^2), separated by a much smaller distance. Dichotomic variations in gap spacing, between $b = 0.46$ mm and $b - \Delta b = 0.40$ mm, are provided by a fiber-glass plate with controlled topography placed on top of the bottom glass plate. The topography consists of copper patches of size 0.4×0.4 mm^2 and height $\Delta b = 0.06$ mm. These patches are randomly distributed in a square grid, occupying 35 % of the surface. Adjacent patches form islands of disorder. The lateral sizes of disorder islands are exponentially distributed, with a characteristic length $\ell_d = 0.6$ mm. The invading liquid (silicone oil) is injected through the medium either at constant flow rate, by means of a syringe pump connected to the inlet, or at constant pressure, by means of an external reservoir, as shown in Fig. 12.5. The oil injected at one end (inlet) displaces the air initially present and forces it to leave the cell at the opposite end (outlet) which is open to the atmosphere. The lateral edges of the cell are sealed, so that the oil flows in the y direction only.

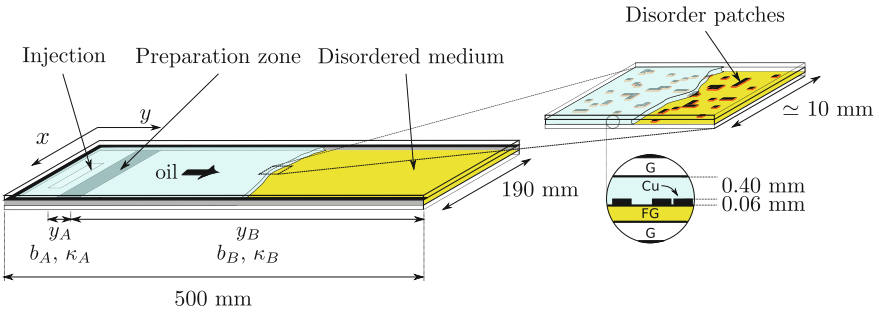

Fig. 12.4 Sketch of our model open fracture. It consists of two horizontal, parallel glass plates (G) and a disorder fiber-glass plate (FG). Squared copper patches (Cu) of lateral sizes $0.4 \times 0.4\,\text{mm}^2$ which occupy 35 % of the surface of the FG plate are randomly distributed on a square grid. The region of interest (ROI) defines the lateral system size $L = 136\,\text{mm}$. The figure is reproduced from [15].

The medium mimics an *open fracture* that features a two-dimensional non-zero aperture field, distributed along a plane. The randomness along the fracture plane makes it more complex than the simple parallel plate model of an open fracture. Although the two-level geometry is different from the geometry measured on natural fractures, which combines a continuously varying aperture field and statistically well-defined random in-plane and out-of-plane spatial correlations, the simplicity of the two-level geometry facilitates theoretical analysis. Indeed, a precise analytical description of the stochastic contributions to the linearized interfacial growth equation that arise in our specific setup from gap randomness along the fracture plane was recently reported [67]. It will be briefly reviewed in Sect. 12.4.

Flow in a horizontal and smooth Hele-Shaw cell is described by a gap-averaged, two-dimensional velocity field $\boldsymbol{v}(x, y)$ which locally obeys Darcy's law, i.e. $\boldsymbol{v}(x, y) = -(\kappa/\mu)\nabla p$, where the hydraulic permeability in the absence of disorder is given by $\kappa = b^2/12$ and μ is the dynamic viscosity of the fluid. A locally variable gap thickness modifies the hydraulic permeability of the cell. For the two-valued gap thickness of our cell the permeability follows the empirical relation [90]:

$$\kappa = \frac{b^2}{12}\left(1 - 0.55\frac{\Delta b}{b}\right)^2, \tag{12.2}$$

and we get for the present setup $\kappa \simeq 0.015\ \text{mm}^2$.

Silicone oils have the advantage of being available in a wide range of viscosities, with nearly identical oil-air surface tension. We have used silicone oils of dynamic viscosities $\mu = 10, 50, 100, 169$ and 350 cP at room temperature, density $\rho \simeq 1000$ kg/m^3, and surface tension $\sigma \simeq 21$ mN/m. Silicone oils fully wet–with zero static contact angle–all surfaces present in the model: glass, copper and fiberglass. To overcome the formation of precursor wetting films in the course of the displacements we prewet the cell with a thin oil layer on each plate before carrying out the experiments.

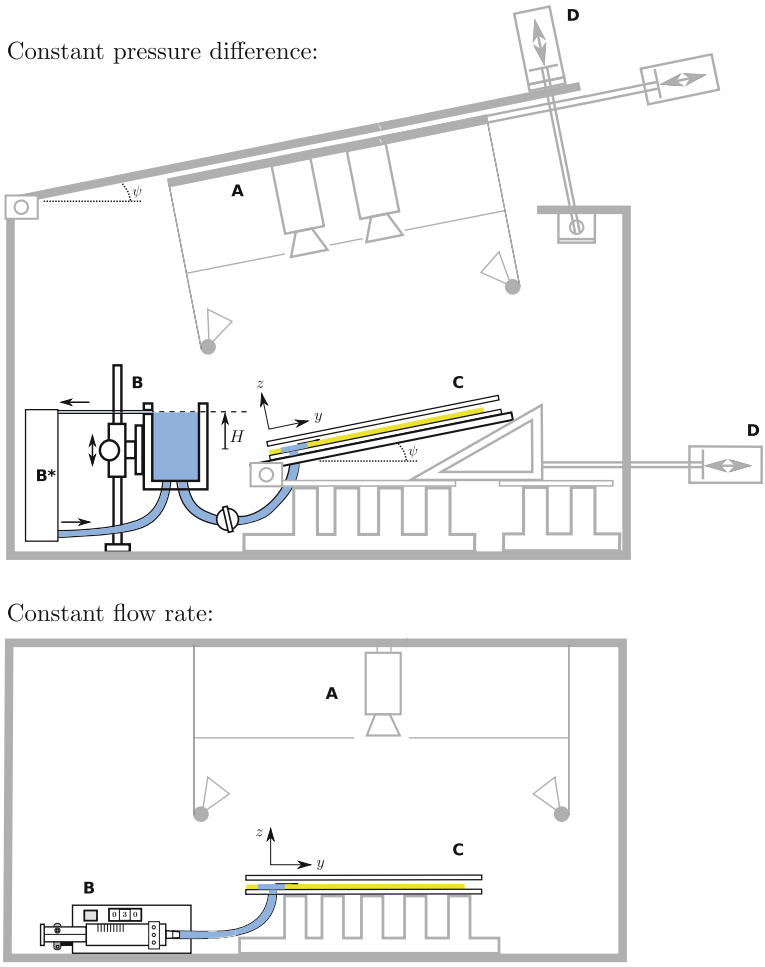

Fig. 12.5 Experimental setups for the two possible driving modes. The setup in the *top panel* is used in constant-pressure-driven displacements, while the setup in the *bottom panel* is used in displacements at constant flow rate. The figure is reproduced from [15]

All the results discussed in the next section correspond to unidirectional displacements in the y direction at constant flow rate. The invading fluid flows in the free gap between the two plates of the cell. The volume of fluid injected per unit time is constant, but the average velocity of the invading front (over the cell width, L) fluctuates in time because the gap thickness of the cell is not spatially uniform. Mean front velocities fall in the range $0.04 < \mathrm{v} < 0.6$ mm/s, so that we explore a wide range of capillary numbers, $6 \times 10^{-5} < \mathrm{Ca} < 2 \times 10^{-3}$, which correspond to nominal lateral correlation lengths $2.6 < \ell_c < 15.3$ mm. Experimental limitations prevent carrying out displacements at arbitrarily small flow rates. Combining the smallest accessible

v and μ we are able to reach a largest ℓ_c of about 12 % of the lateral system size [17]. In order to have accurate enough statistics, each experiment is repeated 15 to 20 times with several disorder realizations.

The advancement of the oil-air front is recorded from above using a high-speed and high-resolution camera. In each experiment an initially flat front propagates for about 150 mm in the y-direction of the cell, to make sure that it has reached a statistically-stationary state of saturated roughness. Next, image recording starts and imbibition fronts are monitored within a measurement window (ROI) centered with the cell. The ROI has lateral size $L = 136$ mm to avoid boundary effects produced by the side walls, and it extends typically 25 to 45 mm in the propagation direction y. The spatial resolution is $r = 0.106$ mm/pixel, so that each square patch of the disorder is covered by more than 4 pixels in either x or y directions. Once the spatial resolution is chosen, the image acquisition rate (up to 200 frames/s) is adjusted to make sure that the front locally advances one pixel at most between consecutive images. Numerical data corresponding to consecutive positions of the front, $h(x, t)$,

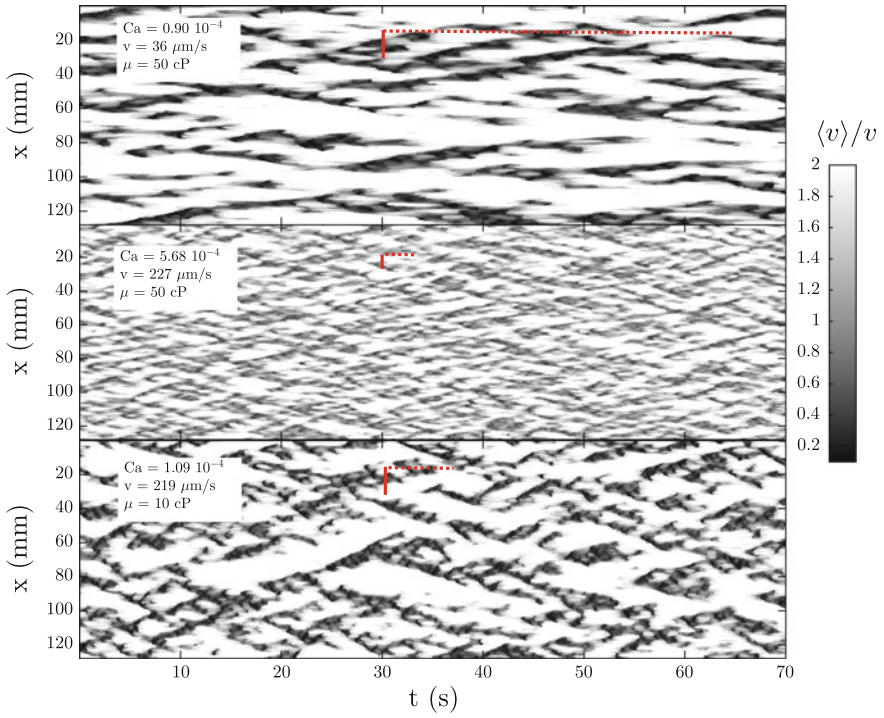

Fig. 12.6 Spatio-temporal maps $v(x, t)$ of the local velocities of imbibition fronts, for three different experiments with various imposed flow rates v and dynamic viscosities of the silicone oils μ, and thus different capillary numbers Ca of the flow. The vertical (*solid*) and horizontal (*dashed*) lines represent the extent of the spatial and temporal correlations respectively

are obtained by applying an edge-tracking algorithm on the recorded frames. An example has been shown in Fig. 12.3.

Our study is based on the analysis of the *local waiting times* of the front. This method of analysis was originally developed to study the dynamics of interfacial cracks [58]. It consists on counting, for all pixels (x, y) within the ROI (recorded image), the number of consecutive images in which the front is found in that pixel, and derive from this number the amount of time, $wt(x, y = h(x, t))$, spent by the front in that position. From this matrix, a *map of local velocities* can be computed as $v(x, y) = r/wt(x, y)$, where r (spatial resolution) is the linear size of one pixel. Each local velocity determined in this way is the mean value of the local front velocity at the pixel resolution. Combining the information contained in the map of local velocities with the front profiles $y = h(x, t)$ provides a *map of spatio-temporal activity*, $v(x, h(x, t))$. Examples of the latter will be shown in Fig. 12.6.

12.4 Dynamics of Slow Imbibition Displacements in Our Model Open Fracture

12.4.1 Theoretical Framework

The fact that we are dealing with *stable* two-phase displacements makes that local deviations of the invading front from its mean position can be considered small compared to their lateral extent. In this approximation, an interfacial equation for the dynamics of the front height, $h(x, t)$, can be derived along the lines of the linear stability analysis of Saffman and Taylor for the viscous fingering problem [83], assuming that the displacing fluid (oil) is much more viscous than the displaced fluid (air), i.e. $\mu \gg \mu_0$. The temporal growth of $\tilde{h}(k)$–the Fourier mode of the front height of wavenumber k–is given by:

$$\frac{1}{\mathrm{v}}\frac{\partial \tilde{h}(k)}{\partial t} = \delta(k) - |k|\tilde{h}(k) - \kappa\frac{\sigma}{\mu \mathrm{v}}|k|k^2\tilde{h}(k) + \text{ quenched-noise terms.} \qquad (12.3)$$

Kronecker's delta, present only in constant flow-rate displacements, accounts for the condition of global mass conservation per unit time. The deterministic part of the equation (the two explicit terms in the right-hand-side, both of them negative) account for viscous damping and surface-tension damping, respectively. Viscous damping (proportional to $|k|$) is dominant at small k (perturbations of long wavelength), while surface-tension damping (proportional to $|k|k^2$) is dominant at large k (perturbations of short wavelength). These two forces cross over at $k_c = [(\mu \mathrm{v}/\sigma)/\kappa]^{1/2}$, which corresponds to the lateral length scale $\ell_c = (\kappa/\mathrm{Ca})^{1/2}$ introduced earlier. The presence of absolute values of k indicates that the front dynamics is non-local, a consequence of the laplacian character of the unperturbed pressure field in the bulk of the invading fluid, as discussed earlier. Instead of a differential equation, non-locality leads to an

integro-differential equation for the deterministic dynamics of $h(x,t)$ in real space. This makes the theoretical description of the dynamics of stable imbibition fronts substantially more complex than most other problems of slowly-driven interfaces [24, 32, 37, 67].

The destabilization of the front is due to forces resulting from the internal structure of the disordered medium. These are included generically in the third term of the right-hand-side of the equation, in the form of quenched-noise terms. Thermal fluctuations are considered comparatively negligible, so that time-dependence is expected to enter only through the interface position $h(x,t)$. In 2003 Pauné and Casademunt derived the precise form of these quenched-noise terms for the specific case of stable imbibition displacements in a horizontal Hele-Shaw cell with fluctuating gap thickness–a setup inspired by our model open fracture [67]. In their work however the variable gap thickness is assumed to vary smoothly in space, $|\nabla b| \ll 1$. It takes the form $b^2(x,y) = b_0^2[1+\zeta(x,y)]$, where $\zeta(x,y)$ is a random variable of zero mean and b_0 is the mean gap thickness. The authors note that fluctuations in gap thickness–a single source of randomness–give rise simultaneously to the three basic physical effects of a porous matrix on the interface motion: local variations of capillary pressure, of permeability, and of available volume. Hence, different (but not independent) quenched-noise terms in (12.3) are generated by those distinct physical mechanisms. First a non–local, conserved (area-preserving) noise term of the form:

$$-\frac{b_0}{12}\frac{\sigma}{\mu v}|k|\tilde{\zeta}(k), \tag{12.4}$$

where $\tilde{\zeta}(k)$ is the Fourier transform of $\zeta(x,h(x))$. This noise term, known as *capillary disorder*, results from capillary-pressure fluctuations. Gap thickness fluctuations give rise also to local permeability variations. Combined with fluid volume conservation, permeability variations produce a second noise term, local and nonconserved, of the form:

$$-\frac{1}{2}\tilde{\zeta}(k). \tag{12.5}$$

This second noise term is called *permeability disorder*. Equating these two quenched-noise terms leads to a second crossover length (between conserved and nonconserved noise) in imbibition displacements, that we introduced earlier: $\ell_\times = b_0/(6\,\mathrm{Ca})$. It gives an estimation of the lateral length scale above which fluctuations in the medium permeability contribute also–together with capillary pressure fluctuations–to the destabilization of the invading front. In very slow displacements, such as the ones considered in the remaining of this chapter, $\ell_\times \gg L > \ell_c$ and permeability disorder can be disregarded in front of capillary disorder. This defines the so-called *capillary regime*. The importance of permeability disorder, however, has been observed experimentally in pressure-driven imbibition displacements [69]. Finally, fluctuations in available volume give rise to a *long-ranged correlated disorder*, $\tilde{\Omega}_{\mathrm{LR}}(k,t)$. In contrast to our earlier expectations, this noise term enters effectively as an annealed (explicitly time-dependent) noise, with:

$$\langle \tilde{\Omega}_{\mathrm{LR}}(k,t)\tilde{\Omega}_{\mathrm{LR}}(k',t')\rangle = \frac{\Delta}{2\pi}|k|\delta(k+k')e^{-|k|\mathrm{v}|t-t'|}, \tag{12.6}$$

where Δ is given by $\langle \zeta(x,y)\zeta(x',y')\rangle = \Delta\delta(x-x')\delta(y-y')$, since ζ is effectively white above the microscopic correlation length of the quenched disorder. Hence $\tilde{\Omega}_{\mathrm{LR}}$ scales as $|k|^{1/2}$ and introduces long-range memory. Numerical computations, however, show that this nonlocal part of the bulk noise can also be neglected in the capillary regime [67].

The relative importance of the destabilizing forces, therefore, is controlled by the capillary number of the displacement, Ca $\sim \mu$v. We have $\ell_c \sim 1/\sqrt{\mathrm{Ca}}$ and $\ell_\times \sim 1/\mathrm{Ca}$. In our setup, the capillary regime ($\ell_\times \gg L > \ell_c$) corresponds to capillary numbers in the range from 6×10^{-5} (the lowest Ca accessible) to about 6×10^{-4}. In this range $15 < \ell_c < 5$ mm, and $1325 < \ell_\times < 125$ mm, respectively. Above Ca $= 6\times10^{-4}$ the dynamics is in a mixed regime in which both capillary and permeability disorder are relevant [72].

12.4.2 Localized Burst Dynamics

Spatio-temporal Correlated Activity Maps

The spatio-temporal field of local velocities $v(x,t)$ computed from $v(x,h(x,t))$ constitutes a convenient representation of the local activity in the course of the imbibition process. Examples of such local activity maps for experiments performed at different imposed flow rates v and dynamic viscosities of the invading fluid μ–and thus different capillary numbers within the capillary regime of the flow–are shown in Fig. 12.6. The figure reveals clearly that the invasion process of our disordered cell is highly fluctuating both spatially and temporally. In all cases regions of low velocities alternate with regions of high velocities (above v), spanning a wide range of temporal and length scales. We observe that the amplitude of the velocity fluctuations are larger at lower viscosities (bottom and middle maps correspond to experiments at similar flow rates v, but viscosities $\mu = 10$ cP and $\mu = 50$ cP respectively) and also at smaller flow rates (top and middle maps correspond to experiments with the same invading fluid of viscosity $\mu = 50$ cP but forced to invade the cell at v $= 36\,\mu$m/s and v $= 227\,\mu$m/s, respectively).

We performed a detailed quantitative analysis of the spatio-temporal correlations of the local velocities $v(x,t)$. First of all, we could show that local velocities are indeed correlated along the fronts–in the x direction–up to the scale ℓ_c at which viscous forces overcome surface tension in damping the interfacial fluctuations [17, 85]. Moreover, we could also show that the amplitude of the local velocity fluctuations is controlled as well by the capillary number, since experiments performed in very different conditions–with very different (μ, v)–but similar Ca present the same statistical distribution of local velocities $P(v/\langle v\rangle)$ [17]. However, analyzing the autocorrelation of the signal $v(x,t)$ in time, $C_v(\Delta t)$, we could show that the

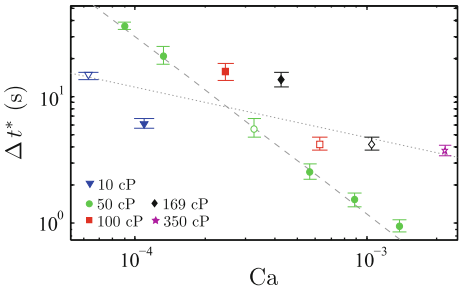

Fig. 12.7 Maximum anticorrelation time Δt^*, extracted from the autocorrelation of the signal $v(x,t)$ in time, as a function of the capillary number Ca. *Dashed* and *dotted lines* are guides to the eye proportional to $\mathrm{v}^{-1.4}$ and $\mu^{-0.4}$, respectively. Open symbols correspond to experiments performed at $\mathrm{v} = 0.13$ mm/s. Reproduced from [17]

temporal correlations of the imbibition fronts during the cell invasion are not simply controlled by the capillary number [17, 85]. Indeed, we could observe that C_v decays as the time lag Δt increases, until it reaches a minimum value below zero (maximum anticorrelation) at Δt^*, before becoming uncorrelated ($C_v \to 0$) at larger time lags. Figure 12.7 displays the evolution of Δt^* for all experimental conditions explored as a function of the capillary number $\mathrm{Ca} \sim \mu \mathrm{v}$. It makes clear that velocity and viscosity do not play the same role in controlling Δt^*. The temporal correlations of the local front velocities depend more strongly on v than on μ. The dashed line goes through experiments performed at different v but same μ and is proportional to a power law $\mathrm{v}^{-1.4}$. Experiments at the same v but different μ correspond to the dotted line, that goes as $\mu^{-0.4}$. This difference can actually be noticed directly on the activity maps shown in Fig. 12.6, by comparing the top and bottom panels for instance. The capillary numbers of those two experiments are rather close, around 10^{-4}, leading indeed to spatial correlations of similar length, around 12 mm. The correlated clusters of fast motion, however, last much longer for the experiment performed at lower flow rate, shown in the top panel ($\Delta t^* \simeq 35$ s). Therefore, by changing μ and v independently we showed that the imbibition front dynamics is not simply controlled by the capillary number $\mathrm{Ca} \sim \mu \mathrm{v}$.

High Velocity Clusters

Spatio-temporal correlations lead to a burst dynamics, clearly apparent on the spatio-temporal maps shown in Fig. 12.6. In order to study the statistical properties of correlated clusters of fast motion, we turn our attention to the spatial map of local velocities $v(x,y)$. We define *local avalanches* as spatially-connected clusters of local velocities $v(x,y)$ higher than an arbitrary threshold v_c. For example, in the bottom panel of Fig. 12.8 we show the spatial distribution of clusters obtained from a thresholded map $v(x,y) > c\langle v \rangle$, with $c = 1.5$.

First of all, it is important to notice that avalanches do not arise trivially from the medium heterogeneities. While, as discussed in Sect. 12.3, the lateral sizes of the disorder patches are exponentially distributed with a characteristic extent

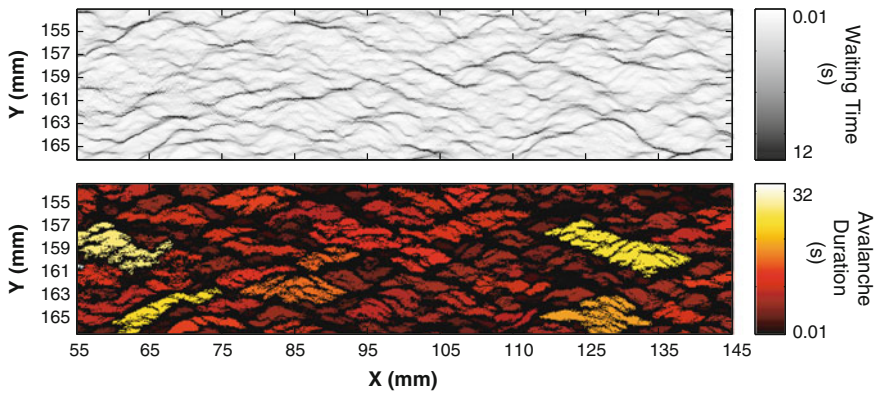

Fig. 12.8 *Top* Map of waiting time fluctuations obtained by the superposition of 10,000 interfaces for an experiment driven at v = 0.134 mm/s with $\mu = 50$ cP. *Bottom* Corresponding spatial distribution of velocity clusters for velocities $v(x, y) > c\langle v\rangle$, with $c = 1.5$. Reproduced from [85]

$\ell_d \simeq 0.6\,\text{mm}$, high velocity clusters are power-law distributed–in size A, lateral extensions L_x, L_y, and duration D–with exponentially decaying cut-offs. The measured power-law exponents appear robust, since they do not evolve within a wide range of velocity thresholds, imposed flow rates, and viscosities of the invading fluid, and therefore are independent of the capillary number Ca. The values of the exponents are $\alpha_A = 1.09 \pm 0.08$ for cluster sizes and $\alpha_D = 1.03 \pm 0.10$ for cluster durations.

We could verify moreover that the various statistical distributions follow scaling relations expected close to a depinning transition: local avalanches have a self-affine anisotropic shape, $L_y \sim L_x^H$, with a local roughness exponent $H \simeq 0.8$; and their lateral extent and size scale with their duration as $L_x \sim D^{1/z_{av}}$, with a dynamic exponent $z_{av} = 1.1 \pm 0.1$, and $A \sim D^{\gamma_{av}}$, where $\gamma_{av} = (1 + H)/z_{av} = 1.8 \pm 0.1$.

On the other hand, the exponential cut-offs of the various power-law distributions that characterize avalanche properties diverge as the imposed flow rate and the viscosity are reduced, and thus as $\text{Ca} \to 0$. We could actually show that the maximum extent of the local avalanches along x scales as $\xi_{L_x} \sim \ell_c \sim 1/\sqrt{\text{Ca}}$. Thus, we could also verify that their maximum size follows $\xi_A \sim \xi_{L_x}\xi_{L_y} \sim \xi_{L_x}^{1+H} \sim \text{Ca}^{(1+H)/2}$. Finally their maximum duration behaves as $\xi_D \sim \xi_{L_y}/\text{v} \sim \ell_c^H/\text{v} \sim \mu^{-H/2}\text{v}^{-(1+H/2)}$. These scaling relations correspond to the spatio-temporal correlations observed and measured on the activity maps of the displacements–as shown in Fig. 12.7 for the temporal correlations.

It is important to mention that the scale-invariant properties of the localized high-velocity bursts, which seem to belong to the realm of a critical depinning transition at $\text{Ca} = 0$, differ significantly from those obtained in phase-field simulations [56, 75]. Such discrepancy may be due to the fact that we could not reach experimentally the critical point at $\text{Ca} = 0$, where a different set of values of the scaling exponents can be expected. Nevertheless, it should be remarked also that the quenched disorder field introduced in phase-field simulations of imbibition displacements, to model capillary

pressure fluctuations, has been so far considered to follow a Gaussian distribution with a correlation length limited to the underlying lattice spacing. This is in contrast with our experiments, where single disorder patches alone have a linear extension of 0.4 mm and disorder islands formed by several patches have a characteristic extension of several pixels, $\ell_d \simeq 0.6$ mm, introducing thus a microscopic correlation length of the quenched disorder.

12.4.3 Dynamics of Global Avalanches

In the previous subsection we discussed the avalanche dynamics of imbibition fronts based on measurements of the interfacial velocity at the local scale of our spatial resolution. It is important to underline that often this local information is not accessible in crackling-noise systems, where a global–spatially averaged–quantity is analyzed instead. Trying to find coarse-grained equivalent descriptions of highly heterogeneous phenomena is widespread in various contexts in physics. In particular, a common theoretical approach to study porous media flows consists in developing volume-averaging or homogenization procedures, aimed at obtaining effective flow behavior at large scale from the up-scaling of phenomena at microscopic scales [96]. Consequently it seems worthwhile to study how the various observables characterizing stable imbibition dynamics evolve with the scale of observation.

We have analyzed the influence of the two controlling parameters of our experiments–the dynamic viscosity of the invading fluid, μ, and the mean velocity associated to the imposed flow rate, v–on the statistical properties of the global velocity at scale ℓ. This global velocity, V_ℓ, is the spatial average of $v(x,t)$ (the spatio-temporal map of local front velocities) over a window of lateral size ℓ: $V_\ell(t) = (1/\ell)\int_\ell v(x,t)dx$. The length scale ℓ could be varied in a wide range, from the spatial resolution of the images up to the width L of the measurement region.

Due to the large fluctuations of the local front velocity, and its spatial and temporal correlations, the global velocity signals $V_\ell(t)$ present very strong fluctuations, which evolve systematically with the parameters μ, v and ℓ, even though the imposed flow rate is constant in our experiments. Indeed, Fig. 12.9 shows typical examples of these time series measured at the largest scale of observation $\ell = L$, corresponding to the three experiments of Fig. 12.6. In all three cases $V_\ell(t)$ is a jerky signal that strongly fluctuates around its mean value. The amplitude of the fluctuations is larger for lower capillary numbers (i.e. lower μ or v). Obviously this is also the case when the measuring window size ℓ is reduced. In the following we analyze the statistical properties of these fluctuating time series.

Statistical Distributions of Global Velocities $V_\ell(t)$

As described earlier the local velocities $v(x,t)$ are spatially correlated along the imbibition front, up to the characteristic scale $\ell_c = \sqrt{\kappa/\mathrm{Ca}}$. Therefore $V_\ell(t)$–the average of this spatially-correlated signal–is expected to display non-Gaussian fluctuations. A large number of studies in various contexts not related to imbibition have shown

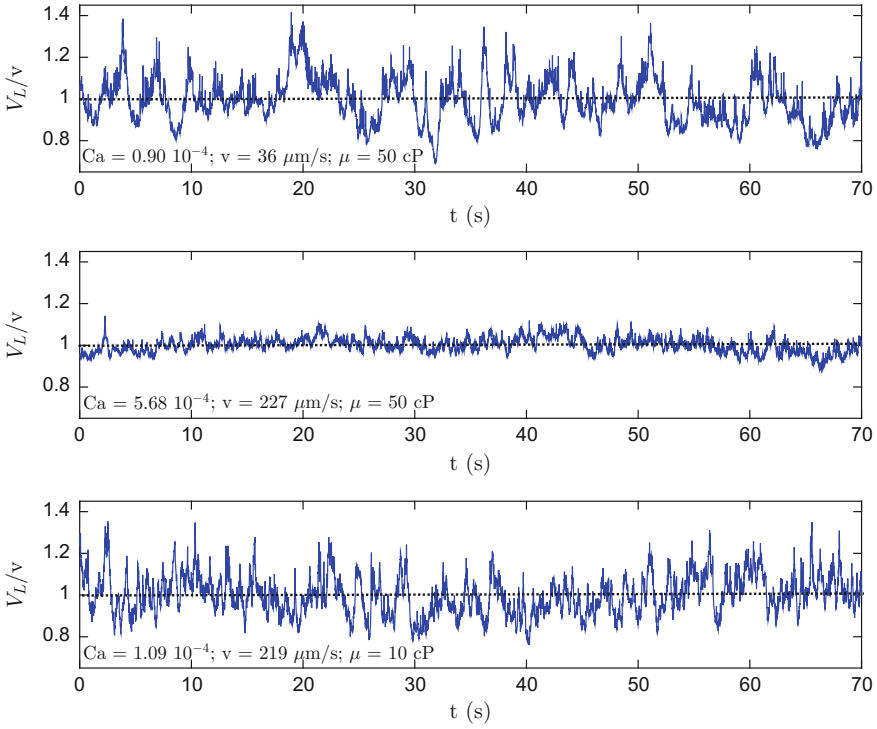

Fig. 12.9 Examples of the temporal evolution of the global velocities of the front, $V_\ell(t)$, spatially-averaged over the lateral size of the region of interest $\ell = L$, for the same three experiments shown in Fig. 12.6. The horizontal *dotted lines* show the imposed mean velocity at the inlet, v

that the fluctuations of global quantities in correlated systems–such as the power consumption in a turbulent flow [73], the magnetization of an XY Ising model [11] or the director orientation of a liquid crystal close to the critical Fréedericksz transition [42]–may be well described by generalized Gumbel (GG) distributions when the correlation length is comparable to the size of the measuring region. The GG distributions display an asymmetric non-Gaussian shape with a large exponential tail:

$$P_a(Y) = \frac{a^a b_a}{\Gamma(a)} \exp\left\{-a\left[b_a(Y + s_a) + e^{-b_a(Y+s_a)}\right]\right\}, \tag{12.7}$$

with $b_a = \sqrt{\psi^1(a)}/\sigma_Y$ and $s_a = \langle Y\rangle + \left(\ln a - \psi^0(a)\right)/b_a$, where $\Gamma(a)$ is the gamma function and $\psi^m(a) = d^{m+1} \ln \Gamma(a)/da^{m+1}$ is the polygamma function of order m. Considering a normalized variable Y (so that the first two moments of the distribution are $\langle Y\rangle = 0$ and $\sigma_Y = 1$), the only free parameter left to fix the shape of the GG distribution is a, related to its skewness by $S_k = \langle Y^3\rangle \sim 1/\sqrt{a}$.

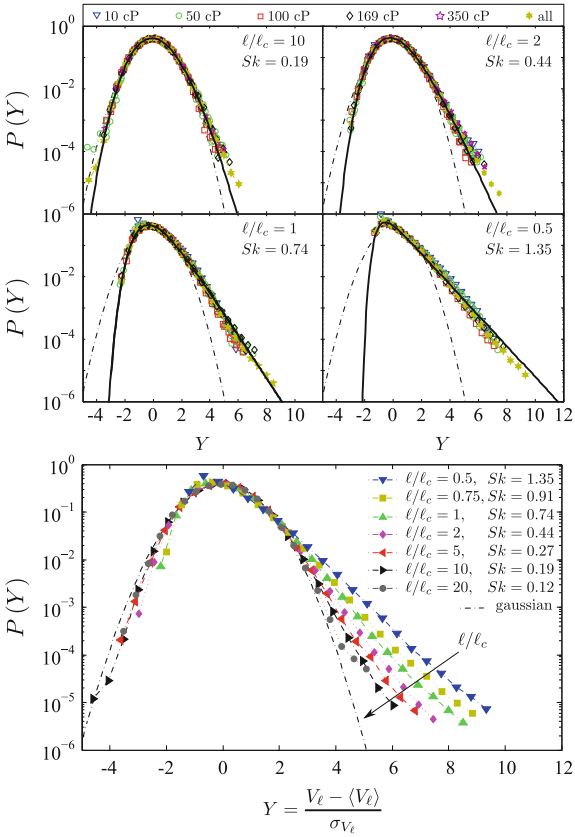

Fig. 12.10 Distributions of the normalized fluctuations of the global velocity, $Y = (V_\ell - \langle V_\ell \rangle)/\sigma_{V_\ell}$, for various values of ℓ/ℓ_c. *Top panels* show $P(Y)$ for all the experiments with different (μ, v) compatible with $\ell/\ell_c = 10$, 2, 1, and 0.5. Distributions for each experiment separately, and for data sets containing data from all experiments, are shown. *Solid lines* correspond to generalized Gumbel distributions with the value of the skewness Sk of the experimental distributions. The *bottom panel* displays $P(Y)$ for data sets containing data from all experiments compatible with ℓ/ℓ_c from 0.5 to 20. *Dashed-dotted lines* in all plots represent a normal distribution. Reproduced from [15]

We could indeed confirm these observations in our imbibition experiments [18, 70]. Figure 12.10 displays the statistical distributions of the normalized global velocity fluctuations $Y = (V_\ell - \langle V_\ell \rangle)/\sigma_{V_\ell}$, where $\langle V_\ell \rangle$ is the temporal average of the signal over the duration of the experiment and σ_{V_ℓ} its standard deviation. The different panels show the probability distributions obtained from various experiments performed with very different values of (μ, v), grouped by a common value of ℓ/ℓ_c. All distributions remarkably collapse, and compare very well with GG distributions of the same skewness. Moreover, the skewness Sk (and thus the non-Gaussian statistics of the global velocity fluctuations $V_\ell(t)$) increases systematically as the measuring length scale ℓ decreases towards the correlation length ℓ_c–determined by the capillary number of the displacement and the permeability of the medium. Hence the ratio ℓ/ℓ_c seems to control the amplitude of the temporal fluctuations of the global front velocity $V_\ell(t)$. Physically it can be interpreted as the number of statistically-independent domains of the interface, $N_{\mathrm{eff}} = \ell/\ell_c$. The theoretical reasons for the ubiquitous occurrence of GG fluctuations in correlated systems, however, are still being investigated [8, 12].

A Turbulent-like Dynamics

In the studies briefly reviewed above we just considered the statistical properties of the amplitude of $V_\ell(t)$–the global (spatially averaged) velocity of the front–at different length scales [70, 71]. More recently we have conducted also a multi-scale analysis of the temporal correlations of this temporal signal [16]. The study is based on the multi-fractal formalism proposed by Parisi and Frisch [31] to characterize the intermittent behavior of velocity signals measured in hydrodynamic turbulence. It consists in analyzing the statistical properties of the velocity increments $\Delta V_\ell(\tau) = V_\ell(t+\tau) - V_\ell(t)$ at different time scales τ.

Figure 12.11 shows the distributions of the normalized velocity increments $Y = (\Delta V_\ell - \langle \Delta V_\ell \rangle)/\sigma$ for increasing time lags τ. $\langle \Delta V_\ell \rangle$ stands for the ensemble average of ΔV_ℓ and σ for its standard deviation. These results were obtained for a given set of experimental conditions, v = 0.053 mm/s and $\mu = 50$ cP, with a measuring window $\ell = L/8 = 17$ mm ($\simeq 1.6\ \ell_c$). They constitute a typical example of the temporal evolution of the distributions of velocity increments. We observe that the shape of these distributions progressively evolves through the temporal scales τ, from being heavy-tailed at short τ towards being nearly Gaussian at longer time lags. Such behavior unveils that the dynamics of the invading front is highly intermittent, with complex temporal correlations on short time intervals.

Analyzing the evolution of the structure functions that characterize the distributions of velocity increments for different viscosities of the invading fluid, different velocities at the inlet, and different length scales ℓ, we were able to identify the parameters controlling the observed intermittent dynamics [16]. Indeed, Fig. 12.12 shows the normalized statistical distributions of spatially-averaged velocity increments $\Delta V_\ell(\tau)$ obtained under various experimental conditions (μ, v), but measured at length scales ℓ and time lags τ such that the ratios ℓ/ℓ_c and τ/τ_c are both fixed. The data collapse shows that the distributions of velocity increments depend specifically on those two parameters only. The characteristic time τ_c sets the temporal range over which intermittency is observed, while the ratio ℓ/ℓ_c controls its intensity. The characteristic time follows accurately the relation $\tau_c = \ell_d/\mathrm{v}$, and thus can be identified

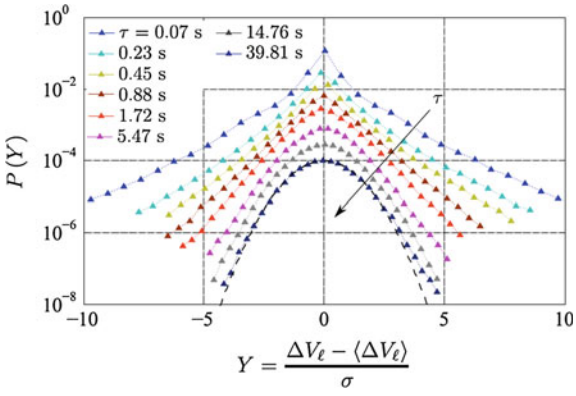

Fig. 12.11 Semi-log plot of $P(Y)$ versus $Y = (\Delta V_\ell - \langle \Delta V_\ell \rangle)/\sigma$ for increasing time lags τ, shifted vertically for visual clarity. The *dashed curve* represents a Gaussian distribution. The experiments were carried out at v = 0.053 mm/s and $\mu = 50$ cP, and analyzed at $\ell = L/8 = 17$ mm. The figure is reproduced from [16]

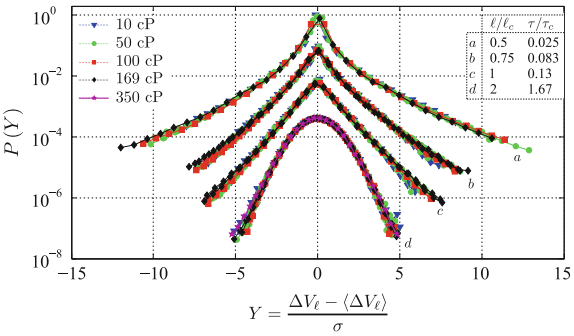

Fig. 12.12 Distributions of $\Delta V_\ell(\tau)$ for very different experimental conditions, with v between 0.036 and 0.55 mm/s and μ between 10 and 350 cP, collapsed for fixed $(\ell/\ell_c, \tau/\tau_c)$. Different distributions are shifted arbitrarily for visual clarity. The figure is reproduced from [16]

with the average time spent by the fluid front to advance over the typical extent ℓ_d of a disorder island in the cell.

In summary, we could demonstrate that slow imbibition displacements in our model disordered medium exhibit all the characteristic features of an intermittent dynamics. Such intermittent–turbulent-like–dynamics results from the local clusters of fast cooperative motion, triggered at the smallest length scales of the medium heterogeneities and distributed up to the correlation length ℓ_c. More work is still required, however, to understand the origin of the positive asymmetry of the distributions of velocity increments observed in our experiments, and also to verify the specific role of the medium heterogeneities of the medium by changing their properties systematically.

Global Avalanches

The large positive fluctuations of the global velocity $V_\ell(t)$ studied previously correspond actually to global avalanches. Those excursions of $V_\ell(t)$ above an arbitrary threshold V_c (usually chosen equal to the imposed mean velocity at the inlet v) have a size S and duration T defined by the area enclosed and the time elapsed between two consecutive threshold-crossings of the signal $V_\ell(t)$, as defined in Fig. 12.13.

We characterized the scaling behavior of these global avalanches in [18, 70]. We could show that their size and duration both follow power-law distributions, with power-law exponents α and τ respectively, and exponentially decaying cut-offs. Figure 12.14 displays the statistical distributions of sizes and durations in terms of the reduced variables $S' = S/\langle S \rangle^{1/(2-\alpha)}$ and $T' = T/\langle T \rangle^{1/(2-\tau)}$, respectively. The distributions were obtained from many experiments performed in various different conditions, with the only constraint that the scale ℓ at which the global velocity V_ℓ was measured was larger than ℓ_c. The data collapse allows to measure accurate values of the power-law exponents, as explained in [71, 76]. We obtained $\alpha = 0.96 \pm 0.05$ for avalanche sizes and $\tau = 1.15 \pm 0.15$ for their duration. Using the values of these two exponents, moreover, we could properly characterize the scaling behavior of the

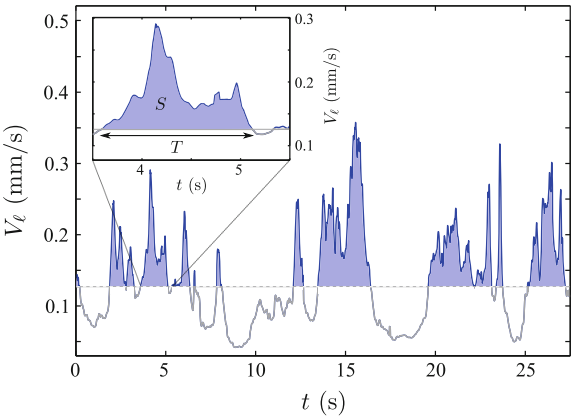

Fig. 12.13 The main panel shows an example of the global velocity signal for $\ell = L$, clipped by its average value. The inset is a single avalanche, of size S and duration T

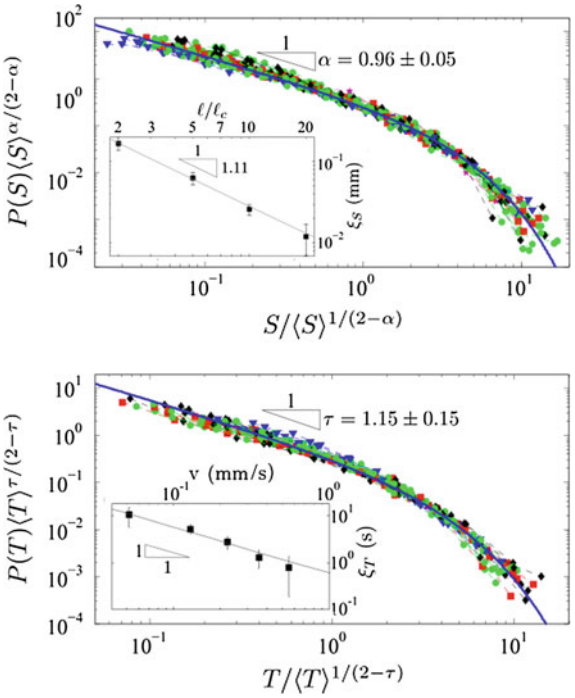

Fig. 12.14 Data collapse of the probability distributions of sizes (*top*) and durations (*bottom*) of the global avalanches, for experiments analyzed at $\ell > \ell_c$. Thirty-four different data sets with various (μ, v, ℓ) are considered. Different symbols correspond to different viscosities. The best fits to a power law with an exponential cutoff are achieved with $\alpha = 0.96$ and $\tau = 1.15$ (*solid lines*). Insets: evolution of the cutoff values of $P(S)$ with ℓ/ℓ_c (*top*) and the cutoff values of $P(T)$ with the imposed inlet velocity v (*bottom*). In the latter case the global avalanches were analyzed from time series $V_\ell(t)$ measured at a scale $\ell = 2\,\ell_c$. *Solid lines* are guides to the eye. Reproduced from [15]

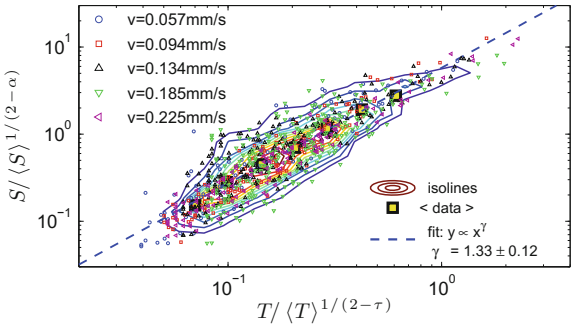

Fig. 12.15 Isolines of the joint distributions $P(S', T')$, where $S' = S/\langle S\rangle^{1/(2-\alpha)}$ and $T' = T/\langle T\rangle^{1/(2-\tau)}$, showing that $S' \propto T'^{\gamma}$, for experiments performed at various imposed flow rates but similar viscosities $\mu = 50$ cP and analyzed at the largest length scale $\ell = L$. A fit gives the value $\gamma = 1.33 \pm 0.12$. Reproduced from [71]

joint distribution of sizes and durations, as shown in Fig. 12.15. The maximum of the distribution followed $S' \propto T'^{\gamma}$, with $\gamma = 1.33 \pm 0.12$ for experiments performed at various inlet velocities, with an oil of viscosity $\mu = 50$ cP, analyzed at the largest length scale $\ell = L$.

Interestingly, in contrast with the scaling behavior of the localized high velocity clusters discussed in Sect. 12.4.2, the values of the scaling exponents of the global avalanches reported here are in good agreement with the ones obtained from phase–field simulations [74, 80]. This result underlines the fact that the avalanche dynamics of stable imbibition fronts is different at small and large scales. This is clearly demonstrated by the different values of γ and γ_{av}, the exponents characterizing the scaling behavior of the joint distributions of sizes and durations of global and local avalanches respectively. The difference is also evident in the way that the cutoffs of $P(S)$ and $P(T)$ (size and duration distributions of the global avalanches) depend on the controlling parameters of the displacements, which is not the same than for the local velocity clusters. As observed in the insets of Fig. 12.14, the cutoff of the distributions of global avalanche sizes, ξ_S, depends on $\ell/\ell_c \sim \ell\sqrt{\mu \mathrm{v}}$, and the cutoff of global avalanche durations depends only on the mean velocity of the interface as $\xi_T \sim 1/\mathrm{v}$. The latter could correspond to the characteristic time τ_c introduced in the previous section, which measured the average time spent by the fluid front to advance over the typical extent ℓ_d of the disorder islands. However more experimental work is needed, again, to change the properties of the disorder in our model fracture in order to confirm the previous results.

Finally, we could show that the scaling exponent γ slightly evolves also with ℓ/ℓ_c [18]. This result makes us suspect that the scaling exponents and the scaling range of the size and duration distributions of global avalanches might depend slightly on the size of the measuring window, ℓ.

12.5 Conclusions and Perspectives

We have considered a very simple realization of a two-phase fluid displacement in a disordered medium: the slow and stable imbibition of a viscous wetting fluid in a model open fracture. Already in such a simple situation, the interplay between stabilizing and destabilizing forces at different length and time scales leads to very rich and complex dynamics, which exhibits spatial and temporal scale-invariance, anomalous fluctuations, and intermittency.

With the setup presented here, the motion of the invading fronts can be monitored with very high spatial and temporal resolution. Our studies show that the displacements take place with strongly correlated local velocities, both in the lateral direction along the advancing front and in the direction of propagation. Spatio-temporal correlations lead to localized velocity bursts, or avalanches, whose scale-invariant properties–with sizes and durations power-law distributed over wide ranges of values–arise from the proximity to a critical depinning transition at $\mathrm{Ca} = 0$.

Avalanche properties (sizes and durations) can be defined and measured for local bursts of activity (local avalanches), and also for the jerky signal $V_\ell(t)$ which is obtained from the local activity by taking its spatial average in a window of lateral size ℓ. This temporal signal plays the role of a *crackling noise* in our system. The jerky advancement of the average position of the front is obviously a consequence of the local burst dynamics, with several clusters of large velocities–correlated or not–occurring at the same time but at different positions along the front. In contrast with the case of fracture fronts [47], however, a theoretical framework linking these different scales of description is still lacking in imbibition.

Part of the difficulty in establishing this link for displacements driven at constant flow rate might lie in the presence of large-scale velocity correlations, induced by the condition of global mass conservation (per unit time) of the fluid that is being forced to invade the cell. This condition, which is not present in other problems of slowly-driven interfaces, introduces correlations over scales much larger than ℓ_c, and it is expected to become increasingly important as the distance of the front to the inlet (where the displacing fluid is injected) increases [1].

A new set of experiments recently performed with fluids of different viscosities has led us to disclose the distinct effect of the imposed flow rate and the dynamic viscosity of the invading fluid on the dynamics of the imbibition process [17, 18]. Spatial properties in the lateral direction (x) are seen to depend only on the capillary number Ca. Indeed, lateral correlations of local velocities are controlled by the characteristic length that arises from local mass conservation, $\ell_c \sim \mathrm{Ca}^{-1/2} \sim (\mu \mathrm{v})^{-1/2}$. Also the amplitude of the fluctuations of the global velocity on scale ℓ, $V_\ell(t)$, and their strongly non-gaussian distribution, are both controlled by Ca through the ratio ℓ/ℓ_c, which accounts for the effective number of degrees of freedom of the invading front. In contrast, temporal properties of the avalanche dynamics, measured either at local or at global scale, do not depend simply on the capillary number. On one hand we measured strong temporal correlations of the local front velocities up to a characteristic time $\Delta t^* \sim \mu^{-0.4} \mathrm{v}^{-1.4}$, which corresponds to the scaling behavior

of the maximum duration of the local bursts, $\xi_D \sim \ell_c^H/\mathrm{v} \sim \mu^{-H/2}\mathrm{v}^{-(1+H/2)}$. On the other hand we showed that the global invasion process exhibits a strongly intermittent dynamics, with temporal correlations and a maximum duration of global avalanches both set by a characteristic time scale that depends only on v, in the form $\tau_c \sim 1/\mathrm{v}$. The proportionality coefficient is compatible with ℓ_d, the characteristic extent of the disorder in the invasion direction, but this parameter has not been changed systematically in our experiments so far.

In order to verify carefully the possible dependence on the size of the measuring window ℓ of the scaling exponents and the scaling range of sizes and durations of the global avalanches, and to get a better understanding of this evolution, we are currently analyzing the scaling behavior of the average shape of the global avalanches–as recently done in the context of interfacial crack fronts [48]. Such analysis will allow us to go beyond the simple measurement of power-law exponents, subjected to large dispersions and error bars [63].

In future experiments we plan to modify systematically different properties of the disorder, such as the extension, height and shape of the defects, the cell coverage and their spatial distribution, in order to study their impact on the morphology and dynamics of stable imbibition fronts at different scales. For instance, the fact that local velocity bursts in our setup propagate nearly balistically, i.e. $L_x \sim D^{1/z_{av}}$ with $z_{av} = 1.10 \pm 0.12$ [17], while a value z_{av} close to 1.6 was found in phase-field simulations of the same kind of displacements [75], might come from the non-negligible microscopic correlation length of the disorder in the experiments.

It seems interesting also to perform in detail a comparative study of the dynamics in model open fractures and in porous media models such as Hele-Shaw cells with glass-bead packings. In this latter type of setting, Dougherty and Carle found that the sizes of local avalanches followed an exponential distribution, with a characteristic size corresponding to the typical pore size [22]. Their results are in strong contrast with our observations in open fractures, and also with the results expected for slowly-driven elastic interfaces in disordered media close to a critical depinning transition. The question is whether spatial correlations between local front velocities cannot grow beyond the size of the pores in a disordered porous medium.

Because of their relevance for specific applications, further advances in the study of imbibition displacements are taking place in more complicated settings. Examples include imbibition in nanoporous matrices with specific correlations of pore structure [34, 82], in arrays of micropillars [9] and in carbon nanotubes [93], miscible displacements in aqueous foams [59], and imbibition displacements of chemically-reacting fronts [2].

Acknowledgments We are grateful to all our collaborators in the subject, and in particular to our former students J. Soriano, R. Planet and X. Clotet. This research is currently funded by MINECO, Spain, through project No. FIS2013-41144-P, and by AGAUR, Generalitat de Catalunya, through grant No. 2014-SGR-878.

References

1. M. Alava, M. Rost, M. Dubé, Imbibition in disordered media. Adv. Phys. **53**, 83–175 (2004)
2. S. Atis, A.K. Dubey, D. Salin, L. Talon, P. Le Doussal, K.J. Wiese, Experimental evidence for three universality clases for reaction fronts in disordered flows. Phys. Rev. Lett. **114**, 234502 (2015)
3. H. Auradou, J.P. Hulin, S. Roux, Experimental study of miscible displacement fronts in rough self-affine fractures. Phy. Rev. E **63**, 066306 (2001)
4. A. Balankin, H. Zapata López, E. Pineda León, D. Morales Matamoros, L. Morales Ruiz, D. Silva López, M. Rodríguez, Depinning and dynamics of imbibition fronts in paper under increasing ambient humidity. Phys. Rev. E **87**, 014102 (2013)
5. A.L. Barabasi, H.E. Stanley, *Fractal Concepts in Surface Growth* (Cambridge University Press, Cambridge, 1995)
6. J. Baró, Á. Corral, X. Illa, A. Planes, E.K.H. Salje, W. Schranz, D.E. Soto-Parra, E. Vives, Statistical similarity between the compression of a porous material and earthquakes. Phys. Rev. Lett. **110**, 088702 (2013)
7. E. Bertin, Global fluctuations and Gumbel statistics. Phys. Rev. Lett. **95**, 170601 (2005)
8. E. Bertin, M. Clusel, Global fluctuations in physical systems: A subtle interplay between sum and extreme value statistics. Int. J. Mod. Phys B **22**, 33113368 (2008)
9. M.L. Blow, H. Kusumaatmaja, J.M. Yeomans, Imbibition through an array of triangular posts. J. Phys. Cond. Mat. **21**, 464125 (2009)
10. D. Bonn, J. Eggers, J. Indekeu, J. Meunier, E. Rolley, Wetting and spreading. Rev. Mod. Phys. **81**, 739805 (2009)
11. S.T. Bramwell, P. Holdsworth, J.-F. Pinton, Universality of rare fluctuations in turbulence and critical phenomena. Nature **396**, 552–554 (1998)
12. S.T. Bramwell, The distribution of spatially averaged critical properties. Nat. Phys. **5**, 443–447 (2009)
13. S. Buldyrev, A.-L. Barabasi, F. Caserta, S. Havlin, H.E. Stanley, T. Vicsek, Anomalous interface roughening in porous media: experiment and model. Phys. Rev. A bf **45**, R8313–R8316 (1992)
14. P. Charbonneau, S.W. McIntosh, H.-L. Liu, T.J. Bogdan, Avalanche models for solar flares. Sol. Phys. **203**, 321–353 (2001)
15. X. Clotet, Imbibition in a model open fracture. Capillary rise, kinetic roughening, and intermittent avalanche dynamics. PhD Thesis, Univ. de Barcelona and ENS-Lyon (2014). Available from: http://hdl.handle.net/10803/284588
16. X. Clotet, J. Ortín, S. Santucci, Disorder-Induced capillary bursts control intermittency in slow imbibition. Phys. Rev. Lett. **113**, 074501 (2014)
17. X. Clotet, J. Ortín, S. Santucci, Experimental study of stable imbibition displacements in a model open fracture: I Local avalanche dynamics. Phys. Rev. E **93**, 012149 (2016)
18. X. Clotet, S. Santucci, J. Ortín, Experimental study of stable imbibition displacements in a model open fracture. II. Scale-dependent avalanche dynamics. Phys. Rev. E **93**, 012150 (2016)
19. T. Cubaud, M. Fermigier, Faceted drops on heterogeneous surfaces. Europhys. Lett. **55**, 239245 (2001)
20. T. Delker, D.B. Pengra, P.-Z. Wong, Interface pinning and the dynamics of capillary rise in porous media. Phys. Rev. Lett. **76**, 2902–2905 (1996)
21. M. Dentz, T. Le Borgne, A. Englert, B. Bijeljic, Mixing, spreading and reaction in heterogeneous media: a brief review. J. Contam. Hydrol. **120–121**, 1–17 (2011)
22. A. Dougherty, N. Carle, Distribution of avalanches in interfacial motion in a porous medium. Phys. Rev. E **58**, 28892893 (1998)
23. G. Drazer, H. Auradou, J. Koplik, J.P. Hulin, Self-affine fronts in self-affine fractures: large and small-scale structure. Phys. Rev. Lett. **92**, 014501 (2004)
24. M. Dubé, M. Rost, K.R. Elder, M. Alava, S. Majaniemi, T. Ala-Nissila, Liquid conservation and non-local interface dynamics in imbibition. Phys. Rev. Lett. **83**, 16281631 (1999)

25. M. Dubé, M. Rost, M. Alava, Conserved dynamics and interface roughening in spontaneous imbibition: a critical overview. Eur. Phys. J. B **15**, 691699 (2000)
26. M. Dubé, M. Rost, K.R. Elder, M. Alava, S. Majaniemi, T. Ala-Nissila, Conserved dynamics and interface roughening in spontaneous imbibition: A phase field model. Eur. Phys. J. B **15**, 701714 (2000)
27. F.A.L. Dullien, *Porous Media: Fluid Transport and Pore Structure*, 2nd edn. (Academic Press, San Diego, 1992)
28. J.F. Duprat, M. Fermigier, F. Goulaouic, P. Jenffer, Two-phase flow in an imperfect Hele-Shaw cell-influence of wettability defects on interface dynamics. C. R. Acad. Sci. **314**, 879882 (1992)
29. S. Field, J. Witt, F. Nori, X. Ling, Superconducting vortex avalanches. Phys. Rev. Lett. **74**, 12061209 (1995)
30. D.S. Fisher, Collective transport in random media: from superconductors to earthquakes. Phys. Rep. **301**, 113150 (1998)
31. U. Frisch, *Turbulence* (Cambridge University Press, Cambridge, 1995)
32. V. Ganesan, H. Brenner, Dynamics of two-phase fluid interfaces in random porous media. Phys. Rev. Lett. **81**, 578–581 (1998)
33. D. Geromichalos, F. Mugele, S. Herminghaus, Nonlocal dynamics of spontaneous imbibition fronts. Phys. Rev. Lett. **89**, 104503 (2002)
34. S. Gruener, Z. Sadjadi, H.E. Hermes, A.V. Kityk, K. Knorr, S.U. Egelhaaf, H. Rieger, P. Huber, Anomalous front broadening during spontaneous imbibition in a matrix with elongated pores. PNAS (Proc. Nat. Acad. Sci. U. S. A.) **109**, 10245–10250 (2012)
35. B. Gutenberg, C.F. Richter, *Seismicity of the Earth and Associated Phenomena* (Princeton University Press, Princeton, 1954)
36. S. He, G.L.M.K.S. Kahanda, P.Z. Wong, Roughness of wetting fluid invasion fronts in porous media. Phys. Rev. Lett. **69**, 3731–3734 (1992)
37. A. Hernández-Machado, J. Soriano, A.M. Lacasta, M.A. Rodríguez, L. Ramírez-Piscina, J. Ortín, Interface roughening in Hele-Shaw flows with quenched disorder: experimental and theoretical results. Europhys. Lett. **55**, 194–200 (2001)
38. G.M. Homsy, Viscous fingering in porous media. Annu. Rev. Fluid Mech. **19**, 271–311 (1987)
39. V. Horvath, F. Family, T. Vicsek, Comment on Self-affine fractal interfaces from immiscible displacement in porous media. Phys. Rev. Lett. **65**, 2289 (1990)
40. V. Horvath, F. Family, T. Vicsek, Dynamic scaling of the interface in two-phase viscous flows in porous media. J. Phys. A **24**, L25–L29 (1991)
41. J.F. Joanny, P.G. de Gennes, A model for contact angle hysteresis. J. Chem. Phys. **81**, 552–562 (1984)
42. S. Joubaud, A. Petrosyan, S. Ciliberto, N. Garnier, Experimental evidence of non-Gaussian fluctuations near a critical point. Phys. Rev. Lett. **100**, 180601 (2008)
43. J. Krug, P. Meakin, Kinetic roughening of Laplacian fronts. Phys. Rev. Lett. **66**, 703–706 (1991)
44. J. Krug, Origins of scale invariance in growth processes. Adv. Phys. **46**, 139282 (1997)
45. M. Lago, M. Araujo, Capillary rise in porous media. J. Coll. Interf. Sci. **234**, 35–43 (2001)
46. T. Laurila, C. Tong, I. Huopaniemi, S. Majaniemi, T. Ala-Nissila, Dynamics and kinetic roughening of interfaces in two-dimensional forced wetting. Eur. Phys. J. B **46**, 553561 (2005)
47. L. Laurson, S. Santucci, S. Zapperi, Avalanches and clusters in planar crack front propagation. Phys. Rev. E **81**, 046116 (2010)
48. L. Laurson, X. Illa, S. Santucci, K.T. Tallakstad, K.J. Måløy, M.J. Alava, Evolution of the average avalanche shape with the universality class. Nat. Commun. **4**, 2927 (2013)
49. P. Le Doussal, K.J. Wiese, Avalanche dynamics of elastic interfaces. Phys. Rev. E **88**, 022106 (2013)
50. L. Leger, J.F. Joanny, Liquid spreading. Rep. Progr. Phys. **55**, 431–486 (1992)
51. R. Lenormand, E. Touboul, C. Zarcone, Numerical models and experiments on immiscible displacements in porous media. J. Fluid Mech. **189**, 165–187 (1988)

52. R. Lenormand, Liquids in porous media. J. Phys. Cond. Matter **2**, A79A88 (1990)
53. K. Li, D. Zhang, H. Bian, C. Meng, Y. Yang, Criteria for Applying the Lucas-Washburn Law. Sci. Rep. **5**, 14085 (2015)
54. P. Lloveras, F. Salvat-Pujol, L. Truskinovsky, E. Vives, Boiling Crisis as a Critical Phenomenon. Phys. Rev. Lett. **108**, 215701 (2012)
55. J.M. López, Scaling approach to calculate critical exponents in anomalous surface roughening. Phys. Rev. Lett. **83**, 4594–4597 (1998)
56. J.M. López, M. Pradas, A. Hernández-Machado, Activity statistics, avalanche kinetics, and velocity correlations in surface growth. Phys. Rev. E **82**, 031127 (2010)
57. K.J. Måløy, J. Feder, T. Jøssang, Viscous fingering fractals in porous media. Phys. Rev. Lett. **55**, 2688 (1985)
58. K.J. Måløy, S. Santucci, J. Schmittbuhl, R. Toussaint, Local waiting time fluctuations along a randomly pinned crack front. Phys. Rev. Lett. **96**, 045501 (2006)
59. R. Mensire, K. Piroird, E. Lorenceau, Capillary imbibition of aqueous foams by miscible and nonmiscible liquids. Phys. Rev. E **92**, 053014 (2015)
60. M.C. Miguel, A. Vespignani, S. Zapperi, J. Weiss, J.R. Grasso, Intermittent dislocation flow in viscoplastic deformation. Nature **410**, 667–671 (2001)
61. S. Moulinet, C. Guthmann, E. Rolley, Roughness and dynamics of a contact line of a viscous fluid on a disordered substrate. Eur. Phys. J. E **8**, 437443 (2002)
62. J.G. Orlandi, J. Soriano, E. Álvarez-Lacalle, S. Teller, J. Casademunt, Noise focusing and the emergence of coherent activity in neuronal cultures. Nat. Phys. **9**, 582 (2013)
63. S. Papanikolaou, F. Bohn, R.L. Sommer, G. Durin, S. Zapperi, J.P. Sethna, Universality beyond power laws and the average avalanche shape. Nat. Phys. **7**, 316320 (2011)
64. L. Paterson, Diffusion-limited aggregation and two-fluid displacements in porous media. Phys. Rev. Lett. **52**, 1621 (1984)
65. A. Paterson, M. Fermigier, P. Jenffer, L. Limat, Wetting on heterogeneous surfaces - experiments in an imperfect Hele-Shaw cell. Phys. Rev. E **51**, 12911298 (1995)
66. A. Paterson, M. Fermigier, Wetting of heterogeneous surfaces: influence of defect interactions. Phys. Fluids **9**, 22102216 (1997)
67. E. Pauné, J. Casademunt, Kinetic roughening in two-phase fluid flow through a random Hele-Shaw cell. Phys. Rev. Lett. **90**, 144504 (2003)
68. O. Perkovic, K. Dahmen, J.P. Sethna, Avalanches, Barkhausen noise and plain old criticality. Phys. Rev. Lett. **75**, 4528 (1995)
69. R. Planet, M. Pradas, A. Hernández-Machado, J. Ortín, Pressure-dependent scaling scenarios in experiments of spontaneous imbibition. Phys. Rev. E **76**, 056312 (2007)
70. R. Planet, S. Santucci, J. Ortín, Avalanches and non-Gaussian fluctuations of the global velocity of imbibition fronts. Phys. Rev. Lett. **102**, 094502 (2009)
71. R. Planet, S. Santucci, J. Ortín, Planet, Santucci, and Ortín reply. Phys. Rev. Lett. **105**, 029402 (2010)
72. R. Planet, S. Santucci, J. Ortín, Roughness and intermittent dynamics of imbibition fronts due to capillary and permeability disorder. J. Contam. Hydrol. **120**, 157–169 (2011)
73. B. Portelli, P.C.W. Holdsworth, J.-F. Pinton, Intermittency and non-Gaussian fluctuations of the global energy transfer in fully developed turbulence. Phys. Rev. Lett. **90**, 104501 (2003)
74. M. Pradas, Avalanches in disordered media. Scaling growth, avalanche dynamics, and microfluidic fronts. Ph.D. Thesis, Univ. de Barcelona (2009)
75. M. Pradas, J.M. López, A. Hernández-Machado, Avalanche dynamics in fluid imbibition near the depinning transition. Phys. Rev. E **80**, 050101 (2009)
76. G. Pruessner, Comment on "avalanches and non-gaussian fluctuations of the global velocity of imbibition fronts". Phys. Rev. Lett. **105**, 029401 (2010)
77. M. Queralt-Martín, M. Pradas, R. Rodríguez-Trujillo, M. Arundell, E. Corvera Poiré, A. Hernández-Machado, Pinning and avalanches in hydrophobic microchannels. Phys. Rev. Lett. **106**, 194501 (2011)
78. J.J. Ramasco, J.M. López, M.A. Rodríguez, Generic dynamic scaling in kinetic roughening. Phys. Rev. Lett. **84**, 2199–2202 (2000)

79. E. Rolley, C. Guthmann, R. Gombrowicz, V. Repain, Roughness of the contact line on a disordered substrate. Phys. Rev. Lett. **80**, 28652868 (1998)
80. M. Rost, L. Laurson, M. Dubé, M. Alava, Fluctuations in fluid invasion into disordered media. Phys. Rev. Lett. **98**, 054502 (2007)
81. M.A. Rubio, C.A. Edwards, A. Dougherty, J.P. Gollub, Self-affine fractal interfaces from immiscible displacements in porous media. Phys. Rev. Lett. **63**, 1685–1688 (1989)
82. Z. Sadjadi, H. Rieger, Scaling theory for spontaneous imbibition in random networks of elongated pores. Phys. Rev. Lett. **110**, 144502 (2013)
83. P.G. Saffman, G.I. Taylor, The penetration of a fluid into a porous medium or Hele-Shaw cell containing a more viscous liquid. Proc. R. Soc. Lond. A **245**, 312–329 (1958)
84. M. Sahimi, *Flow and Transport in Porous Media and Fractured Rock*, 2nd edn. (Wiley-VCH, Weinheim, 2011)
85. S. Santucci, R. Planet, K.J. Måløy, J. Ortín, Avalanches of imbibition fronts: towards critical pinning. Europhys. Lett. **94**, 46005 (2011)
86. E. Schäffer, P.-Z. Wong, Contact line dynamics near the pinning threshold: a capillary rise and fall experiment. Phys. Rev. E **6**, 5257–5277 (2000)
87. H. Schütt, H. Spetzler, Capillary crack imbibition: a theoretical and experimental study using a Hele-Shaw cell. Pure Appl. Geophys. **158**, 627646 (2001)
88. J.P. Sethna, K.A. Dahmen, C.R. Myers, Crack. Noise. Nat. bf **410**, 24250 (2001)
89. Y.D. Shikhmurzaev, J.E. Sprittles, Anomalous dynamics of capillary rise in porous media. Phys. Rev. E **86**, 016306 (2012)
90. J. Soriano, J. Ortín, A. Hernández-Machado, Experiments of interfacial roughening in Hele-Shaw flows with weak quenched disorder. Phys. Rev. E **66**, 031603 (2002)
91. J. Soriano, J.J. Ramasco, M.A. Rodríguez, A. Hernández-Machado, J. Ortín, Anomalous roughening of Hele-Shaw flows with quenched disorder. Phys. Rev. Lett. **89**, 026102 (2002)
92. J. Soriano, A. Mercier, R. Planet, A. Hernández-Machado, M.A. Rodríguez, J. Ortín, Anomalous roughening of viscous fluid fronts in spontaneous imbibition. Phys. Rev. Lett. **95**, 104501 (2005)
93. S. Supple, N. Quirke, Rapid imbibition of fluids in carbon nanotubes. Phys. Rev. Lett. **90**, 214501 (2003)
94. M. Trojer, M.L. Szulczewski, R. Juanes, Stabilizing fluid-fluid displacements in porous media through wettability alteration. Phys. Rev. Appl. **3**, 054008 (2015)
95. E. Vives, J. Ortín, L. Mañosa, I. Ràfols, R. Pérez-Magrané, A. Planes, Distributions of avalanches in martensitic transformations. Phys. Rev. Lett. **72**, 1694–1697 (1994)
96. S. Whitaker, *The Method of Theory and Applications of Transport in Porous Media*, vol. averaging (Kluwer Academic Publishers, The Netherlands, 1999)
97. D. Wilkinson, J.F. Willemsen, Invasion percolation: a new form of percolation theory. J. Phys. A. **16**, 3365 (1983)
98. D. Wilkinson, Percolation model of immiscible displacements in the presence of buoyancy forces. Phys. Rev. A **30**, 520 (1984)
99. T.A. Witten, L.M. Sander, Diffusion-limited aggregation, a kinetic critical phenomenon. Phys. Rev. Lett. **47**, 1400 (1981)
100. S. Zapperi, P. Cizeau, G. Durin, H.E. Stanley, Dynamics of a ferromagnetic domain wall: avalanches, depinning transition and the Barkhausen effect. Phys. Rev. B **58**, 6353–6366 (1998)

Index

E.K.H. Salje et al. (eds.), *Avalanches in Functional Materials and Geophysics*,
Understanding Complex Systems, DOI 10.1007/978-3-319-45612-6